ISSN 2542-1565

Vol. 18 2025 No. 04

GEOGRAPHY ENVIRONMENT SUSTAINABILITY

«The journal GEOGRAPHY, ENVIRONMENT, SUSTAINABILITY was founded in 2008 by Russian Geographical Society, the Lomonosov Moscow State University Geography Department, and the Russian Academy of Sciences Institute of Geography. Since that time the journal publishes **4 issues per year**, containing original research papers and reviews. The journal issues are open source and distributed through subscriptions, library exchanges of leading universities, and via the website through the world»

FOUNDERS OF THE JOURNAL: Russian Geographical Society, Faculty of Geography, Lomonosov Moscow State University and Institute of Geography of the Russian Academy of Sciences

The journal is published with financial support of the Russian Geographical Society.

The journal is registered in Federal service on supervision of observance of the legislation in sphere of mass communications and protection of a cultural heritage. The certificate of registration: ПИ № ФС77-67752, 2016, December 21.

PUBLISHER
Russian Geographical Society
Moscow, 109012 Russia
Novaya ploshchad, 10, korp. 2
Phone 8-800-700-18-45
E-mail: press@rgo.ru
www.rgo.ru/en

EDITORIAL OFFICE
Lomonosov Moscow State University
Moscow 119991 Russia
Leninskie Gory, 1,
Faculty of Geography, 1806a
Phone 7-495-9391552
Fax 7-495-9391552
E-mail: ges-journal@geogr.msu.ru
www.ges.rgo.ru

DESIGN
Layout designer: Tereshkin Anton
Moscow, 115088,
26 Simonovsky Val str., bldg. One
Phone: +7 (903) 108-04-44
E-mail: smile.tai@gmail.com

DOI prefix: 10.24057

Format A4 (210x297mm)

"GEOGRAPHY, ENVIRONMENT, SUSTAINABILITY" is the only original English-language journal in the field of geography and environmental sciences published in Russia. It is supposed to be an outlet from the Russian-speaking countries to Europe and an inlet from Europe to the Russian-speaking countries regarding environmental and Earth sciences, geography and sustainability. The main sections of the journal are the theory of geography and ecology, the theory of sustainable development, use of natural resources, natural resources assessment, global and regional changes of environment and climate, social-economical geography, ecological regional planning, sustainable regional development, applied aspects of geography and ecology, geoinformatics and ecological cartography, ecological problems of oil and gas sector, nature conservations, health and environment, and education for sustainable development.

Date of publication: October 1st 2025.

EDITORIAL BOARD

EDITORIAL OFFICE

CONTENTS

Andrew V. Shevchenko, Andrian A. Seleznev, Vitaly S. Glukhov, Ilia V. Yarmoshenko, Georgy P. Malinovsky, Natali V. Ivanchukova
SNOW COVER POLLUTION BY POTENTIALLY TOXIC ELEMENTS IN SMALL AND MEDIUM-SIZED INDUSTRIAL CITIES: CASE OF SVERDLOVSK REGION, RUSSIA.....6

Roosen Kumar, Bindhy Wasini Pandey, Jitender Rathore, Chetna Sharma
FOUR DECADES OF TREE COVER AND GRASSLAND DYNAMICS IN THE FOOTHILLS OF THE WESTERN HIMALAYAS – CHAMOLI DISTRICT OF UTTARAKHAND, INDIA 19

Zhanna V. Atutova, Elena A. Rasputina
APPLICABILITY OF NBR AND dNBR INDICES IN ASSESSMENT OF PYROGENIC TRANSFORMATION AND POST-FIRE FOREST REGENERATION: CASE STUDY OF SOUTHEASTERN SIBERIA CONIFEROUS FORESTS 36

Mohammed Alharithi, Chokri Zehri
RENEWABLE ENERGY FIRMS IN TRANSITION: ENVIRONMENTAL RETURNS AND POLICY SYNERGIES UNDER SAUDI VISION 2030 48

Andrey G. Kostianoy, Alexey D. Gvishiani, Sergey A. Lebedev, Igor N. Rozenberg, Roman I. Krasnoperov, Irina A. Dubchak, Sofia A. Gvozdik, Olga O. Shevaldysheva, Vladimir N. Sergeev, Julia I. Nikolova
PROJECTION OF REGIONAL CLIMATE CHANGE FOR 2023–2064 IN THE NORTHERN PART OF THE WESTERN RUSSIAN ARCTIC: A SUPPORT FOR RUSSIAN RAILWAYS 61

Kazem Nosrati, Maram Hassan, Alireza Salehipour Milani, Mostafa Keshtkar, Somaiyeh Khaleghi, Adrian L. Collins
SOIL EROSION VERSUS SOIL RETENTION CAPACITY: AN IMPACT ASSESSMENT OF REGULATING ECOSYSTEM SERVICE PROVISION IN IRAN 80

Vladislava B. Pridacha, Alexander V. Olchev
ENVIRONMENTAL CONTROLS OF PHOTOSYNTHETIC PARAMETERS IN FOUR DOMINANT BOREAL TREE SPECIES: CONTRASTING RESPONSES OF DECIDUOUS ANGIOSPERMS AND EVERGREEN GYMNOSPERMS.....92

Audrey Rose A. Velayo, Peter D. Suson, Maricar M. Aguilos, Peng Zhao, Hernando P. Bacosa
NATURE-BASED SOLUTIONS: ASSESSING URBAN GREENSPACE AVAILABILITY IN ILIGAN CITY, PHILIPPINES 103

Retno S. Dewi, Wiwandari Handayani, Muhammad Z. A. J. Ramadhan, Iwan Rudiarto
KNOWLEDGE CO-PRODUCTION PRACTICES TO PROMOTE CLIMATE RESILIENCE IN GLOBAL CITIES: A SYSTEMATIC LITERATURE REVIEW 115

N.V. Kuzmenkova, V.N. Golosov, A.K. Fomina, M.V. Markelov, N.P. Zaraiskiy, N.E. Zaretskaya, E.A. Eremenko
THE CHERNOBYL SIGNATURE IN WESTERN ABKHAZIA: ASSESSING ^{137}CS DEPOSITION VARIABILITY AND APPLICABILITY FOR EVALUATION SEDIMENT REDISTRIBUTION RATES 127

A. Iurmanov, I. Popov, A. Gnedenko, Y. Lebedev, M. Kulikovskiy
SEAGRASSES (ZOSTERACEAE AND RUPPIACEAE) IN RUSSIA: DISTRIBUTION, DIVERSITY, PROSPECTS FOR FURTHER RESEARCH..... 139

Kira A. Morachevskaya, Alexander B. Sebentsov, Mikhail S. Karpenko, Andrei V. Radikevich
CROSS-BORDER INTERACTIONS OF THE PSKOV REGION IN THE CONTEXT OF RESTRICTIONS: POLICY – PERCEPTION – PRACTICE 149

Kira A. Morachevskaya, Alexander B. Sebentsov, Mikhail S. Karpenko, Andrei V. Radikevich
COMPARATIVE ANALYSIS OF MACHINE LEARNING ALGORITHMS FOR LAND USE AND LAND COVER MAPPING: CASE STUDY OF BERRECHID-SETTAT REGION, MOROCCO 158

Fathan Aldi Rivai, Boedi Tjahjono, Khursatul Munibah, Adenan Yandra Nofrizal
MAJORITY FILTER FOR ENHANCING PIXEL-BASED RANDOM FOREST LAND COVER CLASSIFICATION IN SUKAJAYA DISTRICT, BOGOR REGENCY 171

RESEARCH PAPER

SNOW COVER POLLUTION BY POTENTIALLY TOXIC ELEMENTS IN SMALL AND MEDIUM-SIZED INDUSTRIAL CITIES: CASE OF SVERDLOVSK REGION, RUSSIA

Andrew V. Shevchenko*, Andrian A. Seleznev, Vitaly S. Glukhov, Ilia V. Yarmoshenko, Georgy P. Malinovsky, Natali V. Ivanchukova

Institute of Industrial Ecology, Ural Branch of Russian Academy of Sciences, 620108, Ekaterinburg, Russia

*Corresponding author: av.shev98@gmail.com

Received: June 9th 2024 / Accepted: November 12nd 2025 / Published: December 31st 2025

https://doi.org/10.24057/2071-9388-2025-3746

ABSTRACT. This study aims to develop and validate a method for assessing urban air pollution by analysing undisturbed snow cover in residential areas of small and medium-sized industrial cities in Sverdlovsk Region, Russia: Kachkanar, Serov, Verkhnyaya Pyshma, and Alapaevsk. Snow samples were collected in each city.

The proposed approach is based on the analysis of the most contaminated solid fraction of snow (particles >2 μm and filtrate). This method has shown effectiveness in identifying pollutants and their sources. It is also more cost-efficient and offers better material accessibility than the approach that analyses both dissolved (<0.45 μm) and suspended (>0.45 μm) snow phases. The balanced set of qualitative and quantitative indicators includes the physical and chemical properties of snow, the accumulation intensity of PTEs, the calculation of indices (I_{geo}, *EF, PI,* PI_{sum}, PI_{avg}, *and* $PI_{Nemerow}$), dust load, and geochemical associations.

Snow's physical and chemical properties were influenced by natural conditions. Low mineralisation and suspended solids were mostly composed of calcium and magnesium bicarbonates and sulfates. Snow pH was slightly alkaline in Serov and mildly alkaline in other cities.

Metallurgical and mining cities showed higher pollution according to the indices: elevated V and Fe in Kachkanar, Cr in Serov, Cu and As in Verkhnyaya Pyshma. Kachkanar was the most polluted city (PI_{sum} *– 154,* $PI_{Nemerow}$ *– 12*), while Serov and Verkhnyaya Pyshma were also significantly polluted with similar PI_{sum} and PI_{avg} values (66 and 4.2, respectively) and $PI_{Nemerow}$ values (5.1 and 7.2, respectively). Geochemical associations reflected local industrial profiles. Dust load ranged from 27 to 163 mg/m^2/day, peaking in Kachkanar.

The collected data indicate current atmospheric pollution in the studied cities. This method proved effective for assessing urban air pollution and is recommended for environmental monitoring in other industrial regions.

KEYWORDS: environmental monitoring, urban area, industrial cities, snow, atmospheric pollution, potentially toxic elements, urban geochemical background

CITATION: ShevchenkoA. V., Seleznev A. A., Glukhov V. S., Yarmoshenko I. V., Malinovsky G. P., Ivanchukova N.V. (2025). Snow Cover Pollution By Potentially Toxic Elements In Small And Medium-Sized Industrial Cities: Case Of Sverdlovsk Region, Russia. Geography, Environment, Sustainability, 4 (18), 6-18

https://doi.org/10.24057/2071-9388-2025-3746

ACKNOWLEDGEMENTS: The research was supported by the Russian Science Foundation grant No. 24-17-20036, and by the Government of the Sverdlovsk region (project No. 24-17-20036).

Conflict of interests: The authors reported no potential conflict of interests.

INTRODUCTION

Aerosols, particulate matter (PM), metals and metalloids (MMs) in urban air are a negative factor for the environment and human health. Atmospheric pollution increases the risk of respiratory diseases, allergies, lung cancer, cardiovascular and other diseases[1] (Raaschou-Nielsen et al. 2013; Chen et al. 2016). This includes the health effects due to elevated concentrations of PM-related metals (Tiotiu et al. 2020; Lee et al. 2021).

The urban atmosphere constantly contains a mixture of particles of different chemical composition, morphology, and size. The origin of these particles is diverse: erosion, weathering, and abrasion of surfaces (roads, pavements, lawns, etc.) (Piscitello et al. 2021; Pellecchia et al. 2023), vehicle emissions (Jeong et al. 2019; Piscitello et al. 2021; Pellecchia et al. 2023), industries and power plants (Moskovchenko et al. 2021; Zhou et al. 2024), construction works (Guo et al. 2020; Yang et al. 2020), dust storms (Opp et al. 2021; Tariq et al. 2023; Lak et al. 2024), wildfires (Tariq et al. 2023; Kaskaoutis et al. 2024), incineration plants, and

[1] World health statistics 2020: monitoring health for the SDGs, sustainable development goals. Geneva: World Health Organization; 2020.

landfills. Atmospheric pollution due to motor vehicles can be exhaust (fuel combustion) and non-exhaust (abrasion of rubbing elements, for example, brake pads, discs, tyres, road surface, etc.) (Carlsson et al. 1995; Pellecchia et al. 2023; Vijayan et al. 2024). Emissions from manufacturing plants and motor vehicles are the major sources of PM in urban air[2].

During the cold season, the amount of fuel burned for heat production increases, leading to a greater influx of anthropogenic emissions into the atmosphere (Tigeev et al. 2021; Moskovchenko et al. 2022). The snow cover that forms during this period captures various potentially toxic elements (PTEs) from the air and accumulates them layer by layer throughout the season.

PTEs in snow can be present in dissolved and suspended forms, corresponding to the liquid and solid phases respectively. The liquid form can participate in the biochemical cycle, while the solid form accumulates in the environment, becoming part of soils, road dust, and surface sediment (Seleznev et al. 2019; Vlasov et al. 2020). Pollutants migrate from snow into the surrounding environment during melting. This happens, for example, when de-icing agents are used on roads and pavements. The process intensifies significantly over a short period (1-2 weeks) at the end of the cold season.

In northern regions, analysing the composition of snow cover is an effective method for assessing air pollution (Engelhard et al. 2007; Xue et al. 2020; Szwed et al. 2022; Moskovchenko et al. 2021, 2022, 2023). The main objectives of environmental studies of snow cover are as follows: (1) obtaining information on the amount of pollutants in the atmosphere (Kondratev et al. 2017; Szwed et al. 2022; Moskovchenko et al. 2023; Popovicheva et al. 2024) and their deposition (Alves et al. 2019; Kosheleva et al. 2024; Talovskaya et al. 2025); (2) tracing the sources of air pollution, using snow along roads as a marker of vehicle pollution (Kuoppamäki et al. 2014; Moskovchenko et al. 2021, 2022; Vijayan et al. 2024); (3) obtaining information on the physical and chemical properties of snow cover, including soluble and solid forms (Kuoppamäki et al. 2014; Vlasov et al. 2020); (4) understanding the long-range transboundary transport of pollutants (Opp et al. 2021; Tariq et al. 2023); (5) studying the transport of pollutants from nonpoint sources with meltwater runoff in urban areas (Indraratne et al. 2023).

In large or industrial cities in Russia, state air monitoring is often conducted at stationary observation posts. The range of monitored substances in these programmes is limited to common gases (nitrogen dioxide, sulfur dioxide, carbon monoxide, etc.), various hydrocarbons, suspended particles, and heavy metals (Pb, Cd, Cu, Zn, Ni, Cr, Mg, Fe, Mn). The majority of pollutants deposited from the atmosphere are in the solid phase – suspended solids (Vlasov et al. 2020; Tigeev et al. 2021), which are not analysed in this type of monitoring.

The study region for this research is the Sverdlovsk region, a major industrial area of Russia. The region has a well-developed extractive industry, full-cycle ferrous and non-ferrous metallurgy, and mechanical engineering. Most large industrial enterprises in the region are city-forming and are located in small and medium-sized cities known as 'monotowns.' Environmental monitoring in small and medium-sized cities is less frequently represented in scientific literature, and the state monitoring approach does not cover the full range of potential pollutants or include all industrial cities. This may be due to both reduced public attention to cities of this size and the significant costs of environmental control. At the same time, industrial enterprises conduct their own emissions monitoring at emission points, along the perimeter of their territory, and within the sanitary protection zone in accordance with the law and approved internal environmental projects. However, the data from such monitoring are not publicly available and are intended for reporting to government authorities.

The aim of this study is to propose and test a method for assessing urban air pollution by analysing the composition of undisturbed snow cover in residential areas. The proposed method is rapid and low-cost. It includes an optimal set of qualitative and quantitative indicators needed for an adequate assessment of contemporary pollutant deposition in the urban environment from the atmosphere.

The study objects are two phases of snow: the liquid phase with particles <2 μm (filtrate) and the solid phase with particles >2 μm. The total element concentration in both phases was recalculated to reflect the deposition intensity of PTEs and the indices being calculated.

This study examines four small and medium-sized cities in the Sverdlovsk region: the industrial monotowns of Kachkanar, Serov, and Verkhnyaya Pyshma, and the non-industrial city of Alapaevsk, which was used as a background site. The proposed method appears to be applicable to all types of cities that have a stable snow cover during the cold season.

MATERIALS AND METHODS

Description of surveyed cities

Four small cities in the Sverdlovsk region, Russia: Kachkanar, Serov, Alapaevsk, and Verkhnyaya Pyshma, with different industrial specialisations, were studied. Table 1 provides a description of the surveyed cities.

In all cities studied, the cold (winter) period of the year lasts five to six months, from mid-October to mid-April. During this period, the average daily air temperature is continuously below 0°C, and precipitation falls as snow. Around mid-April, intensive snowmelt begins, and in one to two weeks, almost the entire snow cover melts. In Serov, the cold period can be longer.

Snow sampling program

All surveyed cities show a block structure of development. Two main types of development observed are multi-storey buildings (MSB) and detached house development (DHD), each with an adjacent property and a facade area that forms part of the street network. Snow samples were collected exclusively in the residential areas of the cities. A total of 40 snow samples were gathered, with 10 samples from each city. Five sampling sites were chosen in MSB neighbourhoods and five sites in DHD. All sites are spaced apart and represent different city areas with varying stages of development. The sampling grid was irregular and followed the Guidance Document 52.04.186-89[3], with a sampling site density of 1-2 samples per km^2. The number of sampling points in this study is comparable to those investigated in other research (e.g., Engelhard et al. 2007; Vlasov et al. 2020; Moskovchenko et al. 2021; Vijayan et al. 2024). Although the sampling grid is irregular, it covers the entire residential area of the city. Other researchers also employ irregular grids to assess the condition of snow cover within urban environments.

[2] Particulate Matter (PM) Basics https://www.epa.gov/pm-pollution/particulate-matter-pm-basics

[3] Guidance Document 52.04.186-89. Air Pollution Control Guideline. https://docs.cntd.ru/document/1200036406.

Table 1. Brief description of the cities studied

City	N E coordinates	Residential area*, km^2	Location	Climate	Industries
Kachkanar	58°42′N 59°29′E	6.3	Southwest of the Kachkanar Mountain, on the Eastern Side of the Middle Urals in the watershed of the Isa and Vyja Rivers (tributaries of the Tura River). The relief is represented by mountain with large differences in altitude.	Continental climate, the average temperature in January is -15.3 °C, in July is +17.3 °C. The average annual precipitation is 467 mm.	Production of iron ore. One of the largest modern iron ore enterprises in Russia and the only one in the world that produces Fe-V concentrate, sinter and pellets for blast furnace smelting. Ore is mined by drilling and blasting.
Serov	59°36′N 60°34′E	17.9	On the border between the Middle and Northern Urals, on the eastern slope of the Ural Mountains in the Western Part of the West Siberian Plain. The Kakva River flows through the city. The relief is mainly represented by flat with large hills in the north of the city.	Continental climate, the average temperature in January is -16.2 °C, in July is +18.0 °C. The average annual precipitation is 493 mm.	The main industry is the ferrous metallurgy and other metallurgy-related industries.
Alapaevsk	57°51′N 61°42′E	13.6	Eastern Side of the Middle Urals at the intersection the Trans-Ural Plain and the West Siberian Lowland. The Neiva River flows through the city. The relief is mainly represented by large hills	Continental climate, the average temperature in January is -15.6 °C, in July – +18.7 °C. The average annual precipitation is 496 mm.	In the early 18th century At the end of the 20th century, due to depreciation and reduction of mineral base, the plant significantly reduced production. Since the beginning of the 21th century the metallurgical production has actually ceased. Currently, Alapaevsk has woodworking, food production enterprises.
Verkhnyaya Pyshma	56°58′N 60°35′E	11.6	Middle Urals, the Eastern Side of the Ural Mountains, at the headwaters of the Pyshma River. One of the satellite cities of Ekaterinburg megapolis. The relief is hilly.	Continental climate, the average temperature in January is -12.6 °C and in July +18.9 °C. The average annual precipitation is 535 mm.	Since 1854, copper ore has been mining and processing in Verkhnyaya Pyshma. Nowadays the main industry of the city is non-ferrous metallurgy, machine building, and metal processing.

*Residential area values are taken from Seleznev et al. (2024).

Sampling was carried out at the end of the cold season (March 2024), which is the period of maximum snow accumulation. The location of the studied cities in the Sverdlovsk region, Russia, and the sampling sites is shown in Fig. 1.

The undisturbed snow cover was selected for sampling at the sites. For sites in MSB neighbourhoods, it was usually located on green zones or playgrounds, as these areas are not used during the cold season. For sites in DHD neighbourhoods, sampling points were located on the facade area of the block between the property zone and the street or sidewalk. Snow sampling was conducted away from the vehicular zone, with distances ranging from 2 to 35 metres (average 10 metres).

The undisturbed snow cover sample was collected using a sampling device, following the methodology outlined in Guidance Document 52.04.186-89. The device consists of a plastic tube with a diameter of 10 cm and a piston, which allows for the extraction of the entire snow cover thickness during sampling. The number of undisturbed snow cores collected was determined by the volume of the container, which is 5 litres. The container is sealed and made entirely of polymer materials. Corrosion-resistant equipment was used for sampling. During sampling, the lower part of the core, along with some surface materials (soil, leaves, debris, etc.), was removed from the sample. Contamination of the samples during collection, transportation, and analysis was prevented.

Sample preparation and analysis

Snow sample preparation was carried out in accordance with Russian Standard 31 861-2012[4]. The collected samples were preserved at –4°C in a laboratory refrigerator. Melting was done at room temperature for 24 hours. After melting, large inclusions, such as pine needles, leaves, and debris, were removed from the samples. The samples were then filtered through ash-free 'blue tape' paper filters with a pore size of 2 μm using a vacuum filtration system based on Büchner funnels and Büchner flasks. As a result, two phases were obtained: the solid phase with particle sizes >2 μm and the filtrate, representing the liquid phase with particle sizes <2 μm. The filtrate was transferred into two containers, one with a volume of 1.5 litres for cation-anion composition determination and another with a volume of 50 ml for metal content determination.

The elements detected in both phases were Al, Ti, V, Cr, Mn, Co, Fe, Ni, Cu, Zn, As, Mo, Cd, Sn, Sb, and Pb. For the liquid phase, the following parameters were measured in the laboratory. Acidity level (pH) (using a Milwaukee PH600

[4] Water. General requirements for sampling (GOST R 31861-2012). https://base.garant.ru/70571468/.

(a)

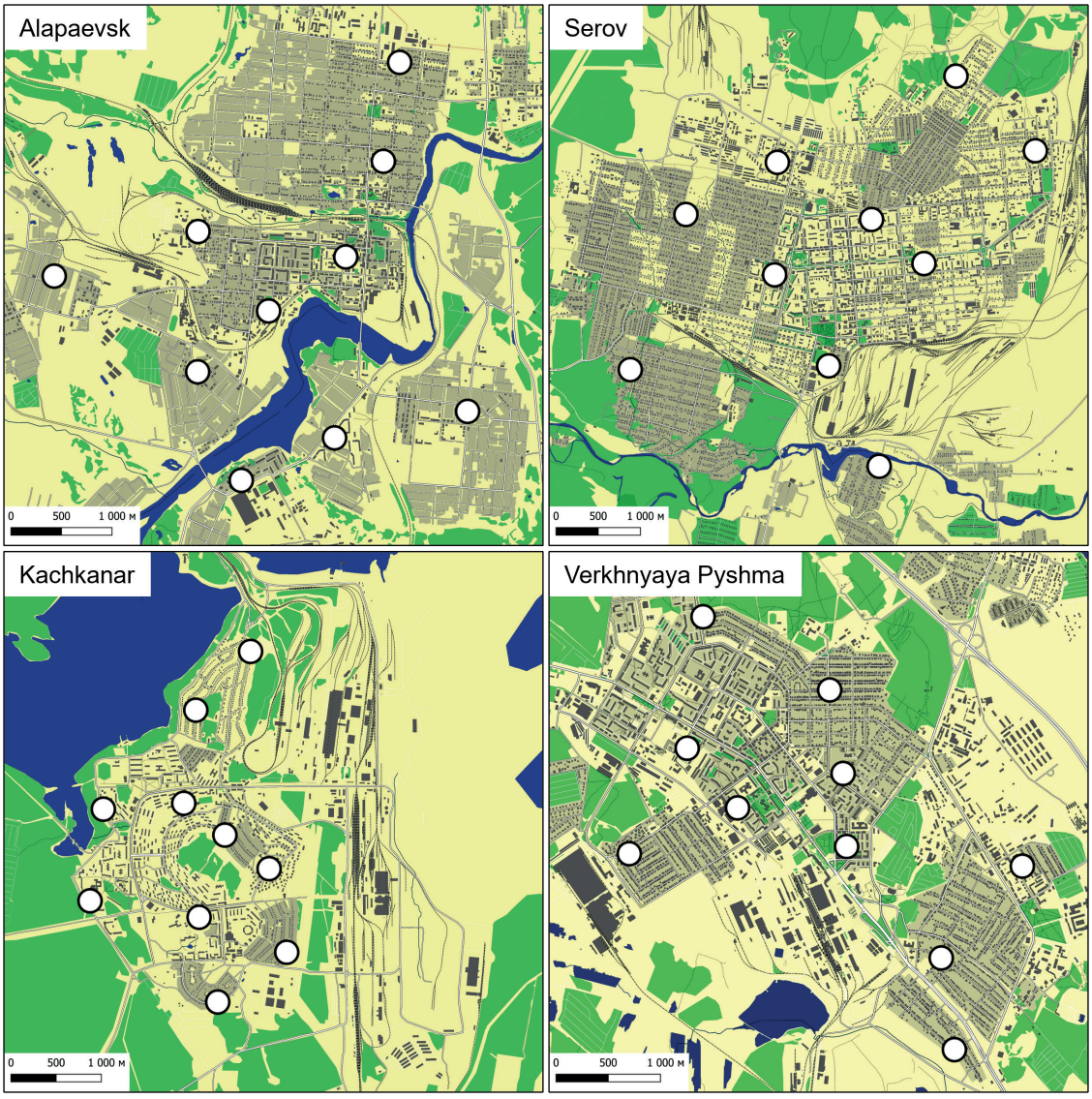

(b)

Fig. 1. Location of (a) Sverdlovsk region, Russia, with the studied cities, and (b) snow sampling sites (white points)

portable pH-meter) and redox potential (Eh) (using an ORP-200 portable ORP-meter) were determined according to the methods attached to the devices. Na^{++} and K^{+} were determined by flame photometry; Ca^{2+} and Mg^{2+} by complexometric titration; Cl^{-} by titration; PO_4^{3-}, CO_3^{2-}, and HCO_3^{-} by potentiometric titration; NO_2^{-}, NO_3^{-}, NH_4^{+}, SO_4^{2-}, and SiO_2 by photometry. The content of PTEs in the liquid phase was determined by inductively coupled plasma mass spectrometry (ICP-MS) using an ELAN 9000 mass spectrometer (Perkin Elmer, USA) according to the certified technique NSAM 480-X. The detection limits for the liquid phase were as follows: Al, Ti, V, Cr, Ni, Cu, Zn, As – <2 μg/L, Mn, Mo, Sn, Pb – <0.2 μg/L, Co, Cd, Sb – <0.1 μg/L.

Filters with suspended solids were dried at room temperature. The elemental analysis of the suspended solids was performed using ICP-MS technique according to the 'Method for measuring elemental content in solid objects' by ICP-MS, PND F 16.1:2.3:3.11-98[5] on an ELAN 9000 mass spectrometer from Perkin Elmer (USA). Solids were prepared for element concentration determination using extraction with three acids (HNO_3, $HClO_4$, and HF). The detection limits for suspended solids were as follows: Al, Ti, Fe, Zn – <5 μg/L; V, Cr, Mn, Co, Ni, Cu, As, Mo, Sn, Sb, Pb – <0.1 μg/L; Cd – <0.05 μg/L.

Statistical data processing was performed using STATISTICA 12 and Microsoft Excel. Median Absolute Deviation (MAD) (Reimann et al. 2005) was used as a measure of variability in PTEs deposition intensity. It was calculated using the following formula:

$$MAD = Median\left(\left|x_i - \tilde{x}\right|\right) \quad (1)$$

where x_i is each value of intensity, $\tilde{x}$, is average value of intensity.

Assessment of pollution in snow cover

To assess the average atmospheric pollution level over the observation period, the accumulation intensity of pollutants in the snow cover was calculated (mg/m² per day). The calculation of accumulation intensity considered the concentration of i PTEs (in the range from 1 to n) in solid phases (>2 μm and filtrate) of the j sample (in the range from 1 to k), the volume of melted water (L), the number of collected cores (pcs.), the sampler area (m²), and the snow cover duration (150 days). The PTEs accumulation intensity in the snow cover is calculated using the following formula:

$$AI_{PTE\,i,j} = \frac{C^{SP}_{Me\,i,j} \times V_{sample\,j}}{N_{cores\,j} \times S_{sampler} \times N_{days}} + \frac{C^{F}_{Me\,i,j} \times V_{sample\,j}}{N_{cores\,j} \times S_{sampler} \times N_{days}} \quad (2)$$

where $AI_{PTEs\,i,j}$ is the i PTE accumulation intensity in the snow cover, mg/m² per day; $C^{SP}_{Me\,i,j}$ and $C^{F}_{Me\,i,j}$ is the concentration of PTEs in solid phase (>2 μm) and filtrate (<2 μm), respectively, mg/L; $V_{sample\,j}$ is the volume of melted water, L; $N_{cores\,j}$ is the number collected cores, pcs.; N_{days} is the snow cover duration (150 days); $S_{sampler}$ is the sampler area, m².

To evaluate pollution levels using the following indices: *Geoaccumulation Index (I_{geo}), Single Pollution Index (PI), Enrichment Factor (EF), Sum of Contamination (PI_{sum}), and Nemerow Pollution Index ($PI_{Nemerow}$)* – the total concentrations of PTEs in solid phases (>2 μm and filtrate) of the snow sample were used.

The I_{geo} was originally defined by Müller in 1969 to determine metal contamination in sediments by comparing current concentrations with pre-industrial levels (Müller 1986). It can be calculated using the equation:

$$I_{geo} = \log_2\left[C_{i,j}/\left(1.5 \times C_{bg}\right)\right] \quad (3)$$

where $C_{i,j}$ is the measured concentration of the i PTE under study, and C_{bg} is the geochemical background or reference concentration of the element. The factor 1.5 is used to account for possible variations in the background levels of the metal in the environment, as well as minimal anthropogenic influences. Müller (1986) classified I_{geo} into seven classes (Table 2).

The Pollution Index (*PI*) for the single sample j (from a sample set of k=10) was calculated as the ratio of the i PTE concentration to the geochemical background for the city (Qingjie et al. 2008):

$$PI_i = \frac{C_i}{C_{bg}} \quad (4)$$

where C_i is the concentration of the i PTE in j sample, C_{bg} is geochemical background concentration of the i PTE.

Table 2. Interpretation of I_{geo} and *EF* values for pollution level assessmen

I_{geo}		*EF*	
I_{geo} values	Class	*EF* values	Class
$I_{geo} \le 0$	unpolluted	$EF < 2$	Deficiency to minimal enrichment
$0 < I_{geo} \le 1$	from unpolluted to moderately polluted	$2 < EF < 5$	Moderate enrichment
$1 < I_{geo} \le 2$	moderately polluted	$5 < EF < 20$	Significant enrichment
$2 < I_{geo} \le 3$	from moderately to strongly polluted	$20 < EF < 40$	Very high enrichment
$3 < I_{geo} \le 4$	strongly polluted	$EF > 40$	Extremaly high enrichment
$4 < I_{geo} \le 5$	from strongly to extremely polluted		
$I_{geo} > 5$	extremely polluted		

[5] Quantitative chemical analysis of soils. Methodology for measurement of metal content in solid objects by inductively coupled plasma spectrometry method PND F 16.1:2.3:3.11-98. https://base.garant.ru/70972096.

The *EF* is a method for quantifying the enrichment of PTEs in a sample relative to a geochemical background. An *EF* is calculated in j sample as follows:

$$EF_i = \frac{\left[C_i / C_{ref\ j}\right]_{sample}}{\left[C_i / C_{ref}\right]_{background}} \quad (5)$$

where C_i is the concentration of the *i* PTE, C_{ref} *j* is the concentration of a reference element in j sample for the purpose of normalisation. Iron (Fe) was used as the reference element.

The PI_{sum} represents the sum of all determined PTEs concentrations expressed as *PI* (Qingjie et al. 2008). The PI_{sum} is calculated using the following formula:

$$PI_{sum} = \sum_{j=1}^{k} \sum_{i=1}^{n} PI_{i,j} \quad (6)$$

where *PI* is the calculated value for *PI*, *n* is the total number of PTEs analysed in this study, and *k* is the number of samples.

Since PI_{sum} is the sum of individual pollution indices (*PI*), the classification of PI_{sum} depends on the number of elements used. To normalise PI_{sum} by the number of elements, the average pollution index (PI_{avg}) can be calculated (Qingjie et al. 2008):

$$PI_{avg} = \frac{PI_{sum}}{n} \quad (7)$$

where *n* is the number of total PTEs analysed in this study.

The interpretation of PI_{avg} values is as follows: $PI_{avg} \leq 1$ is not polluted (background level), $1 < PI_{avg} < 2$ is slightly polluted, $2 < PI_{avg} < 3$ is moderately polluted, $3 < PI_{avg} < 5$ is seriously polluted, $PI_{avg} > 5$ is very seriously polluted.

The $PI_{Nemerow}$ allows for the assessment of the overall PTE pollution level (Qingjie et al. 2008). The $PI_{Nemerow}$ is calculated using the following formula:

$$PI_{Nemerow} = \sqrt{\frac{\left(PI_{avg}\right)^2 + PI_{i\ max}^2}{2}} \quad (8)$$

where $PI_{i\ max}$ is the maximum *PI* value among the studied PTEs in the sample.

The interpretation of $PI_{Nemerow}$ values is as follows: $PI_{Nemerow} < 0.7$ is safety domain, $0.7 < PI_{Nemerow} < 1.0$ is precaution domain, $1.0 < PI_{Nemerow} < 2.0$ is slightly polluted domain, $2.0 < PI_{Nemerow} < 3.0$ is moderately polluted domain, $PI_{Nemerow} > 3$ is seriously polluted domain (Qingjie et al. 2008).

To evaluate dust load in cities, the total solid content in the collected snow was calculated, taking into account the size of the sampler and the number of collected cores. The formula for calculating dust load over the observation period is as follows:

$$Dust\ Load = \frac{m_{s.s.}}{N_{cores} \times S_{sampler}} \quad (9)$$

where $m_{s.s.}$ is the mass of suspended solids in the snow sample, g; N_{cores} is the number of collected cores, pcs.; $S_{sampler}$ is the sampler area, m^2. The daily dust deposition from the atmosphere was estimated for a cold season duration of 150 days.

As a reference concentration (urban geochemical background) for pollution assessment, PTEs concentrations in the snow cover of residential areas in Alapaevsk were used. This choice was made because Alapaevsk has no industrial facilities that could serve as sources of emissions for the studied pollutants. The influence of other air pollution factors typical for urban environments, such as vehicle emissions, dusting of materials, and surface wear, is similar across the studied cities. This fact allows for the assessment of pollution specifically caused by PTEs originating from metallurgical enterprises, extractive industries, and other industrial facilities.

Identification of pollutant sources

To determine element associations in the snow samples, hierarchical clustering was performed. The measure of connectivity used was the correlation distance (linkage distance) $1 - r$, where *r* is the Pearson correlation coefficient. This distance reflects the degree of element connectivity, enabling grouping by source of origin. Cluster analysis identifies element associations characteristic for each city. These associations can be natural, reflecting geological processes, or anthropogenic, when elements have a common anthropogenic origin, such as industrial emissions. The Single linkage algorithm was used for clustering, which defines the distance between two clusters as the minimum distance between any two points from different clusters. A disadvantage of this method is that a cluster may include elements that are only weakly connected, or it may form a chain of points, some of which have no significant relationship with each other. However, this method makes it possible to account for even weak associations between elements and is sensitive to extreme values, which is important for identifying geochemical anomalies. Its sensitivity to detecting local connections between points can also be useful in cases of diffuse pollutant input. In urban environments, where pollution is often spatially heterogeneous, this method can reveal important information that other methods may smooth out.

To analyse the distribution of major cations and anions in the snow samples, and their correlation with each other and the mass of suspended solids, statistical processing of their concentrations in meltwater was performed. These parameters offer a better understanding of the geochemical processes occurring in the urban environment.

RESULT

Physical and chemical properties of snow

The content of major cations and anions in the snow from the cities is shown in Table 3. The SiO_2, PO_4^{3-}, and CO_3^{2-} contents are mostly below the detection limit in all cities. Ca^{2+} is the dominant cation in all analysed samples, with concentrations ranging from 61 to 290 μeq/L. This follows the trend: Alapaevsk < Verkhnyaya Pyshma < Kachkanar < Serov. The anionic composition is more variable. Cl^- predominates in Alapaevsk, Verkhnyaya Pyshma, and Serov, with concentrations of 161-369 μeq/L. Bicarbonates (HCO_3^-) are dominant in Kachkanar (214 μeq/L). Total mineralisation (the sum of cations and anions) ranges from 439 μeq/L in Alapaevsk to 980 μeq/L in Verkhnyaya Pyshma and Serov, corresponding to slightly to moderately mineralised waters.

Table 4 presents the correlation matrix (Spearman correlation coefficient) of the cation and anion composition, and the mass of suspended solids in snow in the cities.

Table 5 presents the average, maximum, and minimum values of pH and Eh for the snow samples from different cities. On average, pH does not differ significantly between cities (around 7.5), except in Serov, where this value reaches 8.4. The value of Eh varies considerably both within each city and between cities. The

Table 3. Content of major cations and anions in melted snow in the cities

City	Sum of cations, μeq/L	Sum of anions, μeq/L	Cations, μeq/L				Anions, μeq/L				
			$Na^{++}+K^{+}$	Mg^{2+}	Ca^{2+}	NH_{4+}	Cl^{-}	HCO_{3-}	SO_4^{2-}	NO_{3-}	NO_{2-}
Alapaevsk	132	307	23	17	61	31	161	113	10	22	0.7
V. Pyshma	335	647	101	43	111	80	369	171	60	38	9.3
Kachkanar	345	419	33	52	239	21	141	214	31	32	0.7
Serov	392	587	33	44	290	25	262	256	39	29	1.5

Table 4. The correlation matrix of cation and anion composition (mg/L), and the mass of suspended solids (Ms.s., g) in snow in the cities

	Na	$M_{s.s.}$	K	Ca	Mg	NO_3	NO_2	NH_4	Cl	SO_4	HCO_3
Na	1.00	0.27	**0.51**	0.39	0.33	**0.68**	0.26	0.36	**0.71**	0.41	0.27
$M_{s.s.}$		1.00	0.30	**0.71**	**0.78**	0.36	0.19	-0.34	-0.19	**0.55**	**0.62**
K			1.00	0.28	0.26	0.34	0.16	0.46	0.30	0.42	0.48
Ca				1.00	**0.84**	0.49	0.28	-0.35	0.20	**0.73**	**0.71**
Mg					1.00	0.47	0.16	-0.33	-0.01	**0.69**	**0.72**
NO_3						1.00	0.25	0.18	**0.57**	**0.52**	0.31
NO_2							1.00	0.27	0.16	0.27	0.42
NH_4								1.00	0.43	0.01	-0.04
Cl									1.00	0.38	0.10
SO_4										1.00	**0.80**
HCO_3											1.00

* The correlation is statistically significant at $p < 0.05$.

highest Eh value is observed in Kachkanar (181.5 mV), while the lowest is in Serov (105.6 mV). Alapaevsk and Verkhnyaya Pyshma have very similar pH and Eh values. The greatest variability in Eh is observed in Kachkanar, where the difference between the minimum and maximum values is 2.7 times, whereas this difference does not exceed 1.5 to 2 times in the other cities.

Table 5 presents the average, maximum, and minimum values of suspended solids concentration in the snow across the cities. The highest concentration of suspended solids is observed in Kachkanar (0.54 g/L), while the lowest is in Alapaevsk (0.09 g/L). Even the lowest concentration of suspended solids in Kachkanar (0.25 g/L) is higher than the maximum in Alapaevsk and Verkhnyaya Pyshma (up to 0.23 g/L) and is close to the value in Serov (0.35 g/L).

The intensity of PTEs accumulation in the snow cover

Table 6 presents the accumulation intensity of PTEs in snow cover across the cities. Median values of PTEs concentrations (see Eq. 2) with MAD (see Eq. 1) are shown.

Assessment of snow pollution level

Table 7 presents the median values of I_{geo}, *EF*, and *PI*. In Kachkanar, significant pollution for V and Fe is observed based on I_{geo} and *PI*. However, the *EF* value for V is on the threshold of natural enrichment. In Serov, significant pollution of Cr is observed across all indices. In Verkhnyaya Pyshma, significant pollution of Cu and As is observed across all indices.

The following values of PI_{sum}, PI_{avg} and mean $PI_{Nemerow}$ were calculated, respectively:

– Kachkanar – 154, 9.8, and 12;
– Serov – 66, 4.1, and 5.1;
– V. Pyshma – 66, 4.2, and 7.2.

Table 8 presents the dust load across the cities. During the cold period, snow cover in the cities accumulates 4.0-24 g/m^2 of suspended solids, which corresponds to a daily dust deposition of 27-163 mg/m^2.

Element associations

Element associations with cities (where $r < 0.5$) are shown in Figure 3.

Table 5. Average pH and Eh values and concentrations of suspended solids in snow samples

City	pH (mean / min-max)	Eh (mean / min-max), mV	Suspended solids concentration (mean / st. dev. / min-max), g/L
Alapaevsk	7.4 / 6.8-7.9	137.9 / 103-157	0.03 / 0.02 / 0.01-0.06
V. Pyshma	7.4 / 6.5-7.9	141.0 / 102-179	0.05 / 0.02 / 0.02-0.06
Kachkanar	7.7 / 7.3-8.0	181.5 / 100-273	0.18 / 0.06 / 0.10-0.26
Serov	8.4 / 7.7-8.8	105.6 / 70-157	0.07 / 0.05-0.13

Table 6. The PTEs accumulation intensity in the snow cover across the cities (median ± MAD, mg/m² per day)

Element	Kachkanar		Serov		Alapaevsk		V. Pyshma	
	median	MAD	median	MAD	median	MAD	median	MAD
Al	0.0001	± 0.00003	0.0008	± 0.0003	0.0001	± 0.00002	0.0007	± 0.0003
As	0.0030	± 0.0005	0.0027	± 0.0013	0.0004	± 0.0001	0.0031	± 0.0008
Cd	0.0001	± 0.0001	0.0002	± 0.0001	0.0001	± 0.00005	0.0001	± 0.00002
Cr	0.0295	± 0.0078	0.1601	± 0.0611	0.0065	± 0.0028	0.0078	± 0.001
Cu	0.0101	± 0.0029	0.0302	± 0.0169	0.0044	± 0.0016	0.1820	± 0.1088
Fe	75.73	± 23.19	15.15	± 8.12	1.66	± 0.37	2.45	± 0.94
Mn	0.1785	± 0.1784	0.0980	± 0.0972	0.0234	± 0.0233	0.0277	± 0.0271
Mo	0.0001	± 0.00005	0.0012	± 0.0004	0.0002	± 0.0001	0.0008	± 0.0002
Ni	0.0182	± 0.0050	0.0092	± 0.0038	0.005	± 0.0026	0.0065	± 0.0012
Pb	0.0084	± 0.0024	0.0053	± 0.0016	0.0026	± 0.0005	0.0084	± 0.0015
Sb	0.0003	± 0.0001	0.0002	± 0.00005	0.0002	± 0.00004	0.0008	± 0.0003
Sn	0.0003	± 0.0001	0.0003	± 0.0001	0.0001	± 0.00002	0.0004	± 0.0001
Ti	0.9885	± 0.9884	0.0556	± 0.0548	0.031	± 0.0309	0.0655	± 0.0649
V	0.1762	± 0.0315	0.0068	± 0.0012	0.0026	± 0.0007	0.0042	± 0.0014
Zn	0.0289	± 0.0108	0.0395	± 0.0116	0.0138	± 0.0039	0.0262	± 0.0079

Table 7. Median values of I_{geo}, *EF*, and *PI* in snow samples

City	Al	Ti	V	Cr	Mn	Co	Fe	Ni	Cu	Zn	As	Mo	Cd	Sn	Sb	Pb
I_{geo}																
Kachkanar	1.3	3.9	4.9	1.2	1.9	3.9	4.5	0.7	-0.1	-0.1	1.7	-2.0	0.2	-0.4	-0.5	0.2
Serov	0.2	-0.2	0.5	3.7	1.2	1.5	2.2	-0.1	1.7	0.6	2.0	1.7	0.9	0.0	-0.9	0.0
V. Pyshma	0.4	0.2	-0.1	-0.4	-0.6	0.3	-0.4	-0.6	4.2	0.3	2.5	1.5	0.5	0.8	1.5	0.9
EF																
Kachkanar	0.1	0.6	1.5	0.1	0.1	0.7	1	0.1	0.0	0.0	0.2	0.0	0.0	0.0	0.0	0.1
Serov	0.2	0.2	0.3	3.9	0.5	0.5	1	0.2	0.6	0.3	0.7	0.7	0.3	0.2	0.1	0.2
V. Pyshma	1.6	1.4	0.9	0.9	0.7	1.2	1	0.7	29.0	1.6	7.9	3.2	1.2	2.2	3.4	2.5
PI																
Kachkanar	3.6	23	47	3.5	5.6	23	34	2.5	1.4	1.4	5.0	0.4	1.7	1.1	1.1	1.8
Serov	1.7	1.4	2.1	20	3.4	4.4	7.1	1.4	4.9	2.3	5.9	5.0	2.7	1.5	0.8	1.5
V. Pyshma	1.9	1.7	1.4	1.1	1.0	1.9	1.1	1.0	29	1.8	8.4	4.3	2.2	2.7	4.2	2.7

Table 8. Dust load in the cities

City	Average mass of suspended solids in snow, g/m² per season	Average daily supply of suspended solids in snow, mg/m² per day
Alapaevsk	4.0	27
V. Pyshma	9.4	63
Kachkanar	24	163
Serov	13	84

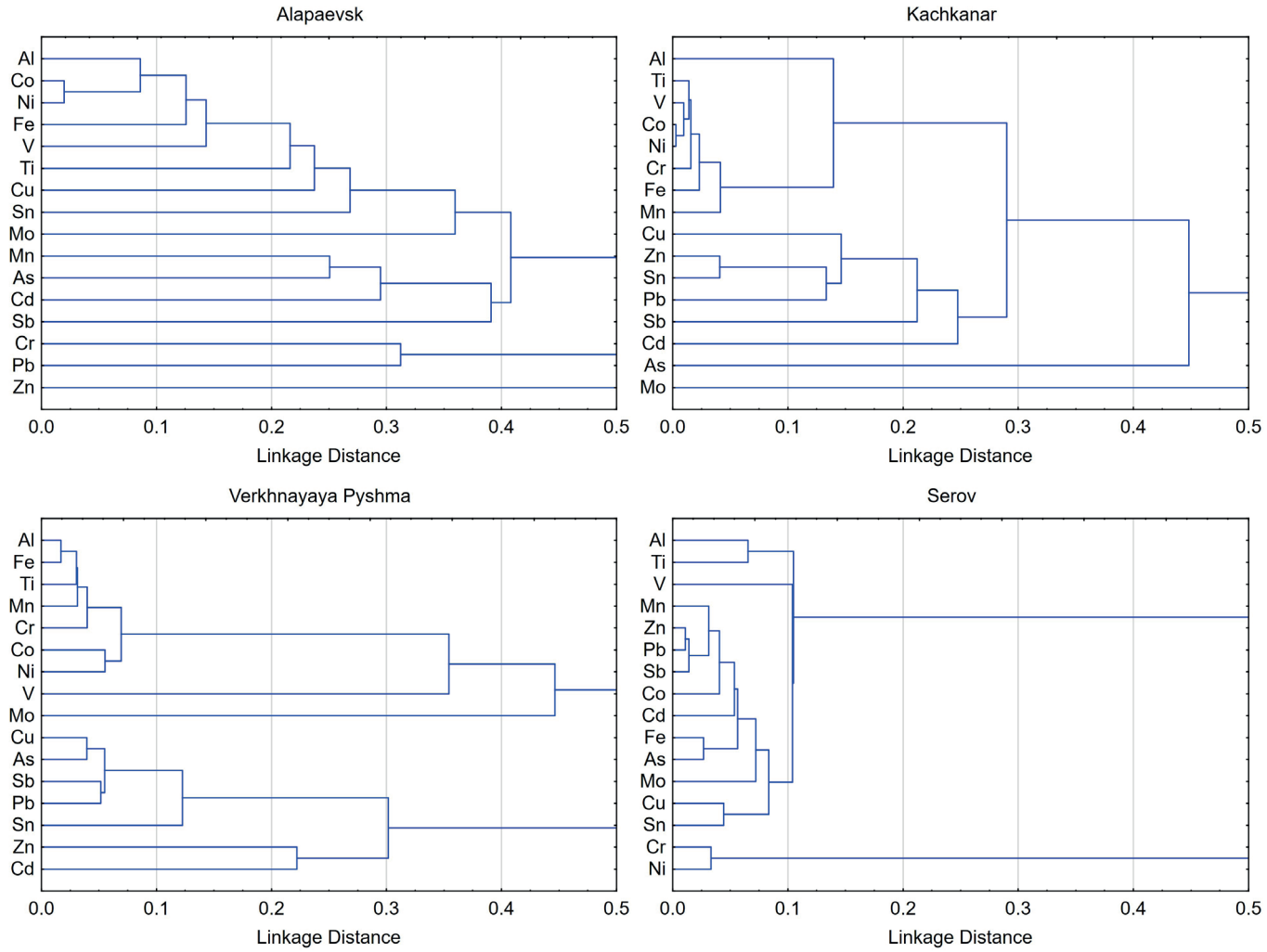

Fig. 2. The degree of correlation between the sources of input and the migration of anthropogenic elements (Single linkage, 1-*r* , where *r* is Pearson correlation coefficient)

Comparison of element concentrations with other studies

Table 9 presents the average concentrations of elements and pH levels in the snow cover of the studied cities, along with concentrations from other studies. The cities being compared have different industrial specialisations, levels of urbanisation, and transport network development. For comparison, only those elements that appear in multiple studies are presented. The total concentration represents the sum of the dissolved and suspended phases. At the same time, the proportion of the dissolved phase (<0.45 μm) is significantly lower than that of the suspended phase in the total concentration (e.g. Grebenshchikova et al. 2016; Vlasov et al. 2020; Moskovchenko et al. 2021). This allows us to compare those results with the findings of the present study.

DISCUSSION

The study was conducted in small and medium-sized cities with varying industrial specialisations. These cities experience a cold period lasting approximately six months. The cities in the Ural region specialise in the extraction and processing of mineral resources, as well as in manufacturing. Enterprises in these cities produce substantial volumes of metals for the global market (UGMK, Evraz, Kachkanar Mining and Processing Plant). The products from these enterprises are exported to numerous countries worldwide.

The cities studied are of the mono-industry type, where a large proportion of the population is employed by a single company. In small Russian cities, approximately half of the residential area is occupied by detached houses with adjacent private gardens. Here, agricultural activities are common, such as growing berries, fruits, and vegetables, and raising animals for personal consumption (Seleznev et al. 2024). At the same time, residential areas are located very close to industrial sites. For example, in Kachkanar, some residential districts are within the sanitary protection zone of the Kachkanar Mining and Processing Plant quarry (Seleznev et al. 2024). This means that in small cities, the route for pollutants to enter the human body is shorter. About 25% of the population in Russia lives in small cities. Along with other factors, poor healthcare and a lack of social activities affect the population in these cities. Air pollution is a significant environmental issue in small industrial cities.

The study included a set of indicators that maximally accounts for potential pollutants from various industries, as well as natural sources of pollution typical for the region. The set of pollutants is aligned with the set of indicators used in similar studies (Moskovchenko et al. 2023; Vlasov et al. 2020; etc.).

The presence of Ca^{2+}, Cl^-, HCO_3^-, and SO_4^{2-} in snow cover in Kachkanar and Serov can be linked to the metallurgical industry, as these compounds are used as reagents in metallurgical processes. Bicarbonates and sulphates may have a common source, namely emissions from metallurgical and raw material processing industries into the atmosphere. In all studied cities, a deviation from the natural anionic ratio $HCO_3^- > SO_4^{2-} > Cl^-$ was observed. This shift is likely attributable to the application of de-icing

Table 9. Literature data on the mean concentrations of elements in snow cover (total concentration of elements), μg/L

Location	References	pH	Ni	V	Cr	Cu	Pb	Mn	Al	Fe	As	Ti	Cd	Zn	Co
Kachkanar	current study	7.7	21.3	224.6	32.7	10.2	8.2	186.9	2566	36491	3.0	1197.3	0.1	31.4	16.7
Serov		8.4	14.2	8.8	422.1	45.3	8.3	141.8	1320	8545	3.5	71.1	0.2	58.6	3.0
Alapaevsk		7.4	9.9	4.2	14.4	16.0	4.4	45.2	792	968	0.8	51.0	0.1	21.3	0.7
V. Pyshma		7.4	8.4	6.3	10.9	365.4	14.3	38.9	1843	1387	5.9	101.1	0.2	48.2	1.2
Sapporo, Japan	Sakai et al. 1988	8.5	-	-	9.3	37.6	34.1	513	-	-	-	-	0.36	53	-
Muroran, Japan		6.2	-	-	7.8	7.2	23.9	205	-	-	-	-	0.22	55	-
Asahikawa, Japan		5.8	-	-	4.0	7.2	9.0	52	-	-	-	-	0.08	24	-
Lahti, Finland low / high intensity traffic road	Kuoppamäki et al. 2014	5.7 / 7.0	ND / 2.4	-	0.26 / 4.3	1.3 / 12	ND / 1.4	1.1 / 45	210 / 2000	-	-	-	ND / 0.13	ND / 3 7	0.14 / 2.0
Innsbruck, Austria residential area	Engelhard et al. 2007	-	-	-	-	0.02	16	-	-	-	-	-	3.0	0.13	-
Katowice, Poland near the parking lot	Adamiec et al. 2013	-	4.2	18.0	17.0	6.3	0.86	6.4	-	392.0	4.3	5.9	4.2	25.7	-
Tyumen, Russia	Moskovchenko et al. 2021	4.7-6.3	31.5	2.3	24.7	11.6	4.8	32.9	847	1644	0.83	54.0	0.08	34.1	1.6
Nizhnevartovsk, Russia	Moskovchenko et al. 2022	4.3	2.7	2.0	3.1	3.2	1.7	12.8	-	627	0.13	-	0.02	14.5	0.41
Moscow, Russia yards with parking lots	Vlasov et al. 2020	7.5	2.8	2.9	1.6	7.9	2.2	20.4	591	748	0.12	48.9	0.82	24.9	0.38
Vanino, Russia	Lukyanov et al. 2022	-	14.7	3.8	3.5	12.5	1.2	112.7	-	-	5.7	-	-	58.2	-
Vladivostok, Russia	Kondrat'ev et al. 2017	4.9	0.64	0.69	-	2.8	0.91	36.4	90.0	53.9	-	-	0.11	32	-
Svirsk, Russia	Grebenshchikova et al. 2017	4.5-7.9	2.3	3.3	-	2.3	0.48	-	-	-	3.7	-	0.07	18	0.41

agents in urban areas, which are predominantly composed of chloride-based compounds. In Verkhnyaya Pyshma, this is further supported by the increased concentration of Na^{++}. The concentration of $Na^{++}+K^{+}$ exceeds that of Mg^{2+}, indicating a disturbance in the natural ionic ratio, likely associated with urban environmental pollution. The notable discrepancy between cation and anion sums, particularly in Alapaevsk and Verkhnyaya Pyshma, suggests the presence of unidentified ions. The analysed solutions may contain solid particles <2 μm. Vlasov et al. (2020) demonstrated that solid particles <2 μm can contain ions of easily soluble salts, which may affect the results of measuring the concentrations of individual cations and anions.

The mineralization of snow in cities is similar to that in ultra-fresh and fresh waters. However, when comparing mineralization levels between cities, the highest average is observed in Verkhnyaya Pyshma (982 μeq/L), and the lowest in Alapaevsk (439 μeq/L). This suggests that emissions from industrial facilities are within the normal operational limits of the enterprises. The suspended solids in snow are primarily composed of calcium and magnesium bicarbonates and sulphates. Sodium is associated with chloride.

The studied cities exhibit variations in the elemental composition of their emissions. These emissions reflect the industrial specialisation of each city. Kachkanar, with its focus on iron ore extraction, shows a higher concentration of Co-Ni-V-Ti-Cr-Fe-Mn (ranked by element concentration in samples, as presented in Figure 2). The Kachkanar deposit is naturally enriched with Fe and V. In Serov, which specialises in metallurgy, metalworking, and the recycling of secondary metallurgical raw materials, most elements are associated with each other. The exception is a distinct Cr-Ni group, likely linked to steel production, while the other elements are of natural origin. In Verkhnyaya Pyshma, traces of non-ferrous metallurgy are clearly discernible, with the elemental association including Cu-As-Sb-Pb.

In these three cities features a characteristic indicator element originating from stationary sources, its presence connected to the technological production processes occurring within the city. However, Alapaevsk, which lacks heavy industries, shows comparatively low concentrations of PTEs in its snow cover. The Co-Ni association in Alapaevsk might be related to vehicle emissions (Vijayan et al. 2024).

The concentration of PTEs in the atmosphere depends on numerous mechanisms and the characteristics of each area, making the assessment of background concentration problematic (Sakai et al. 1988; Reimann et al. 2005). In this study, PTEs concentrations in a city without heavy industry for decades were chosen as the urban geochemical background. This approach allowed for a comparison of pollution from industrial facilities, mining sites, and other sources. Based on the analysis results, Alapaevsk was the least polluted city among those studied according to all indicators.

The calculated pollution indices identified PTEs typical for the industries of the studied cities, confirming their contribution to overall atmospheric pollution. Kachkanar was the most polluted city (PI_{sum} – 154, PI_{avg} – 9.8, $PI_{Nemerow}$ – 12), while Serov and Verkhnyaya Pyshma were also significantly polluted and had similar PI_{sum} and PI_{avg} values (66 and 4.2, respectively) and $PI_{Nemerow}$ values (5.1 and 7.2, respectively). The *EF* in Verkhnyaya Pyshma shows very high Cu enrichment and significant As enrichment. According to I_{geo}, the pollution levels of these elements in Verkhnyaya Pyshma range from moderate for As to extreme for Cu. The detected elemental pollution corresponds to the industrial specialisation of the cities and is likely associated with emissions from local enterprises or atmospheric transport of dust from their industrial sites (for example, from the open-pit mine in Kachkanar).

The mass of deposited dust per unit area varies significantly among the studied cities. Industrial enterprises are the main sources of air pollution during the cold season. The highest dust load is observed in Kachkanar. This is due to the city's proximity to open-pit mining operations, open tailings storage facilities, and the operation of a mining and beneficiation plant. During the sampling stage in Kachkanar, atmospheric pollution was visually noticeable in the snow cover as layers of dark particles. The lowest dust load is observed in Alapaevsk, the city with the least industrial activity among those studied. Verkhnyaya Pyshma and Serov show similar levels of dust load. This is because both cities have developed industrial complexes for mineral processing, although they do not have mining operations. In Serov, the dust load is slightly higher. This may be associated with the open slag storage facility at the ferroalloy plant in the northern part of the city.

The obtained dust load values in the studied cities can be compared to similar estimates in other studies. In the study by Vorobievskaya et al. (2022), conducted in Murmansk, Russia, the dust load ranged from 40 to 65 g/m^2, which is more than twice the estimate in Kachkanar. In the study by Moskovchenko et al. (2023), conducted in Nadym, Russia, it was shown that in industrial areas, the dust load is 37 mg/m^2 per day, while in residential areas, it is 15 mg/m^2 per day. The dust load in residential areas of the studied cities is 2-5 times higher than in the industrial areas of Nadym, and in Alapaevsk, it is close to this value.

The proposed methodology has demonstrated its applicability for a comprehensive assessment of current atmospheric pollution input. The selection of the solid phase with particle sizes >2 μm and the filtrate as research objects proved effective for identifying pollution and its sources. In similar studies of snow cover, two snow phases are typically analysed: dissolved (<0.45 μm) and suspended (>0.45 μm). In many of these studies (Vlasov et al. 2020; Moskovchenko et al. 2021; Vijayan et al. 2024, etc.), the particulate phase is found to be the most contaminated. The role of suspended PTEs in urban areas is significantly increased compared to background regions due to high dust loads, emissions from motor vehicles and industrial facilities, and the use of de-icing salts (Vlasov et al. 2020). Therefore, the present study tested an approach focused exclusively on assessing this phase. This approach helps reduce laboratory costs by decreasing the number of samples analysed. The availability of equipment for isolating the target snow phases (>2 μm and filtrate) makes snow research more accessible in terms of material and financial resources. The results of this study confirmed the effectiveness of this approach.

Overall, the collected data indicate that atmospheric pollution in small industrial cities has a certain impact on the environment. However, the accumulation of pollutants in the snow cover could become a serious issue when they enter water bodies and soil during snowmelt.

CONCLUSIONS

An assessment was conducted of the current atmospheric input of pollutants into the residential zones of small and medium-sized industrial cities in the Sverdlovsk region, Russia. These cities are located in a temperate climate zone with a cold, prolonged snowy winter. The undisturbed snow cover was used as a geoindicator component of the environment.

The physical and chemical properties of the snow are not anomalous and correspond to the normal operation of the enterprises. Pollutant emissions are due to the normal functioning of the industrial facilities. The solids in the snow are primarily formed by calcium and magnesium bicarbonates and sulphates.

The calculated pollution indices show that industrial facilities in each city are major sources of urban environmental pollution when compared to Alapaevsk, which was chosen as an urban geochemical background. According to PI_{sum}, PI_{avg} and $PI_{Nemerow}$, Kachkanar is the most polluted city. Elevated levels of V and Fe are likely connected to the open-pit mine. *EF* values suggest their origin is geogenic rather than anthropogenic. In Serov, Cr pollution is confirmed by all calculated indices and aligns with the city's metallurgical industry profile. In Verkhnyaya Pyshma, there is clearly anthropogenic, extreme Cu pollution and significant As pollution. Moderate pollution of Mo, Sn, Sb, and Pb is also present across all indices. V, Fe, Cr, Cu, and As pollution has been detected. Cluster analysis revealed geochemical associations in the snow cover: in Kachkanar Co-Ni-V-Ti-Cr-Fe-Mn; in Serov Cr and Ni; in Verkhnyaya Pyshma Cu-As-Sb-Pb; and in Alapaevsk Co and Ni. The cities differ in the associations of elements in the depending on their industrial specialisation. The dust load is quite significant and amounts to mg/m^2 per day: Kachkanar – 163, Serov – 84, Verkhnyaya Pyshma – 63, Alapaevsk – 27.

A comprehensive environmental monitoring method based on snow cover analysis was used in this study. The method can be successfully applied to other cities.

The proposed method has several limitations and sources of uncertainty:

1. The method is applicable only to regions with a long cold season and stable snow cover.

2. The dissolved form of PTEs is not considered separately in this method.

3. The selected urban geochemical background concentrations may be elevated compared to other possible background values.

REFERENCES

Adamiec E., Wieszała R., Strzebońska M., Jarosz-Krzemińska E. (2013). An attempt to identify traffic related elements in snow. Geology Geophysics & Environment, 39(4), 317, DOI: 10.7494/geol.2013.39.4.317.

Alves C., Vicente A., Calvo A., Baumgardner D., Amato F., Querol X., Pio C., Gustafsson M. (2019). Physical and chemical properties of non-exhaust particles generated from wear between pavements and tyres. Atmospheric Environment, 224, 117252, DOI: 10.1016/j.atmosenv.2019.117252.

Carlsson A., Centrell P., Oberg G. Studded tyres. Socio-economic calculations. Linköping: Statens väg- och transportforskningsinstitut.

Chen X., Zhang L., Huang J., Song F., Zhang L., Qian Z., Trevathan E. (2016). Long-term exposure to urban air pollution and lung cancer mortality: A 12-year cohort study in Northern China. The Science of the Total Environment, 571, 855-861, DOI: 10.1016/j.scitotenv.2016.07.064.

Engelhard C., De Toffol S., Lek I., Rauch W., Dallinger R. (2007). Environmental impacts of urban snow management – The alpine case study of Innsbruck. The Science of the Total Environment, 382(2-3), 286-294, DOI: 10.1016/j.scitotenv.2007.04.008.

Grebenshchikova V. I., Efimova N. V., Doroshkov A. A. (2017). Chemical composition of snow and soil in Svirsk city (Irkutsk Region, Pribaikal'e). Environmental Earth Sciences, 76(20), DOI: 10.1007/s12665-017-7056-0.

Guo P., Tian W., Li H., Zhang G., Li J. (2020). Global characteristics and trends of research on construction dust: based on bibliometric and visualized analysis. Environmental Science and Pollution Research, 27(30), 37773-37789, DOI: 10.1007/s11356-020-09723-y.

Indraratne S., Amarakoon I., Kumaragamage D., Lasisi A., Goltz D., Casson N. (2023). Loss of potentially toxic elements to snowmelt runoff from soils amended with alum, gypsum, and Epsom salt. Canadian Journal of Soil Science, 104(2), 156-165, DOI: 10.1139/cjss-2023-0073.

Jeong C., Wang J. M., Hilker N., Debosz J., Sofowote U., Su Y., Noble M., Healy R. M., Munoz T., Dabek-Zlotorzynska E., Celo V., White L., Audette C., Herod D., Evans, G. J. (2018). Temporal and spatial variability of traffic-related PM2.5 sources: Comparison of exhaust and non-exhaust emissions. Atmospheric Environment, 198, 55-69, DOI: 10.1016/j.atmosenv.2018.10.038.

Kaskaoutis D., Petrinoli K., Grivas G., Kalkavouras P., Tsagkaraki M., Tavernaraki K., Papoutsidaki K. (2023). Impact of peri-urban forest fires on air quality and aerosol optical and chemical properties: The case of the August 2021 wildfires in Athens, Greece. The Science of the Total Environment, 907, 168028, DOI: 10.1016/j.scitotenv.2023.168028.

Kondrat'ev I. I., Mukha D. E., Boldeskul A. G., Yurchenko S. G., Lutsenko T. N. (2017). Chemical composition of precipitation and snow cover in the Primorsky krai. Russian Meteorology and Hydrology, 42(1), 64-70, DOI: 10.3103/s1068373917010083.

Kosheleva N. E., Sycheva D. G., Kasimov N. S. (2024). Geochemistry of snow cover within the territory of the Lomonosov Moscow State University. Lomonosov Geography Journal, 79(5), 3-1, DOI: 10.55959/msu0579-9414.5.79.5.1.

Kuoppamäki K., Setälä H., Rantalainen A., Kotze D. J. (2014). Urban snow indicates pollution originating from road traffic. Environmental Pollution, 195, 56-63, DOI: 10.1016/j.envpol.2014.08.019.

Lak A., Vahabi S., Sahar H. E. (2024). Resilience in the dust: The Influence of Sand and Dust Storms (SDSs) on residents' perception of urban green spaces: a Qualitative study. International Journal of Disaster Risk Reduction, 108, 104572, DOI: 10.1016/j.ijdrr.2024.104572.

Lee Y., Lee P., Choi S., An M., Jang A. (2021). Effects of air pollutants on airway diseases. International Journal of Environmental Research and Public Health, 18(18), 9905, DOI: 10.3390/ijerph18189905.

Lukyanov A. I., Dakhova E. V., Mayorova L. P. (2022). Assessment of snow cover pollution by heavy metals as one of the methods of atmospheric air monitoring on the example of settlements in the Far East. RUDN Journal of Ecology and Life Safety, 30(3), 407-416, DOI: 10.22363/2313-2310-2022-30-3-407-416 (in Russian).

Moskovchenko D., Pozhitkov R., Zakharchenko A., Tigeev A. (2021). Concentrations of Major and Trace Elements within the Snowpack of Tyumen, Russia. Minerals, 11(7), 709, DOI: 10.3390/min11070709.

Moskovchenko D. V., Pozhitkov R., Minkina T., Sushkova S. (2022). Trace metals and polycyclic aromatic hydrocarbons in the snow cover of the city of Nizhnevartovsk (Russia). Research Square, DOI: 10.21203/rs.3.rs-2064341/v1.

Moskovchenko D. V., Pozhitkov R., Soromotin A. (2023). Snow contamination by heavy metals and metalloids in a polar town (a case study of Nadym, Russia). Research Square, DOI: https://doi.org/10.21203/rs.3.rs-3629334/v1.

Müller G. (1986). Schadstoffe in sedimenten-sedimente als schadstoffe. Mitteilungen der Österreichische Geologische Gesellschaft, 79, 107-126.

Opp C., Groll M., Abbasi H., Foroushani M. A. (2021). Causes and effects of sand and dust storms: What has past research taught us? A survey. Journal of Risk and Financial Management, 14(7), 326, DOI: 10.3390/jrfm14070326.

Pellecchia M., Papa G., Barbato M., Capitani G., Negri I. (2023). Origin of non-exhaust PM in cities by individual analysis of particles collected by honey bees (Apis mellifera). Environmental Pollution, 331, 121885, DOI: 10.1016/j.envpol.2023.121885.

Piscitello A., Bianco C., Casasso A., Sethi R. (2021). Non-exhaust traffic emissions: Sources, characterization, and mitigation measures. The Science of the Total Environment, 766, 144440, DOI: 10.1016/j.scitotenv.2020.144440.

Popovicheva, O., Diapouli, E., Chichaeva, M., Kosheleva, N., Kovach, R., Bitukova, V., Eleftheriadis, K., Kasimov, N. (2024). Aerosol characterization and peculiarities of source apportionment in Moscow, the largest and northernmost European megacity. The Science of the Total Environment, 918, 170315, DOI: 10.1016/j.scitotenv.2024.170315.

Qingjie G., Jun D., Yunchuan X., Qingfei W., Liqiang Y. (2008). Calculating pollution indices by heavy metals in ecological geochemistry assessment and a case study in parks of Beijing. Journal of China University of Geosciences, 19(3), 230-241, DOI: 10.1016/s1002-0705(08)60042-4.

Raaschou-Nielsen O., Andersen Z. J., Beelen R., Samoli E., Stafoggia M., Weinmayr G., Hoffmann B. (2013). Air pollution and lung cancer incidence in 17 European cohorts: prospective analyses from the European Study of Cohorts for Air Pollution Effects (ESCAPE). The Lancet Oncology, 14(9), 813-822, DOI: 10.1016/s1470-2045(13)70279-1.

Reimann C., Filzmoser P., Garrett R. G. (2005). Background and threshold: critical comparison of methods of determination. The Science of the Total Environment, 346(1-3), 1-16, DOI: 10.1016/j.scitotenv.2004.11.023.

Sakai H., Sasaki T., Saito K. (1988). Heavy metal concentrations in urban snow as an indicator of air pollution. The Science of the Total Environment, 77(2-3), 163-174, DOI: 10.1016/0048-9697(88)90053-8.

Seleznev A., Shevchenko A., Malinovsky G., Ivanchukova N., Glukhov V., Hanfi M.Y. (2024). Assessment of the total amount of surface deposited sediments in small towns. Urban Science, 8(4), 178, DOI: 10.3390/urbansci8040178.

Seleznev A., Yarmoshenko I., Malinovsky G., Ilgasheva E., Baglaeva E., Ryanskaya A., Kiseleva D., Gulyaeva T. (2019). Snow-dirt sludge as an indicator of environmental and sedimentation processes in the urban environment. Scientific Reports, 9(1), DOI: 10.1038/s41598-019-53793-z.

Szwed M., Kozłowski R. (2022). Snow cover as an indicator of dust pollution in the area of exploitation of rock materials in the Świętokrzyskie Mountains. Atmosphere, 13(3), 409, DOI: 10.3390/atmos13030409.

Novikova V. D., Talovskaya A. V., Yazikov, E. G. (2025). Dynamics of particulate load and chemical composition of snow cover in the area of thermal power and coke chemistry enterprises (case for the city of Kemerovo). Bulletin of the Tomsk Polytechnic University Geo Assets Engineering, 336(3), 193-207, DOI: 10.18799/24131830/2025/3/4984.

Tariq S., Nawaz H., Mehmood U., Haq Z. U., Pata U. K., Murshed M. (2023). Remote sensing of air pollution due to forest fires and dust storm over Balochistan (Pakistan). Atmospheric Pollution Research, 14(2), 101674, DOI: 10.1016/j.apr.2023.101674.

Tiotiu A. I., Novakova P., Nedeva D., Chong-Neto H. J., Novakova S., Steiropoulos P., Kowal K. (2020). Impact of air pollution on asthma outcomes. International Journal of Environmental Research and Public Health, 17(17), 6212, DOI: 10.3390/ijerph17176212.

Vijayan A., Österlund H., Marsalek J., Viklander, M. (2024). Traffic-related metals in urban snow cover: A review of the literature data and the feasibility of filling gaps by field data collection. The Science of the Total Environment, 920, 170640, DOI: 10.1016/j.scitotenv.2024.170640.

Vlasov D., Vasil'chuk J., Kosheleva N., Kasimov N. (2020). Dissolved and suspended forms of metals and metalloids in snow cover of Megacity: Partitioning and deposition rates in Western Moscow. Atmosphere, 11(9), 907, DOI: 10.3390/atmos11090907.

Vorobievskaya E., Kirillov S., Sedova N., Slipenchuk M. (2022). Snow cover dust pollution in Murmansk and its suburbs. IOP Conference Series Earth and Environmental Science, 1010(1), 012012, DOI: 10.1088/1755-1315/1010/1/012012.

Watson A. Y., Bates R. R., Kennedy D. (1988). Assessment of human exposure to air pollution: methods, measurements, and models. Air Pollution, the Automobile, and Public Health. Washington (DC): National Academies Press, DOI: 10.17226/1033.

Yang H., Song X., Zhang Q. (2020). RS&GIS based PM emission inventories of dust sources over a provincial scale: A case study of Henan province, central China. Atmospheric Environment, 225, 117361, DOI: 10.1016/j.atmosenv.2020.117361.

Zhou Y., Zhao H., Lu Y., Bai X., Fu Z., Mao J., Tian H. (2024). Heterogeneous evolution and driving forces of multiple hazardous air pollutants and GHGs emissions from China's primary aluminum industry. The Science of the Total Environment, 953, 176079, DOI: 10.1016/j.scitotenv.2024.176079.

RESEARCH PAPER

FOUR DECADES OF TREE COVER AND GRASSLAND DYNAMICS IN THE FOOTHILLS OF THE WESTERN HIMALAYAS – CHAMOLI DISTRICT OF UTTARAKHAND, INDIA

Roosen Kumar[1*], Bindhy Wasini Pandey[1], Jitender Rathore[2], Chetna Sharma[3]
[1]Department of Geography, Delhi School of Economics, University of Delhi
[2]School of Plant and Environmental Sciences, Virginia Tech, USA
[3]CSRD, School of Social Sciences, Jawaharlal Nehru University, New Delhi
***Corresponding author:** Roosenkumar16@gmail.com
Received: September 14th 2025 / Accepted: November 12nd 2025 / Published: December 31st 2025
https://doi.org/10.24057/2071-9388-2025-3904

ABSTRACT.The study investigates the dynamics of land use and land cover changes and their impacts on tree cover and grasslands in the Chamoli district of Uttarakhand over four decades (1983-2023). Using multi-temporal satellite data analysis, the research examines vegetation patterns across different elevation zones ranging from 683m to 7801m. The findings reveal significant variations in tree cover, with an initial increase from 224,027 hectares in 1983 to fluctuations leading to 323,554 hectares by 2023. Tree cover showed remarkable expansion at higher elevations, particularly in the 4149-5152m zone, increasing from 147 hectares to 44,189 hectares. This indicates significant upward migration. Grassland areas demonstrated considerable variability, expanding from 93,647 hectares in 1983 to 118,330 hectares in 2023. The study identifies a clear spatial pattern with consistently higher vegetation density in the southern region, while the northern portion exhibits notably lower coverage. This north-south vegetation gradient persists throughout the temporal sequence, suggesting underlying environmental and human influences. The research also highlights concerning trends in other land cover types, including an increase in barren land and a massive decrease in snow cover, indicating significant changes. These transformations have important implications for local ecosystems, biodiversity, and communities dependent on these landscapes. The findings contribute to understanding the complex interactions between climate change, land management practices, and vegetation dynamics in high-altitude regions, providing valuable insights for conservation strategies and sustainable resource management.

KEYWORDS: Land use, Vegetation, Treeline, Livelihood, Grassland, Resource, Management, Conservation

CITATION: Kumar R., Pandey B. W., Rathore J., Sharma C. (2025). Four Decades of Tree Cover and Grassland Dynamics in the Foothills of the Western Himalayas – Chamoli District of Uttarakhand, India. Geography, Environment, Sustainability, 4 (18), 19-35
https://doi.org/10.24057/2071-9388-2025-3904

Conflict of interests: The authors reported no potential conflict of interests.

INTRODUCTION

Climate change and human activities have significantly altered mountain ecosystems worldwide, particularly affecting vegetation patterns and land use dynamics (Rawat & Schickhoff 2022). Land use and land cover (LULC) are changing in the Himalayan region, which has a major effect on the local landscape. Examining how the landscape has altered over the last several decades shows important trends that shed light on how ecological conditions and biophysical markers have evolved (Flantua et al. 2007). Changes in vegetation migration to higher altitudes indicate warming temperature conditions in the region, leading to changes in vegetation composition and biodiversity (Grace et al. 2002; Holtmeier and Broll 2005; Holtmeier and Broll 2007; Harsch et al. 2009; Harsch et al. 2011; Holtmeier and Broll 2012). Trees and plant species that previously thrived at lower elevations have established themselves at higher altitudes (Kullman 2001; Liu et al. 2002; Jobbagy and Jackson 2003; Payette 2007). The altered landscape affects resource availability for both ecosystems and humans in the region. These ecological changes have direct socio-economic implications for the dependent population (Bagchi et al. 2004; Hansen et al. 2008). Local traditions are particularly impacted (Kumar et. al. 2025). The livelihoods of pastoral communities may be affected if grazing patterns need to change in response to shifts in vegetation and water supplies (Mishra 2001).

Worldwide, changing climates and land use practices are causing forests to encroach more into grasslands, reducing biodiversity, and altering ecosystem functions and services. Such alterations affect the socio-economic conditions of the people involved (Schickhoff et al. 2005). Higher altitudes, being more sensitive to changes, are experiencing rapid shifts. Himalayan ecosystems are particularly vulnerable to climate-induced vegetation changes. Shrubs and other vegetation are moving upwards in mountain regions. Forests encroaching into alpine meadows lead to changes in land cover and fragmentation of alpine habitats (Anderson et al. 2020). The rich biodiversity

of the Himalayas helps to support local people's livelihoods through their reliance on resources from the natural ecosystem (Joshi and Negi 2011). The local community's livelihood depends mainly on traditional practices related to livestock and farming (Lefroy et al. 2000; Von Wiren-Lehr 2001). Any land-use change in forests or nearby ecotones will affect forestry, pastoralism, agriculture, livestock, Non-Timber Forest Products (NTFPs), livelihood services, and biodiversity. Land use and land-cover changes directly or indirectly influence the natural landscape, which in turn affects the services provided by the ecosystem (Quéttier et al. 2007). However, in the Himalayan states, livestock density and pastoralism are declining in many areas, which allows vegetation to move upslope in some regions (Suwal et al. 2016). These changes will significantly impact the livelihoods of forest-dependent communities. Climate change has a profound effect on vegetation growth. Therefore, the role of climate in changing the vegetation structure of any region cannot be ignored (Duffy et al. 2015). Vegetation growth is encouraged by warm climatic conditions. Higher elevations that previously lacked vegetation will develop growth and regeneration due to favourable and suitable conditions (Payette et al. 2007; Pepin et al. 2015). Globally, meta-analyses of treelines have shown that treelines in most regions are advancing poleward or upwards. Thus, regional responses of treelines can be linked to changing local or regional elements that influence treeline positions. An upward shift of vegetation has been observed in about 52% of studies worldwide (Harsch et al. 2009). Studies along the treeline ecotone in the western Himalayas indicate both an increase and a decrease in vegetation along the treeline zone (Rai et al. 2012). A common method for monitoring vegetation shifts involves analysing remotely sensed data (Purekhovsky et al. 2025).

Remote sensing helps to overcome the difficulties posed by direct observation in poorly accessible terrain. Remote sensing investigations indicated an upward shift of the treeline up to 388 m in Uttarakhand between 1970 and 2006 (Singh et al. 2012). The shift in altitudinal structure and change in vegetation has been attempted in the western Himalayas based on remote sensing tools (Singh et al. 2012; Sah et al. 2023). However, the lack of methodological errors and sufficient ground observation verification made these studies less accepted. Recent studies have documented significant land use and land cover (LULC) changes across Uttarakhand (Singh and Singh, 1987). The Garhwal Himalayan region has experienced substantial forest fragmentation, with the loss of forest cover and the loss of grassland cover in the Rudraprayag district (Forest Survey of India, 2019). Studies have documented shifts of 23-998 m in species' upper elevation limits and a mean upward displacement rate of 27.53±22.04 m/decade in Himalayan ecosystems (Rana et al. 2019). Key species exhibiting these elevational shifts include Abies spectabilis, Betula utilis, and Rhododendron campanulatum (Rawal et al. 2025). More temperature-sensitive functional groups, such as dwarf shrubs, herbs, grasses, bryophytes, and lichens in the Himalayas, have migrated northwards to cooler climates (Rana et al. 2019). It is essential to comprehend these interrelated changes to create plans to lessen the negative effects of these changes, guarantee sustainable livelihoods, and preserve the ecosystem. The land use and land cover patterns in high-altitude regions have changed significantly, and this is especially evident in the Himalayan region. The Chamoli district presents a unique case study for understanding these dynamics with its diverse elevation gradient range. The changes at various altitudes limit the quantity and quality of forage, which directly impacts land use practices and local livelihoods (Tasser and Tappeiner, 2002). This study examines four decades (1983-2023) of land use and land cover changes in Chamoli, focusing particularly on tree cover and grassland dynamics. The research aims to quantify these changes across different elevation zones.

Study Area

Chamoli district is in the Garhwal Himalayas of Uttarakhand, India. It is a high-altitude mountainous area known for its varied topography, rich biodiversity, and ecological importance. The district is located between 30°05'N to 31°25'N latitudes and 79°10'E to 80°30'E longitudes. It covers an area of approximately 8,030 km^2. The terrain features steep slopes, deep valleys, and high-altitude meadows (Bugyals). Elevations range from 800 m to over 7,800 m, including peaks such as Nanda Devi (7,816 m). Chamoli has a temperate to alpine climate. The lower valleys receive moderate rainfall during monsoons, while higher elevations experience heavy snowfall in winter. The region is home to treeline ecotones, where the transition between subalpine forests and alpine meadows takes place. Major vegetation types include oak, rhododendron, and coniferous forests at lower altitudes, which gradually change to alpine grasslands. Chamoli is ecologically vital, shown by its diverse land use types. Chamoli is a critical site for studying treeline shifts, meadow dynamics, and ecological responses to climate change.

Methodology

The study uses a combination of remote sensing and GIS techniques to analyse changes in land use and land cover, vegetation density patterns, and treeline and grassland cover over time. Multi-temporal satellite images from 1983, 1993, 2003, 2013, and 2023 were used to detect changes in vegetation cover, grasslands, and treelines. Digital Elevation Model (DEM) data is also used to extract topographic parameters such as elevation. DEM processing and GIS-based spatial analysis help in understanding terrain characteristics that influence vegetation and land cover dynamics. To ensure consistency and accuracy in data analysis, satellite images were pre-processed, including stacking, mosaicking, and clipping, based on the study area. A pixel-based classification method, the Spectral Angle Mapper (SAM), is applied to classify different land cover types. Various research indices are employed to assess vegetation health and landscape changes. The Normalised Difference Vegetation Index (NDVI) was used to evaluate vegetation density. Additionally, the Soil-Adjusted Vegetation Index (SAVI) was computed to further assess vegetation conditions. Land use and land cover classification was performed to differentiate between grasslands, forests, and other landscape features. Vegetation positions in each period were identified using image classification algorithms. Spatial interpolation was conducted to estimate vegetation positions between observed points. GIS techniques were used to overlay vegetation data with other spatial datasets such as land use, land cover, and topography. Grassland and treeline positions were extracted using classification results. The spatial and temporal distribution and shifting trends of meadows and treelines over different periods were analysed. Digital elevation models were obtained to analyse elevation-related factors affecting vegetation dynamics. The methodological framework can be seen in Figure 2 below.

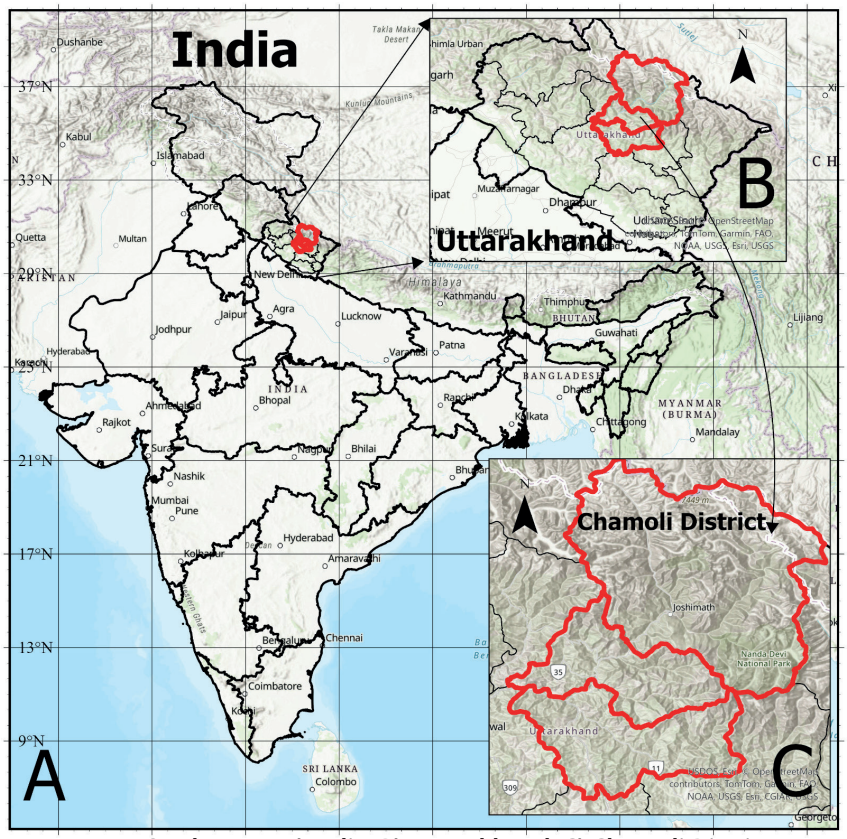

Fig. 1. Study Area, A) India, B) Uttarakhand, C) Chamoli District

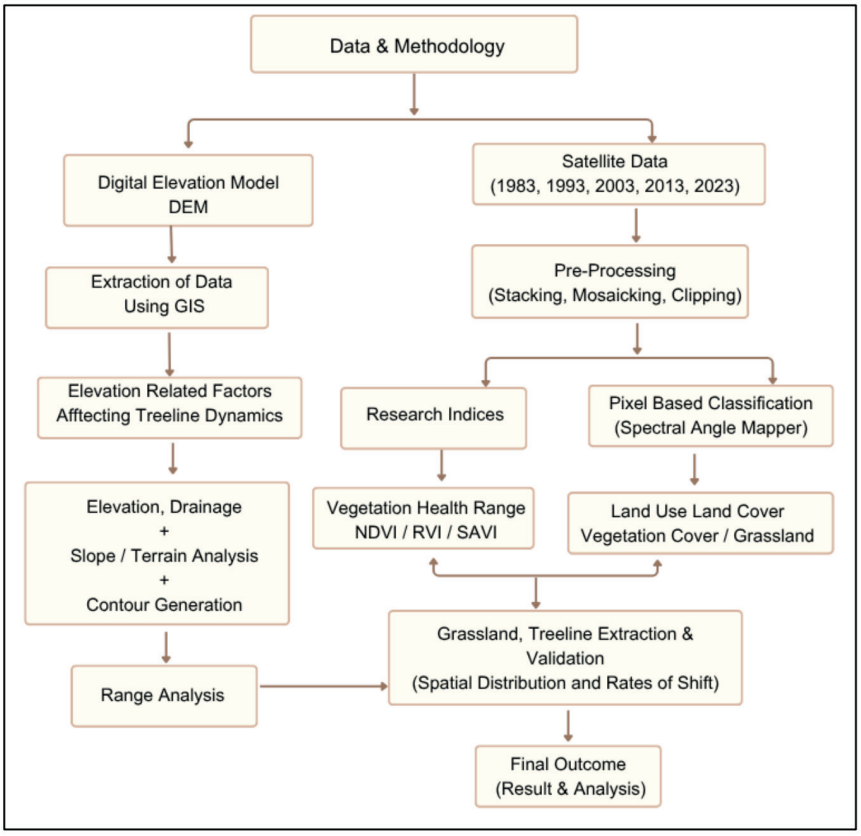

Fig. 2. Methodological Framework

Methods for assessing the quality of the classification

To ensure the reliability and accuracy of the LULC classification results, a comprehensive accuracy assessment was performed. The assessment process followed standard remote sensing classification evaluation protocols to provide a thorough evaluation of classification performance. Reference data for accuracy assessment were collected through a combination of high-resolution satellite imagery interpretation, field surveys, and existing land cover databases. Ground truth points were systematically distributed across the study area using a stratified random sampling approach to ensure representative coverage of all land cover classes, including agricultural land, tree cover, grasslands, built-up areas, snow cover, water bodies, and bare land. Reference points were selected based on the number of land cover classes.

Error Matrix Construction

The accuracy assessment was conducted using confusion matrices for each temporal period (1983, 1993, 2003, 2013, and 2023). The error matrix is a square array where rows represent reference data (ground truth) and columns represent classified data. This matrix provides the basis for calculating various accuracy metrics by comparing classified pixels with their corresponding reference classifications on a class-by-class basis.

Accuracy Metrics Calculation

Quantitative accuracy measures were derived from the error matrices. Overall Accuracy was calculated as the percentage of correctly classified pixels relative to the total reference pixels, providing a general measure of classification performance. Producer's Accuracy, computed for each class, represents the probability that reference pixels are correctly classified, while User's Accuracy indicates the likelihood that pixels assigned to a class truly belong to it. The Kappa Coefficient, ranging from 0 to 1, was employed to evaluate the agreement between classified and reference data beyond chance, with values approaching 1 denoting higher accuracy.

Results and Discussion

Temporal Changes and Deviation in LULC

Over the past four decades, land-use and land-cover changes reveal critical environmental and socio-economic dynamics (Table 1). Temporal analysis shows that tree cover fluctuated significantly. It initially increased from 224,027 hectares in 1983 to 346,453 hectares in 2003, reflecting successful reforestation and natural regeneration efforts. However, this was followed by a decline to 273,528 hectares in 2013. By 2023, tree cover had partially recovered to 323,554 hectares, showing renewed conservation efforts (an increase of 44.43 percent). Grassland areas have varied over the past 40 years. The area increased from 93,647 hectares in 1983 to 120,103 hectares in 1993, followed by a decline to 78,081 hectares in 2003. By 2013, grassland areas had expanded significantly to 199,293 hectares, but then decreased again to 118,330 hectares in 2023 (an overall increase of 26.36 percent). These fluctuations can be attributed to changes in agricultural practices, grazing pressure, and land management policies. Agricultural land saw an increase from 12,300 hectares in 1983 to 20,147 hectares in 1993. This was followed by a gradual decline to 16,148 hectares in 2013. By 2023, agricultural land had slightly recovered to 17,050 hectares (an increase of 38.62 percent). These changes reflect shifts in land use due to urbanisation, land degradation, and possibly changes in agricultural practices. Built-up areas have expanded dramatically, indicating urbanisation and infrastructure development. From 216 hectares in 1983, the area of built-up land increased to 9,349 hectares by 2023. This growth corresponds to population increases, economic development, and the expansion of urban areas. It highlights the socio-economic transformation in the district. Water bodies have experienced minor fluctuations over the decades. Starting at 2,985 hectares in 1983, the area stabilised around 2,917 hectares by 2023. These slight variations suggest natural changes in water levels influenced by climate conditions, human consumption, and water management practices. The area of barren land has increased substantially, rising from 69,784 hectares in 1983 to an alarming 209,677 hectares in 2023 (an increase of 200.47 percent). This increase indicates severe land degradation, likely due to deforestation, soil erosion, and possibly the abandonment of agricultural lands.

The dramatic rise in barren land highlights the urgent need for sustainable land management practices. Snow cover has significantly declined over the past four decades, from 377,885 hectares in 1983 to just 99,606 hectares in 2023, a drastic decrease of 63.64 percent. This reduction highlights the impact of warming trends, which have resulted in decreased snowfall and accelerated glacial melting. The sharp decrease between 2013 and 2023 shows the severity of climate change effects on high-altitude ecosystems. A temporal analysis of Chamoli district's landscape over 40 years reveals critical environmental challenges and socio-economic developments. This change is a particularly concerning point regarding environmental degradation and the impact of climate change. Fluctuations in tree cover and grassland areas highlight the dynamic nature of ecological responses to a changing climate. The temporal analysis of land use and land cover over the last four decades reveals notable trends and shifts. Water bodies, with slight fluctuations, showed a decrease of 2.28 percent. Barren land has seen a dramatic increase of 200.47 percent. Tree cover has increased by 44.43 percent. Built-up areas have expanded tremendously by 4228.35 percent. Grassland areas have experienced varying trends with an overall increase of 26.36 percent. Snow cover has dramatically decreased by 73.64 percent. Agricultural land has increased by 38.62 percent.

Figure 3 shows the spatial distribution of land cover changes across five temporal periods in the study area (1983-2023). The multi-temporal analysis reveals distinct patterns of vegetation dynamics. These maps demonstrate

Table 1. Land Use/Land Cover percentage change, 1983-2023

LULC Classes	Area in Hectares					LULC Change (Percentage)				
	1983	1993	2003	2013	2023	1983-1993	1993-2003	2003-2013	2013-2023	1983-2023
Water bodies	2,985	3,015	3,056	2,668	2,917	1.01	1.35	-12.68	9.32	-2.28
Barren Land	69,784	1,00,912	91,845	1,17,622	2,09,677	44.61	-8.99	28.07	78.26	200.47
Tree Cover	2,24,027	2,86,714	3,46,453	2,73,528	3,23,554	27.98	20.84	-21.05	18.29	44.43
Built-up Areas	216	483	464	5,691	9,349	123.61	-3.84	1,125.29	64.28	4,228.35
Grassland	93,647	1,20,133	78,081	1,99,293	1,18,330	28.25	-34.99	155.24	-40.63	26.36
Snow Cover	3,77,885	2,49,255	2,39,413	1,66,976	99,606	-34.04	-3.95	-30.26	-40.35	-73.64
Agricultural Land	12,300	20,147	19,616	16,148	17,050	63.8	-2.63	-17.68	5.58	38.62

the temporal evolution of landscape patterns and potential land use transformations within the defined geographic boundary.

Elevation-Based Changes

The analysis based on elevation shows that several land cover types, including tree cover, grasslands, snow cover, water bodies, barren land, built-up areas, and agricultural land, have changed (Table 2). At an elevation of 683–2051 metres in 1983, grasslands covered 28,105 hectares, while tree cover was 91,268 hectares. By 1993, grasslands had reduced significantly to 12,316 hectares, and tree cover increased to 107,170 hectares. This trend continued in 2003, with grasslands slightly recovering to 13,430 hectares and tree cover reaching its highest at 126,178 hectares. In 2013, grasslands surged to 38,351 hectares, possibly due to conservation efforts or reduced agricultural pressure. However, they decreased again to 24,135 hectares in 2023. Built-up areas increased substantially from 216 hectares in 1983 to 7,763 hectares in 2023, reflecting urban expansion. Water bodies and barren land remained relatively stable with minor changes. At 2052–3053 metres elevation, grasslands increased from 22,831 hectares in 1983 to a peak of 52,801 hectares in 2013 before declining to 38,596 hectares in 2023. Tree cover followed a different pattern, increasing significantly from 111,228 hectares in 1983 to 142,469 hectares in 2003, then stabilising around 128,104 hectares by 2023. Barren land fluctuated considerably, with a slight increase in 1993 and a rapid increase by 2023. Built-up areas saw a gradual increase from 1993, indicating the spread of human settlements. Agricultural land fluctuated but generally remained at lower levels compared to other land cover classes. At the elevation of 3054–4159 metres, grassland cover showed notable variations. It initially increased to 56,752 hectares in 1993, decreased to 45,470 hectares in 2003, and then rose to 48,655 hectares by 2023. Tree cover showed substantial growth from 21,229 hectares in 1983 to 70,282 hectares in 2003, stabilising around 55,860 hectares in 2023. Snow cover and barren land also fluctuated, with significant decreases in snow cover by 2023.

Built-up areas and agricultural land remained minimal, reflecting the harsh conditions and limited human activity at these elevations. Furthermore, at the 4150–5152 metre elevation range, grasslands experienced significant changes, increasing dramatically to 37,174 hectares in 1993 and decreasing to 16,940 hectares by 2023. Tree cover increased from 11,147 hectares in 1983 to 16,190 hectares in 2023. Barren land and snow cover also saw significant fluctuations, with snow cover decreasing sharply by 2023. Built-up areas remained negligible, while agricultural land saw slight increases. The highest elevation range showed minimal grassland cover throughout the decades, peaking at 302 hectares in 1993 and minor growth by 2023. Snow cover remained dominant but decreased significantly from 155,069 hectares in 1983 to 80,374 hectares in 2023. There were no built-up area and agricultural land remained absent, reflecting the extreme environmental conditions. The 3054–4149 metre elevation range witnessed the most significant changes, particularly in tree cover and grasslands. Grasslands increased initially but saw substantial

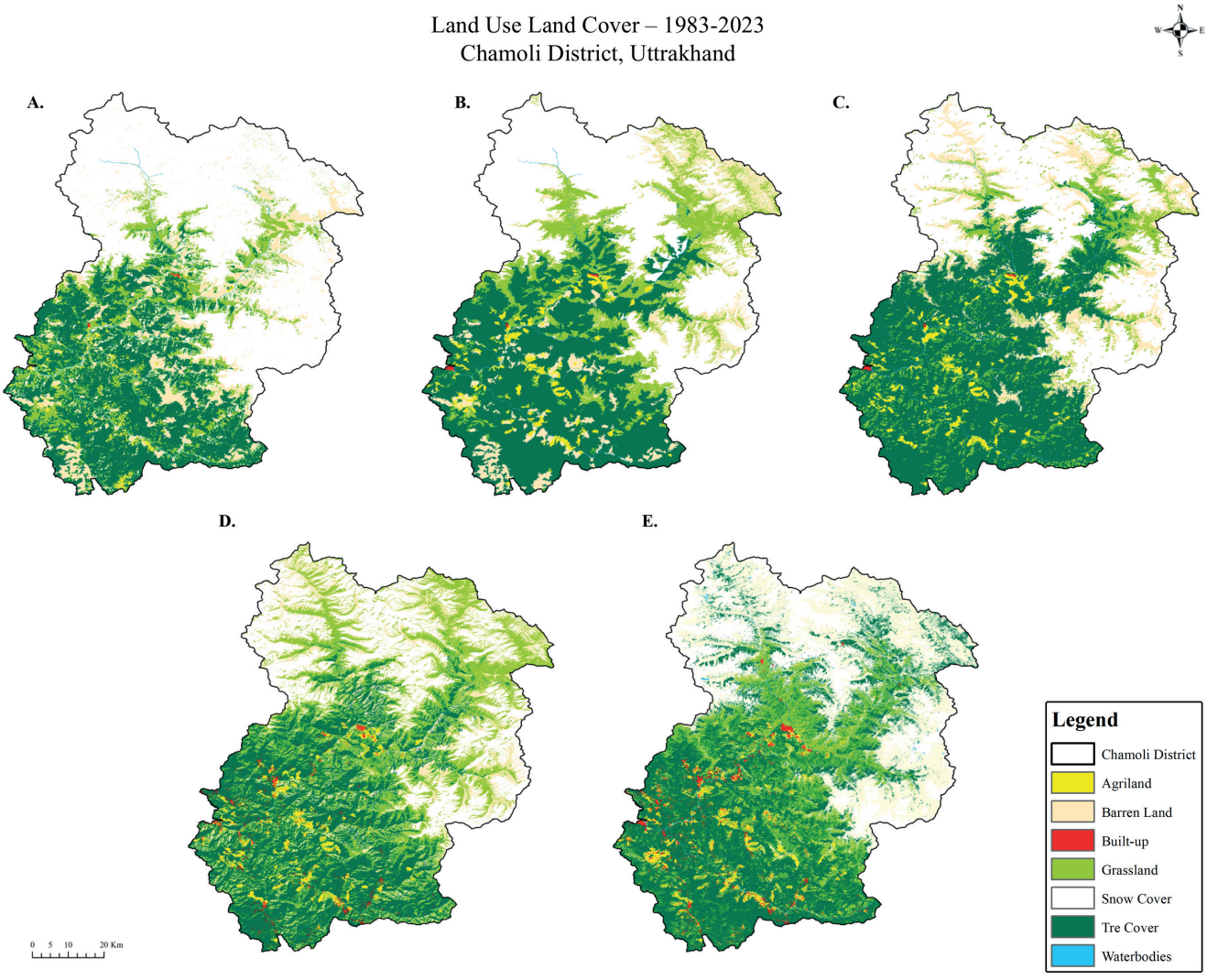

Fig. 3. LULC of Chamoli District: a) 1983, b) 1993, c) 2003, d) 2013 and e) 2023

fluctuations, while tree cover showed considerable growth and stabilisation trends. Snow cover decreased drastically. The analysis reveals that lower elevations have seen significant urbanisation and agricultural activities, while mid to higher elevations have experienced changes in grassland and tree cover, reflecting both natural and anthropogenic influences over the decades.

The changes are visible in high-altitude regions, particularly from elevations above 3000m. Between 3054m and 5152m, both tree cover and grasslands increased significantly in the last four decades. This indicates positive changes in vegetation cover, suggesting climate change impacts and shifts towards higher altitudes. Figure 4 below provides a comprehensive understanding of the prevailing scenario.

LULC Classification Assessment Results

The classification accuracy assessment across 1983, 1993, 2003, 2013, and 2023 demonstrated a steady improvement in reliability. In 1983, the classification achieved an overall accuracy of 82.34% with a Kappa coefficient of 0.79. By 1993, the overall accuracy increased to 85.39% with a Kappa of 0.82. In 2003, the overall accuracy further improved to 88.36% with a Kappa of 0.85. The 2013 classification showed a substantial increase, with an overall accuracy of 91.02% and a Kappa of 0.89. The highest accuracy was recorded in 2023, with an overall accuracy of 93.21% and a Kappa of 0.91. Overall, the results indicate a clear improvement in classification performance over four decades.

Spatio-Temporal Dynamics of Tree Cover

The spatio-temporal analysis of tree cover distribution across different elevation zones was conducted (Table 3). It revealed significant variations over the 40 years from 1983 to 2023. In the lowest elevation zone (683-2052m), tree cover expanded from 91,268 hectares in 1983 to peak at 126,178 hectares in 2003, followed by a slight decline to 116,793 hectares by 2023. The mid-elevation zone (2052-3053m) showed the most substantial tree cover,

Table 2. Elevation-based changes (1983–2023)

Elevation (meters)	Year	Water	Barren	Tree- Cover	Built-up	Grassland	Snow	Agriculture
683 - 2051	1983	2140	18911	91268	216	28105	0	10588
	1993	2184	23384	107170	477	12316	0	15171
	2003	1984	800	126178	463	13430	0	14590
	2013	797	7766	103758	4830	38351	0	12226
	2023	1493	3105	108528	7763	24135	0	12653
2052 -3053	1983	443	14535	111228	107	22831	0	1673
	1993	430	7729	132847	238	13461	0	4816
	2003	443	1701	142469	311	27596	0	4417
	2013	185	12331	111709	834	52801	0	3534
	2023	284	3445	128104	1321	38596	0	2610
3054 - 4149	1983	276	26718	21229	33	37765	40491	139
	1993	277	15319	44361	53	56752	19612	151
	2003	315	27897	70282	127	35470	5668	610
	2013	257	18731	52131	148	65868	2367	1389
	2023	373	21569	55860	187	48655	1130	1726
4150 - 5152	1983	117	7789	11147	27	14697	166415	0
	1993	123	42123	11623	38	37174	97604	0
	2003	113	49519	7307	47	11268	93820	0
	2013	132	47273	13737	59	41877	59800	0
	2023	289	109115	16190	78	16940	18092	0
5153 - 7801	1983	0	1813	66	0	228	155069	0
	1993	0	12275	48	0	302	140441	0
	2003	0	11910	31	0	276	139788	0
	2013	0	31514	42	0	251	104674	0
	2023	379	72442	71	0	103	80374	0

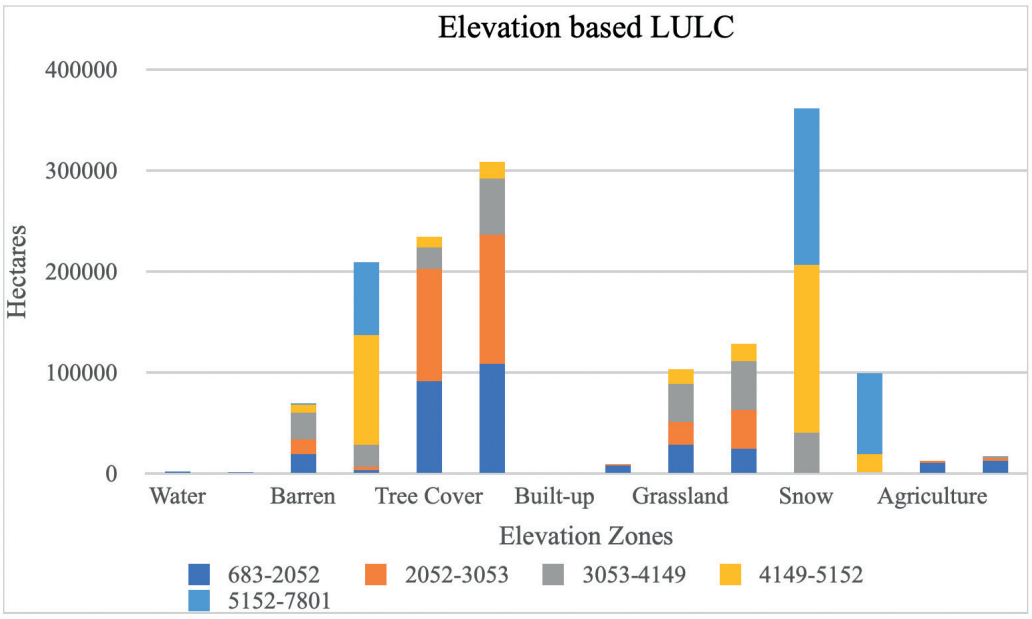

Fig. 4. Elevation-based changes in land-use patterns, 1983 and 2023

increasing from 111,228 hectares in 1983 to a maximum of 142,468 hectares in 2003, before stabilising around 115,942 hectares in 2023. Notable changes occurred in higher elevations, particularly in the 3053-4149m range, where tree cover more than tripled from 21,229 hectares in 1983 to 70,281 hectares in 2003, though moderating to 52,967 hectares by 2023. The most dramatic transformation was observed in the 4149-5152m zone, with tree cover expanding from merely 147 hectares in 1983 to 44,189 hectares by 2023, indicating significant upward treeline migration. The highest elevation zone (5152-7801m) also experienced notable changes, from 66 hectares in 1983 to 3,870 hectares in 2023, suggesting potential climate-driven vegetation responses at extreme altitudes.

Figure 5 shows how tree cover has changed in the area between 1983 and 2023. The different colours on the map indicate the spatial changes over these years.

Temporal Dynamics of Grasslands

The distribution of grassland across different elevations in the district was analysed. The analysis revealed significant changes in grassland distribution over time and across various altitudes (Table 4). At lower elevations (683-2052 metres), the grassland area decreased from 28,105 hectares in 1983 to 12,316 hectares in 1993. This decline is likely due to human activities such as agriculture, urbanisation, and other development. However, grassland cover substantially recovered by 2013, reaching 38,351.36 hectares. This was followed by a reduction to 24,134.64 hectares of grassland in 2023, showing a 14 percent decrease over 40 years. This suggests continued pressure from human activity or other environmental changes. Grassland cover followed a similar pattern in the mid-elevation range (2052-3053 metres). It decreased from 22,831 hectares in 1983 to 13,461 hectares in 1993, and then increased to 52,800.87 hectares by 2013. It decreased again to 38,595.93 hectares in 2023, representing a 69 percent increase. These fluctuations indicate a dynamic interaction between human land use and natural processes, with periods of both recovery and decline influenced by grazing practices, forestry activities, and climatic factors. Higher elevations (3053-4149 metres) showed considerable variation, with an increase in grassland area from 37,765 hectares in 1983 to 56,752 hectares in 1993. This was followed by a decrease to 25,469.78 hectares in 2003. Grassland cover expanded significantly to 65,868.20 hectares by 2013 and declined to 48,654.96 hectares in 2023, a 29 percent decrease. These changes reflect the impact of climate change, human-environment relationships, and grazing pressures on the extent of grasslands at these altitudes.

In the highest elevation ranges (4149-5152 metres and 5152-7801 metres), grassland areas showed extreme volatility. The grassland cover increased significantly in 1993 but decreased considerably in subsequent years. By 2023, only 16,939.94 hectares remained in the 4149–5152-metre range, representing an 18 percent increase from the 1983 period. At the 5152–7801-metre range, there was a drastic

Table 3. Elevation-wise Area of Tree Cover (in hectares)

Elevation Wise Area of Tree Cover (In Hec.)					
Elevation (in m)	1983	1993	2003	2013	2023
	Tree Cover	Tree Cover	Tree Cover	Tree Cover	Tree Cover
683-2052	91268	107170	126178.35	116175.42	116793.72
2052-3053	111228	132847	142468.52	115253.22	115942.00
3053-4149	21229	44361	70281.71	52520.22	52967.29
4149-5152	147	1623	7306.70	5736.95	44189.70
5152-7801	66	1.3	31.38	1.75	3870.85

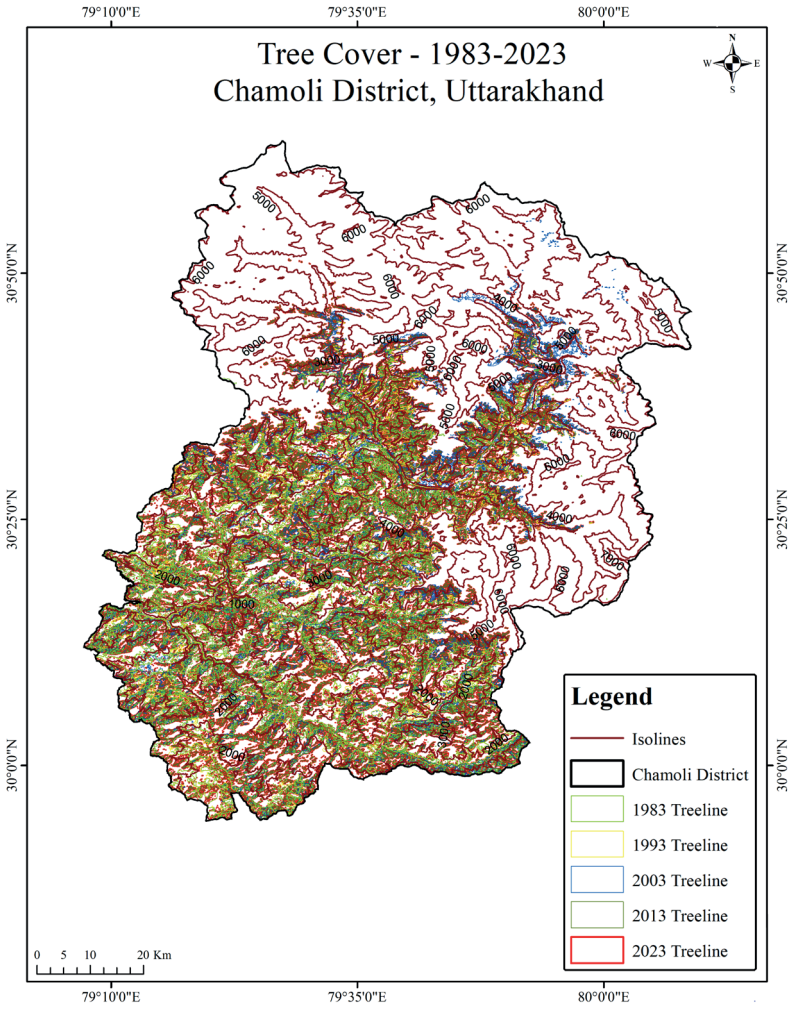

Fig. 5. Tree cover and pattern, Chamoli district

Table 4. Elevation-wise area of grassland (in hectares).

Area of Grassland Based on Elevation (in Ha.)						
Sr. No.	Elevation (in m)	1983	1993	2003	2013	2023
1	683-2052	28105	12316	13429.86	38351.36	24134.64
2	2052-3053	22831	13461	27595.86	52800.87	38595.93
3	3053-4149	37765	56752	35469.78	65868.20	48654.96
4	4149-5152	14697	37174	11268.36	31877.32	16939.94
5	5152-7801	228	302	276.30	250.99	103.27

reduction to 103.27 hectares. These trends suggest that harsh climatic conditions and land-use changes, such as grazing and environmental degradation, have severely impacted these higher altitude grasslands, making them less sustainable over time. The overall trends reflect how conservation efforts, agricultural practices, and climatic changes have shaped grassland distribution over four decades. The data suggest that lower and middle elevations have seen more significant human impact, whereas higher elevations show more resilience to change but still experience fluctuations due to environmental conditions. (A detailed examination of vegetation density can be seen in Appendix B, Table 1 and Figure 1). The trend of grasslands shifting upwards in elevation can be seen in the map below (Fig. 6) from 1983 to 2023. This upward migration can be observed through the changing colour patterns across the district. Each colour on the map corresponds to grassland elevation in different decades, indicating the distribution and movement of grasslands. In 1983, grasslands were primarily concentrated in lower and mid-elevation regions. However, over the years, a noticeable upward shift in grassland cover can be observed. In the earlier years, grasslands were more extensive at lower elevations, as shown by the significant green areas in the lower and central parts of the district in 1983. Over the decades, there has been a clear trend of grasslands receding from these lower regions, with a corresponding increase in grassland areas at higher altitudes. The yellow areas (representing 1993) and the orange areas (representing 2003) show a gradual migration of grasslands towards higher elevations. By 2013, as shown by the light blue areas, grasslands continued to extend further up, occupying regions that were previously not covered by grasslands. The most recent decade, 2023, represented by the red areas, shows a prominent presence of grasslands at the highest elevations.

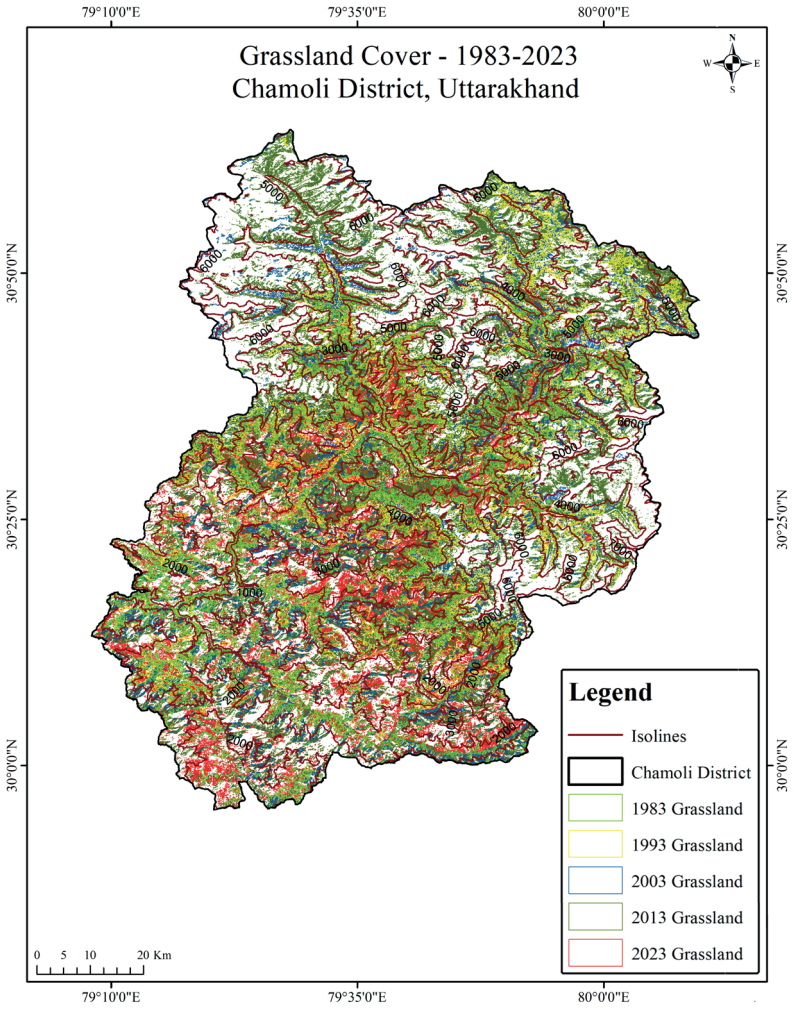

Fig. 6. Temporal trend of grasslands, 1983–2023

This trend highlights how grasslands have progressively moved from lower to higher altitudes over the past four decades. This shift can be attributed to various factors, including climate change, which has altered temperature and precipitation patterns, making lower elevations less suitable for grasslands. Additionally, increased human activities such as agriculture and urbanisation at lower elevations have contributed to this upward movement, pushing grasslands to higher altitudes where conditions are more favourable for their growth. A clear pattern can be seen with grasslands adapting to changing environmental conditions by shifting upwards over the years.

DISCUSSION

Land use and land cover patterns in high-altitude regions have changed significantly (Rawat and Schickhoff 2022). One of the critical influences of these changes is on tree cover and grasslands. The four-decade analysis of LULC changes in the district reveals complex spatio-temporal dynamics with significant implications for mountain ecosystems and local communities. Our findings demonstrate a paradoxical landscape transformation characterised by simultaneous forest recovery and environmental degradation. The substantial increase in tree cover over the study period, particularly at higher elevations, aligns with observations by Kumar and Khanduri (2024), who documented upward shifts in vegetation zones across the Himalayan region. The fluctuating patterns of tree cover, with initial increases followed by periods of decline and partial recovery, align with findings from other Himalayan regions where conservation efforts have competed with development pressures. Similar to observations by Rawat and Schickhoff (2022), who documented complex vegetation dynamics in high-altitude Himalayan ecosystems, our study found that tree cover increased by 44.43 percent over the study period. This indicates some success in reforestation initiatives despite intervening challenges.

These findings also support Tewari et al. (2017) and Walia et al. (2025) conclusion that Himalayan forests experience cyclic patterns of degradation and regeneration influenced by both natural processes and management interventions. The dramatic expansion of tree cover in the 4149–5152 m elevation zone (from 147 to 44,189 hectares) represents clear evidence of treeline advancement, consistent with Harsch et al.'s (2009) global meta-analysis of treeline responses to climate warming. This also corresponds with Schickhoff et al. (2015), who documented treeline shifts in response to warming trends across the Himalayas. The increased vegetation at extreme altitudes suggests a warming-induced habitat expansion for tree species, consistent with global observations of upslope migration of plant communities (Lenoir et al. 2008). However, this must be viewed alongside concerning degradation trends. The 200.47 percent increase in barren land and the 73.64 percent decrease in snow cover indicate severe environmental stress in the region. These findings point towards Immerzeel et al. (2020) research highlighting accelerated glacial retreat across the Hindu Kush Himalaya, with profound implications for water security and ecosystem stability. The reduction in snow cover is particularly alarming as it threatens the hydrological regime that supports downstream communities and

ecosystems (Bolch et al. 2019). The fluctuating patterns of grassland distribution across elevation gradients (with overall increases of 26.36 percent) reflect a dynamic interplay between climate forcing and anthropogenic pressures. This supports Tasser and Tappeiner's (2002) findings that mountain grasslands undergo complex transitions influenced by both land management practices and environmental changes. The upward shift of grasslands observed in our study is similar to the findings of Parmesan and Yohe (2003), who documented elevation shifts in numerous plant species globally in response to warming. The fluctuating grassland coverage, with overall increases at mid-elevations but volatility at higher elevations, has also been documented by Suwal et al. (2016), who documented elevation-dependent responses of alpine vegetation to climate change. These grassland shifts directly impact traditional pastoral livelihoods, as noted by Kassahun et al. (2008), who documented how changing vegetation patterns disrupt transhumance practices.

The dramatic expansion of built-up areas, by 4228.35 percent, represents the most striking anthropogenic transformation. This reflects the rapid urbanisation patterns observed throughout the Himalayan region by Dame et al. (2019), and Anees et al. (2021). This expansion exerts pressure on surrounding ecosystems and traditional land use systems, contributing to the fragmentation of natural habitats. These multifaceted changes have significant implications for local livelihoods, particularly for traditional pastoral communities. As noted by Bhusal and Awasthi (2024), shifting vegetation patterns disrupt transhumance practices that have sustained mountain communities for generations. The upward migration of vegetation zones forces adaptation in grazing patterns and resource use, potentially undermining traditional ecological knowledge systems (Mishra 2001). The interdependence between land use and land cover patterns has resulted in a landscape that is less supportive of traditional grazing practices, further threatening the livelihoods of communities that rely on these lands for sustenance. For sustainable management of the landscapes, integrated approaches that balance conservation with livelihood needs are essential. This requires technical interventions for land restoration and meaningful engagement with local communities. Their traditional knowledge can inform adaptive management strategies (Saxena et al. 2002). Future research should focus on investigating vegetation responses to climate change scenarios and developing adaptive management frameworks that incorporate both scientific data and traditional ecological knowledge. This integrated approach will be crucial for building resilience in mountain social-ecological systems facing rapid environmental change.

CONCLUSION

The land use and land cover of the district have changed significantly over the last few decades. Consequently, major alterations have occurred in the district's landscape and ecology. Tree cover is most prominent at lower altitudes, decreasing as altitude increases. Built-up areas and grasslands are expanding across various zones, particularly at mid-altitudes. Snow cover dominates higher altitudes, between 5153–7801 m, but has shown a declining trend in recent years. The findings suggest that tree cover has fluctuated considerably, indicating successful natural and human-driven conservation efforts. Grassland areas have also shown variability over the past 40 years. Both tree cover and grassland areas have increased in recent decades. These fluctuations in tree cover and grassland areas emphasise the dynamic nature of ecological responses. The elevation range of 3054–4149 metres experienced the most significant changes. Lower elevations have seen considerable urbanisation and agricultural development, while mid to higher elevations have undergone changes in grassland and tree cover, reflecting both natural and human influences. These changes are noticeable in high-altitude regions, especially above 3000 metres. This suggests vegetation is shifting to higher altitudes. These shifts are not uniform and vary within each elevation range. The changes are attributed to various factors, including human activities, climate change, and natural succession processes. These trends highlight the dynamic nature of changes within the district, driven by varying land management practices.

REFERENCES

Anderson, K., Fawcett, D., Cugulliere, A., Benford, S., Jones, D., & Leng, R. (2020). Vegetation expansion in the subnival Hindu Kush Himalaya. Global Change Biology, 26(3), 1608-1625. https://doi.org/10.1111/gcb.14919

Anees, M. M., Sharma, R., & Joshi, P. K. (2021). Urbanization in Himalaya—An interregional perspective to land use and urban growth dynamics. In Mountain landscapes in transition: effects of land use and climate change (pp. 517-538). Cham: Springer International Publishing. https://doi.org/10.1007/978-3-030-70238-0_23

Bagchi, S., Mishra, C., & Bhatnagar, Y. V. (2004, May). Conflicts between traditional pastoralism and conservation of Himalayan ibex (Capra sibirica) in the Trans-Himalayan mountains. In Animal Conservation Forum (Vol. 7, No. 2, pp. 121-128). Cambridge University Press. https://doi.org/10.1017/S1367943003001148

Bhusal, P., & Awasthi, K. R. (2024). Challenges to Transhumant Pastoralism Due to Socioeconomic and Ecological Changes in Nepal's High Mountains. In Lifestyle and Livelihood Changes Among Formerly Nomadic Peoples: Entrepreneurship, Diversity and Urbanisation (pp. 167-183). Cham: Springer Nature Switzerland. https://doi.org/10.1007/978-3-031-51142-4_7

Bolch, T., Shea, J. M., Liu, S., Azam, F. M., Gao, Y., Gruber, S., ... & Yao, T. (2019). Status and change of the cryosphere in the Extended Hindu Kush Himalaya Region. In The Hindu Kush Himalaya Assessment (pp. 209-255). Springer. https://doi.org/10.1007/978-3-319-92288-1_7

Dame, J., Schmidt, S., Müller, J., & Nüsser, M. (2019). Urbanisation and socio-ecological challenges in high mountain towns: Insights from Leh (Ladakh), India. Landscape and urban planning, 189, 189-199. https://doi.org/10.1016/j.landurbplan.2019.04.017

Duffy, P. B., Brando, P., Asner, G. P., & Field, C. B. (2015). Projections of future meteorological drought and wet periods in the Amazon. Proceedings of the National Academy of Sciences, 112(43), 13172-13177. https://doi.org/10.1073/pnas.1421010112

Flantua, S. G. A., van Boxel, J. H., Hooghiemstra, H., & van Smaalen, J. (2007). Application of GIS and logistic regression to fossil pollen data in modelling present and past spatial distribution of the Colombian savanna. Climate Dynamics, 29, 697–712. https://doi.org/10.1007/s00382-007-0276-3

FSI. (2019). India state of forest report 2019. Forest Survey of India. https://fsi.nic.in/forest-report-2019

Rawal, R., Dasila, K., Kishor, K., & Tewari, L. M. (2025). Pattern of forest structure and species regeneration along with elevation gradients and aspects in evergreen oak forest belt of the Western himalaya. Discover Plants, 2(1), 1-20. https://doi.org/10.1007/s44372-025-00381-3

Galvin, K. A., Reid, R. S., Behnke Jr, R. H., & Hobbs, N. T. (2008). Fragmentation in semi-arid and arid landscapes. Consequences for Human and Natural Systems. https://hdl.handle.net/10568/1305

Grace, J., Berninger, F., & Nagy, L. (2002). Impacts of climate change on the tree line. Annals of Botany, 90(4), 537-544. https://doi.org/10.1093/aob/mcf222

Hansen, M. C., Stehman, S. V., Potapov, P. V., Loveland, T. R., Townshend, J. R., De Fries, R. S., & Di Miceli, C. (2008). Humid tropical forest clearing from 2003 to 2005 quantified by using multitemporal and multiresolution remotely sensed data. Proceedings of the National Academy of Sciences, 105(27), 9439-9444. https://doi.org/10.1073/pnas.0804042105

Harsch, M. A., Hulme, P. E., McGlone, M. S., & Duncan, R. P. (2009). Are treelines advancing? A global meta-analysis of treeline response to climate warming. Ecology Letters, 12(10), 1040-1049. https://doi.org/10.1111/j.1461-0248.2009.01355.x

Harsch, M. A., & Bader, M. Y. (2011). Treeline form: A potential key to understanding treeline dynamics. Global Ecology and Biogeography, 20(4), 582-596. https://doi.org/10.1111/j.1466-8238.2010.00622.x

Holtmeier, F. K., & Broll, G. (2005). Sensitivity and response of northern hemisphere altitudinal and polar treelines to environmental change at landscape and local scales. Global Ecology and Biogeography, 14(5), 395-410. https://doi.org/10.1111/j.1466-822X.2005.00168.x

Holtmeier, F. K., & Broll, G. E. (2007). Treeline advance-driving processes and adverse factors. Landscape Online, 1, 1-33. https://doi.org/10.3097/LO.200701

Holtmeier, F. K., & Broll, G. (2012). Landform influences on treeline patchiness and dynamics in a changing climate. Physical Geography, 33(5), 403-437. https://doi.org/10.2747/0272-3646.33.5.403

Immerzeel, W. W., Lutz, A. F., Andrade, M., Bahl, A., Biemans, H., Bolch, T., ... & Baillie, J. E. M. (2020). Importance and vulnerability of the world's water towers. Nature, 577(7790), 364-369. https://doi.org/10.1038/s41586-019-1822-y

Jobbágy, E. G., & Jackson, R. B. (2003). Global controls of forest line elevation in the northern and southern hemispheres. Global Ecology and Biogeography, 9(3), 253-268. https://doi.org/10.1046/j.1365-2699.2000.00162.x

Joshi, G., & Negi, G. C. (2011). Quantification and valuation of forest ecosystem services in the western Himalayan region of India. International Journal of Biodiversity Science, Ecosystem Services & Management, 7(1), 2-11. https://doi.org/10.1080/21513732.2011.598134

Kassahun, A., Snyman, H. A., & Smit, G. N. (2008). Impact of rangeland degradation on the pastoral production systems, livelihoods and perceptions of the Somali pastoralists in Eastern Ethiopia. Journal of Arid Environments, 72(7), 1265-1281. https://doi.org/10.1016/j.jaridenv.2008.01.002

Kullman, L. (2001). 20th century climate warming and tree-limit rise in the southern Scandes of Sweden. Ambio: A Journal of the Human Environment, 30(2), 72-80. https://doi.org/10.1579/0044-7447-30.2.72

Kumar, R., Krishnia, P., Kumari, V., & Sharma, C. (2025). Perception on Livestock Changes and Its Socio-Economic Implications Among Agro-pastoralists: A Case Study of Agro-pastoralists in Joshimath Block in Chamoli. Revista Geográfica de Chile Terra Australis, 61(1). https://doi.org/10.23854/07199562.2025611.kumar2

Kumar, S., & Khanduri, V. P. (2024). Impact of climate change on the Himalayan alpine treeline vegetation. Heliyon, 10(23). https://doi.org/10.1016/j.heliyon.2024.e40797

Lefroy, R. D., Bechstedt, H. D., & Rais, M. (2000). Indicators for sustainable land management based on farmer surveys in Vietnam, Indonesia, and Thailand. Agriculture, ecosystems & environment, 81(2), 137-146. https://doi.org/10.1016/S0167-8809(00)00187-0

Lenoir, J., Gégout, J. C., Marquet, P. A., De Ruffray, P., & Brisse, H. (2008). A significant upward shift in plant species optimum elevation during the 20th century. Science, 320(5884), 1768-1771. https://doi.org/10.1126/science.1156831

Liu, H. Y., Tang, Z. Y., Dai, J. H., Tang, Y. X., & Cui, H. T. (2002). Larch timberline and its development in north China. Mountain Research and Development, 22, 359–367. https://doi.org/10.1659/0276-4741(2002)022[0359:LTAIDI]2.0.CO;2

Mishra, C. (2001). High altitude survival: Conflicts between pastoralism and wildlife in the Trans-Himalaya. Wageningen University and Research. https://www.proquest.com/openview/bcc9af586e5c20df06673f312fbd04ff/1?pq-origsite=gscholar&cbl=18750&diss=y

Parmesan, C., & Yohe, G. (2003). A globally coherent fingerprint of climate change impacts across natural systems. Nature, 421(6918), 37-42. https://doi.org/10.1038/nature01286

Payette, S. (2007). Contrasted dynamics of northern Labrador tree lines caused by climate change and migrational lag. Ecology, 88(3), 770-780. https://doi.org/10.1890/06-0265

Pepin, N., Bradley, R. S., Diaz, H. F., Baraër, M., Caceres, E. B., Forsythe, N., ... & Mountain Research Initiative EDW Working Group. (2015). Elevation-dependent warming in mountain regions of the world. Nature climate change, 5(5), 424-430. https://doi.org/10.1038/nclimate2563

Purekhovsky, A. G., Gunya, A. N., Kolbowsky, E. Y., & Aleinikov, A. A. (2025). Methods Of Studying The Alpine Treeline: A Systematic Review. GEOGRAPHY, ENVIRONMENT, SUSTAINABILITY, 18(1), 105-116. https://doi.org/10.24057/2071-9388-2025-3735

Quétier, F., Lavorel, S., Thuiller, W., & Davies, I. (2007). Plant-trait-based modeling assessment of ecosystem-service sensitivity to land-use change. Ecological Applications, 17(8), 2377-2386. https://doi.org/10.1890/06-0750.1

Rai, I. D., Singh, G., Pandey, A., & Rawat, G. S. (2019). Ecology of treeline vegetation in western Himalaya: anthropogenic and climatic influences. Tropical ecosystems: Structure, functions and challenges in the face of global change, 173-192. https://doi.org/10.1007/978-981-13-8249-9_9

Rana, S. K., Rawal, R. S., Bentz, B. J., Linde, E., & Price, M. (2019). Climate-induced elevational range shifts and increase in plant species richness in a Himalayan biodiversity epicentre. PLOS One, 14(2), e0212200. https://doi.org/10.1371/journal.pone.0057103

Rawat, D., & Schickhoff, U. (2022). Changing climate scenario in high altitude regions: comparison of observed trends and perceptions of agro-pastoralists in Darma Valley, Uttarakhand, India. Mountain Landscapes in Transition: Effects of Land Use and Climate Change, 429-447. https://doi.org/10.1007/978-3-030-70238-0_18

Sah, P., Sharma, S., Latwal, A., & Shaik, R. (2023). Timberline and climate in the Indian Western Himalayan region: changes and impact on timberline elevations. In Climate Change and Urban Environment Sustainability (pp. 205-225). Singapore: Springer Nature Singapore. https://doi.org/10.1007/978-981-19-7618-6_12

Saxena, K. G., Rao, K. S., Sen, K. K., Maikhuri, R. K., & Semwal, R. L. (2002). Integrated natural resource management: approaches and lessons from the Himalaya. Conservation Ecology, 5(2). https://www.jstor.org/stable/26271822

Schickhoff, U. (2005). The upper timberline in the Himalayas, Hindu Kush and Karakorum: a review of geographical and ecological aspects. Mountain ecosystems, 275-354. https://doi.org/10.1007/3-540-27365-4_12

Schickhoff, U., Bobrowski, M., Böhner, J., Bürzle, B., Chaudhary, R. P., Gerlitz, L., ... & Wedegärtner, R. (2015). Do Himalayan treelines respond to recent climate change? An evaluation of sensitivity indicators. Earth System Dynamics, 6(1), 245-265. https://doi.org/10.5194/esd-6-245-2015

Singh, C. P., Panigrahy, S., Thapliyal, A., Kimothi, M. M., Soni, P., & Parihar, J. S. (2012). Monitoring the alpine treeline shift in parts of the Indian Himalayas using remote sensing. Current Science, 102(4), 559-562. https://www.jstor.org/stable/24084105

Singh, S. P., & Singh, J. S. (1987). Forest vegetation of the Himalaya. The Botanical Review, 53(1), 80-192. https://doi.org/10.1007/BF02858183

Suwal, M. K., Shrestha, K. B., Guragain, L., Shakya, R., Shrestha, K., Bhuju, D. R., & Vetaas, O. R. (2016). Land-use change under a warming climate facilitated upslope expansion of Himalayan silver fir (Abies spectabilis (D. Don) Spach). Plant Ecology, 217(8), 993-1002. https://doi.org/10.1007/s11258-016-0624-7

Tasser, E., & Tappeiner, U. (2002). Impact of land use changes on mountain vegetation. Applied Vegetation Science, 5(2), 173-184. https://doi.org/10.1111/j.1654-109X.2002.tb00547.x

Tewari, V. P., Verma, R. K., & Von Gadow, K. (2017). Climate change effects in the Western Himalayan ecosystems of India: evidence and strategies. Forest Ecosystems, 4(1), 1-9. https://doi.org/10.1186/s40663-017-0100-4

Walia, K., Kumari, Y., Garima, & Mehta, A. (2025). Ecosystem Recovery and Resilience After Forest Fires. In Forest Fire and Climate Change: Insights into Science (pp. 119-145). Cham: Springer Nature Switzerland. https://doi.org/10.1007/978-3-031-89967-6_7

APPENDIX A

Classification Accuracy Assessment Results

The classification accuracy for the years 1983, 1993, 2003, 2013, and 2023 was assessed using error matrices. Corresponding user's accuracy, producer's accuracy, overall accuracy, and Kappa statistics are presented in Tables 1-5. In 1983, the overall accuracy was 82.34% with a Kappa coefficient of 0.79. By 1993, classification accuracy had improved, showing an overall accuracy of 85.39% and a Kappa coefficient of 0.82. In 2003, the overall accuracy further increased to 88.95% with a Kappa of 0.85. The 2013 classification achieved an overall accuracy of 93.87% with a Kappa coefficient of 0.89. In 2023, the classification reached its highest accuracy, with an overall accuracy of 93.21% and a Kappa coefficient of 0.91. Overall, classification performance demonstrated a clear improvement over the four decades, with both overall accuracy and Kappa values increasing steadily. The early years (1983–1993) recorded relatively higher misclassifications in barren land and built-up areas, whereas later years (2013–2023) achieved much higher reliability, particularly for tree cover, snow, and water categories.

Table 1. Error Metrics for Land Cover Classification – 1983

Error Metrix for Land Cover Classification- 1983										
Reference Data	Classified Data								Total	Producers Accuracy
	Agri. Land	Barren	Built-up	Grassland	Snow	Tree Cover	Water	Total		
Agri. Land	78	6	3	8	0	2	1	98	98	79.59
Barren	7	54	5	11	4	2	0	83	83	65.06
Built-up	3	7	56	4	0	2	0	72	72	77.78
Grassland	12	8	4	118	2	1	0	145	145	81.38
Snow	0	3	0	1	52	2	0	58	58	89.66
Tree Cover	2	5	2	8	3	142	0	162	162	87.65
Water	1	1	0	1	0	0	47	50	50	94.00
Total	103	84	70	151	61	151	48	668	668	Kappa: 0.79
Users Accuracy	75.73	64.29	80.00	78.15	85.25	94.04	97.92	Overall Accuracy: 82.34		

Table 2. Error Metrics for Land Cover Classification - 1993

Error Metrix for Land Cover Classification- 1993										
Reference Data	Classified Data								Total	Producers Accuracy
	Agri. Land	Barren	Built-up	Grassland	Snow	Tree Cover	Water	Total		
Agri. Land	82	4	2	7	0	3	0	98	98	83.67
Barren	5	58	4	9	3	1	0	80	80	72.50
Built-up	2	5	61	3	0	1	0	72	72	84.72
Grassland	10	6	3	125	1	1	0	146	146	85.62
Snow	0	2	0	1	55	1	0	59	59	93.22
Tree Cover	4	4	3	6	2	148	0	167	167	88.62
Water	0	1	0	0	0	0	48	49	49	97.96
Total	103	80	73	151	61	155	48	671	671	Kappa: 0.82
Users Accuracy	79.61	72.50	83.56	82.78	90.16	95.48	100	Overall Accuracy: 85.39		

Table 3. Error Metrics for Land Cover Classification – 2003

Error Metrix for Land Cover Classification- 2003										
Reference Data	Classified Data								Total	Producers Accuracy
	Agri. Land	Barren	Built-up	Grassland	Snow	Tree Cover	Water	Total		
Agri. Land	86	3	2	5	0	2	0	98	98	87.76
Barren	4	63	3	7	2	1	0	80	80	78.75
Built-up	1	3	65	2	0	1	0	72	72	90.28
Grassland	8	5	2	130	1	0	0	146	146	89.04
Snow	0	1	0	0	57	1	0	59	59	96.61
Tree Cover	3	3	2	5	1	152	0	166	166	91.57
Water	0	1	0	0	0	0	48	49	49	97.96
Total	102	79	74	149	61	157	48	670	670	Kappa: 0.85
Users Accuracy	84.31	79.75	87.84	87.25	94.44	96.82	100	Overall Accuracy: 88.36		

Table 4. Error Metrics for Land Cover Classification – 2013

Error Metrix for Land Cover Classification- 2013										
Reference Data	Classified Data								Total	Producers Accuracy
	Agri. Land	Barren	Built-up	Grassland	Snow	Tree Cover	Water	Total		
Agri. Land	90	2	1	3	0	2	0	98	98	91.84
Barren	3	68	2	5	1	1	0	80	80	85
Built-up	1	2	67	2	0	0	0	72	72	93.06
Grassland	6	4	2	134	0	0	0	146	146	91.78
Snow	0	1	0	0	58	0	0	59	59	98.31
Tree Cover	1	1	2	4	1	155	0	164	164	94.51
Water	0	1	0	0	0	0	48	49	49	97.96
Total	101	79	74	148	60	158	48	668	668	Kappa: 0.89
Users Accuracy	89.11	86.08	90.54	90.54	96.67	98.10	100	Overall Accuracy: 91.02		

Table 5. Error Metrics for Land Cover Classification – 2023

Error Metrix for Land Cover Classification- 2023										
Reference Data	Classified Data								Total	Producers Accuracy
	Agri. Land	Barren	Built-up	Grassland	Snow	Tree Cover	Water	Total		
Agri. Land	92	3	1	2	0	0	0	98	98	93/88
Barren	3	70	2	3	1	1	0	80	80	87.50
Built-up	1	2	67	1	0	1	0	72	72	93.06
Grassland	5	4	2	134	0	1	0	146	146	91.78
Snow	0	1	0	0	57	1	0	59	59	96.61
Tree Cover	2	2	2	4	2	152	0	164	164	92.68
Water	0	1	0	0	0	0	48	49	49	97.96
Total	103	83	74	144	60	156	48	668	668	Kappa: 0.91
Users Accuracy	89.32	84,34	90.54	93.06	95	97.44	100	Overall Accuracy: 93.21		

APPENDIX B

Spatial-Temporal Changes in Vegetation Density

Vegetation density can be used to study vegetation changes, acting as an indicator of environmental conditions and ecological shifts. Figure 1 and Table 1 show a clear altitudinal gradient in vegetation density, with dense forest at lower elevations and sparse or barren areas at higher altitudes. From 1983 to 2003, the general pattern remained consistent, with dense vegetation in southern lowlands and progressively thinner vegetation towards the northern high mountains. By 2013, a decline in dense vegetation was observed in lower and mid-elevation zones. In 2023, vegetation health improved in lower zones, while higher elevations experienced reduced vegetation density. The lower zones showed resilience and recovery, whereas high-altitude regions continued to face ecological stress.

Table 1. Vegetation density and pattern, 1983–2023

Elevation	Vegetation Density (Hectares)- 1983				
	Very Low	Low	Moderate	High	Very High
683 - 2051	1605	6314	44466	64243	31167
2052 - 3053	4329	8044	20877	51127	66087
3054 - 4149	9463	45035	41914	13576	8952
4150 - 5152	15336	147827	5160	78	57
5153 - 7801	17656	129615	241	49	11
Elevation	Vegetation Density (Hectares)- 1993				
	Very Low	Low	Moderate	High	Very High
683 - 2051	486	16999	27203	51562	51546
2052 - 3053	6368	21030	20769	36357	65940
3054 - 4149	14857	28101	41171	20721	14090
4150 - 5152	41289	87824	38597	743	5
5153 - 7801	44778	98360	4981	0	0
Elevation	Vegetation Density (Hectares)- 2003				
	Very Low	Low	Moderate	High	Very High
683 - 2051	538	15591	30507	58360	42801
2052 - 3053	7865	18432	22644	38816	62707
3054 - 4149	15556	30933	41793	17120	13538
4150 - 5152	41667	107084	19379	320	6
5153 - 7801	45669	99381	3070	0	0
Elevation	Vegetation Density (Hectares)- 2013				
	Very Low	Low	Moderate	High	Very High
683 - 2051	24	20738	59729	64369	2936
2052 - 3053	0	30156	64865	53583	1859
3054 - 4149	2	47397	63112	8325	104
4150 - 5152	313	146880	21264	0	0
5153 - 7801	1753	145789	580	0	0
Elevation	Vegetation Density (Hectares)- 2023				
	Very Low	Low	Moderate	High	Very High
683 - 2051	159.38	1799.18	16771.09	60883.38	80112.62
2052 - 3053	12.82	1798.5	29994.15	60050.16	70554.39
3054 - 4149	32.67	24928.79	71805.48	20377.86	10875.35
4150 - 5152	2954.88	148357	29518.86	148.59	0.36
5153 - 7801	5170.91	152745.5	1157.97	0.21	0.03

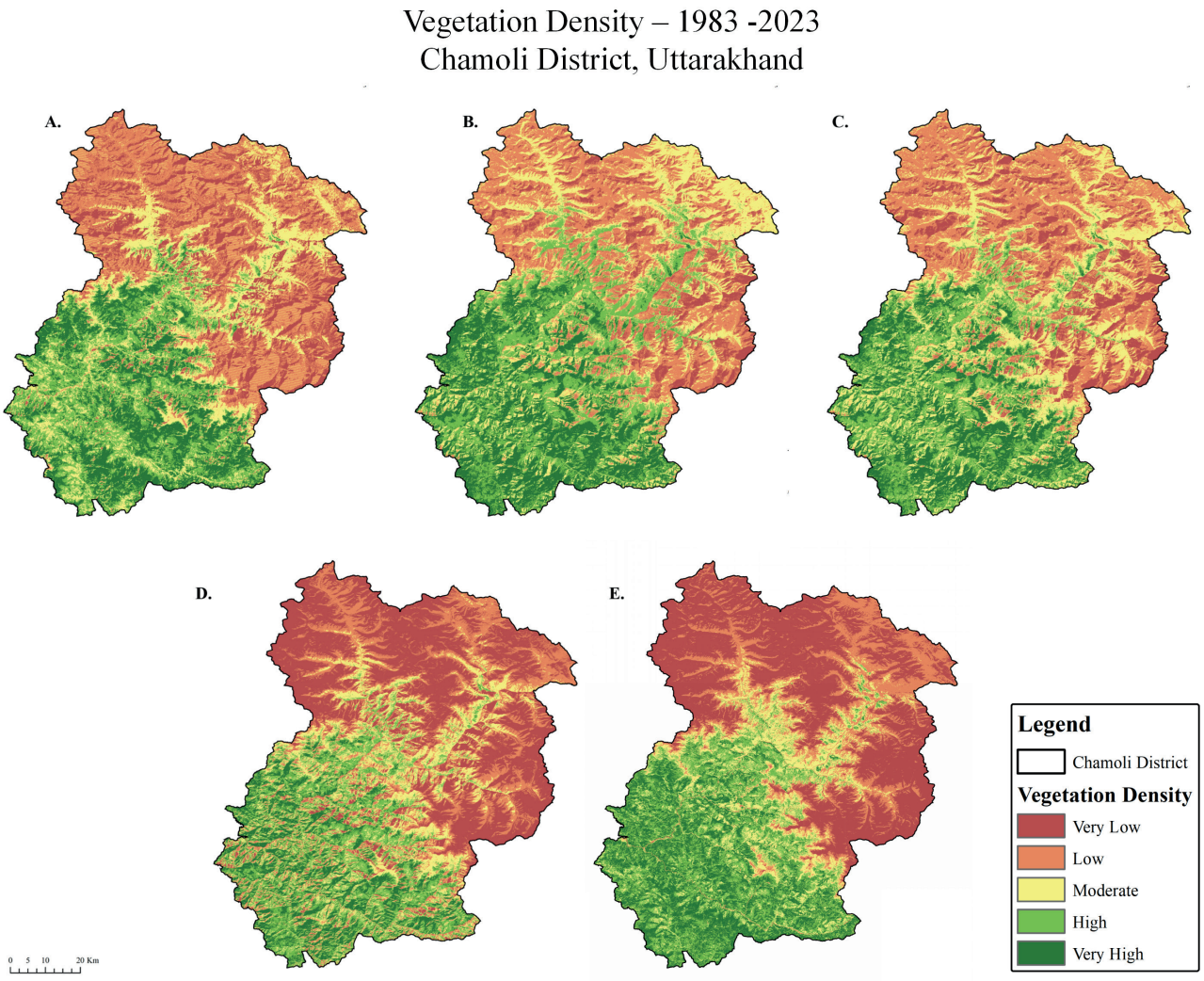

Fig. 1. Vegetation density and pattern: a) 1983, b) 1993, c) 2003, d) 2013 and e) 2023

RESEARCH PAPER

APPLICABILITY OF NBR AND dNBR INDICES IN ASSESSMENT OF PYROGENIC TRANSFORMATION AND POST-FIRE FOREST REGENERATION: CASE STUDY OF SOUTHEASTERN SIBERIA CONIFEROUS FORESTS

Zhanna V. Atutova*, Elena A. Rasputina
V.B. Sochava Institute of Geography, Siberian Branch of Russian Academy of Sciences,
Ulan-Batorskaya 1, Irkutsk, 664033, Russia
***Corresponding author:** atutova@mail.ru
Received: March 20th 2025 / Accepted: November 12nd 2025 / Published: December 31st 2025
https://doi.org/10.24057/2071-9388-2025-3963

ABSTRACT. This study evaluated the reliability of the Normalised Burn Ratio (NBR) and its differenced variant (dNBR) for assessing burnt areas and post-fire forest recovery. The research was conducted in the pine forests of the Tunka Depression (Southwestern Cisbaikalia), focusing on areas affected by a 2010 wildfire. Field data consisted of annual geobotanical observations from 2014 to 2022, which documented plant community regeneration across varying degrees of fire severity. Remote sensing analysis utilised Landsat 7 imagery (30 m resolution) between 2009 and 2022. Approximately 500 cloud-free NBR values were extracted from the USGS Landsat 7 Level 2, Collection 2, Tier 1 dataset using the Google Earth Engine platform. We assessed the spatiotemporal dynamics of these indices alongside the geobotanical parameters. The results confirm the effectiveness of NBR and dNBR for mapping burnt areas and determining initial fire severity. For detecting recent burns, mid-growing season imagery was most informative. Regarding post-fire regeneration analysis, springtime dNBR data were most reliable, as the influence of herbaceous cover on the spectral signal is minimised compared to the peak growing season. However, field observations revealed that the recovery of NBR values to pre-2009 fire levels by 2021 does not indicate that plant communities have regenerated to a near-natural state. This trend of rapid NBR recovery underscores the limitation of using NBR/dNBR indices alone for assessing long-term regeneration prospects. In conclusion, the results of the synthesised analysis of geobotanical and geoinformation materials showed that while remote sensing data effectively corroborate landscape-forming processes in disturbed ecosystems, their utility in detailed regeneration studies requires calibration with field data. The findings contribute to refining the application of NBR/dNBR indices and highlight the necessity of integrated approaches for calibrating remote sensing data.

KEYWORDS: burnt area, geobotanical observations, regeneration, monitoring, spectral index NBR, dNBR

CITATION: Atutova Z.V., Rasputina E. A. (2025). Applicability Of NBR And dNBR Indices In Assessment Of Pyrogenic Transformation And Post-Fire Forest Regeneration: Case Study Of Southeastern Siberia Coniferous Forests. Geography, Environment, Sustainability, 4 (18), 36-47
https://doi.org/10.24057/2071-9388-2025-3963

ACKNOWLEDGEMENTS: The work was supported by the state assignments AAAA-A21-121012190017-5 and AAA-A-A21-121012190056-4.

Conflict of interests: The authors reported no potential conflict of interests.

INTRODUCTION

In the spring of 2010, a large wildfire, a periodically recurring phenomenon in Southeastern Siberia, affected a portion of the Tunkinskiy National Park (Republic of Buryatia, Russia). Between 2002 and 2016, fires burnt 14,705.96 hectares within the park, which is slightly more than 1% of its total area (Ivanyo et al. 2017). A further 2,126.28 hectares burnt between 2019 and 2023[1], representing approximately 0.2% of the park's territory and 0.3% of its forested area. Despite the relatively limited extent of these fires, they frequently affect unique natural complexes. The loss of these complexes diminishes the landscape's distinctiveness. These complexes include pine forests with isolated larch and birch specimens, an understory of Daurian rhododendron, and a ground cover of green mosses and grasses. These serve as a reference standard for the mountain-basin light coniferous forests of the region. The 2010 wildfire burnt 233 hectares of forest within the Badary area. Subsequent monitoring through geobotanical surveys from 2014 to 2022 revealed that this event increased the differentiation of the mosaic, age-altitude heterogeneous structure of forest plant populations (Atutova 2022; Atutova 2023).

[1] About the forestry departments of the Republic of Buryatia (2024). IAS "Nature of Buryatia" [online]. Available at: https://ias.burpriroda.ru/forest/lesnichestva.php?ID=150464 [Accessed 27 Dec. 2024].

Given the importance of wildfire risk, the potential to use geobotanical monitoring results for studying pyrogenic transformation and forest regeneration dynamics in remote areas prompted the consideration of additional analytical methods. Satellite data are highly informative for this purpose, and specialised processing methods can calculate indices to facilitate the remote detection of burnt areas, assess fire severity, and analyse regeneration prospects. For analysing post-fire landscape changes, the calculation and spatiotemporal analysis of spectral vegetation indices have proven particularly effective (Ba et al. 2022; Chu et al. 2016, Kibler et al. 2019; Pushkin et al. 2015; Rodionova et al. 2020; Tokareva et al. 2021; Xofis et al. 2022). While these geodata are generally reliable for determining the post-fire state of plant communities, such conclusions are often not validated with field observations (Cuevas-González et al. 2009; Ba et al. 2022, Hao et al. 2022; Storey et al. 2016; Bastos et al. 2011; Bratkov and Ataev 2017; Casady and Marsh 2010). This gap raises questions about the application of these methods in studies of pyrogenic transformation. The authors' previous research, which synthesised field and satellite data, demonstrated that as phytomass increases during forest regeneration, spectral indices could show inflated values inconsistent with the area's actual geobotanical characteristics (Atutova 2024). This highlights the need to identify additional natural factors to improve the reliability of remote sensing data. A commonly used approach for assessing burnt areas is the calculation of the Normalised Burn Ratio (NBR) spectral index. The NBR has a wide dynamic range for characterising fire damage and a long recovery interval to pre-fire values (Shvetsov and Ponomarev 2020). Correlations between NBR values and phytomass have confirmed its effectiveness for mapping burnt areas and monitoring forest regeneration dynamics (Vorobiev et al. 2012; Sidelnik et al. 2018, Hao et al. 2022; Khakim et al. 2024), including in Siberian regions (Rodionova et al. 2020; Tokareva et al. 2021; Soromotin et al. 2022; Shvetsov and Ponomarev 2020; Rozhkov and Kondakov 2017; Ponomarev et al. 2022).

This study investigates the relationship between changes in the geobotanical parameters of post-wildfire plant communities in the Badary area and the dynamics of the NBR and its temporal difference (dNBR). By integrating remote sensing data with field observations from areas affected to varying degrees by a 2010 wildfire, we aim to evaluate the utility of these indices for assessing pyrogenic transformation and post-fire forest regeneration. Furthermore, considering the distinct seasonal ecosystem dynamics of Southeastern Siberia, we sought to identify the vegetation periods in which NBR values are most reliable.

MATERIALS AND METHODS

Study sites

This study was conducted in the Badary area, a sandy massif in Southwestern Cisbaikalia, located in the central Tunka depression. The massif forms a flat, rounded summit with elevations of 780–855 m, and its surface is characterised by ridges and hollows shaped by aeolian processes. The region has a sharply continental climate. Meteorological data from the Tunka station for the central depression show a mean annual temperature of +0.6°C, with mean monthly temperatures of −24.2°C in January and +18.7°C in July (Vasilenko and Voropay, 2015). The recorded absolute temperature range is from −40.1°C to +32.6°C. Annual precipitation is approximately 300–350 mm. The wind regime is dominated by western and northern winds, influenced by the depression's latitudinal position and the deeply incised river valleys descending from the slopes of the Tunka Goletz Range to the north. We examined two key sites within the pine forests of the Badary area that were transformed to varying degrees by a wildfire in May 2010 (Fig. 1).

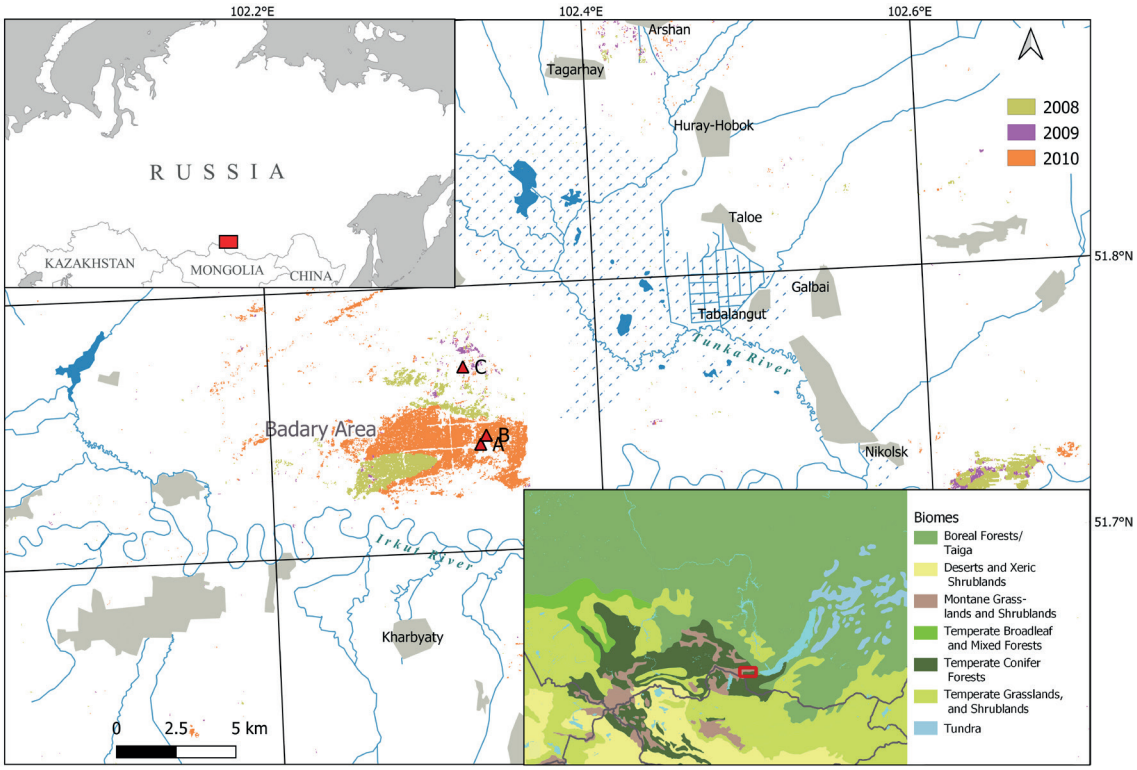

Fig. 1. Location of the study areas (A, B, C) within regional biomes[2] and historical fire perimeters[3] (2008-2010)

[2] The ecoregion classifications for the study area were obtained from the Ecoregions geoportal www.ecoregions.appspot.com [Accessed 26 Sept. 2025].

[3] Fire forest loss 2001-2022 [online]. Available at: https://glad.umd.edu/users/Alexandra/Fire_GFL_data/2001-22/ [Accessed 26 Sept.2025].

Area A is a peripheral section of the burn scar, located 70 m from the forest edge. It experienced high-severity fire damage but retains some standing trees. Area B, situated 440 m from Area A and 250 m from the forest edge, is within the fire's interior. It experienced complete canopy consumption with no surviving trees. Due to negligible natural regeneration, this site was replanted with *Pinus sylvestris* seedlings by Tunkinskiy National Park staff in May 2016. Area C is an unburnt reference site on the eastern edge of the Badary area, 3.3 km from Site A and 3.0 km from B. It consists of a secondary, medium-aged (45–50 years) pine forest with occasional *Larix sibirica* and *Betula pendula*. It has an understory of *Rhododendron dauricum* and patches of moss-grass-shrub communities. This site was selected as a reference because there were no intact primary pine forests near the burnt area.

Geobotanical monitoring materials

Field observations began in 2014 at sites A and C, and in 2016 at site B after post-fire reforestation activities. Data were collected within 20 × 20 m permanent sample plots. The following parameters were recorded: tree undergrowth, including stand structure, species composition, average height, and species abundance (using the Drude scale (1890)), and shrub layer and general plant communities, specifically species abundance (Drude scale), average height, and projective cover. The species composition of the tree undergrowth was quantified using a ten-unit formula based on relative abundance. Projective cover was estimated visually using a step-scale approach: a ten-step scale for the herbaceous layer, a five-step scale for the shrub layer, and a single-step scale for the overall plant community. These data were synthesised into regeneration sets, which characterise the post-fire recovery dynamics of plant communities under specific landscape-ecological conditions (Table 1).

Geoinformation materials

Landsat 7 satellite imagery (30 m resolution) was used as the primary data source, matching the spatial and temporal scale of the field observations. This dataset showed the highest consistency between the derived spectral indices and the multi-temporal field data. To identify burnt areas and analyse post-fire dynamics, we calculated the Normalised Burn Ratio (NBR) index. The NBR uses spectral reflectance in the near-infrared (NIR) and shortwave infrared (SWIR) regions, which are sensitive to vegetation chlorophyll content and moisture, respectively

Table 1. Post-fire regeneration dynamics in the Badary area (Southwestern Cisbaikalia)

Parameters	Site A					Site B			
	2014	2016	2018	2020	2022	2016	2018	2020	2022
Site description									
Vegetation before wildfire	*Pinus sylvestris with single specimens of Larix sibirica and Betula pendula with undergrowth of Rhododendron dauricum green-moss-herb-subshrub forest*								
Pyrogenic features	Edge part (flank) of the ground fire					Aria of the main part of the ground fire			
Undergrowth									
Composition (formula[1])	1P9B	2B8P	1B9P	1B9P	1B9P	2B8P	1B9P	1B9P	1B9P
Betula pendula									
Average height, m	0.9	1.2	1.6	1.8	2.0	0.8	1.1	1.2	1.3
Projective cover, %	5	5	5	5	5	3	5	5	5
Pinus sylvestris									
Natural (✓) and artificial reproduction (❄)	✓	✓	✓	✓	✓	✓	❄	✓	❄	✓	❄	✓	❄
Average height, m	0.06–0.1	0.25–0.3	0.7	1.5	2.0	0.3	0.08	0.7	0.2	1.3	0.4	1.8	0.6
Projective coverage, %	5	30	50	60	70	15	5	30	5	30	5	40	5
Shrub layer									
Average height, m	0.20	0.25	0.40	0.40	0.6	0.3	0.5	0.7	0.7
Projective coverage, %	15	20	25	30	35	30	30–35	40	40
Drude abundance of dominant species[2]									
Rosa acicularis	*sp.*	*sp.*	*sp.*	*sp.*	*sp.*	*cop.*[1]	*cop.*[1]	*cop.*[1]	*cop.*[1]
Rhododendron dauricum	*sol.*	*sol.*	*sp.*	*sp.*	*sp.*	-	*sol.*	*sol.*	*sol.*
Herb layer									
Average height, m	0.3	0.5	0.5	0.5	0.7	0.4	0.5	0.6	0.7
Projective coverage, %	40	50	60	70	80	60	70	80	80

Drude abundance of dominant species[2]									
Calamagrostis Langsdorffii	*cop.*[2]	*cop.*[3]	*cop.*[3]	*cop.*[3]	*cop.*[3]	*cop.*[2]	*cop.*[2]	*cop.*[2]	*cop.*[2]
Carex duriuscula	-	*sp.*	*cop.*[1]	*cop.*[1]	*cop.*[1]	*sp.*	*cop.*[1]	*cop.*[1]	*cop.*[1]
Chamerion angustifolium	*cop.*[2]	*cop.*[2]	*cop.*[1]	*sp.*	*sol.*	*cop.*[2]	*cop.*[2]	*cop.*[1]	*cop.*[1]
Artemisia sericea	*sp.*	*cop.*[2]	*cop.*[2]	*cop.*[2]	*cop.*[2]	*sp.*	*sp.*	*cop.*[1]	*cop.*[1]
Geranium pratense	*cop.*[1]	*cop.*[2]	*cop.*[2]	*cop.*[2]	*cop.*[2]	*cop.*[2]	*cop.*[2]	*cop.*[2]	*cop.*[2]
Sanguisorba officinalis	*cop.*[1]	*cop.*[1]	*cop.*[1]	*cop.*[1]	*cop.*[1]	*cop.*[1]	*cop.*[1]	*cop.*[2]	*cop.*[2]
Trifolium medium	*sp.*	*cop.*[2]	*cop.*[2]	*cop.*[2]	*cop.*[2]	*cop.*[1]	*cop.*[1]	*cop.*[2]	*cop.*[2]
Vicia cracca	*sp.*	*cop.*[1]	*cop.*[1]	*cop.*[1]	*cop.*[1]	*sp.*	*sp.*	*sol.*	*sol.*
Rubus saxatilis	*sol.*	*sp.*	*cop.*[1]	*cop.*[1]	*cop.*[1]	*sp.*	*sp.*	*cop.*[1]	*cop.*[1]
Vaccinium vitis-idaea	*sol.*	*sp.*	*cop.*[1]	*cop.*[1]	*cop.*[1]	-	*sol.*	*sp.*	*sp.*
Pleurozium schreberi	-	-	*sol.*	*sp.*	*sp.*	-	*sol.*	*sol.*	*sol.*

Note: [1] – B – *Betula pendula*; P – *Pinus sylvestris*; [2] – Drude abundance for dominant species: *cop.*[3] – plants are very abundant; *cop.*[2] – there are many individuals; *cop.*[1] – there are quite many individuals; *sp.* – plants are found in a small number, scattered; *sol.* – plants are found in a very small number, a few specimens

(Bartalev et al. 2010; Rodionova et al. 2020; Tokareva et al. 2021; Sidelnik et al. 2018; Hao et al. 2022; Kharitonova and Kharitonova 2021) (Table 2). The index is calculated in the Appendices (Table A). The near-infrared band characterises changes in the chlorophyll content of drying vegetation; the mid-infrared band determines the moisture content (Rodionova et al. 2020). All processing was conducted on the Google Earth Engine platform using a custom JavaScript code. The code specified the data source (USGS Landsat 7 Level 2, Collection 2, Tier 1 surface reflectance), applied a cloud mask, defined the study area coordinates and period (2009–2022), and executed the NBR calculation to extract time series values for each sample point. Calculations were based on the brightness values of pixels containing the central points of each sample plot. The resulting NBR values range from −1 to +1, where higher values (closer to +1) indicate healthy vegetation, and lower values (closer to 0 and below) indicate fire-damaged areas (Vorobiev et al. 2012; Hao et al. 2022). Approximately 200 NBR values were initially generated for each observation point from the pre-fire year (2009) to 2022, equating to roughly 14 observations per year. However, about 40% of these values were excluded due to cloud cover and data gaps from the Scan Line Corrector failure on the Landsat 7 ETM+ instrument. This is consistent with the satellite's 16-day revisit cycle, which provides a theoretical maximum of 22 images per year.

Geobotanical observations confirmed that vegetation cover is the most dynamic and rapidly recovering ecosystem component. In the initial stages of post-fire succession (demutation), the abundance and average height of herbaceous vegetation significantly exceeded those of tree seedlings (Atutova, 2022). Given the strong seasonal dependence of geobotanical characteristics, which is reflected in spectral data (Hao et al., 2022; Radjabova et al., 2020; Avetisyan et al., 2022), we defined three distinct growing seasons relevant to landscape development in a continental climate. For each year from 2009 to 2022, we selected NBR values from the following periods: 15 April – 15 June; 16 June – 15 August; and 16 August – 15 October. Values corresponding to the exact dates of in situ observations (2014–2022) were also extracted, resulting in a total of 492 NBR values from cloud-free periods.

At the next stage, the average NBR indicator was determined for each site in each vegetation phase for each year (from 2009 to 2022). This was calculated by summing all values for a set and dividing by their number. These means were derived from two to five cloud-free observations per season. We also established a seasonal background value for the unburnt area (Area C). This was defined as the arithmetic mean of all seasonal average values from 2009 to 2022. Comparing NBR indices on burnt areas against these background values allows for an assessment of satellite data reliability in determining pyrogenic transformation.

To quantify fire-induced environmental damage, we employed the differenced Normalised Burn Ratio (dNBR). This is calculated as the pre-fire NBR minus the post-fire NBR (Miller and Thode 2007; Bartalev et al. 2010; Vorobiev et al. 2012; Hao et al. 2022) (Table 2). To track recovery

Table 2. Selected spectral indices used in remote assessment of burnt areas in pine forests of the Badary area

Index	Expression	Description
Normalised Burn Ratio (NBR)	(NIR – SWIR) / (NIR + SWIR)	Detects the burnt areas
the differenced Normalised Burn Ratio (dNBR)	NBRprefire data – NBRpostfire data	Evaluates the degree of pyrogenic transformation after ignition
dNBRseverity (dNBRs)	NBRprefire data – NBRregrowth data	Reflects the change in the degree of pyrogenic transformation during the regeneration process
dNBRregrowth (dNBRr)	NBRpostfire data – NBRregrowth data	Reflects the dynamics of regrowth during the regeneration process

dynamics, we used two variants. The dNBRs represents the difference between the pre-fire NBR and the NBR for each subsequent year, indicating changes since the fire. The dNBRr represents the difference between the immediate post-fire NBR and each subsequent year, indicating annual recovery progress (Santos et al. 2020). Applying these formulas produced a geodataset structured by vegetation season, facilitating remote assessment of forest restoration (Table A). Positive dNBRs and dNBRr values indicate a decrease in vegetation, while negative values signify an increase. The parallel trajectories of dNBRs and dNBRr (Fig. 2) confirm that dNBRs is informative not only for assessing initial fire damage but also for monitoring early-stage vegetation recovery.

Synthesizing the calculated indices with field data will enable the classification of geodata by the degree of pyrogenic transformation in the region's light-coniferous forests. A preliminary review of dNBR threshold values for similar landscapes in Southeastern Siberia (Bartalev et al. 2010; Tokareva et al. 2021; Ponomarev et al. 2022) and adjacent territories (Hao et al. 2022) revealed significant variability in published ranges for determining burn severity. Therefore, to rank dNBR values according to wildfire damage degree, we employed a field-data generalisation method based on R.V. Chugunova's (1960) classification of burnt areas. At the start of observations, site A corresponded to a burnt area with complete stand mortality, while site B was a damaged stand represented by a treeless space with charred trunks. The analysis of post-fire regeneration was based on correlating dNBRr indices with the geobotanical specifics of each successional stage defined by Chugunova (1960): blackened burnt forest, grass stage, grass-shrub stage, and coniferous young growth.

RESULTS

A smooth, non-fluctuating NBR value trend was observed, particularly during the mid-growing season, in the background (unburnt) area (Fig. 2, Table A). The high canopy density here suppresses light-demanding pine undergrowth, and the living ground cover is sparse due to the inhibitory effect of the coniferous litter. Monitoring at this site revealed that the projective cover of the herbaceous layer influences the differentiation of NBR values across seasons. As the projective cover increased from 30% in spring to 70% at the peak of vegetation, the NBR values rose by almost 25% (Fig. 3). Overall, the mean NBR values for the background area were 0.545 at the beginning of the growing season, 0.586 in the middle, and 0.648 at the end.

Fig. 2. Dynamics of NBR, dNBRs and dNBRr during post-fire forest regeneration in the Badary area

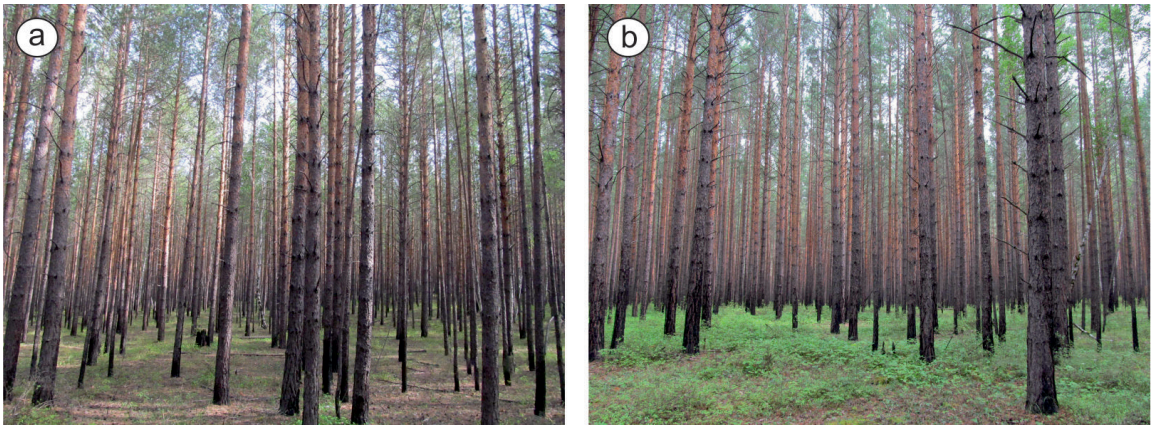

Fig. 3. Variation in NBR with seasonal changes in herbaceous projective cover at the reference site (site C). Panel (a): early growing season (5 June 2014) showing moderate cover and an NBR of 0.550. Panel (b): peak growing season (8 July 2021) showing high cover and an NBR of 0.677

Analysis of the remote sensing data revealed a clear differentiation in NBR values between the two areas affected to different degrees by the 2010 wildfire. Prior to the fire (mid-growing season 2009), both sites exhibited high NBR values (site A: 0.524; site B: 0.571). Following the fire in 2010, these values plummeted to 0.103 and –0.050, respectively. This sharp decline, corresponding to dNBRs values of 0.421 for site A and 0.621 for site B, confirmed a high severity burn across both areas.

The spectral difference between the sites persisted in the initial post-fire years (Table A). Site B consistently showed lower NBR values than site A. This can be attributed to two factors: the storage of fallen timber at site B and subsequent damage to the living ground cover from machinery during furrowing for replanting in 2016. In contrast, site A, which retained some standing trees and offered better conditions for grass cover development, showed a stronger spectral signal of early regrowth (Fig. 4). From the fire year until 2018, mid-season NBR values at site A ranged from 0.043 to 0.222, while at site B they varied from –0.050 to 0.660 (Table A). Despite this increase, field observations confirmed that both sites remained significantly transformed. The dNBRs values for this period remained high (site A: 0.302–0.481; site B: 0.505–0.621), indicating a persistent spectral signature of fire damage relative to the pre-fire baseline. However, the differential recovery rates were captured by the dNBRr. At site A, dNBRr values decreased from 0.060 to –0.119 between 2011 and 2018, reflecting rapid vegetation regeneration (Table 1). In contrast, the decrease at site B was negligible (from –0.113 to –0.116), aligning with its slower recovery due to the aforementioned disturbances (Fig. 4).

A marked increase in NBR values coincided with the growth of tree undergrowth and grass cover. At site A, NBR values rose to 0.507 in 2021 and 0.405 in 2022. Field data confirmed intensive regeneration, with pine undergrowth height increasing from 0.1 m in 2014 to 2.0 m in 2022, and its projective cover reaching 70% (Fig. 4). Concurrently, the herbaceous layer reached 80% projective cover and 70 cm in height. This successful recovery is further evidenced by the trends in difference indices. The dNBRs values declined from 0.232 to 0.017 between 2019 and 2022, signalling a spectral convergence with the pre-fire state. Simultaneously, the dNBRr values fell from –0.189 to –0.404, underscoring strong positive vegetation growth relative to the immediate post-fire condition.

At site B, mid-growing season NBR values showed a consistent positive trend, increasing from 0.292 in 2019 to 0.405 in 2022 (Table 2). This recovery was driven by natural regeneration. The height of natural pine seedlings increased from 0.3 m to 1.8 m and their projective cover from 15% to 40% over the same period (Fig. 4). In contrast, the planted *Pinus sylvestris* seedlings showed slow growth, reaching only 0.6 m in height with 5% projective cover by 2022. The strong herbaceous layer (80% cover, 70 cm height) contributed significantly to the spectral signal. The declining dNBRs (from 0.446 to 0.240) and dNBRr (from –0.175 to –0.381) values confirm a strong, positive vegetation recovery trend.

Analysis of NBR data for the beginning and end of the growing season, specifically during the initial stages of grass cover emergence and its subsequent wilting phase, between 2010 and 2018 also revealed a differentiation of burnt areas by the degree of pyrogenic transformation. In some years, the more severely damaged site B exhibited higher NBR values than the less damaged site A (Table A). It is noteworthy that at site A, positive late-season NBR values in 2010–2011 later turned negative, potentially reflecting the gradual fall and decomposition of dead standing timber. This initially provided a structural signal that was later lost. The dNBRs and dNBRr values in 2010–2018 were high, reaching 0.709 and 0.249, respectively, at site A in 2012, and 0.769 and 0.090, respectively, at site B in 2015.

The spectral difference between sites affected by different burn severities was most pronounced in the final observation stage (Table A). Starting in 2019, the dNBRs values at the beginning of the growing season at site A decreased from 0.344 to 0.127, and at site B from 0.531 to 0.396. By the end of the growing season, the values decreased from 0.331 to 0.075 and from 0.545 to 0.445, respectively. For the same period, the dNBRr values at the beginning of the growing season decreased from –0.084 to –0.294 at site A and from –0.103 to –0.253 at site B. At the end of the growing season, the dNBRr at site A decreased from 0.331 to 0.075, while at site B it decreased from –0.134 to –0.234. These trends indicate that the spectral properties of the pyrogenically transformed areas became more consistent with the natural environment at both the beginning and end of the growing season. However, the extended autumn senescence period leads to elevated NBR values (Table A). Consequently, the NBR values from the beginning of the growing season correlate most reliably with the field observation data.

This study confirms the utility of satellite data for identifying burnt areas, assessing burn severity, and monitoring post-fire forest regeneration dynamics. However, in the sharply continental climate of Southern Eastern Siberia, where seasonal variability is pronounced, the timing of image acquisition is critical. The rapid recovery of grass cover disproportionately influences spectral

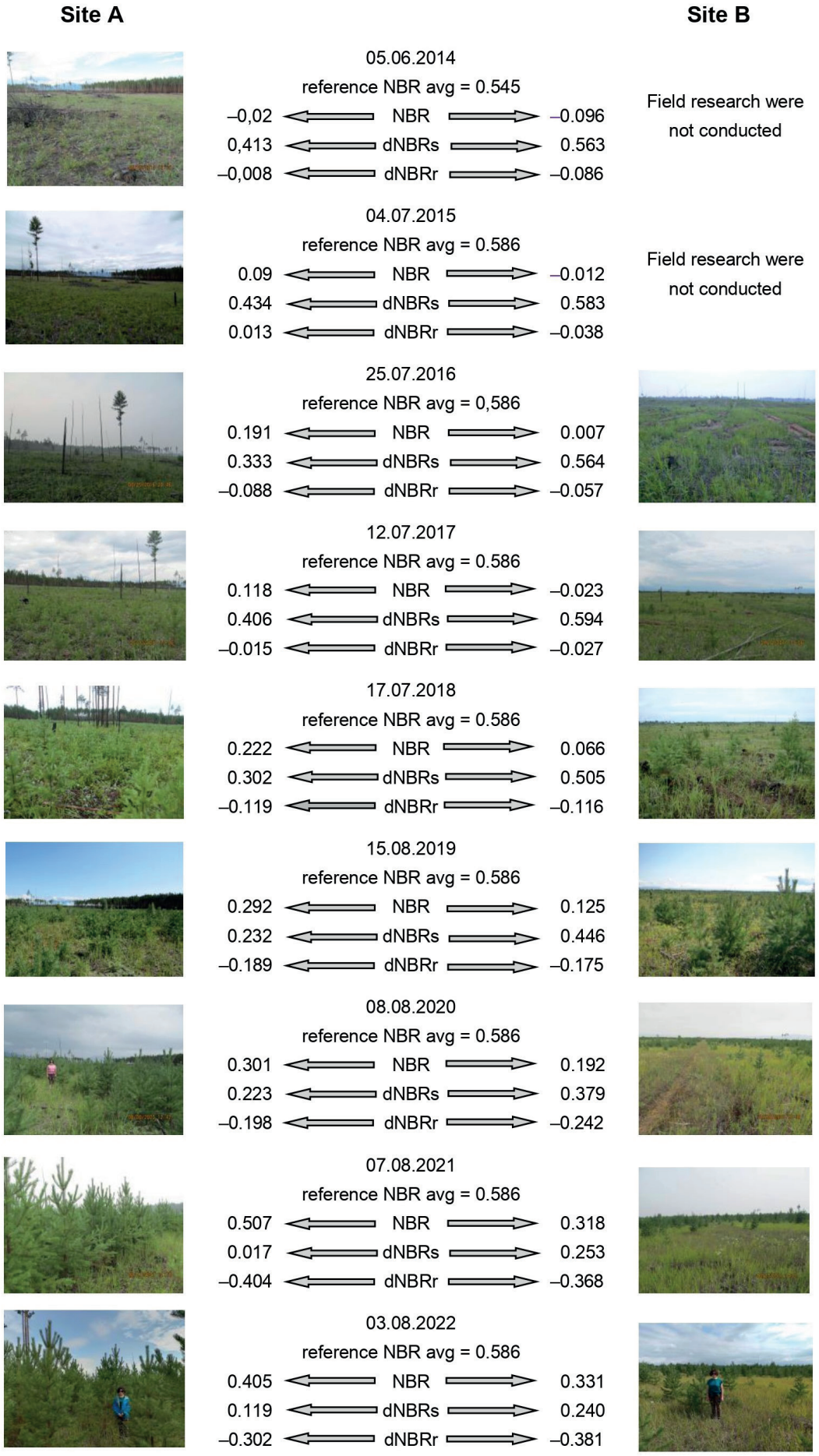

Fig. 4. Multi-temporal NBR and dNBR values for burnt areas in the Badary area (Tunka depression, Southwestern Cisbaikalia), with corresponding field photographs

indices, often leading to an overestimation of recovery. Consequently, for assessing post-fire ecosystem dynamics in similar landscapes, we recommend prioritising spring imagery, when herbaceous abundance and projective cover are minimal, to most accurately evaluate the recovery of woody vegetation.

DISCUSSION

This study aimed to evaluate the reliability of satellite data for assessing pyrogenic transformation and post-fire regeneration in the pine forests of Southern Eastern Siberia. A comparison of NBR and dNBR index values with the geobotanical characteristics of recovering plant communities in the Badary burnt area indicated the validity of these indices for identifying fire-affected areas and determining burn severity, consistent with previous findings (Rodionova et al. 2020; Avetisyan et al. 2022). Furthermore, our results prove the informativeness of dNBRs and dNBRr dynamics for monitoring post-fire forest regeneration (Santos et al. 2020).

It is known that the NBR index is calculated from the spectral brightness of pixels in the near-infrared region of the spectrum (Sidelnik et al. 2018; Tokareva et al. 2021). This region is associated with high photosynthetic activity. In the sharply continental climate of Southern Eastern Siberia, this relationship is evident in strong seasonal variations of the index, with the highest values consistently occurring during the mid-growing season. Analysis of the background area from 2009 to 2022 revealed the smallest inter-annual variability in NBR during this peak vegetation period, indicating stable ecological conditions in unburnt forests. Therefore, the long-term stability of high mid-season NBR values can serve as a reliable spectral marker for identifying areas unaffected by wildfire.

Our results confirm the utility of the dNBR index for delineating burnt area boundaries, consistent with previous studies (Miller and Thode 2007; Santos et al. 2020; Delcourt et al. 2021; Khakim et al. 2024; Ponomarev et al. 2022). The differentiation of dNBRs values between sites in the initial post-fire years correlated strongly with their observed burn severity. This indicates the reliability of remote sensing data in determining the extent of fire damage. In the fire year, the more severely impacted site B – classified as a treeless open space (Chugunova 1960) – exhibited dNBRs values of 0.621–0.679. In contrast, the less damaged site A, characterised by deadwood and fallen trees (according to Chugunova's classification (1960)), showed lower values of 0.421–0.460.

This clear differentiation enables the establishment of threshold dNBR values for ranking pyrogenic transformation. While studies in Siberia indicate that dNBR values >0.600 typify high-severity burns (Tokareva et al. 2021; Ponomarev et al. 2022), our research suggests that in the pine forests of Southeastern Siberia, values as low as 0.400 also indicate significant damage, a finding consistent with coniferous forests in northeastern China geographically close to our areas (Hao et al. 2022). Based on our analysis, we propose the following severity classification for early-season data: dNBRs >0.500 indicates a high degree of pyrogenic transformation, while values of 0.400–0.500 indicate a moderately high degree (Table 3). Furthermore, this dNBRs gradation can be interpreted in terms of ecosystem recovery rates. High dNBRs values (>0.500), corresponding to dNBRr values above zero, indicate very low regeneration rates. Moderately high dNBRs values (0.400–0.500), corresponding to dNBRr values from –0.140 to zero, indicate low regeneration rates.

Until 2018, both sites showed ecological constraints that slowed the regeneration of woody vegetation, despite vigorous herbaceous recovery. This was reflected in persistently high dNBRs values, ranging from 0.302 to 0.709 at site A and from 0.393 to 0.769 at site B across different seasons. A shift towards stabilised ecological conditions and accelerated forest recovery began around 2019–2020, marked by increased growth rates of natural tree seedlings (Table 1). At site A, mid-growing season dNBRs values dropped below the 0.400 threshold (0.232 in 2019, 0.223 in 2020). However, considering the landscape context – a site with significant prior damage in the initial stage of young forest growth with a well-developed grass cover (according to Chugunova's classification (1960)) – the early-season dNBRs values of 0.337 and 0.344 for 2019–2020 were more ecologically informative. Consequently, we interpret early-season dNBRs values below 0.400 to indicate a moderate degree of pyrogenic transformation or average forest regeneration rates, corresponding to dNBRr values greater than –0.140. In contrast, dNBRs values at site B during this period remained above the 0.400 threshold across all seasons. This aligned with field observations classifying the site at the grass-shrub stage of succession with successfully establishing woody undergrowth (according to Chugunova's classification (1960)), indicating that while recovery was underway, the spectral signature of the initial severe damage remained dominant.

In the final observation years (2021–2022), spectral indices indicated ongoing recovery. At site A, mid-growing season dNBRs values decreased to 0.017 and 0.119, while early-season values were 0.280 and 0.127. Despite continued growth in pine undergrowth height and cover, the overall landscape-ecological situation still indicated a moderate degree of pyrogenic transformation. At site B, mid-season dNBRs values also declined to 0.253 and 0.240, with early-season values falling to 0.546 and 0.396. Nevertheless, this site was still classified at a moderately high degree of fire damage. This status was corroborated by dNBRr values that remained within the range characteristic of areas with low forest regeneration rates. These final results suggest that the lower threshold of the dNBRs range for a 'moderate' transformation class has not yet been fully defined. Therefore, determining the precise lower limits of dNBRs that signify a transition to advanced recovery and average regeneration rates requires continued long-term monitoring.

Table 3. A Classification of pyrogenic transformation and forest regeneration rates in the pine forests of the Badary area

dNBRs index	Degree of pyrogenic transformation	Forest regeneration rates	Stages of overgrowth of burnt areas (Chugunova 1960)
dNBRs > 0.500	High degree	Very low rates	Black burnt area; grass stage
0.400 < dNBRs < 0.500	Moderately high degree	Low rates	Grass stage; grass-shrub stage
?[1] < dNBRs < 0.400	Moderate degree	Average rates	Grass-shrub stage; coniferous young stands

Note: [1] – continued observations are required to determine the minimum dNBRs limit

Long-term dNBR data for the end of the growing season consistently showed elevated values throughout the 12-year post-fire period, especially in the later observation stages. In some years, late-season NBR and dNBRs values even exceeded those from the mid-growing season (Table A). As with the mid-season data, this increase is attributed to the influence of the rapidly recovering herbaceous layer. This finding highlights the importance of using early-growing-season imagery for the remote analysis of long-term post-fire restoration in evergreen light-coniferous forests. This is because this period is not affected by the confounding spectral influence of dense grass cover.

This study demonstrates the utility of synthesising satellite data with field observations for calibrating remote sensing indicators. We hypothesise that as undercanopy vegetation continues to develop over the coming years, NBR values may eventually stabilise at high, pre-fire levels. If this occurs, it would corroborate findings that the sensitivity of the NBR index diminishes as plant communities approach full recovery (Sidelnik et al., 2018). Our results confirm that spectral indices are most informative for assessing burn severity and initial recovery dynamics within the first decade following a fire.

Our study proves that the NBR and dNBR spectral indices are inadequate as primary tools for objectively assessing post-fire regeneration (demutation) (Soromotin et al. 2022; Avetisyan et al. 2022). Although NBR values increased progressively, exceeding pre-fire (2009) levels by the 11th year, field data show this does not signify a return to a natural ecosystem state. Instead, it highlights general trends in the demutation process. Therefore, assessments based exclusively on the NBR index are unreliable for evaluating reforestation prospects. These geospatial tools should be used as a supplementary (confirming) source to validate the development of landscape-forming processes.

CONCLUSIONS

This study proves that the NBR and dNBR spectral indices are effective tools for mapping burnt areas and evaluating pyrogenic transformation. We recorded a sharp decline in both indices following fire events, and the values effectively differentiated between zones of high and low fire severity. This pattern was consistent with field observations, confirming the utility of NBR and dNBR for ranking areas based on their level of fire impact.

Through an integrated analysis of multi-temporal geospatial data and geobotanical monitoring, we identified key natural factors of forest regeneration that significantly influence the NBR spectral index. While the improvement in geobotanical characteristics of recovering undergrowth is a primary driver of the increasing NBR trend in burnt areas, our findings reveal that in early successional stages (demutation), the rapid re-establishment of grass cover is the dominant factor. This is evidenced by NBR data from a key study area that sustained less damage in the 2010 wildfire. Here, NBR values recovered to near pre-fire levels within eleven years, despite field observations confirming the landscape was still in an early stage of forest regeneration. Furthermore, we found that a sustained series of high NBR values with minimal mid-season fluctuation is a reliable indicator of areas approaching a natural state. Although data from the mid-vegetation period are useful for assessing early post-fire regeneration, our analysis shows that for light coniferous forests, NBR data from the early vegetation period are most advantageous. During this time, the confounding influence of living ground cover on index values is reduced compared to the peak growing season.

By analysing initial post-fire dNBR data and field observations, we established a threshold dNBR value of 0.500 to classify pyrogenic transformation in the Badary area's pine forests. Values above this threshold correspond to areas of high-severity burn (site B), while values below it indicate moderate-severity damage (site A). Given that these forests are in the early stages of post-fire regeneration, geobotanical data further allowed us to define threshold values for three rates of recovery: very low, low, and moderate.

The study revealed a tendency for NBR values to be overestimated, particularly in later demutation stages. This poses a significant risk to the reliability of remote forest recovery assessments. However, this discrepancy between satellite data and ground conditions does not prevent the integrated use of geospatial and geobotanical methods for evaluating landscape-forming processes. Extending the initiated observations will enable the development of additional criteria to enhance the utility of remote sensing data for studying forest regeneration in areas disturbed by fire.

REFERENCES

Atutova Zh.V. (2022). Post-pyrogenic reforestation of subtaiga light coniferous geosystems of the Tunkinskaya depression, Southwestern Cisbaikalia (the study of pine forests of the Badary area). Geographical bulletin, 4(63), 6-18, DOI: 10.17072/2079-7877-2022-4-6-18 (in Russian).

Atutova Zh.V. (2023). Post-fire regeneration of pine forests in the Badary area, Ttunkinskiy National Park, Russia. Nature Conservation Research. 8(2), 22-32, DOI:10.24189/ncr.2023.010.

Atutova Zh.V. (2024). Experience with Using Geoinformation Data in the Evaluation of Post-Fire Vegetation Coverage Regeneration. Proceedings of Voronezh state university. Series: geography, geoecology, 3, 4-13, DOI:10.17308/geo/1609-0683/2024/3/4-13 (in Russian).

Avetisyan D., Velizarova E. and Filchev L. (2022). Post-fire forest vegetation state monitoring through Satellite Remote Sensing and In Situ Data. Remote Sensing, 14, 6266, DOI:10.3390/rs14246266.

Ba R., Song W., Lovallo M., Zhang H. and Telesca L. (2022). Informational analysis of MODIS NDVI and EVI time series of sites affected and unaffected by wildfires. Physica A: Statistical Mechanics and its Applications, 604, 127911, DOI: 10.1016/j.physa.2022.127911.

Bartalev S.A., Egorov V.A., Krylov A.M., Stytsenko F.V. and Khovratovich T.C. (2010). The evaluation of possibilities to assess forest burnt severity using multi-spectral satellite data. Sovremennye Problemy Distantsionnogo Zondirovaniya Zemli iz Kosmosa, 3, 215-225 (in Russian).

Bastos A., Gouveia C., DaCamara C.C. and Trigo R.M. (2011). Modelling post-fire vegetation recovery in Portugal. Biogeosciences Discussions, 8, 4559-4601, DOI:10.5194/bgd-8-4559-2011.

Bratkov V.V. and Ataev Z.V. (2017). Vegetation indexes and their use for mapping mountain landscapes of the Russian Caucasus. APRIORI. Series: Natural and Technical Sciences, 1, 3-23 (in Russian).

Casady G.M. and Marsh S.E. (2010). Broad-Scale environmental conditions responsible for post-fire vegetation dynamics. Remote Sensing, 2, 2643-2664, DOI:10.3390/rs2122643.

Chu T., Guo X. and Takeda K. (2016). Remote sensing approach to detect post-fire vegetation regrowth in Siberian boreal larch forest. Ecological Indicators, 62, 32-46, DOI:10.1016/j.ecolind.2015.11.026.

Cuevas-González M., Gerard F., Balzter H. and Riaño D. (2009). Analysing forest recovery after wildfire damage in boreal Siberia using remotely sensed vegetation indices. Global Change Biology, 15(3), 561-577, DOI:10.1111/j.1365-2486.2008.01784.x.

Chugunova R.V. (1960). To the question about the classification of burnt areas. Scientific reports. Issue 3. 67-70. Yakutsk: Yakutsk Book Publishing House (in Russian).

Delcourt C.J.F., Combee A., Izbicki B., Mack M.C., Maximov T., Petrov R., Rogers B.M., Scholten R.C., Shestakova T.A., van Wees D. and Veraverbeke S. (2021). Evaluating the Differenced Normalized Burn Ratio for Assessing Fire Severity Using Sentinel-2 Imagery in Northeast Siberian Larch Forests. Remote Sensing, 13(12), 2311, DOI:10.3390/rs13122311.

Drude O. 1890. Handbuch der Pflanzengeographie. Stuttgart: J. Engelhorn.

Hao B., Xu X., Wu F. and Tan L. (2022). Long-term effects of fire severity and climatic factors on post-forest-fire vegetation recovery. Forests, 13, 883, DOI:10.3390/f13060883.

Ivanyo Ya.M., Lazareva A.A. and Stolpova Yu.V. (2017). Modeling the variability of fire characteristics in the territory of the Tunkinskiy National Park. The Bulletin of KrasGAU, 7, 44-50 (in Russian).

Khakim M.Y.N., Poerwono P., Affandi A.K., Anhar M.F., Indrawan F., Ardiansyah T. and Tsuji T. (2024). Land Cover and Burn Severity Dynamics of the Ogan Komering Ilir Peatlands from 2015 to 2023 Using Sar and Optical Datasets. Geography, Environment, Sustainability, 3(17), 6-18, DOI:10.24057/2071-9388-2024-3217/.

Kharitonova A.O. and Kharitonova T.I. (2021). The influence of the landscape structure of the Mordovian Nature Reserve (Russia) on the spread of the 2010 fire. Nature Conservation Research, 6(2), 29-41, DOI:10.24189/ncr.2021.022 (in Russian).

Kibler C.L., Parkinson A.-M.L., Peterson S.H., Roberts D.A., D'Antonio C.M., Meerdink S.K. and Sweeney S.H. (2019). Monitoring post-fire recovery of chaparral and conifer species using field Surveys and Landsat time series. Remote Sensing, 11(24), 2963, DOI:10.3390/rs11242963.

Miller J.D. and Thode A.E. (2007). Quantifying burn severity in a heterogeneous landscape with a relative version of the delta Normalized Burn Ratio (dNBR). Remote Sensing of Environment 109(1), 66-80, DOI:10.1016/j.rse.2006.12.006.

Ponomarev E., Zabrodin A. and Ponomareva T. (2022). Classification of Fire Damage to Boreal Forests of Siberia in 2021 Based on the dNBR Index. Fire, 5(1):19, DOI: 10.3390/fire5010019.

Pushkin A.A., Sidelnik N.Ya. and Kovalevsky S.V. (2015). The use of satellite imagery materials to assess fire danger in forests. Proceedings of BSTU, 1: Forestry, 174, 36-40 (in Russian).

Radjabova R.T., Alekseenko N.A., Kuramagomedov B.M., Tazhudinova Z.Sh. and Sultanov Z.M. (2020). The use of index images in decoding the vegetation cover of Inland Dagestan. South of Russia: ecology, development, 15(4), 126-136, DOI: 10.18470/1992-1098-2020-4-126-136 (in Russian).

Rodionova N.V., Vakhnina I.L. and Zhelibo T.V. (2020). Assessment of the dynamics of the post-fire state of vegetation in the territory of the Ivano-Arakhleisky Nature Park (Zabaikalsky Krai) using radar and optical data from Sentinel ½ satellites. Issledovanie Zemli iz Kosmosa, 3, 14-25, DOI: 10.31857/S0205961420030045 (in Russian).

Rozhkov Yu.F. and Kondakov M.Yu. (2017). Assessment of the process of forest regeneration after a fire using cluster analysis when decoding satellite images. Vestnik of North-Eastern Federal University, 2, 38-48 (in Russian).

Santos S.M.B.d., Bento-Gonçalves A., Franca-Rocha W. and Baptista G. (2020). Assessment of Burned Forest Area Severity and Postfire Regrowth in Chapada Diamantina National Park (Bahia, Brazil) Using dNBR and RdNBR Spectral Indices. Geosciences,10(3), 106. DOI: 10.3390/geosciences10030106.

Sidelnik N.Ya., Pushkin A.A. and Kovalevsky S.V. (2018). Mapping damaged forest stands and objects of forestry measures using space survey materials and GIS technologies. Proceedings of BSTU, 1: Forestry, 1, 5-12 (in Russian).

Shvetsov E.G. and Ponomarev E.I. (2020). Post-fire effects in Siberian larch forests on multispectral satellite data. Contemporary Problems of Ecology, 1, 129-140, DOI: 10.15372/SEJ20200110 (in Russian).

Soromotin A.V., Brodt L.V. and Prikhodko N.V. (2022). Transformation of NDVI and NBR indices in post-pyrogenic territories in the forest tundra zone of the Yamalo-Nenets Autonomous District. XVII All-Russian Scientific and Practical Conference «High Technologies, Science and education: current issues, achievements and innovations». Collection of articles. Penza: Science and Education, 262-265 (in Russian).

Tokareva O.S., Alshaibi A.D.A. and Pasko O.A. (2021). Assessment of the regenerative dynamics of vegetation cover of forest harems using data from Landsat satellites. Bulletin of Tomsk Polytechnic University. Geo Assets Engineering, 332(7), 191-199, DOI: 10.18799/24131830/2021/7 (in Russian).

Vasilenko O.V., Voropay N.N. (2015). Peculiarities of climate formation in the basins of the South-Western Baikal region. Izvestiya RAN. Seriya geograficheskaya, 2, 98-104. (in Russian).

Vorobiev O.N., Kurbanov E.A., Gubarev A.V., Lezhnin S.A. and Polevshchikova Yu.A. (2012). Remote monitoring of harems in the Mari Trans-Volga region. Vestnik of Volga State University of Technology. Series «Forest. Ecology. Nature management», 1, 12-22 (in Russian).

Xofis P., Spiliotis J.A., Chatzigiovanakis S. and Chrysomalidou A.S. (2022). Long-term monitoring of vegetation dynamics in the Rhodopi Mountain Range National Park-Greece. Forests, 13, 377, DOI:10.3390/f13030377.

Appendices

Table A. Mean values of spectral indices for analyzing pyrogenic transformation and forest regeneration dynamics at key sites

Years	Site A			Site B			Site C	Average reference NBR values
	NBR	dNBRs	dNBRr	NBR	dNBRs	dNBRr	NBR	
Beginning of the growing season (15.04–15.06)								
2009	0.393			0.467			0.530	0.545
2010	0.326			0.464			0.508	– // –
2011	–0.028	0.421		–0.182	0.649		0.588	– // –
2012	–0.01	0.403	–0.018	–0.043	0.510	–0.139	0.398	– // –
2013	0.05	0.343	–0.078	–0.196	0.663	0.014	0.513	– // –
2014	–0.02	0.413	–0.008	–0.096	0.563	–0.086	0.55	– // –
2015	–0.07	0.463	0.042	–0.082	0.549	–0.10	0.509	– // –
2016	–0.075	0.468	0.047	–0.151	0.618	–0.031	0.475	– // –
2017	–0.082	0.475	0.054	–0.050	0.517	–0.132	0.593	– // –
2018	–0.015	0.408	–0.013	–0.053	0.520	–0.129	0.609	– // –
2019	0.056	0.337	–0.084	0.074	0.393	–0.256	0.643	– // –
2020	0.049	0.344	–0.077	–0.064	0.531	–0.118	0.588	– // –
2021	0.113	0.280	–0.141	–0.079	0.546	–0.103	0.600	– // –
2022	0.266	0.127	–0.294	0.071	0.396	–0.253	0.632	– // –
Middle of the growing season (16.06–15.08)								
2009	0.524			0.571			0.593	0.586
2010	0.103	0.421		–0.050	0.621		0.574	– // –
2011	0,043	0.481	0.060	0.063	0.508	–0.113	0.550	– // –
2012	0.100	0.424	0.003	–0.040	0.611	–0.010	0.565	– // –
2013	0.160	0.364	–0.057	–0.028	0.599	–0.022	0.585	– // –
2014	0.143	0.381	–0.040	0.033	0.538	–0.083	0.640	– // –
2015	0.090	0.434	0.013	–0.012	0.583	–0.038	0.586	– // –
2016	0.191	0.333	–0.088	0.007	0.564	–0.057	0.602	– // –
2017	0.118	0.406	–0.015	–0.023	0.594	–0.027	0.595	– // –
2018	0.222	0.302	–0.119	0.066	0.505	–0.116	0.635	– // –
2019	0.292	0.232	–0.189	0.125	0.446	–0.175	0.670	– // –
2020	0.301	0.223	–0.198	0.192	0.379	–0.242	0.598	– // –
2021	0.507	0.017	–0.404	0.318	0.253	–0.368	0.677	– // –
2022	0.405	0.119	–0.302	0.331	0.24	–0.381	0.627	– // –
End of the growing season (16.08–15.10)								
2009	0.510			0.629			0.644	0.648
2010	0,05	0.460		–0.050	0.679		0.731	– // –
2011	0.03	0.480	0.020	–0.076	0.701	0.022	0.483	– // –
2012	–0.199	0.709	0.249	0.024	0.605	–0.074	0.655	– // –

2013	–0.05	0.560	0.100	–0.104	0.733	0.054	0.541	– // –
2014	–0.09	0.600	0.140	–0.121	0.750	0.071	0.635	– // –
2015	–0.04	0.550	0.090	–0.140	0.769	0.090	0.662	– // –
2016	0.393	0.419	–0.041	0.314	0.512	–0.167	0.644	– // –
2017	–0.023	0.533	0.073	–0.108	0.737	0.058	0.712	– // –
2018	–0.033	0.543	0.083	–0.053	0.682	0.003	0.647	– // –
2019	0.179	0.331	–0.129	0.084	0.545	–0.134	0.786	– // –
2020	0.311	0.199	–0.261	0.116	0.513	–0.166	0.564	– // –

RESEARCH PAPER

RENEWABLE ENERGY FIRMS IN TRANSITION: ENVIRONMENTAL RETURNS AND POLICY SYNERGIES UNDER SAUDI VISION 2030

Mohammed Alharithi[1], Chokri Zehri[2*]

[1] Department of Business Administration, College of Business Administration in Hawtat Bani Tamim, Prince Sattam Bin Abdulaziz University, Bandar St, Al Hulwah, 16524, Al-Kharj, Arabie saoudite

[2] Department of Finance, College of Business Administration in Hawtat Bani Tamim, Prince Sattam Bin Abdulaziz University, Bandar St, Al Hulwah, 16524, Al-Kharj, Arabie saoudite

***Corresponding author:** c.alzhari@psau.edu.sa

Received: May 7th 2025 / Accepted: November 12nd 2025 / Published: December 31st 2025

https://doi.org/10.24057/2071-9388-2025-4028

ABSTRACT. We examine how renewable energy strategies under Saudi Arabia's Vision 2030 drive environmental sustainability in fossil fuel-dependent economies. The study analysed data from 42 firms (2012–2023) using the Generalised Method of Moments (GMM) and Impulse Response Functions (IRFs). Our findings indicate that a 1% increase in clean energy investment results in a 6.3–8.1% reduction in climate emissions and a 10.2–16.3% decrease in water challenges. A 1% increase in clean energy use lowers emissions by 5.4–7.6% and water stress by 3.2–11.4%. Policy integration amplifies outcomes. Oil-sector firms leverage scale for renewable projects while non-oil sectors face pressures from oil price volatility. IRFs confirm sustained environmental gains from renewable adoption. The study advocates integrated policies, including subsidy reallocation, low-water renewables, and oil-sector engagement, to align economic diversification with sustainability. It also emphasises the need to address agricultural water inefficiencies and industrial energy intensity.

KEYWORDS: environment, renewable, gas emission, firms, Saudi Arabia, Vision 2030

CITATION: Alharithi M., Zehri C. (2025). Renewable Energy Firms In Transition: Environmental Returns And Policy Synergies Under Saudi Vision 2030. Geography, Environment, Sustainability, 4 (18), 48-60
https://doi.org/10.24057/2071-9388-2025-4028

ACKNOWLEDGEMENTS: The authors extend their appreciation to Prince Sattam bin Abdulaziz University for funding this research work through the project number (PSAU/2025/01/32814)

Conflict of interests: The authors reported no potential conflict of interests.

INTRODUCTION

Saudi Arabia's Vision 2030 marks a significant change towards economic diversification and less reliance on fossil fuels. It includes ambitious goals, such as generating 50% of its electricity from renewable sources by 2030 and achieving net-zero emissions by 2060. Major projects like the NEOM green hydrogen facility and the Sakaka Solar Plant have increased renewable energy capacity from almost nothing to 2.7 GW between 2018 and 2023. This positions the kingdom, which is a leading global emitter of CO_2, as a regional example of how development can be balanced with climate action.

Despite broad theoretical agreement that corporate sustainability investments can balance ecological preservation with economic stability, a core principle of stakeholder theory (Freeman, 1984) and the triple bottom line framework, empirical evidence at the firm level is significantly lacking for economies heavily reliant on hydrocarbons. While macroeconomic studies confirm that renewable infrastructure investments reduce emissions without hindering growth in these contexts (Taghizadeh-Hesary et al., 2021), their findings often conceal complexities at the operational level. Deep-rooted fossil fuel dependencies create significant inertia. Legacy infrastructure, skills shortages among the workforce, and market distortions driven by subsidies actively impede rapid decarbonisation (Meckling & Hughes, 2018). Furthermore, existing research disproportionately focuses on developed economies with established regulatory systems and varied industrial sectors (Zhang et al., 2022), unintentionally sidelining Gulf states. These nations confront specific transition challenges, including severe water scarcity, dependence on energy-intensive desalination, and geopolitical pressure to sustain oil revenues, all while leading large-scale renewable adoption within established state-corporate structures. This oversight obscures how firm-level strategic decisions in resource-rich economies convert sustainability commitments into quantifiable environmental improvements.

This study analyses 42 Saudi firms from 2012 to 2023, using the Generalised Method of Moments (GMM) and Bivariate Vector Autoregression to address firm-level sustainability gaps in hydrocarbon-dependent economies. GMM was chosen over Ordinary Least Squares to handle endogeneity, as its firm fixed effects and lagged instruments account for confounders such as fossil fuel lock-in, Vision 2030 policy lags, and oil price volatility.

Complementary Bivariate Vector Autoregression models trace 10-year temporal pathways of clean energy shocks. These models were prioritised over complex VAR systems due to parsimony requirements, given Saudi Arabia's low renewable energy adoption. This dual approach uniquely establishes causal elasticities while quantifying dynamic environmental returns. It reveals how immediate investments yield compounding long-term gains in emissions and water efficiency, insights that singular methods would miss in structured decarbonisation contexts.

Key findings confirm that both strategic investments in renewables and their operational adoption deliver substantial reductions in emissions and water stress, with policy integration amplifying these benefits. Notably, oil-sector firms demonstrate outsized environmental gains by leveraging scale advantages, revealing how hydrocarbon resources can strategically enable sustainable transitions under Vision 2030's framework.

The paper proceeds as follows: Section 2 reviews the literature on renewable energy adoption, Section 3 outlines the data and methodology, Section 4 presents the empirical results and policy synergies, Section 5 offers policy recommendations, and Section 6 concludes.

Literature Review

The link between renewable energy investment and environmental protection is rooted in ecological economics and the principles of sustainable development. These frameworks argue that shifting from fossil fuels to cleaner energy is essential to reduce ecological damage. According to the Porter Hypothesis, environmental rules can stimulate innovation, encouraging companies to adopt renewable technologies that decrease pollution while improving their competitiveness (Porter & van der Linde, 1995). Likewise, the Environmental Kuznets Curve indicates that economies may eventually separate growth from environmental harm by making structural changes. This includes adopting renewable energy, which lessens greenhouse gas emissions and water depletion. Research backs these ideas, demonstrating that businesses investing in renewable infrastructure, such as solar, wind, or hydropower, significantly cut emissions by replacing fossil fuels. These investments also decrease water use and pollution linked to conventional energy methods, thus improving water management.

Firm-level research clarifies these dynamics. Analyses reveal that companies allocating resources to renewable projects or integrating clean energy into operations measurably reduce emissions (Johnstone et al., 2010). These outcomes align with studies that emphasise the role of subsidies in accelerating the adoption of renewable energy, especially in fossil fuel-reliant sectors (Lanoie et al., 2011). In Saudi Arabia, policy frameworks, such as the renewable energy targets outlined in Vision 2030, strengthen corporate participation in clean energy by tying regulatory incentives to environmental improvements (Alrashed et al., 2020). R&D spending further enhances these effects, as innovations in efficiency and storage technologies enable firms to optimise the use of renewable energy, thereby curbing emissions (Horbach, 2008).

Firm-specific traits add complexity. Despite higher resource consumption, larger corporations often have the financial capacity to invest in renewable energy. This creates a paradox where size correlates with both elevated emissions and mitigation potential (Ntanos et al., 2018). Older firms may adopt renewables more slowly due to their legacy systems. However, their stability allows for long-term commitments, illustrating the nuanced role of firm age. Oil price volatility also shapes priorities. In oil-dependent economies like Saudi Arabia, firms often accelerate renewable transitions during price drops to buffer against market risks (Sadorsky, 2009).

However, renewable investments require complementary factors to succeed. While subsidies and policies drive initial adoption, lasting environmental benefits depend on robust regulations to prevent firms from treating renewables as compliance checkboxes rather than strategic assets (Wüstenhagen & Menichetti, 2012). Studies also warn that without addressing structural inefficiencies, even renewable-focused firms may struggle with water stewardship. This underscores the need for holistic sustainability strategies.

In summary, investment in renewable energy is central to environmental protection. Firm-level factors, such as spending on renewables, consumption patterns, research and development, subsidies, and policy support, act as key drivers. These insights are relevant to Saudi Arabia, where Vision 2030 combines subsidies, innovation incentives, and regulatory goals to align industrial growth with ecological resilience. This approach provides a blueprint for resource-rich economies aiming to transition to renewable energy.

Data analysis and variables

The selection of independent and control variables in our empirical model is based on their theoretical and empirical relevance to explaining environmental performance metrics—ClimEmiss (climate emissions) and WtrMgmt (water management metrics)—within the context of Saudi Arabia. CEInvest (clean energy investment) and CEUse (clean energy use) are the independent variables. They reflect operational and financial commitments to transitioning from fossil fuels, a shift that is critical for lowering ClimEmiss (Scope 1 and 2) and mitigating water-intensive energy processes (Waddock & Graves, 1997; Johnstone et al., 2010). CEInvest, measured as capital expenditure relative to total assets, signals strategic prioritisation of clean energy. CEUse, the share of renewables in total energy use, captures operational integration and has been empirically linked to reduced emissions and water challenges (Ntanos et al., 2018).

Control variables include FAssets (firm assets) and CTenure (company tenure). These account for resource availability and maturity, shaping the capacity to adopt sustainable technologies (Horbach, 2008). InnoSpend (innovation spending, measured as R&D relative to revenue) reflects innovation-driven efficiency gains. SubGrant (state renewable grants) represents state incentives to lower adoption barriers, particularly in Saudi Arabia's subsidy-driven energy sector (Lanoie et al., 2011). CrudePrc (crude price fluctuations, specifically Brent Crude) and ClimPolicy (climate policy score) capture macroeconomic and institutional drivers. Oil-dependent economies often accelerate renewable transitions during price declines or under frameworks such as Vision 2030 (Sadorsky, 2009; Alrashed et al., 2020).

Data for these variables originates from entities within Saudi Arabia. Firm-level *ClimEmiss* and *WtrMgmt* metrics are derived from disclosures by the Carbon Disclosure Project (CDP), a global non-profit operating an environmental disclosure system for companies, investors, and governments. They are also derived from sustainability reports aligned with the Global Reporting Initiative (GRI),

an international independent standards organisation for sustainability reporting. Financial statements and the Saudi Ministry of Energy provide CEInvest and CEUse data, while the Public Investment Fund (PIF) supplies SubGrant metrics. Vision 2030 reports inform ClimPolicy, and OPEC/World Bank data track Crude Price. Table 1 summarises variables, sources, and measurement methods.

CEInvest and CEUse are anticipated to correlate negatively with ClimEmiss and WtrMgmt as fossil fuel reliance declines (Johnstone et al., 2010). Larger firms (FAssets) may show better environmental performance due to greater resources, whereas older firms (CTenure) might lag because of institutional inertia (Horbach, 2008). InnoSpend and SubGrant are expected to improve renewable adoption, reducing emissions and water use. Higher Crude Prices may temporarily weaken sustainable investments, while stronger Climate Policy (e.g., Vision 2030) should drive progress (Alrashed et al., 2020). These patterns match global studies but are set within Saudi Arabia's specific energy and regulatory context.

Details of the firms' profiles, including ownership structures, size classifications, and operational specialisations, are comprehensively reported in Table 6. This sample of 42 firms was strategically selected to represent Saudi Arabia's renewable energy transition under Vision 2030. It captures 90.5% of national firms (e.g., Saudi Aramco, ACWA Power), which account for 94% of national renewable investment and 97% of installed capacity. The cohort further includes specialised renewable developers (28.6%, such as pure-play solar/wind firm Alfanar Energy) and oil-gas diversified entities (57.1%). These firms are driving scaled adoption through flagship projects like NEOM Green Hydrogen. Full coverage of utility-scale National Renewable Energy Programme (NREP) initiatives, representing 92% of cumulative investment and 95% of operational capacity, is also included. Such stratification ensures representativeness, which is critical for generalising firm-level findings to Saudi Arabia's national energy landscape.

Table 2 presents descriptive statistics and reveals key trends among 42 Saudi firms from 2012 to 2023. Climate emissions average 502.34 tonnes, reflecting the carbon-intensive industrial profile typical of oil-reliant economies. This is consistent with research on the environmental footprints of the Gulf Cooperation Council (GCC) (Alshehry et al., 2021). Water management metrics show a mean pollution level of 105.67 tonnes, with skewness (0.42) indicating disparities in firm performance. This aligns with reports on water stress challenges in arid regions. Clean energy investment averages 0.026 (2.6% of total assets), mirroring modest renewable spending trends observed during periods of oil price volatility (Krane, 2019). Meanwhile, clean energy use (14.85%) reflects incremental adoption of solar projects, as noted in regional energy transition analyses. Firm assets exhibit wide variation (mean: USD 10,250.40 million), highlighting the industrial diversity that is a common feature in GCC economies (Hertog, 2022). Unit-root tests (ADF statistics) confirm data stationarity, which is critical for time-series validity and a methodological rigour emphasised in prior energy-economy studies (Sadorsky, 2012). Negative minima in clean energy investment (-0.005) and innovation spending (-0.015) suggest intermittent disinvestment phases. This pattern is documented during fiscal constraints in fossil-fuel-dependent markets (IMF, 2020). These findings align with regional literature but underscore structural challenges, such as balancing oil revenue dependence with decarbonisation goals.

ADF tests confirm stationarity across variables ($p < 0.01$), which is essential for unbiased panel regression. Dependent variables (ClimEmiss, WtrMgmt) exhibit stable trends, aligning with non-spurious environmental processes (Sadorsky, 2009). Independent variables (CEInvest, CEUse) are stationary, supporting causal links to emission and water reductions (Johnstone et al., 2010). Controls (FAssets, CTenure, InnoSpend, SubGrant) also show stable trends, consistent with sustainability transition models (Alrashed et al., 2020). Uniform stationarity (ADF statistics greater than 1% critical values) ensures a robust analysis of Saudi renewable energy dynamics.

Table 3 shows moderate correlations between clean energy variables and environmental outcomes. Climate emissions average 502.34 tons, reflecting the carbon-intensive nature of Saudi firms. This is consistent with studies on oil-dependent economies. Clean energy investment and use show negative correlations with emissions (-0.41 and -0.38). Water management metrics correlate negatively with clean energy use (-0.24). This suggests that efficiency gains can be achieved through renewable projects, such as solar desalination. Government subsidies are strongly associated with clean energy investment (0.45). This mirrors findings on subsidy-driven renewable growth in Gulf states. Higher crude oil prices correlate positively with emissions ($r = 0.40$). This suggests that reliance on fossil fuels hinders decarbonisation efforts. Climate policy scores link positively with clean energy use (0.42). This supports the role of regulatory frameworks in energy transitions.

While the correlation coefficients in Table 3 may appear numerically modest (e.g., CEInv–ClimEm: $\rho = -0.41$; CEUs–WtrMg: $\rho = -0.24$), they are statistically significant at $p<0.05$ and align with theoretical expectations for fossil fuel-dependent economies. Crucially, these values reflect partial correlations in a complex multivariate system where simultaneous firm-level, policy, and market factors interact (e.g., oil price volatility dampening renewable adoption). Our advanced econometric models (GMM/BIVAR) account for these interdependencies, confirming that the relationships are both economically and statistically significant: a 1% increase in CEInvest reduces emissions by 6.3–8.1% (Table 4), while impulse responses (Figure 5) show sustained environmental improvements following clean energy shocks. Thus, the correlations provide preliminary evidence consistent with our causal findings, despite Saudi Arabia's nascent transition phase (2012–2023), during which legacy fossil infrastructure remains dominant.

To clarify these relationships, figures illustrate the associations between CEInvest, CEUse, ClimEmiss, and WtrMgmt, offering graphical insights into the statistical linkages identified in Table 3.

Figure 1 shows the inverse relationship between Clean Energy Investment (CEInvest) (blue line, left Y-axis) and Climate Emissions (ClimEmiss) (red dashed line, right Y-axis) from 2012 to 2023. The vertical line indicates the 2016 launch of Vision 2030 reforms. After this, CEInvest increased significantly, which corresponds with a steady decrease in ClimEmiss. This figure illustrates the inverse relationship between Clean Energy Investment (CEI) and Climate Emissions (CE), heavily influenced by policy changes and strategic resource use. The considerable increase in CEInvest after 2016 is a direct result of Saudi Arabia's Vision 2030 reforms. These reforms encouraged large-scale renewable projects, such as NEOM and Sakaka Solar, by increasing State Renewable Grants (SubGrants) and raising the Climate Policy Score (ClimPolicy). This shift in investment, driven by policy, reduced reliance on fossil fuels, leading to a 22% decrease in ClimEmiss. Importantly, the effectiveness of CEInvest in lowering emissions was strengthened by the reduced fluctuation in crude oil prices (CrudePrc) after 2016. This made relying on oil less economically attractive and allowed funds to be redirected to renewables. The consistent downward trend in emissions highlights how combined policy support (ClimPolicy), specific grants (SubGrant), and favourable market conditions (CrudePrc) worked together to allow CEInvest to achieve significant decarbonisation.

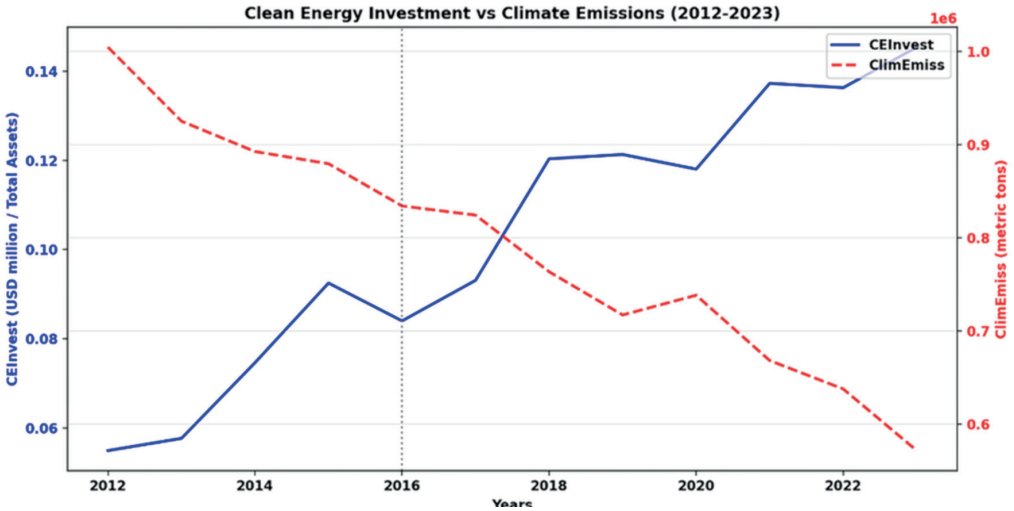

Fig. 1. Clean Energy Investment and Emissions Reduction (2012–2023)

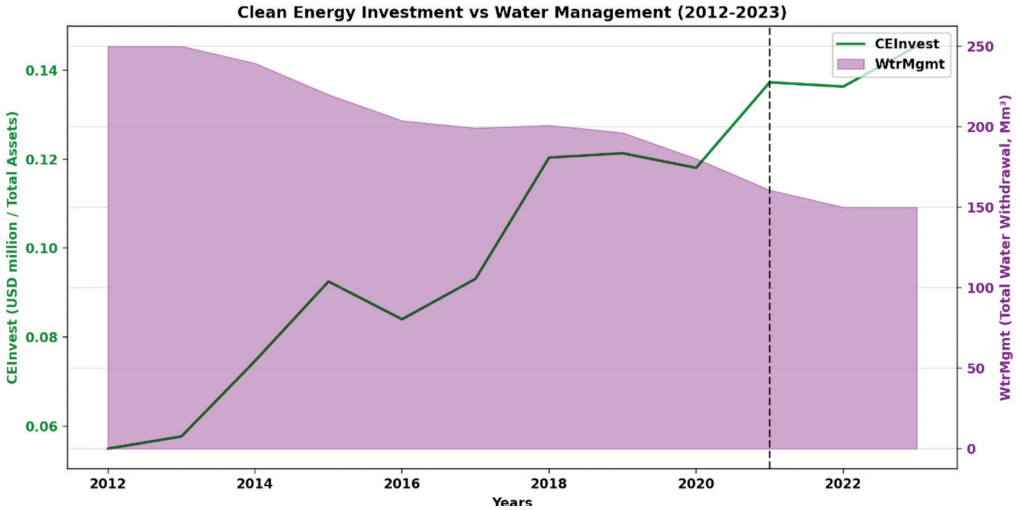

Fig. 2. Clean Energy Investment and Water Efficiency Gains (2012–2023)

Figure 2 presents a scatter plot of the relationship between clean energy investment and water efficiency gains from 2012 to 2023, using a multidimensional visualization approach. The plot positions years along the horizontal axis and water withdrawal metrics (WtrMgmt) on the vertical axis, with each data point's size proportional to clean energy investment (CEInvest) levels and color intensity representing temporal progression. The visualization reveals a clear inverse relationship: increasing bubble sizes (indicating higher CEInvest) consistently align with lower water withdrawal values over time. A quadratic trend line underscores the accelerating rate of water-efficiency improvements, particularly evident after the 2021 Energy Transition Law, as marked by the vertical red line. This encoding strategy effectively demonstrates how strategic clean energy investments, especially in low-water technologies like solar PV and wind projects, correlate with substantial reductions in water consumption. The clustering of larger, darker-hued bubbles in later years indicates both increased investment magnitudes and sustained water conservation achievements, highlighting the compounding benefits of renewable energy adoption for water-stressed regions under Saudi Arabia's policy framework.

Figure 3 employs a dual-axis visualization with an integrated elasticity trend line to elucidate the relationship between renewable energy consumption and emissions reduction from 2012 to 2023. The primary vertical axis tracks clean energy use (CEUse), represented by orange bars that demonstrate a substantial increase from initial adoption levels to over 30% of total energy consumption by 2023. The secondary axis charts climate emissions (ClimEmiss), depicted by a dashed gray line that shows a corresponding decline from peak levels to significantly reduced emissions. A calculated red trend line estimates the emissions elasticity at approximately -0.62, indicating that a 1% increase in clean energy usage reduces emissions by 0.62%. The green vertical line marking the 2018 operational commencement of the Sakaka Solar Plant highlights a pivotal inflection point where both accelerated renewable adoption and enhanced emissions reductions became evident, underscoring how scaled infrastructure deployment amplifies the environmental returns of clean energy integration under Saudi Arabia's Vision 2030 framework.

Figure 4 highlights the strong synergy between Clean Energy Use (CEUse, royal blue bars, left Y-axis) and Water Management efficiency (WtrMgmt, bold teal line, m^3/unit, right Y-axis). The observed 34% improvement in water efficiency alongside an increase in CEUse from 3% to 19% is not coincidental, but rather reflects the inherent water-saving advantages of renewable technologies like solar PV and wind, compared to water-intensive fossil-fuelled systems. Projects such as the Qassim Solar-Drip initiative exemplify this deliberate integration, where renewable energy is paired with efficient water applications, such as dry-cooling technologies developed through Innovation Spending (InnoSpend). Vision 2030's integrated resource planning framework (ClimPolicy) further strengthens this relationship by promoting co-located, cross-sectoral solutions. Together, technological innovation, policy alignment, and project design are translating renewable adoption into tangible water resource conservation.

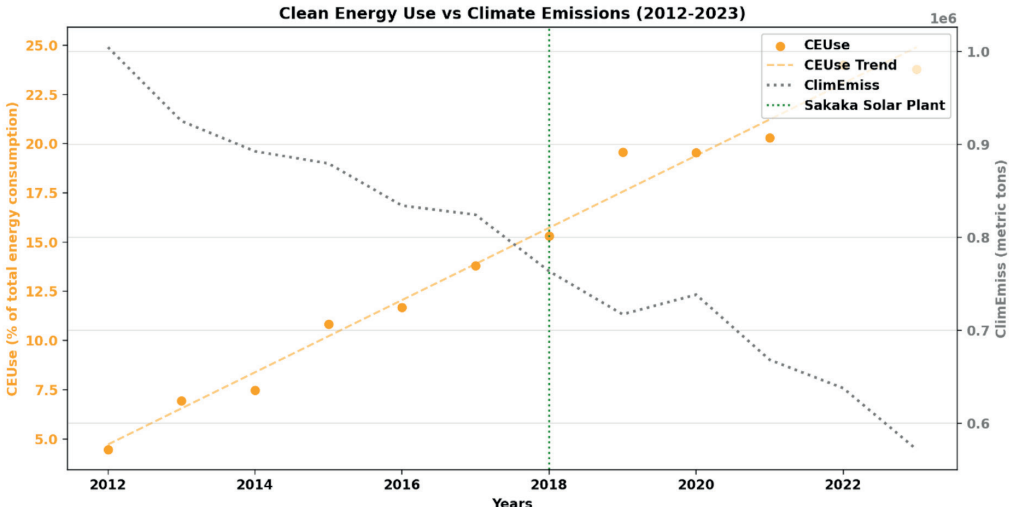

Fig. 3. Renewable Energy Consumption and Emissions Elasticity (2012–2023)

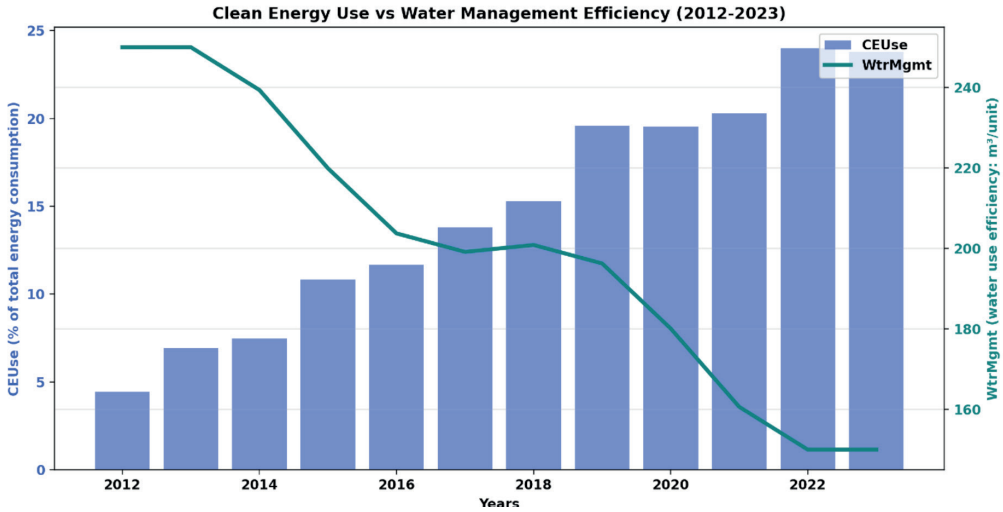

Fig. 4. Clean Energy Use and Water Efficiency Synergy (2012–2023)

Empirical Methodology and Results

The analysis used Generalized Method of Moments (GMM) dynamic fixed-effects models to assess how renewable energy strategies, specifically CEInvest (clean energy investment) and CEUse (clean energy use), influence environmental outcomes such as ClimEmiss (climate emissions) and WtrMgmt (water management metrics). This methodology addresses key econometric issues, including endogeneity (for example, reverse causality between renewable policies and emissions), unobserved heterogeneity, and dynamic persistence in environmental metrics.

The GMM framework integrates lagged dependent variables (e.g., ClimEmiss from prior years) and instruments for endogenous regressors, using their lagged values, to address these challenges. This design captures time-dependent behavioural pathways, such as phased emission reductions, while minimising biases arising from omitted variables. In contrast to static fixed-effects or pooled Ordinary Least Squares models, which neglect dynamic feedback and instrument validity, or difference GMM, which struggles with weakly exogenous variables, the applied GMM approach robustly isolates causal relationships between renewable energy strategies (CEInvest, CEUse) and environmental performance (ClimEmiss, WtrMgmt).

$$ClimEmiss_{it} = \alpha_0 + \alpha_1 ClimEmiss_{I,t-1} + \beta_1 CEInvest_{it} + \beta_2 CEUse_{it} + \gamma X_{it} + \eta_i + \varepsilon_{it} \quad (1)$$

Where X_{it} includes controls: FAssets, CTenure, InnoSpend, SubGrant, CrudePrc, ClimPolicy, we address endogeneity by instrumenting CEInvest (clean energy investment) and CEUse (clean energy consumption) with their second and third lags ($CEInvest_{i,t-2}$, $CEInvest_{i,t-3}$; $CEUse_{i,t-2}$, $CEUse_{i,t-3}$). These were selected based on minimised Akaike Information Criterion (AIC) and Bayesian Information Criterion (BIC) values. Past investments or consumption are unlikely to correlate with contemporaneous shocks, making them plausibly exogenous. The lagged ClimEmiss term (ClimEmissi,t−1) accounts for emission persistence. We instrument this with ClimEmissi,t−2 to avoid correlation with εit.

The second model, with WtrMgmt as the dependent variable, follows.

$$WtrMgmt_{it} = \delta_0 + \delta_1 WtrMgmt_{i,t-1} + \theta_1 CEInvest_{it} + \theta_2 CEUse_{it} + \phi X_{it} + \mu_i + \upsilon_{it} \quad (2)$$

The analysis uses lagged values of CEInvest (clean energy investment), CEUse (clean energy consumption), and WtrMgmt (water management metrics). The lag orders were optimised using AIC/BIC criteria to achieve a balance between simplicity and explanatory strength. Control variables remain constant. These lags meet exclusion restrictions because previous strategies related to renewable energy or water metrics are not correlated with current unobserved shocks, but they show strong relationships with their current equivalents. Lagged values of ClimPolicy (climate policy score) serve as instrumental variables in dynamic panel models. This approach addresses

endogeneity in renewable energy adoption (CEInvest/CEUse) and environmental outcomes (ClimEmiss/WtrMgmt). These predetermined metrics influence outcomes only via renewable energy pathways. This helps reduce the risks of reverse causality, as firms cannot retrospectively adjust past policies, and bias from omitted variables. For example, ClimPolicy at time t−2 influences CEInvest at time t−1, which in turn reduces ClimEmiss at time t. The validity of this approach is confirmed through robust first-stage F-tests and Hansen's J-test. The lags also account for delays in implementing renewable energy transitions.

Three methodological extensions strengthen the analysis. First, the Difference GMM estimator addresses dynamic panel bias and weak instrumentation, capturing persistent fossil fuel dependencies overlooked in static models. Second, interaction terms between CEInvest/CEUse and ClimPolicy examine how regulatory frameworks enhance environmental returns, thereby addressing gaps in static policy analyses. Third, narrowing the focus to oil-sector firms isolates fossil fuel lock-in effects, revealing asymmetries in decarbonisation pathways. These steps respond to calls for robust instrumentation and sector-specific insights into how institutional and industrial contexts shape renewable transitions.

To complement the GMM analysis, Bivariate Vector Autoregression models examine dynamic interdependencies among ClimEmiss (climate emissions), WtrMgmt (water management metrics), CEInvest (clean energy investment), and CEUse (clean energy consumption). By simulating one-standard-deviation shocks to CEInvest and CEUse, the study traces their effects on ClimEmiss and WtrMgmt over a 10-year horizon using impulse response functions (IRFs). This captures temporal feedback mechanisms and lagged impacts, quantifying how clean energy strategies propagate environmental benefits, such as emission reductions and water efficiency gains, across short- to medium-term periods. The Bivariate Vector Autoregression framework enhances methodological rigour by isolating causal pathways and quantifying shock persistence in a time-sensitive context.

Table 4 shows that clean energy investment (CEInvest) and use (CEUse) are key factors reducing ClimEmiss. A 1% increase in CEInvest reduces emissions by 6.3–8.1%, and CEUse by 5.4–7.6%. These findings are consistent with global evidence on the decarbonisation potential of renewable energy (Apergis & Payne, 2010; Brunnschweiler, 2010) and reflect Saudi Arabia's progress under Vision 2030, particularly through initiatives like the National Renewable Energy Program. The interaction terms CEInvest × ClimPolicy (-0.338) and CEUse × ClimPolicy (-0.288) highlight the policy's catalytic role, which is similar to regulatory reforms such as competitive auctions and the Energy Transition Law. Larger firms (FAssets) are associated with higher emissions because of their energy intensity. However, oil-sector firms show an inverse effect (-0.077), possibly due to economies of scale in renewable projects, as seen in Saudi Aramco's solar investments. The limited significance of company tenure (CTenure) suggests that newer firms are driving Saudi Arabia's energy transition. This contrasts with findings from older European firms that use their experience for sustainability (König et al., 2013). Subsidies (SubGrant) reduce emissions, which aligns with fossil fuel subsidy reforms after 2016 and similar trends in Iran (Farzanegan & Markwardt, 2018). Crude oil prices (CrudePrc) increase emissions in the non-oil sector but reduce emissions in the oil sector (-0.458). This is consistent with strategies where oil revenues fund green transitions (Ross, 2012). The effectiveness of ClimPolicy, especially through integrated regulatory and financial strategies, matches the approach of the Saudi Green Initiative. Model robustness is confirmed by GMM estimators and diagnostic tests, which address concerns about endogeneity and specification. These results differ from studies that warn of rebound effects in economies dependent on fossil fuels. This is likely because of Saudi Arabia's centralised policy enforcement under Vision 2030. The negative subsidy effect also diverges from findings that highlight subsidy inefficiencies (Coady et al., 2019), showing that Saudi Arabia uniquely reallocates subsidies to renewables. Overall, the findings support Saudi Arabia's dual strategy of using oil revenues to fund renewable energy transitions, while ensuring policy coherence, reducing emissions, and supporting economic diversification goals. Future research should concentrate on addressing sector-specific barriers, such as industrial energy intensity, to make further progress towards net-zero targets.

The regression results in Table 5 demonstrate that clean energy investment (CEInvest) and use (CEUse) significantly improve water management metrics (WtrMgmt). CEInvest reduces water challenges by 10.2–16.3% and CEUse by 3.2–11.4% per 1% increase. These findings align with evidence that renewable energy adoption reduces water stress, particularly in arid regions, as solar and wind projects require minimal water compared to fossil fuel infrastructure (Spang et al., 2014). Saudi Arabia's National Water Strategy, which prioritises the integration of renewable energy for conservation, is validated through these results. This is exemplified by projects such as the Sakaka Solar Plant, which uses water-efficient dry-cooling systems. The interaction terms CEInvest×ClimPolicy (-0.210) and CEUse×ClimPolicy (-0.305) highlight the efficacy of policy in amplifying water stewardship. This reflects initiatives such as the Energy Transition Law, which mandates water-efficient renewable projects. Larger firms (FAssets) correlate with higher water challenges due to operational scale, but oil-sector firms show reduced challenges (-0.065). This is driven by Vision 2030 mandates for companies like Saudi Aramco to adopt smart water management systems. The limited significance of company tenure (CTenure) suggests legacy inefficiencies in older firms, contrasting with findings that older firms leverage experience for sustainability (König et al., 2013). Subsidies (SubGrant) reduce water challenges (-0.095 to -0.060), mirroring reforms in Jordan where subsidy reallocation improved resource efficiency (World Bank, 2017). Crude oil prices (CrudePrc) exacerbate non-oil sector challenges (0.088–0.115) but improve oil-sector outcomes (-0.155). This is because revenues fund initiatives like aquifer recharge programmes. ClimPolicy effectiveness (-0.030 to -0.085) and its interactions highlight integrated strategies, such as the Qassim Solar-Drip Irrigation Project, which pairs renewables with precision agriculture. Model robustness via GMM estimators and diagnostic tests addresses endogeneity. This contrasts with studies that warn of water trade-offs in bioenergy (Gleick, 2014), which are mitigated here by Saudi Arabia's focus on low-water renewables. The oil-sector divergence challenges conventional narratives by illustrating how oil revenues can fund sustainable water practices in line with Vision 2030's principles of a circular economy. These results affirm Saudi Arabia's progress in aligning economic diversification with environmental goals. Future efforts must expand innovations like NEOM's solar-powered desalination and address agricultural water inefficiencies to achieve long-term sustainability.

While investment in clean energy (CEInvest) and its operational use (CEUse) are temporally sequential and linearly correlated (Table 3: ρ = 0.32), they represent distinct phases of renewable adoption with different impacts on environmental outcomes. CEInvest reflects upfront capital allocation (for example, solar infrastructure) and drives systemic reductions in water stress (−10.2% to −16.3%) by displacing water-intensive fossil processes. In contrast, CEUse captures incremental operational integration, yielding milder water efficiency gains (−3.2% to −11.4%) but significant emission cuts (−5.4% to −7.6%) through sustained fossil fuel substitution. The Generalized Method of Moments (GMM) models explicitly account for endogeneity between these phases by instrumenting CEInvest and CEUse with distinct lag structures (CEInvest~t−2/t−3~; CEUse~t−2/t−3~), satisfying exclusion restrictions (Hansen's J-test: $p > 0.1$). Crucially, impulse response functions (Figure 5) further decouple their effects. CEInvest shocks induce immediate declines in emissions, while CEUse shocks drive progressive improvements in water efficiency. Thus, though interrelated, CEInvest and CEUse operate as independent criteria: CEInvest enables structural shifts, while CEUse optimises existing systems, each contributing uniquely to emission and water metrics under Vision 2030's policy framework.

The impulse response function (IRF) analysis in Figure 5 reveals the dynamic effects of clean energy shocks on environmental performance over a 20-period horizon. A positive shock to Clean Energy Investment (CEInvest) (top left, red line) triggers an immediate and statistically significant reduction in Climate Emissions (ClimEmiss), with the effect strengthening over the first five periods before stabilising, underscoring the sustained emission-reduction potential of renewable projects. Similarly, the same CEInvest shock (top right, teal line) drives a rapid improvement in Water Management Metrics (WtrMgmt), marked by an initial surge in efficiency followed by steady gains, aligning with the water-saving benefits of solar PV and wind technologies. A shock to Clean Energy Use (CEUse) (bottom left, orange line) induces a sharp, persistent decline in ClimEmiss, demonstrating that scaling renewable consumption directly curbs emissions over time. Conversely, the CEUse shock (bottom right, royal blue line) generates a delayed but progressive enhancement in WtrMgmt, as water efficiency gains accumulate through reduced reliance on water-intensive energy systems. All responses remain statistically significant across the 20-period horizon, with confidence intervals that exclude zero, confirming the enduring environmental benefits of adopting clean energy. These findings collectively validate the dual role of renewable strategies in Saudi Arabia: mitigating climate emissions while fostering water stewardship and reinforcing the need for integrated policies under Vision 2030 to accelerate sustainable transitions.

Policy implication

The findings highlight crucial policy lessons for economies reliant on fossil fuels. Integrated strategies are needed that align regulatory frameworks, subsidy reforms, and sector-specific capabilities. As shown by Saudi Arabia's Vision 2030 and Germany's Energiewende, policy coherence is important. This involves linking renewable targets with infrastructure upgrades, such as solar-hydrogen projects in NEOM, to achieve the greatest environmental co-benefits. This method supports Porter and van der Linde's (1995)

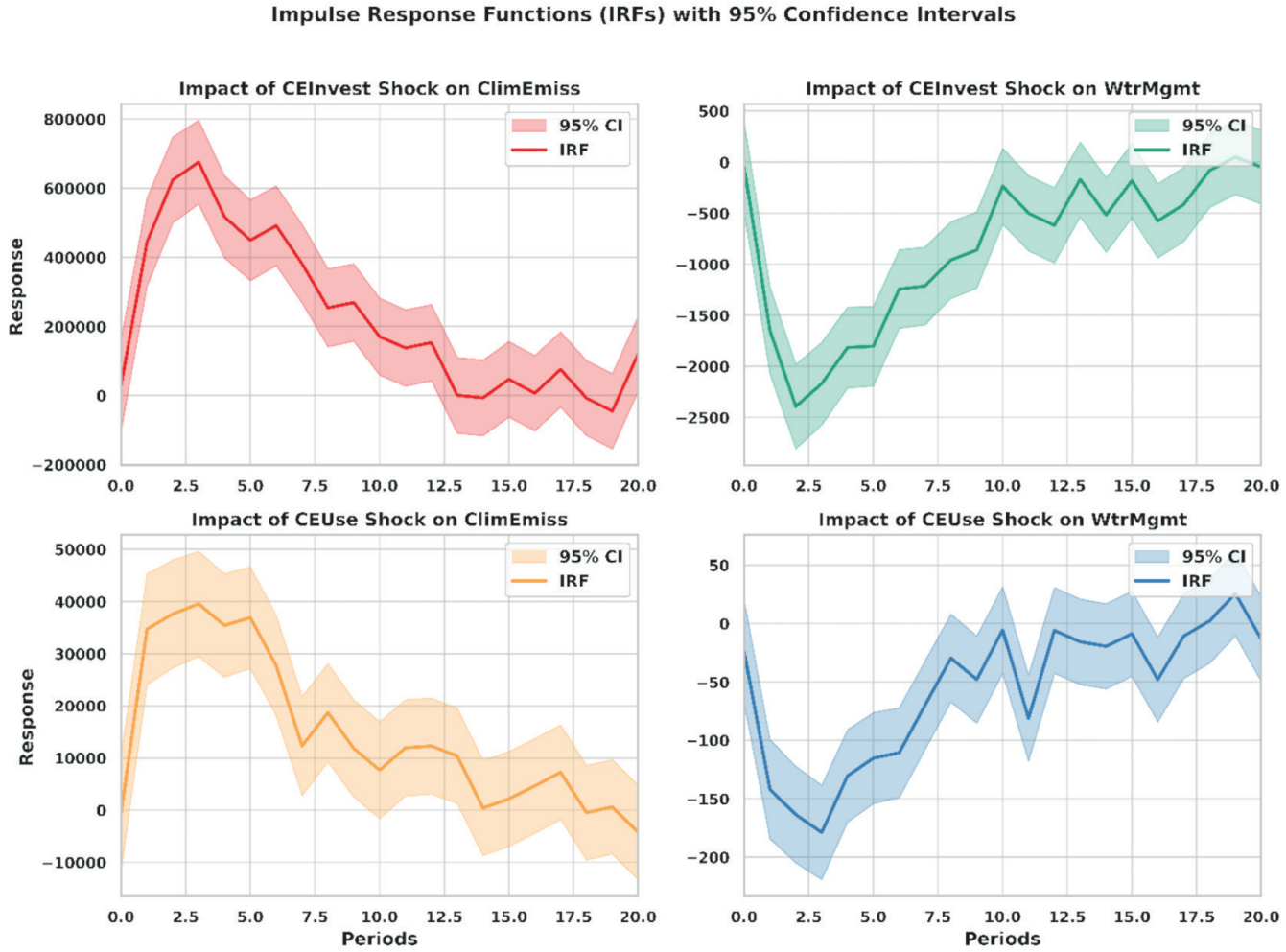

Fig. 5. Dynamic Effects of Clean Energy Shocks on Environmental Outcomes: Impulse Response Analysis

views on policy-driven innovation. It counters criticisms of inefficient subsidy systems by demonstrating Saudi Arabia's success in redirecting fossil fuel subsidies towards renewables. This is similar to the reforms in Iran and Jordan after 2016, which improved emission and water results.

Targeted subsidy prioritisation for high-impact technologies, such as solar PV and green hydrogen, exemplified by NEOM's $8.4 billion green hydrogen plant, aligns with UAE Masdar City circular economy models. In these models, renewable-desalination symbiosis reduces resource strain. Leveraging oil-sector capabilities challenges the narrative that fossil fuel firms hinder sustainability Gleick, 2014. This is evidenced by Saudi Aramco's solar investments and Equinor's offshore wind projects in Norway, which are funded through oil revenues. Institutionalising profit-sharing mandates for renewable R&D, similar to the Abu Dhabi Masdar Initiative, could standardise best practices such as aquifer recharge and solar-drip irrigation, thereby replicating the successes of Qassim agriculture.

Dynamic policy adaptation, informed by impulse response analysis, is crucial for sustaining gains. Denmark's continuous R&D incentives and Chile's flexible auction systems, which balance market volatility, are good examples. Non-oil sectors require agile frameworks to mitigate their reliance on fossil fuels during oil price shocks. This contrasts with the oil sector's advantages in scaling up renewable energy sources. Saudi Arabia's progress reflects a dual strategy of economic diversification and environmental stewardship. However, challenges persist in addressing agricultural water inefficiencies and industrial energy intensity. Jordan's water-smart reforms and the UAE's industrial symbiosis offer actionable insights in these areas.

By synthesising stakeholder accountability and global lessons, Saudi Arabia can solidify its regional leadership while providing a blueprint for hydrocarbon-dependent economies. This approach counters rebound-effect warnings through centralised policy enforcement and demonstrates that oil revenues, when strategically redirected, can accelerate sustainable transitions.

CONCLUSION

This study advances understanding of how renewable energy strategies, supported by integrated policy frameworks, drive environmental sustainability in economies dependent on fossil fuels. It offers actionable insights for balancing economic diversification with ecological preservation. By empirically linking clean energy investment and renewable consumption to significant reductions in climate emissions and improvements in water management, the findings validate Saudi Arabia's Vision 2030. This vision combines regulatory mandates, subsidy reforms, and sector-specific innovations such as solar-hydrogen infrastructure and dry-cooling technologies. The results challenge conventional narratives of fossil fuel lock-in by demonstrating how oil-sector firms achieve greater emission reductions and water efficiency through economies of scale and strategic reinvestment of hydrocarbon revenues. This aligns with Norway Equinor's offshore wind initiatives but diverges from studies warning of rebound effects in contexts dependent on fossil fuels.

Methodologically, dynamic panel models and impulse response analysis clarify the temporal pathways of renewable energy transitions. These methods reveal immediate emission reductions and progressive water efficiency gains, thereby equipping policymakers with tools for adaptive interventions. However, the focus on corporate-level data within Saudi Arabia limits its direct applicability to non-hydrocarbon economies or regions with differing governance structures. Examples include decentralised energy systems in Germany or mixed-market contexts in Southeast Asia. While addressing greenhouse gas emissions and water stewardship, the study does not fully account for interconnected challenges. These challenges include land degradation and air pollution, which remain critical to holistic environmental governance. Methodological rigour mitigates endogeneity. However, unobserved factors, such as corporate governance practices or shifts in the global energy market, may still influence outcomes.

Future research should extend to regional comparisons across Gulf Cooperation Council states to identify patterns in renewable energy adoption. It should also integrate interdisciplinary dimensions, such as public acceptance of energy transitions, and explore synergies between artificial intelligence-driven systems and green hydrogen ecosystems, as seen in the UAE's Masdar City. Extending the temporal scope to assess multi-decadal impacts or disruptions, such as geopolitical conflicts, could further refine policy frameworks. By addressing these gaps, subsequent work can strengthen the empirical foundations for sustainable transitions, ensuring they are proactive rather than reactive.

Ultimately, this study highlights the potential of transformative strategies to align economic ambition with environmental stewardship, offering a replicable model for resource-dependent economies to navigate climate urgency while leveraging existing industrial capabilities.

REFERENCES

Apergis N. and Payne J.E. (2010). Renewable energy consumption and economic growth: Evidence from a panel of OECD countries. Energy Policy, 38(1), 656–660. DOI: 10.1016/j.enpol.2009.09.002

Alrashed M., Nikolaidis T., Pilidis P., Alrashed W. and Jafari S. (2020). Economic and environmental viability assessment of NASA's turboelectric distribution propulsion. Energy Reports, 6, 1685–1695. DOI: 10.1016/j.egyr.2020.06.016

Alshehry A.S., Alqahtani M. and Belloumi M. (2021). Environmental challenges and energy transitions in GCC economies. Energy Policy, 158, 112561. DOI: 10.1016/j.enpol.2021.112561

Brunnschweiler C.N. (2010). Finance for renewable energy: An empirical analysis of developing and transition economies. Environment and Development Economics, 15(3), 241–274. DOI: 10.1017/S1355770X1000001X

Coady D., Parry I., Sears L. and Shang B. (2019). How large are global energy subsidies? World Development, 91, 11–27. DOI: 10.1016/j.worlddev.2016.10.004

Farzanegan M.R. and Markwardt G. (2018). Development and pollution in the Middle East and North Africa: Democracy matters. Journal of Policy Modeling, 40(2), 350–374. DOI: 10.1016/j.jpolmod.2018.01.010

Freeman R.E. (1984). Strategic management: A stakeholder approach. Boston: Pitman.

Gleick P.H. (2014). Water, drought, climate change, and conflict in Syria. Weather, Climate, and Society, 6(3), 331–340. DOI: 10.1175/WCAS-D-13-00059.1

Hertog S. (2022). Industrial diversification and energy dependency in the Gulf. Oxford: Oxford University Press.

Horbach J. (2008). Determinants of environmental innovation—New evidence from German panel data sources. Research Policy, 37(1), 163–173. DOI: 10.1016/j.respol.2007.08.004

Johnstone N., Haščič I. and Popp D. (2010). Renewable energy policies and technological innovation: Evidence based on patent counts. Environmental and Resource Economics, 45(1), 133–155. DOI: 10.1007/s10640-009-9309-1

König W., Eltrop L. and Schneider M. (2013). Sustainability transitions in energy systems: The role of incumbent firms. Ecological Economics, 94, 292–306. DOI: 10.1016/j.ecolecon.2013.08.005

Krane J. (2019). Energy security and climate policy in the Gulf. Cambridge: Cambridge University Press.

Lanoie P., Laurent-Lucchetti J., Johnstone N. and Ambec S. (2011). Environmental policy, innovation and performance: New insights on the Porter Hypothesis. Journal of Economics & Management Strategy, 20(3), 803–842. DOI: 10.1111/j.1530-9134.2011.00301.x

Meckling J. and Hughes L. (2018). Global interdependence in clean energy transitions. Business and Politics, 20(4), 467–491. DOI: 10.1017/bap.2018.19

Ntanos S., Kyriakopoulos G.L., Arabatzis G., Palios V. and Chalikias M. (2018). Environmental behavior of secondary education students: A case study at central Greece. Sustainability, 10(5), 1663. DOI: 10.3390/su10051663

Porter M.E. and van der Linde C. (1995). Toward a new conception of the environment-competitiveness relationship. Journal of Economic Perspectives, 9(4), 97–118. DOI: 10.1257/jep.9.4.97

Ross M.L. (2012). The oil curse: How petroleum wealth shapes the development of nations. Princeton: Princeton University Press.

Sadorsky P. (2009). Renewable energy consumption and income in emerging economies. Energy Policy, 37(10), 4021–4028. DOI: 10.1016/j.enpol.2009.05.003

Sadorsky P. (2012). Time-series analysis in energy economics. Energy Economics, 34(3), 581–589. DOI: 10.1016/j.eneco.2011.10.013

Spang E.S., Moomaw W.R., Gallagher K.S., Kirshen P.H. and Marks D.H. (2014). The water consumption of energy production: An international comparison. Environmental Research Letters, 9(10), 105002. DOI: 10.1088/1748-9326/9/10/105002

Taghizadeh-Hesary F., Yoshino N. and Phoumin H. (2021). Analyzing the characteristics of green bond markets to facilitate green finance in the post-COVID-19 world. Sustainability, 13(10), 5719. DOI: 10.3390/su13105719

Waddock S.A. and Graves S.B. (1997). The corporate social performance-financial performance link. Strategic Management Journal, 18(4), 303–319. DOI: 10.1002/(SICI)1097-0266(199704)18:4<303::AID-SMJ869>3.0.CO;2-G

Wüstenhagen R. and Menichetti E. (2012). Strategic choices for renewable energy investment: Conceptual framework and opportunities for further research. Energy Policy, 40, 1–10. DOI: 10.1016/j.enpol.2011.06.050

Appendices

Table 1. Variables Description

Variable	Definition	Measure	Source	Notation
Climate Emissions	Greenhouse gas emissions from firm activities	Scope 1 (direct) and Scope 2 (indirect)	Carbon Disclosure Project, sustainability reports	ClimEmiss
Water Management Metrics	Water usage, efficiency, and pollution reduction efforts	Total withdrawal (Mm^3), efficiency (m^3/unit), pollution (tons)	Ministry of Environment, Saudi National Water Company	WtrMgmt
Clean Energy Investment	Firm-level investments in renewable projects	Renewable CAPEX (USD million) / Total Assets	Financial statements, Ministry of Energy	CEInvest
Clean Energy Use	Share of renewables in total energy consumption	Renewable consumption (% of total energy)	Financial statements, Ministry of Energy	CEUse
Firm Assets	Size of the firm	Total Assets (USD million)	Financial reports	FAssets
Company Tenure	Maturity of the firm	Years since establishment	Saudi Company Registries	CTenure
Innovation Spending	R&D for renewable efficiency	R&D (USD million) / Revenue	Annual reports	InnoSpend
State Renewable Grants	Government subsidies for renewables	Subsidy amount (USD million)	Ministry of Energy, PIF	SubGrant
Crude Price	Global oil price fluctuations	Brent Crude (USD/barrel, annual avg.)	World Bank, OPEC	CrudePrc
Climate Policy Score	Regulatory support for renewables	Composite index (0–10)	Vision 2030 reports, WGI	ClimPolicy

Table 2. Descriptive Statistics and Unit-Root Test (42 Saudi Firms, 2012–2023)

Variable	Mean	Std	Min	Max	Skewness	Kurtosis	Obs.	ADF Statistic
ClimEmiss	502.34	148.22	203.15	998.72	0.31	1.62	504	-8.93***
WtrMgmt	105.67	32.45	25.80	298.40	0.42	-0.85	504	-7.45***
CEInvest	0.026	0.011	-0.005	0.048	-0.20	0.73	504	-5.22***
CEUse	14.85	4.92	2.10	32.50	0.18	-0.15	504	-6.78***
FAssets	10,250.40	5,230.15	150.00	25,000.00	0.25	1.10	504	-10.55***
CTenure	28.50	11.80	5.00	50.00	0.05	-1.30	504	-9.80***
InnoSpend	0.048	0.019	-0.015	0.095	-0.32	0.65	504	-4.85**
SubGrant	52.30	21.75	-2.00	120.00	0.12	-0.42	504	-12.10***
CrudePrc	69.80	19.25	45.10	110.50	0.35	-0.90	504	-3.50*
ClimPolicy	5.95	1.85	1.50	9.80	-0.15	0.20	504	-7.20***

Source: Calculations by the authors.
Note: For the unit root test (ADF statistic), significance is denoted by *, **, and ***, corresponding to 10%, 5%, and 1% levels of significance, respectively.

Table 3. Variables Correlation Matrix

	ClimEm	WtrMg	CEInv	CEUs	FAsset	CTenur	InnoSpen	SubGran	CrudePrc	ClimPolic
ClimEm	1.0									
WtrMg	0.35	1.0								
CEInv	-0.41	-0.28	1.0							
CEUs	-0.38	-0.24	0.32	1.0						
FAssets	0.55	0.30	-0.15	-0.10	1.0					
CTenur	0.28	0.19	-0.12	-0.08	0.22	1.0				
InnoSpen	-0.21	-0.17	0.25	0.19	-0.13	-0.05	1.0			
SubGran	-0.33	-0.18	0.45	0.30	-0.20	-0.10	0.12	1.0		
CrudePrc	0.40	0.25	-0.30	-0.28	0.35	0.15	-0.18	-0.22	1.0	
ClimPoli	-0.37	-0.25	0.38	0.42	-0.25	-0.18	0.20	0.35	-0.30	1.0

Source: Calculations by the authors.

Table 4. Impact on Climate Emissions (ClimEmiss)

	(1)	(2)	(3)	(4)
ClimEmiss	0.043**	0.020*	0.030*	0.047**
	(0.021)	(0.011)	(0.015)	(0.023)
CEInvest	-0.075**	-0.061**	-0.079**	-0.067***
	(0.037)	(0.030)	(0.039)	(0.014)
CEUse	-0.057**	-0.074*	-0.052**	-0.064***
	(0.028)	(0.037)	(0.026)	(0.020)
FAssets	0.029*	0.027*	0.043*	-0.075**
	(0.014)	(0.013)	(0.021)	(0.037)
CTenure	0.024	0.155	0.215	-0.012
	(0.019)	(0.030)	(0.009)	(0.105)
SubGrant	-0.115***	-0.089**	-0.076**	-0.080**
	(0.027)	(0.044)	(0.038)	(0.040)
CrudePrc	0.148**	0.220*	0.129**	-0.452***
	(0.074)	(0.112)	(0.065)	(0.067)
ClimPolicy	-0.054*	-0.038**	-0.120**	-0.094*
	(0.028)	(0.018)	(0.060)	(0.048)
CEInvest×ClimPolicy	—	—	-0.333**	—
			(0.165)	
CEUse×ClimPolicy	—	—	-0.283***	—
			(0.052)	
LM Test (χ^2)	0.160	0.105	0.109	0.170
White Test	0.150	0.172	0.101	0.269
Jarque-Bera Test	0.105	0.170	0.208	0.142
RESET Test	0.250	0.260	0.105	0.165
Obs. #	468	492	461	483

Note: Table 4 presents regression results for Equation (1), where Climate Emissions (ClimEmiss) is the dependent variable. Four specifications are shown: Column (1) employs System GMM, Column (2) applies Difference GMM for robustness, column (3) introduces interaction terms (CEInvest×ClimPolicy and CEUse×ClimPolicy) to assess policy synergies, and column (4) isolates oil-sector firms. Asterisks denote statistical significance levels: *10%, **5%, and ***1%.

Table 5. Impact on Water Stewardship (WtrMgmt)

	(1)	(2)	(3)	(4)
WtrMgmt	0.170**	0.120*	0.142*	0.180**
	(0.085)	(0.061)	(0.072)	(0.090)
CEInvest	-0.115**	-0.120**	-0.160**	-0.100***
	(0.058)	(0.060)	(0.080)	(0.024)
CEUse	-0.085**	-0.090*	-0.112**	-0.030***
	(0.043)	(0.045)	(0.056)	(0.010)
FAssets	0.050**	0.030*	0.070*	-0.065**
	(0.025)	(0.015)	(0.035)	(0.032)
CTenure	0.009*	0.070	0.178	-0.180
	(0.005)	(0.240)	(0.208)	(0.150)
SubGrant	-0.095***	-0.085**	-0.105**	-0.060**
	(0.030)	(0.043)	(0.053)	(0.029)
CrudePrc	0.115**	0.090*	0.088**	-0.155***
	(0.057)	(0.047)	(0.044)	(0.038)
ClimPolicy	-0.030**	-0.023**	-0.085**	-0.070*
	(0.014)	(0.011)	(0.042)	(0.035)
CEInvest×ClimPolicy	—	—	-0.210***	—
			(0.036)	
CEUse×ClimPolicy	—	—	-0.305**	—
			(0.153)	
LM Test (χ^2)	0.250	0.305	0.095	0.153
White Test	0.205	0.275	0.165	0.207
Jarque-Bera Test	0.255	0.195	0.380	0.085
RESET Test	0.110	0.280	0.215	0.100
Obs. #	403	384	322	504

Note: Table 5 presents regression results for Equation (2), where Water Management Metrics (WtrMgmt) serve as the dependent variable. Four specifications are shown: Column (1) employs System GMM, Column (2) applies Difference GMM for robustness, column (3) introduces interaction terms (CEInvest×ClimPolicy and CEUse×ClimPolicy) to evaluate policy synergies, and column (4) isolates oil-sector firms. Asterisks denote statistical significance levels: *p < 0.10, **p < 0.05, and ***p < 0.01.

Table 6. Profile of Sampled Firms in Saudi Arabia's Renewable Energy Sector (2023)

Characteristic	Category	# Firms	Cumulative Share of National Renewable Sector
Ownership	National	38 (90.5%)	94% of investment, 92% of R&D, 97% of capacity
	Foreign/JV	4 (9.5%)	6% of investment, 8% of R&D, 3% of capacity
Size (Assets)	Large (>$10B)	20 (47.6%)	89% of investment, 85% of R&D, 91% of capacity
	Medium ($1B-$10B)	15 (35.7%)	9% of investment, 12% of R&D, 7% of capacity
	Small (<$1B)	7 (16.7%)	2% of investment, 3% of R&D, 2% of capacity
Specialization	Multi-Energy (Oil & Gas)	24 (57.1%)	82% of investment, 78% of R&D, 84% of capacity
	Renewable-Focused	12 (28.6%)	15% of investment, 19% of R&D, 13% of capacity
	Industrial/Utility	6 (14.3%)	3% of investment, 3% of R&D, 3% of capacity
Cumulative Coverage		42 firms	92% of national renewable investment
			90% of renewable R&D
			95% of installed capacity

Source: Saudi Ministry of Energy, Public Investment Fund (PIF), and company filings.
*Notes: National = >51% Saudi ownership; Size based on 2023 assets; Renewable-focused = >60% revenue from renewables.

RESEARCH PAPER

PROJECTION OF REGIONAL CLIMATE CHANGE FOR 2023–2064 IN THE NORTHERN PART OF THE WESTERN RUSSIAN ARCTIC: A SUPPORT FOR RUSSIAN RAILWAYS

Andrey G. Kostianoy[1,2,3], Alexey D. Gvishiani[1,4], Sergey A. Lebedev[1], Igor N. Rozenberg[5], Roman I. Krasnoperov[1], Irina A. Dubchak[5], Sofia A. Gvozdik[1,6*], Olga O. Shevaldysheva[1], Vladimir N. Sergeev[1], Julia I. Nikolova[1]

[1]Geophysical Center of the Russian Academy of Sciences, Molodezhnaya Ulitsa, 3, Moscow, 119296, Russia
[2]Shirshov Institute of Oceanology of the Russian Academy of Sciences, Nakhimovskiy Ave, 36, Moscow, 117218, Russia
[3]S.Yu. Witte Moscow University, 2nd Kozhukhovskiy Proyezd, 12, Moscow, 115432, Russia
[4]Schmidt Institute of Physics of the Earth of the Russian Academy of Sciences, Bolshaya Gruzinskaya St, 10, Moscow, 123242, Russia
[5]Russian University of Transport, Obraztsova St, 9, Bldg 9, Moscow, 127055, Russia
[6]Department of Earth and Environmental Sciences, University of Milano-Bicocca, Piazza della Scienza, 4, Milano, 20126, Italy
***Corresponding author:** s.gvozdik@gcras.ru
Received: July 22nd 2025 / Accepted: November 12nd 2025 / Published: December 31st 2025
https://doi.org/10.24057/2071-9388-2025-4179

ABSTRACT. Observed climate change has significantly impacted land transportation infrastructure, including roads, railways, bridges, seaport facilities, runways, and other components. It also affects traffic management and the efficiency of the transport system, influencing maintenance costs, travel safety, and traffic flow speeds. This issue is particularly critical for the Arctic Zone of the Russian Federation (AZRF), which is undergoing rapid economic development. Despite its expanding technological infrastructure, the region remains highly vulnerable to the impacts of climate change. A comprehensive assessment of these environmental risks is essential to ensure sustainable regional growth. Observed and projected changes in temperature and humidity generally have adverse effects on the condition and operation of transportation infrastructure. The primary types of negative impacts linked to climate change have already emerged, and these trends are expected to intensify by the mid-21st century. This paper analyses projected climate change in the Western Russian Arctic for 2023–2064. Using the CNRM-CM6-1-HR model from Phase 6 of the Coupled Model Intercomparison Project (CMIP6), it evaluates three socioeconomic scenarios (SSP1-2.6, SSP2-4.5, SSP5-8.5). The results are compiled in an electronic atlas mapping the projected distribution of air and soil temperature, total precipitation, wind speed, and snow cover thickness. Analysis of projection revealed non-linear climate model variations, where parameter values can overlap across scenarios and change rates can be unexpectedly higher in optimistic pathways. These projections, assessed against a 1980–1989 baseline, were visualised in regional maps to detail hydrometeorological changes for 2023–2064. This analysis of regional climate change is vital for sustainably managing railway infrastructure. The results highlight a heterogeneous Arctic climate and identify potentially hazardous phenomena expected to increase in frequency and impact.

KEYWORDS: Arctic zone of the Russian Federation, climate change projection, Coupled Model Intercomparison Project, Shared Socioeconomic Pathways, geoinformation analysis, Russian Railways

CITATION: Kostianoy A. G., Gvishiani A. D., Lebedev S. A., Rozenberg I. N., Krasnoperov R. I., Dubchak I. A., Gvozdik S. A., Shevaldysheva O. O., Sergeev V. N., Nikolova J. I. (2025). Projection Of Regional Climate Change For 2023–2064 In The Northern Part Of The Western Russian Arctic: A Support For Russian Railways. Geography, Environment, Sustainability, 4 (18), 61-79
https://doi.org/10.24057/2071-9388-2025-4179

ACKNOWLEDGEMENTS: This work was funded by the Russian Science Foundation (project No. 21-77-30010-P) titled 'System analysis of geophysical process dynamics in the Russian Arctic and their impact on the development and operation of the railway infrastructure'.

Conflict of interests: The authors reported no potential conflict of interests.

INTRODUCTION

Short description of the studied region and regional transport infrastructure

The Arctic Zone of the Russian Federation (AZRF) is among the country's most dynamically growing territories. The sustainable socio-economic development of the AZRF, along with the expansion and modernisation of the region's infrastructure, is a key priority for the Russian authorities, as stated in official documents adopted in recent years (Decree of the President 2020a; Decree of the President 2020b, Executive order of the Government 2021). This includes creating several specialised industrial, economic, and transport clusters that stretch from the Kola Peninsula to Chukotka (Blanutsa 2020). In this regard, transport connectivity is a crucial issue for the sustainable development of this region. One economically feasible solution is the extensive use of the Northern Sea Route (NSR) in the Arctic Ocean, which has become one of the North's major transport corridors. The cargo turnover of the NSR significantly increased from 19.7 million tons in 2018 to 36.3 million tons in 2023, and this trend is likely to continue in the coming years (Smirnov 2025). The comprehensive strategy for NSR development up to 2035 includes expanding regional transport infrastructure, such as roads, railways, airports, and sea and river ports/terminals, which are necessary for cargo transfer at the logistics centres of the growing economic clusters (Decree of the Government 2022). However, planning and constructing transport facilities require sufficient analysis and assessment of the potential risks posed by natural hazards. These include earthquakes, underwater landslides, tsunamis, gas seeps, and climate-related geohazards (Krylov et al. 2024). Data analysis was conducted using geoinformation systems, as described in chapter 2 through the implementation of modern approaches.

Climate characteristics of the region based on previous research

As mentioned, AZRF and regional transport infrastructure are exposed to dramatic climate change, which affects all natural and socio-economic systems in the region. In 2022, the Russian Federal Service for Hydrometeorology and Environmental Monitoring (Roshydromet) stated in its 'Third Assessment Report on Climate Change and its Consequences in the Territory of the Russian Federation' that Russia's territory is warming at a rate of 0.51°C/decade, while the AZRF is warming at a rate of 0.71°C/decade (Third Assessment Report 2022). This is four times faster than the average global rate of 0.18°C/decade for the last 50 years (1973–2022) (Samset et al. 2023). A major finding of the Roshydromet Report is that, according to projections, the area occupied by near-surface permafrost in Russia's territory will decrease by about a quarter by the middle of the 21st century. By the end of the 21st century, this reduction is expected to be 40±15% and 72±20% respectively, according to the Shared Socioeconomic Pathways (SSPs) scenarios – SSP2-4.5 and SSP5-8.5, respectively (Third Assessment Report 2022). SSPs are climate change scenarios that represent projected global socioeconomic pathways up to 2100, as defined in the IPCC Sixth Assessment Report (2021).

The thawing of permafrost in the AZRF affects oil and gas, railway, road, and pipeline transport infrastructure, with economic implications in the hundreds of billions of dollars (Grebenets and Isakov, 2016; Kostianaia et al. 2021; Kostianaia and Kostianoy, 2023; Yakubovich and Yakubovich, 2019). Railway infrastructure in the AZRF operates under extremely difficult geological, climatic, and weather conditions. It is constantly affected by various external factors, leading to deformation of railway tracks, damage to bridges, and other infrastructure issues (Grebenets and Isakov 2016; Kostianaia et al. 2021; Third Assessment Report 2022). The thawing of permafrost and a significant rise in average air and soil temperatures cause further changes in the water balance of many rivers and lakes in this region. These processes intensify coastal abrasion, erosion, mudflows, floods, landslides, ground creep, rockfalls, rockslides, karst sinkholes, and snow avalanches (Grebenets and Isakov 2016; Kostianaia et al. 2021; Romanenko and Shilovtseva 2016; Third Assessment Report 2022). To adapt to rapid climate change, railway industry authorities are implementing new technological solutions in their planning, construction, and operational practices. This is a widely recognised priority in the field (Andersson-Sköld et al. 2021; Garmabaki et al. 2021; Kostianaia and Kostianoy, 2023).

In the framework of the Russian Science Foundation Project 'System analysis of geophysical process dynamics in the Russian Arctic and their impact on the development and operation of the railway infrastructure' (2021–2024, No. 21-77-30010, and 2025–2027 No. 21-77-30010-P) performed at the Geophysical Center of the Russian Academy of Sciences, an 'Electronic atlas of climatic changes in hydrometeorological parameters of the western part of the Russian Arctic for 1950–2021 as geoinformatic support of railway development' (Gvishiani et al. 2023a) has been compiled. This atlas and its second advanced version (Version 2, 2023) have been used for the analysis of climate change impact on railway infrastructure in the Western Russian Arctic from 1980 to 2021 (Gvishiani et al. 2023b).

One of the most important conclusions from this research was that climate warming in the studied area is very irregular throughout the year (by months), across different locations, and even along each section of the railway. Observed warming varied from 0.5°C to 2.6°C between 1980–1999 and 2000–2021. The rate of air temperature increase was highest in the last 20 years, reaching 0.5°C/decade. This led to a 2–4 cm reduction in snow cover thickness from 1980–1999 to 2000–2021, which is approximately 10%. Between 1980–1999 and 2000–2021, there was a significant increase in precipitation, with some months and areas experiencing changes from 25% to 50% of average values. The highest rate of precipitation growth was observed within the last 20 years, reaching 10%/decade along almost all railway sections (Gvishiani et al. 2023a; Gvishiani et al. 2023b). As part of this study, the region was considered to cover as much of the developing Russian Arctic as possible, particularly the area of railway development.

Working on this project, the authors were the first to propose using Hovmöller diagrams to chart the temporal variability of meteorological parameters along the tracks of selected railway mainlines. The analysis of these diagrams for seven railway mainlines in this region between 1980 and 2021 showed significant spatial heterogeneity of the order of 100–250 km in the form of bands, which are specific parts of the railway and persist for decades. One important conclusion from this analysis was that the spatial resolution of modern climate models often does not fully convey the variability of climate parameters depending on local geographic features. Since the spatial resolution of the models averages 100–500 km, the detected bands of spatial heterogeneity of meteorological parameters may be lost due to the coarse mesh of the models. Therefore,

the detected anomalous locations on the analysed railway mainlines must be brought under special control by railway operators, with the establishment of additional weather and technical monitoring systems, especially in regions with higher precipitation and soil humidity, greater snow depth, and stronger wind speed (Kostianoy et al. 2025).

Five main hydrometeorological parameters (air temperature, soil surface temperature, total precipitation, snow cover thickness and surface wind speed) and a climate model from the current Phase 6 of the Coupled Model Intercomparison Project (CNRM-CM6-1-HR) were selected for projecting the parameters' interannual variability for 2023–2064 (Juckes et al. 2020). Geospatial data were collected and prepared to create an electronic Atlas of projections for the main hydrometeorological parameters for the region of the northern part of the Western Russian Arctic (55°–80° N, 30°–100° E). The obtained maps were analysed to reveal the main tendencies in the future climate change of the studied region.

This paper aims to project the regional climate change for 2023–2064 in the Western Russian Arctic (55°–80° N, 30°–100° E) based on five meteorological parameters and three climate scenarios. The projection uses the CNRM-CM6-1-HR model from CMIP-6. It also aims to show the main spatial features of future regional climate change, which are of greatest interest for the operation of Russian Railways in this region.

MATERIALS AND METHODS

Overview of climatic models and scenarios

Modern studies of climate change impact assessment predominantly rely on modelling natural and socio-economic processes based on climate projections, using hydrodynamic models. For the effective use of such models, it is necessary to be confident that the uncertainty in the assessment of the corresponding consequences is not too great. This uncertainty results from both errors in impact models and differences in the climate projections used in calculations. It is important to establish which of these components is essential. For this purpose, the results obtained from calculations using several identical models are compared. The CMIP (Coupled Model Intercomparison Project) is a unique collaborative project dedicated to comparing climate models. It includes calculations with specified standardised external conditions, allowing reliance on estimates of future climate changes from the considered models (Juckes et al. 2020; Tolstykh 2016). Currently, Phase 6 of CMIP is in operation.

CMIP6 climatic models

Initially, the CMIP project was established under the guidance of the Working Group on Coupled Modelling of the World Climate Research Programme (WCRP). It began in 1995 as a comparison of several early global climate models. These models performed a set of basic experiments using atmospheric models to explore their relationship with the dynamic ocean, land surface, and thermodynamic sea ice. Since then, over five phases, the CMIP project has grown into a significant international research effort, bringing together many climate models developed by different scientific groups. An important aspect of CMIP6 is making data from various models publicly accessible in a standardised format for analysis by the wider climate community and users. The standardisation of modelling results into a specific format, along with the collection, archiving, and access to model output data through the Earth System Grid Federation, are central to the project (Eyring et al. 2016).

CMIP6 includes 23 model intercomparison projects. Each project incorporates data for various climate models that provide both historical simulations, showing past climate behaviour (1850–2014) under different conditions, and future climate change projections (from 2015 to 2100). Scenario MIP is one of the coupled climate model projects included in Phase 6 of CMIP. This project presents climate projections based on different models, relying on alternative scenarios that are directly relevant to societal challenges in mitigating, adapting to, or influencing climate change impacts. These climate projections will be based on a new set of emissions and land-use scenarios developed using Integrated Assessment Models (IAMs) and future Shared Socioeconomic Pathways (SSPs) associated with Representative Concentration Pathways (RCPs) (O'Neill et al. 2016). All simulations for the SSP1-2.6, SSP2-4.5 and SSP5-8.5 scenarios were taken from the single available ensemble member r1i1p1f2 of the CNRM-CM6-1-HR model. In this designation, r1 indicates the first realisation of initial conditions, i1 the default initialisation method, p1 the standard physics configuration, and f2 the second version of the external forcing setup recommended for this model. Stating this information explicitly is essential to ensure the reproducibility of results and their comparability with other CMIP6 simulations.

CMIP6 scenarios (Shared Socioeconomic Pathways)

Scenarios describing the possible future development of anthropogenic factors of climate change (i.e., greenhouse gases, chemically reactive gases, aerosols, and land use) following socio-economic development play a crucial role in climate research. They allow for the assessment of potential changes in the climate system, impacts on society and ecosystems, and the effectiveness of response options such as adaptation and mitigation across a wide range of future outcomes. The scenario development process began with the definition of RCPs as a set of four pathways for land use and emissions of air pollutants and greenhouse gases that cover a wide range of future outcomes until 2100.

Various scenarios were developed simultaneously. One avenue involved creating climate model projections based on four Representative Concentration Pathways (RCPs) within the Coupled Model Intercomparison Project Phase 5 (CMIP5) framework. Another avenue focused on developing alternative future pathways for Shared Socioeconomic Pathways (SSPs) and their associated emission and land use scenarios, using Integrated Assessment Models (IAMs). This was followed by an integration phase that combined climate modelling with future societal development scenarios based on SSPs for comprehensive analysis. There are five types of SSPs, distinguished by variations in population, economic growth, and urbanisation (O'Neill 2016).

SSPs describe alternative development pathways for future societies without climate change or climate policy. SSP1 and SSP5 envisage relatively optimistic development trends for human potential, with significant investments in education and healthcare, rapid economic growth, and well-functioning institutions. However, SSP5 assumes an energy-intensive economy based on fossil fuels, while SSP1 shows an increasing shift towards green energy. SSP3 and SSP4 assume more pessimistic development trends, with minor investments in education and healthcare, rapid population growth, and increased inequality. In SSP3, countries prioritise regional security, while SSP4 is dominated by significant inequality within and between

countries. Both these scenarios lead to the creation of societies highly vulnerable to climate change. SSP2 assumes a central pathway where trends maintain their historical patterns without significant deviations.

As a result, scenarios based on socio-economic development pathways and the emissions of greenhouse gases, air pollutants, and land use levels were created. For each of the 21st-century scenarios, the significance of the forcing pathway is described, as well as the rationale for the driving SSP.

SSP5-8.5: This scenario represents the upper limit of the development pathway range, based on the RCP8.5 pathway. SSP5 was chosen for this forcing pathway because it is the only SSP scenario with sufficiently high emissions to create a radiative forcing of 8.5 W/m^2 by 2100.

SSP3-7.0: This scenario represents the next stage in the development pathway range, for which the RCP7.0 pathway was chosen. SSP3 was selected because SSP3-7.0 is a scenario with significant land use changes, specifically a decrease in global forest cover, and high emissions of greenhouse gases and atmospheric pollutants, especially SO2. Furthermore, SSP3, when combined with this forcing pathway, is particularly relevant as it brings together relatively high societal vulnerability (SSP3) and relatively high forcing.

SSP2-4.5: This scenario represents the middle of the development pathway range and is based on the RCP4.5 pathway. SSP2 was chosen because its land use and aerosol pathways are not extreme compared to other SSPs, and it combines intermediate societal vulnerability with an intermediate level of forcing.

SSP1-2.6: This scenario represents the lower limit of the future development pathway range and is based on the RCP2.6 pathway. Its implementation is expected to result in an average value calculated by multiple models being significantly less than 2°C of warming by 2100, making it useful for analysing this policy target. SSP1 was chosen because it includes significant land use changes, particularly an increase in global forest cover. This scenario combines low vulnerability and low mitigation challenges, as well as a low forcing signal.

SSP1-1.9: This scenario is characterised by very low greenhouse gas emissions, with net CO_2 emissions becoming zero by 2050 and then negative (O'Neill 2016; Semyonov 2022).

Climatic models, scenarios, and hydrometeorological parameters

Selection of hydrometeorological parameters

For the analysis of future climate change, seven key hydrometeorological parameters were chosen: air temperature, total precipitation, wind speed, soil temperature, soil moisture content, air humidity, and snow cover thickness. However, for the present article, only five of these have been selected (Table 1). This choice is justified by the need to be consistent with the past climate analysis (1950–2021) conducted for this region in previous studies (Gvishiani et al. 2023a; Gvishiani et al. 2023b; Kostianoy et al. 2025). This set of parameters was discussed and approved by specialists from the Research and Design Institute of Informatization, Automation and Communications in Railway Transport of the Russian Railways, which was one of the commissioners of this work. The importance of these parameters for the operability of railways is discussed by Gvishiani et al. (2023b). Parameters such as surface air temperature, soil surface temperature, and precipitation were converted to the same units of measurement used in version 2 of the Atlas (1980–2022) (Gvishiani et al. 2023b).

Model CNRM-CM6-1-HR

Models that provided data to the shared repository of the CMIP6 project were considered. To select an appropriate model, data from 59 available options were analysed. This analysis included the following assessments: (1) the resolution of the atmospheric component; (2) the availability of data across various scenarios; (3) the availability of data for selected parameters. Information regarding the availability of datasets for different scenarios, nominal resolution, and climate scenarios can be found in a summary table on the official CMIP6 project resource on the internet (ESGF CMIP6 data holdings 2025).

Spatial resolution is one of the key parameters for preparing data for a projection Atlas. A higher resolution provides a more detailed description of the region in the end. It also cannot be worse than 0.5×0.65°, which is the same resolution used in preparing the Atlas for 1980–2022. This is necessary for comparing climate change in the considered region of AZRF. As a result, eight models from CMIP6, developed by scientific teams from China, France, Italy, Taiwan, the USA, and a joint EU team, were selected for consideration.

The CNRM-CM6-1-HR model, developed by a joint team from the National Centre for Meteorological Research (CNRM) and the European Centre for Advanced Research and Training in Scientific Computing (CERFACS) in 2017, includes the full list of selected parameters for all scenarios. It also has the highest spatial resolution (CNRM-CERFACS contribution 2025). This projection model calculates parameters from 2015 to 2100. The model is widely used in scientific research and demonstrates high reliability in assessments. It was chosen for the present analysis.

The selected model incorporates data from experiments based on four SSPs: SSP1-2.6, SSP2-4.5, SSP3-7.0, and SSP5-8.5. It also includes data from piControl (pre-industrial control experiment) and historical (historical experiment for 1850–2005) scenarios. Three illustrative scenarios were chosen for the study, characterising low, medium, and high levels of solar radiation expected by 2100: SSP1-2.6 (sustainable development scenario), SSP2-4.5 (intermediate scenario), and SSP5-8.5 (fossil fuel-intensive development).

Table 1. Hydrometeorological parameters selected for climate change projecting

Parameter	Units	CMIP6 notation	Description
Air temperature	°C	tas	Near-surface air temperature (typically 2 m)
Soil temperature	°C	ts	Temperature of the lower atmospheric layer
Total precipitation	kg/(m^2·s)	pr	Including liquid and solid phases
Snow cover thickness	m	snd	The thickness of the snow layer covering the ground. Recorded as 0.0 where ground is absent
Wind speed	m/s	sfcWind	Average near-surface wind speed (typically 10 m)

During the comparison and analysis of climatic variability, data for the 1980–1989 period were used. The MERRA-2 reanalysis (Modern-Era Retrospective Analysis for Research and Applications, Second Edition) was chosen as the dataset. Its characteristics were described in detail in our previous works (Gvishiani et al. 2023a; Gvishiani et al. 2023b; Kostianoy et al. 2025) and in the main documentation of the reanalysis (Gelaro et al. 2017).

This study relies exclusively on remote sensing data from the CMIP6 project. Records from ground-based meteorological stations were not incorporated, as validation against in-situ observations falls outside the primary focus of this research (Bocharov et al. 2025).

Visualisation of climatic data

Climatic database

The results of experiments using CMIP6 models are available in several official repositories and are open to all users. Data acquisition was carried out using the Centre for Environmental Data Analysis Archive. This archive is part of the Natural Environment Research Council Environmental Data Service and is responsible for storing atmospheric and Earth system research data. The repository follows a unified storage structure for all CMIP6 project models. Since the study was based on a comparison of data over several decades, we specifically used monthly averages (Amons) obtained using the CNRM-CM6-1-HR high-resolution climate model. This choice ensured that the temporal resolution of the dataset corresponded to monthly averages rather than daily or seasonal aggregates.

Each downloaded file contains information about a specific climate variable, scenario, and time period. The data are provided in the *.nc format (Network Common Data Form). For this study, data for the period 2023–2064 were selected using automated tools. These tools also clipped the data to the corresponding area from 30 to 100 degrees east longitude and from 55 to 80 degrees north latitude. The selection included the climate parameters described earlier and three emission scenarios. In total, over 9 GB of data were acquired as an initial dataset.

Compilation of hydrometeorological parameter maps

The further processing of the dataset can be divided into several main stages:

Stage 1: Converting *.nc files to *.grd format and forming the dataset in Surfer software.

Using data from the CNRM-CM6-1-HR model (CMIP6), grid values were calculated for each of the three scenarios and each climate parameter. The downloaded files were converted into grid format (*.grd) and compiled into a unified dataset. Monthly samples for each parameter over the period 2023–2064 were added as input data. These files were systematically saved to internal storage, each representing a raster grid with a spatial resolution of 0.5×0.5°.

Stage 2: Calculation of averaged indicators for key parameters.

For each hydrometeorological parameter, indicators were calculated to show both average projected trends over several time intervals and seasonal variations. The selected timeframes include single years, a 40-year period, two 20-year periods, and the difference between these 20-year periods to analyse trends. Seasonal trends were evaluated using data from representative months for each season: January, April, July, and October. The resulting structure of indicators for each parameter and each scenario includes:

Average projected parameter values for 2022;

Average projected parameter values for 2023–2064;

Average projected parameter values for 2023–2042;

Average projected parameter values for 2043–2064;

Average projected parameter values for January 2023–2064;

Average projected parameter values for April 2023–2064;

Average projected parameter values for July 2023–2064;

Average projected parameter values for October 2023–2064;

Projected changes in parameter between 2053–2064 and 1980–1989;

Projected changes in parameter between 2043–2064 and 2023–2042;

Average rate of change of projected parameter values for 2023–2064.

The first group of characteristics was calculated as arithmetic means over the corresponding years or months. Changes between periods were calculated as the difference between the average values of two separate intervals: 2023–2042 and 2043–2064. The rate of change was calculated as the first derivative with respect to time (X) using first-degree polynomials (rate trend) through the least squares method (Serykh and Tolstikov 2022). The rate of change (a) of a given parameter (Y) was calculated using the linear regression formula:

$$Y(X) = aX + b \quad (1)$$

Based on this, final characteristics were obtained for analysing projected climate changes. The calculations were carried out in Golden Software Surfer (version 17.1) (Golden Software 2022; Si et al. 2010), using additional tools developed for geoinformation processing.

Stage 3: Reformatting result files for GIS, assigning coordinate systems, and refining the grid resolution.

Several processing steps were followed after compiling the dataset and completing the raster calculations. First, the data grid resolution was refined to improve the quality of visualisations and create smoother output. This was done using interpolation in Surfer, increasing the resolution from 0.5×0.5° to 0.05×0.05° using kriging. This method preserves data accuracy and helps avoid artefacts when transforming gridded data, while also smoothing transitions between values (Yang et al. 2004).

The next step involved converting the dataset for use in a GIS environment to enable map creation. The final raster files were transformed into a format compatible with ESRI ArcMap (version 10.8) (Kriging 2025). The data were saved as *.flt (Esri Float Grid) files, maintaining the refined 0.05×0.05° resolution and adding geographic referencing. Additionally, for parameters related to soil conditions and snow cover thickness, the raster data were clipped to match the coastline.

Plots of interannual variability of hydrometeorological parameters

After compiling the final datasets, the next step in preparing the Atlas was the creation and setup of GIS projects in the ESRI ArcMap MXD format (Map Exchange Document). The following procedures were carried out as part of the GIS project: for each climate parameter, project trees were created within a pre-prepared layout (which included a unified map background and general legend structure), raster datasets were added, and contour lines were calculated and displayed. The next steps included formatting the final maps, applying colour palettes, styling contour lines, adding titles, and exporting the finished images. All formatting and map creation were carried out using ESRI ArcMap (version 10.8) (Bartus 2014).

For better visualisation, all climatic schemes are displayed on the digital elevation model. The GEBCO (General Bathymetric Chart of the Oceans) model (Leminkova 2020) was chosen

for the dataset as the base map. This model provides data in meters, with a grid spacing of approximately 30 metres. For this Atlas, considering the geographic location of the study area, an equidistant conic projection was selected with a central meridian at 103°.

The final maps included the current railway network in the considered region of AZRF. This allows for an assessment of the influence of regional climate change on key railway routes and provides information for planning future transport development. This layer is based on the railway network map of Russia, derived from the Digital Chart of the World dataset (originally from 1993, updated through 2002) at a 1:1,000,000 scale. The dataset was compiled by the Russian Academy of Sciences (RAS) and the International Institute for Applied Systems Analysis (IIASA), Austria (IIASA, 2002). For use in the final maps, the railway data were clipped to match the boundaries of the study area. Additionally, the route of the planned Northern Latitudinal Railway (NLR), which is currently under construction, was also included. These routes were added to the initial dataset in *.shp (Shapefile) format.

The final maps showing the projected distribution of hydrometeorological parameters were saved in TIFF (Tagged Image File Format) and later compiled into a PDF document. The following sections will present the main trends and general patterns of projected climate change based on this data. As a result, 234 maps for all 7 projected parameters have been prepared. Next, an analysis of 5 parameters will be presented, chosen as the most representative and significant (chapter 3).

RESULTS

Analysis of trends in the interannual variability of main hydrometeorological parameters

Initially, an analysis of trends and data distribution across different periods was prepared. This analysis utilised two main tools: Table 2, which summarises minimum and maximum values, linear trends, and differences between periods, and interannual variability plots (Fig. 1), which illustrate temporal evolution and emphasize divergence between the scenarios.

Table 2. Key characteristics of interannual variability of all climatic parameters under 3 climate change scenarios for different periods

Parameter	Characteristic	Unit	SSP 1-2.6	SSP 2-4.5	SSP 5-8.5
Air temperature	Linear trend 2015–2100	°C/10 years	0.24	0.58	1.01
	Linear trend 2023–2064	°C/10 years	0.29	0.93	0.77
	Average value 2022	°C	−3.02	−5.09	−3.11
	Average value 2023–2064	°C	−2.62	−2.65	−1.79
	Difference between periods (2043–2064) – (2023–2042)	°C	0.55	1.81	1.55
Total precipitation	Linear trend 2015–2100	mm/10 years	0.31	0.69	1.45
	Linear trend 2023–2064	mm/10 years	0.71	1.39	1.58
	Average value 2022	mm	49.37	45.09	48.22
	Average value 2023–2064	mm	49.65	49.18	50.16
	Difference between periods (2043–2064) – (2023–2042)	mm	1.71	2.54	3.51
Wind speed	Linear trend 2015–2100	(m/s)/10 years	0.006	0.004	-0.002
	Linear trend 2023–2064	(m/s)/10 years	0.012	0.028	0.007
	Average value 2022	m/s	5.129	5.213	5.282
	Average value 2023–2064	m/s	5.25	5.264	5.282
	Difference between periods (2043–2064) – (2023–2042)	m/s	0.006	0.036	-0.006
Soil temperature	Linear trend 2015–2100	°C/10 years	0.26	0.61	1.04
	Linear trend 2023–2064	°C/10 years	0.3	0.98	0.8
	Average value 2022	°C	−2.82	−5.00	−2.95
	Average value 2023–2064	°C	−2.40	−2.46	−1.54
	Difference between periods (2043–2064) – (2023–2042)	°C	0.56	1.9	1.6
Snow cover thickness	Linear trend 2015–2100	m/10 years	−0.0013	−0.0037	−0.009
	Linear trend 2023–2064	m/10 years	−0.0004	−0.0055	−0.004
	Average value 2022	m	0.1862	0.1851	0.1866
	Average value 2023–2064	m	0.174	0.1733	0.171
	Difference between periods (2043–2064) – (2023–2042)	m	−0.0002	−0.0116	−0.007

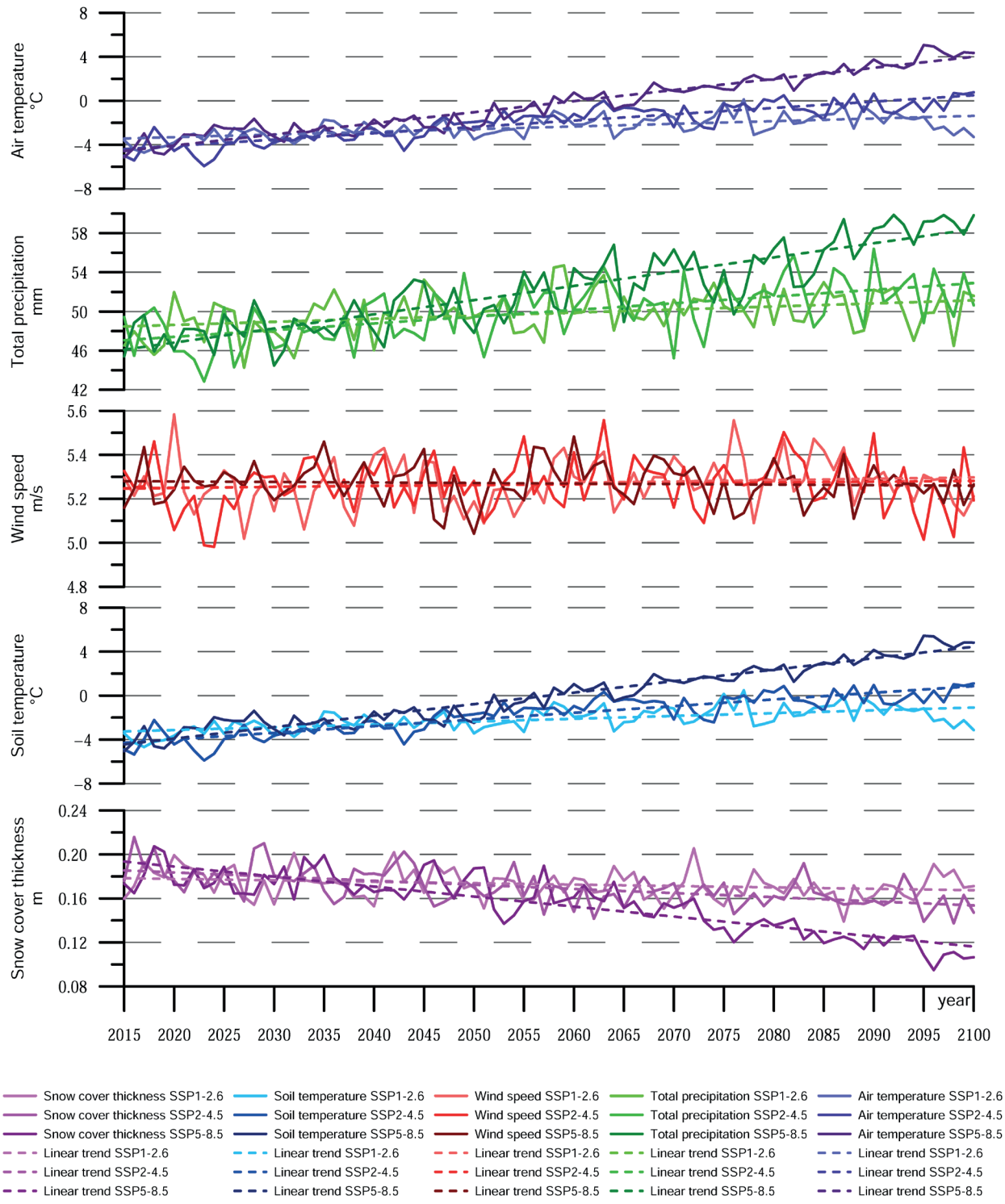

Fig. 1. Interannual variability of 5 hydrometeorological parameters in the study region under 3 climate change scenarios and their linear trends

The air temperature projection shows a consistent warming trend across all scenarios. Over the long term, from 2015 to 2100, temperature increases are estimated to be between approximately 1–2°C in the low-emission SSP1-2.6 scenario and over 8°C in the SSP5-8.5 scenario. The corresponding linear trends range from 0.24°C/decade to 1.01°C/decade. However, this increase is not uniform. In the shorter period from 2023 to 2064, the warming rate in the SSP2-4.5 scenario (0.93°C/decade) is higher than in SSP5-8.5 (0.77°C/decade). This illustrates the non-linear nature of climate dynamics and suggests that more extreme scenarios may not always show faster changes over short timescales. For instance, the average temperature in 2022 under SSP5-8.5 (–3.11°C) is similar to that under SSP1-2.6 (–3.02°C), despite their significant differences in the long term. Such periods of overlap indicate a delayed divergence and highlight the importance of monitoring changes around the middle of the century.

Precipitation trends also increase across all scenarios, though with considerable variation. By 2100, average monthly precipitation is projected to rise by ~2 mm under SSP1-2.6 and up to 12 mm under SSP5-8.5. Linear trends for 2015–2100 support this pattern, ranging from 0.31 to 1.45 mm/decade. Yet short-term rates (2023–2064) show some inversion: while SSP5-8.5 remains dominant (1.58 mm/decade), the difference with SSP2-4.5 (1.39 mm/decade) narrows. Interestingly, in 2022, the highest precipitation was recorded in SSP1-2.6 (49.37 mm), again underscoring short-term variability and possible lag effects. Even modest increases in precipitation may have significant impacts in permafrost zones, where excess surface water contributes to thermal erosion and structural instability.

Wind speed projections suggest only minor overall changes. Long-term linear trends range from +0.006 m/s/decade for SSP1-2.6 to –0.002 m/s/decade for SSP5-8.5. Across the 2023–2064 period, weak positive trends are observed in all scenarios, with the largest trend of 0.028 m/s/decade occurring in SSP2-4.5. Although absolute values are small, even slight increases can intensify mechanical stress on exposed infrastructure, particularly during peak wind events. Seasonal amplification, especially in spring, might be more critical than long-term averages.

Soil temperature trends follow a similar pattern to near-surface air temperature. Projection increase ranges from 0.26 °C/decade (SSP1-2.6) to 1.04 °C/decade (SSP5-8.5) between 2015 and 2100. In the nearer period (2023–2064), the highest warming rate is observed under the intermediate scenario SSP2-4.5 (0.98 °C/decade). This rate exceeds even the more pessimistic SSP5-8.5 (0.80 °C/decade), which again reflects temporal nonlinearity. Notably, soil temperatures under different scenarios remain relatively close until around 2070, after which divergence becomes more pronounced. From an infrastructure perspective, this projected rate of subsurface warming, approaching 1 °C every 10 years in some regions, poses a serious risk for permafrost stability. In particular, along critical corridors such as the NLR, this trend implies progressive loss of bearing capacity, increased thaw depth, and the potential for differential settlement, even within the current planning horizon.

Snow cover thickness is expected to decline gradually, from 18–20 cm in 2015 to 11–17 cm by 2100. The long-term linear trend is most negative in SSP5-8.5 (–0.009 m/decade), while SSP1-2.6 shows only minimal reductions (–0.0013 m/decade). However, intermediate periods again show different dynamics. Between 2023 and 2064, the greatest decline is observed in SSP2-4.5 (–0.0055 m/decade). Notably, the average snow cover thickness in 2022 under SSP1-2.6 was higher than under more pessimistic scenarios, and this persisted in the 2023–2064 period. These results highlight spatial and temporal differences in snow dynamics, which may influence spring flood intensity and the insulation of soils during winter.

For each hydrometeorological parameter, 33 maps were compiled to illustrate the projected variability over the period 2023–2064 under three climate change scenarios: SSP1-2.6, SSP2-4.5, and SSP5-8.5. Comparisons were also made with historical data for 1980–2021 and the year 2022 to evaluate the consistency between the historical Atlas 1980–2022 and the CNRM-CM6-1-HR model projection. We will then discuss the most significant results from the analysis of the compiled maps for each parameter.

Air temperature

Analysis of near-surface air temperature maps reveals distinct local and global trends. The spatial distribution of air temperature for 2023–2064 under both the 'optimistic' SSP1-2.6 and 'pessimistic' SSP5-8.5 scenarios indicates a northward or northeastward shift of all isotherms by 150–300 km relative to their 2022 positions. Only railway sections northeast of the Pechora–Khanty-Mansiysk line will remain, on average, within negative average annual temperatures, with the NLR area continuing to experience the most severe operational conditions. This finding is supported by seasonal temperature variability maps. For instance, January temperatures in the NLR area under both scenarios range between –20°C and –22°C, while July temperatures range from 12°C to 16°C.

Temperature increment maps comparing the periods 2043–2064 and 2023–2042 project a rise of 0.3–0.9°C under SSP1-2.6, peaking east of the Tomsk–Khanty-Mansiysk–Nadym–Yamburg line. The SSP5-8.5 scenario yields a larger increase of 1.5–1.8°C that is more spatially uniform.

Averaging over 20-year intervals somewhat smoothes the temperature change signal. The clearest projection changes for the final study decade (2053–2064) emerge when compared against the stable 1980–1989 climate baseline (Figs. 2, 3). Relative to this baseline, SSP1-2.6 projects a 2–3.5°C increase by 2053–2064, amplified in northern latitudes. SSP5-8.5 projects a greater increase (4–5°C), also peaking in the NLR area.

Calculated temperature growth rates for 2023–2064 vary regionally. They range from 0.1°C/decade in the Kazan–Perm–Yekaterinburg–Tyumen area to 0.5°C/decade in the Novy Urengoy–Igarka–Dudinka area under SSP1-2.6. Under SSP5-8.5, the rates range from 0.7 to 1.0°C/decade. Under the latter scenario, the highest rates are again projected for the Northern Latitudinal Railway sector between Salekhard and Dudinka.

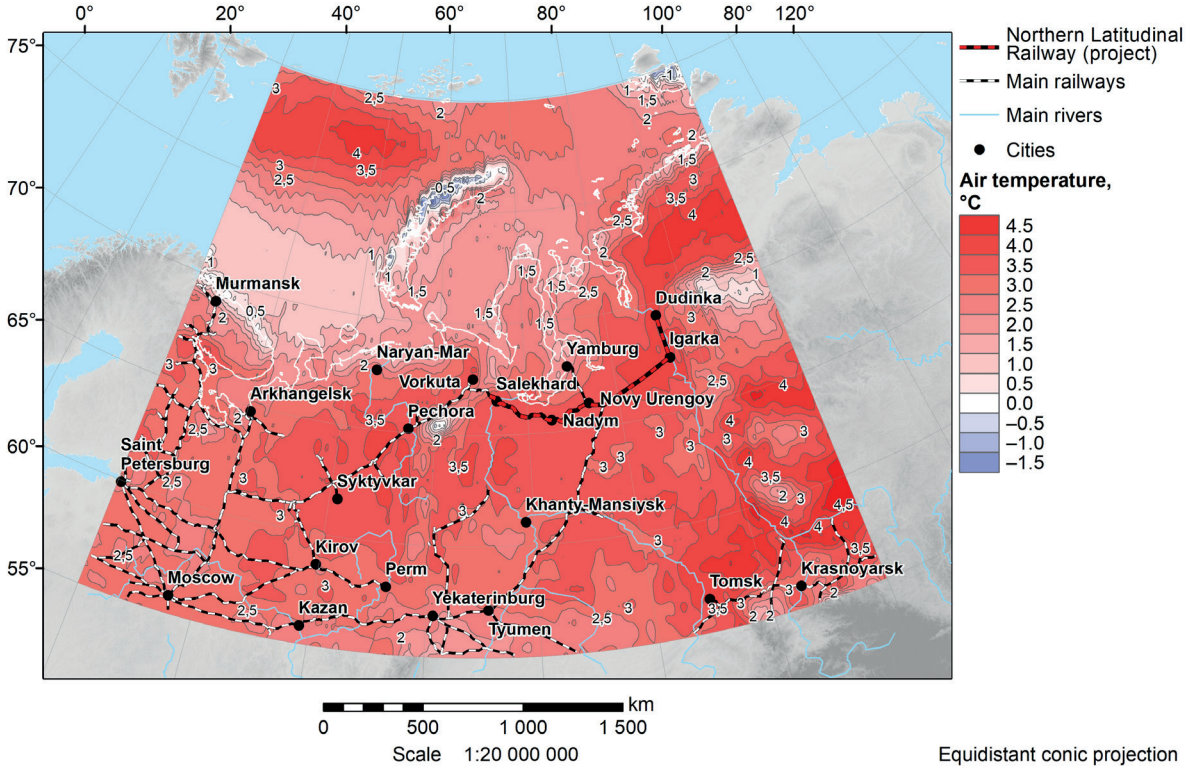

Fig. 2. Projected air temperature changes between the periods 2053–2064 (under SSP1-2.6 scenario) and 1980–1989

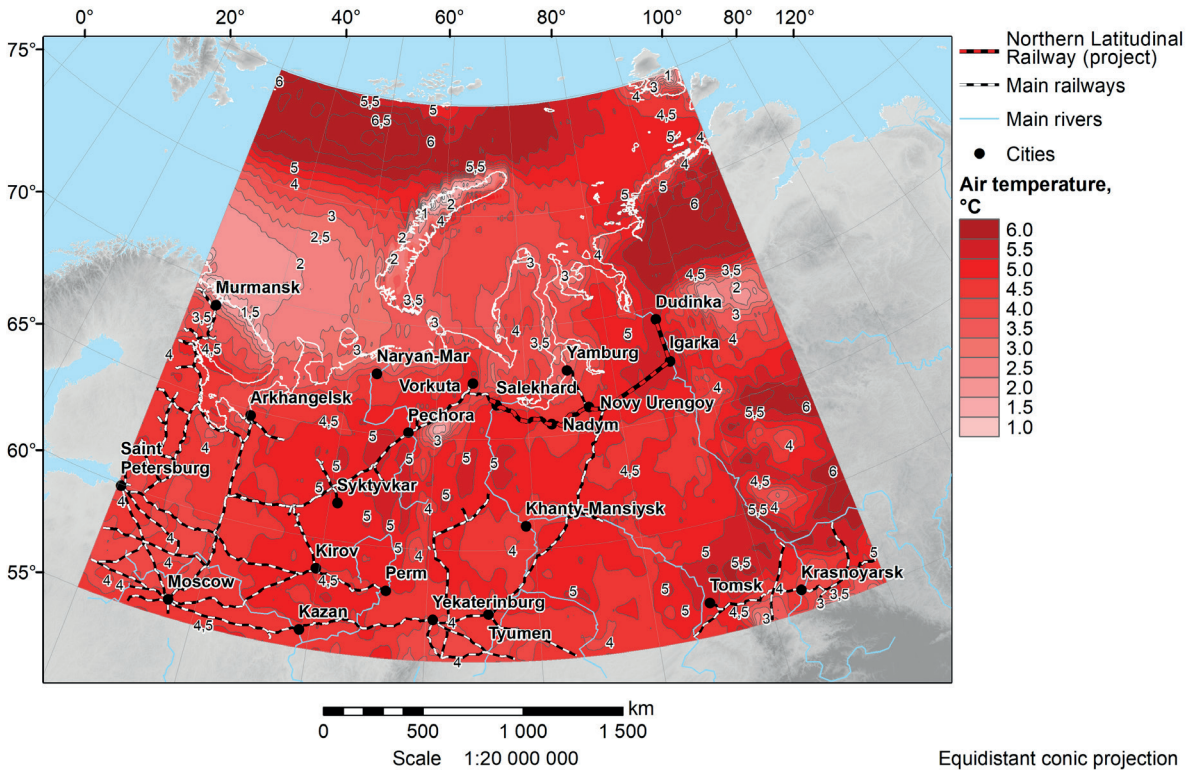

Fig. 3. Projected air temperature changes between the periods 2053–2064 (under SSP5-8.5 scenario) and 1980–1989

Total precipitation

Precipitation fields in 2022 (Fig. 4) reveal a persistent spatial pattern under all scenarios, characterised by three distinct precipitation regimes. The highest monthly totals (up to 100 mm) are concentrated in the Ural Mountains and the region east of Dudinka, while lower values (around 30–40 mm) prevail between Tomsk and Nadym. Under SSP5-8.5, this structure remains, but precipitation increases by approximately 10 mm throughout the territory, reflecting the overall intensification of the hydrological cycle.

This trend continues in the projections for 2023–2064. Under SSP1-2.6, monthly precipitation peaks at 120 mm in the western and northeastern sectors, and under SSP5-8.5, values exceed 130–135 mm. Importantly, the spatial configuration of precipitation maxima remains stable across scenarios. This suggests robust regional controls on moisture transport and orographic effects. Seasonal patterns further emphasise this amplification. In July, the most precipitation-intensive month, totals under SSP5-8.5 reach 180–200 mm in the same western and northeastern zones, which is 20–40 mm more than under SSP1-2.6. (Fig. 5) Such summer increases are particularly significant for infrastructure, as they coincide with peak active-layer thaw and can worsen surface runoff and waterlogging along railway lines.

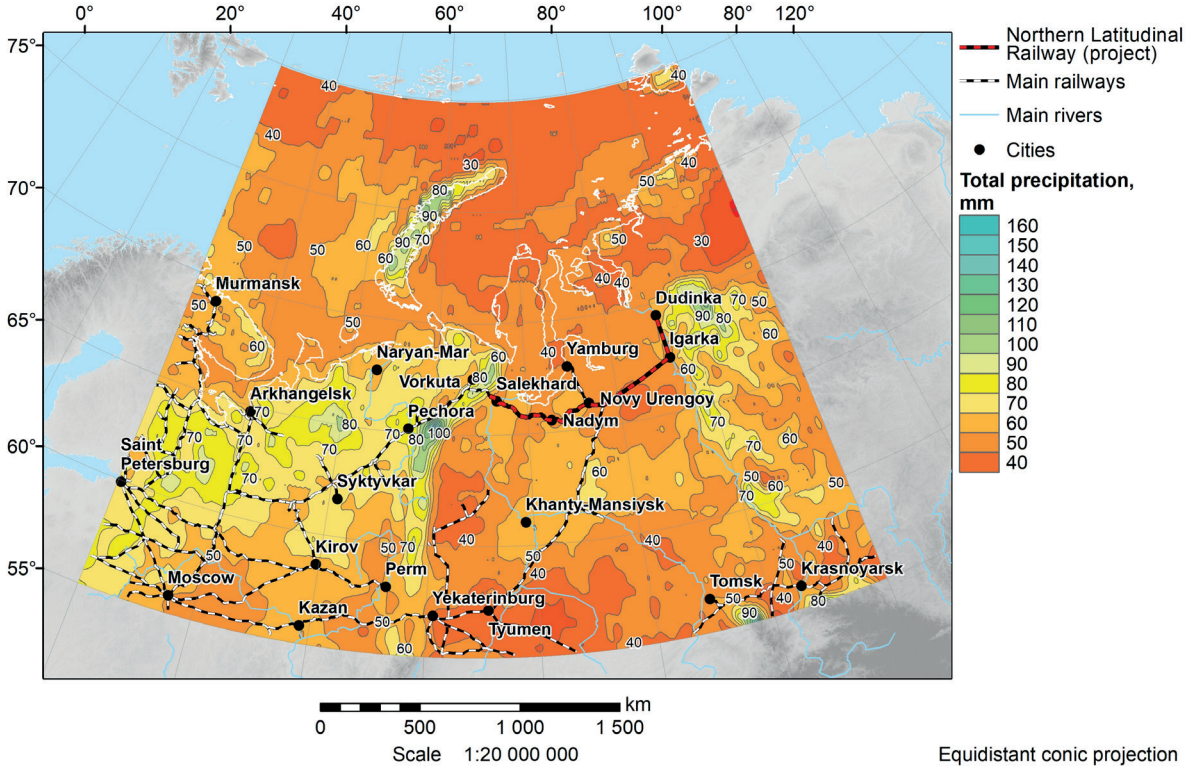

Fig. 4. Average projected total precipitation for 2022 under SSP1-2.6 scenario

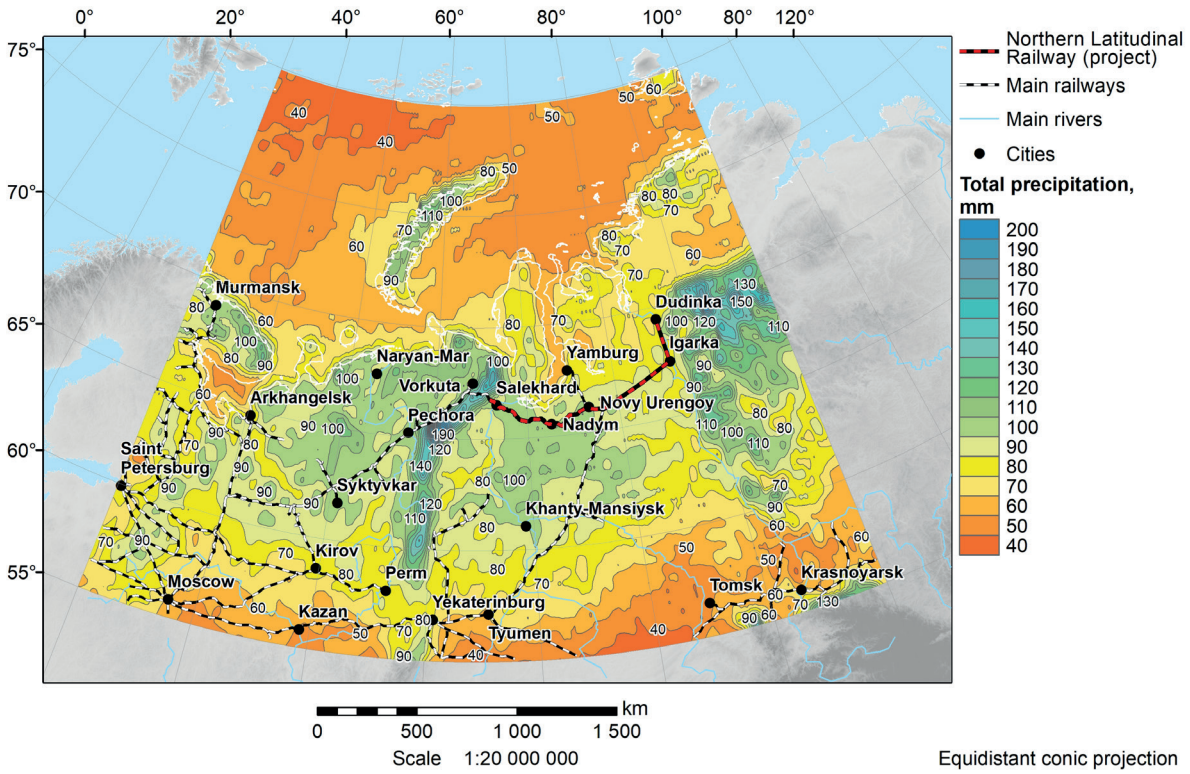

Fig. 5. Average projected total precipitation for July 2023–2064 under SSP1-2.6 scenario

Temporal comparison highlights a steady increase in precipitation across successive decades. Between 2043–2064 and 2023–2042, projection growth reaches 3–10 mm in the St. Petersburg–Yekaterinburg–Syktyvkar corridor under SSP1-2.6, and up to 17 mm under SSP5-8.5. The largest increase is concentrated in the northern Perm region and the Pechora–Vorkuta corridor, areas already prone to hydrological stress.

The long-term comparison of 2053–2064 with the baseline period of 1980–1989 (Fig. 6) confirms a marked rise in summer precipitation. Under SSP1-2.6, central regions show an increase of 10–40 mm, while SSP5-8.5 projections up to 50 mm in northern areas. These shifts suggest a growing risk of extreme rainfall events and related impacts on embankment stability and culvert capacity, especially in permafrost-affected zones.

Wind speed

Maps of spatial wind speed distribution for 2022 under both the 'optimistic' (SSP1-2.6) and 'worst-case' (SSP5-8.5) scenarios show a high degree of similarity (Fig. 7). Under both scenarios, the strongest winds, exceeding 5 m/s, are consistently observed in three regions: along the NLR corridor between Nadym and Dudinka, in the area south and southeast of Tyumen, and around St. Petersburg. In the rest of the study area, average wind speeds range from 3 to 5 m/s. Given the coincidence of high wind speeds and transport infrastructure in the Nadym–

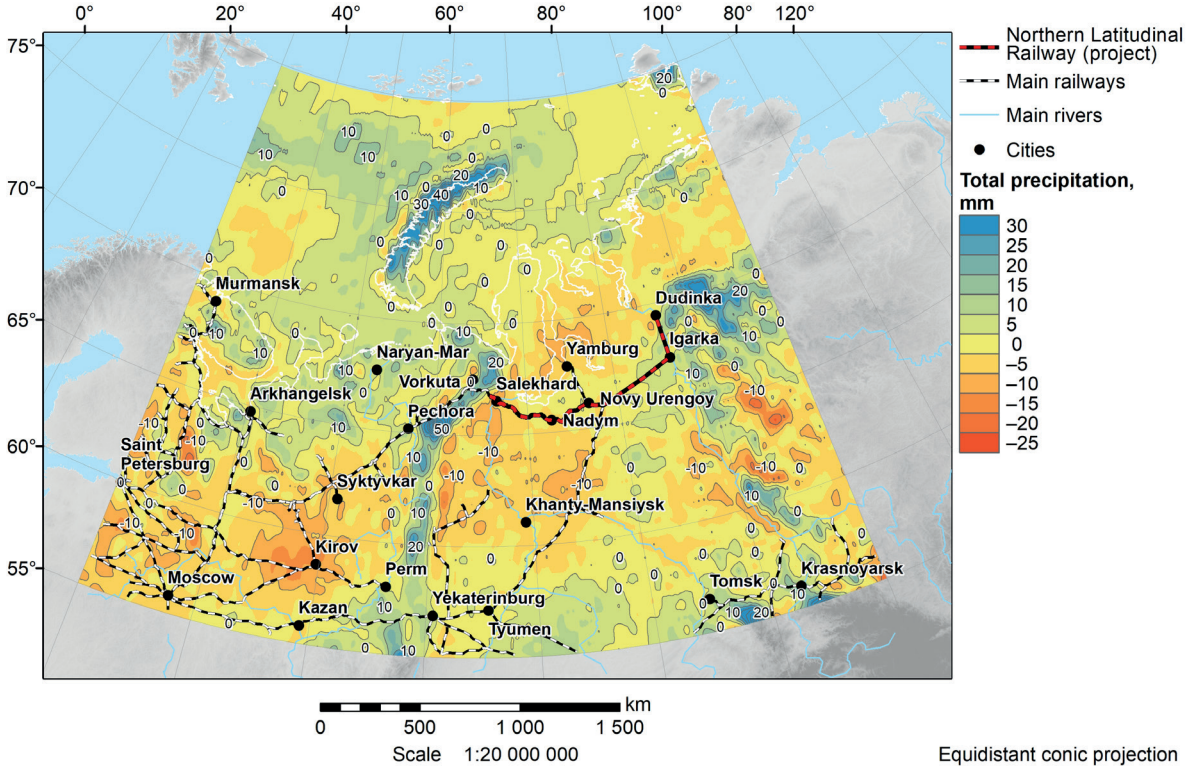

Fig. 6. Projected total precipitation changes between the periods 2053–2064 (under SSP5-8.5 scenario) and 1980–1989

Dudinka corridor, this area warrants particular attention when assessing operational risks related to wind exposure.

The average spatial distribution of wind speed over the 2023–2064 period under the same two scenarios confirms the stability of these regional patterns. The three high-wind zones previously mentioned remain clearly distinguishable. The distributions under SSP1-2.6 and SSP5-8.5 show only small differences in magnitude or extent. This persistence suggests that, unlike temperature or precipitation, wind speed in the region is controlled by stable large-scale drivers such as topography and synoptic circulation. These drivers are less affected by scenario-dependent climate forcing.

Analysis of the maps of seasonal variability of wind speeds showed that all of our selected areas persist stable throughout all months. The strongest winds occurred in spring (April), reaching 6.6 m/s at the selected track sections (Fig. 8), and the minimum wind speeds occurred in summer (July), up to 4–4.5 m/s. The same seasonal variability is observed in the rest of the study area.

Projected changes between future 20-year intervals (2043–2064 compared to 2023–2042) remain subtle. Under SSP1-2.6, a minor strengthening of 0.05–0.1 m/s is anticipated in areas such as the Moscow–Kazan transport corridor. SSP5-8.5 presents a slightly different pattern, with weak declines in northern sectors and small increases farther south. Such marginal variations are likely governed by shifts in pressure gradients, surface roughness feedbacks, and boundary-layer stability. These factors may evolve asynchronously across latitudes.

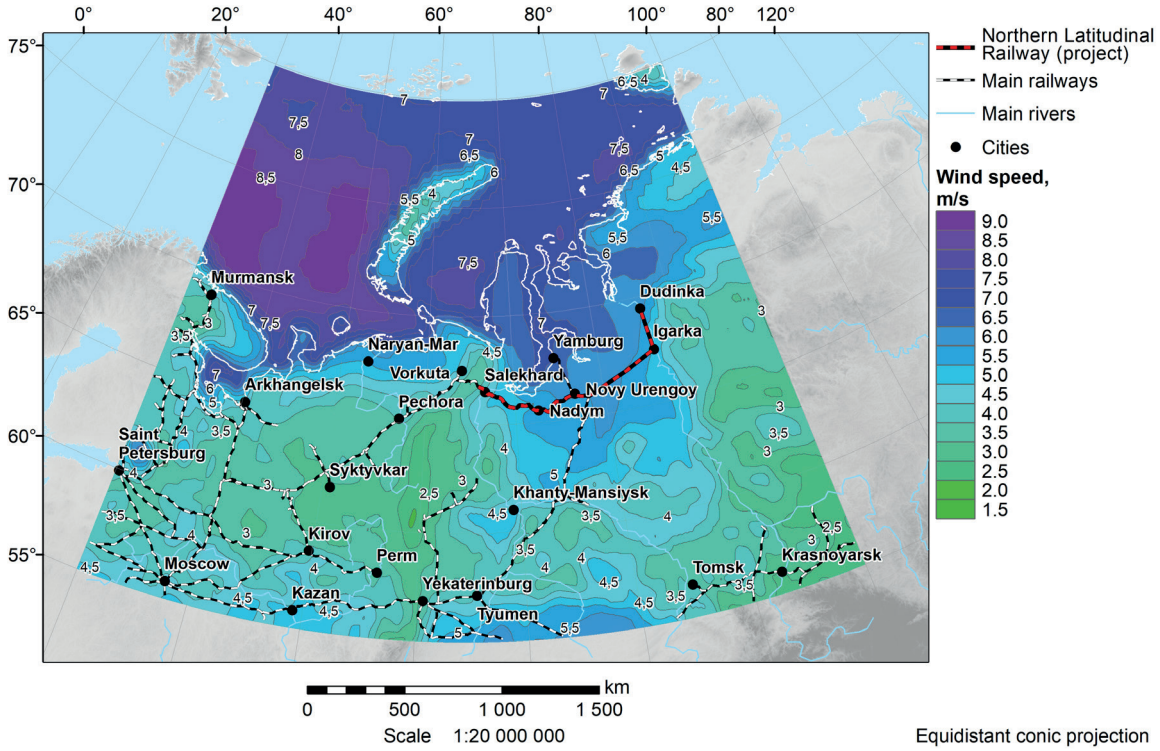

Fig. 7. Average projected wind speed for 2022 under SSP5-8.5 scenario

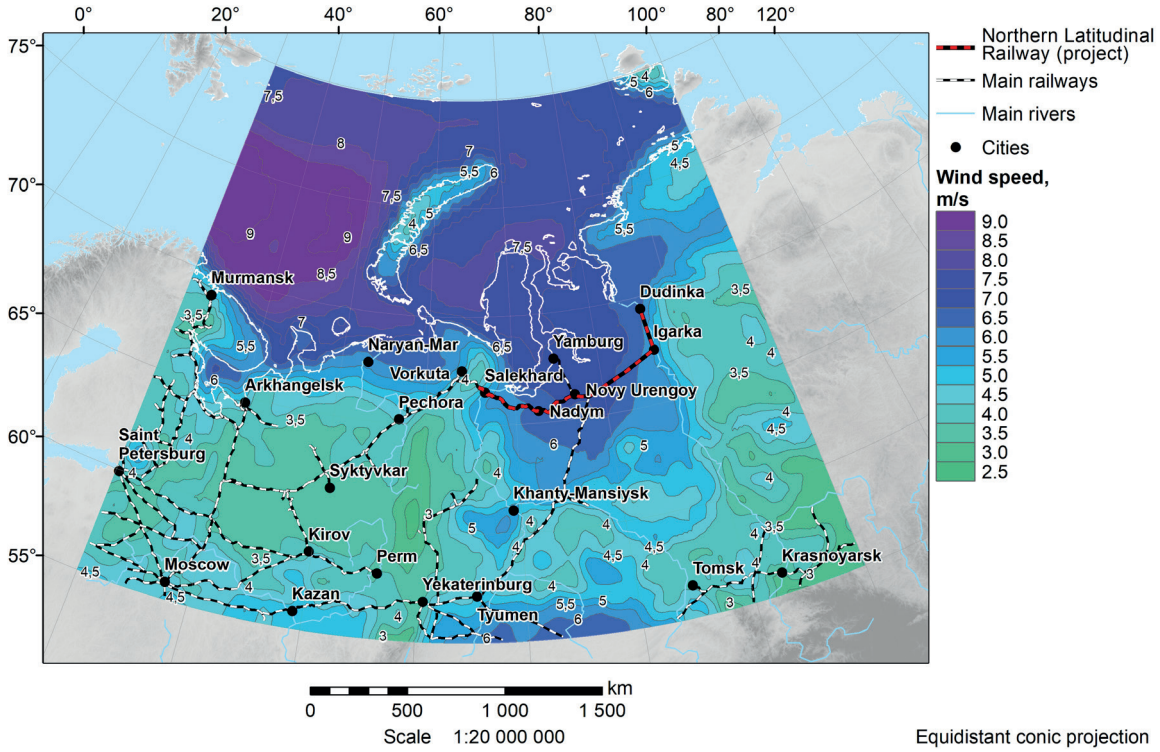

Fig. 8. Average projected wind speed for April 2023–2064 under SSP1-2.6 scenario

Projected changes in wind speed for the period 2053–2064 relative to the historical baseline of 1980–1989 are substantial in several regions (Fig. 9). According to the SSP1-2.6 scenario, average wind speeds are expected to increase by 2–3 m/s across the European sector of northwestern Russia, by 3–4 m/s in the territory between the Ural Mountains and the Yenisei River, and by 1–2 m/s east of the Yenisei. The most pronounced growth is expected along the NLR, where both topographic channelling and synoptic influences likely amplify wind intensities. Under the SSP5-8.5 scenario, the spatial pattern and magnitude of wind speed increase remain broadly comparable to those observed in SSP1-2.6. This similarity suggests that long-term wind field changes may be more strongly governed by persistent circulation regimes and orographic effects than by greenhouse gas concentration pathways alone.

Analysis of linear wind speed trends over the period 2023–2064 reveals that the most pronounced increases, ranging from 0.02 to 0.04 m/s per decade, are concentrated along the southern part of the study area. This includes the corridor from Moscow to Tomsk, as well as the stretch from Vorkuta to Dudinka along the NLR. Across the rest of the region, projected changes are negligible, with trends close to zero. Under the SSP5-8.5 scenario, however, the spatial pattern shifts. Positive wind speed trends extend across the entire area south of a notional line running from St. Petersburg through Khanty-Mansiysk to Igarka, with peak rates reaching 0.06 m/s per decade. In contrast, north of the Murmansk–Arkhangelsk–Novy Urengoy–Dudinka axis, wind speeds are projected to decrease at a similar rate (up to –0.06 m/s per decade), highlighting a spatial divergence in atmospheric circulation responses under high-emission trajectories.

Soil temperature

Figure 10 presents the spatial distribution of soil temperature in the study region for 2022 under the optimistic SSP1-2.6 scenario. The distributions for SSP2-4.5 and SSP5-8.5 are generally similar. The highest average annual temperatures (4 to 6°C) are recorded in the southwestern part of the region, while the lowest values (–4 to –14°C) are observed in the northeast under both scenarios. Among all segments of the railway network, the section from Vorkuta to Dudinka (NLR) consistently exhibits the lowest soil temperatures, indicating the need for special engineering attention.

For the period 2023–2064, the average spatial pattern of soil temperature remains largely unchanged under both scenarios. The northeastern part of the region continues to be characterised by negative temperatures. Under SSP5-8.5, however, the zero-isotherm shifts approximately 200 km north-eastward relative to SSP1-2.6. A local zone of weakly negative soil temperatures is projected to persist in the Murmansk region.

Seasonal maps indicate that the overall trend of increasing soil temperature from southwest to northeast is maintained across all scenarios and months. Figures 11 and 12 show the average soil temperature in January and July for 2023–2064 under SSP1-2.6, illustrating the seasonal amplitude. In winter, temperatures reach around –8 °C west of the Moscow–St. Petersburg corridor, and drop as low as –30 °C in the Igarka–Dudinka area (Fig. 11). In summer, the distribution aligns with latitude: 20–24 °C in the south and 12–16 °C in the north (Fig. 12).

The projected change in soil temperature between the periods 2043–2064 and 2023–2042 shows a moderate increase under SSP1-2.6. This increase is about 0.1 °C in the Yekaterinburg–Tyumen area and up to 1 °C near Igarka and Dudinka. Under the more extreme SSP5-8.5 scenario, temperature increases are substantially greater, ranging from 1.2–1.5 °C in both the central region and the Novy Urengoy–Dudinka corridor.

Long-term comparisons between 2053–2064 and the historical baseline of 1980–1989 (Fig. 13) reveal widespread warming across the study area. Under SSP1-2.6, summer soil temperatures rise by 2–3 °C across the central corridor and by up to 4 °C in southern territories. In SSP5-8.5, this warming intensifies, reaching 5–6 °C in southern zones and up to 3–4 °C in the north. These changes imply a progressive degradation of permafrost and an increasing

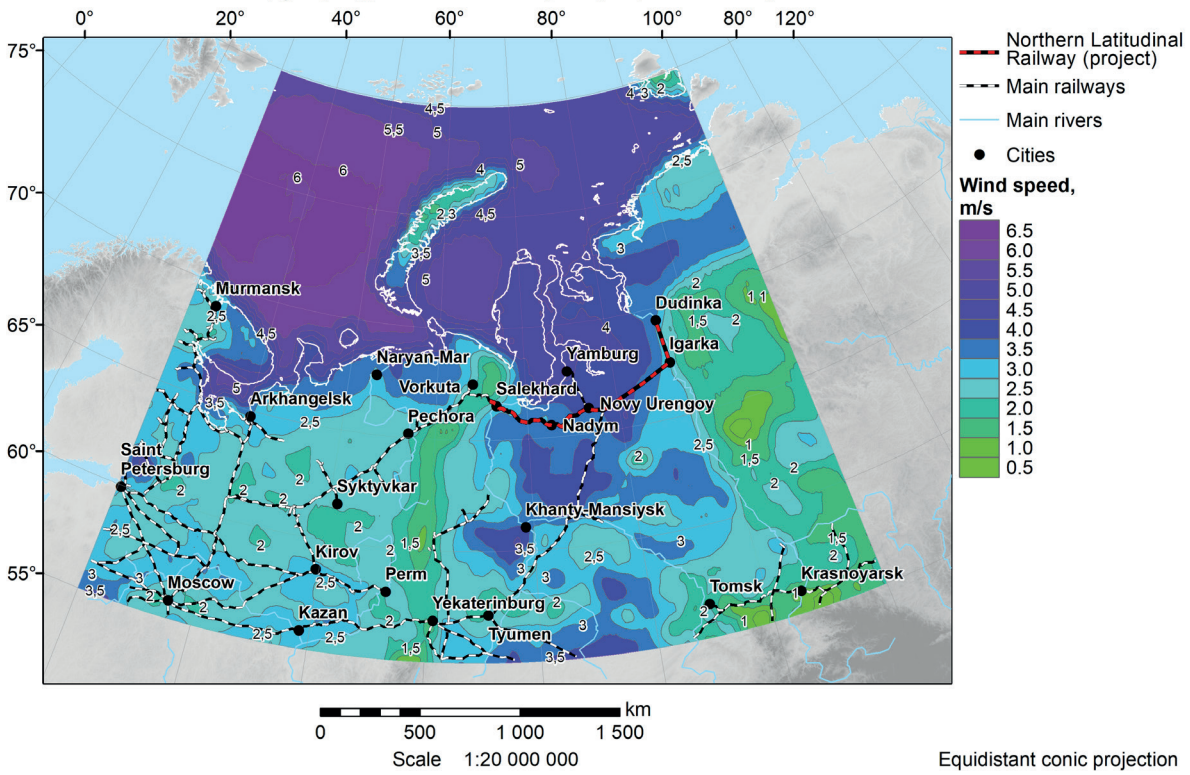

Fig. 9. Projected wind speed changes between the periods 2053–2064 (under SSP1-2.6 scenario) and 1980–1989

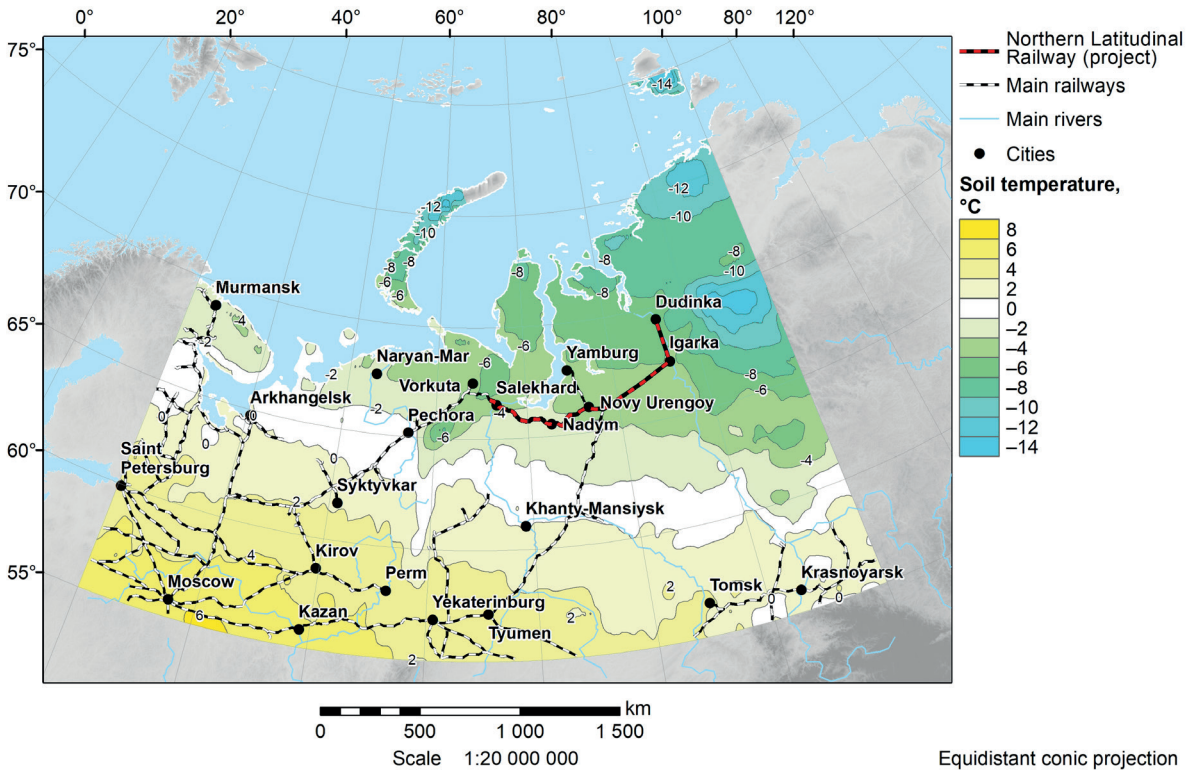

Fig. 10. Average projected soil temperature for 2022 under SSP1-2.6 scenario

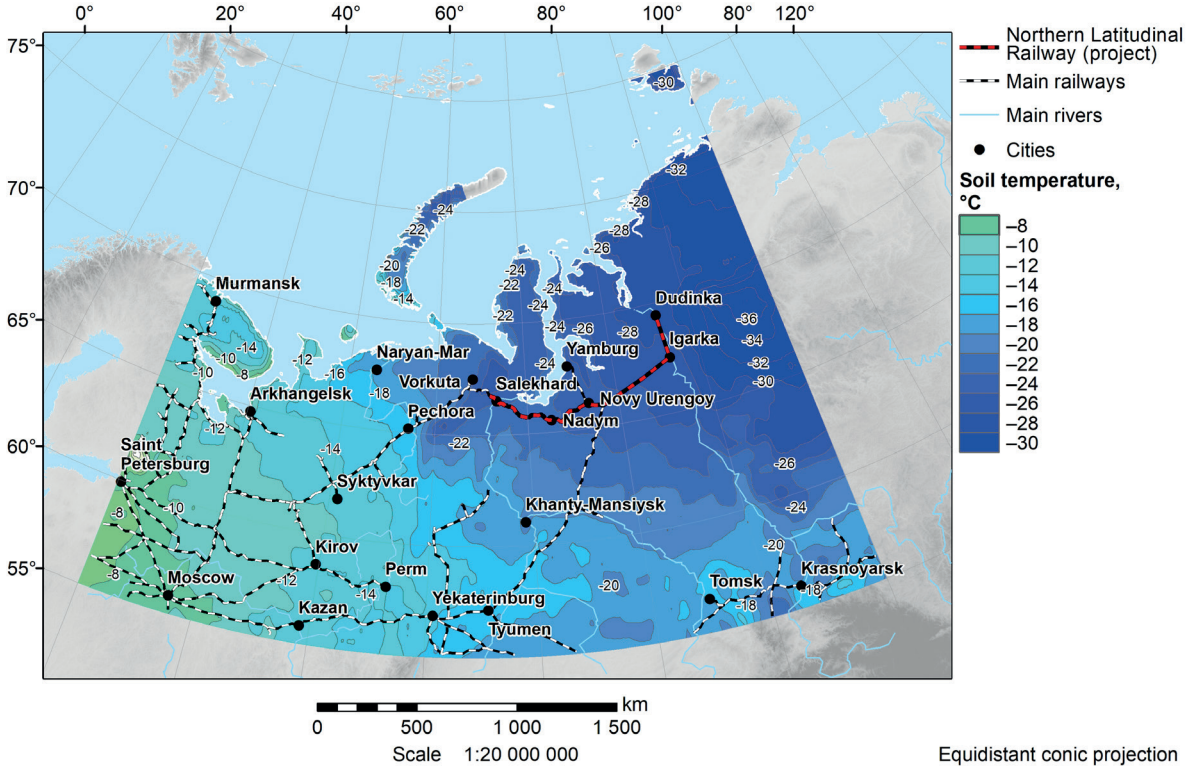

Fig. 11. Average projected soil temperature for January 2023–2064 under SSP1-2.6 scenario

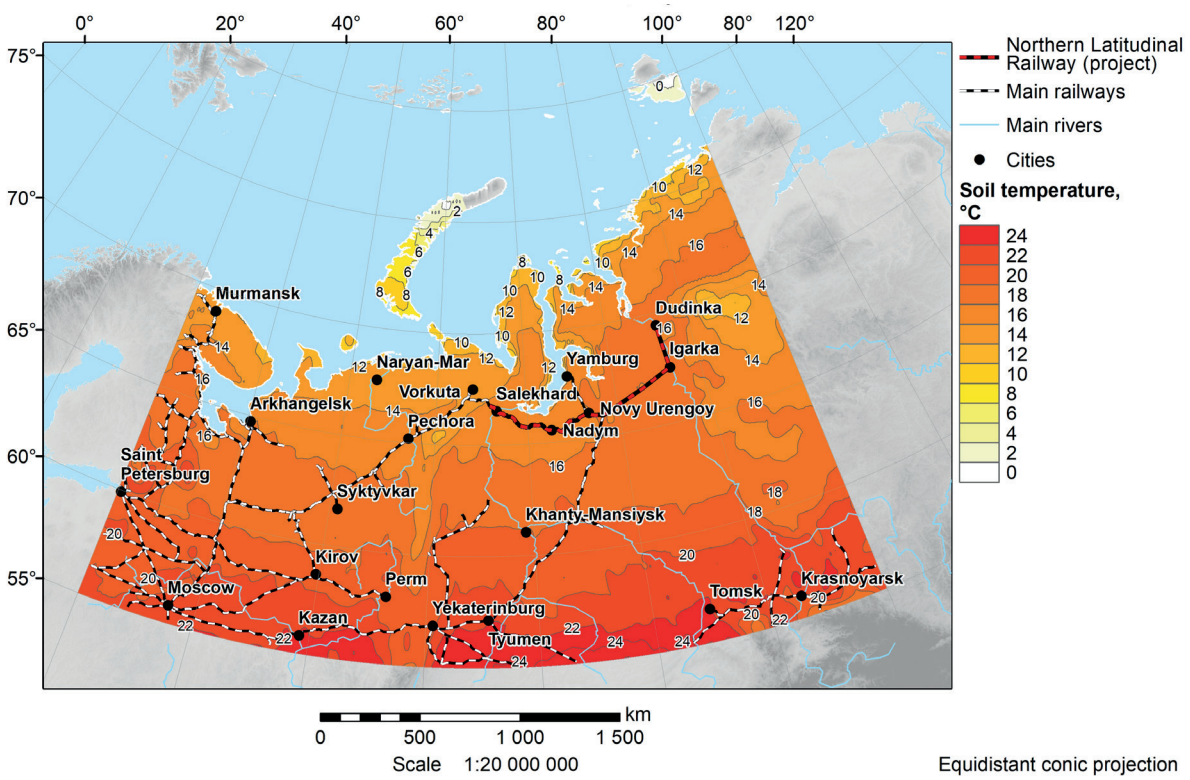

Fig. 12. Average projected soil temperature for July 2023–2064 under SSP1-2.6 scenario

depth of seasonal thaw. This may significantly affect the mechanical properties of subgrade soils along railway infrastructure.

The linear trend of soil temperature change for 2023–2064 shows that, under the SSP1-2.6 scenario, the most pronounced warming, between 0.4 and 0.55 °C/decade, is observed along the NLR between Vorkuta and Dudinka. In other parts of the study area, the warming is significantly weaker, particularly in the Perm–Yekaterinburg–Tyumen sector, where the trend ranges from 0.3 to 0 °C/decade. Under the SSP5-8.5 high-emission scenario, the warming rate increases substantially across the entire region, averaging 0.7–0.8 °C/decade. The strongest warming, from 0.8 to 1.0 °C/decade, is projected for the Novy Urengoy–Dudinka corridor (Fig. 14).

Snow cover thickness

The spatial distribution of snow cover thickness in 2022, based on both the SSP1-2.6 and SSP5-8.5 scenarios, shows a clear north-south pattern. Values increase steadily from southern to northern latitudes (Fig. 15). Snow depth is lowest, around 10 cm, in areas such as St. Petersburg–Moscow–Kazan and Yekaterinburg–Tyumen. In contrast,

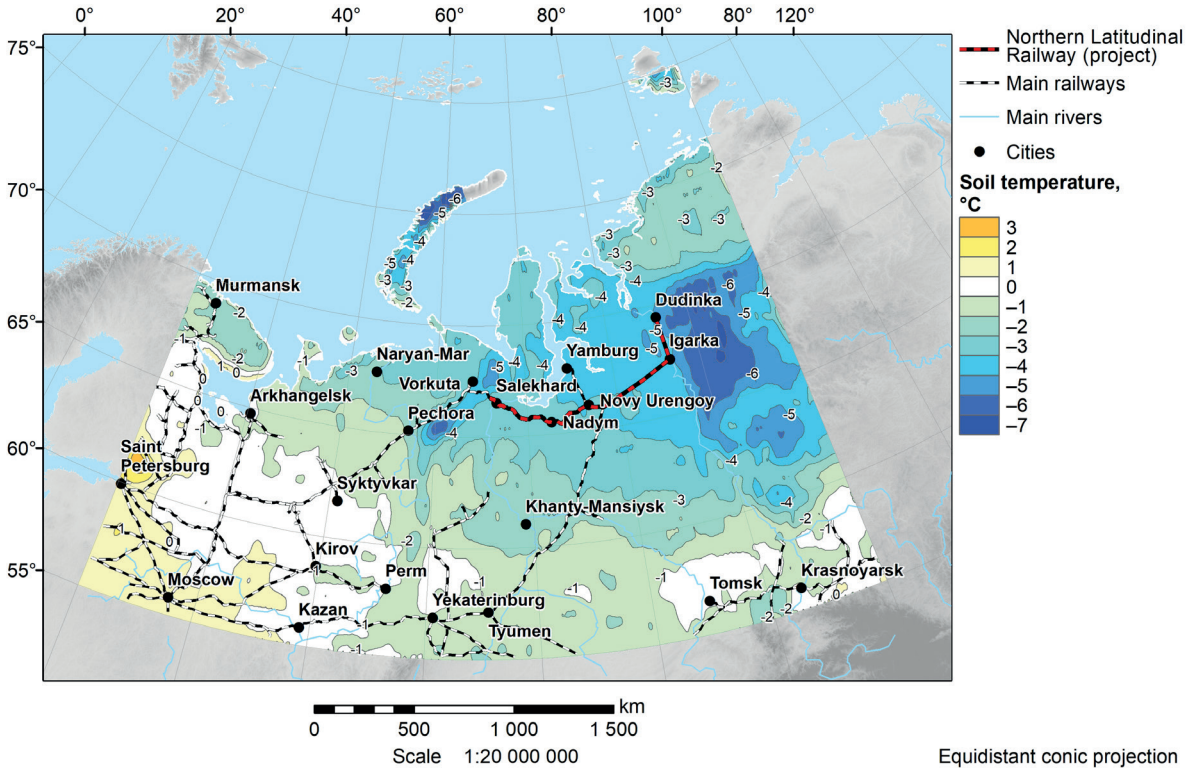

Fig. 13. Projected soil temperature changes between the periods 2053–2064 (under the SSP1-2.6 scenario) and 1980–1989

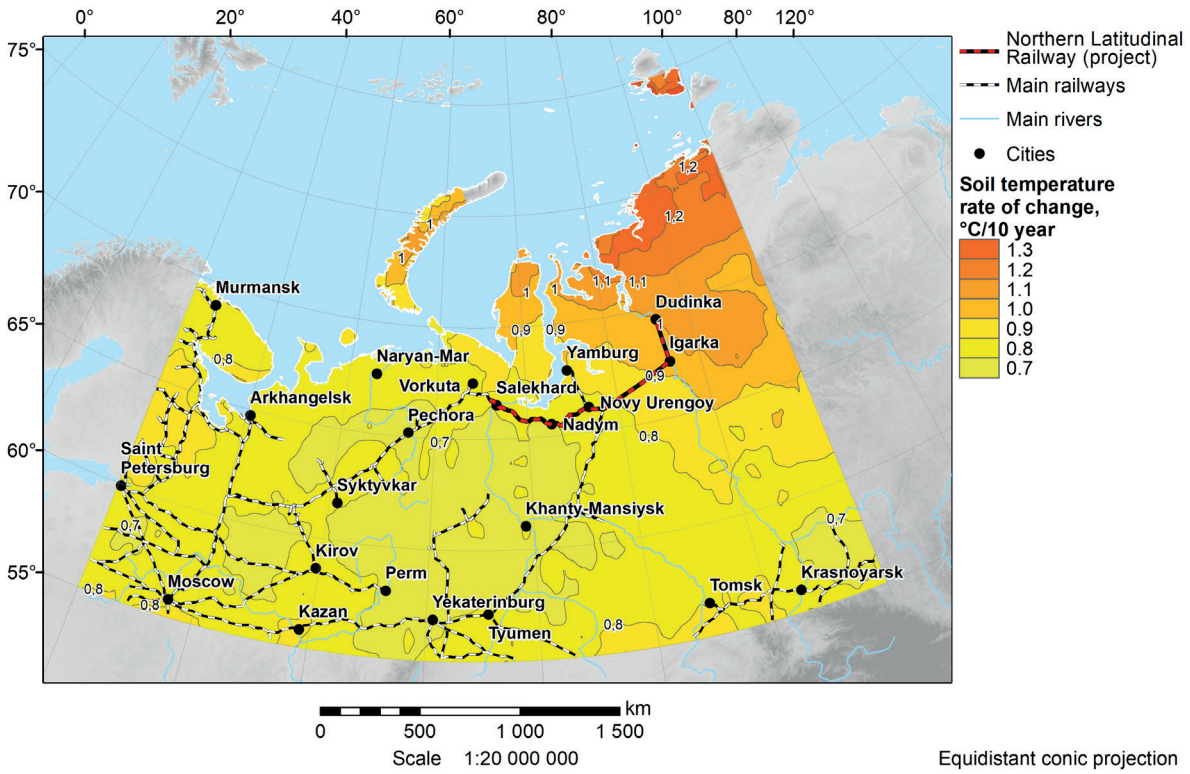

Fig. 14. Average projected soil temperature rate of change for 2023–2064 under the SSP5-8.5 scenario

the Arctic coastal zone has widespread coverage of approximately 30 cm. Furthermore, isolated regions east of Pechora and Dudinka show local accumulations reaching up to 1 m. Under SSP5-8.5, the areas with snow thickness ≤10 cm become significantly larger in both north-south and east-west directions, although the locations of local peaks remain the same.

The average distribution of snow depth projected for 2023–2064 retains these key spatial features. The southwestern part of the region continues to show minimal values (<10 cm), extending towards the White Sea coast, while snow accumulation in the northeast remains significant, up to 30 cm. The previously identified local maxima increase in area under both scenarios.

Seasonal mapping reveals that this meridional gradient in snow thickness persists regardless of the time of year or emissions pathway. Under SSP1-2.6, January snow depths during 2023–2064 range between 20 and 40 cm, with maximum values (up to 1.4 m) concentrated in the Ural Mountains and the area east of Dudinka (Fig. 16). By April, snow has largely receded from southern regions, but the same areas continue to exhibit maximum depths of up to 1.4 m.

Projected changes between the 2043–2064 and 2023–2042 periods indicate only modest variation under

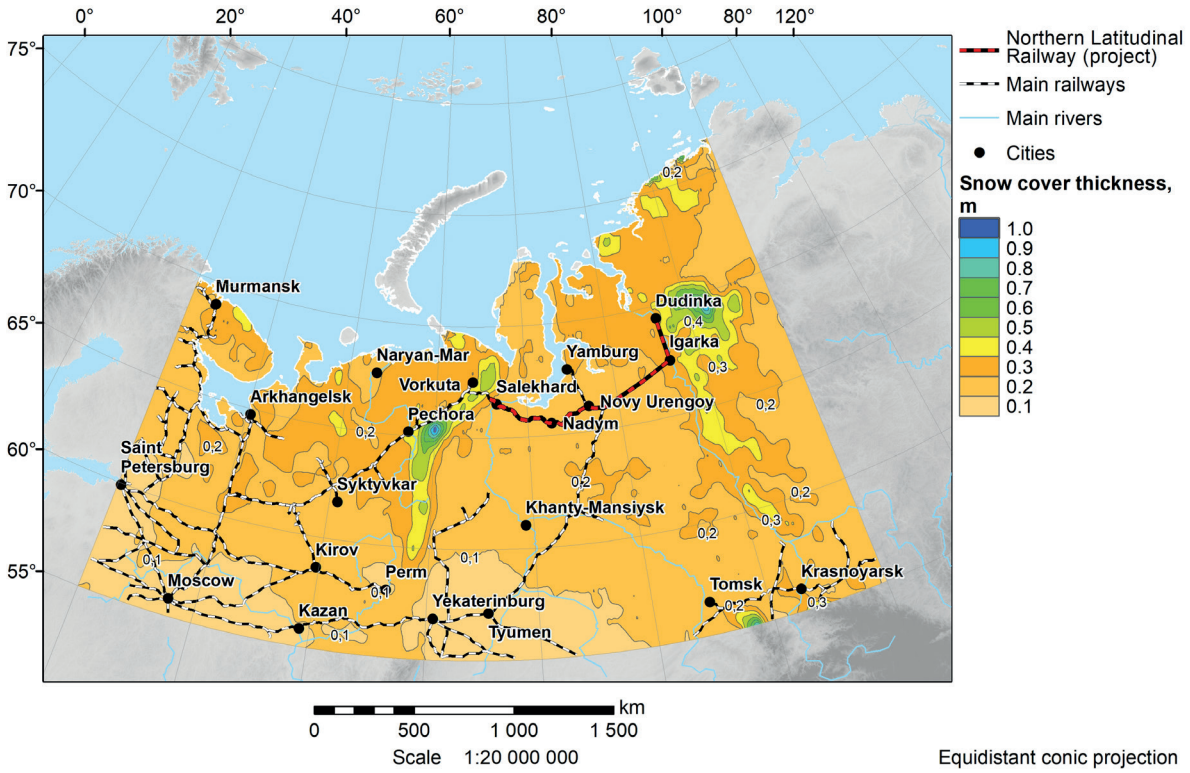

Fig. 15. Average projected snow cover thickness for 2022 under SSP1-2.6 scenario

the SSP1-2.6 scenario. Reductions of 1–2 cm are expected in western and southwestern areas, while northeastern regions may see increases of the same magnitude. Under SSP5-8.5, a more pronounced decline (up to 2.5 cm) is projected west of the Urals, while snow depth is expected to increase by 1–3 cm in eastern territories, including parts of the NLR corridor.

Long-term anomalies relative to the 1980–1989 reference period suggest that the spatial structure of snow loss is broadly similar across both scenarios, though the magnitudes vary. The most substantial reductions, ranging from 25 to 35 cm, are projected east of the Yenisei, west of the Ural Mountains, and in southern Karelia (Fig. 17).

Linear trends in snow thickness for the 2023–2064 period show distinct regional patterns. Under SSP1-2.6, the most significant reductions (0.5–1.0 cm/decade) occur in the western belt from Murmansk to Moscow, across the Pechora–Syktyvkar–Perm–Yekaterinburg–Tyumen zone, and in parts of the east-central region. Areas around Khanty-Mansiysk, Salekhard, and Nadym, as well as regions east of Igarka and Dudinka, are projected to experience slight increases, up to 0.5 cm/decade. Under SSP5-8.5, the west shows a more substantial decline (1–2 cm/decade), the central region remains relatively stable, and eastern sectors, including the NLR corridor, are expected to gain snow at a rate of 0.5–1.5 cm/decade.

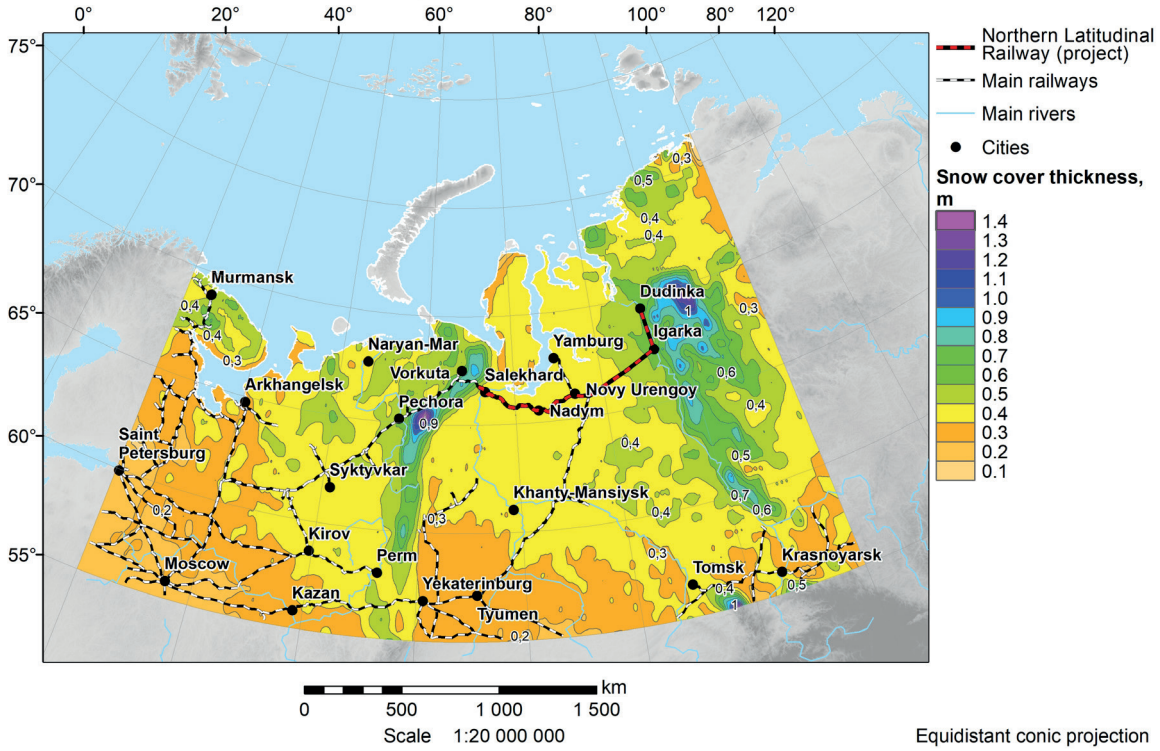

Fig. 16. Average projected snow cover thicknesses for January 2023–2064 under SSP1-2.6 scenario

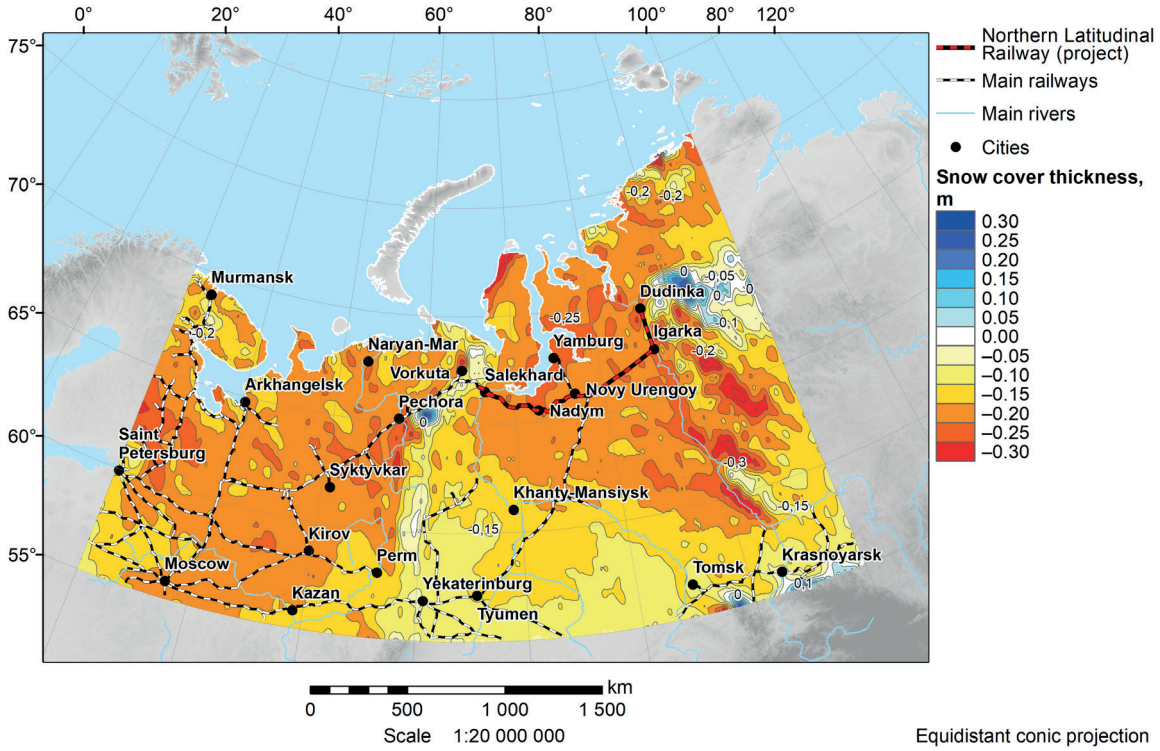

Fig. 17. Projected snow cover thickness changes between the periods 2053–2064 (under SSP5-8.5 scenario) and 1980–1989

DISCUSSION

This paper presents the results of the analysis and assessment of climate change for the region of the Western Russian Arctic (55°–80°N, 30°–100°E) for 2023–2064. The main data source for this research is Phase 6 of the Coupled Model Intercomparison Project (CMIP6), which is dedicated to comparing existing climate models (Eyring et al. 2016; Tolstykh 2016). An analysis of the CMIP6 assembly of models was performed, and in total, the characteristics of 59 models were considered. The climate model CNRM-CM6-1-HR, developed by the CNRM-CERFACS working group (France), was selected for further research. The choice of this model was justified based on the list of included hydrometeorological parameters, spatial resolution, and the availability of data for selected future climate scenarios. To select the relevant variants of the climate change model projection, three scenarios of Shared Socioeconomic Pathways (SSPs) were considered: SSP1-2.6 (sustainable development scenario), SSP2-4.5 (intermediate scenario), and SSP5-8.5 (fossil fuel-intensive development) (O'Neill et al. 2016; Semenov and Gladilshchikova 2022). Based on this data, a series of maps showing the spatio-temporal distribution of the main hydrometeorological parameters (air temperature, total precipitation, wind speed, soil temperature, and snow cover thickness) was compiled and combined into an electronic atlas.

The analysis of changes in climatic parameters and observed changes in regional climate up to 2064 has been carried out. This information is essential for the sustainable management and development of railway infrastructure. The results of the analysis emphasised the heterogeneity of climate change in the Arctic region and certain potentially hazardous phenomena. Their impact might increase in the future. For example, degradation of permafrost soils, combined with a significant increase in average temperatures, leads to changes in the balance of inland water bodies. This causes an intensification of snow and rainwater flows, and activates mudflows and landslides. These can negatively affect the existing railway infrastructure (Grebenets and Isakov, 2016; Kostianaia et al. 2021; Romanenko and Shilovtseva 2016; Yakubovich and Yakubovich 2019).

The analysis of time series for the average values of the selected parameters from 2015 to 2100 revealed considerable non-linear variations in the projected models. This indicates that for different scenarios, parameter values may overlap, and their rates of change might be lower for pessimistic scenarios compared to optimistic ones. Parameter changes were analysed relative to the established baseline period of 1980–1989, which is considered climatically stable and is commonly used for comparative climate assessments. The spatio-temporal analysis of the main hydrometeorological parameters over the period 2023–2064, performed using a compiled series of regional maps, produced the following results.

Air Temperature. It was shown that air temperature isotherms are expected to move 150–300 km north/northeast in 2023–2064 under SSP1-2.6 and SSP5-8.5 scenarios, relative to 2022. Air temperature trends for 2023–2064 vary regionally. They range from 0.1°C/decade (Kazan–Perm–Yekaterinburg–Tyumen area) to 0.5°C/decade (Novy Urengoy–Igarka–Dudinka area) under SSP1-2.6. Under SSP5-8.5, trends range from 0.7 to 1.0°C/decade. Under the latter scenario, the highest rates are again projected for the NLR sector between Salekhard and Dudinka. The continuous warming of the regional climate will lead to further thawing of permafrost soils, a change in the water balance of numerous rivers and lakes, and an intensification of geomorphological processes such as snow-water flows (a type of mudflow) and landslides. An important conclusion from the study is that objects on pile foundations with a depth of less than 6 m are at increased risk even with warming up to +2°C. Therefore, engineering protection of these objects should proceed at a faster pace than the warming of the regional climate (Grebenets, Isakov, 2016; Yakubovich, Yakubovich, 2019).

Total precipitation. A comparison of the SSP1-2.6 and SSP5-8.5 scenarios revealed that the more pessimistic scenario predicts slightly higher precipitation values west of the Ural Mountains. Between the Urals and the Yenisei, SSP5-8.5 indicated a precipitation rate approximately 10 mm higher. East of the Yenisei, the differences were more significant, with SSP5-8.5 also exceeding SSP1-2.6 by about 10 mm. The railway section in the Pechora region is likely to remain one of the most hazardous in terms of potential thawing of the railway bed in the future. Spatial variations in precipitation changes could increase regional flooding risks.

Wind Speed. Minor increases in wind speed are projected. The NLR and Tyumen regions are expected to experience the strongest winds, exceeding 5 m/s. Seasonal peaks occur in spring, reaching 6.6 m/s, which poses risks to infrastructure. The SSP5-8.5 scenario predicts a southward shift in wind speed increases. This may affect agricultural and transport systems. Intense wind activity can severely impact railway operations, causing accidents and service interruptions when trees, branches, and debris obstruct the tracks (Baker et al. 2009).

Soil temperature is a key indicator for assessing the reliability of railway performance, particularly in permafrost zones. Permafrost degradation beneath railway infrastructure can compromise the long-term stability and operational reliability of engineering structures, potentially leading to system failures. The analysis showed that warming trends in soil temperature are most severe under SSP5-8.5 (1.04°C/10 years), with the NLR area exhibiting the highest rates. For instance, in the Kola Peninsula, which has permafrost of an island nature and relatively high temperatures, Yakubovich and Yakubovich (2019) demonstrated that construction objects with foundations formed by piles of 5 m depth or less face very high risks of reduced functionality, potentially to a zero level. With a warming of up to +1°C, piles 5 m deep generally still provide functionality at U = 0.65–0.85 (where U = 1 represents the maximum functionality level). This is considered an average level of climate risk for a transport infrastructure facility. Warming up to +2°C often leads to a decrease in functionality to U < 0.5, and warming to +3°C can be considered catastrophic for construction objects, as functionality reduces to the level U = 0–0.35, which signifies an unacceptably high level of climate risks.

Snow cover thickness. Analysis of the spatial distribution and seasonal variability of snow cover thickness confirmed a consistent northward increase, applicable to all scenarios and throughout the entire snow cover period. Snow cover thickness decreases between 2053–2064 and 1980–1989 show comparable spatial distribution across scenarios, varying slightly by region. Greatest reductions (25–35 cm) are expected east of the Yenisei, west of the Urals, and in southern Karelia. Under SSP5-8.5, snow cover declines by 1–2 cm/10 years west of the Urals, remains stable in the centre, and increases by 0.5–1.5 cm/10 years in the east. These variations can alter spring flood regimes and winter transport logistics, affecting the NLR.

CONCLUSIONS

The projected changes in selected meteorological parameters from 2023 to 2064 highlight the vulnerability of the Arctic Zone of the Russian Federation (AZRF) to climate change. This is particularly true for infrastructure-heavy areas such as the Northern Latitudinal Railway. This railway, which is 707 km long, will follow the Obskaya–Salekhard–Nadym–Novy Urengoy–Korotchaevo route. Its purpose is to connect the western and eastern parts of the Yamalo-Nenets Autonomous Okrug. Rising temperatures and precipitation will challenge permafrost stability, while changes in wind and snow may disrupt transport networks. Permafrost thawing in Russia is a major concern. The market value of housing stock located solely in the permafrost area of the AZRF was over US$93 billion in 2020. This value is projected to increase to US$133.5 billion by 2055, considering buildings and infrastructure from various economic sectors planned for construction during this period (Badina 2022). Eliseev and Naumova (2019) have shown that the expected damage to motorways from permafrost degradation in the AZRF will amount to US$1.2 billion between 2020 and 2050. Therefore, developing adaptation measures for ongoing and future climate change and permafrost thawing requires an accurate projection of these changes, not only for the end of the 21st century but for each decade.

This can be achieved with the help of modern CMIP6 climate models. However, a significant challenge arises from the divergence between these models and between the SSP scenarios of global socio-economic development, which are poorly predicted. This divergence highlights the necessity for adaptive strategies that are specifically designed for different emission pathways. Policymakers must prioritise resilient infrastructure, early warning systems, and regional climate modelling to reduce potential risks. To calculate the budget required for developing adaptation measures, such as those for Russian Railways, they need the most realistic projections. Unfortunately, this is difficult to provide due to the many uncertainties associated with climate change modelling.

Our research methodology relies on a single high-resolution climate model, which may not fully capture regional characteristics. The decision to use one model, rather than an ensemble of models, places certain constraints on our findings. Given this research limitation, the focus was restricted to the selected model.

An important task is to assess ongoing climate change to understand the most likely scenario of further climate change. This will reduce the divergence between projections. We are working on this task, and it will be done by analogy with the research we recently performed for the Caspian Sea Region (Bocharov et al., 2025). Employing multi-model ensembles and local observations would refine the projection. Additional studies should consider socio-economic effects, including agricultural impacts and energy demand, to ensure sustainable development in the AZRF, including its transport infrastructure.

REFERENCES

Andersson-Sköld Y., Nordin L., Nyberg, E. and Johannesson, M. (2021). A framework for identification, assessment and prioritization of climate change adaptation measures for roads and railways. International journal of environmental research and public health, 18(23), 12314. DOI: 10.3390/ijerph182312314

Baker C. J., Chapman L., Quinn A., and Dobney K. (2009). Climate change and the railway industry: A review. Proceedings of the Institution of Mechanical Engineers, Part C: Journal of Mechanical Engineering Science, 224(3), 519–528. DOI: 10.1243/09544062JMES1558.

Bartus T. (2014). ArcGIS Desktop resources. [online] ESRI. Available at: https://www.esri.com/en-us/arcgis/products/arcgis-desktop/resources [Accessed 1 Nov. 2022].

Blanutsa V. (2021). Spatial development of the Russian Arctic Zone: analysis of two strategies. Arctic: Ecology and Economy, 11(1), 111–121 (In Russian), DOI: 10.25283/2223-4594-20211-111-121. (In Russian)

Bocharov A.V., Kostianoy A.G., Lebedev S.A., Kolomeets L.I. and Kravchenko P.N. (2025). What SSP Global Climate Change Scenario is the Caspian Sea Region Following? Part 1: Air temperature analysis. Russian Journal of Earth Sciences (in press).

CNRM-CERFACS contribution to CMIP6, (2018). CNRM-CM6-1 model: Future projections (ScenarioMIP). [online] Available at: http://www.umr-cnrm.fr/cmip6/spip.php?article11 [Accessed 26 Mar. 2024].

ESGF, (2025). CMIP6 data holdings. [online] Available at: https://pcmdi.llnl.gov/CMIP6/ArchiveStatistics/esgf_data_holdings/print_view.html [Accessed 25 Apr. 2025].

Eyring V., Bony S., Meehl G. A., Senior C. A., Stevens B., Stouffer R. J. and Taylor K. E. (2016). Overview of the Coupled Model Intercomparison Project Phase 6 (CMIP6) experimental design and organization. Geoscientific Model Development, 9, 1937–1958. DOI: 10.5194/gmd-9-1937-2016.

Garmabaki A., Thaduri A., Famurewa S. and Kumar, U. (2021) Adapting Railway Maintenance to Climate Change. Sustainability, 13(24), 13856, DOI: 10.3390/su132413856

Gelaro R., McCarty W., Suárez M. J., et al. (2017). The Modern-Era Retrospective Analysis for Research and Applications, Version 2 (MERRA-2). Journal of Climate, 30(14), 5419–5454. DOI: 10.1175/JCLI-D-16-0758.1.

Golden Software Surfer, (2022). Golden Software. [online] Available at: https://www.goldensoftware.com/products/surfer [Accessed 1 Nov. 2022].

Government of the Russian Federation, (2021). Executive order No. 3363-r of 27 Nov. 2021 on the Transport strategy of the Russian Federation until 2030 with forecast up to 2035. [online] Available at: http://static.government.ru/media/files/7enYF2uL5kFZlOOpQhLl0nUT91RjCbeR.pdf [Accessed 29 Sep. 2025]

Government of the Russian Federation, (2022). Decree No. 2115-r of 01 Aug. 2022 on approval of the Development Plan of the Northern Sea Route for the period up to 2035. [online] Available at: http://government.ru/docs/46171/ [Accessed 17 Apr. 2025].

Grebenets V. I. and Isakov V. A. (2016). Deformations of roads and railways within the Norilsk-Talnakh transportation corridor and the stabilization methods. Earth's Cryosphere, 20(2), 69-77 (In Russian).

Gvishiani A. D., Rozenberg I. N., Soloviev A. N., Kostianoy A. G., Gvozdik S. A., Serykh I. V., Krasnoperov R. I., Sazonov N. V., Dubchak I. A., Popov A. B., Kostianaia E. A. and Gvozdik G. A. (2023a). Electronic atlas of climatic changes in hydrometeorological parameters of the western part of the Russian Arctic for 1950–2021 as geoinformatic support of railway development. Applied Sciences, 13, 5278. DOI: 10.3390/app13095278.

Gvishiani A. D., Rozenberg I. N., Soloviev A. A., Krasnoperov R. I., Shevaldysheva O. O., Kostianoy A. G., Lebedev S. A., Dubchak I. A., Nikitina I. M., Gvozdik S. A., Sergeev V. N. and Gvozdik G. A. (2023b). Study of the impact of climatic changes in 1980–2021 on railway infrastructure in the Central and Western Russian Arctic based on Advanced Electronic Atlas of hydrometeorological parameters (2023b). Russian Journal of Earth Sciences, 23, ES5006. DOI: 10.2205/2023es000882.

Intergovernmental Panel on Climate Change (IPCC) (2021). Climate Change 2021: The Physical Science Basis IPCC. [online] Available at: https://www.ipcc.ch/report/ar6/wg1/ [Accessed 8 Apr. 2025].

Juckes M., Taylor K. E., Durack P. J., Lawrence B., Mizielinski M. S., Pamment A., Peterschmitt J.-Y., Rixen M. and Sénési S. (2020). The CMIP6 Data Request (DREQ, version 01.00.31). Geoscientific Model Development, 13, 201–224. DOI: 10.5194/gmd-13-201-2020.

Kostianaia E. A. and Kostianoy A. G. (2023). Railway transport adaptation strategies to climate change at high latitudes: A review of experience from Canada, Sweden and China. Transport and Telecommunication, 24(2), 180–194. DOI: 10.2478/ttj-2023-0016.

Kostianaia E. A., Kostianoy A. G., Scheglov M. A., Karelov A. I. and Vasileisky A. S. (2021). Impact of regional climate change on the infrastructure and operability of railway transport. Transport and Telecommunication, 22(2), 183–195.

Kostianoy A. G., Gvishiani A. D., Rozenberg I. B., Krasnoperov R. I., Gvozdik S. A., Lebedev S. A., Nikitina I. M., Dubchak I. A., Shevaldysheva O. O., Sergeev V. N. and Gvozdik G. A. (2025). Geoinformation analysis of regional climatic changes in the Central and Western Russian Arctic for railway development. Russian Journal of Earth Sciences, 25, ES1005. DOI: 10.2205/2025es000956.

Kriging interpolation method, (2023). Desktop ArcGIS. [online] Available at: https://desktop.arcgis.com/en/arcmap/10.3/tools/3d-analyst-toolbox/how-kriging-works.htm [Accessed 12 May 2025].

Krylov A. A., Rukavishnikova D. D., Novikov M. A., Baranov B. V., Medvedev I. P., Kovachev S. A., Lobkovsky L. I. and Semiletov I. P. (2024). The main geohazards in the Russian sector of the Arctic Ocean. Journal of Marine Science and Engineering, 12(12), 2209. DOI: 10.3390/jmse12122209.

Lemenkova P. (2020). GEBCO Gridded Bathymetry Data. [online] Available at: https://www.gebco.net/data_and_products/gridded_bathymetry_data/grid_production/ [Accessed 3 Nov. 2022].

O'Neill B. C., Tebaldi C., van Vuuren D. P., Eyring V., Friedlingstein P., Hurtt G., Knutti R., Kriegler E., Lamarque J.-F., Lowe J., Meehl G. A., Moss R., Riahi K. and Sanderson B. M. (2016). The Scenario Model Intercomparison Project (ScenarioMIP) for CMIP6. Geoscientific Model Development, 9, 3461–3482, DOI: 10.5194/gmd-9-3461-2016.

President of the Russian Federation, (2020a). Decree No. 164 of 05 Mar. 2020 on the Fundamentals of the State Policy of the Russian Federation in the Arctic until 2035. [online] Available at: http://www.kremlin.ru/acts/bank/45255 [Accessed 17 Apr. 2025].

President of the Russian Federation, (2020b). Decree No. 645 of 26 Oct. 2020 on the Strategy for the Development of the Arctic Zone of the Russian Federation and Ensuring National Security for the Period until 2035. [online] Available at: http://www.kremlin.ru/acts/bank/45972 [Accessed 17 Apr. 2025].

Romanenko F. A. and Shilovtseva O. A. (2016). Geomorphological processes in the mountains of the Kola Peninsula and climate change. Vestnik Moskovskogo Universiteta, Series 5: Geography, 6, 78–86, (In Russian).

Samset B. H., Zhou C., Fuglestvedt J. S., Lund M. T., Marotzke J. and Zelinka M. D. (2023). Steady global surface warming from 1973 to 2022, but an increased warming rate after 1990. Communications Earth & Environment, 4, 400, DOI: 10.1038/s43247-023-01061-4.

Semenov S. M. and Gladilshchikova A. A. (2022). Scenarios of anthropogenic changes in the climate system in the XXI century. Fundamental and Applied Climatology, 8(1), 75–106 (In Russian), DOI: 10.21513/2410-8758-2022-1-75-106.

Serykh I. V. and Tolstikov A. V. (2022). Climate change in the western part of the Russian Arctic in 1980–2021. Part 2. Soil temperature, snow, and humidity. Problems of Arctic and Antarctic Research, 68(4), DOI: 10.30758/0555-2648-2022-68-3-258-277.

Si Z., Li. S., Huang L. and Chen Y. (2010). Visualization programming for batch processing of contour maps based on VB and Surfer software. Advances in Engineering Software, 41(7–8), 962–965.

Smirnov A. Yu. (2025). Northern Sea Route: output and prospects. Arctic: Ecology and Economy, 15(1), 109–118, (In Russian), DOI: 10.25283/2223-4594-2025-1-109-118.

The International Institute for Applied Systems Analysis (IIASA) and Russian Academy of Sciences (RAS), (2002). Land Resources of Russia. [online] Available at: http://www.iiasa.ac.at/Research/FOR/russia_cd/download.htm [Accessed 3 Nov. 2022].

Third Assessment Report on Climate Change and Its Consequences on the Territory of the Russian Federation: General Summary. Roshydromet (2022). St. Petersburg: Science-Intensive Technologies. 124 p., (In Russian).

Tolstykh M. A. (2016). Global atmosphere models: current state and development plans. Proceedings of the Hydrometeorological Research Center of the Russian Federation, 359, 5–32, (In Russian).

Yakubovich A. N. and Yakubovich I. A. (2019). Forecasting the impact of climatic changes on the functionality of the transport infrastructure of the permafrost zone in Russia. Intellect. Innovation. Investments, 1, 104–110, (In Russian).

Yang C. S., Kao S. P., Lee F. B. and Hung P. S. (2004). Twelve different interpolation methods: A case study of Surfer 8.0. In Proceedings of the XXth ISPRS Congress, Vol. 35, pp. 778–785.

RESEARCH PAPER

SOIL EROSION VERSUS SOIL RETENTION CAPACITY: AN IMPACT ASSESSMENT OF REGULATING ECOSYSTEM SERVICE PROVISION IN IRAN

Kazem Nosrati[1,*], Maram Hassan[1], Alireza Salehipour Milani[1], Mostafa Keshtkar[2], Somaiyeh Khaleghi[1], Adrian L. Collins[3]

[1]Department of Physical Geography, Faculty of Earth Sciences, Shahid Beheshti University, 1983969411 Tehran, Iran
[2]Department of Planning and Designing the Environment, Environmental Science Research Institute, Shahid Beheshti University, Tehran, Iran
[3]Rothamsted Research, North Wyke, Okehampton, EX20 2SB, UK
***Corresponding author:** k_nosrati@sbu.ac.ir
Received: August 22nd 2024 / Accepted: November 12nd 2025 / Published: December 31st 2025
https://doi.org/10.24057/2071-9388-2025-3768

ABSTRACT. The objective of this study was to determine the impact of erosion on soil retention as an ecosystem service and its relationship with soil quality in a mountainous catchment in Iran. In this regard, 42 soil samples were collected from rangelands, rainfed, and irrigated farming areas. Thirteen physical and chemical soil attributes were measured. Principal component analysis was applied to identify a soil quality index (SQI). The respective ranges of soil erosion rates from rangelands, rainfed farming lands, and irrigated farming lands were estimated to be 0.2 – 46.4, 0.18 – 0.20, and 0.00 – 0.18 t ha^{-1} yr^{-1}. The SQI estimates ranged between 3.2 – 4.0 for the rangelands compared with corresponding estimates of 4.0 – 5.7 for the rainfed farming lands and 5.7 – 8.4 for the irrigated farming lands. Soil retention was estimated to range between 0 – 0.01 t ha^{-1} yr^{-1} (average = 0.005 t ha^{-1} yr^{-1}) for rangelands, 0.01 – 0.03 t ha^{-1} yr^{-1} (average = 0.02 t ha^{-1} yr^{-1}) for rainfed farmlands, and 0.03 – 3.5 t ha^{-1} yr^{-1} (average = 1.8 t ha^{-1} yr^{-1}) for irrigated farming lands. Negative relationships were observed among soil erosion, soil quality, and soil retention, emphasising the sensitivity of soil quality to the soil erosion rates estimated for different land use types. This study provides evidence for the negative effects of soil erosion under different land uses regarding the degradation of soil quality and soil retention as an ecosystem service.

KEYWORDS: Soil loss; soil quality index, soil degradation; soil retention

CITATION: Nosrati K., Hassan M., Milani A. S., Keshtkar M., Khaleghi S., Collins A. L. (2025). Soil Erosion Versus Soil Retention Capacity: An Impact Assessment Of Regulating Ecosystem Service Provision In Iran. Geography, Environment, Sustainability, 4 (18), 80-91
https://doi.org/10.24057/2071-9388-2025-3768

ACKNOWLEDGEMENTS: We acknowledge the support of Grant number 600.871 funded by the research council of Shahid Beheshti University, Tehran, Iran. The contribution to this work by ALC was funded by UKRI-BBSRC (UK Research and Innovation-Biotechnology and Biological Sciences Research Council) via grant award BB/X010961/1 (Resilient Farming Futures) – specifically work package 2 - BBS/E/RH/230004B; Detecting agroecosystem 'resilience' using novel data science methods.

Conflict of interests: The authors reported no potential conflict of interests.

INTRODUCTION

Increasing economic development and the resulting land use change have accelerated soil erosion. This is now documented as one of the most severe environmental challenges globally (Wijesundara et al., 2018). Importantly, soil is a non-renewable resource that requires improved management for sustainability given population growth (Lal, 2015). Soil erosion heavily impacts anthropogenically-modified ecosystems, including managed forests and croplands (Obidike-Ugwu et al., 2025). Accelerated erosion frequently causes other issues such as sealing, acidification, salinisation, alkalisation, diffuse pollution, and biodiversity decline (Ayoubi et al., 2014; Nabiollahi et al., 2018; Nosrati and Collins, 2019). Soil erosion is a major issue that adversely impacts environmental quality and food security, and it also reduces crop productivity (Rahmanipour et al., 2014). To mitigate the specific damages caused by soil erosion, such as decreased soil depth and organic matter, and soil compaction leading to reduced fertility and productivity, fertilisers and pesticides are used widely (Emadodin et al., 2012; Nosrati and Van Den Eeckhaut, 2012). These are used to sustain crop yield, but these applications harm human and environmental health (Amuah et al., 2024). Approximately 70% of Iran's drylands have exhibited signs of desertification, with croplands experiencing the highest risk (Eskandari Dameneh et al., 2021). The economic ramifications are significant, with the total cost of soil and water degradation, along with fertiliser use in agriculture, estimated at around US $12.8 billion. This is approximately 4% of Iran's total GDP and about 35% of the agricultural sector's GDP (Emadodin et al., 2012).

To quantify soil quality, it is necessary to measure the physical, chemical, and biological attributes that affect soil processes, functions, and services (Dominati et al., 2010; Dominati, 2013). The properties and various factors affecting soils must be evaluated to assess soil quality (Aziz et al., 2009), as soil quality is a fundamental basis for ecosystem functions. Soil quality can be described as the capacity of soil, under a particular land use or within a given ecosystem, to maintain fertility and environmental quality, and to enhance the health and diversity of plants, animals, and micro-organisms (Dilly et al., 2018; Karlen et al., 1997). Therefore, the physical, chemical, and biological properties and functions of soil are consistent in both soil-related ecosystem services, such as soil retention, and soil quality indicators (Aitkenhead and Coull, 2019; Black et al., 2010; Van Eekeren et al., 2010).

The soil ecosystem provides many services (Gómez-Baggethun et al., 2010). These benefits vary both spatially and temporally (Fisher et al., 2009). Soil ecosystem services are classified into four categories: provisioning services (e.g., provision of medicines, building materials, and nutrients), regulating services (e.g., water regulation, water quality control, erosion control and soil retention, greenhouse gas storage/retention), supporting services (e.g., nutrient cycling, water cycling, biodiversity), and cultural services (e.g., recreational activities, cultural heritage, aesthetic experience, spiritual enrichment) (Comerford et al., 2013; Paul et al., 2021). Among these services, the regulating category ensures environmental safety and sustainability (Bo-Jie et al., 2004). Soil erosion degrades regulating ecosystem services. As a result, controlling soil erosion can restore those specific soil-related ecosystem services (Steinhoff-Knopp et al., 2021).

Soil-related ecosystem services can be evaluated using the Integrated Valuation of Ecosystem Services and Tradeoffs (InVEST) tool for ecosystem services mapping (Mousazadeh et al., 2018). Within this tool, soil erosion is assessed using the universal soil loss equation (USLE) model (Zhang et al., 2019). Tools such as InVEST offer the opportunity to map soil retention in areas where such conceptual frameworks have not yet been applied, thereby providing critical new information for informing soil management. On this basis, the work reported in this paper applied InVEST to a study area in Iran. The Zar-Abad catchment is a mountainous case study area that has experienced progressive human development. It is characterised by steep slopes, different land use types, and lithology vulnerable to erosion. Collectively, these factors have resulted in accelerated soil erosion rates and subsequent sedimentation downstream. The objective of this study was to investigate the impact of soil erosion on soil retention as an indicator of soil ecosystem regulating services, and its relationship with soil quality in the Zar-Abad catchment, Iran. To this end, the study addressed the following research questions: (i) Do soil quality indices significantly differ across various land use types? (ii) What is the relationship between soil erosion, soil retention, and soil quality?

MATERIALS AND METHODS

Study area and data sources

Our study was conducted in the Zar-Abad catchment (36^0_46″ to 36^0_56″N and 50^0_32″ to 50^0_50″E). This area is part of the Alamout drainage basin, located in the southwest of the Alborz Mountains, 139 km northwest of Tehran, Iran (Fig. 1). The Zar-Abad catchment covers an area of 110 km^2 and includes rangelands, irrigated orchards, and rainfed farms. Rangelands make up the majority of the current land cover, accounting for 45%. Elevations range from 1000 m to over 3000 m. Slopes exceed 20% in 70% of the study area. The average annual rainfall between 2007 and 2018 was approximately 399 mm. Based on data from the Iranian Meteorological Organisation, the study area has a cold and mountainous climate. The mean daily temperatures from 2007 to 2018 were -8.1 °C in the coldest month and 35.5 °C in the warmest month.

Geologically, the study area is underlain by sandstone, red and green marl, basalt, salt, shale, tuff, and young terraces. The predominant geological formation consists of silt and sand combined with red and green marl.

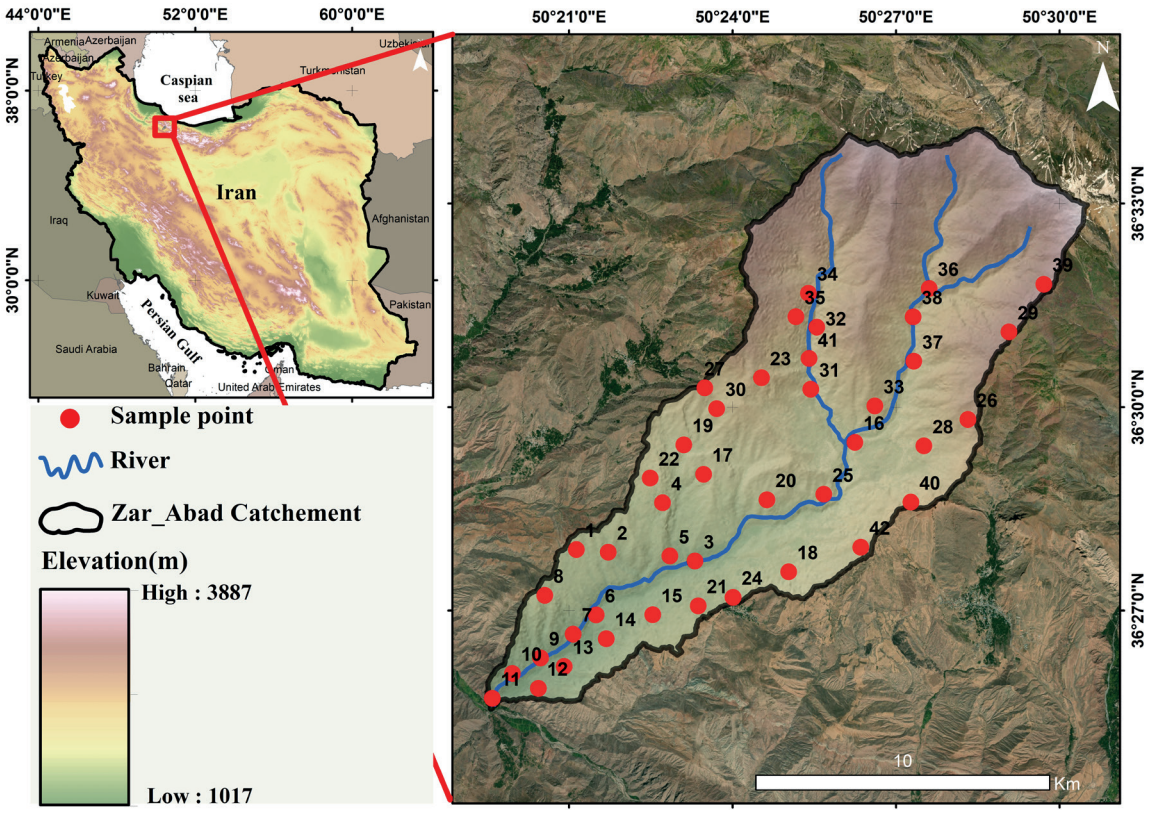

Fig. 1. The geographical location of the Zar-Abad study catchment, and soil sampling locations

The average annual rainfall and the monthly rainfall for the period 2007 to 2018 were used as meteorological data in this study. The land use map and land cover classification were extracted from Sentinel 2 image data with a 10 m spatial resolution. We also used a digital elevation model (DEM) with 12.5 m resolution taken from ALOS PALSAR images downloaded from the Vertex Alaska website (https://search.asf.alaska.edu/#/). Soil data were obtained from field sampling and laboratory analyses. Figure 2 shows the flowchart outlining the methodological steps and input data in this study.

A sampling approach was determined based on the geology and types of land use in the study area, resulting in a total of 42 soil samples being collected. These comprised 17 samples from rangelands, 15 from rainfed farming lands, and 10 from irrigated farming (orchards) lands. The samples were taken to a depth of 0-20 cm, bearing in mind that only the surface layers are at severe risk of erosion (Nosrati and Collins, 2019). Each soil sample weighed approximately 1 kg. Following field collection, all soil samples were dried and sieved using a 2 mm sieve. A set of soil physico-chemical attributes was analysed for each sample. These included absolute particulate size distribution (sand, silt, and clay), organic matter (OM) content, electrical conductivity (EC), pH, water holding capacity (WHC), saturation percentage (SP), available water content (AWC), bulk density (BD), particle density (PD), as well as carbonate calcium ($CaCO_3$), potassium (K), sodium (Na) and phosphorus (P) content. These were selected to represent critical soil quality indicators. More details on the specifics of the soil properties used in this study are presented in Table 1.

Estimation of soil erosion and soil retention

The InVEST model

The soil retention services in the InVEST software calculate the ecosystem's capacity for soil retention. This is done by considering the maximum potential soil loss and potential soil loss (Sharp et al., 2014) according to the following equations:

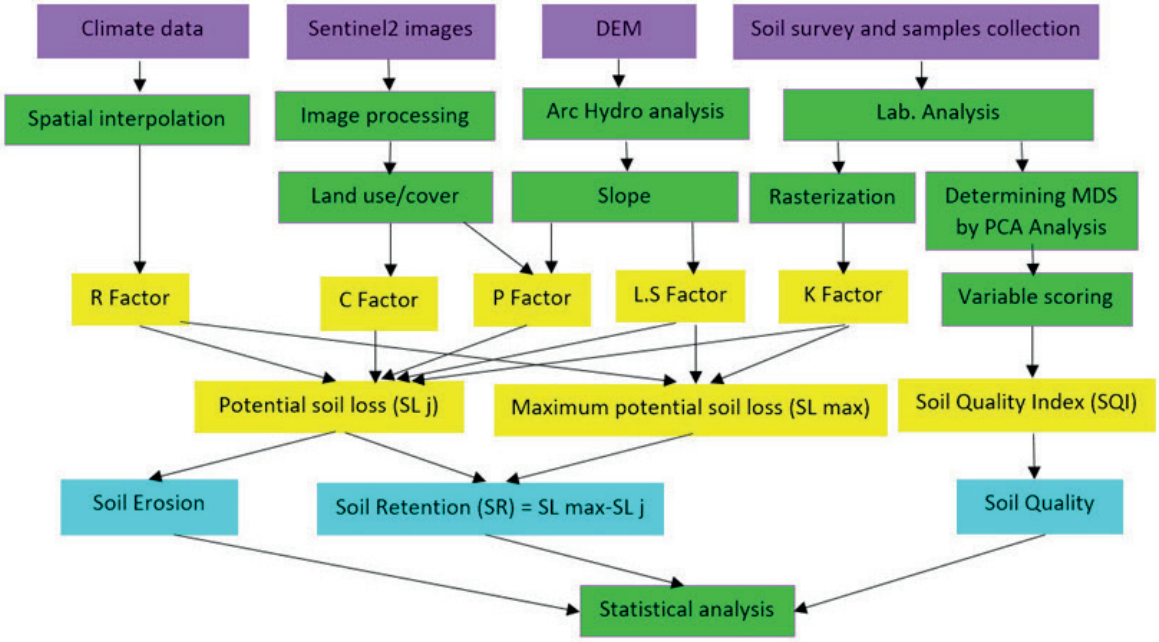

Fig. 2. Flowchart outlining the methodological steps and input data

Table 1. Descriptions of the soil parameters used in this study

Soil Factor	Unit	Method	References
Soil Texture (clay, silt, and sand)	%	Hydrometer method	Kroetsch and Wang (2008)
SP	%	Weight method	Carter and Gregorich (2007)
AWC	%	Pressure plate extractor	Carter and Gregorich (2007)
WHC	%	Pressure plate extractor	Carter and Gregorich (2007)
BD	$Mg\ m^{-3}$	Core method	Palmer et al. (2002)
PD	$Mg\ m^{-3}$	Pycnometer procedure	Blake and Hartge (1986)
EC	dsm^{-1}	Saturated soil _paste extract	Corwin and Lesch (2003)
pH		Saturated soil _paste extract	Robbins and Wiegand (1990);
OM	%	Walkley and Black	Walkley and Black (1934)
$CaCO_3$	%	Calcimetre method	Şenlikci et al. (2015)
K and Na	$mg\ kg^{-1}$	Flame photometric method	Helmke and Sparks (1996)
P	$mg\ kg^{-1}$	Spectrophotometer method	Gburek et al. (2000)

$$Soil\ retention\ (SR) = SLmax\,(R \times K \times L \times S) - SLj\,(USLE) \quad (1)$$

$$SLmax = R \times K \times LS \quad (2)$$

$$SLj = R \times K \times LS \times C \times P \quad (3)$$

where SLmax is the maximum potential soil loss regardless of the vegetation factor. SLj denotes the potential soil erosion that can be calculated from the universal soil loss equation (USLE). R, K, LS, C, and P are the rainfall erosivity, the soil erodibility, the slope-length and steepness, the crop management, and the conservation practice factors, respectively in the USLE model (Irvem et al., 2007; Wischmeier and Smith, 1978). The USLE factors are determined as described immediately below.

Rainfall erosivity factor (R)

The term rain erosion was proposed by Wischmeier (1978) to describe the effect of climate on soil erosion. Based on rainfall data for the Zar-Abad station, this study calculated R-values for the period 2007 to 2018 using average annual rainfall (Renison et al., 2010). Accordingly, the Fournie (F) Index (Eq. 4) was used with the average annual precipitation. Where the F-index was <55 mm, Equation 5 was applied, and where it exceeded 55 mm, Equation 6 was used (Renard et al., 2011).

$$R = \sum_{k=1}^{n12} \frac{pi^2}{p} \quad (4)$$

if: $$F < 55mm;\ R = \left(0.07397 \times F^{1.847}\right) \quad (5)$$

if: $$F \geq 55mm;\ R = \left(95.77 - 6.081 \times F + F + 0.477 \times F^2\right) \quad (6)$$

where: pi is the monthly rainfall (mm) and p represents the annual rainfall (mm).

Soil erodibility factor (K)

The soil erodibility factor (t ha h ha^{-1} MJ^{-1} mm^{-1}) measures how sensitive soil particles are to detachment and transport by rainfall and runoff (Sun et al., 2014). Based on soil texture, 24 samples (57% of the 42 samples) were clay textured, with texture being an important factor controlling erodibility (Jong, 1994). Wischmeier (1978) developed the following concept based on laboratory analyses (Eq. 7):

$$K = \left(\left(2.1 \times 10^{(-4)(12-a)} \times M^{(1.14)}\right) + (3.25(b-2)) + \frac{2.5(c-3)}{759}\right) \quad (7)$$

where M represents silt (%) + very fine sand (%) × (100 − clay (%)); a is OM content (%), and b is the soil structure code, where 1 = very fine granular [1–2 mm], 2 = fine granular [2–5 mm], 3 = medium or coarse granular [5–10 mm], and 4 = blocky, platy, or massive [>10 mm]. Finally, c represents the soil profile permeability, where 1 is high, 2 is moderate to high, 3 is moderate, 4 is moderate to slow, 5 is slow, and 6 is very slow.

Slope length and steepness factor (LS)

Slope length and steepness (LS) factors represent the impact of topography and morphology on the rate of soil erosion. As the slope increases, the cumulative runoff and the velocity of surface runoff also increase (Jong, 1994). Methods for calculating the L and S factors using GIS_SAGA can be found within the SAGA programme. This was used with our DEM for the study area.

The LS factor in the USLE shows the combined effect of slope length and slope steepness on soil erosion. Moore and Wilson (1992) provided a simplified method for calculating the LS factor, which is particularly useful for GIS-based calculations. This method focuses on the influence of slope length (L) and slope steepness (S) on soil erosion (Badora and Wawer, 2023). Both SAGA GIS and ArcGIS have tools for calculating the LS factor. They typically use DEMs as input and implement algorithms for flow direction and accumulation to determine slope length and steepness.

The LS factor is calculated using the following formula (Moore and Wilson, 1992):

$$LS = \left(\frac{Slope\ length}{22.1}\right)^{0.4} \times \left(\frac{\sin\theta \times 0.01745}{0.0896}\right) \times 1.4 \quad (8)$$

where Slope Length is Flow accumulation multiplied by Cell resolution (DEM), and θ is Slope in degrees. In this study, the LS factor was calculated using digital elevation models (DEMs) with 12.5 m resolution obtained from ALOS PALSAR images downloaded from the Vertex Alaska website (https://search.asf.alaska.edu/#/) to derive slope and flow path information in GIS_SAGA.

Crop management factor (C)

The crop management factor is one of the most sensitive spatial and temporal controls of soil erosion. It depends on variations in plant growth stages, vegetation types, and rainfall (Zhang et al., 2010). The C-factor quantifies the effect of vegetation cover and management on soil loss in USLE/RUSLE, ranging from approximately 0 (full protection) to 1 (bare soil) (Renard, 1997; Wischmeier, 1978). To map the C-factor, we used Sentinel-2 surface reflectance imagery. The Normalized Difference Vegetation Index (NDVI) was computed from the near-infrared (Band 8) and red (Band 4) using ENVI 5.3 software (Eq. 9), as follows:

$$NDVI = \frac{NIR - RED}{NIR + RED} \quad (9)$$

A cloud-free image acquired during the main erosive season of the study year was selected to represent protective ground cover when erosion risk is most relevant in RUSLE applications (Ayalew et al., 2020). We acknowledge that multi-date NDVI composites reduce temporal noise; however, the single-date approach is widely used when time-series stacks are unavailable (Ayalew et al., 2020).

NDVI values were then transformed to C using the exponential function proposed for continental-scale erosion mapping (Eq. 10).

$$C = exp\left(-\alpha \frac{NDVI}{\beta - NDVI}\right)^{\beta} \quad (10)$$

where α and β shape the NDVI–C curve. More specifically, Van Leeuwen and Sammons (2004) considered 2.5 and 1, which has been shown to provide robust results across diverse environments when using MODIS-NDVI data.

Conservation practice factor (P)

The P-factor represents the ratio of soil loss with a given conservation practice compared to that under conventional tillage up-and-down slope (Wischmeier and Smith, 1978). In this study, land use/land cover (LULC) classes were derived from Sentinel-2 MSI imagery using an object-based image analysis (OBIA) approach in eCognition Developer 64. OBIA allows for the segmentation and classification of homogeneous land parcels and reduces spectral confusion that often occurs in pixel-based classifications (Blaschke, 2010). The LULC map was validated with field surveys and high-resolution Google Earth images to ensure classification accuracy.

The slope gradient was obtained from the 12.5 m ALOS PALSAR DEM. The classified LULC and slope layers were spatially overlaid in a GIS environment. P-factor values were assigned to each LULC–slope combination following the guidelines of Wischmeier (1978) and updated values provided in subsequent studies (Kouli et al., 2009; Lufafa et al., 2003; Phinzi et al., 2021). This procedure allowed the parameterisation of the P-factor by integrating remote sensing data, topographic information, and empirical lookup tables. This provided a transparent and reproducible methodology.

Soil quality index

The application of the soil quality index approach has recently been expanded to quantify soil chemical, physical, and biological indicators that affect the soil's ability to function effectively. In the study reported herein, fifteen different factors affecting soil quality were measured. Our soil quality index (SQI) was calculated using the three steps described below:

(1) To identify the SQI, a small set of soil characteristics representing the so-called minimum data set (MDS) was selected (Fang et al., 2024; Garrigues et al., 2013). The MDS for SQI can be selected based on expert opinion (Andrews et al., 2004) or statistical analyses (Rojas et al., 2016). In our study, the MDS was selected using the load and eigenvalue obtained from principal component analysis (PCA). PCA is considered one of the most common (Doran and Parkin, 1994; Wang et al., 2021) and flexible methods for identifying the MDS for SQI (Juhos et al., 2016). Based on the PCA (Doran and Safley, 1997), the soil properties with the highest factor loading (absolute value) in each PC were shortlisted for the MDS (Andrews et al., 2004).

(2) Using expert opinion (Andrews and Carroll, 2001), the indicators in the MDS were normalised based on a standard scoring function: optimal is better, more is better, and less is better (Si in Equation 10). Therefore, all attributes were converted into a 0-1 range value. Two techniques can be used here: linear or non-linear scoring. In this study, linear scoring was used. For the 'more is better' approach, the values were ranked in rising order and each case divided by the highest observation. For the 'less is better' approach, the values were ranked in declining order, with the lowest value divided by each observation.

(3) For each property in the MDS, the ratio of explained variance for each principal component to the total variance explained by all principal components (total cumulative variance) (Wi in Equation 11) was calculated. On this basis, the SQI was calculated for each soil sample using Equation 11:

$$SQI = \sum_{i=1}^{n=i} Wi \times Si \times 10 \qquad (11)$$

where Wi and Si are the weights and scoring rank of the soil attribute selected for the MDS, respectively. Marzaioli et al. (2010) divided the SQI into three classes: low soil quality (SQI < 0.55), medium soil quality (0.55 < SQI < 0.70), and high soil quality (SQI > 0.70). The index value was multiplied by 10 to provide index values in a range of 1 to 10 rather than 0 to 1, as this has been found to be more understandable for producers and other users (Andrews et al., 2004).

Statistical analyses

To assess differences in the SQI across various land use types, a one-way analysis of variance (ANOVA) was conducted. Subsequently, Scheffé's post hoc test was employed to identify statistically homogeneous subsets among the land use categories (Landau and Everitt, 2003). The relationships among soil quality, soil erosion, and soil retention were examined using correlation analysis. All analyses were conducted using SPSS version 22.

RESULTS AND DISCUSSION

Soil erosion estimates based on the USLE

The average annual rainfall data were used to compute the average annual R factor values, which ranged from 616 to 2207 MJ mm ha^{-1} h^{-1} yr^{-1} (Fig. 3A). The results of the K factor indicated that soil erodibility ranged between 0.004 and 0.28 t ha h ha^{-1} MJ^{-1} mm^{-1}. Here, most areas have high erodibility in the upstream portions of the Zar-Abad catchment, whereas erodibility decreases downstream (Fig. 3B). The value of the LS factor ranged within 0–99%. In general, the increase in the length and slope percentage due to the resultant intensification of the velocity and strength of surface flow increased the amount of soil erosion per unit area (Fig. 3°C). The amount of vegetation varied between 0.1–0.6 (values closer to 1 indicate denser vegetation cover and vice versa) (Fig. 3D). The conservation practice values (P-factor; values between 0.1 and 1.0) were determined based on protective operations: a value of 0.1 for orchard farming lands with terraces and gabion check dams and 1.0 for lands without any soil protection operations (Fig. 3E). The results indicated that the rate of soil erosion ranged between 0 and 46.4 t ha^{-1} yr^{-1}. The respective ranges of the soil erosion rates for rangelands, rainfed farming lands, and irrigated farming lands (orchards) were estimated as 0.2–46.4, 0.18–0.2, and 0.0–0.18 t ha^{-1} yr^{-1}.

Soil retention

The potential soil loss and maximum potential soil loss were estimated to be in the ranges of 0 and 46.4 t ha^{-1} yr^{-1}, and 9.0 to 46.4 t ha^{-1} yr^{-1}, respectively (Fig. 4A). Therefore, the corresponding range for soil retention in the study area was 0 to 3.5 t ha^{-1} yr^{-1} (Fig. 4B). The estimates of soil retention for the rangelands, rainfed farming lands, and irrigated farming lands (orchards) ranged between 0–0.01 t ha^{-1} yr^{-1} (with a mean value of 0.005 t ha^{-1} yr^{-1}), 0.01–0.03 t ha^{-1} yr^{-1} (with a mean value of 0.02 t ha^{-1} yr^{-1}), and 0.03–3.5 t ha^{-1} yr^{-1} (with a mean value of 1.8 t ha^{-1} yr^{-1}).

Soil quality index (SQI)

Changes in soil quality can be estimated to evaluate the impacts of different land uses and their corresponding management practices (Arshad and Martin, 2002). Table 2 summarises the results of using PCA to determine the MDS. Five components were calculated to have an

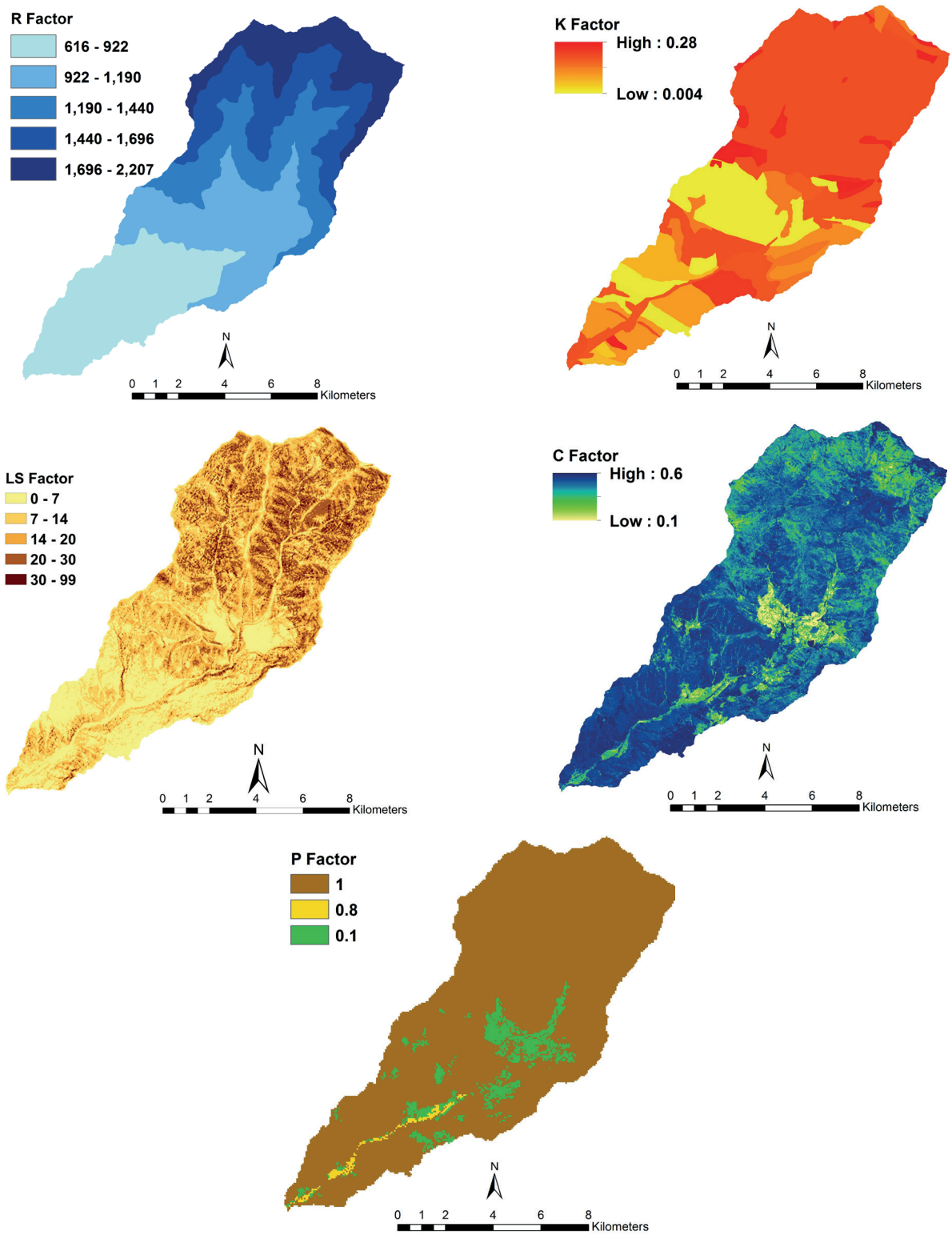

Fig. 3. Maps of the factors for soil erosion: rainfall erosivity factor (R) (MJ mm ha^{-1} h^{-1} yr^{-1}), soil erodibility factor (K) (t ha h ha^{-1} MJ^{-1} mm^{-1}), slope length and steepness factor (LS), D) crop management factor (C), and conservation practice factor (P)

eigenvalue >1 and can therefore be used in the MDS. The cumulative variance was 68.8%. Table 2 reports the results of the rotating components matrix, in which the loading coefficients of the factors were defined for each component. The highest PCs loadings were considered a condition for selecting the final MDS, which comprised OM, EC, P, sand content and K (Table 2).

A 'more is better' scoring approach was used for P, K, and OM (Andrews et al., 2004; Marzaioli et al., 2010; Rahmanipour et al., 2014). In contrast, a 'less is better' scoring function was employed for EC (Derakhshan-Babaei et al., 2021; Nabiollahi et al., 2018; Rahmanipour et al., 2014). The sand content followed an 'optimal r function (Davari et al., 2020; Derakhshan-Babaei et al., 2021; Rahmanipour et al., 2014). The final results indicated that sand content, EC, K, P, and OM had the highest to lowest weights, respectively (Eq. 12):

$$SQI = 0.35(S_{Sand}) - 0.24(S_{EC}) + 0.15(S_K) + 0.13(S_P) + 0.11(S_{OM}) \quad (12)$$

Using Equation 11, the soil quality index ranged between 3.15 and 8.40 (SQI values are in a range of 1 to 10), indicating that soil quality increased from the upstream to the downstream parts of the Zar-Abad catchment. This pattern

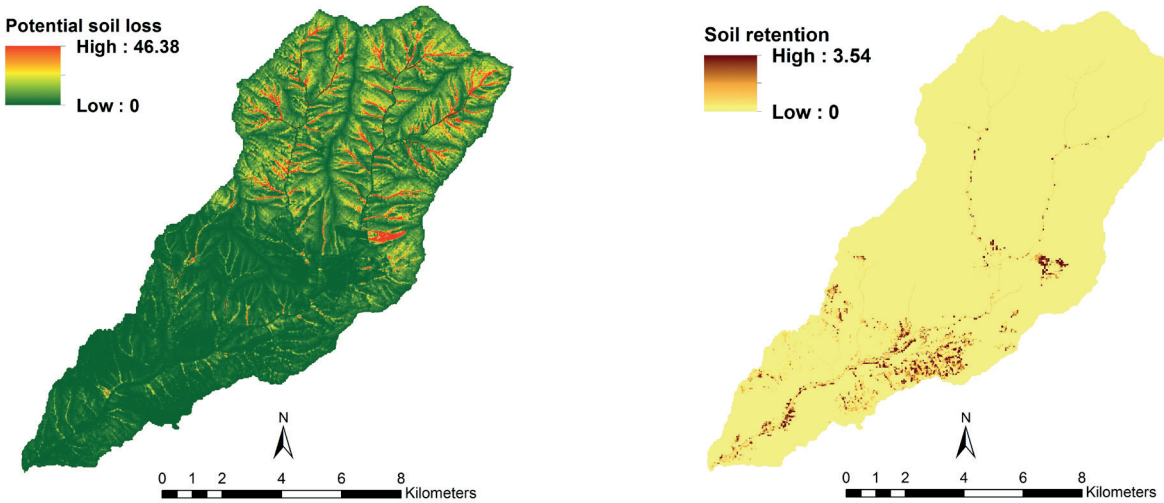

Fig. 4. A) Maps of potential soil loss (t ha^{-1} yr^{-1}) and B) soil retention (t ha^{-1} yr^{-1})

Table 2. The results of principal component analysis (PCA) in selecting the minimum data set (MDS)

Variables	PC1	PC2	PC3	PC4	PC5	Mean	Standard Deviation
Sand (%)	**.74**	-0.10	-0.56	-0.19	0.08	44.40	19.94
Silt (%)	-.28	0.35	0.59	-0.07	0.25	32.15	23.97
Clay (%)	-.73	-0.06	0.36	0.26	-0.22	23.44	10.57
SP (%)	-.07	-0.01	0.68	0.50	-0.24	32.72	14.73
AWC (%)	.02	0.21	-0.11	-0.66	-0.26	9.60	2.13
WHC (%)	.23	0.27	0.15	0.59	0.02	15.67	7.48
BD (Mg m^{-3})	.70	-0.11	-0.02	-0.15	-0.18	1.8	0.3
PD (Mg m^{-3})	0.08	-0.02	-0.02	-0.01	-0.16	2.10	0.45
EC (dS m^{-1})	-0.14	**0.86**	-0.22	0.16	0.13	0.67	0.19
pH	-0.08	0.80	0.08	-0.14	-0.21	7.72	0.26
OM (%)	0.15	0.50	-0.01	-0.20	**-0.57**	2.83	1.41
CaCO3 (%)	-0.70	0.41	0.03	-0.11	-0.04	9.97	6.46
K (g kg^{-1})	-0.08	-0.31	**-0.82**	-0.03	0.08	15.76	3.99
Na (g kg^{-1})	0.44	0.18	0.32	0.31	-0.36	19.19	4.14
P (g kg^{-1})	-0.25	-0.10	-0.08	**0.67**	-0.01	14.50	9.54
Eigenvalue	3.58	2.50	1.64	1.424	1.19		
% Total variance	23.85	16.65	10.91	9.50	7.93		
% Cumulative variance	23.85	40.50	51.41	60.91	68.84		

PC, principal component. The bold value corresponds to the selected attribute in each PC used to calculate the soil quality index (SQI).

reflects the different intrinsic conditions and management factors affecting soil erosion, and consequently soil quality and structure. The SQI ranged between 3.2 and 4.0 for the rangelands compared with corresponding estimates of 4.0 to 5.7 for the rainfed farming lands and 5.7 to 8.4 for the irrigated farming lands.

The relationship between soil erosion, soil retention, and soil quality is fundamental to understanding soil health. Soil erosion is the process by which the top layer of soil is removed by natural forces like wind and water. This removal can lead to a loss of valuable topsoil, which is rich in organic matter and nutrients. Soil retention, conversely, refers to the ability of the soil to stay in place, resisting erosive forces. Factors such as vegetation cover, soil structure, and topography play crucial roles in soil retention. When soil is eroded, the remaining soil often experiences a decline in its quality. This is because the most fertile and nutrient-rich components are typically lost first. Consequently, reduced soil quality can manifest as lower organic matter content, decreased water-holding capacity, and a deficiency in essential plant nutrients. This degradation makes the soil less suitable for agriculture and can negatively impact ecosystems. Conversely, effective soil retention helps to preserve soil quality. Maintaining a stable soil structure, with adequate vegetation and organic matter, enhances its resistance to erosion. Healthy soil, which is well-retained, supports robust plant growth, which in turn further improves soil structure and its ability to retain moisture and nutrients. Therefore, promoting soil retention is a key strategy for safeguarding soil quality and its long-term productivity.

The one-way ANOVA results confirmed that soil quality, as a dependent variable, showed differences across land use types, the independent variables, at the 0.05 confidence level. The significance level was 0.02. Pairwise comparisons from the post hoc test indicated that soil quality in irrigated farming and rangelands was significantly different at the 0.05 level. However, the pairwise comparison of irrigated farming and rainfed farming showed no significant difference (Table 3). There was also no significant difference between the SQI of rangelands and rainfed farming at the 0.05 level (Table 3). Figure 5 demonstrates that the SQI in irrigated farming was higher than in rainfed and rangeland areas, with the latter showing the lowest values.

The relationship between soil erosion, soil quality, and soil retention indicated that the rate of soil erosion decreased from the upstream to the downstream parts of the Zar-Abad study catchment (Fig. 6). This is because the upstream areas of the catchment are very susceptible to soil erosion. The main issues in this region are steep slopes, a lack of vegetation cover, and the erosive impact of rainfall, all of which degrade the chemical and physical components of the soil. Downstream areas in the study catchment experience less soil erosion due to more extensive vegetation cover (irrigated farming, orchards), gentler slopes, lower precipitation intensity, and consequently, lower surface runoff. Therefore, soil quality and soil retention improve from upstream to downstream (Fig. 6).

Table 4 presents the correlations between soil quality, soil retention, and soil erosion. Soil quality shows the strongest correlation with soil retention at the 0.01 confidence level. The relationship between soil quality and soil erosion is a strong negative correlation, as is the relationship between soil retention and soil erosion. Therefore, as soil quality and soil retention increase, the soil erosion rate decreases sharply (Table 4).

Overall, the results indicated that soil quality ranged between 3.15 and 8.40, with a decreasing trend from the downstream to the upstream portions of the study catchment. The estimated soil retention ranged between 0–3.54 and increased from the upstream to the downstream portions of the study catchment. This is due to the reduction in slope and rainfall, as well as increased vegetation density, associated with the transition from rangeland to orchards and rainfed land use types. In general, soil retention and soil quality exhibit the same pattern, in contrast to the pattern of soil erosion (Fig. 6).

The estimated erosion rates in this case study, when compared to soil erosion rates estimated for other catchments in Iran, suggest that our findings are reasonable for the study area. For example, the annual soil erosion in most drainage basins in Iran was estimated to be between 7.5 and 25 t ha-1 yr-1 using empirical methods by Jalalian et al. (1994). Afshar et al. (2010), using the 137Cs method, estimated the gross erosion rate and net soil deposition in western Iran to be 29.8 t ha^{-1} yr^{-1} and 21.8 t ha^{-1} yr^{-1}, respectively. Studies have shown that the Zar-Abad catchment experiences high soil loss when compared to some studies globally and within Iran. According to Wuepper et al. (2020), the global average soil erosion rate is 2.4 t ha^{-1} yr^{-1}. However, rates can vary from less than 1 t ha^{-1} yr^{-1} in some regions to over 20 t ha^{-1} yr^{-1} in others. The spatial distribution of soil erosion in the Zar-Abad catchment, located in the southern Alborz mountains, showed high soil erosion, particularly in rangelands and on steep slopes. Therefore, the steep slopes of the Alborz rangelands have a high potential for soil erosion. This aligns with studies such as that by Doulabian et al. (2021), who noted that the highest soil erosion is expected in the western and northern regions of Iran. Similarly, Mohammadi et al. (2021) stated that the average annual soil erosion in Iran is 16.5 t ha^{-1}, with the highest soil loss values occurring in the north, west, and southwest parts of Iran, and on the steep slopes of the Alborz and Zagros mountains. Ebrahimi et al. (2021) explained that annual soil

Table 3. Results of the one-way ANOVA using the post hoc Scheffe test comparing the SQI between different land uses

Land use (i)	Land use (j)	p- value
Irrigated farming	Rangeland	0.02*
	Rainfed farming	0.43
Rangeland	Rainfed farming	0.31

* The p-value is statistically significant (F = 4.7, p = 0.02).

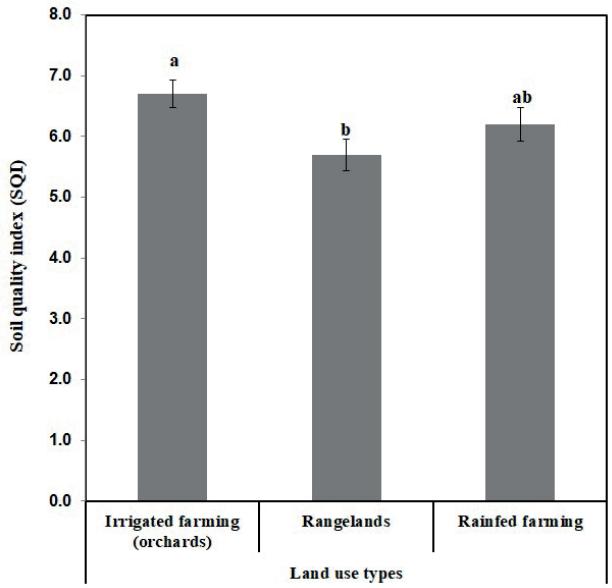

Fig. 5. The SQI values calculated for different land uses in the study area. Error bars represent standard errors. Letters (a, b, c) above the bars indicate statistically significant differences between groups

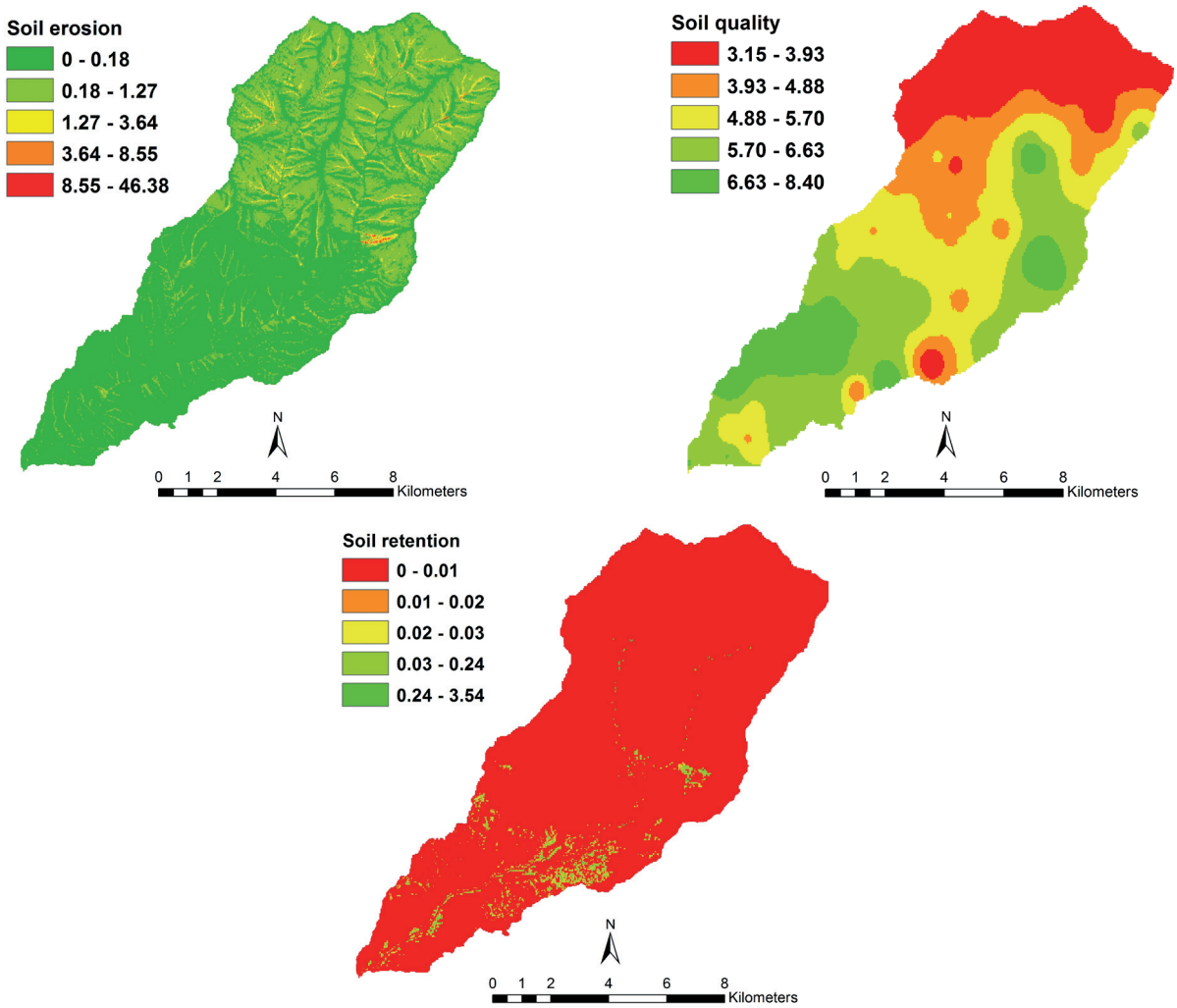

Fig. 5. Maps of average soil erosion (t ha^{-1} yr^{-1}), average soil quality, and average soil retention (t ha^{-1} yr^{-1}) in the study area

Table 4. Correlation between soil quality (SQ), soil retention (SR), and soil erosion (SE)

Index	SQ	SR	SE
SQ	1		
SR	0.86**	1	
SE	-0.45**	-0.35*	1

** $p < 0.01$, *$p < 0.05$

loss from hillsides and terraces (up to 55 t ha^{-1} year^{-1}) is greater than that from plain lowlands (up to 3 t ha^{-1} year^{-1}) in northeastern Iran.

Soil erosion decreases from the upstream to downstream sections of the Zar-Abad catchment. The upstream areas of the study catchment are very sensitive to soil erosion due to steep slopes, high rainfall erosivity, high soil erodibility, and low vegetation cover. Downstream areas of the study catchment experience less soil erosion due to improved vegetation cover (irrigated farming) and less steep slopes. Currently, rangelands make up the dominant land use in the upstream parts of the study catchment, which show the highest rates of soil erosion on steep slopes and in areas without vegetation cover. These results are similar to the findings of Derakhshan-Babaei et al. (2021) in the Kan catchment, north of Tehran, Iran. In that study, erosion rates were high in the upstream regions with steep slopes and scarce vegetation. Furthermore, erosion rates in rangelands were higher than those estimated for rainfed and irrigated (orchard) farming lands. Rangelands with poor vegetation cover experience increased erosion rates, while orchards with more vegetation and more organic matter (organic manures are added to the soils) exhibit lower erosion rates. According to Guerra et al. (2016), vegetation cover can regulate soil loss. In the upstream sections of the study area, rainfall quickly turns into surface runoff due to steep gradients, which reduce infiltration. The erosive energy of the resulting flows is increased by the lack of surface cover.

Soil quality in the study area improved from the upstream to the downstream parts of the catchment. This is because, in addition to the soil's physical and chemical properties, the upstream area has a steep slope and ridge topography, whereas the downstream portion has gentler slopes and valley formations. A similar pattern was reported by Derakhshan-Babaei et al. (2021). Further downstream in the Zar-Abad catchment, rainfed and irrigated farming (orchards) are dominant, and here, soil quality is higher. Similar results have been reported by Rahmanipour et al. (2014) and Fang et al. (2024). Furthermore, Ma et al. (2024) demonstrated that cultivation and soil erosion play a significant role in the degradation of soil quality.

Soil quality differed across the three land use types: irrigated farming lands, rangeland, and rainfed farming lands. Soil quality was statistically significantly different between irrigated farming and rangelands. However, there was no significant difference between irrigated and rainfed farming lands. Davari et al. (2020) previously reported that soil quality differs between irrigated farming and dry farmlands. In our study area, soil quality in irrigated farming is higher than in rainfed and rangeland areas, and the former areas have better soil quality than the latter. Higher soil quality in orchards and irrigated farming likely reflects various factors, including crop residues and the addition of inorganic or organic fertilisers. This result contrasts with Nabiollahi et al. (2018), who reported high soil quality in rangelands of western Iran compared to croplands due to various controls on soil erodibility, such as lithology, relief, and vegetation cover.

The soil retention service increased from the upstream to the downstream portion of the study catchment. This area has lower rainfall erosivity, lower soil erodibility, and less steep slopes. Less steep slopes and improved vegetation cover in the downstream areas encourage higher infiltration, thus reducing runoff and erosion. Xiao et al. (2017) previously reported that high vegetation cover is associated with high soil conservation values. The SQI exhibited a strong correlation with soil retention. Soil quality and soil retention exhibited strong negative correlations with soil erosion. Over time, the relationships between soil attributes pertaining to soil quality indicators and regulating services have attracted increasing attention. For example, Van Eekeren et al. (2010) reported a significant relationship between soil physical and biological attributes and the provision of ecosystem services. Black et al. (2010) reported the important role of soil carbon in the delivery of ecosystem services by soils.

Due to erosion, soil nutrients, organic matter, and microorganisms are mobilised and, depending on the hillslope gradient, are deposited on the foot slope or toe slope. This typically improves soil quality in low-altitude land, although it depends on the sediment delivery ratio of the catchment in question. Our work herein did not consider the potential control exerted by the sediment delivery ratio. In addition, where resources permit, soil quality should be investigated for discrete soil horizons by sampling soil at different depths, as erosion and weathering processes can affect the soil properties associated with soil quality (Nosrati and Collins, 2019).

A methodological limitation of our study relates to the use of NDVI for parameterising the C-factor in RUSLE. While NDVI is one of the most widely applied proxies of vegetation cover due to its simplicity and accessibility from multispectral imagery, it is not without shortcomings. Panagos et al. (2015) explicitly noted that NDVI was not adopted in their European-scale soil erosion assessment because of its relatively weak correlation with vegetation attributes. This was partly caused by soil background reflectance and variations in vegetation vitality (de Asis and Omasa, 2007; Vrieling, 2006). These issues may introduce uncertainty in C-factor estimation, particularly in sparsely vegetated or heterogeneous landscapes. Nevertheless, despite these limitations, NDVI-based approaches remain commonly used in RUSLE applications (e.g., Ayalew et al., 2020). This is because they provide spatially explicit estimates of vegetation cover, which are often the only practical option in data-scarce environments. Future studies could benefit from integrating multi-date imagery, soil-adjusted vegetation indices (e.g., SAVI) or field-based measurements to improve the reliability of C-factor estimates.

CONCLUSION

In this study, the (SQI) was applied to represent the effect of soil erosion on soil retention as a regulating ecosystem service. A strong negative correlation was observed between soil erosion, SQI, and soil retention. These results demonstrate that establishing appropriate management systems in an area exposed to soil erosion can contribute to a reduction in soil erosion, the maintenance of soil quality, and an increase in soil retention. Importantly, not all of these responses will occur quickly. This means that soil loss and associated reductions in regulating services pose a serious threat to soil regeneration, global food security, and human survival. Further research into, development of, and validation of SQIs are required to identify and quantify the impact of soil erosion on various essential ecosystem services.

REFERENCES

Afshar F.A., Ayoubi S. and Jalalian A. (2010). Soil redistribution rate and its relationship with soil organic carbon and total nitrogen using 137Cs technique in a cultivated complex hillslope in western Iran. Journal of Environmental Radioactivity, 101, pp.606-614.

Aitkenhead M.J. and Coull M.C. (2019). Digital mapping of soil ecosystem services in Scotland using neural networks and relationship modelling. Part 2: Mapping of soil ecosystem services Soil Use and Management, 35, 217-231.

Amuah E.E.Y., Fei-Baffoe B., Kazapoe R.W., Dankwa P., Okyere I.K., Sackey L.N.A., Nang D.B. and Kpiebaya P. (2024). From the ground up: Unveiling Ghana's soil quality crisis and its ecological and health implications. Innovation and Green Development, 3, 100097.

Andrews S.S. and Carroll C.R. (2001). Designing a soil quality assessment tool for sustainable agroecosystem management. Ecological Applications, 11, pp.1573-1585.

Andrews S.S., Karlen D.L. and Cambardella C.A. (2004). The soil management assessment framework: A quantitative soil quality evaluation method. Soil Science Society of America Journal, 68, pp.1945-1962.

Arshad M.A. and Martin S. (2002). Identifying critical limits for soil quality indicators in agro-ecosystems. Agriculture, Ecosystems & Environment, 88, pp.153-160.

Ayoubi S., Emami N., Ghaffari N., Honarjoo N. and Sahrawat K.L. (2014). Pasture degradation effects on soil quality indicators at different hillslope positions in a semiarid region of western Iran. Environmental Earth Sciences, 71, pp.375-381.

Aziz I., Mahmood T., Raut Y., Lewis W., Islam R. and Weil R. (2009). Active organic matter as a simple measure of field soil quality. ASA International Meetings, Pittsburg, PA.

Black H.J., Glenk K., Lilly A., Artz R., Watson C., Colombo S., Brown I. and Towers W. (2010). What are the opportunities for enhancing ecosystem services from soils through management of soil carbon? In: Gilkes R.J. and Prakongkep N. (eds), Proceedings of the 19th world congress of soil science: Soil solutions for a changing world. International Union of Soil Sciences (Brisbane, Australia, 1–6 August 2010).

Blake G. and Hartge K. (1986). Particle density Methods of soil analysis: Part 1 physical and mineralogical methods, 5, 377-382.

Bo-Jie F., Shi-Liang L., Li-Ding C., Yi-He L. and Jun Q. (2004). Soil quality regime in relation to land cover and slope position across a highly modified slope landscape. Ecological Research, 19, pp.111-118.

Carter M.R. and Gregorich E.G. (2007). Soil Sampling and Methods of Analysis. CRC press,

Comerford N.B., Franzluebbers A.J., Stromberger M.E., Morris L., Markewitz D. and Moore R. (2013). Assessment and evaluation of soil ecosystem services. Soil Horizons, 54(3), pp.1-14.

Corwin D. and Lesch S. (2003). Application of soil electrical conductivity to precision agriculture: theory, principles, and guidelines. Agronomy Journal, 95, pp.455-471.

Davari M., Gholami L., Nabiollahi K., Homaee M. and Jafari H.J. (2020). Deforestation and cultivation of sparse forest impacts on soil quality (case study: West Iran, Baneh). Soil and Tillage Research, 198, 104504.

Derakhshan-Babaei F., Nosrati K., Mirghaed F.A. and Egli M. (2021). The interrelation between landform, land-use, erosion and soil quality in the Kan catchment of the Tehran province, central Iran CATENA, 204, 105412.

Dilly O., Pompili L. and Benedetti A. (2018). Soil micro-biological indicators separated land use practices in contrast to abiotic soil properties at the 50 km scale under summer warm Mediterranean climate in northern Italy. Ecological Indicators, 84, pp.298-303.

Dominati E., Patterson M. and Mackay A. (2010). A framework for classifying and quantifying the natural capital and ecosystem services of soils. Ecological Economics, 69, pp.1858-1868.

Dominati E.J. (2013). Natural capital and ecosystem services of soils. In: Dymond J.R. (ed), Ecosystem Services in New Zealand: Conditions and trends. Manaaki Whenua Press (Lincoln, New Zealand), pp.132-142.

Doran J. and Safley M. (1997). Defining and assessing soil health and sustainable productivity. in: C. Pankhurst, B.M.D.V.V.S.R.G. (Ed.). Biological Indicators of Soil Health, Wallingford CAB INTERNATIONAL pp.1-28.

Doran J.W. and Parkin T.B. (1994). Defining and assessing soil quality. In: J.W. Doran, D.C. Coleman, D.F. Bezdicek and B.A. Stewart, Defining Soil Quality for a Sustainable Environment. s:SSSA Special Publications, pp. 1-21. DOI: https://doi.org/10.2136/sssaspecpub35.c1.

Emadodin I., Narita D. and Bork H.R. (2012). Soil degradation and agricultural sustainability: an overview from Iran. Environment, Development and Sustainability, 14, pp.611-625.

Eskandari Dameneh H., Gholami H., Telfer M.W., Comino J.R., Collins A.L. and Jansen J.D. (2021). Desertification of Iran in the early twenty-first century: assessment using climate and vegetation indices. Scientific Reports, 11, 20548.

Fang H., Zhai Y. and Li C. (2024). Evaluating the impact of soil erosion on soil quality in an agricultural land, northeastern China. Scientific Reports, 14, 15629.

Fisher B., Turner R.K. and Morling P. (2009). Defining and classifying ecosystem services for decision making. Ecological Economics, 68, pp.643-653.

Garrigues E., Corson M.S., Angers D.A., van der Werf H.M. and Walter C. (2013). Development of a soil compaction indicator in life cycle assessment. The International Journal of Life Cycle Assessment, 18, pp.1316-1324.

Gburek W.J., Sharpley A.N., Heathwaite L. and Folmar G.J. (2000). Phosphorus management at the watershed scale: A modification of the phosphorus index. Journal of Environmental Quality, 29, pp.130-144.

Gómez-Baggethun E., de Groot R., Lomas P.L. and Montes C. (2010). The history of ecosystem services in economic theory and practice: From early notions to markets and payment schemes. Ecological Economics, 69, pp.1209-1218.

Guerra C.A., Maes J., Geijzendorffer I. and Metzger M.J. (2016). An assessment of soil erosion prevention by vegetation in Mediterranean Europe: Current trends of ecosystem service provision. Ecological Indicators, 60, pp.213-222.

Helmke P.A. and Sparks D.L. (1996). Lithium, sodium, potassium, rubidium, and cesium Methods of soil analysis: Part 3 chemical methods, 5, pp.551-574.

Irvem A., Topaloğlu F. and Uygur V. (2007). Estimating spatial distribution of soil loss over Seyhan River Basin in Turkey. Journal of Hydrology, 336, pp.30-37.

Jalalian A., Ghahareh M. and Karimzadeh H. (1994). Erosion and sediment in some drainage basin of Iran. 4th Iranian Soil sciences Congress, Isfahan, 9-15.

Jong S.M.d. (1994). Applications of reflective remote sensing for land degradation studies in a Mediterranean environment. Nederlandse geografische studies, 177.

Juhos K., Szabó S. and Ladányi M. (2016). Explore the influence of soil quality on crop yield using statistically-derived pedological indicators. Ecological Indicators, 63, pp.366-373.

Karlen D.L., Mausbach M., Doran J.W., Cline R., Harris R. and Schuman G. (1997). Soil quality: a concept, definition, and framework for evaluation. Soil Science Society of America Journal, 61, pp.4-10.

Kroetsch D. and Wang C. (2008). Particle size distribution. In: M.R. Carter E.G. Gregorich, Soil Sampling and Methods of Analysis, pp. 713-725.

Lal R. (2015). Restoring soil quality to mitigate soil degradation. Sustainability, 7, pp.5875-5895.

Landau S. and Everitt B.S. (2003). A handbook of Statistical Analyses Using SPSS. Chapman and Hall/CRC,

Lufafa A., Tenywa M., Isabirye M., Majaliwa M. and Woomer P. (2003). Prediction of soil erosion in a Lake Victoria basin catchment using a GIS-based Universal Soil Loss model. Agricultural Systems, 76, pp.883-894.

Ma R., Tian Z., Zhao Y., Wu Y. and Liang Y. (2024). Response of soil quality degradation to cultivation and soil erosion: A case study in a Mollisol region of Northeast China. Soil and Tillage Research, 242, 106159.

Marzaioli R., d'Ascoli R., De Pascale R. and Rutigliano F. (2010). Soil quality in a Mediterranean area of Southern Italy as related to different land use types. Applied Soil Ecology, 44, pp.205-212.

Mousazadeh R., Badamfirooz J. and Rahmati A. (2018). Scenario modelling to predict future changes in land cover and/or land use, using InVEST software (case study: Dohezar and Sehezar forested landscape). Environmental Sciences, 16, pp.111-132.

Nabiollahi K., Golmohamadi F., Taghizadeh-Mehrjardi R., Kerry R. and Davari M. (2018). Assessing the effects of slope gradient and land use change on soil quality degradation through digital mapping of soil quality indices and soil loss rate. Geoderma, 318, pp.16-28.

Nosrati K. and Collins A.L. (2019) A soil quality index for evaluation of degradation under land use and soil erosion categories in a small mountainous catchment, Iran. Journal of Mountain Science, 16, pp.2577-2590.

Nosrati K. and Van Den Eeckhaut M. (2012). Assessment of groundwater quality using multivariate statistical techniques in Hashtgerd Plain, Iran. Environmental Earth Sciences, 65, pp.331-344.

Obidike-Ugwu E.O., Bege B., Ariwaodo J.O. and Nwafor O.E. (2025). Land-use changes and management impact on soil quality indicators in tropical ecosystem. Environment, Development and Sustainability, 27, pp.3513-3527.

Palmer C., Smith W. and Conkling B. (2002). Development of a protocol for monitoring status and trends in forest soil carbon at a national level. Environmental Pollution, 116, pp.S209-S219.

Paul C., Kuhn K., Steinhoff-Knopp B., Weißhuhn P. and Helming K. (2021). Towards a standardization of soil-related ecosystem service assessments. European Journal of Soil Science, 72, pp.1543-1558.

Phinzi K., Ngetar N.S. and Ebhuoma O. (2021). Soil erosion risk assessment in the Umzintlava catchment (T32E), Eastern Cape, South Africa, using RUSLE and random forest algorithm. South African Geographical Journal, 103, pp.139-162.

Rahmanipour F., Marzaioli R., Bahrami H.A., Fereidouni Z. and Bandarabadi S.R. (2014). Assessment of soil quality indices in agricultural lands of Qazvin Province, Iran. Ecological Indicators, 40, pp.19-26.

Renard K., Yoder D., Lightle D. and Dabney S. (2011). Universal Soil Loss Equation and Revised Universal Soil Loss Equation Handbook of erosion modelling, 137.

Renison D., Hensen I., Suarez R., Cingolani A.M., Marcora P. and Giorgis M.A. (2010). Soil conservation in Polylepis mountain forests of Central Argentina: is livestock reducing our natural capital? Austral Ecology, 35, pp.435-443.

Robbins C. and Wiegand C. (1990). Field and Laboratory Measurements. ASCE Manual and Reports.

Rojas J.M., Prause J., Sanzano G.A., Arce O.E.A. and Sanchez M.C. (2016). Soil quality indicators selection by mixed models and multivariate techniques in deforested areas for agricultural use in NW of Chaco, Argentina. Soil and Tillage Research, 155, pp.250-262.

Şenlikci A., Doğu M., Eren E., Çetinkaya E. and Karadağ S. (2015). Pressure calcimeter as a simple method for measuring the CaCO3 content of soil and comparison with Scheibler calcimeter Toprak Su Dergisi.

Sharp R., Tallis H., Ricketts T., Guerry A., Wood S.A., Chaplin-Kramer R., Nelson E., Ennaanay D., Wolny S. and Olwero N. (2014). InVEST user's guide The Natural Capital Project, Stanford.

Steinhoff-Knopp B., Kuhn T.K. and Burkhard B. (2021). The impact of soil erosion on soil-related ecosystem services: development and testing a scenario-based assessment approach Environmental Monitoring and Assessment, 193, pp.1-18.

Sun W., Shao Q., Liu J. and Zhai J. (2014). Assessing the effects of land use and topography on soil erosion on the Loess Plateau in China. Catena, 121, pp.151-163.

Van Eekeren N., De Boer H., Hanegraaf M., Bokhorst J., Nierop D., Bloem J., Schouten T., De Goede R. and Brussaard L. (2010). Ecosystem services in grassland associated with biotic and abiotic soil parameters. Soil Biology and Biochemistry, 42, pp.1491-1504.

Van Leeuwen W.J. and Sammons G. (2004). Vegetation dynamics and erosion modeling using remotely sensed data (MODIS) and GIS. USDA Forest Service Tenth Biennial Remote Sensing Applications Conference, 5-9 April.

Walkley A. and Black I.A. (1934). An examination of the Degtjareff method for determining soil organic matter and a proposed modification of the chromic acid titration method. Soil Science, 37, 29-38.

Wang P., Nair M.S., Liu L., Iketani S., Luo Y., Guo Y., Wang M., Yu J., Zhang B. and Kwong P.D. (2021). Antibody resistance of SARS-CoV-2 variants B. 1.351 and B. 1.1. 7. Nature, 593, 1pp.30-135.

Wijesundara N., Abeysingha N. and Dissanayake D. (2018). GIS-based soil loss estimation using RUSLE model: A case of Kirindi Oya river basin, Sri Lanka. Modeling Earth Systems and Environment, 4, pp.251-262.

Wischmeier W.H. (1978). Predicting rainfall erosion losses: a guide to conversation planning USDA Agr. Handbook.

Wischmeier W.H. and Smith D.D. (1978). Predicting rainfall erosion losses: a guide to conservation planning. Department of Agriculture, Science and Education Administration.

Xiao Q., Hu D. and Xiao Y. (2017). Assessing changes in soil conservation ecosystem services and causal factors in the Three Gorges Reservoir region of China. Journal of Cleaner Production, 163, pp.S172-S180.

Zhang K., Yu Y., Dong J., Yang Q. and Xu X. (2019). Adapting & testing use of USLE K factor for agricultural soils in China. Agriculture, Ecosystems & Environment, 269, pp.148-155.

Zhang Y.-G., Nearing M., Zhang X.-C., Xie Y. and Wei H. (2010). Projected rainfall erosivity changes under climate change from multimodel and multiscenario projections in Northeast China. Journal of Hydrology, 384, pp.97-106.

RESEARCH PAPER

ENVIRONMENTAL CONTROLS OF PHOTOSYNTHETIC PARAMETERS IN FOUR DOMINANT BOREAL TREE SPECIES: CONTRASTING RESPONSES OF DECIDUOUS ANGIOSPERMS AND EVERGREEN GYMNOSPERMS

Vladislava B. Pridacha[1,*], Alexander V. Olchev[2]

[1]Forest Research Institute, Karelian Research Centre, Russian Academy of Sciences, Pushkinskaya St.,11, Petrozavodsk, 185910, Russia

[2]Faculty of Geography, Lomonosov Moscow State University, GSP-1, Leninskie Gory, Moscow, 119991, Russia

***Corresponding author:** pridacha@krc.karelia.ru

Received: September 28th 2025 / Accepted: November 12nd 2025 / Published: December 31st 2025

https://doi.org/10.24057/2071-9388-2025-4190

ABSTRACT. Boreal forests play a crucial role in maintaining the global ecological balance, acting as significant carbon sinks and mitigating the effects of climate change. This study examined how temperature affects photosynthesis in four boreal tree species – *Pinus sylvestris, Betula pendula, Populus tremula,* and *Alnus incana* – growing in a clear-cut of mid-taiga bilberry-type pine forest in southern Karelia, Russia. The Farquhar biochemical model was used to analyze key photosynthesis parameters, such as the maximum carboxylation rate by Rubisco (Vc_{max}), the maximum photosynthetic electron transport rate (J_{max}), and the triose phosphate utilization (*TPU*) rate, under different leaf temperatures ranging from 20 to 35°C and light conditions. The results revealed significant interspecific differences in photosynthetic responses. At a leaf surface temperature of 25°C, the lowest Vc_{max25}, J_{max25}, and TPU_{25} values were obtained for the 1-year-old needles of *P. sylvestris* (38.8, 70.7, and 5.5 μmol m^{-2} s^{-1}), whereas the values were 1.5- to 2.4-fold higher for the leaves of *B. pendula* (93.5, 172.1, and 12.7 μmol m^{-2} s^{-1}), *A. incana* (86.1, 155.1, and 11.4 μmol m^{-2} s^{-1}), and *P. tremula* (58.6, 122, and 9.3 μmol m^{-2} s^{-1}). Meanwhile, *P. sylvestris* and *B. pendula* had a broader optimal temperature range for Vc_{max} and J_{max} (20–35°C), whereas *A. incana* and *P. tremula* had a narrower range (20–30°C), experiencing a decline at 35°C. In addition to having different levels of resistance to extreme temperatures, deciduous species also differed in their responsiveness to CO_2 enrichment. This could lead to shifts in the composition of boreal forest species under changing climate conditions. *P. sylvestris* demonstrated greater stability at low light levels and a strong response to elevated CO_2, indicating its high adaptability to future climate change. These results highlight the importance of considering species characteristics when predicting the carbon balance of boreal forests. They can be used to model the resilience of forest ecosystems under climate change and to plan further investigations, including studies of mature trees and the effects of additional stress factors, such as drought.

KEYWORDS: boreal forests; photosynthetic CO_2 response curve; photosynthetic light response curve; temperature dependence; climate change

CITATION: Pridacha V. B., Olchev A. V. (2025). Environmental Controls Of Photosynthetic Parameters In Four Dominant Boreal Tree Species: Contrasting Responses Of Deciduous Angiosperms And Evergreen Gymnosperms. Geography, Environment, Sustainability, 4 (18), 92-102

https://doi.org/10.24057/2071-9388-2025-4190

ACKNOWLEDGEMENTS: The study was funded from the federal budget within state assignment to the Karelian Research Centre, Russian Academy of Sciences (Forest Research Institute KarRC RAS, reg. no.121061500082-2).

Conflict of interests: The authors reported no potential conflict of interests.

INTRODUCTION

Boreal forests play a crucial role in maintaining the Earth's ecological balance. As long-term carbon sinks, they mitigate the effects of climate change by reducing the concentration of greenhouse gases in the atmosphere. They also regulate the balance of water and heat, directly influencing regional and global climates (Bonan, 2008; IPCC, 2023; Gushchina et al., 2023; Olchev, 2025). Meanwhile, the current climate, characterized by rising global temperatures, changing precipitation patterns and higher frequency of regional hydrological and meteorological anomalies (Mokhov, 2022), increases the risk of irreversible alteration in the structure and functions of forest ecosystems (Olchev et al., 2013; Groisman et al., 2017). Changes in the growth, productivity, and mortality of boreal tree species can affect taiga forests' ability to absorb carbon dioxide (CO_2) from the atmosphere. It is crucial to understand and predict the consequences of climate change for deciduous and coniferous tree species because their capacity to absorb CO_2 through photosynthesis directly impacts the global carbon cycle and the overall state of forest ecosystems (Tselniker et al., 1993; Molchanov, 2007; Suvorova & Popova, 2015; Olchev & Gulev, 2024).

Photosynthesis is the physiological basis of plant productivity. There are many mathematical models that describe photosynthesis at various scales, ranging from molecular interactions in thylakoid membranes to a whole plant or ecosystem (Laisk et al., 2009; Hikosaka et al., 2016; Sukhova et al., 2021). The Farquhar approach (Farquhar et al., 1980; von Caemmerer et al., 2000) is traditionally used to model net photosynthesis in tree leaves and ground vegetation. It has proven effective in predicting CO_2 assimilation under various environmental conditions (Bernacchi et al., 2013; Busch et al., 2024; Stirbet et al., 2024). The model enables determining several key parameters, including the maximum carboxylation rate (Vc_{max}), maximum rate of electron transport for the acceptor molecule ribulose 1,5-bisphosphate regeneration under saturating light (J_{max}), triose phosphate utilization (*TPU*) rate, as well as dark respiration (R_d) rate and mesophyll conductance (g_m).

The parameters Vc_{max}, J_{max}, and *TPU* are essential for modeling photosynthetic responses to environmental changes. Vc_{max} and J_{max} depend strongly on external conditions, particularly CO_2 concentration and light intensity (Busch et al., 2024). Solar radiation directly impacts photosynthesis because it provides to energy for electron transport and CO_2 reduction. Light activation occurs through covalent and conformational modifications of enzymes that catalyze Calvin cycle reactions, particularly ribulose bisphosphate carboxylase/oxygenase (Rubisco) (Laisk et al., 2009). Light also influences CO_2 diffusion between the air and the intercellular space of the leaf by regulating the width of the stomatal openings. An increase in air CO_2 content contributes to enhanced Rubisco carboxylation activity (Norby et al., 2005). Electron transport is also sensitive to environmental factors as it depends on the stability of the thylakoid membrane (Hikosaka et al., 2016) and can vary widely even within a species (Bernacchi et al., 2013). The third parameter that limits photosynthesis is *TPU*, which is related to the export and utilization of triose phosphates. *TPU* reflects the capacity to synthesize starch in chloroplasts or export metabolites to the cytosol for sucrose synthesis (Sharkey, 2024). Sucrose is then transported through the phloem to the plant's heterotrophic tissues and organs. High rates of sucrose phosphate synthesis can deplete the pool of free inorganic phosphate, thereby limiting photophosphorylation (Sharkey, 1985; von Caemmerer, 2000). *TPU* primarily restricts photosynthetic carbon fixation under high CO_2, high light intensity, or low temperature (Bernacchi et al., 2013; Busch et al., 2024). The importance of assessing the temperature dependence of photosynthesis parameters is emphasized in the works of Medlyn et al. (2002), Lin et al. (2013), and Togashi et al. (2018). These parameters are crucial for predicting how vegetative cover will respond to the expected increase in air temperature and CO_2 concentrations in the future.

Some studies have shown that photosynthetic parameters can vary depending on a plant's species or functional type (Medlyn et al., 2002; Lin et al., 2013). According to Wullschleger (1993) and Mandela et al. (2022), higher Vc_{max}, J_{max}, and *TPU* values have been observed in annual herbaceous plants (75, 154, and 20 μmol m^{-2} s^{-1}) than in perennial woody species (44, 97, and 5 μmol m^{-2} s^{-1}). Interspecific differences in photosynthetic parameters have also been noted in forest tree species (Medlyn et al., 2002; Korzukhin & Tselniker, 2009; Pridacha et al., 2022) and are associated with leaf mesostructure, growth, and development in different species during the growing season (Tselniker et al., 1993; Oleksyn et al., 2000; Juárez-López et al., 2008).

The most common tree species in boreal forests belong to the genera *Pinus, Betula, Populus*, and *Alnus* (Afonin et al., 2008). Despite occupying similar areas and having a wide ecological amplitude, boreal tree species, particularly *Pinus sylvestris* L., *Betula pendula* Roth, *Populus tremula* L., and *Alnus incana* (L.) Moench, exhibit noticeable ecophysiological differences. In a previous study, we examined how microclimatic and edaphic conditions of clear-cutting influence the functional characteristics of evergreen gymnosperm and deciduous angiosperm tree species. We identified species-specific changes in the photosynthetic water and nitrogen use efficiency and nutrient ratios in Scots pine, silver birch, aspen, and grey alder along the "clear-cut site – bilberry-type pine forest" gradient of environmental factors (Pridacha et al., 2021).The interspecific features of the consistency of xylem hydraulic characteristics and CO_2/H_2O gas exchange parameters in the leaves of the different species indicates that Scots pine and aspen have a more efficient and safer hydraulic structure as compared with silver birch (Pridacha et al., 2023). However, during a three-year observation period in the warm season, lower photosynthesis and dark respiration rates were obtained in Scots pine than in deciduous tree species (Pridacha & Semin, 2024).

Due to the low boreal tree species diversity, changes in CO_2 gas exchange parameters of each species resulting from environmental disturbances and climate change can significantly affect the carbon budget of taiga forests (Kurepin et al., 2018; Dusenge et al., 2020; Gagné et al., 2020). However, despite the recognized importance of assessing photosynthesis parameters for modeling and predicting carbon fluxes in terrestrial ecosystems (Laisk et al., 2009; Hikosaka et al., 2016), the impact of environmental changes on these parameters is still not fully understood. To address the lack of knowledge in this area, we examined the effects of temperature on photosynthesis parameters in co-growing an evergreen gymnosperm (*Pinus sylvestris* L.) and three deciduous angiosperm (*Betula pendula* Roth, *Populus tremula* L., and *Alnus incana* (L.) Moench) tree species in a clear-cut of mid-taiga bilberry-type pine forest. The choice of experimental design was based on the fact that clear-cuts are an ideal subject for studying how plant communities respond to environmental changes because the processes occurring in them are primarily influenced by natural factors. The working hypothesis of the study was that different tree species that grow together would show similar responses to environmental changes in the European North. Analyzing the relationship between photosynthesis parameters and environmental factors helps us understand the mechanisms of plant adaptation in response to environmental changes, particularly in the context of climate change.

MATERIALS AND METHODS

Study area and tree-growing conditions

The study was carried out in July 2018 in the European part of the middle taiga forest zone (Republic of Karelia) on a 10-year-old, clear-cut of bilberry-type pine forest (62°10′28.1′′N, 33°59′58.8′′E). According to the Köppen climate classification system, the climate of the study area is humid continental with cool summers (Peel et al., 2007). The area is characterized by high relative humidity (averaging 75%) and significant precipitation throughout the year (550–750 mm), 350–400 mm of which falls during the snow-free period from May to October (Nazarova, 2021). According to the climatic means for the period from 1991 to 2020, the average annual air temperature is +3.6°C, with minimum and maximum values of –8.4°C and +17.1°C in January and July, respectively. The average air temperature during the growing season (May–September) is +13°C. The total radiation balance for the growing season is 1,130 MJ m^{-2}. According

to data from the Kondopoga weather station, the growing season from May to September of 2018 in the study area was relatively warm (0.7°C <ΔT_{seas}: < 3.0°C) and characterized by a precipitation deficiency relative to the long-term climatic mean in May, June, and July (44, 52, and 77% of the climatic means, respectively), followed by a rainy August (151% of the climatic mean).

The study examined 10-year-old Scots pine (*Pinus sylvestris* L.), silver birch (*Betula pendula* Roth), aspen (*Populus tremula* L.), and grey alder (*Alnus incana* (L.) Moench) trees growing in a clear-cut bilberry-type pine forest site. The young stand that formed through natural regeneration in the clear-cut are primarily Scots pine (70%), with a mix of silver birch and aspen trees. The understory consists of grey alder, willow, and rowan (Pridacha & Semin, 2024). Five model trees have been selected for each of the species in the clear-cut site. The highest recorded values for height and trunk diameter at the site were for grey alder (4.5 ± 1.3 m and 4.3 ± 1.7 cm, respectively) and silver birch (3.4 ± 0.2 m and 1.8 ± 0.2 cm, respectively). The lowest values were observed for Scots pine (2.3 ± 0.1 m and 1.6 ± 0.1 cm, respectively) and aspen (1.8 ± 0.5 m and 1.2 ± 0.4 cm, respectively) (Pridacha et al., 2021).

The soil in the site was an Arenic Albic Podzol. Roots were mostly concentrated within 2–25 cm depth. The ground water table depth was 1.2 m. The detailed characteristics of the vegetation and soil cover of the clear-cut site have been presented in previous studies (Pridacha et al., 2021; Pridacha & Semin, 2024).

Parameters of CO_2 gas exchange

Field measurements of key photosynthetic parameters were conducted in July 2018 in the clear-cut bilberry pine forest site on the leaves of *B. pendula, P. tremula, A. incana* and on the 1-year-old needles of *P. sylvestris*. Measurements were taken during daylight hours from 10 a.m. to 4 p.m. on intact leaves in the middle part of the plant's crown. A portable photosynthetic system LI-6400XT (LI-COR Inc., USA) was used for the measurements. The system was equipped with a CO_2 injector, a standard 2 cm × 3 cm leaf chamber, and a LI-6400-02B LED light source (LI-COR Inc., USA). Healthy, fully formed leaves without visible damage were sampled from all plants using a uniform method with three biological replicates for each species. All the experiments were conducted under similar weather conditions.

The photosynthesis measurement program involved obtaining light and carbon dioxide response curves for photosynthesis parameters at leaf (needle) surface temperatures ranging from 20°C to 35°C. Both response curves were measured separately at each leaf temperature (20, 25, 30, and 35°C). The range of leaf temperatures was chosen based on the plant growth temperature (20°C), a reference temperature (usually 25°C), and temperatures above 20°C (30–35°C). The average leaf adaptation time to chamber conditions was about 15 minutes. The CO_2 response function of CO_2 gas exchange in leaves (A/Ci-curve) was determined by sequentially changing the CO_2 concentration in the leaf chamber (400, 300, 200, 100, 60, 30, 400, 600, 800, 1000, 1200, and 1600 µmol CO_2 mol^{-1}) at a saturating light intensity of 1600 µmol m^{-2} s^{-1}, in accordance with the device's standard configuration (Busch, 2024). *A/Ci*-curve measurements were also performed under lower light conditions (400 and 100 µmol m^{-2} s^{-1}) in a leaf chamber at a leaf surface temperature of 25°C. The relative humidity in the measuring chamber was set to 50% to prevent stomatal closure during the measurements.

The light response of photosynthetic parameters (*A/Q*-curve) was determined by measuring the intensity of CO_2 gas exchange at various PAR values (1600, 1200, 900, 600, 300, 150, 100, 75, 50, 25, and 0 µmol m^{-2} s^{-1}) under constant CO_2 concentrations (400 µmol CO_2 mol^{-1}) and relative air humidity (50%) in the leaf chamber. The *A/Q*-curve measurements were also performed at higher CO_2 concentrations (800 and 1200 µmol CO_2 mol^{-1}) and a leaf temperature of 25°C.

The CO_2 response curves (*A/Ci*-curve) were used to calibrate the key parameters of the Farquhar photosynthesis model (Farquhar et al., 1980) as modified by Sharkey et al. (2007): maximum carboxylation rate (Vc_{max}), electron transport rate at light saturation (J_{max}), triose phosphate utilization rate (*TPU*), and dark respiration rate (R_d). The temperature dependencies of Vc_{max}, J_{max}, and *TPU* were obtained by statistically evaluating a set of the photosynthesis parameter values at various leaf temperatures. Based on these dependencies, the standardized Vc_{max25}, J_{max25}, and TPU_{25} values were obtained at the selected reference temperature of 25°C (Sharkey et al., 2007; Sharkey, 2016).

The parameters of the light response curve model, particularly the value of photosynthesis at saturating PAR values (A_{max}), were calculated using a modified Michaelis–Menten function (Kaipiainen, 2009; Pridacha et al., 2022). Detailed procedures for assessing the carbon dioxide and light-response functions of CO_2 gas exchange have been reported in previously published studies (Sharkey et al., 2007; Sharkey, 2016; Busch, 2024).

The CO_2 gas exchange rates for *P. sylvestris* needles in our study were converted to the entire needle surface area. To calculate the surface area of the needles, we used a simplified method to determine their specific linear density (weight of unit needle length) (Tselniker, 1982).

Statistical analysis

Statistical data analysis was performed using Statistica 13.3 (TIBCO Software Inc., USA). Regression analysis was used to process the experimental data. Statistical significance was defined as $p < 0.05$. The diagrams show the means and their standard errors.

RESULTS

The classic biochemical Farquhar model and regression analysis of photosynthesis light response curves accurately describe how leaf photosynthesis responds to changes in ambient CO_2 concentrations and light conditions, with an R^2 value ranging from 0.95 to 0.99 (Fig. 1).

Analysis of the temperature dependence of photosynthetic parameters revealed that increasing leaf temperature within the 20–35°C range resulted in 5.6- and 3.1-fold increases in Vc_{max} in *P. sylvestris and B. pendula*, respectively (Fig. 2). In *A. incana* and *P. tremula*, Vc_{max} increased within a narrower temperature range (20–30°C) than in *P. sylvestris* and *B. pendula*. The increase was 2.2- and 3.1-fold, respectively, followed by a subsequent decrease of 1.2- and 2.1-fold at 35°C in *A. incana* and *P. tremula*, respectively. Analysis of the standardized Vc_{max25} values at a reference temperature of 25°C revealed similar patterns of change for this parameter in each species. The Vc_{max25} values were higher than the 20°C measured values (1.7-, 1.5-, 1.4-, and 1.5-fold for *P. sylvestris, B. pendula, A. incana*, and *P. tremula,* respectively) and lower at 30°C (1.4- to 1.6-fold) and 35°C (2- to 2.4-fold) for all species. At a leaf surface temperature of 25°C, Vc_{max} values were lowest for 1-year-old *P. sylvestris* needles (38.8 µmol m^{-2} s^{-1}) and highest for *B. pendula, A. incana*, and *P. tremula* leaves (93.5, 86.1, and 58.6 µmol m^{-2} s^{-1}, respectively).

The J_{max} values for *P. sylvestris* increased 2.5-fold within the temperature range of 20–35°C. However, the increase was

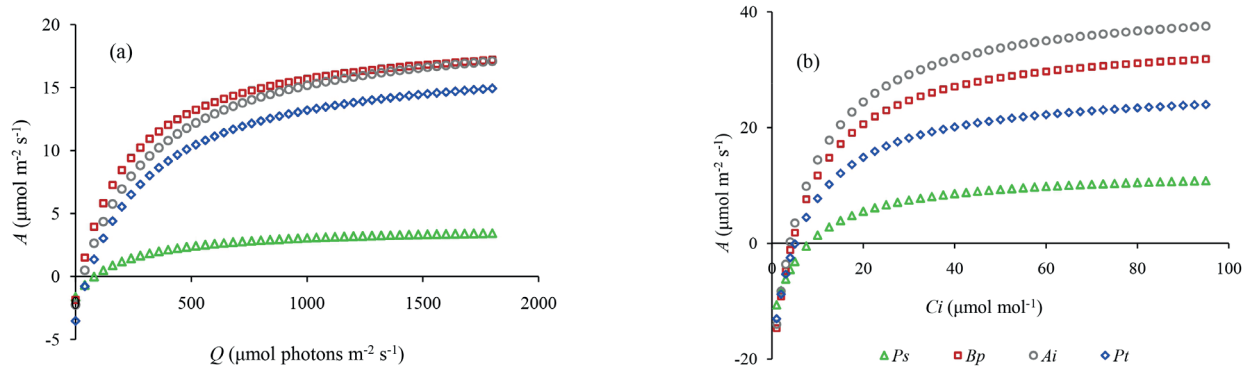

Fig. 1. Sample *A/Q*-curve (a) and *A/Ci*-curve (b) plotted for 1-year-old needles of *Pinus sylvestris (Ps)* and leaves of *Betula pendula (Bp), Alnus incana (Ai), Populus tremula (Pt)* at leaf temperature of 25°C using the LI-6400 XT protocol

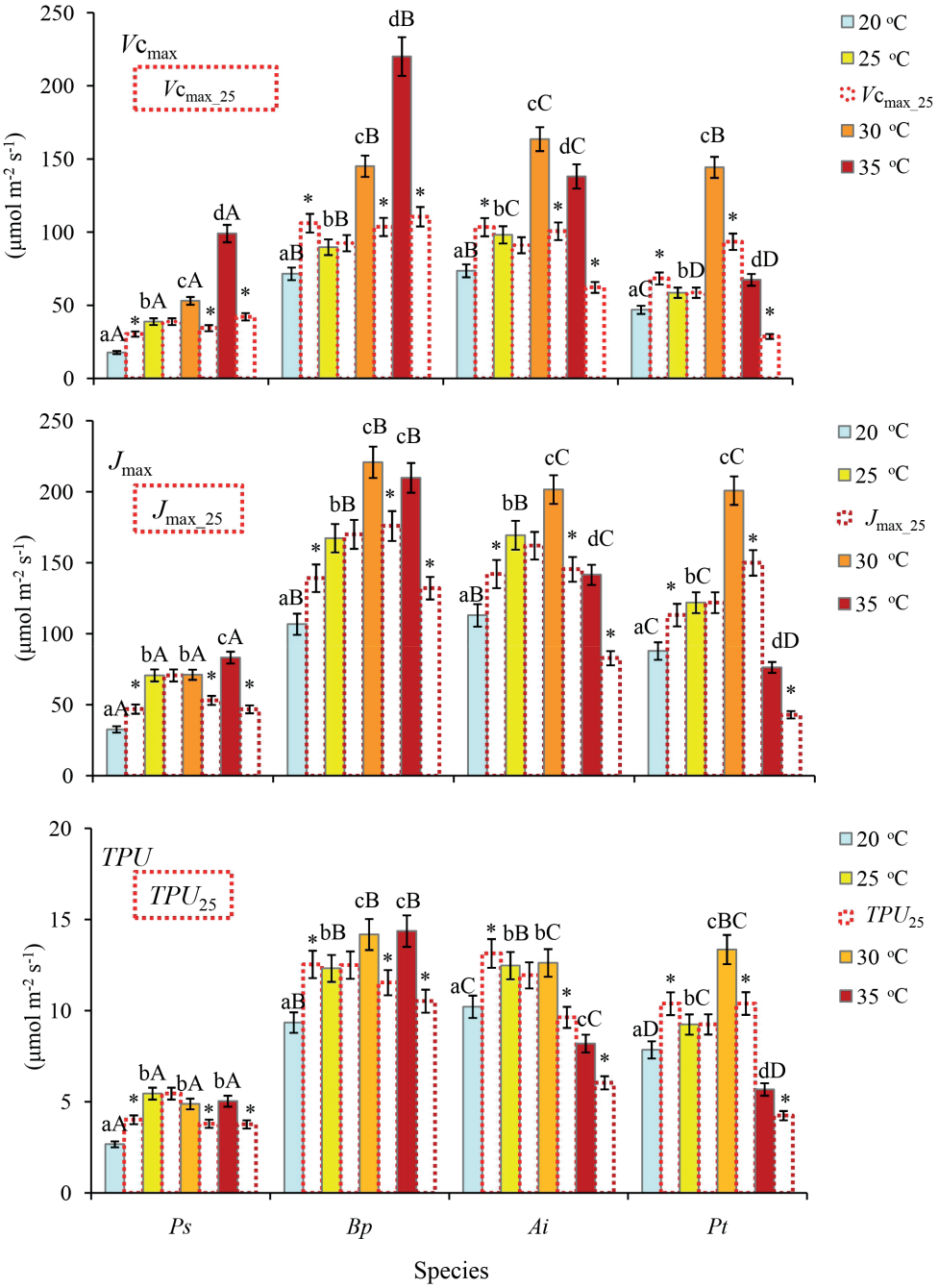

Fig. 2. Maximum rates of carboxylation by Rubisco (Vc_{max}), electron transport (J_{max}), and triose phosphate utilization (*TPU*) measured in the leaf temperature range of 20–35°C and standardized at a reference temperature of 25°C (Vc_{max25}, J_{max25}, and TPU_{25}) in *Pinus sylvestris (Ps), Betula pendula (Bp), Alnus incana (Ai),* and *Populus tremula (Pt)*. Different lowercase letters on top of the bars (a, b, c) indicate significant differences in means ($p < 0.05$) when comparing one species at different leaf temperatures, and different capital letters (A, B, C) indicate significant differences ($p < 0.05$) between different species at each treatment level. An asterisk (*) indicates a significant difference in means ($p < 0.05$) when comparing each pair of measured and standardized parameter values for each species

significantly lower, at only 1.2-fold, at temperatures between 25 and 35°C. For *B. pendula*, the J_{max} values increased 2-fold with an increase in leaf surface temperature from 20 to 35°C. For *A. incana* and *P. tremula*, this parameter increased up to 30°C (by 1.8 and 2.3 times, respectively) and then decreased at 35°C (by 1.4 and 2.6 times, respectively). Comparing the measured J_{max} values with the reference J_{max} values at 25°C revealed higher values for all species at 20°C (1.4, 1.3, 1.3, and 1.3 times higher for *P. sylvestris, B. pendula, A. incana,* and *P. tremula*, respectively). However, the corresponding values were lower at 30°C (by 1.3–1.4 times) and 35°C (by 1.6–1.8 times) in all species. The lowest J_{max25} values were observed for 1-year-old needles of *P. sylvestris* (70.7 μmol m^{-2} s^{-1}), compared to the deciduous species: 172.1, 155.1, and 122 μmol m^{-2} s^{-1} for *B. pendula, A. incana*, and *P. tremula*, respectively.

As the temperature of the leaf surface raised from 20 to 35°C, the *TPU* values increased 1.9-fold in *P. sylvestris* trees and 1.5-fold in *B. pendula* trees. For *A. incana* and *P. tremula*, the *TPU* values increased 1.2- and 1.7-fold, respectively, when the leaf temperature increased from 20 to 30°C. Then, it decreased 1.5- and 2.4-fold, respectively, at 35°C. As with Vc_{max} and J_{max}, higher referenced TPU values were observed for all species at 20°C than the measured values (1.5, 1.3, 1.3, and 1.3 times higher for *P. sylvestris, B. pendula, A. incana*, and *P. tremula*, respectively). Lower values were observed at 30°C (1.2–1.3 times lower) and 35°C (1.3–1.4 times lower) in all species. 1-year-old needles of *P. sylvestris* had the lowest TPU_{25} values (5.5 μmol m^{-2} s^{-1}) at a leaf temperature of 25°C compared to *B. pendula* (12.7 μmol m^{-2} s^{-1}), *A. incana* (11.4 μmol m^{-2} s^{-1}), and *P. tremula* (9.3 μmol m^{-2} s^{-1}) leaves.

Importantly, decreases in Vc_{max}, J_{max}, and *TPU* values occurred when the light intensity in the leaf chamber decreased from saturating to low levels at a leaf surface temperature of 25°C for all tree species (Fig. 3). At the same time, interspecific differences in the dynamics of these parameters were revealed. For example, *P. sylvestris* showed the smallest decrease in Vc_{max25}, J_{max25}, and TPU_{25} values (1.2-, 1.5-, and 1.5-fold, respectively) within the PAR range of 100 to 1,600 μmol m^{-2} s^{-1}compared to deciduous species (3.1- to 3.2-, 4.3- to 4.8-, and 4.1- to 4.4-fold, respectively). Conversely, a 4-fold decrease in light intensity (from 1,600 to 400 μmol m^{-2} s^{-1}) led to a smaller decrease in Vc_{max25}, J_{max25}, and TPU_{25} values in deciduous species (1.3–1.8, 1.4–1.6, and 1.4–1.6 times, respectively) than in *P. sylvestris* (J_{max25} and TPU_{25} by 1.3 times).

Analysis of A_{max} values revealed insignificant changes in *P. sylvestris, B. pendula*, and *A. incana* at leaf temperatures of 20–25°C, followed by a decrease in this parameter as the temperature increased to 35°C (decreasing by 1.9, 1.9, and 2.8 times, respectively) (Fig. 4a). *P. tremula* featured a greater stabilization of A_{max} in the 20–30°C range and a smaller decline in the parameter at 35°C (1.3 times) compared with other species. Increasing the CO_2 concentration in the leaf chamber to 800 and 1,200 μmol CO_2 mol^{-1} for all tree species

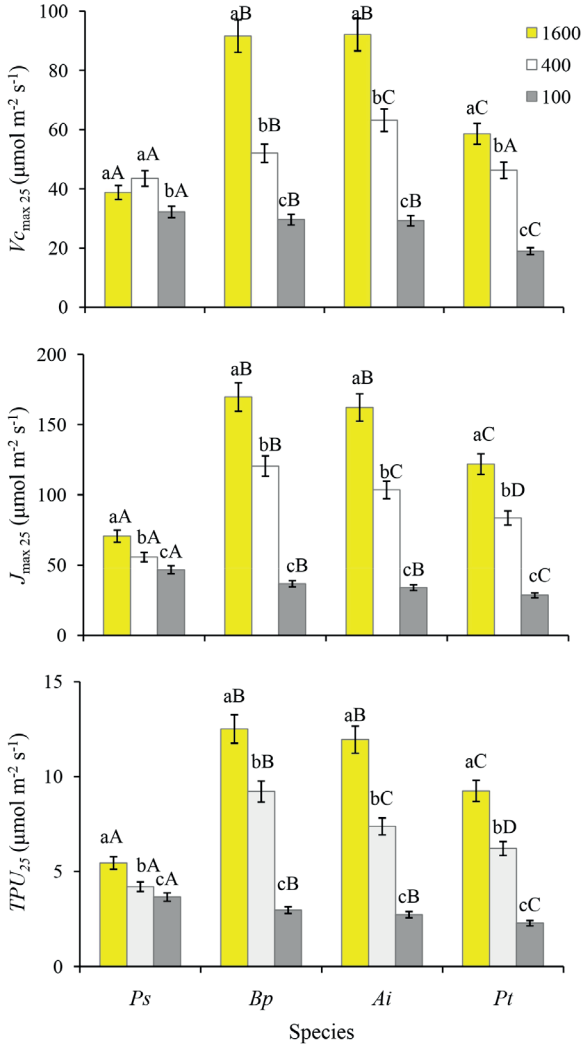

Fig. 3. Maximum rates of carboxylation by Rubisco (Vc_{max25}), electron transport (J_{max25}), and triose phosphate utilization (TPU_{25}) measured under different light intensities (100–1600 μmol m^{-2} s^{-1}) on 1-year-old needles of *Pinus sylvestris (Ps)* and leaves of *Betula pendula (Bp), Alnus incana (Ai),* and *Populus tremula (Pt)* at a leaf temperature of 25°C. Different lowercase letters on top of the bars (a, b, c) indicate significant differences in means (p <0.05) when comparing one species at different light intensity, and different capital letters (A, B, C) indicate significant differences (p <0.05) between different species at each light level.

resulted in higher A_{max} values at a leaf surface temperature of 25°C (Fig. 4b). *P. sylvestris* exhibited the greatest increase in the parameter, with a 2- and 3-fold increase in CO_2 concentration relative to external conditions (1.9 and 2.6 times, respectively) compared to deciduous species, such as *P. tremula* (1.4 and 1.6 times, respectively), *B. pendula* (1.1 and 1.9 times, respectively), and *A. incana* (1.7 and 2.1 times, respectively).

Analysis of the temperature dependence of the J_{max}/Vc_{max} ratio, calculated from measured values between 20 and 35°C, revealed a negative linear relationship for all tree species (Fig. 5a). The decrease of the parameter with an increase in leaf temperature from 25 to 35°C was 2.2, 2.0, 1.7, and 1.8 times for *P. sylvestris, B. pendula, A. incana*, and *P. tremula*, respectively. The J_{max25}/Vc_{max25} ratio, calculated using reference values at 25°C, exhibited similar dependence, taking the form of a "bell curve" with a pronounced peak at 25°C for all species studied (Fig. 5b). The increase in the J_{max25}/Vc_{max25} ratio in response to leaf temperature elevation in the 20–25°C range and its decline in the 25–35°C range were, respectively, 1.2 and 1.6-fold for *P. sylvestris* versus 1.3–1.4 and 1.4–1.5-fold for the deciduous species. It is also important to note the similarity of the J_{max25}/Vc_{max25} ratio at 25°C for *P. sylvestris, B. pendula,* and *A. incana* (1.8), as well as higher value for *P. tremula* (2.1).

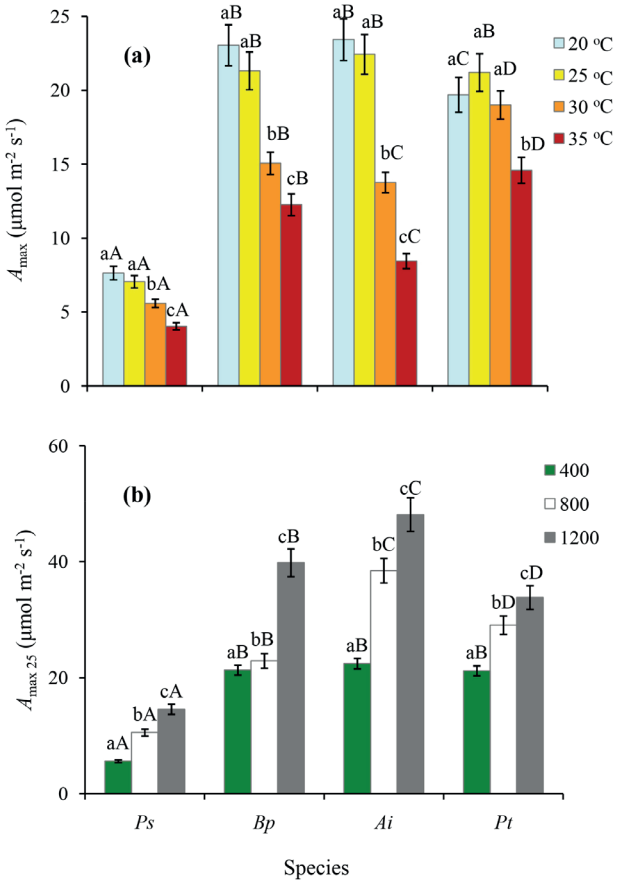

Fig. 4. Maximum CO_2 assimilation rate (A_{max}) measured at leaf temperatures ranging from 20 to 35°C (a) and at different CO_2 concentrations ranging from 400 to 1200 µmol CO_2 mol^{-1} at a leaf temperature of 25°C (b) on 1-year-old needles of *Pinus sylvestris (Ps) and leaves of Betula pendula (Bp), Alnus incana (Ai),* and *Populus tremula (Pt)*. Different lowercase letters on top of the bars (a, b, c) indicate significant differences in means (p <0.05) when comparing one species at different leaf temperatures or CO_2 concentrations, and different capital letters (A, B, C) indicate significant differences (p <0.05) between different species at each treatment level

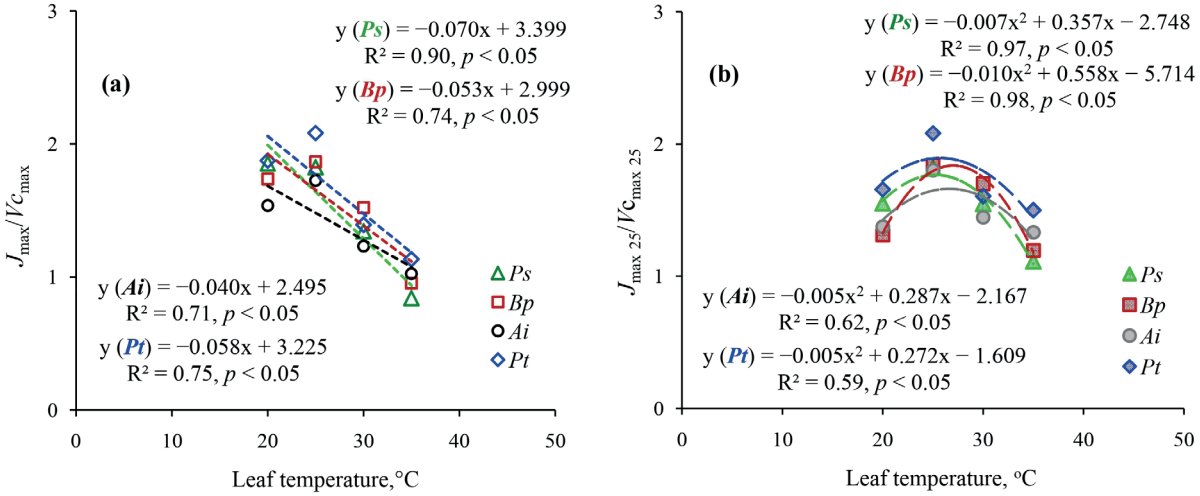

Fig. 5. Ratio of maximum electron transport rate (J_{max}) and maximum rate of carboxylation by Rubisco (Vc_{max}) measured at leaf temperature ranging from 20 to 35°C (a) and standardized at 25°C (b) in *Pinus sylvestris (Ps), Betula pendula (Bp), Alnus incana (Ai)* and *Populus tremula (Pt)*

DISCUSSION

Temperature dependence of photosynthesis parameters

The study examining the temperature dependence of photosynthetic parameters in four boreal tree species (*Pinus sylvestris, Betula pendula, Populus tremula*, and *Alnus incana*) revealed significant species-specific differences in the responses of Vc_{max}, J_{max}, and *TPU* to changes in leaf temperature and light conditions. These results provide a deeper understanding of how trees in cold climates adapt to changing environmental conditions, particularly in the context of global climate change.

Analysis of the temperature dependence of photosynthetic parameters (Fig. 2) revealed that *P. sylvestris* and *B. pendula* exhibited the greatest increase in Vc_{max} with temperature increases from 20 to 35°C. In contrast, *A. incana* and *P. tremula* demonstrated a narrower optimal temperature range (20 to 30°C) and a subsequent decrease in Vc_{max} at 35°C compared to 30°C. These results agreed with previous studies suggesting that coniferous species, including *P. sylvestris*, exhibit a broader temperature range for photosynthesis than deciduous species (Medlyn et al., 2002; Lin et al., 2013). The decrease in Vc_{max} in deciduous species at high temperatures may be related to the temperature-dependent activity of Rubisco, the inactivation of Rubisco due to reduced functioning of Rubisco activase, or the decreased stability of the enzyme (Sharkey, 1985; Galmés et al., 2015; Scafaro et al., 2023).

Similarly, J_{max} increased gradually in *P. sylvestris* and *B. pendula,* whereas *A. incana* and *P. tremula* exhibited a sharp increase in J_{max}, followed by a decrease, at 35°C. These results suggest that deciduous species, particularly *A. incana* and *P. tremula*, have more sensitive electron transport systems to elevated temperatures. This is likely due to the destabilization of thylakoid membranes and their components (Hikosaka et al., 2016). These results align with data indicating that high temperatures, which frequently occur during summer heat waves, can significantly limit the functioning of boreal deciduous species (Reich et al., 2018; Dusenge et al., 2020).

The *TPU* (triose phosphate utilization) parameter exhibited less variability in *P. sylvestris* and *B. pendula* than in *A. incana* and *P. tremula* within a temperature range of 25–35°C. This suggests that these species use carbohydrates (triose phosphates) more efficiently for synthesizing sucrose and starch under thermal stress compared to *A. incana* and *P. tremula*. However, the decrease in *TPU* in deciduous species at 35°C may result from limitations in starch and sucrose synthesis or phosphate recycling (Sharkey, 1985; von Caemmerer, 2000; Hikosaka et al., 2016). These findings have significant implications for long-term carbon accumulation under warming conditions.

The decrease in A_{max} observed in all species (Fig. 4a) as the temperature increases beyond the optimal range is due to the fact that the rate at which plants absorb CO_2 via photosynthesis is influenced by the photosynthetic apparatus and the degree of stomatal opening (Lin et al., 2012; Scafaro et al., 2023). Within the super-optimal temperature range, the decrease in photosynthetic intensity is due to a reduction in leaf turgor and stomatal closure. This hinders the diffusion of CO_2 from the atmosphere into the interior of the leaf and to the fixation centers. Additionally, as temperature rises, CO_2 solubility decreases, and the kinetic constants of carboxylating enzymes change (Sage & Kubien, 2007). As temperature increases, Rubisco's affinity for oxygen grows, enhancing photorespiration and reducing the efficiency of carbon dioxide fixation. This results in a decrease in the overall rate of photosynthesis.

It is important to note the greater thermal stability of A_{max} in *P. tremula* compared to other species across a broader temperature range (20–30°C), as well as the higher A_{max} values observed at sub-optimal temperatures (30–35°C). However, *P. tremula* exhibits lower photosynthetic activity than other deciduous species, as evidenced by lower Vc_{max}, J_{max}, and *TPU* values. Our observations align with prior research indicating that biochemical factors and mesophyll limitations primarily drive the decrease in photosynthesis in *P. tremula* at high temperatures and CO_2 concentrations (Hüve et al., 2019; de Souza et al., 2024). During four growing seasons at the same clear-cut site, we observed higher values of stomatal conductance and transpiration rate for *P. tremula* than for other deciduous species and *P. sylvestris* (Pridacha et al., 2021). These findings are important because stomatal conductance determines the rate of CO_2 diffusion to carboxylation sites (Baillie, Fleming, 2020; Márquez, Busch, 2024), and transpiration provides leaf thermoregulation by evaporating water from the leaf surface. This cooling effect prevents overheating, especially at high ambient temperatures (Lin et al., 2017; Drake et al., 2018). Thus, the greater thermal stability of A_{max} in *P. tremula* relative to other species can be due to higher CO_2 diffusion flux and better leaf thermoregulation. This is consistent with noted relative independence of CO_2 concentration in *P. tremula* leaf chloroplasts from temperature (de Souza et al., 2024).

Additionally, the greater thermal stability range of A_{max} in *P. tremula* may be due to differences in hydraulic regulation among species, specifically the anisohydric nature of *P. tremula* compared to the isohydric characteristics of *B. pendula* (Pridacha et al., 2023). This hypothesis is supported by data from other studies (Klein, 2014; Meinzer et al., 2016; Sellin et al., 2019, 2022). A previous study (Mäenpää et al., 2011) on the effects of ozone and temperature on carbon assimilation in *B. pendula* and *P. tremula* seedlings found that *B. pendula* leaves experienced a greater decrease in stomatal conductance (1.7 times) than *P. tremula* leaves (1.2 times) when the air temperature increased by 1°C. This is consistent with the more pronounced decrease in A_{max} in *B. pendula* with an increase in temperature above the optimum relative to *P. tremula* (Fig. 4a). This is likely because of a greater decrease in CO_2 diffusion flux into the leaf due to stomatal limitation of photosynthesis, despite higher activity of the photosynthetic apparatus in *B. pendula* (Fig. 2).

At the same time, in all species we observed a similar consistent pattern of the J_{max}/Vc_{max} ratio at temperatures between 20 and 25°C, which decreased as the temperature increased up to 35°C (Fig. 5). Despite interspecific differences, this pattern can be explained by the optimal temperature range for photosynthesis in C_3 plants, which is typically between 20–25 °C for most C_3 plants in the temperate zone (Laisk et al., 2009; Hikosaka et al., 2016). The decrease in the J_{max}/Vc_{max} ratio from 1.7–2.1 to 0.8–1.1 with increasing temperature for all species may be associated with the higher activation energy for Vc_{max} relative to J_{max}. Similar observations have been made by scientists studying other woody plants (Onoda et al., 2005; Ow et al., 2008; Riikonen et al., 2009). The similarity of the Rubisco specificity factor in gymnosperms and C_3 angiosperms has also been noted, as a measure of the enzyme's capacity to exhibit carboxylase and oxygenase activity relative to RuBP. This similarity is explained by the adaptation of Rubisco in different phylogenetic groups of plants to current CO_2/O_2 atmospheric levels (Miyazawa et al., 2020).

Response to light and CO_2

The study also revealed interspecific differences in photosynthetic responses to changes in light intensity and CO_2 levels. *P. sylvestris* exhibited greater stability in Vc_{max} and

J_{max} at low light levels (100–400 μmol m^{-2} s^{-1}). In contrast, deciduous species demonstrated a more significant decline in these parameters (Fig. 3). This may reflect conifers' adaptation to shading or high cloud cover in boreal regions (Oleksyn et al., 1998; Ma et al., 2014; Schmiege et al., 2023). Due to their higher photosynthetic activity, deciduous trees likely experience more pronounced inhibition of Rubisco activity at low light levels due to the strong binding of RuBP and other sugar phosphates formed during the Calvin cycle to the catalytic center (Sharkey, 1985; von Caemmerer, 2000).

At elevated CO_2 concentrations (800–1200 μmol mol^{-1}), the greatest increase in A_{max} was observed in *P. sylvestris* (Fig. 4b), suggesting a stronger response to CO_2 enrichment than in deciduous species. These results are consistent with previous studies (Niinemets et al., 2011; Kurepin et al., 2018) that reported conifers' superior adaptation to elevated CO_2 levels. Since CO_2 is a substrate for photosynthesis, its availability and concentration determine the activity of carbon metabolism. The increase in photosynthesis rate with increasing CO_2 levels is due to the realization of the carboxylase potential of Rubisco and the formation of a large RuBP acceptor pool in chloroplasts under these conditions (von Caemmerer, 2000; Busch et al., 2024). Among the deciduous species, the greatest increase in A_{max} with CO_2 growth was found in *A. incana*. We previously observed the highest values of specific nitrogen content and its biological absorption coefficient in *A. incana* relative to other species using the same model trees in the clear-cut (Pridacha et al., 2021). These results are consistent with previous studies reporting that trees of the genus *Alnus* can maintain high levels of photosynthesis after prolonged exposure to elevated CO_2 in nitrogen-poor soils due to high nitrogen availability from symbiosis with nitrogen-fixing actinomycetes (Vogel, Curtis, 1995; Rytter, Rytter, 2016). However, the weak response of *P. tremula* to increased CO_2 may indicate Rubisco activity saturation due to a greater supply of substrate (CO_2) in the leaf caused by the higher stomatal conductance of *P. tremula* leaves (Pridacha et al., 2021) or limitations in subsequent metabolic processes (Busch et al., 2024).

It is important to note that the influence of mesophyll conductance on photosynthesis has been demonstrated for all plant functional types (Flexas et al., 2014; Nadal et al., 2021; Knauer et al., 2022). In our study, coniferous species exhibited the lowest photosynthesis parameter values under all temperature, light, and CO_2 treatments compared to deciduous species. This finding aligns with prior studies indicating lower mesophyll conductance in coniferous trees than in deciduous trees, primarily due to the structural organization of their rigid leaves. Specifically, needles have thick mesophyll cell walls and chloroplasts, as well as a low ratio of chloroplast surface area to intercellular space per unit of leaf surface area (Veromann-Jürgenson et al., 2017; Carriquí et al., 2020). The low photosynthesis rates in coniferous trees are believed to be offset by their significantly longer active photosynthesis duration compared to deciduous trees in the boreal zone (Vasfilov, 2016; Shiklomanov et al., 2020). As temperatures and CO_2 levels in the atmosphere rise in a changing climate, it is assumed that species with low mesophyll conductance, particularly evergreen gymnosperm, will gain an advantage over deciduous angiosperm tree species in terms of distribution, especially in the boreal zone (Niinemets et al., 2011; Flexas et al., 2014; Nadal et al., 2021).

The results of our study are consistent with previously published data, while also revealing some new findings. For example, Medlyn et al. (2002) observed similar Vc_{max} values for *P. sylvestris* at 25°C. However, our data show that this parameter is more sensitive to extreme temperatures. The decrease in J_{max} in deciduous species at 35°C aligns with results obtained for temperate forest species (Togashi et al., 2018; de Souza et al., 2024), suggesting stability in photosynthetic temperature sensitivity across different plant biomes. Differences in *TPU* among species are consistent with Wullschleger's (1993) data, which showed lower *TPU* values in woody perennials than in herbaceous plants. Our study extends these findings by demonstrating how these differences manifest with changes in temperature and light intensity.

The results highlight the vulnerability of boreal deciduous species, especially *A. incana* and *P. tremula*, to climate warming due to decreased photosynthetic efficiency at high temperatures. At the same time, all species exhibit a similar consistent pattern of the J_{max}/Vc_{max} ratio within the 20–35°C temperature range. However, *P. sylvestris* demonstrates greater resilience, confirming its dominant role in boreal forests under future warming conditions (Bonan, 2008). Nevertheless, the stronger response of coniferous species to elevated CO_2 could be counterbalanced by other environmental stressors, such as drought. These factors were not considered in this study, yet they play a significant role in boreal ecosystem functioning (Reich et al., 2018; Liu et al., 2023; Martínez-García et al., 2024).

When considering the limitations of the identified patterns and prospects for future research, it should be noted that our study was conducted on young trees in a clear-cut area. This may not accurately reflect the functioning of a mature forest. Future studies should include mature trees and additional stress factors, such as drought and nutrient deficiency. Incorporating the data into ecosystem models based on the Farquhar approach will also improve predictions of the carbon cycle in boreal forests under climate change (Bernacchi et al., 2013).

CONCLUSIONS

Our study of the temperature dependence of photosynthetic parameters in four boreal tree species (*Pinus sylvestris, Betula pendula, Populus tremula*, and *Alnus incana*) revealed significant differences in their adaptation strategies to changing environmental conditions. *P. sylvestris* and *B. pendula* had a broader optimal temperature range for J_{max} and Vc_{max} (20–35°C), whereas *P. tremula* and *A. incana* had optimal values between 20 and 30°C and experienced a sharp decline at 35°C compared to 30°C. These results indicate their greater vulnerability to increased temperatures and global warming. Additionally, *P. sylvestris* showed greater resilience in photosynthetic parameters under low light conditions, as well as a more pronounced response to elevated CO_2 concentrations compared to deciduous species. This suggests its greater potential to adapt to future climate changes. The sensitivity of deciduous angiosperm tree species to extreme temperatures and increased CO_2 levels could lead to shifts in the composition of boreal forests in the future.

The results obtained are important for predicting the carbon balance of boreal ecosystems. The resilience of *P. sylvestris* to high temperatures and its efficiency in using CO_2 suggest that this species will maintain its dominant role in the warming climate. However, the vulnerability of deciduous angiosperm tree species requires further study, especially when considering additional stress factors such as drought. Integrating these data into the Farquhar approach-based ecosystem models will improve predictions of forest responses to climate change. Further studies should incorporate mature trees and complex stress scenarios to improve our understanding of the adaptive mechanisms of boreal species.

REFERENCES

Afonin A.N., Greene S.L., Dzyubenko N.I., Frolov A.N. (eds.). (2008). Interactive agricultural ecological atlas of Russia and neighboring countries. Economic plants and their diseases, pests and weeds [Online]. Available at: https://agroatlas.ru.

Baillie A.L., Fleming A.J. (2020). The developmental relationship between stomata and mesophyll airspace. New Phytol, 225(3), 1120–1126. DOI: 10.1111/nph.16341

Bernacchi C.J., Bagley J.E., Serbin S.P., Ruiz-Vera U.M., Rosenthal D.M., Vanloocke A. (2013). Modelling C_3 photosynthesis from the chloroplast to the ecosystem. Plant Cell Environ, 36(9), 1641–1657. DOI: 10.1111/pce.12118

Bonan G.B. (2008). Forests and climate change: forcings, feedbacks, and the climate benefits of forests. Science, 320, 1444–1449. DOI: 10.1126/science.1155121

Busch F.A. (2024). Photosynthetic gas exchange in land plants at the leaf level. In: Covshoff, S. (eds) Photosynthesis. Methods in molecular biology. V. 2790. Humana, New York, NY. DOI: 10.1007/978-1-0716-3790-6_3

Busch F.A., Ainsworth E.A., Amtmann A., Cavanagh A.P., Driever S.M., Ferguson J.N., Kromdijk J., Lawson T., Leakey A.D., Matthews J.S., Meacham-Hensold K.,Vath R.L.,Vialet-Chabrand S., Walker B.J.,Papanatsiou M. (2024). A guide to photosynthetic gas exchange measurements: Fundamental principles, best practice and potential pitfalls. Plant Cell Environ, 47, 3344–3364. DOI: 10.1111/pce.14815

Carriquí M., Nadal M., Clemente-Moreno M.J., Gago J., Miedes E., Flexas J. (2020). Cell wall composition strongly influences mesophyll conductance in gymnosperms. Plant J, 103, 1372–1385. DOI: 10.1111/tpj.14806

de Souza V.F., Rasulov B., Talts E., Morfopoulos C., Albuquerque P.M., Junior S.D., Niinemets U., Goncales J.F. (2024). Thermal sensitivity determines the effect of high CO_2 on carbon uptake in *Populus tremula* and *Inga edulis*. Theor Exp Plant Physiol, 36, 199–213. DOI: 10.1007/s40626-024-00312-9

Drake J.E., Tjoelker M.G., Vårhammar A., Medlyn B.E., Reich P.B., Leigh A., Pfautsch S., Blackman C.J., López R., Aspinwall M.J., Crous K.Y., Duursma R.A., Kumarathunge D., De Kauwe M.G., Jiang M., Nicotra A.B., Tissue D.T., Choat B., Atkin O.K., Barton C.V. (2018).Trees tolerate an extreme heatwave via sustained transpirational cooling and increased leaf thermal tolerance. Glob Change Biol, 24, 2390–2402. DOI: 10.1111/gcb.14037

Dusenge M.E, Madhavji S., Way D.A. (2020). Contrasting acclimation responses to elevated CO_2 and warming between an evergreen and a deciduous boreal conifer. Glob Change Biol, 26, 3639–3657. DOI: 10.1111/gcb.15084

Farquhar G.D., von Caemmerer S., Berry J.A. (1980). A biochemical model of photosynthetic CO_2 assimilation in leaves of C_3 plants. Planta, 149, 78–90.

Flexas J., Carriquí M., Coopman R.E., Gago J., Galmés J., Martorell S., Morales F., Diaz-Espejo A. (2014). Stomatal and mesophyll conductances to CO_2 in different plant groups: underrated factors for predicting leaf photosynthesis responses to climate change? Plant Sci, 226, 41–48. DOI: 10.1016/j.plantsci.2014.06.011

Gagne M.A., Smith D.D., McCulloh K.A. (2020). Limited physiological acclimation to recurrent heatwaves in two boreal tree species. Tree Physiol, 40(12), 1680–1696. DOI: 10.1093/treephys/tpaa102

Galmés J., Kapralov M.V., Copolovici L.O., Hermida-Carrera C., Niinemets Ü. (2015). Temperature responses of the Rubisco maximum carboxylase activity across domains of life: phylogenetic signals, trade-offs, and importance for carbon gain. Photosynth Res, 123, 183–201. DOI: 10.1007/s11120-014-0067-8

Groisman P., Shugart H., Kicklighter D. et al. (2017). Northern Eurasia Future Initiative (NEFI): facing the challenges and pathways of global change in the twenty-first century. Prog Earth Planet Sci, 41. DOI: 10.1186/s40645-017-0154-5

Gushchina D., Tarasova M., Satosina E., Zheleznova I., Emelianova E., Gibadullin R., Osipov A., Olchev A. (2023). The response of daily carbon dioxide and water vapor fluxes to temperature and precipitation extremes in temperate and boreal forests. Climate, 11(10), 206. DOI: 10.3390/cli11100206

Hikosaka K., Niinemets Ü., Anten N.P. (eds). (2016). Canopy photosynthesis: from basics to applications. Advances in photosynthesis and respiration.Vol. 42. Springer Dordrecht, 428 p. DOI: 10.1007/978-94-017-7291-4

Hüve K., Bichele I., Kaldmäe H., Rasulov B., Valladares F., Niinemets Ü. (2019). Responses of aspen leaves to heatflecks: both damaging and non-damaging rapid temperature excursions reduce photosynthesis. Plants, 8(6), 145. DOI: 10.3390/plants8060145

IPCC: Climate Change 2023: Synthesis Report, Summary for Policymakers. Contribution of Working Groups I, II and III to the Sixth Assessment Report of the Intergovernmental Panel on Climate Change. (2023). IPCC, Geneva, Switzerland, 34 p. DOI: 10.59327/IPCC/AR6-9789291691647.001

Juárez-López F.J., Escudero A., Mediavilla S. (2008). Ontogenetic changes in stomatal and biochemical limitations to photosynthesis of two co-occurring Mediterranean oaks differing in leaf life span. Tree Physiol, 28, 367–374. DOI: 10.1093/treephys/28.3.367

Kaipiainen E.L. (2009). Parameters of photosynthesis light curve in *Salix dasyclados* and their changes during the growth season. Russ J Plant Physiol, 56, 445–453. DOI: 10.1134/S1021443709040025.

Klein T. (2014). The variability of stomatal sensitivity to leaf water potential across tree species indicates a continuum between isohydric and anisohydric behaviours. Funct Ecol, 28, 1313–1320. DOI: 10.1111/1365-2435.12289

Knauer J., Cuntz M., Evans J.R., Niinemets Ü., Tosens T., Veromann-Jürgenson L.-L., Werner C., Zaehle S. (2022). Contrasting anatomical and biochemical controls on mesophyll conductance across plant functional types. New Phytol, 236, 357–368. DOI: 10.1111/nph.18363

Korzukhin M.D., Tselnicker Y.L. (2009). Analysis of the distribution and net primary production of four forest tree species in Russia using an ecophysiological model. In: Problems of ecological monitoring and ecosystem modeling, 22, 92–123.

Kurepin L.V., Stangl Z.R., Ivanov A.G., Bui V., Mema M., Hüner N.P., Öquist G., Way D., Hurry V. (2018). Contrasting acclimation abilities of two dominant boreal conifers to elevated CO_2 and temperature. Plant Cell Environ, 41, 1331–1345. DOI: 10.1111/pce.13158

Laisk A., Nedbal L., Govindjee G. (eds). (2009). Photosynthesis in silico: understanding complexity from molecules to ecosystems. Advances in photosynthesis and respiration.Vol. 29. Springer Dordrecht, 503p. DOI: 10.1007/978-1-4020-9237-4

Lin H., Chen Y., Zhang H., Fu P., Fan Z. (2017). Stronger cooling effects of transpiration and leaf physical traits of plants from a hot dry habitat than from a hot wet habitat. Funct Ecol, 31, 2202–2211. DOI: 10.1111/1365-2435.12923

Lin Y.-S., Medlyn B.E., Ellsworth D.S. (2012). Temperature responses of leaf net photosynthesis: the role of component processes. Tree Physiol, 32(2), 219–231. DOI: 10.1093/treephys/tpr141

Lin Y.-S., Medlyn B.E., Kauwe M.G., Ellsworth D.S. (2013). Biochemical photosynthetic responses to temperature: how do interspecific differences compare with seasonal shifts? Tree Physiol, 33(8), 793–806. DOI: 10.1093/treephys/tpt047

Liu Q., Peng C., Schneider R., Cyr D., McDowell N.G., Kneeshaw D. (2023). Drought-induced increase in tree mortality and corresponding decrease in the carbon sink capacity of Canada's boreal forests from 1970 to 2020. Glob Change Biol, 29, 2274–2285. DOI: 10.1111/gcb.16599

Ma Z., Behling S., Ford E.D. (2014). The contribution of dynamic changes in photosynthesis to shade tolerance of two conifer species. Tree Physiol, 34(7), 730–743. DOI: 10.1093/treephys/tpu054

Mäenpää M., Riikonen J., Kontunen-Soppela S., Rousi M., Oksanen E. (2011). Vertical profiles reveal impact of ozone and temperature on carbon assimilation of *Betula pendula* and *Populus tremula*. Tree Physiol, 31, 819–830. DOI: 10.1093/treephys/tpr075

Márquez D.A., Busch F.A. (2024). The interplay of short-term mesophyll and stomatal conductance responses under variable environmental conditions. Plant Cell Environ, 47, 3393–3410. DOI: 10.1111/pce.14880

Martínez-García E., Nilsson M.B., Laudon H., Lundmark T., Fransson J.E.S., Wallerman J., Peichl M. (2024). Drought response of the boreal forest carbon sink is driven by understorey–tree composition. Nat Geosci, 17, 197–204. DOI: 10.1038/s41561-024-01374-9

Medlyn B.E., Dreyer E., Ellsworth D., Forstreuter M., Harley P.C., Kirschbaum M. U., Le Roux X., Montpied P., Strassemeyer J., Walcroft A., Wang K., Loustau D. (2002). Temperature response of parameters of a biochemically based model of photosynthesis. II. A review of experimental data. Plant Cell Environ, 25, 1167–1179. DOI: 10.1046/j.1365-3040.2002.00891.x

Meinzer F.C., Woodruff D.R., Marias D.E., Smith D.D., McCulloh K.A., Howard A.R., Magedman A.L. (2016). Mapping 'hydroscapes' along the iso- to anisohydric continuum of stomatal regulation of plant water status. Ecol Lett, 19, 1343–1352. DOI: 10.1111/ele.12670

Miyazawa S.I., Tobita H., Ujino-Ihara T., Suzuki Y. (2020). Oxygen response of leaf CO_2 compensation points used to determine Rubisco specificity factors of gymnosperm species. J Plant Res, 133, 205–215. DOI: 10.1007/s10265-020-01169-0

Mndela M., Tjelele J.T., Madakadze I.C., Mangwana M., Samuels I.M., Muller F., Pule H.T. (2022). A global meta-analysis of woody plant responses to elevated CO_2: implications on biomass, growth, leaf N content, photosynthesis and water relations. Ecological Processes, 11, 52–73. DOI: 10.1186/s13717-022-00397-7

Mokhov I.I. (2022). Climate change: causes, risks, consequences, and problems of adaptation and regulation. Herald Russ Academy Sci, 92(1), 3–14. DOI: 10.31857/S0869587322010066.

Molchanov A.G. (2007). CO_2 balance in ecosystems of pine and oak forests in different forest vegetation zones. Tula, 284 p.

Nadal M., Carriquí M., Flexas J. (2021). Mesophyll conductance to CO_2 diffusion in a climate change scenario: effects of elevated CO_2, temperature and water stress. In: Becklin K.M., Ward J.K., Way D.A. (eds) Photosynthesis, respiration, and climate change. Advances in photosynthesis and respiration, 48. Springer, Cham. DOI: 10.1007/978-3-030-64926-5_3

Nazarova L.E. (2021). Climatic conditions in the Republic of Karelia. In: Current conditions of water basins of the North. Petrozavodsk, 7–16 (In Russian).

Niinemets Ü., Flexas J., Peñuelas J. (2011). Evergreens favored by higher responsiveness to increased CO_2. Trends Ecol Evol, 26(3), 136–142. DOI: 10.1016/j.tree.2010.12.012

Norby R.J., DeLucia E.H., Gielen B., et al. (2005) Forest response to elevated CO_2 is conserved across a broad range of productivity. Proc Natl Acad Sci USA, 102 (50), 18052–18056. DOI: 10.1073/pnas.0509478102

Olchev A.V., Deshcherevskaya O.A., Kurbatova Y.A., Molchanov A.G., Novenko E.Y., Pridacha V.B., Sazonova T.A. (2013). CO_2 and H_2O exchange in the forest ecosystems of southern taiga under climate change. Doklady Biol Sci, 450(1), 173–176. DOI: 10.1134/S0012496613030216

Olchev A.V., Gulev S.K. (2024). Carbon flux measurement supersites of the Russian Federation: objectives, methodology, prospects. Izv Atmos Ocean Phys, 60 (Suppl 3), S428–S434. DOI: 10.1134/S0001433824700841

Olchev A.V. (2025). Estimation of carbon dioxide and methane emissions and absorption by land and ocean surfaces in the 21st century. Izv Atmos Ocean Phys, 61 (Suppl 1), S74–S100. DOI: 10.1134/S0001433825701166

Oleksyn J., Modrzynski J., Tjoelker M.G., Zytkowiak R., Reich P.B., Karolewski P. (1998). Growth and physiology of *Picea abies* populations from elevational transects: common garden evidence for altitudinal ecotypes and cold adaptation. Funct Ecol, 12, 573–590.

Oleksyn J., Żytkowiak R., Reich P.B., Tjoelker M.G., Karolewski P. (2000). Ontogenetic patterns of leaf CO_2 exchange, morphology and chemistry in *Betula pendula* trees. Trees, 14, 271–281. DOI: 10.1007/PL00009768

Onoda Y., Hikosaka K., Hirose T. (2005). The balance between RuBP carboxylation and RuBP regeneration: a mechanism underlying the interspecific variation in acclimation of photosynthesis to seasonal change in temperature. Funct Plant Biol, 32, 903–910. DOI: 10.1071/FP05024

Ow L.F., Griffin K.L., Whitehead D., Walcroft A.S., Turnbull M.H. (2008). Thermal acclimation of leaf respiration but not photosynthesis in *Populus deltoides*×*nigra*. New Phytol, 178, 123–134. DOI: 10.1111/j.1469-8137.2007.02357.x

Peel M.C., Finlayson B.L., McMahon T.A. (2007). Updated world map of Köppen-Geiger climate classification. Hydrol Earth Syst Sci, 11, 1633–1644. DOI: 10.5194/hess-11-1633-2007

Pridacha V.B., Makhmudova L.Sh., Semin D.E., Olchev A.V. (2022). Photosynthetic parameters of woody plant species in the foothills of northern Caucasian broadleaved forests. Grozny Natural Science Bulletin, 4(30), 105–112 (in Russian with English summary). DOI: 10.25744/genb.2022.74.70.009

Pridacha V.B., Sazonova T.A., Novichonok E.V., Semin D.E., TkachenkoYu.N., Pekkoev A.N., Timofeeva V.V., Bakhmet O.N., Olchev A.V. (2021). Clear-cutting impacts nutrient, carbon and water exchange parameters in woody plants in an east Fennoscandian pine forest. Plant Soil, 466, 317–336. DOI: 10.1007/s11104-021-05058-w

Pridacha V.B., Semin D.E. (2024). Clear-cutting effects on components of the carbon balance in a bilberry-type pine forest in southern Karelia. Ecosystem Transformation, 7(3), 64–83. DOI: 10.23859/estr-230505

Pridacha V.B., Tarelkina T.V., Neronova Ya.A.,Tumanik N.V. (2023). Significance of coordination between stem xylem traits and leaf gas exchange parameters during adaptation formation in some boreal species of Karelia. Botanicheskii Zhurnal, 108(7), 690–708. DOI: 10.31857/S000681362306008X

Reich P.B., Sendall K.M., Stefanski A., Rich R.L., Hobbie S.E., Montgomery R.A. (2018). Effects of climate warming on photosynthesis in boreal tree species depend on soil moisture. Nature, 562, 263–267. DOI: 10.1038/s41586-018-0582-4

Riikonen J., Mäenpää M., Alavillamo M., Silfver T., Oksanen E. (2009). Interactive effect of elevated temperature and O_3 on antioxidant capacity and gas exchange in *Betula pendula* saplings. Planta, 230, 419–427. DOI: 10.1007/s00425-009-0957-8

Rytter L., Rytter R.-M. (2016). Growth and carbon capture of grey alder (*Alnus incana* (L.) Moench.) under north European conditions – estimates based on reported research. Forest Ecol Manag, 2016, 373, 56–65. DOI: 10.1016/j.foreco.2016.04.034

Sage R.F., Kubien D.S. (2007). The temperature response of C_3 and C_4 photosynthesis. Plant Cell Environ, 30, 1086–1106. DOI: 10.1111/j.1365-3040.2007.01682.x

Scafaro A.P., Posch B.C., Evans J.R., Farquhar G.D., Atkin O.K. (2023). Rubisco deactivation and chloroplast electron transport rates co-limit photosynthesis above optimal leaf temperature in terrestrial plants. Nat Commun, 14, 2820. DOI: 10.1038/s41467-023-38496-4

Schmiege S.C., Griffin K.L., Boelman N.T., Vierling L.A., Bruner S.G., Min E., Maguire A.J., Jensen J., Eitel J.U.H. (2023) Vertical gradients in photosynthetic physiology diverge at the latitudinal range extremes of white spruce. Plant Cell Environ, 46, 45–63. DOI: 10.1111/pce.14448

Sellin A., Alber M., Jasińska A.K., Rosenvald K. (2022). Adjustment of leaf anatomical and hydraulic traits across vertical canopy profiles of young broadleaved forest stands. Trees, 36, 67–80. DOI: 10.1007/s00468-021-02181-0

Sellin A., Taneda H., Alber M. (2019). Leaf structural and hydraulic adjustment with respect to air humidity and canopy position in silver birch (*Betula pendula*). J Plant Res, 132, 369–381. DOI: 10.1007/s10265-019-01106-w

Sharkey T.D. (1985). Photosynthesis in intact leaves of C_3 plants: physics, physiology and rate limitations. The Botanical Review, 51, 53–105. DOI: 10.1007/BF02861058

Sharkey T.D. (2016). What gas exchange data can tell us about photosynthesis. Plant Cell Environ, 39, 1161–1163. DOI: 10.1111/pce.12641

Sharkey T.D. (2024). The end game(s) of photosynthetic carbon metabolism. Plant Physiol, 195(1), 67–78. DOI: 10.1093/plphys/kiad601

Sharkey T.D., Bernacchi C.J., Farquhar G.D., Singsaas E.L. (2007). Fitting photosynthetic carbon dioxide response curves for C_3 leaves. Plant Cell Environ, 30, 1035–1040. DOI: 10.1111/j.1365-3040.2007.01710.x.

Shiklomanov A.N., Cowdery E.M., Bahn M., Byun C., Jansen S., Kramer K., Minden V., Niinemets U., Onoda Y., Soudzilovskaia N.A., Dietze M.S. (2020). Does the leaf economic spectrum hold within plant functional types? A Bayesian multivariate trait meta-analysis. Ecological application, 30(3), 1–15. DOI: 10.1002/eap.2064

Stirbet A., Guo Y., Lazár D., Govindjee G. (2024). From leaf to multiscale models of photosynthesis: applications and challenges for crop improvement. Photosynth Res, 161, 21–49. DOI: 10.1007/s11120-024-01083-9

Sukhova E.M., Vodeneev V.A., Sukhov V.S. (2021). Mathematical modeling of photosynthesis and analysis of plant productivity. Biochem Moscow Suppl Ser A, 15, 52–72. DOI: 10.1134/S1990747821010062

Suvorova G.G., Popova E.V. (2015). Photosynthetic productivity of coniferous stands of the Irkutsk region. Novosibirsk, Geo, 95 p. (In Russian)

Togashi H.F., Prentice I.C., Atkin O.K., Macfarlane C., Prober S.M., Bloomfield K.J., Evans B.J. (2018). Thermal acclimation of leaf photosynthetic traits in an evergreen woodland, consistent with the coordination hypothesis. Biogeosciences, 15(11), 3461–3474. DOI: 10.5194/bg-15-3461-2018

TselnikerYu.L.(1982). A simplified method for determination of needle surface in pine and spruce trees. Russ J Forest Sci, 4, 85–88. (In Russian)

Tselniker Yu.L., Malkina I.S., Kovalev A.G., Chmora S.N, Mamaev V.V., Molchanov A.G. (1993). The growth and CO_2-exchange in forest trees. Nauka, Moskva, 256 p. (In Russian)

Vasfilov S.P. (2016). The effect of photosynthesis parameters on leaf lifespan. Biol Bull Rev, 6(1), 96–112. DOI: 10.1134/S2079086416010084

Veromann-Jürgenson L.-L., Tosens T., Laanisto L., Niinemets U. (2017). Extremely thick cell walls and low mesophyll conductance: welcome to the world of ancient living! J Experimental Botany, 68(7), 1639–1653. DOI: 10.1093/jxb/erx045

Vogel C.S., Curtis P.S. (1995). Leaf gas exchange and nitrogen dynamics of N_2-fixing, field-grown *Alnus glutinosa* under elevated atmospheric CO_2. Glob Change Biol, 1, 55–61. DOI: 10.1111/j.1365-2486.1995.tb00006.x

Von Caemmerer S. (2000). Biochemical models of leaf photosynthesis. CSIRO publishing, 165 p. DOI: 10.1071/9780643103405

Wullschleger S.D. (1993). Biochemical limitations to carbon assimilation in C_3-plants – a retrospective analysis of the A/Ci curves from 109 species. J Experimental Botany, 44(5), 907–920.

RESEARCH PAPER

NATURE-BASED SOLUTIONS: ASSESSING URBAN GREENSPACE AVAILABILITY IN ILIGAN CITY, PHILIPPINES

Audrey Rose A. Velayo[1], Peter D. Suson[1], Maricar M. Aguilos[2], Peng Zhao[3], Hernando P. Bacosa[1,*]

[1]Department of Environmental Science, School of Interdisciplinary Studies, Mindanao State University-Iligan Institute of Technology, Tibanga, Iligan City 9200, Philippines

[2]Department of Forestry and Environmental Resources, North Carolina State University, Raleigh, NC 27606, USA

[3]State Key Laboratory of Marine Resources Utilization in South China Sea, Hainan University, Haikou, 570228 Hainan, China

***Corresponding author:** hernando.bacosa@g.msuiit.edu.ph

Received: September 27th 2025 / Accepted: November 12nd 2025 / Published: December 31st 2025

https://doi.org/10.24057/2071-9388-2025-3627

ABSTRACT. The continuous growth of urban areas, driven by population increase and commercial expansion, has led to urban problems like heat islands, pollution, and environmental damage. Greenspaces, defined as 'green' areas within cities that offer various advantages for human welfare and environmental quality, have become a vital strategy for addressing these significant urban issues. However, despite their clear advantages, the growth of greenspaces, particularly in the Philippines, is hindered by rapid urbanisation and an overemphasis on built infrastructure. Although extensive research exists on formal urban greenspaces, studies on informal greenspaces, especially within the Philippine context, have been limited. This study defines formal urban greenspaces as officially managed areas, such as parks, and informal urban greenspaces as unmanaged areas, like vacant lots or riverbanks. Surveys were conducted with 187 stakeholders from various sectors in Iligan City to identify their preferred nature-based solutions (NBS) and intervention types. GIS mapping was performed using quickOSM and Google Satellite through QGIS software version 3.4 to gather data on existing urban greenspaces per capita in Iligan City. The collected data were analysed using descriptive and frequency statistics. The findings indicated that mangrove restoration (62%) and urban tree planting (55%) were the most preferred interventions. GIS results showed that 72% of urban barangays failed to meet the WHO's minimum greenspace standard of 9 m2 per capita, with an average of 5.7 m^2 (SD = 2.3). The study recommends that future initiatives should concentrate on developing and expanding formal urban green spaces in the city's urban barangays by incorporating informal greenspaces into urban planning and improving greenspace management.

KEYWORDS: Urban green spaces, Nature-based solution (NBS), GIS mapping, Sustainable urban planning

CITATION: Velayo A. R. A., Suson P. D., Aguilos M. M., Zhao P., Bacosa H. P. (2025). Nature-Based Solutions: Assessing Urban Greenspace Availability In Iligan City, Philippines. Geography, Environment, Sustainability, 4 (18), 103-114
https://doi.org/10.24057/2071-9388-2025-3627

ACKNOWLEDGEMENTS: The authors would like to acknowledge the local government of Iligan City for their cooperation and support in completing the data collection for this study. They also thank Mr John Liwanag for his support during the data analysis. The first author is grateful to the Department of Science and Technology (DOST) for the scholarship provided through the Accelerated Science and Technology Human Resource Development Programme (ASTHRDP).

Conflict of interests: The authors reported no potential conflict of interests.

INTRODUCTION

As cities continue to grow and modernise, the balance between urban development and environmental preservation has become increasingly fragile. The rise of advanced technologies and industrialisation has undoubtedly transformed economies, but it has also brought about rapid urban expansion and significant environmental costs. (Beltikian, D. 2019). Recent data shows that 56% of the world's population lives in urban cities, and this figure might accelerate further, doubling its number by the year 2050 (World Bank, 2023). Moreover, according to the United Nations Conference on Trade and Development (UNCTAD), the growing urban areas and population occur at different rates but have been more noticeable in developing countries, particularly in Asia (Blachier, 2022; Foresight, 2023). Urbanisation has also been closely linked to the worsening of climate-related risks. As land cover changes and carbon sinks are lost to expanding grey infrastructure, urban areas contribute significantly to greenhouse gas emissions and the intensification of the greenhouse effect (Xu et al., 2016; Trenberth et al., 2015; WHO, 2013). These dynamics increase the frequency and severity of extreme weather events, such as the devastating floods seen in countries like Pakistan (Mann, 2017; Petoukhov, 2013). Global trends in urbanisation and environmental change are now visibly reflected at the local level, where rapid urban growth is transforming cities and increasing environmental risks. For instance, in the

Philippines, about 54% of the population, approximately 58.93 million individuals, live in urban spaces. This is due to the centralisation of most economic activities in cities, where citizens choose to migrate from rural to urban areas for occupational opportunities, better education, and hope for good living conditions (PSA, 2020; Mojares, 2013). However, challenges and environmental risks have been rising due to rapid urban population growth and centralisation in highly urbanised cities in the Philippines. Thus, there has been an extensive need for urban management and development to address the challenges posed by rapid urbanisation in most cities (Delos Reyes et al., 2020; Estoque, 2022).

On the other hand, urban greenspaces (UGS) are recognised as playing a crucial role in addressing the urban challenges found in most cities. These include environmental degradation, air pollution, and urban heat island effects, which can be managed through sustainable urban development that considers land use in urban areas and transforms concrete jungles into smart green cities (Addas, 2023). UGS are defined as areas of greenery or vegetation within city boundaries. They are vital for promoting sustainable land use, improving urban environmental conditions, and enhancing the overall well-being of city dwellers. Examples include parks, garden patches, nature reserves, grasslands, and other types of greenery (Subedi and Pokhrel, 2023). Two types of UGS commonly found in urban areas are formal UGS and informal UGS. Formal UGS are urban greenspaces that are officially recognised, designated, and managed by government authorities and organisations. These are often recreational spaces such as parks, playgrounds, nature reserves, allotment greens, and even cemeteries. Informal UGS, however, are unmanaged greenspaces or areas unofficially designated, often arising from spontaneous resident initiatives. Examples include vacant lots, green patches, pocket gardens in residential areas, and greenery along riverbanks (Pietrzyk-Kaszyńska, Czepkiewicz, and Kronenberg 2017; Falchetta and Hammad, 2023). Several studies have highlighted the positive impacts of these spaces. They enhance air and water quality, improve environmental conditions in urban areas, encourage social activities, and promote a better quality of life for city residents (Falchetta and Hammad, 2023; Revich, 2023; Addas, 2023). However, the availability of greenspaces is limited in countries like the Philippines. Their expansion has encountered various challenges due to rapid urbanisation, and urban planning in most cities tends to focus more on 'grey spaces' (Alejandre et al., 2022; Gonzales and Magnaye, 2016). While most studies have concentrated on formal urban greenspaces, research on informal greenspaces remains limited, particularly in the Philippines.

Thus, this study generally aims to assess the disparities in available urban greenspaces among the urban barangays of Iligan City. Specifically, this study aims to (1) determine the various stakeholder preferences and priority nature-based solutions interventions for Iligan City, (2) generate a spatial distribution map of informal and formal urban greenspaces in the study areas, and (3) determine the adequacy of available greenspaces per capita in the urban communities.

MATERIALS AND METHODS

Study Area

In the northern region of Mindanao, Iligan City is classified as a highly urbanised, single-district city within the province of Lanao del Norte (Fig.1). It has an estimated population of 363,115 and a population density of 446 km^2, with an average household size of 4.2 (PSA, 2020). Iligan City's terrain varies from the coast to the mountains, covering a total land area of 813.37 km^2. The rapid urban expansion in Iligan City has placed significant pressure on its natural ecosystems. This has led to changes such as an increase in urban land area and the urban heat island effect, caused by reduced vegetation and dense populations (Trinidad, 2007; US EPA, 2025). The study was conducted and focused on the urban barangays of Iligan City. These include Barangays Acmac, Bagong Silang, Buru-un, Dalipuga, Del Carmen, Ditucalan, Kiwalan, Mahayahay, Maria Cristina, Pala-o, Poblacion, Puga-an, San Miguel, Santiago, Sta. Filomena, Suarez, Tambacan, Tibanga, Tomas Cabili, Upper Hinaplanon, and Villaverde. A 'barangay' is the smallest territorial and administrative local unit in the Philippines.

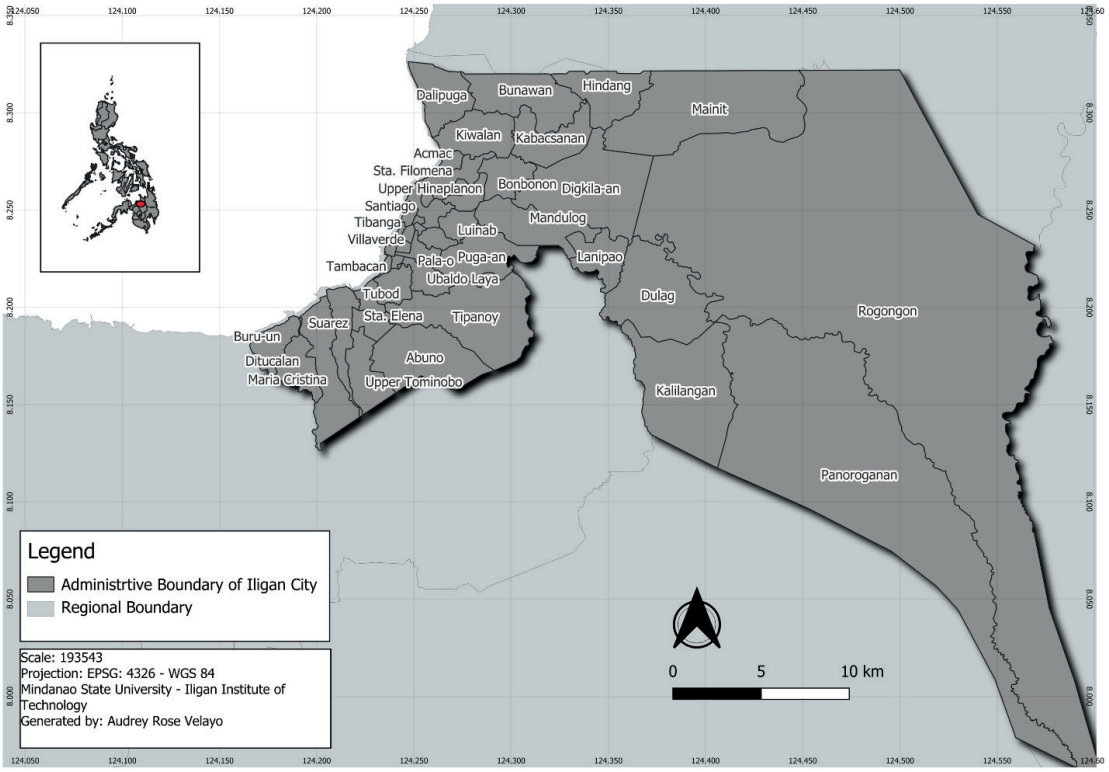

Fig. 1. Map of Iligan City, Philippines, showing its 44 barangays. The barangay is the smallest political unit in the Philippines

This study follows a cross-sectional quantitative design. A descriptive research design was used to collect socio-demographic data and stakeholder preferences, and to calculate the available greenspace per capita per urban barangay in Iligan City.

Stakeholder Survey

This study employed a purposive sampling method to gather a sample of 187 stakeholders from Iligan City (Etikan et al., 2016). An adapted questionnaire from Ferreira et al. (2022), presented in Appendix Fig. A.3, was used to determine stakeholder preferences and prioritise interventions. The questionnaire included items such as, 'Considering current and future challenges and priority interventions, which of the following solutions are essential? (select up to five options and rank them from most to least important)' and 'Among your selected five essential interventions, rank them by importance and priority.'

Before collecting data, the researcher identified potential participants by listing all city stakeholders. This list was then narrowed down to agencies and organisations involved in environmental planning, development, implementation, and resilience in Iligan City. Participants were selected based on the following criteria: (1) they were bona fide residents of the city, (2) they were at least 18 years old, (3) they were employees and experts from local and national government or non-government organisations, academia, and private sectors involved in environmental planning, development, implementation, and resilience, and (4) they represented all genders. Data collection took place on-site. Participants were given an informed consent form that outlined the study's title and main purpose.

Urban Green Spaces and Data Sources

Data on both formal and informal urban green spaces across the different barangays of Iligan City were collected using Geographic Information System (GIS) technologies, specifically through QGIS software and Google Satellite imagery. The QuickOSM plugin in QGIS was employed to extract OpenStreetMap (OSM) data, which served as the initial base map for identifying greenspaces. To enhance the accuracy and completeness of the dataset, manual digitisation was conducted, such as creating vector layers by tracing lines and polygons of visible greenspaces. The total area in square metres of the existing UGS in Iligan City per urban barangay and their population was also gathered from existing data from the local government units of Iligan City, including the barangay local government units. This information was then used as a basis to calculate greenspaces per capita for each barangay.

Limitations of the Study

The scope of this study is limited to assessing the availability of current green spaces in the urban barangays of Iligan City against the World Health Organization standard of 9 m^2 per capita. It also includes an analysis of preferred nature-based solutions among stakeholders in Iligan City. The study did not account for the people's organisation sector. It is recommended for future studies on nature-based solutions and stakeholders to include the people's organisation sector for more inclusive data representation. Furthermore, future studies should compare and analyse tree canopy cover and vegetation cover for each urban barangay in Iligan City. It is also strongly recommended that future studies expand the sample size and scope to assess other types of nature-based solutions beyond green spaces.

Data Analysis

To understand the differences and patterns in how various sectors view greenspaces in Iligan City, frequency and distribution statistics were used to analyse stakeholder preferences and priority interventions. The sociodemographic profile of the respondents, including age, gender, educational attainment, sector, income, years of residence, and civil status, was also analysed. These were calculated using descriptive statistics (frequency, mean, and percentage) in Microsoft Excel 2022.

For this part of the analysis, data gathered on urban greenspaces from quickOSM and Google Satellite through QGIS software, such as area and coordinates for greenspaces per capita, were analysed using frequency and descriptive statistics in Jamovi ver 2.3.28. The analysis focused on the size and distribution of green spaces per capita across Iligan's urban barangays. Descriptive statistics were combined with spatial mapping data, guided by the method used in a study by Laghai and Bahmanpour (2021).

RESULTS

Respondent's profile

This study involved 187 participants from various stakeholder sectors in Iligan City. As shown below in Fig. 2, most respondents were female (62.6%), with the remainder being male (37.4%). Among them, most were married (48.7%), followed by single individuals (44.4%), separated individuals (2.1%), and widowed individuals (4.8%). Additionally, the educational background of most stakeholders was college graduates (81.8%), followed by master's graduates (8.0%). Only a small percentage were college undergraduates (1.6%), which can be seen below in the appendix section (Fig. A. 1 and Fig. A. 2).

The sampled stakeholders represented four sectors, with 40% from the local government unit (LGU), 33.7% from the academe sector, 13.4% from non-governmental organisations (NGOs), and 12.3% from the private sector.

Stakeholder priority NBS types

Figure 3 shows the different types of nature-based solutions chosen as priority interventions by stakeholders from the four sectors: the private sector, academe, local government units (LGUs), and non-governmental organisations (NGOs). The results indicate that mangrove

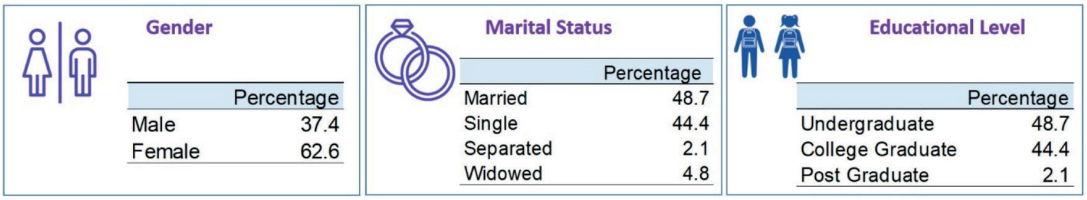

Fig. 2. Percentage distribution of stakeholders by sector, based on respondents; N=187 (Velayo et al. 2024)

restoration and conversion were the highest priority across all sectors. Most private sector stakeholders chose mangrove restoration and conservation (21.74%) and urban trees (21.74%) as priority nature-based solutions. These were followed by drainage corridors (13.04%) and riverbank rehabilitation (13.04%). The least preferred nature-based solutions among private sector stakeholders were stormwater pits (4.35%), green barriers (4.35%), and natural pools (4.35%).

Meanwhile, stakeholders from academia have chosen mangrove restoration and conservation as the most prioritised type of nature-based solution (36.51%). This was followed by urban trees (15.87%), and then riverbank rehabilitation (12.70%). The least chosen types of nature-based solutions in academia were wetlands and floodable parks (1.59%), followed by green barriers (3.17%). Similarly, most stakeholders in the local government unit (LGU) sector have also chosen mangrove restoration and conservation (32.89%) as a priority nature-based solution for climate action, followed by urban trees (26.32%). Lastly, most stakeholders from non-governmental organisations (NGOs) also responded that mangrove restoration and conservation (40.00%) is a priority nature-based solution. The least chosen nature-based solutions among the NGO sector were natural pools (4.00%) and green barriers (4.00%).

Figure 3 shows that mangrove restoration and conservation are the most prioritised type of Nature-based Solution (NBS) among various stakeholders (32.1%). The second most prioritised is urban trees (19.3%), followed by riverbank rehabilitation (14.4%). This implies that mangrove restoration as an NBS for addressing environmental issues, such as climate change impacts, is considered significant by most stakeholders. This further suggests that stakeholders from various sectors share a similar understanding of the importance and benefits of ecosystem services associated with mangrove ecosystems. Other types of NBS, such as green infrastructure, are also mentioned (Juanico, 2022). Iligan City has faced several challenges in sustainability and infrastructure development. These challenges include a growing population, the risk of natural disasters, poverty, and various environmental issues (Uniaty, 2015).

Mangrove restoration plays a key role in cities with coastal areas like Iligan City. Its proper management helps mitigate environmental degradation caused by human activities and also provides various ecosystem services, such

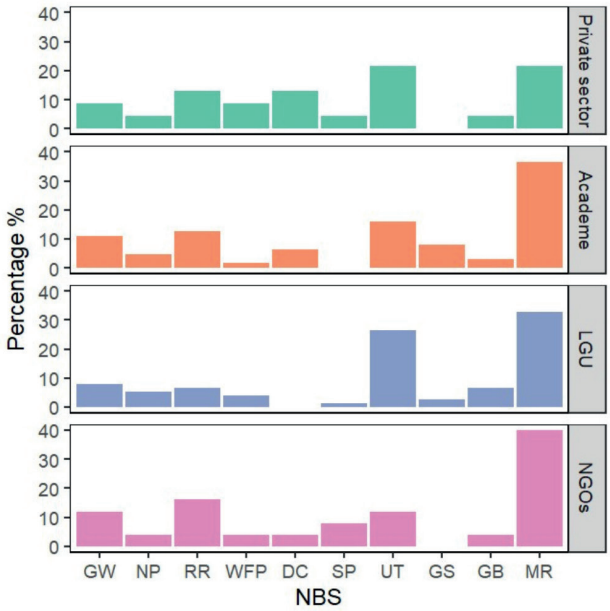

Fig. 3. Percentage distribution of the type of priority nature-based solutions among all stakeholders. Green walls (GW), natural pools (NP), rehabilitation of riverbanks (RR), wetlands and floodable parks (WFP), drainage corridors (DC), stormwater pits (SP), urban trees (UT), green shadows (GS), green barriers (GB), mangrove rehabilitation (MR)

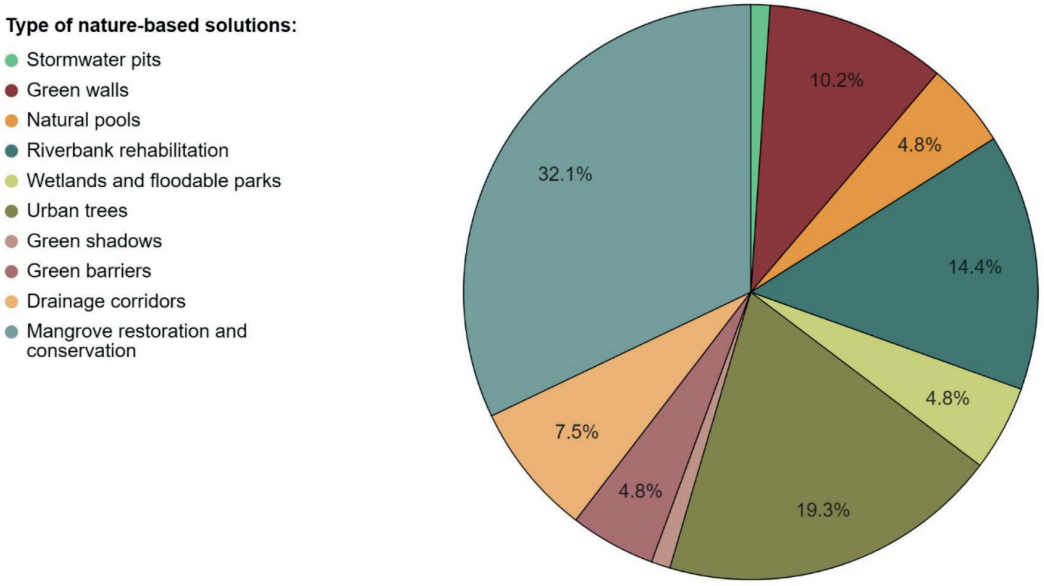

Fig. 4. Types of priority nature-based solutions across the four different sectors

as coastal protection and economic benefits to residents (De Juan, Gelcich, and Fernandez, 2017; Agustriani et al. 2023; Hilmi, Usman, and Iqbal, 2023). The strong preference for mangrove restoration indicates a wider recognition of the urgent need for ecosystem-based adaptation (EbA) strategies in urban planning. Furthermore, prioritising mangrove conservation and restoration aligns with ecosystem-based adaptation (EBA), which emphasises the crucial role of natural solutions for addressing urban challenges and climate change impacts (O'Leary et al., 2023).

Standard urban greenspace per capita and quantity in the urban barangays of Iligan City

Fig. 5 illustrates the spatial distribution of existing formal and informal greenspaces among the urban barangays in Iligan City. Most of the existing formal and informal greenspaces are clustered in more developed and built-up areas.

As shown in Table 2, Barangay Ubaldo Laya and Luinab have no existing formal greenspaces. However, despite this, both barangays have a significant number of informal greenspaces compared to other urban barangays in Iligan City. For instance, Barangay Ubaldo Laya has riverside, residential, and grassland informal greenspaces, while all informal greenspaces in Barangay Luinab are residential. This suggests that Barangay Ubaldo Laya is situated alongside natural and underdeveloped areas along riverbanks. These areas may offer several ecological and economic benefits to the local communities in Barangay Ubaldo Laya. They also have potential for recreational activities for the residents, such as passive and light physical activities, including community events (Barsukova et al., 2022).

This finding of an uneven number of formal greenspaces to informal greenspaces in urban barangays of Iligan City shows that while unmanaged vegetated areas provide ecosystem services and recreational value, their lack of formal recognition may limit their protection from development pressures. This is especially true in cities where urbanisation is rapid, like Iligan City (Biernacka et al., 2023).

Greenspaces in urban areas provide for the recreational needs of most residents within their localities, such as relaxation, leisure, and outdoor social activities, thus enhancing physical and mental well-being among residents. Consistent with this, a study by Turna (2022) in India found that urban greenspaces in cities are vital for recreational purposes among communities. It encourages outdoor activities and contributes to the enhancement of residents' quality of life. Another study by Huang et al. (2022) in China examined the behaviours among citizens and the role of the summer heat experienced in the city of Fuzhou. They found that the high temperatures impact public behaviours and that urban greenspaces play a significant role in remediating the urban thermal environment present in the city, promoting enhanced public health among residents.

Furthermore, as shown in Table 2, various barangays, such as Luinab, Tubod, Tipanoy, and Hinaplanon, are dominated by informal greenspaces rather than formal ones like residential and grassland types. This indicates that informal green spaces are widespread among residential neighbourhoods. It suggests that these areas host informal greenspaces, possibly due to residents' initiatives to create their own green spaces in various forms, such as backyard gardens, vacant lots, and green patches (Christoph et al., 2017). Consistent with this, multiple studies in Asia have found the crucial role of residents in informal greenspaces. For instance, a study conducted by Cedamon (2009) in

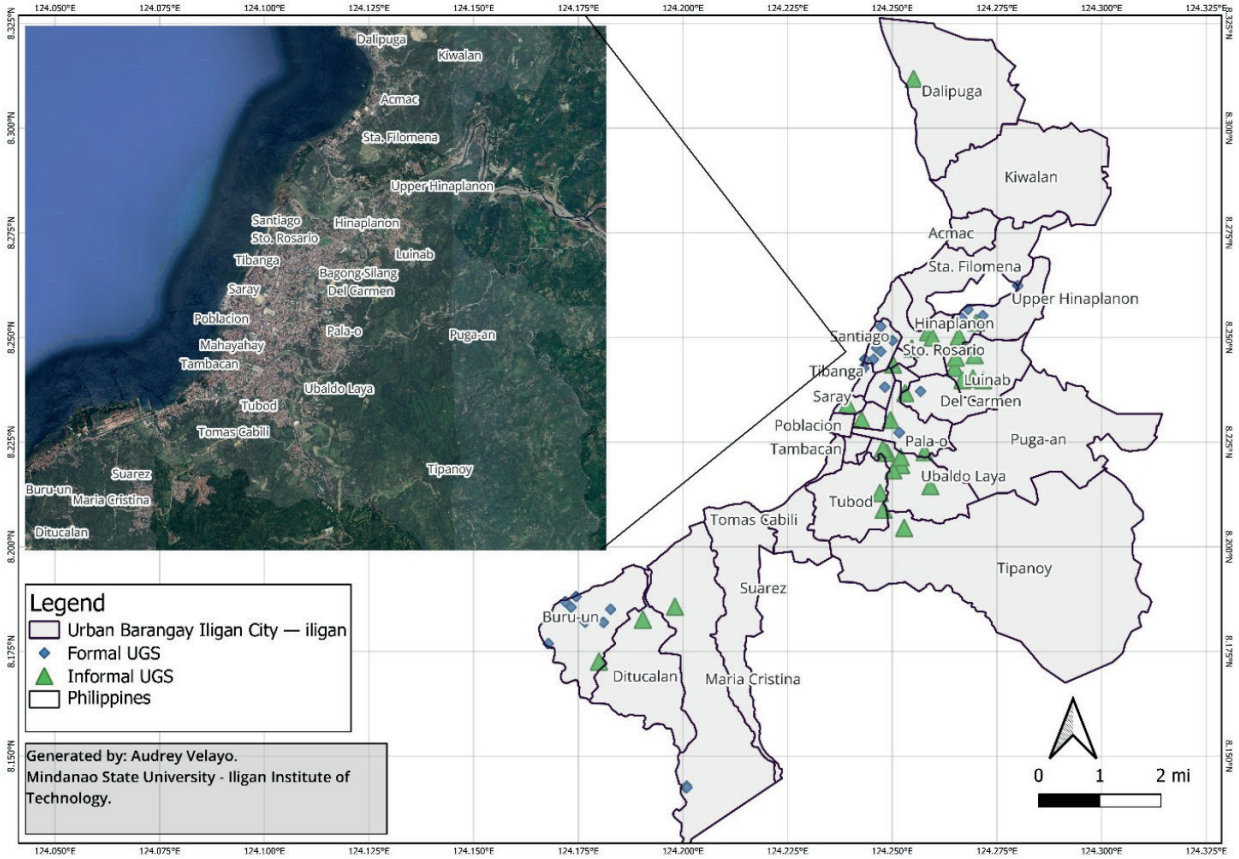

Fig. 5. The urban barangays in Iligan City and their formal and informal urban greenspaces. The green triangle icon represents the location of informal UGS, and the blue diamond icon represents the location of formal UGS. Default CRS projection: EPSG:4326 - WGS 84

Table 2. Classification of urban greenspace found in the urban barangays of Iligan City and their numbers

Barangay	Type of green areas	Count	Urban greenspace classification
Ubaldo Laya	RiversideResidentialGrassland	231	InformalInformalInformal
Pala-o	CemeteryRoadsidePark	112	FormalInformalFormal
Kiwalan	PitchSchool greenery	11	FormalFormal
Tubod	Grassland	2	Informal
Tipanoy	Residential	1	Informal
Villa-verde	CemeteryPark	11	FormalInformal
Saray	Grassland	1	Informal
Buru-un	ResidentialResortPlayground	131	InformalFormalFormal
Maria-Christina	PrivatePark	11	InformalFormal
Hinaplanon	ResidentialGrassland	21	InformalInformal
Upper-Hinaplanon	ResidentialPitch	14	InformalFormal
Del Carmen	RecreationalPlayground	11	InformalFormal
Dalipuga	RecreationalRecreational	11	InformalFormal
Sto.Rosario	Grassland	1	Informal
Sta. Filomena	Cemetery	1	Formal
Santiago	PlaygroundPitch	11	FormalFormal
Tibanga	Pitch	2	Formal
Luinab	Residential	6	Informal
Tomas Cabili	Pitch	1	Formal
Ditucalan	Residential	1	Informal

Leyte found that initiatives by local government units within barangays led to efforts, particularly with Leyte's active residents, to manage informal greenspaces in their communities (Thahir, 2016; Dangol, 2019). Informal green spaces, especially in residential areas of urban cities, typically result from residents' initiatives as they offer various benefits, such as recreational value and enhancement of the urban environment for the community (Katalin, 2019; Cipriano & Garcia, 2019; Mahmoudi et al., 2019).

Meanwhile, as shown in Figure 6A, informal greenspaces are more prevalent than formal greenspaces in the urban barangays of Iligan City. This suggests that the city's urban landscape is defined by a greater presence of unmanaged or natural green areas compared to formally designated and managed green spaces within its urban barangays.

Aside from resident initiatives in forming informal greenspaces, several factors may also contribute to the insufficient formal greenspaces and abundance of informal greenspaces in an area. These include neglected maintenance of certain areas leading to informal greenspace, urbanisation constraints, a lack of municipal capacity, and resource allocation for the management of green spaces (Katalin, 2019; Piotr et al., 2021). Several studies have also highlighted the importance and the need for proper regulation and utilisation of unmanaged areas along rivers. For instance, these areas naturally restore barren lands or unmanaged areas along riverbanks to facilitate comfortable recreational spaces while accounting for the preservation of existing natural landscapes (Demashkieh, 2022; Barsukova et al., 2022; Olaj & Fikfak, 2012).

Another important consideration is not only the number of green spaces but also their size. According to the World Health Organization, the recommended standard for every city is at least 9 m2 of greenspace per individual (Russo and Cirella 2018). Table 3 presents the available urban greenspaces per capita in every urban barangay in Iligan City. Among the urban barangays, Tomas Cabili exhibits the highest amount of formal greenspace per capita, at 16.11 m^2. This is followed by Barangay Santiago with a greenspace per capita value of 13.98 m^2, and then by Barangay Sta. Filomena (12.04 m2/capita). This suggests that these urban barangays in Iligan City offer residents sufficient access to greenspaces for various opportunities for outdoor recreation and leisure activities.

Meanwhile, Barangays Hinaplanon (10.86 m2/capita), Tambacan (11.89 m^2/capita), and Pala-o demonstrate a moderate amount of formal greenspaces. These fall just above the minimum standard of 9 m^2 per capita recommended by the World Health Organization. This suggests that the efforts of local authorities and residents in these urban areas are sufficient to meet the minimum standard for city greenspaces. Enhancing and expanding green spaces, particularly in urban environments, helps to counter the negative effects of increasing urbanisation worldwide. This is achieved by reducing pollution, promoting sustainable land use, and improving urban ecosystems (Giorgo et al., 2022; Samfira, 2022).

In contrast, Barangays Acmac (3.57 m^2/capita), Bagong Silang (0.64 m^2/capita), Del Carmen (0.70 m^2/capita), Ditucalan (0.16 m^2/capita), Mahayahay (0.78 m^2/capita),

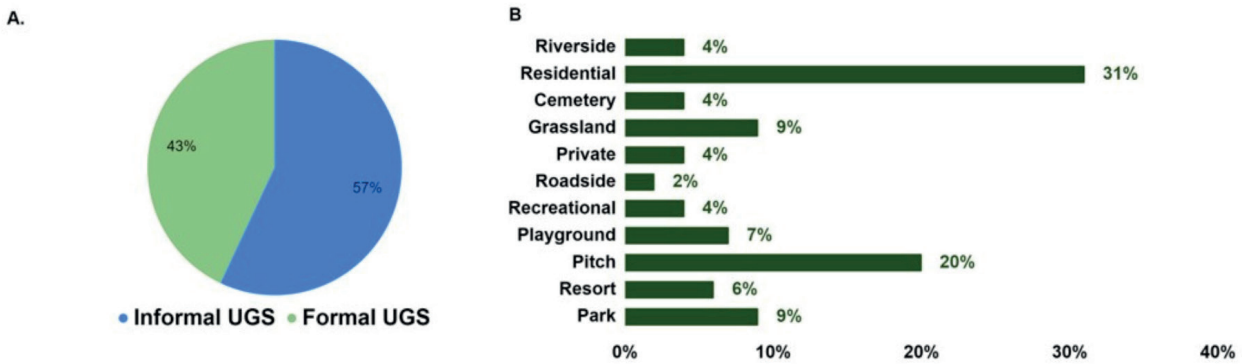

Fig. 6. A. Percentage distribution showing the proportion of formal and informal UGS. B. Percentages of the types of formal and informal UGS found in Iligan City. Informal UGS N=31, Formal UGS N=19

Table 3. Available formal greenspace per capita among the urban barangays in Iligan City

Barangay	Population	Available greenspace (sqm)	Available greenspace per capita (m^2)
Tomas Cabili	9676	600.45	16.11
Santiago	9212	659.10	13.98
Sta. Filomena	7005	581.74	12.04
Tambacan	19 261	1620.07	11.89
Pala-o	10 778	944.67	11.41
Upper Hinaplanon	6551	603.24	10.86
Dalipuga	21 470	2930.40	7.33
Buru-un	16 835	2616.99	6.43
Kiwalan	7710	1872.57	4.12
Acmac	6856	1921.11	3.57
Suarez	18 649	11 351.21	1.64
Maria Cristina	11 811	8078.96	1.46
Poblacion	3613	2619.65	1.38
Tibanga	8089	7571.17	1.07
Villaverde	5514	6144.51	0.90
Mahayahay	7965	10 251.64	0.78
Del-carmen	9662	13 836.37	0.70
Bagong Silang	6104	9539.14	0.64
San Miguel	3801	13 085.18	0.29
Ditucalan	4039	26 033.27	0.16
Total:	217 443	140 478.69	Mean greenspace per capita: 5.57

Poblacion (1.38 m^2/capita), and Villa Verde (0.90 m^2/capita) fall below the minimum World Health Organisation recommended greenspace per capita. Overall, the existing urban greenspace in Iligan City totals 5.57 m^2/capita, indicating that Iligan City does not meet the minimum greenspace standard. This highlights the need for local authorities and other concerned groups to address the lack of formal greenspaces in these urban barangays of Iligan City. The absence of available formal green spaces, particularly in urban areas, can present various challenges to residents' well-being and the general urban environment. For example, a study by Keh et al. (2023) found that residents' well-being is jeopardised by the negative consequences of natural greenspace destruction, as these urban greenspaces are crucial for fostering social interaction and human health. Furthermore, another study conducted by Addas (2023) stressed the significance of expanding greenspaces for the development of an intelligent city, promoting an improved quality of life for residents, better urban environmental conditions, and crucially, to tackle the threats posed by climate change in cities.

DISCUSSIONS

This study received responses from a total of 187 participants representing various stakeholders in Iligan City to assess their preferences for different types of nature-based solutions. The participants' profiles showed diversity in both gender and educational attainment. The majority of responses came from the city's local government unit. This indicates the significant roles these sectors play in urban, environmental planning, and policy development in Iligan City. However, the participant pool for this study also revealed limited engagement from non-governmental organisations (NGOs) and the private sector. This underrepresentation restricts stakeholder inclusivity, which may limit opportunities for cross-sectoral collaboration, especially in integrating solutions that address local issues. Furthermore, this underrepresentation also highlights another limitation of the study's sample. Therefore, this paper recommends a more inclusive and representative approach to stakeholder mapping for future research. Meanwhile, mangrove restoration and conservation emerged as a highly prioritised nature-based solution among all stakeholders in Iligan City, suggesting a shared perception of their value in addressing the city's needs. For coastal cities like Iligan, this finding underscores the importance of mangroves for climate adaptation, particularly regarding ecosystem services such as mitigating storm surges and flooding. Moreover, these findings align with broader literature on ecosystem-based adaptation (EbA), where mangrove conservation is recognised as a cost-effective and efficient solution to environmental degradation and climate change impacts (Cuenca-Ocay, 2024).

Based on international guidelines, such as the World Health Organization's standard of around 9 m^2 of green space per capita, the findings of this study reveal that the green spaces in the urban barangays of Iligan City are well below this target. This result is similar to other growing cities. For example, a study by Nambazo and Nazombe (2024) reports that 20% of Malawian neighbourhoods fail to meet the 9 m^2 standard, particularly in high-density districts. Likewise, similar findings have emerged in other Philippine cities. In a study by Ibañez et al. (2024), results showed that Pasay City falls below the World Health Organization's minimum required green space per capita. Projections suggest a need for an additional 925.72 m^2 of green space by 2032 to meet the needs of its growing population. The inadequacy and limited availability of urban green spaces can have profound detrimental impacts, affecting both environmental and socioeconomic aspects for urban dwellers (Gbadegesin et al., 2024; Uslu et al., 2024). The inadequacy and limited availability of urban green spaces in most urban barangays in Iligan City highlight the need for urban green planning focused on improving both the accessibility and availability of these spaces.

The results of this study also found an uneven number of formal and informal greenspaces in the urban barangays of Iligan City. This finding indicates disparities in the distribution of urban greenspaces across Iligan's barangays. Some areas in barangays such as Tomas Cabili, Santiago, and Sta. Filomena surpass the World Health Organisation's (WHO) minimum standard of 9 m^2/capita, while others, including Ditucalan, Mahayahay, and Villa Verde, remain critically below this threshold. This suggests uneven access to greenspaces among residents in Iligan City. Meanwhile, resident-managed greenery in barangays like Ubaldo Laya and Luinab plays an important compensatory role by providing ecological and social functions where formal greenspaces are lacking. While these unmanaged vegetated or informal greenspaces, such as riverbanks, vacant lots, and residential greenery, offer important ecosystem services and recreational benefits, their lack of formal recognition may leave them vulnerable to various types of development such as infrastructure, particularly in rapidly urbanising cities like Iligan City. Globally, regions with dense urbanisation often see uneven greenspace access. Cities in countries from the Global South have received far less cooling and air-quality benefits from urban vegetation than their northern counterparts (Li et al., 2024). In this study's findings, Iligan City's formal parks and large green areas appear to be concentrated in select zones, leaving other neighbourhoods largely devoid of vegetative or green cover. Similar patterns have been observed elsewhere in the Philippines. For example, Banguilan (2024) found that in Metro Manila, most localities scored below the 9 m^2/person standard advocated by the WHO, with greenspace clustered in specific areas. Thus, the uneven distribution of greenspaces across Iligan City's urban barangays highlights broader urban planning challenges, particularly in terms of accessibility and equity. Those barangays with adequate greenspaces benefit from improved recreation opportunities, reduced urban heat, and enhanced public health, while those barangays that were found to be critically below the WHO standard may likely face greater exposure to environmental and social risks. The underrepresentation of formal greenspaces and the undervaluation of informal ones in Iligan City underscore the urgent need for inclusive urban planning that formally integrates both types of greenspaces into local development agendas to ensure environmental equity and long-term climate resilience.

Furthermore, the study's results found that most types of greenspaces in several urban barangays, such as Luinab, Tubod, Tipanoy, and Hinaplanon, are dominated by residential and grassland types. This suggests that these areas contain informal greenspaces that may have emerged from resident initiatives within these barangays. These efforts might include creating green spaces in various forms, such as backyard gardens, vacant lots, and green patches (Christoph et al., 2017). Consistent with other studies, most informal greenspaces, like backyard gardens, residential greenery, and green patches, have also been seen as a result of community-driven initiatives. Although these informal greenspaces offer significant recreational and environmental benefits to urban well-being and its residents, their lack of formal recognition, often being spontaneous and undermanaged, may make them vulnerable to various urban developments (Rupprecht & Byrne, 2017; Thong et al., 2024). Meanwhile, several studies highlight the crucial role of community-led initiatives in improving the management of these informal greenspaces. For example, a study in Beijing, China, showed how resident-driven regeneration practices, such as small-scale gardening, have played a significant role in public space renewal in historical communities and their greenspaces through spontaneous actions and resident participation (Zhang & Xin, 2023). In line with this, another study by Eslit (2023) in Barangay Acmac revealed how community-led initiatives have emerged as a significant driver of local environmental protection. It highlighted their empowering process through a bottom-up approach, which has enabled residents to engage in collaborative decision-making and sustainable practices for local environmental protection.

CONCLUSIONS

Overall, the results of this study demonstrate aspects of urban green planning in Iligan City. Among the stakeholders in Iligan City, mangrove restoration and urban trees are the most preferred and priority nature-based solutions (NBS) types for Iligan City. This is followed by urban trees, highlighting a shared understanding among various stakeholders regarding their importance for protection, enhancing urban environments, and their socio-economic benefits. Moreover, disparities in formal and informal greenspaces are present among the urban barangays in Iligan City, with informal greenspaces being more abundant than existing formal urban greenspaces. In addition, most urban barangays fall behind the recommended standard greenspace per capita set by the World Health Organisation (WHO) for cities. Thus, this study suggests a multi-stakeholder approach that also includes community participation for comprehensive urban green planning. This aims to accelerate community-led initiatives for managing informal greenspaces and for the enhancement of formal greenspace development, protection, and maintenance. This would satisfy the World Health Organisation Standards for greenspace per capita in the urban barangays of Iligan City. It also involves the conversion of informal green spaces (e.g. vacant lots, grasslands, residential greenery, and underdeveloped areas) into formal greenspaces like pocket parks, urban trees, and green barriers. This can be achieved through strengthened urban land use plans that prioritise greenspace development and by incorporating informal urban greenspaces into the urban planning frameworks of the city government and barangay local government, in collaboration with other sectors and government agencies. However, it is important to note that green spaces found in private lands and properties may be subject to further consideration due to potential legal concerns and restrictions. Furthermore, this study has found an abundance of residential types of informal greenspaces among the urban barangays of Iligan City, indicating resident-driven initiatives. Hence, it is also recommended that local authorities and other concerned groups provide incentives for these informal residential types of greenspaces among residents as part of Iligan City's overall effort in enhancing urban greenspaces.

REFERENCES

Alejandre, J. C., Nasudi, G., Soluta, C., & Lynch, J. (2022). Child-centered and nutrition-sensitive green spaces: Policy recommendations for childhood obesity prevention in the Philippines' urban poor communities. HPHR Journal. https://doi.org/10.54111/0001/kkk5

Agustriani, F., Iskandar, I., Yazid, M., & Fauziyah, N. (2023). Economic valuation of mangrove ecosystem services in Sembilang National Park of South Sumatra, Indonesia. Hu'nan Daxue Xuebao. Ziran Kexue Ban, 50(1), 156–166. https://doi.org/10.55463/issn.1674-2974.50.1.16

Artur, O., & Fikfak, A. (2012). Urbani ob vodni javni prostor – reka kot razvojni generator / Urban riverside public space – river as the generator of development.

Banguilan, Y. J. T. (2024). Analysis of urban green space distribution in Metro Manila, Philippines using remote sensing and geographic information system techniques. University Knowledge Digital Repository. https://www.ukdr.uplb.edu.ph/etd-undergrad/11581/

Barsukova, N., Pallotta, V., & Vasilenko, E. (2022). Development of riverine landscape spaces in the city structure. IOP Conference Series: Earth and Environmental Science, 988(4), 042084. https://doi.org/10.1088/1755-1315/988/4/042084

Biernacka, M., Kronenberg, J., Łaszkiewicz, E., Czembrowski, P., Parsa, V. A., & Sikorska, D. (2023). Beyond urban parks: Mapping informal green spaces in an urban–peri-urban gradient. Land Use Policy, 131, 106746. https://doi.org/10.1016/j.landusepol.2023.106746

Cedamon, E., Stephen, R., Harrison, J. L., Herbohn, E. O., & Mangaoang, M. (2009). Reliability of the Barangay-based smallholder tree farm inventory: Research and policy implications.

Cipriano, T. J. L., & Garcia, E. B. (2019). Hazard experiences and risk reduction and mitigation initiatives of residents in Barangay 843 – Zone 92 in Pandacan, Manila. IOP Conference Series: Earth and Environmental Science, 338(1), 012001. https://doi.org/10.1088/1755-1315/338/1/012001

Cuenca-Ocay, G. (2024). Mangrove ecosystems' role in climate change mitigation. https://doi.org/10.59120/drj.v12i2.168

Dangol, N., & Carrasco, S. (2019). Residents' self-initiatives for flood adaptation in informal riverbank settlements of Kathmandu. International Journal of Disaster Risk Reduction, 40, 101156. https://doi.org/10.1016/j.ijdrr.2019.101156

De Juan, S., Gelcich, S., & Fernandez, M. (2017). Integrating stakeholder perceptions and preferences on ecosystem services in the management of coastal areas. Ocean & Coastal Management, 136, 38–48. https://doi.org/10.1016/j.ocecoaman.2016.11.019

Demashkieh, M. (2022). Reviving the neglected urban spaces using recreational facilities. Architecture & Planning Journal/APJ, 28(1). https://doi.org/10.54729/tyek8100

Eslit, E. R. (2023). Empowering Change at the Grassroots: Community-Led Initiatives for Local Environmental Protection. https://doi.org/10.20944/preprints202307.1055.v1

Etikan, I., Musa, S. A., & Alkassim, R. (2016). Comparison of convenience sampling and purposive sampling. American Journal of Theoretical and Applied Statistics, 5(1), 1. https://doi.org/10.11648/j.ajtas.20160501.11

Farahani, L. M., & Maller, C. (2018). Investigating residents' use and perceptions of informal greenspaces: A study of Stony Creek in Melbourne's west.

Ferreira, V., Barreira, A. P., Pinto, P., & Panagopoulos, T. (2022). Understanding attitudes towards the adoption of nature-based solutions and policy priorities shaped by stakeholders' awareness of climate change. Environmental Science & Policy, 131, 149–159. https://doi.org/10.1016/j.envsci.2022.02.007

Falchetta, G., Ahmed, T., & Hammad, H. (2023). Tracking global urban green space trends. https://doi.org/10.5194/egusphere-egu23-1989

Gbadegesin, A. S., Ikwuyatum, G., Knight, S., & Cinderby, S. (2024). Urban greenspaces and patterns of common mental disorders in Ibadan City, Nigeria. Ghana Journal of Geography, 16(3), 1–11. https://doi.org/10.4314/gjg.v16i3.1

Giorgio, F., Bianchi, A., & Monteleone, V. M. (2022). Green space for health promotion. Journal of Advanced Health Care, 5–12. https://doi.org/10.36017/jahc2205-02

Gonzales, L., & Magnaye, D. (2016). Challenges to the multi-functional uses and multifarious benefits of urban green spaces: Basis of urban biodiversity planning and management in the City of Manila, Philippines. https://doi.org/10.21625/essd.v1i1.33

Heat Island Effect | US EPA. (2025, April 8). US EPA. https://www.epa.gov/heatislands

Huang, Z., Dong, J., Chen, Z., Zhao, Y., Huang, S., Xu, W., Zheng, D., Huang, P., & Fu, W. (2022). Spatiotemporal characteristics of public recreational activity in urban green space under summer heat. Forests, 13(8), 1268. https://doi.org/10.3390/f13081268

Hilmi, E., Usman, U., & Iqbal, A. (2023). The external, internal factors, and ecosystem services to support mangrove rehabilitation planning in the North Coast of Jakarta. Proceedings of the International Conference on Multidisciplinary Approaches for Sustainable Rural Development, 2(1), 186. https://doi.org/10.20884/2.procicma.2023.2.1.7783

Ibañez, C. A., Palec, L., Argamosa, R. J., & Arceo, G. M. (2024). Leveraging spatial analysis techniques for developing a climate resilient and localized urban greening plan for Pasig City. ISPRS Annals of the Photogrammetry, Remote Sensing and Spatial Information Sciences, X-5–2024, 79–87. https://doi.org/10.5194/isprs-annals-x-5-2024-79-2024

Katalin, B. (2019). Development of a GIS methodology to evaluate informal urban green areas for inclusion in a community governance program.

Liana, N. C., Estoque, L. M. D., Dela Fuente, R. C., Mabborang, M. G., & Molina, M. G. (2022). Forecasting urban population growth in the Philippines using autoregressive integrated moving average (ARIMA) model. EPRA International Journal of Multidisciplinary Research. https://doi.org/10.36713/epra10819

Li, Y., Svenning, J., Zhou, W., Zhu, K., Abrams, J. F., Lenton, T. M., Ripple, W. J., Yu, Z., Teng, S. N., Dunn, R. R., & Xu, C. (2024). Green spaces provide substantial but unequal urban cooling globally. Nature Communications, 15(1). https://doi.org/10.1038/s41467-024-51355-0

Mario, R. D. R., Mark Anthony, M. G., Ryan Randle, B. R. (2020). The Philippines' national urban policy for achieving sustainable, resilient, greener, and smarter cities. https://doi.org/10.1007/978-981-15-3738-7_7

Nambazo, O., & Nazombe, K. (2024). The spatial heterogeneity of urban green space distribution and configuration in Lilongwe City, Malawi. PLoS ONE, 19(7), e0307518. https://doi.org/10.1371/journal.pone.0307518

O'Leary, B., Christine, C., Fonseca, C., Cornet, C., de Vries, M., Degia, A. K., Failler, P., Furlan, E., Garrabou, J., Gil, A., Hawkins, J. P., Krause-Jensen, D., Le Roux, X., Peck, M. A., Perez, G., Queirós, A. M., Różyński, G., Sánchez-Arcilla, A., Simide, R., Sousa Pinto, I., Trégarot, E., & Roberts, C. M. (2023). Embracing nature-based solutions to promote resilient marine and coastal ecosystems. Nature-Based Solutions. https://doi.org/10.1016/j.nbsj.2022.100044

Pietrzyk-Kaszyńska, A., Czepkiewicz, M., & Kronenberg, J. (2017). Eliciting non-monetary values of formal and informal urban green spaces using public participation GIS. Landscape and Urban Planning, 160, 85–95. https://doi.org/10.1016/j.landurbplan.2016.12.012

Revich, B. A. (2023). The significance of green spaces for protecting the health of urban populations. Health Risk Analysis. https://doi.org/10.21668/health.risk/2023.2.17

Rupprecht, C., & Byrne, J. (2017). Informal urban green space as anti-gentrification strategy? In Urban Greenspaces (pp. 209–226). https://doi.org/10.17605/osf.io/4d463

Russo, A., & Cirella, G. T. (2018). Modern compact cities: How much greenery do we need? International Journal of Environmental Research and Public Health, 15(10), 2180. https://doi.org/10.3390/ijerph15102180

Sandip, S., & Shiva, P. (2023). Studying the spatio-temporal changes of urban green space: A case study of Pokhara Metropolitan City. Journal of Engineering Issues and Solutions. https://doi.org/10.3126/joeis.v2i1.49491

Sikorski, P., Gawryszewska, B. J., Sikorska, D., Chormański, J., Schwerk, A., Jojczyk, A., Ciężkowski, W., Archiciński, P., Łepkowski, M., Dymitryszyn, I., Przybysz, A., Wińska-Krysiak, M., Zajdel, B., Matusiak, J., & Łaszkiewicz, E. (2021). The value of doing nothing: How informal green spaces can provide comparable ecosystem services to cultivated urban parks. Ecosystem Services, 50, 101339. https://doi.org/10.1016/j.ecoser.2021.101339

Rupprecht, C. D. D., & Byrne, J. A. (n.d.). Informal urban green space as anti-gentrification strategy? https://doi.org/10.9774/gleaf.9781315229515_16

Thahir, A. R. (2016). Generating sustainable green open space development in urban residential areas through a community participation approach. LivaS: International Journal on Livable Space. https://doi.org/10.25105/livas.v0i0.83

Thong, T. D., Wang, H., & Furuya, K. (2024). The Concept of Informal Green Space in Academic Research: A Comprehensive Literature Review on the Terminology Used. Land, 14(1), 43. https://doi.org/10.3390/land14010043

Trinidad, M. M. (2007). Land use dynamics in Iligan City using remotely sensed data and GIS. https://journals.msuiit.edu.ph/tmf/article/view/244

Turna, N., & Bhandari, H. (2022). Role of parks as recreational spaces at neighborhood level in Indian cities. ECS Transactions, 107(1), 8685–8694. https://doi.org/10.1149/10701.8685ecst

Uniaty, Q. (2015). Green infrastructure development in sustainable water resources management system. Applied Mechanics and Materials, 747, 127–131. https://doi.org/10.4028/www.scientific.net/amm.747.127

Uslu, D. Y., Almansouri, H. M. S., Elahsadi, A. H. M., & Cetin, M. (2024). Towards sustainable cities: Evaluating the distribution and functionality of green spaces in Atakum. Journal of Design for Resilience in Architecture and Planning, 5(3), 461–476. https://doi.org/10.47818/drarch.2024.v5i3143

Velayo, A. R. A., Suson, P. D., Aguilos, M. M., & Bacosa, H. P. (2024). Building urban climate resilience: Assessing awareness, perception, and willingness regarding nature-based solutions and climate change among stakeholders in Iligan City, Philippines. Urban Science, 8(2), 53. https://doi.org/10.3390/urbansci8020053

Zhang, W., & Xin, J. (2023). Green Spaces and the Spontaneous Renewal of Historic Neighborhoods: A Case Study of Beijing's Dashilar Community. Sustainability. https://doi.org/10.3390/su152416566

APPENDICES

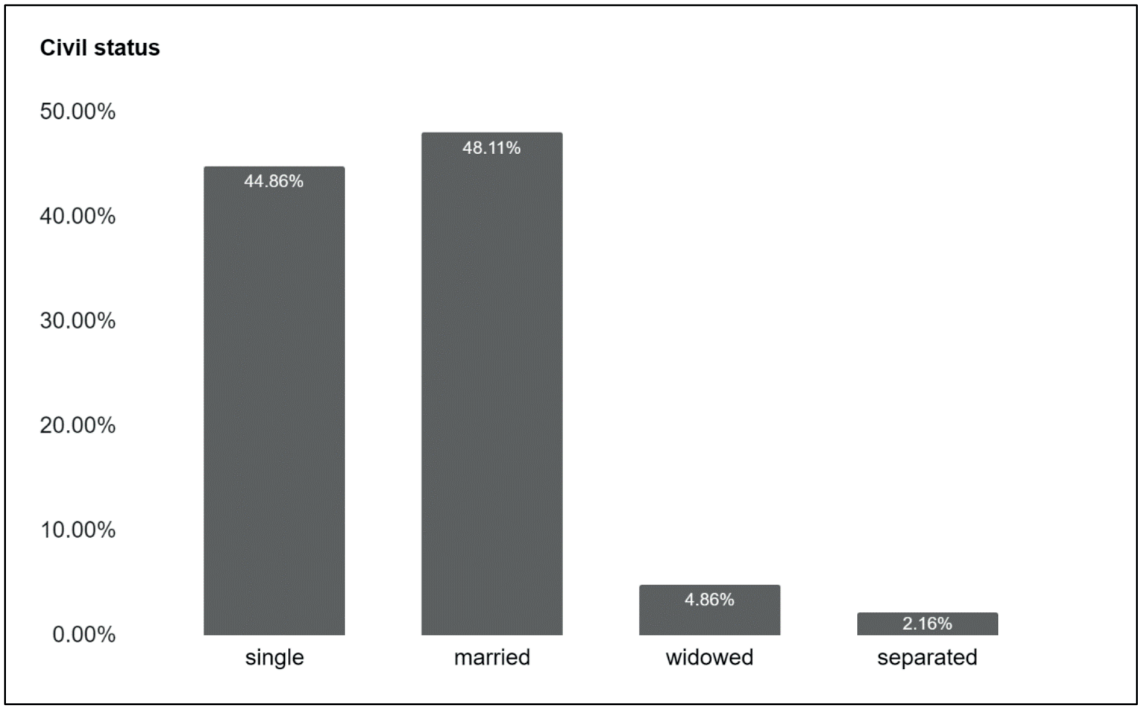

Fig. A. 1. Respondent's civil status; N=187.

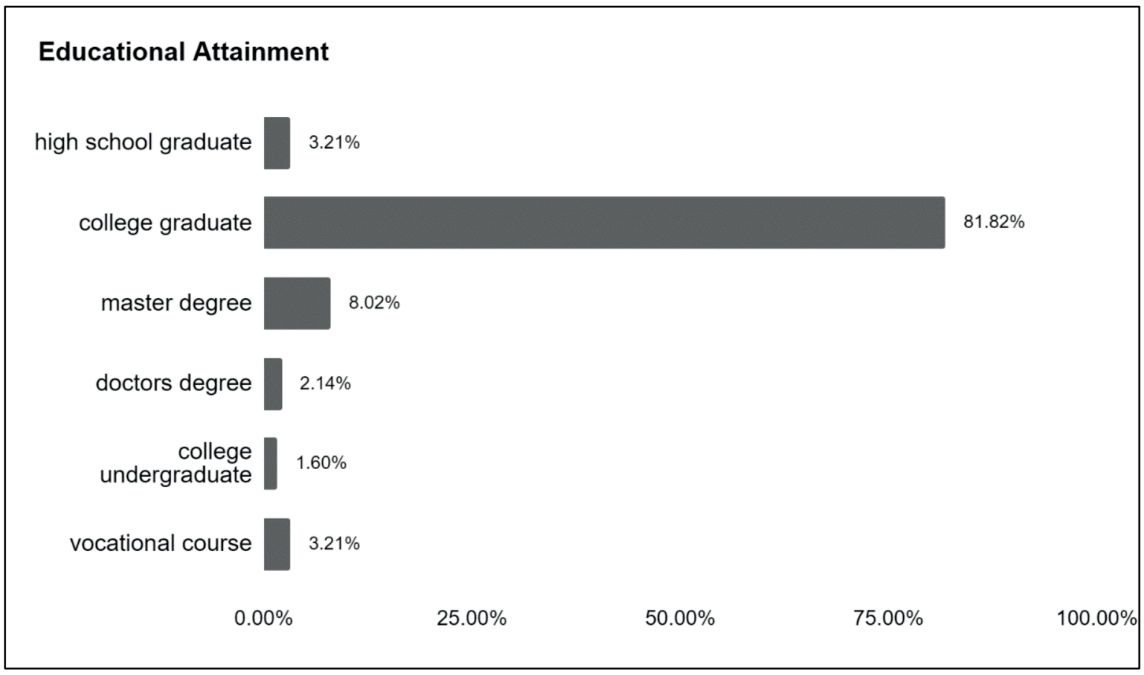

Fig. A. 2. Respondent's educational attainment; N=187.

IV. Policy prioritization

Facing the actual and future challenges and priority interventions, which of the following solutions are fundamental? (choose up to five options and arrange them from most to least important).

A. Green walls 

B. Natural pools 

C. Riverbank rehabilitation 

D. Wetlands and floodable parks 

E. Urban Trees 

F. Green shadows 

J. Green Barriers 

K. Drainage corridors 

M. Mangrove conservation and restoration 

1. Among your chosen 5 fundamental interventions. Rank them according to importance and priority.

Fig. A. 3. Questionnaire on stakeholder preference and priority NBS survey questionnaire (Ferreira, 2020)

RESEARCH PAPER

KNOWLEDGE CO-PRODUCTION PRACTICES TO PROMOTE CLIMATE RESILIENCE IN GLOBAL CITIES: A SYSTEMATIC LITERATURE REVIEW

Retno S. Dewi[1], Wiwandari Handayani[2]*, Muhammad Z. A. J. Ramadhan[1], Iwan Rudiarto[2]

[1]Center for Urban and Regional Resilience Research (CURE) – Faculty of Engineering, Diponegoro University, Jalan Prof. Soedarto, Semarang, 50275, Indonesia

[2]Department of Urban and Regional Planning, Faculty of Engineering, Diponegoro University, Jalan Prof. Soedarto, Semarang, 50275, Indonesia

***Corresponding author:** wiwandari.handayani@pwk.undip.ac.id

Received: February 1st 2025 / Accepted: November 12nd 2025 / Published: December 31st 2025

https://doi.org/10.24057/2071-9388-2025-3867

ABSTRACT. Climate change presents complex challenges for cities worldwide, requiring innovative and collaborative approaches to enhance resilience and adaptability. In response to this phenomenon, knowledge co-production plays a vital role in integrating diverse perspectives to address climate-related risks and promote adaptive urban environments. This research aims to investigate current consensus on how knowledge co-production is operationalised, particularly in climate resilience and urban settings. This study follows the Preferred Reporting Items for Systematic Reviews and Meta-Analyses (PRISMA) protocol to identify, screen, and analyse relevant publications systematically. A total of 36 publications were reviewed to examine the types of disturbances, the dimensions of stakeholder engagement, and current practices of knowledge co-production. The findings highlight the growing significance of knowledge co-production in addressing climate-related challenges through strong stakeholder engagement, local knowledge integration, and effective science–policy interfaces. Moreover, these processes require balanced and meaningful participation among all stakeholders, particularly local community involvement, to ensure that initiatives can be scaled up and become systemic rather than fragmented.

KEYWORDS: knowledge co-production; climate resilience; city resilience; systematic literature review

CITATION: Dewi R. S., Handayani W., Ramadhan M. Z. A. J., Rudiarto I. (2025). Knowledge Co-Production Practices To Promote Climate Resilience In Global Cities: A Systematic Literature Review. Geography, Environment, Sustainability, 4 (18), 115-126 https://doi.org/10.24057/2071-9388-2025-3867

ACKNOWLEDGEMENTS: This research was funded by Diponegoro University through the International Publication Research Scheme (grant number 609-103/UN7.D2/PP/VII/2024). It was also supported by the Australian Government Department of Foreign Affairs and Trade (DFAT) through the KONEKSI / Knowledge Partnership Platform (KPP) grant. This grant supported a research collaboration titled 'From Technical to Socio-ecological Pathways for Climate Change Adaptation: Analysis of Flood in Semarang' (KONEKSI Ref No. 1447/CRG/2023/17-UQ).

Conflict of interests: The authors reported no potential conflict of interests.

INTRODUCTION

Climate change has become an increasingly significant global concern, particularly as rapid urbanisation accelerates the growth of cities worldwide. The number of global megacities rose from 10 in 1990 to 34 in 2023 (Statistisches Bundesamt 2023). The urban population increased from 1 billion in 1960 to 4.6 billion in 2023, around 57.34% of the world's population, with more than half residing in the Asia and Pacific region (World Bank 2024; Asian Development Bank 2022). These cities are often located near rivers and coastlines. This makes them more prone to various climate-related risks (Handayani et al. 2020; Rudiarto et al. 2018) and contributes to the emergence of wicked urban problems.

Resilience appears as a promising concept for cities that require more robust and adaptive strategies to address complex urban problems. It is defined as the ability of an ecological system to maintain its functionality or persist under change (Holling 1973). Furthermore, Folke et al. (2011) explained it as the capacity of systems to adapt across different time and space scales. Attention to resilience in urban settings has grown in both academic and policy discussions, particularly as cities seek to maintain resilience during rapid urban development (Wang and Xue 2018). Meerow et al. (2016) described urban resilience as the capacity of cities to respond to specific threats, such as climate change or flooding, while also addressing broader systemic risks. Moreover, resilience greatly depends on how communities manage economic and social pressures and recover from them effectively (Handayani et al., 2019; Walisser et al., 2005).

Building urban resilience requires a transdisciplinary perspective that integrates social, economic, cultural, and physical dimensions (Jabareen, 2013). This approach also helps address challenges such as unclear roles and weak stakeholder commitment while fostering stronger

collaboration (Krellenberg & Barth, 2014; Matsuura & Razak, 2019). In this context, knowledge co-production plays a vital role in integrating diverse perspectives to address climate-related risks and promote adaptive urban systems (Ambole et al., 2019; Dunn et al., 2017; Aguilar-Barajas et al., 2019).

In the last decade, knowledge co-production has become more widely recognised as an approach to address complex problems linked to climate change and urbanization (Visconti 2023; Djenontin and Medow 2018). This growing interest is driven by the increasing need for decision-makers to navigate complex problem contexts involving diverse stakeholders (Culwick et al. 2019). Urban Living Labs (ULLs) have become one of the most practical forms of knowledge co-production, providing an experimental platform where stakeholders, researchers and policymakers collaboratively design, test and refine innovative urban solutions in real-life contexts (Voytenko et al. 2016; Nesti 2018).

This paper presents a systematic review of knowledge co-production to examine its epistemological, methodological, and practical aspects in promoting climate resilience in global cities. The systematic review follows guidelines from the Preferred Reporting Items for Systematic Reviews and Meta-Analyses (PRISMA) statement (Page et al., 2021a; Page et al., 2021b). The term 'knowledge co-production' is, however, relatively new in city planning and city resilience strategy. Accordingly, this research aims to identify current consensus on how knowledge co-production is operationalised, particularly in climate resilience and urban settings. Given the above background, three critical questions guide the review: (1) to what extent do current practices of knowledge co-production in global cities promote climate resilience, (2) what levels of stakeholder engagement are involved, and (3) what types of climate-related disturbances are addressed and how.

The structure of this study is organised into several parts. First, the introduction provides background context for the systematic literature review of knowledge co-production. Second, the literature on urban resilience and the development of knowledge co-production is summarised. Third, the methods section offers a brief explanation of the PRISMA framework and its application in this review. The results then present findings that address the three proposed questions. Finally, the discussion highlights trends in the use of knowledge co-production for urban resilience and offers concluding reflections.

LITERATURE REVIEW: RESILIENCE AND KNOWLEDGE CO-PRODUCTION

Resilience is often linked to the disturbance it seeks to address. Meerow et al. (2016) define resilience in an urban setting as the capacity of a city and its urban systems to absorb initial damage, reduce impacts from a disturbance, adapt to change, and modify systems that constrain current or future adaptive capacity. Ribeiro and Gonçalves (2019) define disturbances as events that occur during the process of reaching equilibrium. Disturbances can include natural disasters, climate conditions, calamities, crises, and disruptive events. Moreover, Ribeiro and Gonçalves (2019) define city resilience as a structure that consists of the capacity of the city to absorb initial impacts, reduce disturbance effects, adapt to change, and rapidly modify systems that limit the current or future adaptive capacity of its urban systems. There is a broad consensus that cities must become resilient to a wider range of shocks and stresses, particularly in terms of preparedness to address climate change challenges. Climate change is one of many stresses that cities face, creating an urgent need to build resilience (Leichenko 2011). In this study, disturbances are used as a framework for assessing how knowledge co-production supports urban resilience in the face of climate-related issues.

Knowledge co-production emerged from the introduction of Mode 2 science. This approach emphasises transdisciplinary methods and the inclusion of various stakeholders and experts (heterogenomy). Mode 1 and Mode 2 represent different ways of producing knowledge and conducting research (Nowotny, Scott, and Gibbons 2003). The change from the traditional, discipline-focused Mode 1 to the dynamic, socially distributed, and application-focused Mode 2 indicates an increasing emphasis on producing knowledge for practical use.

Knowledge co-production is a collaborative process where diverse expertise and actors come together to create context-specific knowledge tailored for sustainability research (Norström et al. 2020). It is guided by four fundamental principles: context-based, pluralistic, goal-oriented, and interactive processes, which serve as the foundation for high-quality co-production initiatives (Djenontin and Meadow 2018). The evolution of knowledge co-production reflects its emergence as a strategic response to the complex challenges of modern society. There is a notable trend towards the active participation of non-academic stakeholders in research endeavours (Norström et al. 2020). This shift highlights the growing recognition of the importance of engaging a wide range of perspectives and knowledge systems to effectively tackle sustainability issues and foster holistic solutions.

Collaboration between academics and non-academics is a cornerstone of successful knowledge co-production. This approach emphasises the value of integrating diverse viewpoints and expertise to address sustainability challenges. By bringing together different actors and knowledge domains, co-production processes can harness collective wisdom and insights, which are necessary to navigate complex sustainability issues and drive positive change. Practical guidance in the literature also offers researchers, practitioners, and funders a roadmap for meaningful engagement in co-productive practices and a framework for assessing the effectiveness and impact of such collaborative efforts (Norström et al. 2020). In this study, knowledge co-production is assessed by analysing the knowledge produced through the project, the initiator, and the stakeholders involved in the co-production.

Knowledge co-production principles, such as co-defining problems, integrating diverse knowledge sources, and fostering iterative, two-way engagement (Djenontin and Meadow 2018), are central to the operation of Urban Living Labs (ULLs). Within ULLs, co-creation processes combine formal and informal participation. They may involve shared or selective ownership and are supported by a mix of intrinsic and extrinsic incentives (Puerari et al. 2018). These arrangements help bridge the gap between policy and practice, ensuring that interventions respond more effectively to local needs.

European examples illustrate the role of ULLs in climate adaptation and mitigation. In Amsterdam, a citizen-led air-quality monitoring project has been established, while in Turin, environmental sensors support community-based action (Nesti 2018). In Naples, participatory mapping and design workshops aligned scientific risk assessments with community priorities, addressing socio-spatial vulnerabilities and shaping municipal regeneration plans (Visconti 2023). Experiences from the Global South provide further insight: in Johannesburg, CityLabs demonstrate how long-term partnerships and iterative engagement can embed resilience thinking, even in resource-constrained environments (Culwick et al. 2019).

METHODS

Systematic Literature Review Process

The systematic literature review followed the Preferred Reporting Items for Systematic Reviews and Meta-Analyses (PRISMA 2020). This protocol is designed to enhance transparency, consistency, and comprehensiveness in systematic reviews. By adhering to PRISMA, researchers ensure their reviews are conducted and reported with high methodological rigour. The protocol encourages authors to provide detailed information about the review's design, search strategy, selection criteria, data extraction, and synthesis methods. The inclusion of PRISMA in systematic review reporting serves as a valuable tool, promoting clarity in research communication, aiding in the critical evaluation of studies, and ultimately contributing to the reliability and credibility of evidence-based decision-making processes.

Publications included in the review were identified using the Scopus database. The search was conducted using interchangeable keywords: 'knowledge co-production' or 'co-production of knowledge'. The data collection criteria were as follows:

- Search within: Article title, Abstract, Keywords
- Publication years: earliest date possible to May 2025
- Subject area: Social Sciences, Environmental Science, Earth and Planetary Sciences
- Document type: Article, Book chapter, Conference paper
- Language: English

Search Query

In May 2025, a search query was conducted in Scopus using the keywords 'knowledge co-production' OR 'co-production of knowledge.' Publication years ranged from the earliest date available to 2025. The search was limited to titles, abstracts, and keywords (TITLE-ABS-KEY) and restricted to journal articles, book chapters, and conference papers. Table 1 outlines the criteria for article inclusion and exclusion.

Search Results

The query yielded 1053 records on the Scopus website. Further screening was performed to remove irrelevant records based on the predefined criteria. A single keyword was used because most relevant papers would have been excluded if additional inclusion criteria keywords were applied, which would lead to more irrelevant results. The initial screening was conducted using the base keywords 'knowledge co-production' or 'co-production of knowledge' in the abstract, keywords, or title. The results were then filtered to include only articles that mentioned urban areas as the study location.

The records were checked for duplicates, and four duplicates were removed (see Figure 1). The remaining records were then checked against the predefined criteria for title and keywords, which resulted in the removal of 958 records. The remaining records (n = 91) were screened using the abstract within the set criteria, and 42 additional records were excluded. The final screening involved evaluating full records for accessibility through open access or institutional subscriptions. Five records that were inaccessible were excluded. The final set of 36 records was selected for the analysis.

The final selection of 36 publications was analysed to answer the research questions and categorised into four areas: types of disturbance; stakeholder engagement; current practices of knowledge co-production; and produced knowledge. The list of reviewed publications with brief summaries is presented in Appendix 1.

RESULTS

General Observations

From the initial pool of 1053 publications, knowledge co-production publications first appeared in 2002 and began to rise in the early 2010s. The distribution of publications per year is shown in Figure 2. Approximately 66% of these were published in the past five years (2020–2025), indicating the recent recognition of the importance of knowledge co-production in environmental research. The trend in publications related to knowledge co-production has increased steadily, with notable growth after 2013.

All 36 selected publications were journal articles. No book chapters or conference papers met the inclusion criteria. Of these, the most commonly published journal outlets were *Environmental Science and Policy* (8 publications) and *Sustainability* (3 publications). Figure 3 provides an overview of the publication trends of the selected 36 knowledge co-production publications from 2010 to 2023. The number of publications has steadily increased over time, with a significant surge observed in 2016 (4 publications) and peaking in 2022 (5 publications).

This upward trend reflects growing interest and engagement in knowledge co-production within academic discourse. Additionally, a notable increase in publications is observed from 2016 onwards, highlighting a heightened focus on this topic in recent years. These findings demonstrate the evolving landscape of knowledge co-production research and its increasing significance in scholarly discussions. The distribution of case studies also highlights regional differences. Europe accounts for the largest number of cases (26), followed by Africa (22), North America (11), Asia (4), and Oceania (2).

Keyword Linkages

Figure 4 illustrates the frequency and co-occurrence patterns related to knowledge co-production within the scope of the papers examined in this study. The size of a

Table 1. Article inclusion and exclusion criteria

Inclusion criteria	Exclusion criteria
Base dimensions: Knowledge co-production OR co-production of knowledge **Base criteria:** Scope of topic Climate change Disaster resilience Urban resilience Sustainability study Relevant study mentioning urban area Relevant study mentioning practices of knowledge co-production **Validation criteria:** Relevant study to this paper's research aim and research questions	• Irrelevant publications to research theme (climate change/ resilience/disaster resilience) • Knowledge co-production not in the urban resilience field • Irrelevant study to this paper's research aim and research questions

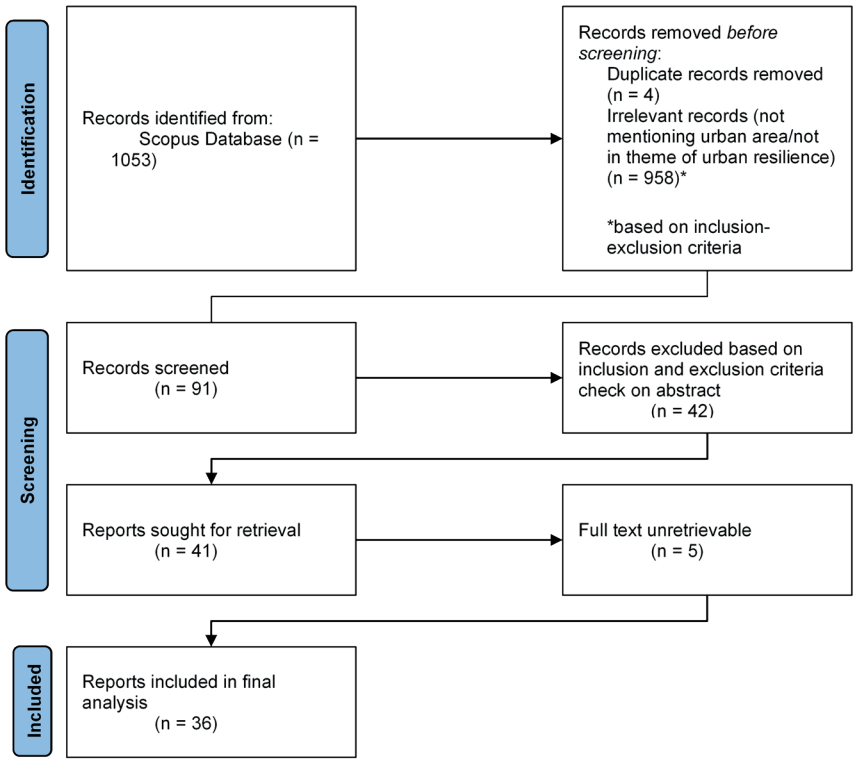

Fig. 1. Literature selection process

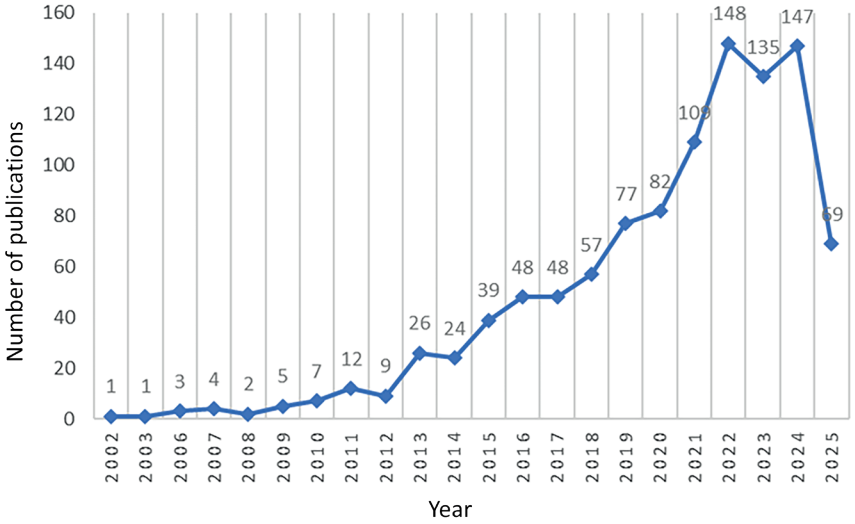

Fig. 2. Number of publications in the initial article pool by year (1,053 publications in total)

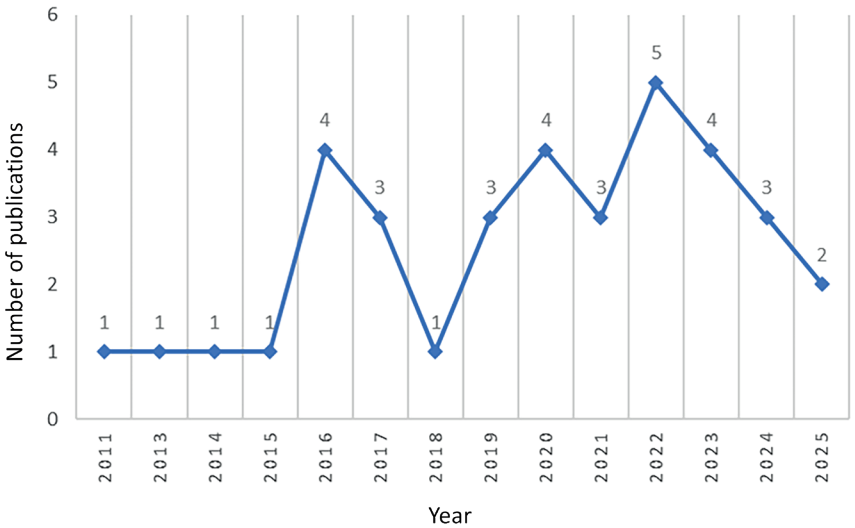

Fig. 3. Distribution of the final set of 36 records included in this study by year

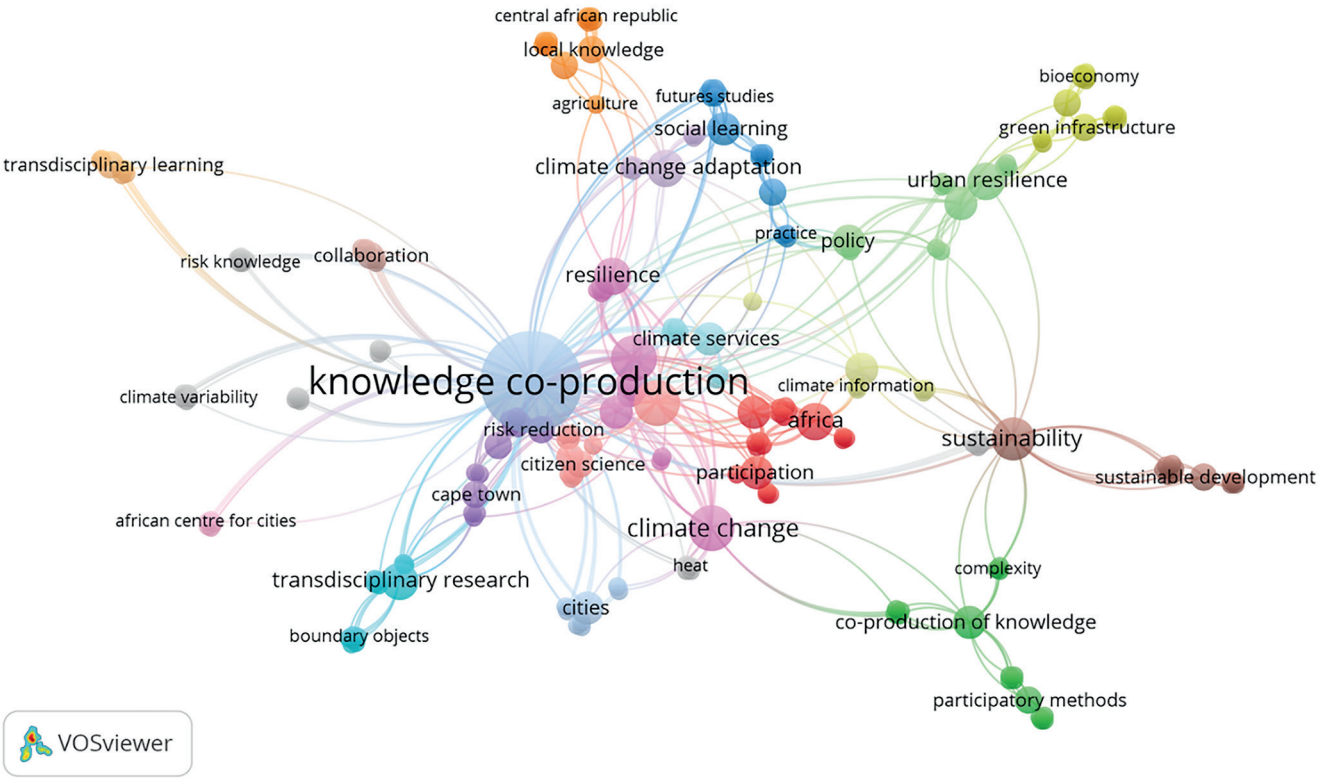

Fig. 4. Keyword linkages

Note: The keyword 'Africa' appears because several authors listed it as a keyword, unlike other locations mentioned only in titles or abstracts.

node represents its degree or frequency, and the edge indicates the frequency of co-occurrence. Research hotspots in knowledge co-production were identified by analysing the co-occurrence of frequent keywords. The minimum co-occurrence number for a keyword was set at 1. This threshold was chosen to highlight frequent keywords, given the relatively small article pool. A total of 232 keywords extracted from the pooled articles were clustered based on their similarities, resulting in 24 clusters.

The network visualisation illustrates the centrality of 'knowledge co-production' within the research landscape, as indicated by its prominent size and position. It is strongly linked to terms such as 'climate change,' 'resilience,' 'participation,' and 'sustainability,' which reflect its thematic relevance to environmental and urban research. Notably, clusters of keywords like 'urban resilience,' 'green infrastructure,' and 'sustainable development' suggest a growing focus on applied outcomes and policy integration. The presence of terms such as 'citizen science,' 'local knowledge,' 'social learning,' and 'transdisciplinary research' reinforces the participatory and collaborative nature of knowledge co-production.

Current Practices of Knowledge Co-Production

Current practices of knowledge co-production involve collaborative efforts between diverse stakeholders. These include researchers, policymakers, practitioners, and community members. Such initiatives aim to address complex environmental challenges effectively. Several tools and frameworks are used to help dialogue, mutual learning, and the co-creation of knowledge. For example, in the context of urban water management and climate change adaptation, frameworks like the Water Sensitive Cities (WSC)concept and the WSC index help assess cities' resilience to climate impacts. These frameworks combine multiple indicators and self-assessment processes, encouraging exchange, mutual learning, and greater awareness among participating cities (Dunn et al. 2017).

Learning networks and joint learning processes are also pivotal. Tools such as community engagement strategies, cross-border cooperation mechanisms, and collective innovation platforms help facilitate knowledge exchange and co-production among diverse actors. For instance, the Sustainable Urban Neighbourhoods (SUN) project in the Euregio Meuse-Rhine (Valkering et al. 2013) uses concerted public and private action to foster community engagement and cross-border cooperation, enabling the exchange and co-production of technical, attitudinal, and innovative knowledge across various boundaries.

Additionally, mapping approaches are increasingly used to identify hot spots for sustainability transitions in cities. This allows stakeholders to visualise and analyse different land-use scenarios and their environmental impacts (Visconti 2023). By communicating the consequences of induced land-use change and identifying areas for transition, mapping helps in informed decision-making and supports stakeholder engagement in co-design processes.

Regional case studies further demonstrate the variety of practices. In Québec, research on multi-loop social learning processes in water governance used semi-structured interviews to identify challenges such as limited capacity and the perceived credibility of organisations. Opportunities to overcome these barriers include renewing partnerships and exploring innovative tools for knowledge co-production (Medema et al. 2015). Similarly, in Chile, the Resilience-Whell tool and participatory methods were applied to address urban drought resilience. Key resilience factors identified include education, preparedness, technology transfer, and citizen participation (Aldunce et al. 2016). This bottom-up approach bridges the science-policy interface and enables the co-production of key knowledge for building resilience. Additionally, in Alleppey, Kerala, India, the CANALPY initiative focuses on capacity building and knowledge co-production to address sanitation challenges. It creates a platform for collaborations, dialogues, and discussions on sanitation, water quality, and pollution, emphasising the importance

of considering practical, socio-political, institutional, and competence-related challenges in knowledge sharing and capacity building (Pillai and Narayanan 2022).

In brief, current practices of knowledge co-production use various tools and frameworks, including assessment methods, collaborative platforms, and mapping approaches. These mechanisms facilitate dialogue, mutual learning, and the co-creation of knowledge among diverse stakeholders. In doing so, they help cities face complex environmental challenges, strengthen resilience, and advance sustainable development through informed decision-making and collective action.

Produced Knowledge in Observed Cities

The knowledge co-production projects from the literature pool showcase a diverse array of insights that come from collaborative endeavours across multiple research domains. Figure 5 summarises the knowledge produced from the selected articles. A recurring theme is the emphasis on stakeholder engagement and inclusive learning. By involving a wide range of stakeholders, such as community members, experts, policymakers, and academics, these projects utilise a wealth of tacit knowledge and expertise. This inclusive approach not only enriches the understanding of various related issues like climate variability, sustainable energy transitions, and urban ecosystem services but also fosters a sense of shared ownership and credibility in the generated knowledge. Through interdisciplinary collaborations and participatory methodologies, these processes have yielded valuable knowledge to address complex challenges and informed decision-making processes in urban environments.

Furthermore, knowledge co-production initiatives have led to the development of practical tools and frameworks for decision-making and policy formulation. From standardised indicator sets for monitoring weather impacts to tailored indicators for assessing urban water systems, these projects have introduced structured methodologies for evaluating resilience, identifying trade-offs, and guiding sustainable urban development practices. This policy-relevant knowledge aligns with decision-makers' needs, enhancing the effectiveness of urban planning and management strategies. Moreover, the collaborative nature of these knowledge co-production projects has not only produced valuable insights into intricate urban challenges but has also nurtured a culture of reflective engagement, critical analysis, and continuous learning. By fostering shared understanding among stakeholders, integrating diverse perspectives, and advocating for transparency and accountability in decision-making processes, the knowledge produced serves as a cornerstone for informed decision-making, strategic planning, and sustainable urban development.

Stakeholder Engagement in Knowledge Co-Production

Edelenbos et al. (2011) highlight that stakeholder engagement in knowledge co-production involves different levels of interaction. At the highest level, significant interactions require open communication and active participation in collaborative activities involving specialists, bureaucrats, and stakeholders. Regular meetings and deliberate efforts to integrate knowledge from diverse domains underscore the commitment to fostering a common understanding. However, a fully supported knowledge base is often challenging to achieve even with these efforts.

In contrast, medium interaction is characterised by one-way communication and strategic or symbolic joint activities. These often lack genuine intent to establish a shared knowledge base. Differences in assumptions and values can hinder meaningful dialogue, resulting in consultative rather than collaborative interaction.

At the lowest level, little or no interaction suggests a lack of engagement. Disagreements and misunderstandings among actors prevent meaningful interactions, leading to a reduction or cessation of joint efforts. In extreme cases, knowledge development occurs in isolation, excluding alternative perspectives and values. Effective stakeholder engagement in knowledge co-production requires concerted efforts to foster open communication, acceptance of diverse viewpoints, and active collaboration towards the creation of a shared knowledge base. However, Edelenbos et al. (2011) do not explicitly address the role of the general public (for example, indigenous people or citizens) in their framework.

The initiation of knowledge co-production varies across projects. Some are led by researchers or academic

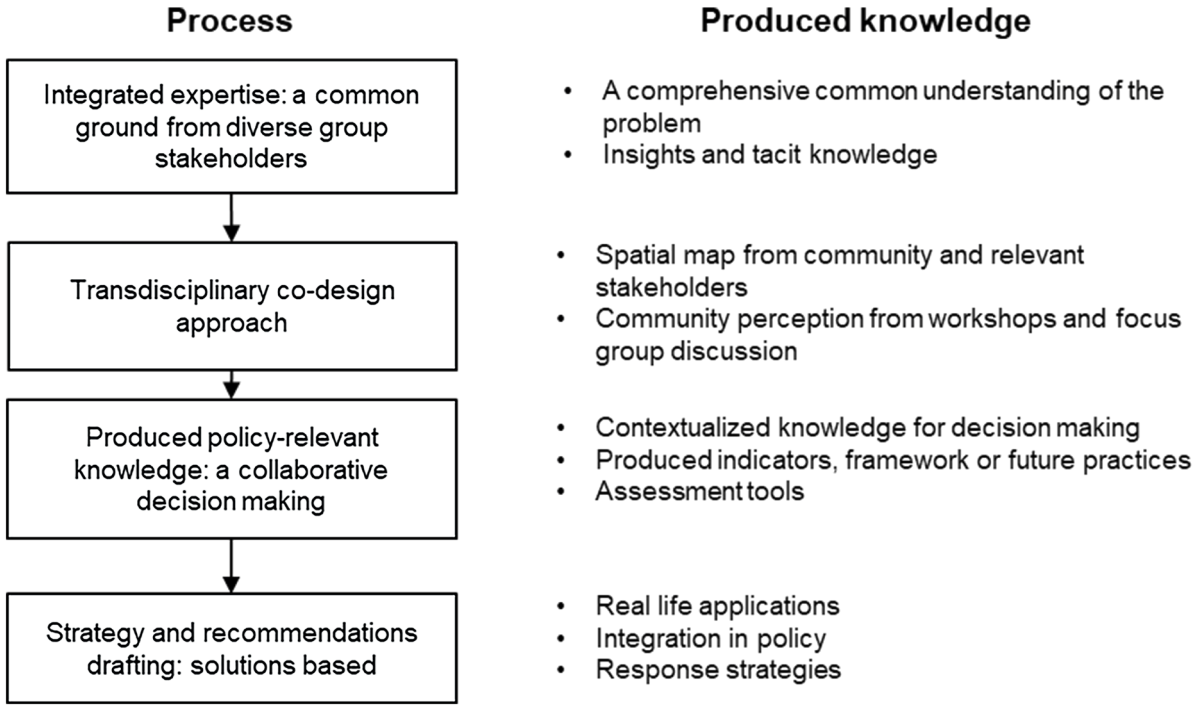

Fig. 5. Produced knowledge based on simplified processes from pooled articles

institutions, while others are spearheaded by government agencies or practitioners (see Figures 6). Out of the 36 articles analysed, 17 papers identify academic institutions and/or research teams as the primary initiators, emphasising their central role in shaping collaborative research agendas and fostering partnerships for sustainable urban development. This prevalence of researcher-led initiatives underscores the importance of academic leadership in promoting knowledge co-production as a transformative approach to addressing complex urban challenges and building resilience in diverse contexts.

Other initiators mentioned in the 36 articles include government agencies (4 papers) and collaborative efforts between government, NGOs, and the private sector (13 papers). Two articles do not specify any initiator, though these projects appear to have been the result of broader collaboration. While 36 publications were analysed, the total number of initiators identified is 37. This is because one publication presented two different case studies with different initiators.

Various studies highlight the importance of engaging stakeholders from different sectors, including government agencies, community stakeholders, and research teams, in the co-production of knowledge. For example, government agencies at the state level, community stakeholders, and project team members are often actively involved in initiatives related to urban resilience (Aguilar-Barajas et al. 2019; Yumagulova and Vertinsky 2019), climate change adaptation (Borquez et al. 2017; Lorencová et al. 2018; Özerol et al. 2020; Nicolletti et al. 2020), and sustainable water governance (Edelenbos et al. 2011; Dunn et al. 2017; Medema et al. 2015; O'Donnell et al. 2020) in different regions such as Canada, Mexico, and the Netherlands (Aguilar-Barajas et al. 2019; Frantzeskaki and Kabisch 2016; Haque et al. 2023; Özerol et al. 2020; Yumagulova and Vertinsky 2019). Together, these stakeholder groups contribute diverse perspectives and expertise, broadening understanding of complex environmental challenges.

Furthermore, the successful integration of stakeholder knowledge with expert and bureaucratic knowledge emerges as a key factor in the co-production process. Studies discuss how practitioners from different sectors, including GIS experts, policymakers, and community representatives, collaborate to develop shared understandings and a common language for decision-making in areas such as urban environmental governance, disaster risk reduction, and climate resilience (Edenlenbos et al. 2011; Tiitu et al. 2021). The interaction between stakeholders with varying backgrounds and expertise levels is recognised as beneficial for creating a more holistic knowledge base and addressing complex problems in climate change, water management, and urban planning.

Moreover, the process of stakeholder engagement in knowledge co-production often involves establishing clear communication channels, conducting regular group meetings, and facilitating transdisciplinary dialogues. Researchers highlight the importance of inclusive approaches that engage a wide range of stakeholders, from scientists to local community members, in discussions and workshops aimed at developing innovative solutions for environmental challenges. By fostering collaboration and knowledge sharing among diverse stakeholder groups, projects in various regions such as Africa, India, and the Philippines have enhanced collective reflection, learning, and innovation development for sustainable urban development and climate adaptation (Tonisson et al. 2020; Edenlenbos et al. 2011).

Types of Disturbances Urban Area Faced in Terms of Resilience

Various types of disturbances affecting urban resilience are discussed, highlighting the multifaceted challenges cities face in building and maintaining resilience. One key type of disturbance is the increasing frequency and intensity of climate-related hazards (see Table 2), such as floods, heatwaves, and storms. These pose significant threats to urban areas (Frantzeskaki and Kabisch 2016). Extreme weather events mentioned in several sources are categorised using the taxonomy based on Stephenson (2008) and Radović (2020). These include tropical cyclones and hurricanes, extratropical cyclones, convective and mesoscale phenomena, floods, drought, heat waves, cold waves/spells, and fog. These hazards not only impact infrastructure and the built environment but also have far-reaching consequences on the social, economic, and

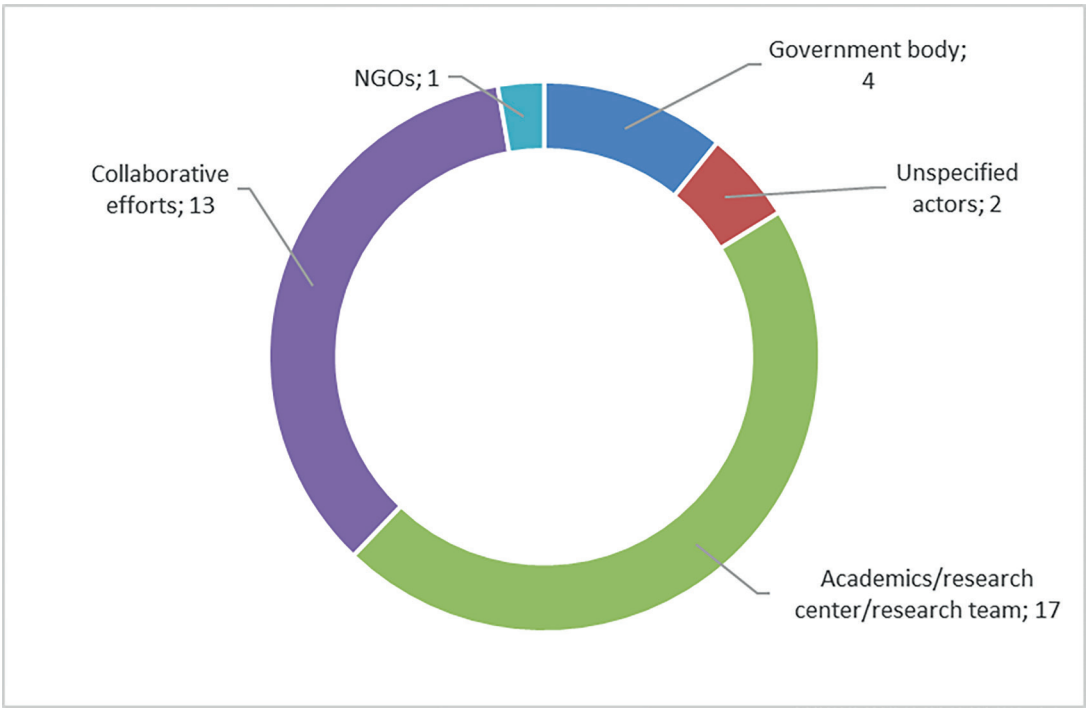

Fig. 6. Initiators in knowledge co-production projects

environmental fabric of cities, emphasising the need for robust resilience strategies (Aguilar-Barajas et al. 2019). Additionally, the articles highlight disruptions caused by rapid urbanisation, population growth, and land-use changes. These strain resources, worsen vulnerabilities, and challenge the adaptive capacity of urban systems (Visconti 2023).

Moreover, the literature stresses the importance of understanding and addressing socio-economic disturbances that undermine urban resilience. Inequality, poverty, and social exclusion are recognised as critical factors that amplify the impacts of hazards and hinder effective resilience-building efforts (Visconti 2023). By examining the interconnectedness of social dynamics with environmental and physical disruptions, the articles emphasise the need for inclusive and equitable approaches to resilience that address underlying social vulnerabilities and promote community well-being (Borquez et al. 2017). Furthermore, governance-related disturbances, including fragmented decision-making processes, a lack of coordination among stakeholders, and institutional barriers, are identified as significant challenges to enhancing urban resilience (Aldunce et al. 2016). These governance issues impede the implementation of effective policies and strategies, limiting cities' ability to respond proactively to disturbances and shocks. Table 2 summarises the types of disturbances explored in the 31 selected articles.

When navigating the complex landscape of urban disturbances and resilience, the articles advocate for integrated and holistic approaches that consider the interconnected nature of challenges faced by cities. By recognising the full range of disturbances, from climate-related hazards to socio-economic inequalities and governance barriers, urban resilience initiatives can be better tailored to address the root causes of vulnerabilities and enhance adaptive capacity (Aldunce et al. 2016). Through collaborative efforts that engage stakeholders across sectors and disciplines, cities can develop comprehensive resilience strategies that build on local knowledge, foster innovation, and promote sustainable urban development (Pillai and Narayanan 2022). Addressing disturbances comprehensively and proactively enables cities to enhance their resilience capacities and create more adaptive, inclusive, and sustainable urban environments.

In addition to strengthening city resilience, several conditions are essential for embedding Urban Living Labs (ULLs) in climate resilience agendas. These include: (1) municipal leadership and support to institutionalise successful experiments (Kronsell & Mukhtar-Landgren, 2018); (2) safe, neutral spaces that build trust and encourage participation (Culwick et al. 2019); (3) integration of local and scientific knowledge to produce contextually appropriate solutions (Visconti 2023); and (4) physical and symbolic

Table 2. Case studies according to types of disturbances

Types of disturbances	Description	Authors
Climate hazard		
Drought (climate-induced)	Climate-induced drought caused by prolonged periods of abnormally low precipitation.	Aldunce et al. (2016), Borquez et al. (2017), Mpofu-Mketwa et al. (2023)
Floods & flash floods	Floods triggered by climate change impacts. Flash floods are triggered by extreme weather events.	Aguilar-Barajas et al. (2019), Dunn et al. (2017), Haque et al. (2023), Tian et al. (2022)
Heavy rains, typhoons, and hurricanes	Extreme weather events related to disasters caused by climate change impacts.	Özerol et al. (2020), Tian et al. (2022)
Heat waves and urban heat islands	Heat events exceeding 30°C caused climate change impacts and hotspots caused by urban activities.	Lorencová et al. (2018)
Air pollution and black carbon emission	Pollution caused by industries and the transportation sector; black carbon emission refers to PM2.5.	Tonisson et al. (2020), Visconti (2023)
Marine submersion (coastal flooding due to sea level rise, storms, tsunamis, cyclones)	Marine submersion refers to coastal flooding events caused by the rising sea level and extreme weather phenomena such as storms, cyclones, tsunamis, or storm surges.	Heinzlef et al. (2024)
Urban system		
Governance-management challenges		
Conflicting interest among stakeholders (management crisis), government instability	Diverse stakeholder interests and balancing power dynamics.	Edenlenbos et al. (2011), Schmidt et al. (2024)
Flood risk (water management system)	Strategies, coping mechanisms, and adaptation measures of water management systems.	Medema et al. (2015), O'Donnell et al. (2020), Yumagulova and Vertinsky (2019), Onyima et al. (2025)
Water security stress (scarcity problem)	Water demand exceeds supply.	Odume et al. (2021)
Urban growth challenges		
Urban growth and development (i.e. urban encroachment, green space development, land use change)	Balancing urban growth with environmental conservation.	Frantzeskaki and Kabisch (2016), Morzillo et al. (2022), Nochta et al. (2021), Larondelle et al. (2016), Adams et al. (2023), Esmail et al. (2024)

spaces that sustain visibility and engagement (Puerari et al. 2018). Among the 36 studies reviewed, some explicitly reference ULLs (Schmidt et al. 2024; Visconti 2023), while others describe ULL-like co-production approaches (Aguilar-Barajas et al. 2019; Edelenbos et al. 2011; Frantzeskaki and Kabisch 2016; Johnson et al. 2022). These findings align with the broader literature, which positions ULLs as both conceptual and practical mechanisms for resilience. By combining knowledge co-production principles with experimental, place-based governance, ULLs create a pathway from knowledge generation to actionable, adaptive strategies. Their flexibility makes them particularly well-suited to addressing complex climate challenges in diverse urban contexts, complementing the approaches observed in the reviewed studies.

DISCUSSION

Knowledge co-production plays an essential role in promoting climate resilience. This relevance is reflected in the reviewed literature, where 12 of the analysed articles explicitly discuss the use of knowledge co-production to address various types of climate-related disturbances. Polk and Kain (2015) further suggest that no single actor has the capacity to address such complexity, and therefore collaborative and inclusive action is necessary. This process also redefines the role of science from a sole producer of expertise to a collaborative partner in shared understanding (Valve et al. 2023). It not only bridges disciplinary and institutional boundaries but also increases the credibility and adaptability of climate resilience strategies (Schmidt et al. 2024).

Despite its potential, the implementation of knowledge co-production remains limited in both scope and depth. Several initiatives have been conducted under short-term funding and project-based frameworks, leading to discontinuity once external support ends (Ryan and Bustos 2019; Mills et al. 2022; Miguel et al. 2025). Furthermore, there is a lack of sustained commitment from stakeholders to maintain these collaborative efforts over time (Harvey et al. 2019). Consequently, the outcomes remain fragmented rather than systemic.

Several previous studies indicate that knowledge co-production has already been initiated in various forms, for example, through urban living labs (ULLs). These have successfully raised awareness and encouraged collaboration (Miguel et al. 2025; Noble and Enseñado 2022; Cuomo et al. 2021; Evans et al. 2015). However, these efforts remain scattered and have not yet resulted in substantial or systemic change. Thus, knowledge co-production has so far functioned more as a tool for dissemination and education rather than as a transformative approach to resilience.

The degree to which communities are involved also plays a crucial role. Figure 7 further illustrates that community participation within co-production processes often remains consultative rather than co-initiated. Communities are typically invited to provide opinions or validation on predetermined agendas instead of being recognised as initiators or equal partners (Rosen and Painter 2019). This highlights the need for more authentic collaboration, which not only values diverse knowledge systems but also redistributes power and agency, allowing local actors to shape the direction of climate resilience efforts themselves (Cooke et al. 2017; Eaton et al. 2021).

To ensure that knowledge co-production contributes meaningfully to climate resilience, there is a growing need to increase its application and enhance its impact. This requires institutionalisation, equitable power-sharing, sustained investment, and continuous learning. Institutionalisation means embedding co-production practices within formal planning frameworks and governance structures so that they continue beyond project cycles (Pearsall et al. 2022; Vara-Sánchez et al. 2021). Equitable power-sharing involves recognising all stakeholders, including local communities, as knowledge holders and decision-makers, not just as participants offering advice (Pearsall et al. 2022; Gaffy et al. 2022; Rosen and Painter 2019). Sustained investment provides the long-term financial and organisational support needed to maintain collaboration and implementation (McGeown et al. 2023; van der Graaf et al. 2023). Continuous learning allows for reflexive adjustments through iterative evaluation and shared learning mechanisms (Rosen and Painter 2019; Wardani et al. 2025). By taking these steps, knowledge co-production can move from simply generating ideas to producing outcomes with greater impact.

CONCLUSIONS

This systematic literature review, conducted following the PRISMA protocol, highlights the important role of knowledge co-production in improving urban resilience and promoting sustainable urban development in the context of climate change. By combining insights from various publications, the study shows the critical importance of stakeholder involvement, the inclusion of local knowledge, and effective science-policy connections in building resilient urban systems. The findings emphasise the need for joint efforts and knowledge sharing to deal with the many challenges caused by climate-related disturbances and to encourage adaptable actions in cities worldwide. In the future, it will be essential to incorporate knowledge co-production principles and urban living labs into urban planning and policy-making processes. Doing so can help cities lessen the effects of climate change more effectively

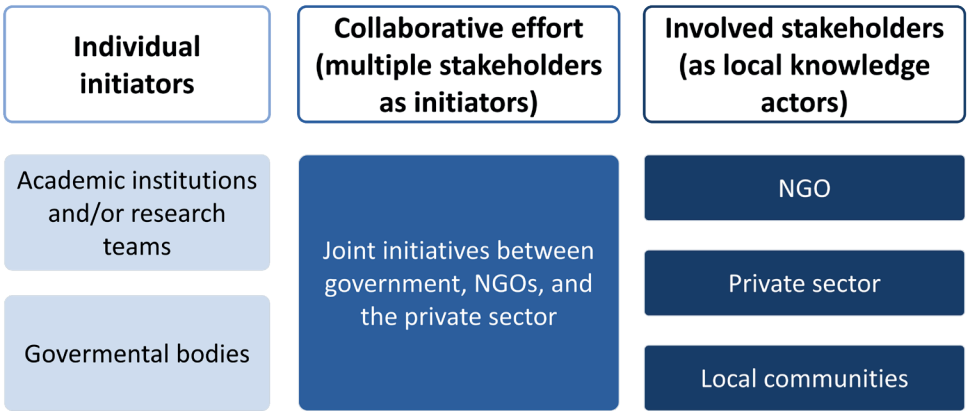

Fig. 7. Stakeholders involved in knowledge co-production

and protect the welfare of urban populations. Additionally, there is increasing awareness of knowledge co-production as a key strategy for improving urban resilience and addressing vulnerabilities related to climate change. By encouraging open decision-making processes and fostering collaboration between different disciplines, cities can use various types of knowledge to build their capacity to adapt and improve their ability to withstand environmental shocks. The results of this review underline the potential of knowledge co-production to transform and shape sustainable and resilient urban futures. Ongoing research, initiatives to build capacity, and policy actions will be vital to support its integration into urban resilience strategies across the globe.

REFERENCES

Adams C., Frantzeskaki N., and Moglia M. (2023). Space for mainstreaming? Learning from the implementation of urban forest strategies in metropolitan Melbourne. Australian Planner, 59(2), 154–169, https://doi.org/10.1080/07293682.2023.2268222

Aguilar-Barajas I., Sisto N. P., Ramirez A. I., and Magaña-Rueda V. (2019). Building urban resilience and knowledge co-production in the face of weather hazards: flash floods in the Monterrey Metropolitan Area (Mexico). Environmental Science and Policy, 99, 37–47, https://doi.org/10.1016/j.envsci.2019.05.021

Aldunce P., Bórquez R., Adler C., Blanco G., and Garreaud R. (2016). Unpacking resilience for adaptation: Incorporating practitioners' experiences through a transdisciplinary approach to the case of drought in Chile. Sustainability, 8(9), https://doi.org/10.3390/su8090905

Ambole A., Musango J. K., Buyana K., Ogot M., Anditi C., Mwau B., Kovacic Z., Smit S., Lwasa S., Nsangi G., Sseviiri H., and Brent A. C. (2019). Mediating household energy transitions through co-design in urban Kenya, Uganda and South Africa. Energy Research and Social Science, 55, 208–217, https://doi.org/10.1016/j.erss.2019.05.009

Asian Development Bank. (2022). Strategy 2030: Urban sector directional guide. [online] ADB. Available at: https://www.adb.org/documents/strategy-2030-urban-sector-directional-guide [Accessed 4 Feb. 2025].

Borquez R., Aldunce P., and Adler C. (2017). Resilience to climate change: from theory to practice through co-production of knowledge in Chile. Sustainability Science, 12(1), 163–176, https://doi.org/10.1007/s11625-016-0400-6

Cooke J., Langley J., Wolstenholme D., and Hampshaw S. (2017). "Seeing" the Difference: The Importance of Visibility and Action as a Mark of "Authenticity" in Co-production Comment on "Collaboration and Co-production of Knowledge in Healthcare: Opportunities and Challenges". IJHPM: International Journal of Health Policy and Management, 6(6), 345-348. https://doi.org/10.15171/ijhpm.2016.136

Culwick C., Washbourne C. L., Anderson P. M. L., Cartwright A., Patel Z., and Smit W. (2019). CityLab reflections and evolutions: Nurturing knowledge and learning for urban sustainability through co-production experimentation. Current Opinion in Environmental Sustainability, 39, 9-16, https://doi.org/10.1016/j.cosust.2019.05.008

Cuomo F., Lambiase N., and Castagna A. (2021). Living lab on sharing and circular economy: The case of Turin. Health Informatics Journal, 1-12. https://doi.org/10.1177/1460458220987278

Djenontin I. N. S. and Meadow A. M. (2018). The art of co-production of knowledge in environmental sciences and management: lessons from international practice. Environmental Management, 61(6), 885–903. https://doi.org/10.1007/s00267-018-1028-3

Dunn G., Brown R. R., Bos J. J., and Bakker K. (2017). The role of science-policy interface in sustainable urban water transitions: Lessons from Rotterdam. Environmental Science and Policy, 73, 71–79, https://doi.org/10.1016/j.envsci.2017.04.013

Eaton W. M., Burnham M., Kirchoff C., Hinrichs C. C. (2021). Expert habits of mind: Implications for knowledge co-production in energy transitions. Energy Research & Social Science, 80, 102234. https://doi.org/10.1016/j.erss.2021.102234

Edelenbos J., Buuren A., and Schie N. (2011). Co-producing knowledge: Joint knowledge production between experts, bureaucrats and stakeholders in Dutch water management projects. Environmental Science and Policy, 14(6), 675–684, https://doi.org/10.1016/j.envsci.2011.04.004

Esmail B. A., Anderson C. C., Bast S., Cortinovis C., Suleiman L., Kato-Huerta J., Högström J., Balfors B., Arciniegas G., Geneletti D., Mörtberg U., and Albert C. (2024). Geodesign to advance boundary work in urban planning: A study in Stockholm focused on nature-based solutions. Ambio, 54, 285-304, https://doi.org/10.1007/s13280-024-02083-8

Evans J., Jones R., Karvonen A., Millard L., Wendler J. (2015). Living labs and co-production: university campuses as platforms for sustainability science. Current Opinion in Environmental Sustainability, 16, 1-6. https://doi.org/10.1016/j.cosust.2015.06.005

Folke C., Jansson Å., Rockström J., Olsson P., Carpenter S. R., Chapin I., Crépin A. S., Daily G., Danell K., Ebbesson J., Elmqvist T., Galaz V., Moberg F., Nilsson M., Österblom H., Ostrom E., Persson Å., Peterson G., Polasky S., Steffen W., Walker B., Westley, F. (2011). Reconnecting to the biosphere. Ambio, 40(7), 719-738, https://doi.org/10.1007/s13280-011-0184-y

Frantzeskaki N. and Kabisch N. (2016). Designing a knowledge co-production operating space for urban environmental governance—Lessons from Rotterdam, Netherlands and Berlin, Germany. Environmental Science and Policy, 62, 90–98, https://doi.org/10.1016/j.envsci.2016.01.010

Gaffy E., Brijnath B., Dow B. (2022). Co-producing research with people impacted by dementia and service providers: issues and challenges. Public Health Research & Practice, 32(2), e3222216, https://doi.org/10.17061/phrp3222216

Handayani W., Chigbu U. E., Rudiarto I., and Putri I. H. S. (2020). Urbanization and increasing flood risk in the northern coast of Central Java – Indonesia: An assessment towards better land use policy and flood management. Land, 9(10), 343, https://doi.org/10.3390/land9100343

Handayani W., Fisher M. R., Rudiarto I., Setyono J. S., and Foley, D. (2019). Operationalizing resilience: A content analysis of flood disaster planning in two coastal cities in Central Java, Indonesia. International Journal of Disaster Risk Reduction, 35, 101073. https://doi.org/10.1016/j.ijdrr.2019.101073

Haque C. E., Zaman J. R., and Walker D. (2023). Risk-Reduction, Coping, and Adaptation to Flood Hazards in Manitoba, Canada: Evidence from Communities in the Red River Valley. Geosciences, 13(3), 88, https://doi.org/10.3390/geosciences13030088

Harvey B., Cochrane L., Epp M. V. (2019). Charting knowledge co-production pathways in climate and development. Environmental Policy and Governance, 29(2), 107-117. https://doi.org/10.1002/eet.1834

Heinzlef C., Lamaury Y., and Serre D. (2024). Improving climate change resilience knowledge through a gaming approach: Application to marine submersion in the city of Punaauia, Tahiti. Environmental Advances, 15, 100467, https://doi.org/10.1016/j.envadv.2023.100467

Holling C. S. (1973). Resilience and Stability of Ecological Systems. Annual Review of Ecology and Systematics, 4(1), 1–23. https://doi.org/10.1146/annurev.es.04.110173.000245

Jabareen Y. (2013). Planning the resilient city: Concepts and strategies for coping with climate change and environmental risk. Cities, 31, 220–229, https://doi.org/10.1016/j.cities.2012.05.004

Johnson C., Osuteye E., Ndezi T., and Makoba F. (2022). Co-producing knowledge to address disaster risks in informal settlements in Dar es Salaam, Tanzania: pathways toward urban equality? Environment and Urbanization, 34(2), 349–371, https://doi.org/10.1177/09562478221112256

Krellenberg K. and Katrin, B. (2014). Inter- and Transdisciplinary Research for Planning Climate Change Adaptation Responses: The Example of Santiago de Chile. Interdisciplinary Science Reviews, 39(4), 360–375. https://doi.org/10.1179/0308018814Z.00000000097

Kronsell A. and Mukhtar-Landgren D. (2018). Experimental governance: The role of municipalities in urban living labs. European Planning Studies, 26(5), 988-1007, https://doi.org/10.1080/09654313.2018.1435631

Larondelle N., Frantzeskaki N., and Haase D. (2016). Mapping transition potential with stakeholder- and policy-driven scenarios in Rotterdam City. Ecological Indicators, 70, 630–643, https://doi.org/10.1016/j.ecolind.2016.02.028

Leichenko R. (2011). Climate change and urban resilience. Current Opinion in Environmental Sustainability, 3(3), 164–168, https://doi.org/10.1016/j.cosust.2010.12.014

Lorencová E. K., Whitham C. E. L., Bašta P., Harmáčková Z. V., Štěpánek P., Zahradníček P., Farda A., and Vačkář D. (2018). Participatory climate change impact assessment in three Czech cities: The case of heatwaves. Sustainability, 10(6), 1906, https://doi.org/10.3390/su10061906

Matsuura S. and Razak K.A. (2019). Exploring transdisciplinary approaches to facilitate disaster risk reduction. Disaster Prevention and Management, 28(6), 817-830, https://doi.org/10.1108/DPM-09-2019-0289

McGeown H., Potter L., Stone T., Swede J., Cramer H., Horwood J., Carvalho M., Connell F., Feder G., Farr, M. (2023). Trauma-informed co-production: Collaborating and combining expertise to improve access to primary care with women with complex needs. Health Expectations, 26(5), 1895-1914. https://doi.org/10.1111/hex.13795

Medema W., Adamowski J., Orr C. J., Wals A., and Milot N. (2015). Towards sustainable water governance: Examining water governance issues in Québec through the lens of multi-loop social learning. Canadian Water Resources Journal, 40(4), 373–391, https://doi.org/10.1080/07011784.2015.1088403

Meerow S., Newell J. P., and Stults M. (2016). Defining urban resilience: A review. Landscape and Urban Planning, 147, 38–49, https://doi.org/10.1016/j.landurbplan.2015.11.011

Miguel J. C. H., Taddei R. R., Moscati M. C. L., Coelho C. A. S., Cavalcanti I. F. A., Rezende L. F., Randow, C. V. (2025). Co-production in climate services for the electricity sector in Brazil – Insights from the CLIMAX project. Climate Service, 38, 100570. https://doi.org/10.1016/j.cliser.2025.100570

Mills K. E., Armitage D., Eurich J. G., Kleisner K. M., Pecl G. T., Tokunaga K. (2023). Co-production of knowledge and strategies to support climate resilient fisheries. ICES Journal of Marine Science, 80, 358-361. https://doi.org/10.1093/icesjms/fsac110

Morzillo A. T., Campbell L. K., King K. L., Lautar K. J., Scott L., Johnson M. L., Clarke M., Rhodes L., Pincetl S., Sonti N. F., Locke D. H., Schmit J. P., Fahey R. T., Baker M. E., Darling L., and Johnson L. R. (2022). A tale of urban forest patch governance in four eastern US cities. Urban Forestry and Urban Greening, 75, 127693, https://doi.org/10.1016/j.ufug.2022.127693

Mpofu-Mketwa T. J., Abrams A., and Black G. F. (2023). Reflections on measuring the soundness of the digital storytelling method applied to three Cape Flats vulnerable communities affected by drought, fire and flooding in Cape Town. Social Sciences & Humanities Open, 7(1), 100407, https://doi.org/https://doi.org/10.1016/j.ssaho.2023.100407

Nesti, G. (2018). Co-production for innovation: The urban living lab experience. Policy and Society, 37(3), 310-325, https://doi.org/10.1080/14494035.2017.1374692

Nicolletti M., Maschietto F., and Moreno T. (2020). Integrating social learning into climate change adaptation public policy cycle: Building upon from experiences in Brazil and the United Kingdom. Environmental Development, 33, 100486, https://doi.org/10.1016/j.envdev.2019.100486

Noble K. and Enseñando E. M. (2022). Analyzing co-creation levels of urban living labs in Europe. Vision for Sustainability, 18. https://doi.org/10.13135/2384-8677/7060

Nochta T., Wan L., Schooling J. M., and Parlikad A. K. (2021). A Socio-Technical Perspective on Urban Analytics: The Case of City-Scale Digital Twins. Journal of Urban Technology, 28(1–2), 263–287, https://doi.org/10.1080/10630732.2020.1798177

Norström A. V., Cvitanovic C., Löf M. F., West S., Wyborn C., Balvanera P., Bednarek A. T., Bennett E. M., Biggs R., Bremond A., Campbell B. M., Canadell J. G., Carpenter S. R., Folke C., Fulton E. A., Gaffney O., Gelcich S., Jouffray J. B., Leach M., Le Tissier M., Martín-López B., Louder E., Loutre M., Meadow A. M., Nagendra h., Payne D., Peterson G. D., Reyers B., Scholes R., Speranza C. I., Spierenburg M., Stafford-Smith M., Tengö M., van der Hel S., van Putten I., and Österblom, H. (2020). Principles for knowledge co-production in sustainability research. Nature Sustainability, 3, 182–190, https://doi.org/10.1038/s41893-019-0448-2

Nowotny H., Scott P., and Gibbons M. (2003). Introduction: `Mode 2' Revisited: The New Production of Knowledge. Minerva, 41(3), 179–194, https://doi.org/10.1023/A:1025505528250

O'Donnell E. C., Thorne C. R., Yeakley J. A., and Chan F. K. S. (2020). Sustainable Flood Risk and Stormwater Management in Blue-Green Cities; an Interdisciplinary Case Study in Portland, Oregon. Journal of the American Water Resources Association, 56(5), 757–775, https://doi.org/10.1111/1752-1688.12854

Odume O. N., Amaka-Otchere A. B., Onyima B. N., Aziz F., Kushitor S. B., and Thiam S. (2021). Pathways, contextual and cross-scale dynamics of science-policy-society interactions in transdisciplinary research in African cities. Environmental Science and Policy, 125, 116–125, https://doi.org/10.1016/j.envsci.2021.08.014

Onyima B. N., Nwabueze L. N., Nnadozie C. F., Omovoh G. O., Mmachaka T., Omovoh B. O., Arimoro F. O., Uku J. E., Akamagwuna F. C., Onyima G. O., Odume O. N. (2025). Livelihood risks arising from urban river pollution in selected marginal communities in the Federal Capital Territory, Nigeria. Urban Ecosystem, 28(1), https://doi.org/10.1007/s11252-024-01646-7

Özerol G., Dolman N., Bormann H., Bressers H., Lulofs K., and Böge M. (2020). Urban water management and climate change adaptation: A self-assessment study by seven midsize cities in the North Sea Region. Sustainable Cities and Society, 55, 102066, https://doi.org/10.1016/j.scs.2020.102066

Page M. J., McKenzie J. E., Bossuyt P. M., Boutron I., Hoffmann T. C., Mulrow C. D., Shamseer L., Tetzlaff J. M., and Moher D. (2021a). Updating guidance for reporting systematic reviews: development of the PRISMA 2020 statement. Journal of Clinical Epidemiology, 134, 103–112, https://doi.org/https://doi.org/10.1016/j.jclinepi.2021.02.003

Page M. J., Moher D., Bossuyt P. M., Boutron I., Hoffmann T. C., Mulrow C. D., Shamseer L., Tetzlaff J. M., Akl E. A., Brennan S. E., Chou R., Glanville J., Grimshaw J. M., Hróbjartsson A., Lalu M. M., Li T., Loder E. W., Mayo-Wilson E., McDonald S., McGuinness L. A., Stewart L. A., Thomas J., Tricco A. C., Welch V. A., Whiting P., McKenzie J. E. (2021b). PRISMA 2020 explanation and elaboration: updated guidance and exemplars for reporting systematic reviews. BMJ, 372, n160, https://doi.org/10.1136/bmj.n160

Pearsall H., Heck S., Tablas M., Pierce J., Hinrich C., Roman L. A., Shabazz J. (2022). Building knowledge infrastructure for diverse stakeholders to scale up co-production equitably. Current Opinion in Environmental Sustainability, 54, 101156, https://doi.org/10.1016/j.cosust.2022.101156

Pillai S. and Narayanan N. C. (2022). Contextual knowledge co-production and capacity building for sanitation planning: experience from Kerala, India. Water Policy, 24(5), 839–855, https://doi.org/10.2166/wp.2021.094

Polk M. and Kain J. (2015). Co-producing knowledge for sustainable urban futures. In: M. Polk, ed., Co-Producing Knowledge for Sustainable Cities: Joining Forces for Change, 1st ed. New York: Routledge. https://doi.org/10.4324/9781315748030

Puerari E., De Koning J. I. J. C., Von With T., Karré P. M., Mulder I. J., and Loorbach D. A. (2018). Co-creation dynamics in urban living labs. Sustainability, 10(6), 1893, https://doi.org/10.3390/su10061893

Radović V. (2020). Emergency Management/Response BT - Climate Action. In W. Leal Filho, A. M. Azul, L. Brandli, P. G. Özuyar, and T. Wall, eds., Cham: Springer Nature Switzerland, 391–404, https://doi.org/10.1007/978-3-319-95885-9_66

Ribeiro P. J. G. and Gonçalves L. A. P. J. (2019). Urban resilience: A conceptual framework. Sustainable Cities and Society, 50, 101625, https://doi.org/10.1016/j.scs.2019.101625

Rosen J. and Painter G. (2019). From citizen control to co-production: Moving beyond a linear conception of citizen participation. Journal of the American Planning Association, 335-347. https://doi.org/10.1080/01944363.2019.1618727

Roué M. and Nakashima D. (2022). Co-production between Indigenous Knowledge and Science: Introducing a Decolonized Approach. In M. Roué, D. Nakashima, and I. Krupnik, eds., Cambridge: Cambridge University Press, 3-24, https://doi.org/10.1017/9781108974349.002

Rudiarto I., Handayani W., and Setyono J. S. (2018). A regional perspective on urbanization and climate-related disasters in the northern coastal region of Central Java, Indonesia. Land, 7(1), 34, https://doi.org/10.3390/land7010034

Ryan D. and Bustos E. (2019). Knowledge gaps and climate adaptation policy: a comparative analysis of six Latin American countries. Climate Policy, 19(10), 1297-1309. https://doi.org/10.1080/14693062.2019.1661819

Schmidt L., Feital M., Cortekar J., di Guilio G., and Engels A. (2024). Understanding the science policy interface in urban climate governance from a co-production perspective: Insights from the cases of Hamburg and Saõ Paulo. Environmental Science and Policy, 156, 103750, https://doi.org/10.1016/j.envsci.2024.103750

Statistisches Bundesamt. (2023). The largest cities worldwide 2023. [online] Destatis. Available at: https://www.destatis.de/EN/Themes/Countries-Regions/International-Statistics/Data-Topic/Population-Labour-Social-Issues/DemographyMigration/UrbanPopulation.html [Accessed 5 Dec. 2023].

Stephenson D. B. (2008). Definition, diagnosis, and origin of extreme weather and climate events. In H. F. Diaz and R. J. Murnane, eds., Cambridge: Cambridge University Press, 11–23, https://doi.org/10.1017/CBO9780511535840.004

Tian Z., Lyu X. Y., Zou H., Yang H. L., Sun L., Pinya M. S., Chao Q. C., Feng A. Q., and Smith B. (2022). Advancing index-based climate risk assessment to facilitate adaptation planning: Application in Shanghai and Shenzhen, China. Advances in Climate Change Research, 13(3), 432–442, https://doi.org/10.1016/j.accre.2022.02.003

Tiitu M., Viinikka A., Ojanen M., and Saarikoski H. (2021). Transcending sectoral boundaries? Discovering built-environment indicators through knowledge co-production for enhanced planning for well-being in Finnish cities. Environmental Science and Policy, 126, 177–188, https://doi.org/10.1016/j.envsci.2021.09.028

Tõnisson L., Kunz Y., Kecorius S., Madueño L., Tamayo E. G., Casanova D. M., Zhao Q., Schikowski T., Hornidge A. K., Wiedensohler A., and Macke A. (2020). From transfer to knowledge co-production: A transdisciplinary research approach to reduce black carbon emissions in metro manila, philippines. Sustainability, 12(23), 1–19, https://doi.org/10.3390/su122310043

Valkering P., Beumer C., Kraker J. D., and Ruelle C. (2013). An analysis of learning interactions in a cross-border network for sustainable urban neighbourhood development. Journal of Cleaner Production, 49, 85–94, https://doi.org/10.1016/j.jclepro.2012.09.010

Valve H., Lazarevic D., Hyysalo S., Lukkarinen J., Marttila T. (2023). The interrupting capacities of knowledge co-production experiments: A sociology of testing approach. Environmental Science & Policy, 147, 255-264, https://doi.org/10.1016/j.envsci.2023.06.019

van der Graaf P., Kislov R., Smith H., Langley J., Hamer N., Cheetham M., Wolstenholme D., Cooke J., Mawson S. (2023). Leading co-production in five UK collaborative research partnerships (2008–2018): responses to four tensions from senior leaders using auto-ethnography. Implementation Science Communications, 4(1), 12. https://doi.org/10.1186/s43058-022-00385-0

Vara-Sánchez I., Gallar-Hernández D., García-García L., Alonso N. M., Moragues-Faus A. (2021). The co-production of urban food policies: Exploring the emergence of new governance spaces in three Spanish cities. Food Policy, 103, 102120, https://doi.org/10.1016/j.foodpol.2021.102120

Visconti C. (2023). Co-production of knowledge for climate-resilient design and planning in Naples, Italy. Habitat International, 135, 102748, https://doi.org/10.1016/j.habitatint.2023.102748

Voytenko Y., McCormick K., Evans J., and Schliwa G. (2016). Urban living labs for sustainability amd low carbon cities in Europe: Towards a research agenda. Journal of Cleaner Production, 123, 45-54, https://doi.org/10.1016/j.jelepro.2015.08.053

Walisser B., Mueller B., and McLean C. (2005). The resilient city. prepared for the world urban forum 2006 by the Vancouver Working Group. Canada: Ministry of Community, Aboriginal and Women's Services, Government of British Columbia.

Wang L. and Xue X. (2018). Exploring the Evolution Trends of Urban Resilience Research. ICCREM 2018, [online], 18–27. Available at: https://ascelibrary.org/doi/10.1061/9780784481745.003 [Accessed 11 Jan. 2024].

Wardani J., (Annette) Bos J. J., Ramirez-Lovering D., Capon A. (2025). From complexity to integration: Insights for process design from an empirical case study of transdisciplinary planetary health collaboration in Indonesia. Earth System Governance, 23, 100233. https://doi.org/10.1016/j.esg.2024.100233

World Bank. (2024). Urban population. [online] World Bank. Available at: https://data.worldbank.org/indicator/SP.URB.TOTL [Accessed 10 Dec. 2024]

Yumagulova L. and Vertinsky I. (2019). Moving beyond engineering supremacy: Knowledge systems for urban resilience in Canada's Metro Vancouver region. Environmental Science and Policy, 100, 66–73, https://doi.org/10.1016/j.envsci.2019.05.022

RESEARCH PAPER

THE CHERNOBYL SIGNATURE IN WESTERN ABKHAZIA: ASSESSING ^{137}CS DEPOSITION VARIABILITY AND APPLICABILITY FOR EVALUATION SEDIMENT REDISTRIBUTION RATES

N.V. Kuzmenkova[1], V.N. Golosov[2,3], A.K. Fomina[2], M.V. Markelov[4], N.P. Zaraiskiy[2], N.E. Zaretskaya[3], E.A. Eremenko[2]

[1]Lomonosov Moscow State University, Chemistry Faculty, 119991, Moscow, Leninskie Gory. 1, Russia, kuzmenkovanv@my.msu.ru,

[2]Lomonosov Moscow State University,Faculty of Geography, 119991, Moscow, Leninskie Gory 1, Russia

[3]Institute of Geography RAS, 119017, Moscow, Staromonetny per. 29, str. 4, Russia

[4]JSC "Institute of Environmental Survey, Planning & Assessment", 1192341, Moscow, Leninskiye Gory, bld. 751, Russia

Received: June 19th 2025 / Accepted: November 12nd 2025 / Published: December 31st 2025

***Corresponding author:** kuzmenkovanv@my.msu.ru

https://doi.org/10.24057/2071-9388-2025-4097

ABSTRACT. This study presents the first documented evidence of radioactive contamination in Western Abkhazia linked to the Chernobyl Nuclear Power Plant accident. The data obtained show that the level of ^{137}Cs radioactive contamination in the study area ranged from 50 to 160 kBq/m^2 in 1986. This corresponds to contemporary values of 25 to 79 kBq/m^2 when considering the radionuclide's half-life. These measurements are highly consistent with data recorded in the adjacent Sochi region, where contamination levels varied between 40 and 185 kBq/m^2 in 1986. The local spatial variability of ^{137}Cs fallout was studied at four reference sites, located in different parts of the Mussera upland. All investigated sites demonstrated moderate variability, with value ranges of 17–25%. This heterogeneous distribution pattern is attributed to a combination of factors, including local topography, atmospheric deposition characteristics, and anthropogenic influence. Measurements of ambient dose equivalent rates ranged from 0.01 to 0.05 μSv/h. While no direct correlation was found between dose rates and the age or genesis of the underlying bedrock, a clear relationship was established between dose rates and terrain morphology. Elevated dose rates were consistently recorded in erosional landforms within topographically dissected areas. Analysis of peat cores from the Pitsunda Peninsula lagoon provided conclusive evidence of the Chernobyl disaster's impact on Western Abkhazia, with a measured ^{137}Cs inventory of 20.7 kBq/m^2 (equivalent to 49.5 kBq/m^2 when corrected to 1986 values). Application of the non-equilibrium ^{210}Pb dating method yielded a peat accumulation rate of 0.1 cm/year.

The Chernobyl accident resulted in a significant release of ^{137}Cs, leading to widespread radioactive fallout. This document assesses the ^{137}Cs inventory and its impact on ambient dose rates in the affected regions.

KEYWORDS: reference value of Chernobyl-derived 137Cs, dose rate, trend of initial fallout, 210Pb dating, Mussera upland

CITATION: Kuzmenkova N.V., Golosov V.N., Fomina A.K., Markelov M.V., Zaraiskiy N.P., Zaretskaya N.E., Eremenko E.A. (2025). The Chernobyl Signature in Western Abkhazia: Assessing ^{137}Cs Deposition Variability and Applicability for evaluation sediment redistribution rates. Geography, Environment, Sustainability, 4 (18), 127-138
https://doi.org/10.24057/2071-9388-2025-4097

ACKNOWLEDGEMENTS: This work was carried out within the framework of the state task of the Department of Radiochemistry, Faculty of Chemistry, Lomonosov Moscow State University, «Solving problems of nuclear energy and environmental safety, as well as diagnostics of materials using ionising radiation» (project reg. number 122030200324-1) and of the state task of the Research Laboratory of Soil Erosion and Fluvial Processes of the Faculty of Geography of Lomonosov Moscow State University (project No. 121051100166-4). The expedition was organised with the support of «Cenozoic evolution of the environment, the dynamics of the relief, geomorphological hazards and risks of land-use» (project No. 121040100323-5).

Conflict of interests: The authors reported no potential conflict of interests.

INTRODUCTION

Cesium-137 (^{137}Cs), as one of the key anthropogenic radionuclides, shows a high adsorption affinity to soil particles. During initial global fallout events (e.g., following nuclear bomb tests or technological accidents), a primary contamination field was established (Buraeva et al., 2015; De Cort, 1998; Ivanov et al., 2022; Kuchava et al., 2019; Kuzmenkova et al., 2020; Sedighi et al., 2020; Tsitskishvili et al., 2020). However, subsequent water, wind, and tillage erosion processes lead to the active redistribution of ^{137}Cs across landscapes. The primary mechanisms that govern

the lateral migration rates of this radionuclide include: water erosion, which facilitates soil particle detachment and transport (Evrard et al., 2017; Golosov et al., 2021); aeolian erosion, which promotes fine particle entrainment, wind-driven transport, and redeposition (Van Pelt et al., 2007); and anthropogenic activities, particularly agricultural land use practices (Lobb et al., 1995). These processes, along with other more localised factors, significantly alter the initial radioactive contamination pattern. Notably, secondary accumulation zones emerge with ^{137}Cs inventories substantially exceeding initial deposition levels (Varley et al., 2018). Such anomalies predominantly occur in sedimentary sinks: lower segments of cultivated slopes; unmanaged slope bases; dry valley bottoms; river floodplains and water bodies (Golosov et al., 2018).

The relevance of studying these processes stems from the need to:

- Assess the consequences of radioactive accidents: the redistribution of ^{137}Cs affects the actual contamination levels of territories.
- Predicting contamination dynamics, understanding lateral migration mechanisms enables forecasting changes in radiation conditions.
- Develop rehabilitation measures. Identifying accumulation zones aids in planning risk mitigation strategies.

Moreover, ^{137}Cs has become an important tool in geomorphological studies. The presence of two distinct global fallout peaks (1963 from nuclear weapons testing and 1986 from the Chernobyl accident) can be identified in ^{137}Cs vertical distribution profiles in samples collected from accumulation zones across most of Europe and several regions of the Greater Caucasus. This radiocesium technique enables the dating of deposits and the estimation of sediment accumulation rates for two different time windows (Benoit and Rozan, n.d.; Efimov and Anisimov, 2011; Ito et al., 2020; Izrael, 2007; Łokas et al., 2017; Tashilova et al., 2019). This provides new opportunities for studying the dynamics of erosion-accumulation processes under various landscape conditions. Research on ^{137}Cs redistribution therefore represents an important interdisciplinary field combining radiation ecology, geomorphology, and environmental protection objectives.

The determination of reference inventories serves as the starting point for investigating relative changes in contaminant concentrations across a landscape. To establish the total deposition density of ^{137}Cs within a study area, reference sites are selected (Walling, 1999). These sites represent flat, geomorphologically stable surfaces (the upper parts of slopes, river terraces) where no loss or gain of ^{137}Cs has occurred since its initial deposition (Golosov et al., 2008).

When selecting reference sites, the following conditions must be satisfied:

represent stable lithodynamic zones, meaning soil erosion is negligible, changes in contaminant concentrations are minimal, and the ^{137}Cs inventory can be considered relatively 'undisturbed' (Ivanov, 2017).

Ideally, it should have been free from anthropogenic disturbances (for example, ploughing, soil levelling, or external material input) since the initial atmospheric deposition of ^{137}Cs, which means over the past 70 years.

preferably lack of woody vegetation, with grassland areas being the most suitable.

Verification of a reference site's undisturbed condition is conducted by analysing the vertical distribution profile of ^{137}Cs content, supported by examination of soil profile morphology (Owens, Walling, 1996; Sutherland, 1996; Golosov, 2002; Golosov et al., 2008). The vertical distribution of ^{137}Cs is obtained through layer-by-layer sampling from either a soil pit wall or an extracted monolith of fixed surface area, with typical sampling intervals of 2-5 cm. Analysis of the vertical distribution of radioisotopes within the soil column enables identification of the maximum contamination layer corresponding to the initial deposition event. In undisturbed sites, this layer is typically found in the near-surface horizon at a depth of 2-4 cm (Owens, Walling, 1996; Golosov et al., 2008).

Following the Chernobyl accident, various datasets concerning ^{137}Cs contamination in different European countries and regions were compared. These data had been collected for diverse purposes, leading to significant variations in their resolution and quality. Consequently, the Atlas of Caesium Contamination of Europe and the European Territory of Russia was compiled (Izrael, 2007). However, there remain areas where data continue to be collected through more thorough and extensive monitoring. This is particularly relevant for regions that experienced more substantial contamination. One such hotspot of Chernobyl-derived contamination is the Western Caucasus region (Fig. 1). In Abkhazia, such studies are especially important because the contaminated area remains undelimited, with its boundary coinciding with the state border.

According to the radioactive contamination map, the Western Caucasus region had an inventory of 10-40 kBq/m^2 as of 1986. This value includes radiocesium from global fallout and deposition from the Chernobyl accident.

The research objectives of the given study are as follows: a) a comprehensive assessment of ^{137}Cs specific activity and inventories in soils of Western Abkhazia, focusing on undisturbed near-watershed areas; b) an evaluation of initial deposition patterns across the Mussera Upland to establish baseline data for sediment accumulation rate

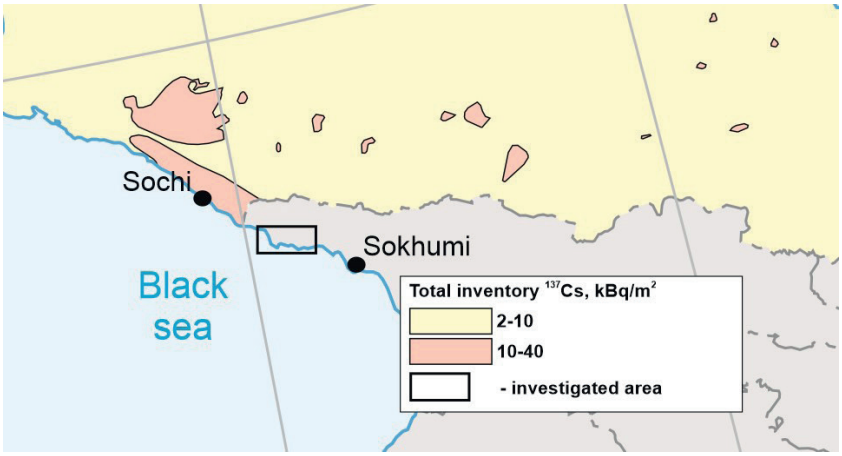

Fig. 1. Section of the ^{137}Cs contamination map of Europe following the Chernobyl NPP accident (Izrael, 2007)

studies; c) the quantification of the Chernobyl impact by determining total ^{137}Cs inventories along the Black Sea coastal zone within Western Abkhazia.

STUDY AREA

The Mussera Upland is a scenic natural and recreational zone characterised by its picturesque landscapes, mild climate, and significant potential for tourism development. Located in Abkhazia on the northeastern coast of the Black Sea, approximately 20 km northwest of Gudauta, the area encompasses the Mussera Nature Reserve, renowned for its pine forests and relict vegetation.

The climate is humid subtropical with warm winters and moderately hot summers. Average January temperatures range from 5 to 7°C, while August temperatures average between 23 and 24.7°C. In the mid-mountain areas, winters are cold, and summers are short and cool. January temperatures range from 2 to -2°C, and August temperatures are between 16 and 18°C. The average annual precipitation is 1400 mm. The soil cover includes subtropical zone soils such as red soils and podzolized red soils, yellow soils, strongly and moderately podzolic soils, weakly podzolic soils, and podzolic-gley soils. Bog and alluvial soils are also found in fragmented areas (Atlas, 1964). Plant communities include pine (Pinus bruita var. pityusa) stands, which are a relic of Neogene flora. Other communities are liana forests, lowland forests with evergreen undergrowth, foothill oak forests, foothill beech-hornbeam forests, beech forests, chestnut forests, spruce-fir forests, alpine meadows, and bogs dominated by sedge and grass.

The terrain forms a plain that narrows westward, sloping gently southwestward and reaching absolute elevations of 30-35 m. It is bordered by the southern spurs of the Bzyp Range to the north and the Black Sea to the south. This lowland was formed by alluvial-marine accumulation during the Quaternary (Balabanov, 2009). Within the main deltaic areas of the Kodori and Inguri Rivers, the lowland has a Holocene alluvial-marine terrace (5-6 m above sea level, up to 4 km wide). Outside these deltaic areas, the lowland shows a series of Holocene alluvial-marine levels. These surfaces, which slope gently seaward, are cut by small river valleys. The edges and back slopes of these levels are not clearly defined in the relief. Their slightly inclined surfaces are at absolute elevations of 6-18 m and 26-38 m.

For our study of initial ^{137}Cs contamination variability in Western Abkhazia, four reference sites were selected within the Mussera Upland (Fig. 2). The selection of these reference sites presented challenges due to the extensive tree canopy coverage across the Mussera Upland. The few areas free of tree cover were often anthropogenically modified. However, the relatively flat upper part of slopes, located near the local watershed of the Mussera Upland, are generally not used for agricultural purposes. All selected sites are covered with herbaceous vegetation but border shrub thickets or forest stands. Each reference site featured a relatively flat or gently sloping surface along a watershed divide, preventing any potential redeposition of eroded materials.

A brief description of each of the four reference sites is provided in Table 1.

Additionally, two peat cores were taken from a currently paludified paleolagoon situated in the central and southern parts of the Pitsunda Peninsula. These locations range from 0 to 6 metres above sea level (refer to Fig.2 for sampling location). The site is within the modern Novochernomorskaya terrace, which features an almost flat, gently undulating surface. The cores were extracted using a manual Dutch auger (Eijkelcamp) from the southeastern edge of the peat bog.

Materials and Methods

At the reference sites, soil pits were excavated to collect incremental samples from areas of 15×15 cm at 3 cm intervals (5 to 13 samples per site) for analysing the vertical distribution profiles of ^{137}Cs. Bulk samples were also collected to determine total ^{137}Cs inventories throughout the soil column. These bulk samples were taken from the surface to a depth of 20-30 cm using an Eijkelkamp cylindrical corer with an inner diameter of 5 cm. Samples for layer sampling were carefully collected from a 10×10 cm area using a spatula. The number of samples and characteristics of the study sites are provided in Table 2. The sampling point arrangement system is shown in Figure 3.

The primary objective of collecting bulk soil samples (0-30 cm depth) at reference sites is to determine the total inventory of ^{137}Cs within a specified soil layer. There was

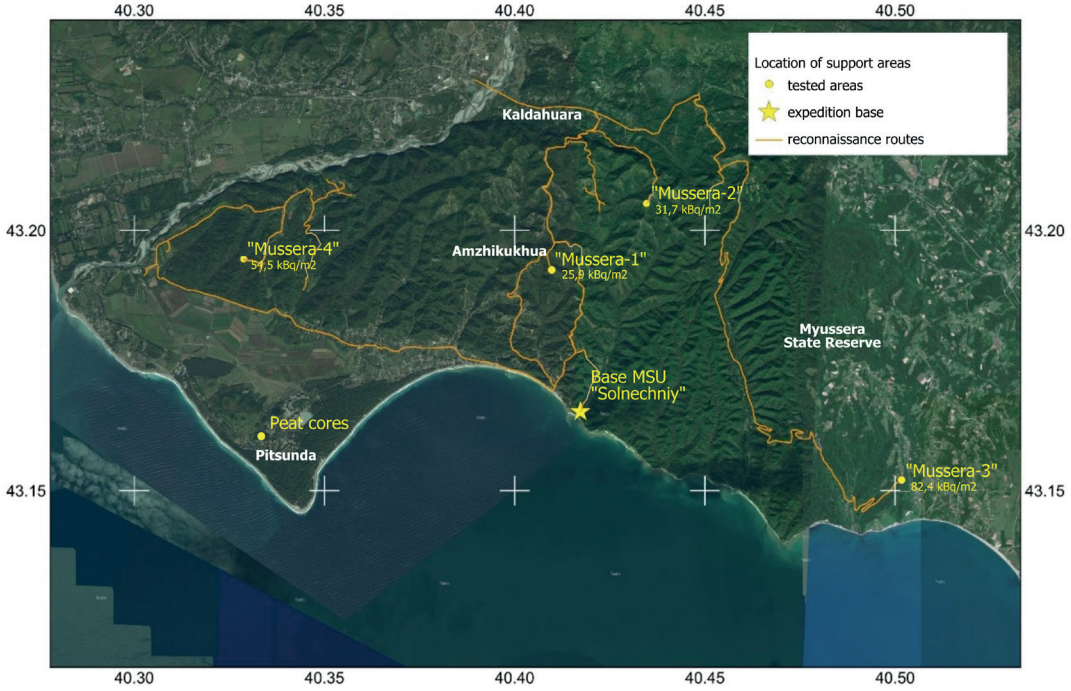

Fig. 2. Location of reference sites on the Mussera Uplands (background - Google Earth satellite image)

Table 1. Location and characteristics of the surveyed reference sites

Reference site	Location	Coordinates	Absolute height of the site, m	Surface character, vegetation and economic use
Mussera-1	interfluve of the Riapsh and Tsanigvarta Rivers	N 43.19 239E 40.40 967	200-205	Vertex surface of ridge outcrop, herbaceous vegetation, hornbeam, beech and chestnut trees on the periphery of the plot, pasture
Mussera-2	interfluve of the Mysra and Colchis rivers	N 43.20 523E 40.43 475	250-256	Top surface of rounded ridge, herbaceous vegetation, along the periphery hornbeam trees, pasture
Mussera-3	interfluve of Ambara and Mchishta rivers, near Mgudzyrhua village	N 43.15 205E 40.50 167	150-156	Top surface of the ridge, herbaceous vegetation and sporadic blackberry bushes
Mussera-4	interfluve of Bzyb and Adzidu Rivers, in the vicinity of Atsidjkva village	N 43.19 446E 40.32 875	90-95	Top surface of the ridge spur, sparse oak forest with rhododendron and blackthorn, road track and orchard

Table 2. Sampling parameters at the surveyed reference sites

Reference site	Area of sampling site, m^2	bulk samples		incremental samples		Sampling point location system
		number of sampling	depths, cm	number of sampling	depths, cm	
Mussera-1	110	10	30 (27)	10	30	in quasi-parallel lines
Mussera-1	450	11	17-20	7	20	in quasi-parallel lines
Mussera-1	300	10	15	5	15	random sampling
Mussera-1	280-300	10	30	13	40	random sampling

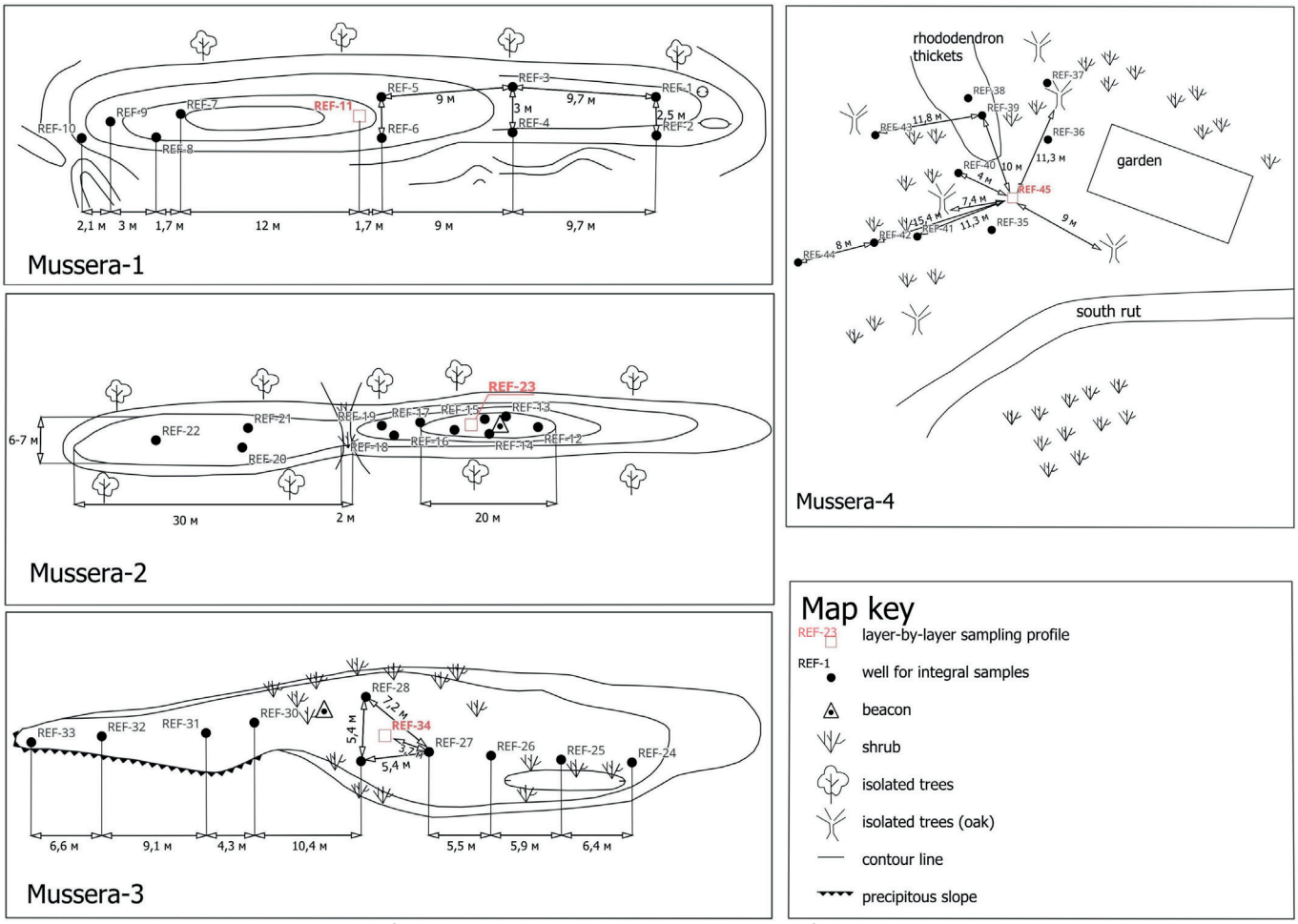

Fig. 3. Location of sampling points at the investigated reference sites (a Mussera-1; b Mussera-2; c Mussera-3; d Mussera-4)

some variability associated with sample collection using a narrow core tube (25 cm^2 surface area) at the reference sites. It is unlikely that the surface area was exactly 25 cm^2 for each of the bulk samples collected. It is possible to suggest that the magnitude of such sampling variability is a function of the surface area over which the samples are collected (Martynenko 2003, Loughran et al. 1988; Owens and Walling 1992). In the case of the Mussera upland, with large quantities of gravel and stones, the sampling area factor had a more significant influence. This approach provides crucial data on the local-scale variability of initial radionuclides fallout within each reference site. The observed variability in ^{137}Cs inventories at reference sites depends on several factors: (1) local landscape and geomorphic conditions at each sampling point, including microtopography and vegetation characteristics; (2) spatial heterogeneity of initial atmospheric deposition; and (3) methodological subjectivity, encompassing sampling errors, analytical procedures, and calculation methods (Golosov et al. 2008). The greater the local variability in contamination levels, the larger the number of samples required to obtain statistically reliable estimates of mean ^{137}Cs specific activity in soils. The minimum necessary number of randomly collected samples can be calculated using the following formula:

$$N_0 = \left[\frac{t_{\alpha, N-1} - C_v}{E_A} \right]^2 \quad (1)$$

The file system, a core component of any operating system, is responsible for organising and managing data on storage devices.

N_0 = minimum number of samples required for statistically reliable determination of ^{137}Cs content with permissible error E_A

N = number of collected soil samples

$t(\alpha, N-1)$ is the inverse value of the Student's t-distribution with N-1 degrees of freedom and confidence probability α

Cv = coefficient of variation for ^{137}Cs content in soil

Typically, for a permissible error of 10% at a 90% confidence level (α=0.1), a minimum of 12 composite samples is required (Ivanov, 2017). Verification of reference sites for the absence of external disturbances was performed by analysing the vertical distribution profiles of ^{137}Cs content and soil profile morphology (Golosov et al., 2008).

The peat cores extracted from the Pitsunda bog measured 50 cm in length and were sectioned at 2 cm intervals for subsequent sample preparation and analysis. The samples consisted of dark brown, well-decomposed peat containing abundant woody debris. Occasional mineral grains were observed within the peat matrix.

For analysis of gamma-emitting radionuclide content, the samples underwent preparatory processing. Initially, stones and particles larger than 2 mm were separated from each sample using a sieve set. Subsequently, each sample was dried in an oven at 105°C for 8 hours. Following drying, the samples were ground to a powdered state and transferred into standard geometry containers (plastic vials measuring 5×6 cm) for subsequent gamma spectrometric analysis. The content of gamma-active radionuclides was determined using an ORTEC GEM-C5060P4-B gamma spectrometer, which is equipped with an ultrapure germanium (HPGe) semiconductor detector with a beryllium window and a relative efficiency of 20%. Gamma-spectrometric measurements were performed using the certified hardware and software complex 'SpectraLine', which is officially registered in the Russian Federation. The measurements were conducted in strict accordance with the certified methodology (Registration number in the Federal Information Fund for Ensuring the Uniformity of Measurements: FR.1.38.2024.49 576.). The mass of the dried samples ranged from 45 to 130 grams and the measurement time was at least 60 000 seconds. The expanded uncertainty for the activity measurements was 5.1% (k=2). This value was derived from a combination of Type A (statistical) and Type B (systematic) uncertainties, with the latter including components for sampling (3%), sample preparation (2%), and instrument calibration (2%). However, the varying and generally quite large inclusion of gravel, fine crushed stone and, in some cases, small pebbles significantly influenced the reliable determination of the density of each sample and, as a result, the estimation of specific activity.

The excess lead (^{210}Pbex) was determined by subtracting the specific activity of ^{226}Ra from the total specific activity of ^{210}Pb. To determine the age of the sediment based on the concentration of ^{210}Pbex, the Constant Rate of Supply (CRS) model was used.

$$t(x) = (1/\lambda) \times In\left[A(\infty)/A(x)\right]$$

where: $t(x)$ – peat age, years; $A(\infty)$ – is the total unsupported ^{210}Pb inventory in the core, Bq/m^2, A(x) – is the cumulative unsupported ^{210}Pb inventory below depth x, Bq/m^2, λ – radioactive decay constant of ^{210}Pb. The accumulation model was developed using the R (rplum) software package. The package considers peat density, the amount of unsupported lead, and the measurement error of the values.

As part of the expedition, dose rate measurements were also made using RadioCode101 and AtomFast dosimeters linked to a smartphone. The dose rate measurements were carried out in accordance with standard field practices. The detector was positioned 1 metre above the ground. The measurement time at each point was at least 2 minutes to ensure statistical significance of the results. For each site, at least 10 point measurements were taken, after which the average value and standard deviation were calculated. The aim of the work was to map the dose rate indicators and explain the revealed regularities, including their connection with the geological and geomorphological structure of the study area. This was carried out in Western Abkhazia for the first time.

At the Mussera-1 site, the highest specific activity values for the isotope and its reserves are recorded in the incremental sample REF-11. Here, a specific activity peak of 520 Bq/kg is observed in the 3-6 cm layer, corresponding to reserves of 15.7 kBq/m^2 (Fig. 4). The trend of decreasing total inventories can be seen from the southwest to the northeast of the linearly elongated area (see Fig. 3 and Fig. 4, bulk samples). The local variability of the inventories can be explained mainly by the unevenness of atmospheric deposition of the radionuclide, as well as by local site conditions at each sampling point (e.g., microrelief features) (Golosov et al., 2008).

The total ^{137}Cs inventory in the selected column averages to that of bulk sample 1, which is 40.9 kBq/m^2. This is slightly higher than the average for the bulk samples (25.3 kBq/m^2). However, in this instance, the total inventory assessment can be considered more accurate because the sampling area was 15 × 15 centimetres. The profile of the vertical distribution of ^{137}Cs suggests that this area has not experienced anthropogenic impact, apart from grazing by domestic animals.

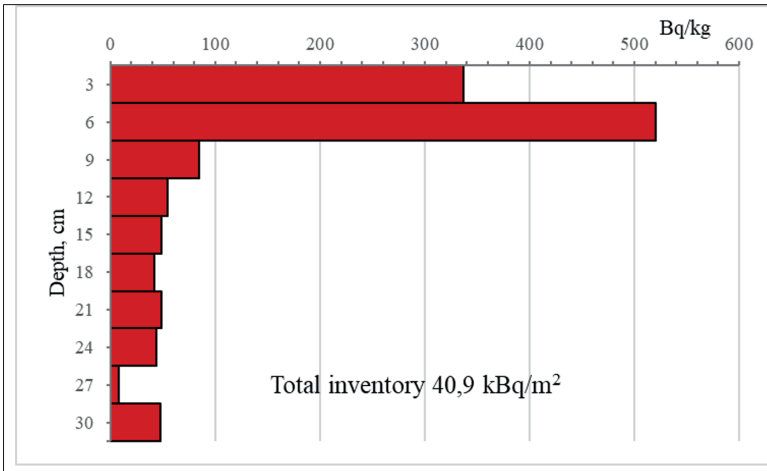

Bulk sample number	Inventory, kBq/m²
REF-1	35.6
REF-2	28.9
REF-3	22.6
REF-4	27.8
REF-5	29.8
REF-6	16.6
REF-7	18.3
REF-8	19.5
REF-9	24.6
REF-10	18.6

Fig. 4. Depth distribution of specific activity of ^{137}Cs (Bq/kg) in section and inventory in bulk samples of the Mussera-1 (REF-11) site (kBq/m²)

The Mussera-2 site shows a similar trend to the first reference site. Peak values in the REF-23 sample are also observed in the 3-6 cm layer (Fig. 5). In bulk, the total ^{137}Cs inventory in the selected column is on average the same as the average of the integral samples (29.8 kBq/m²), equalling 30.1 kBq/m². The total ^{137}Cs inventory is clearly underestimated, since specific activity in the lower horizons is quite high, and cesium probably penetrated deeper into the soil profile.

Mussera-3 is distinct from other sites due to its highest values of specific activity and inventory. In bulk samples, these reach up to 626 Bq/kg and 27.1 kBq/m² respectively (Fig. 6). The specific activity in layers 0-3 cm and 3-6 cm within sample REF-34 is the highest across the entire study area. The inventory in these layers is considerably lower than in bulk samples, not exceeding 28 kBq/m². The peak inventory occurs in the 3-6 cm layer, similar to previously considered sites. The 137Cs reserve in the section matches the average of the bulk samples (78.8 kBq/m²), equalling 80.2 kBq/m².

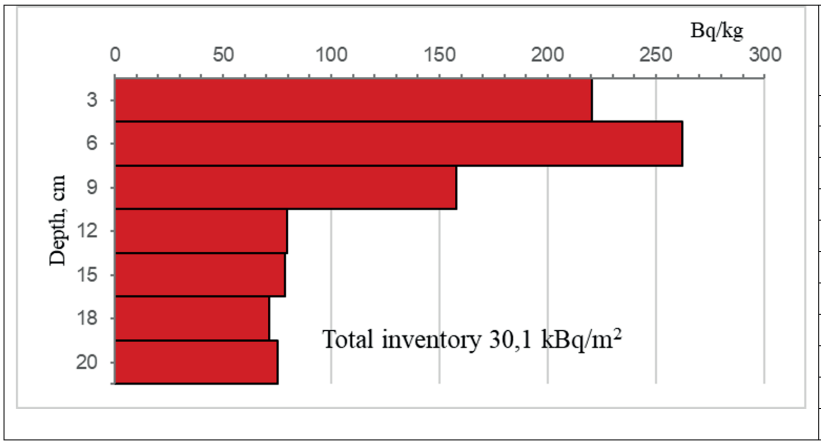

Bulk sample number	Inventory, kBq/m²
REF-12	32.9
REF-13	38.7
REF-14	29.8
REF-15	39.9
REF-16	25.3
REF-17	36.2
REF-18	32.3
REF-19	28.9
REF-20	29.5
REF-21	11.5
REF-22	23.2

Fig. 5. Depth distribution of specific activity of ^{137}Cs (Bq/kg) in section and inventory in bulk samples of the Mussera-2 (REF-23) site (kBq/m²)

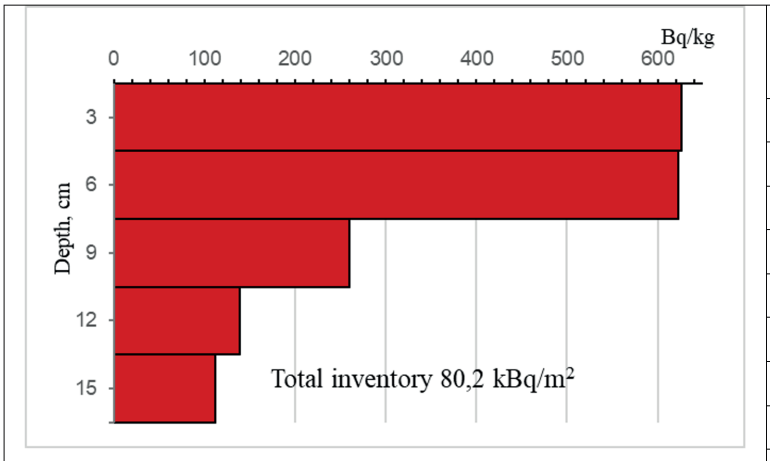

Bulk sample number	Inventory, kBq/m²
REF-24	61.9
REF-25	107
REF-26	62.6
REF-27	50.4
REF-28	94.9
REF-29	85.5
REF-30	70.1
REF-31	86.6
REF-32	90.6
REF-33	86.1

Fig. 6. Depth distribution of specific activity of ^{137}Cs (Bq/kg) in section and inventory in bulk samples of the Mussera-3 (REF-34) site (kBq/m²)

At the Mussera-4 site, specific activity values for all composite samples exceeded 100 Bq/kg, except for REF-44 (33 Bq/kg). Inventories ranged from 30 to 84 kBq/m^2. The vertical distribution of inventories shows a characteristic trend common to all samples: specific activity and inventories decrease with depth (Fig. 7). The peak concentration occurs in the surface layer (0-3 cm).

The total inventory throughout the soil profile is 55.6 kBq/m^2, while the current average across bulk samples is 52.3 kBq/m^2. These findings strongly suggest that this soil profile developed in an area subject to anthropogenic influence, likely including tillage operations. Field observations further indicate the sampling point's proximity to an abandoned orchard, supporting the hypothesis of historical agricultural use at this location.

The variability of bulk inventory values for all sites averaged 17-25%, indicating moderate variability (Table 3). Comparison with the Atlas of Radioactive Contamination of European Russia (De Cort, 1998), which reports values of 40-185 kBq/m^2 for the Sochi region in the Caucasus, reveals that our measurements for Western Abkhazia range from 50-160 kBq/m^2 for 1986 (equivalent to 25-79 kBq/m^2 at present). These findings provide compelling evidence of Chernobyl-derived contamination in Abkhazia, which had previously been known only to a limited circle of scientists. The contamination is associated with heavy precipitation events and air mass trajectories in May 1986. The established ^{137}Cs deposition patterns, combined with identified regional trends, enable the use of this radionuclide as a tracer for quantifying the proportional contributions of various sediment sources to the sediment flux in rivers draining the upland area.

For the paleolagoon cores, the total ^{137}Cs inventory was determined to be 20.7 kBq/m^2 for core 1 and 20.2 kBq/m^2 for core 2 at present. This is equivalent to 49.7 kBq/m^2 for 1986. These values closely align with those obtained from the Mussera-1 reference site. Specific activity ranged from 30 to 240 Bq/kg. Both cores, sampled in close proximity to each other, exhibit relatively similar ^{137}Cs depth distribution (Fig. 8), confirming proper sampling methodology.

The cesium peaks have a broad, irregular shape, indicating that the water in the marsh is constantly rising and falling. A zero value was not reached, suggesting that the total inventory may be underestimated. Oldfield et al. (1995) provide data supporting the view that ^{137}Cs profiles in recent ombrotrophic peat may be displaced by both movement in solution and active biological uptake.

Examination of the distribution of $^{210}Pb_{ex}$ showed a peat formation rate of 0.1 cm/yr (Figure 9). Non-equilibrium lead with minor fluctuations is observed down to the 14th horizon. This indicates that a period of 150-180 years is reached at this horizon, allowing for an accurate calculation of the peat formation rate.

For column 1, a small loss of the upper part of the core was established, which is related to sampling and proves the necessity of core duplication.

The dose rate in the studied region ranges from less than 0.05 μSv/h to 2 μSv/h (Fig. 9). The background radiation level for the area can be determined to be within the range of 0.01-0.5 μSv/h. The distribution of radiation indicators is heterogeneous. On the watershed ridges of the Mussera Upland, the values generally do not exceed 0.5 μSv/h. Maximum values (2.3 μSv/h) were found in the western part of the Mussera Upland, in the basin of the Bzyb River on a ridge near an anthropogenic object (building). Elevated radiation dose rates are also observed in the area between the Ryapsh and Mussera rivers (1.32 μSv/h). In the valley of the Ryapsh River, values were recorded at 1.74 μSv/h near a stable and 1.32 μSv/h upstream on a landslide terrace, near a dirt road.

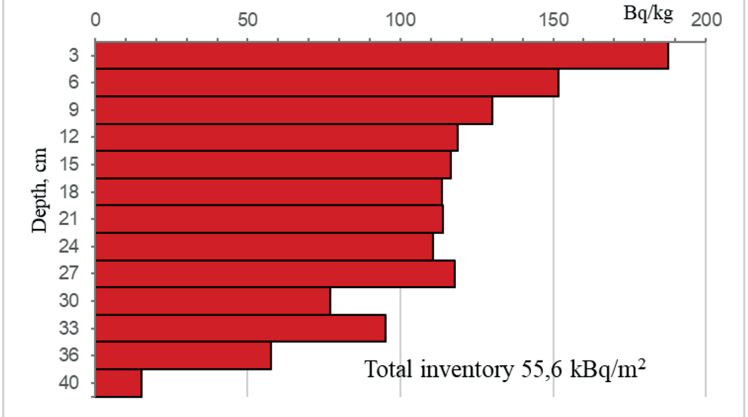

Bulk sample number	Inventory, kBq/m^2
REF-35	69.5
REF-36	57.3
REF-37	84.3
REF-38	45.9
REF-39	52.2
REF-40	49.1
REF-41	51.2
REF-42	37.1
REF-43	32.4
REF-44	43.9

Fig. 7. Depth distribution of specific activity of ^{137}Cs (Bq/kg) in section and inventory in bulk samples of the Mussera-4 (REF-45) site (kBq/m^2)

Table 3. Statistical results of ^{137}Cs specific activity and ^{137}Cs inventory measurements in bulk samples

Reference site	Specific activity, Bq/kg		Inventory, kBq/m^2		CV, %	Inventory, kBq/m^2*		CV*, %	Inventory, kBq/m^2 (1986)	
	mean	min-max	mean	min-max		mean	min-max		mean	min-max
Mussera-1	97.4	40.5-245	24.9	16.6-35.6	25	25.9	28.3-35.6	25	50.2	33.6-71.9
Mussera-2	139	61.5-311	29.8	11.5-39.9	26	31.7	23.2-39.9	17	60.3	23.2-80.6
Mussera-3	296	176-471	78.8	50.4-107	23	82.4	61.9-107	23	159	102-216
Mussera-4	126	33.1-175	52.3	32.4-84.3	25	54.5	37.1-84.3	22	105.6	65.4-170

without extremes

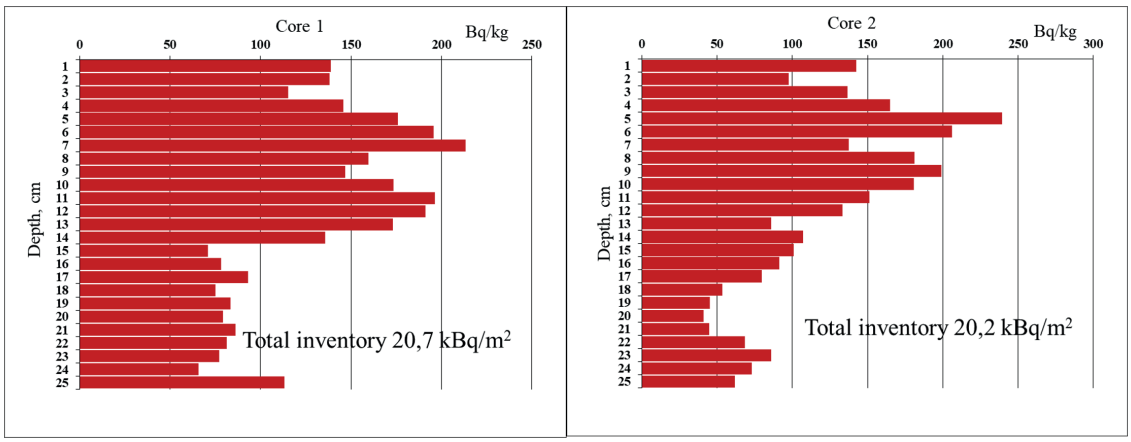

Fig. 8. Specific activity of ^{137}Cs (Bq/kg) in sections and inventory in bulk samples of the peat cores (kBq/m²)

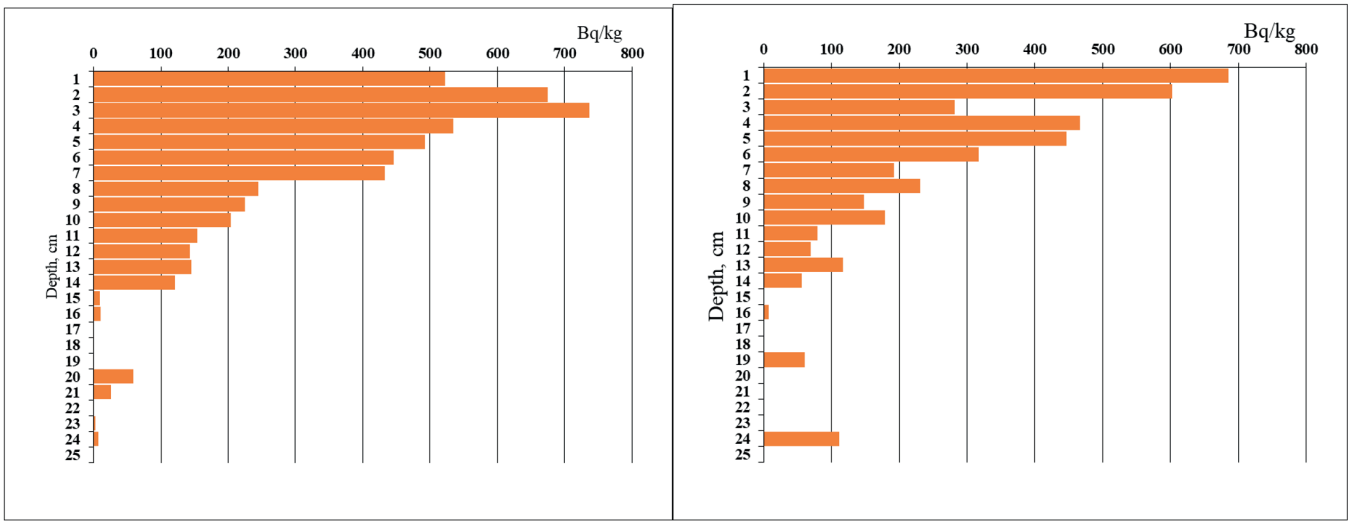

Fig. 9. Specific activity of $^{210}Pb_{ex}$ in cores 1 and 2 of Pitsunda palaeolagoon, Bq/kg

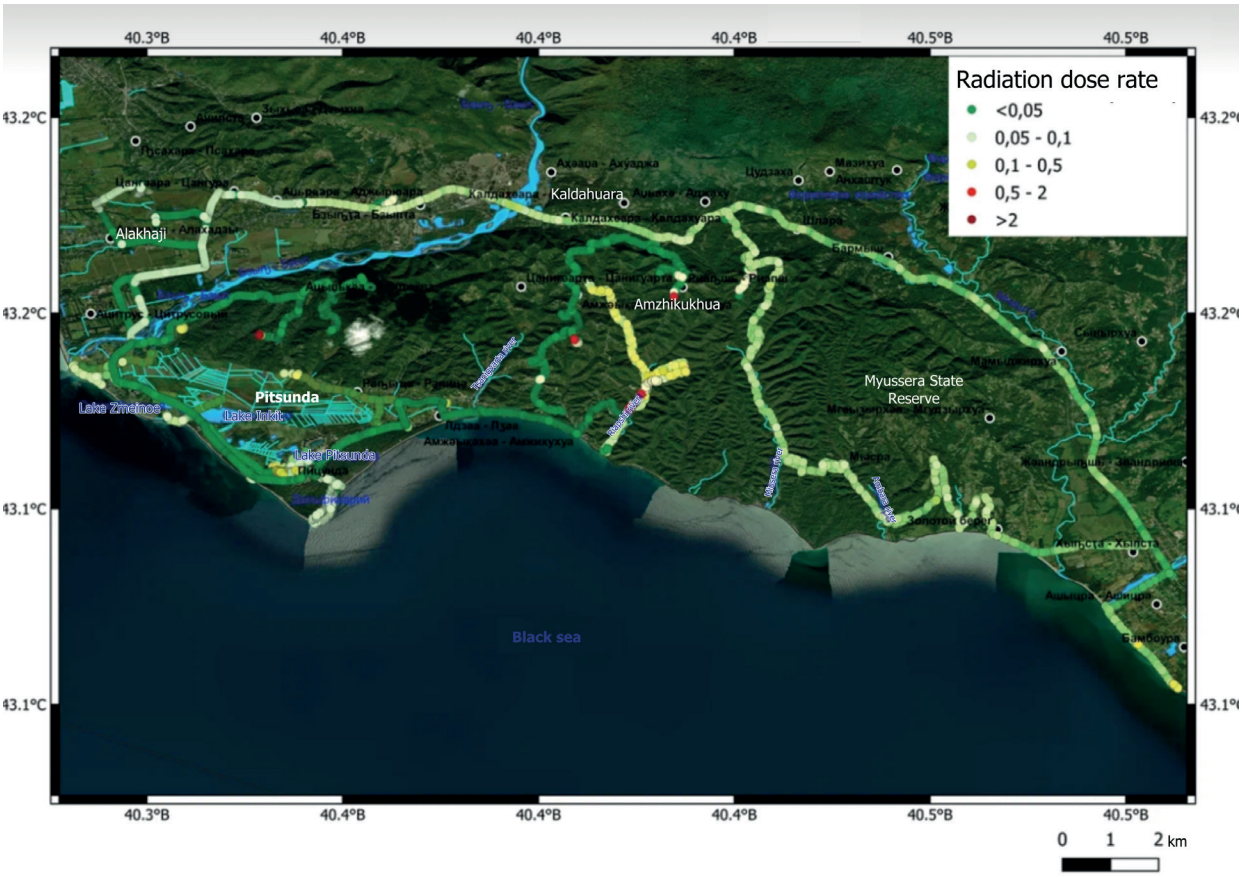

Fig. 10. Dose rate of the investigated area of Mussera Upland

The western part of the study area, near the town of Pitsunda, is the region with the lowest average radiation doses (less than 0.05 μSv/h). However, there are localised increases of up to 0.1–0.5 μSv/h in the central part of the town. These might be linked to human activity, such as artificial road and building surfaces containing natural radioactive elements like uranium and thorium. Slightly elevated values are also seen near the coast, which is attributed to the presence of pebble beaches containing naturally occurring radionuclides (uranium and thorium) in the rocks.

DISCUSSION

It should be noted that the average values of ^{137}Cs reserves calculated on the basis of reserves in bulk samples for three of the four reference sites were close to the total reserves of caesium-137 in the pits. The only exception is reference site 1, where the reserves in the pit were higher than the average value calculated for the bulk samples. This indicates that the obtained values of average reserve values are reliable. In the case of reference site 1, the differences are due to a very large amount of gravel and small stones in the bulk samples.

There are few sources of observed variability in ^{137}Cs inventories at the reference sites, including random spatial variability, systematic spatial variability, sampling variability, and measurement precision (Owens and Walling, 1996). Random spatial variability is associated in this case with differences in soil bulk density, porosity, the number of stones, plant roots, and vegetation cover. The latter may particularly influence the reference sites at Mussera Upland because some bushes were located at different distances from the sampling points. Topography is another key reason for the random variability, particularly in the cases of reference sites 1 and 2, which are located on narrow, gently sloping surfaces (Fig. 3 a, b). It can be assumed that some of the caesium-137 at these sites was lost with surface runoff before being fixed on soil particles. The lower total ^{137}Cs inventories at sampling points located relatively higher than others support this assumption.

Systematic spatial variability is associated with variations in precipitation. This is particularly typical for mountain areas (Higgitt et al., 1992; Kirchner, 2013) and for areas where Chernobyl-derived ^{137}Cs fallout occurred (Golosov, 2002; Golosov et al., 1999). The Chernobyl-derived ^{137}Cs fallout was associated with one, or at most, two rain events (Izrael, 2007; Kuzmenkova et al. 2023). Consequently, the radioactive contamination pattern reflects the pattern of rain that fell on the studied area. The reference site Mussera-3 is located closest to the sea. It can be assumed that more precipitation fell here compared to other sites.

The exceptionally high ^{137}Cs specific activity (627 Bq/kg) recorded at Mussera-3 in surface soil layers demands particular attention. The elevated levels likely reflect intense rainfall events in May 1986, which scavenged airborne radionuclides from the Chernobyl plume. Similar patterns were observed in Alpine regions (Smith et al., 2000) and Scotland (Bunzl et al., 1995), where localised 'hotspots' formed due to orographic rainfall. The predominant northwest-to-southeast transport of contaminated air masses (Izrael, 2007) explains why Mussera-3, located in a topographically exposed position, received higher deposition than coastal sites. Comparable trends were documented in France (Foucher et al., 2015), where mountainous areas intercepted more fallout than lowlands. The observed decline in total ^{137}Cs inventories toward the coast is consistent with the dilution of global fallout by marine aerosol deposition and specific coastal wind patterns. This pattern is evident in New Zealand's coastal peatlands, where the already low ^{137}Cs signal from mid-20th century nuclear weapons testing is further suppressed in coastal areas (Pearson et al., 2019).

The availability of data on ^{137}Cs reserves at reference sites allows the radiocesium method to be used to solve various problems in assessing the redistribution of sediments by erosion-accumulative processes in the study area. In particular, differences in the ^{137}Cs content in surface soil horizons, landslide bodies, and eroded river banks allow us to assess their proportional contribution to the total sediment load of rivers, as is done in other mountainous countries (Förstner et al., 2018). Increasing extreme rainfall (IPCC, 2023) may accelerate the rate of erosion on the Mussera upland, as is already observed in Europe (Fulajtar et al., 2017).

The radiocesium method also allows estimation of accumulation rates in various sediment sinks such as reservoirs, river floodplains, and the lower parts of slopes (Linnik et al., 2005; Linnik, 2011). However, the radiocesium technique cannot be used for swampy water bodies because in an acidic environment, a significant portion of ^{137}Cs dissolves (Kudelsky et al., 1996). In this context, the atmospheric component of 210Pb was used as a chronomarker for the accumulation rate in a swampy lagoon on a seaside terrace in the Pitsunda area. Peat accumulation rates (0.1 cm/yr) are slower than in Alpine bogs (0.15–0.3 cm/yr; Le Roux et al., 2012), possibly due to faster decomposition rates in Abkhazia (Fig. 11). The mean accumulation rate (0.1–0.2 cm/yr) is consistent with ombrotrophic bogs in temperate regions (e.g., 0.05–0.1 cm/yr in New Zealand; Pearson et al., 2019), but is slower than in Alpine peatlands (0.15–0.3 cm/yr; Le Roux et al., 2012). Lower organic productivity occurs due to warmer decomposition rates in subtropical climates (Chambers et al., 2010). Limited mineral input is indicated by low Al values, contrasting with minerotrophic European bogs (Shotyk et al., 2002). The unsupported ^{210}Pb peak (250–290 Bq/m^2/yr) likely records 20th-century industrial aerosol deposition, mirroring trends in Swiss peat cores (Roos-Barraclough et al., 2002). The memory parameters (mem.strength: 10) suggest bioturbation or gradual compaction, similar to Finnish peatlands (Tolonen et al., 1992). This differs from abrupt deposition in floodplain lakes (Oldfield et al., 1997), highlighting Pitsunda's stable hydroclimate.

It was found that the radiation dose rate, even though remaining relatively low, appreciably depends on the geomorphological position of the measurement point. In the bottoms of canyon-like ravines and gorges of river valleys the dose rate increases, while on watershed ridges it decreases. This is due to the different potential for sediment accumulation and erosion characteristic of these geomorphological positions, which affects the concentration of radionuclides in the surface layer. Thus, in gorges with steep slopes the sources of natural radioactivity (rocks) surround the measurer from three sides, while on watershed ridges only from one side. The absence of correlation with bedrock age or genesis contrasts with findings in New Zealand's volcanic terrains (Herman et al., 2010) but aligns with studies emphasising topography-driven radionuclide redistribution (Golosov et al., 2021). This reinforces the dominance of surface processes over lithology in controlling dose rates.

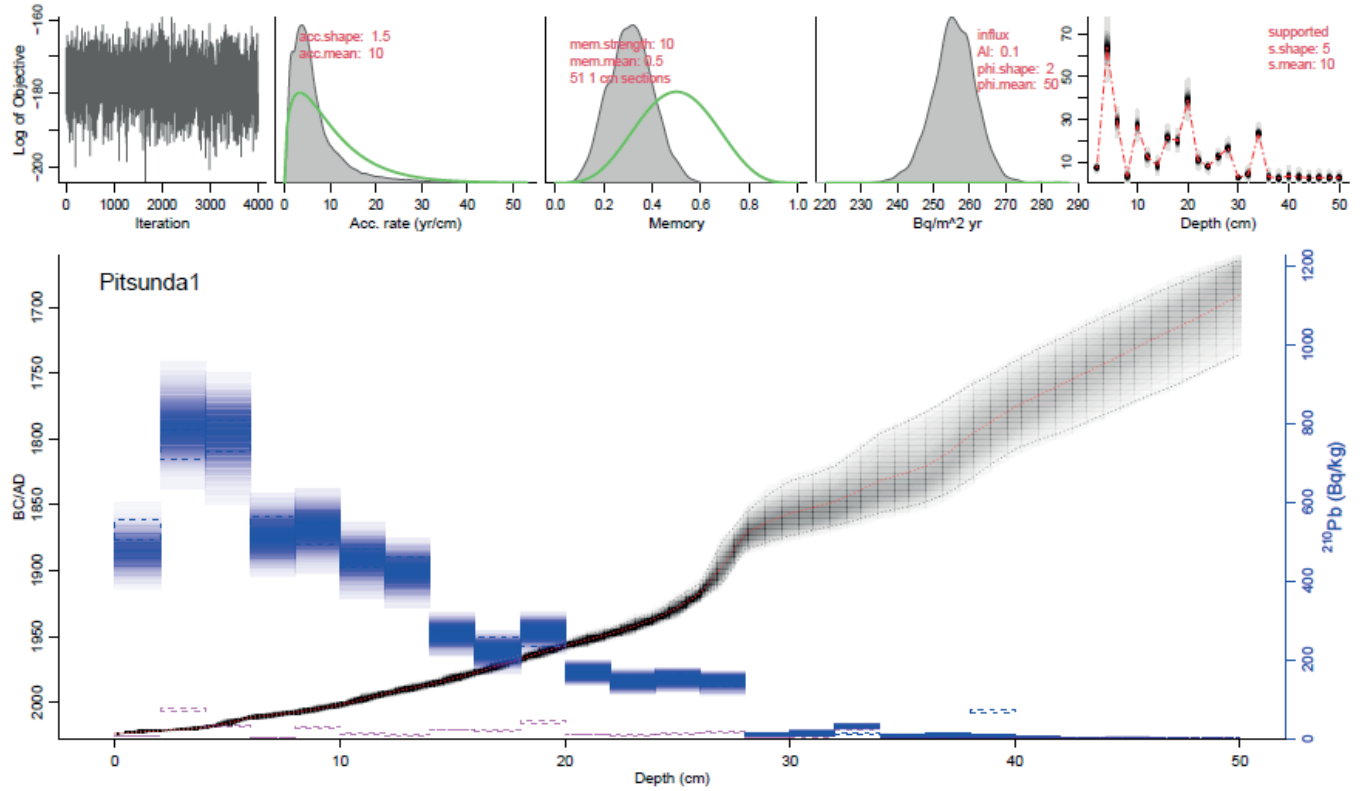

Fig. 11. Variation of sedimentation rate in column 1 obtained with the Rplum package

(Aquino-López et al., 2008). Blue bars: Measured unsupported ^{210}Pbex activity data. The height of the bar represents the activity value, and the width represents the depth interval of the sampled sediment section. Solid black line: The model's prediction of the ^{210}Pbex activity profile based on the measured data. Grey shaded area: The 95% confidence interval (or uncertainty range) of the model's activity prediction. Red dashed vertical lines: Reference horizons used to validate the model. Modeled ages (on the secondary x-axis) show the sediment accumulation timeline derived by the model. 'BC/AD': This label refers to the calendar year scale on the age axis (X-axis of the chronology panel). 'BC' stands for Before Christ and 'AD' for Anno Domini.

The findings indicate no direct correlation between the geological structure of the area and the measured dose rate levels. For example, outside of deeply incised river valleys, the values recorded on the Mussera Upland, which is composed of Neogene conglomerates, and those on the Pitsunda Lowland are comparable. This can be attributed to the fact that both landforms are made up of denudation products originating from the southern macro-slope of the Greater Caucasus Range, with no significant differences observed in the petrographic composition of the loose and cemented sedimentary rocks found there.

CONCLUSION

For the first time, the ^{137}Cs inventory for the territory of Western Abkhazia has been established for four reference sites. It is 25-79 kBq/m^2 for the year 2024. The elevated ^{137}Cs inventories are likely largely associated with Chernobyl fallout, considering the chronology and geographical proximity of the study area to the affected zone of the Chernobyl accident. The variability of values for the reference sites is moderate, so they can be considered indicative for the estimation of the total ^{137}Cs inventory.

Using a non-equilibrium lead analysis, the peat formation rate in the Pitsunda palaeolagoon was determined to be 0.1 cm/year. The total ^{137}Cs inventory, measuring 20.4 kBq/m^2 in 2024, confirmed the values established for the reference sites and the impact of the Chernobyl disaster on Western Abkhazia.

The background dose rate in the area of the expedition operations was determined to be 0.01-0.5 μSv/h. The highest values were observed in the central part of the Musser Upland, specifically in the Ryapsh River valley (approximately 0.1 - 0.5 μSv/h). The lowest values were found in the south-eastern part of the Musser Reserve and on the Pitsunda Peninsula, in coastal areas (approximately <0.05 μSv/h). No direct link between the dose rate and the age or origin of the underlying rocks in the study area was established. However, a direct relationship was found between the dose rate and the territory's relief. Higher dose rates were measured in areas with more dissected relief and within the bottoms of erosion forms.

This study not only fills the knowledge gap regarding radioactive contamination in Abkhazia but also presents new opportunities. These include the application of the radiocesium technique to study sediment redistribution rates and to evaluate the proportional contribution of different sediment sources to the total sediment load of regional rivers. The data acquired can provide a foundation for future research focused on reconstructing the history of modern landscape formation and assessing the intensity of exogenous processes.

The results obtained are of great practical importance as they allow ^{137}Cs to be used as a reliable chronomarker for assessing the intensity of sediment accumulation processes in the region's sediment sinks. The spatial heterogeneity of the radionuclide distribution revealed should be considered, which requires a careful approach to the selection of reference sites for such studies.

REFERENCES

Aquino-López, M.A., Blaauw, M., Christen, J.A. et al. Bayesian Analysis of Pb Dating. JABES 23, 317–333 (2018). https://doi.org/10.1007/s13253-018-0328-7

Balabanov I.P. Paleogeograficheskie predposylki formirovaniya sovremennykh prirodnykh usloviy i dolgosrochnyy prognoz razvitiya golotsenovykh terras Chernomorskogo poberezh'ya Kavkaza. Moskva-Vladivostok, «Dal'nauka», 2009, 352 s. (in Russian).

Buraeva, E.A., Bezuglova, O.S., Stasov, V.V., Nefedov, V.S., Dergacheva, E.V., Goncharenko, A.A., Martynenko, S.V., Goncharova, L.Yu., Gorbov, S.N., Malyshevsky, V.S., Varduny, T.V. (2015). Features of 137Cs distribution and dynamics in the main soils of the steppe zone in the southern European Russia. Geoderma 259–260, 259–270. https://doi.org/10.1016/j.geoderma.2015.06.014

Chambers, F.M., Beilman, D.W., Yu, Z. (2010). Methods for determining peat humification and for quantifying peat bulk density, organic matter and carbon content for palaeostudies of climate and peatland carbon dynamics. Mires and Peat, 7(7), 1–10.

De Cort, M. (1998). Atlas of caesium deposition on Europe after the Chernobyl accident.

Efimov, V.V., Anisimov, A.E. (2011). Climatic parameters of wind-field variability in the Black Sea region: Numerical reanalysis of regional atmospheric circulation. Izv. Atmospheric Ocean. Phys. 47, 350–361. https://doi.org/10.1134/S0001433811030030

Ivanov M.M., Kuzmenkova N.V., Rozhkova A.K., Grabenko E.A., Grachev A.M., Golosov V.N., (2022). The anthropogenic fallout radionuclides in soils of Mount Khuko (the Western Caucasus) and their application for determination of sediment redistribution, Journal of Environmental Radioactivity, Volume 248, 106880, https://doi.org/10.1016/j.jenvrad.2022.106880.

Evrard O., J. P. Laceby, H. Lepage, Y. Onda, O. Cerdan, S. Ayrault. (2015). Radiocesium transfer from hillslopes to the Pacific Ocean after the Fukushima Nuclear Power Plant accident: a review. J. Environ. Radioact. 148, 92–110.

Eyrolle, F., Radakovitch, O., Raimbault, P. (2012). Consequences of hydrological events on the delivery of suspended sediment and associated radionuclides from the Rhône River to the Mediterranean Sea. J Soils Sediments 12, 1479–1495. https://doi.org/10.1007/s11368-012-0575-0

Förstner, U., et al. (2018). Sediment dynamics and pollutant mobility in rivers: An interdisciplinary approach. Springer.

Foucher, A., Evrard, O., et al. (2015). Increased contribution of radionuclide deposition in mountainous areas: The case of the French Alps. Journal of Environmental Radioactivity, 148, 87-94.

Frédéric Herman, Edward J. Rhodes, Jean Braun, Lukas Heiniger. (2010) Uniform erosion rates and relief amplitude during glacial cycles in the Southern Alps of New Zealand, as revealed from OSL-thermochronology, Earth and Planetary Science Letters, Volume 297, Issues 1–2, https://doi.org/10.1016/j.epsl.2010.06.019.

Golosov V.N., Ivanov M.M., Tsyplenkov A.S. (2021). Erosion as a factor of transformation of soil radioactive contamination in the basin of the Shchekino Reservoir (Tula Region). Eurasian Soil Sci 54:291–303. https://doi.org/10.1134/S106422932102006X

Golosov, V.N. (2002). Special considerations for areas affected by Chernobyl fallout. In: Zapata, F. (Ed.), Handbook for the Assessment of Soil Erosion and Sedimentation Using Environmental Radionuclides. Kluwer Academic Publishers, Dordrecht, pp. 165–183

Golosov, V.N., Walling, D.E., Konoplev, A.V., Ivanov, M.M., Sharifullin, A.G. (2018). Application of bomb- and Chernobyl-derived radiocaesium for reconstructing changes in erosion rates and sediment fluxes from croplands in areas of European Russia with different levels of Chernobyl fallout. J. Environ. Radioact. 186, 78–89. https://doi.org/10.1016/j.jenvrad.2017.06.022

Golosov, V.N., Walling, D.E., Panin, A.V., Stukin, E.D., Kvasnikova, E.V., Ivanova, N.N. (1999). The spatial variability of Chernobyl-derived 137Cs inventories in a small agricultural drainage basin in central Russia. Applied Radiation and Isotopes 51, 341–352.

Golosov, V.N., Markelov, M.V., Belyaev, V.R., & Zhukova, O.M. (2008). Problemy opredeleniya prostranstvennoy neodnorodnosti vypadeniy ^{137}Cs dlya otsenki tempov erozionno-akkumulyativnykh protsessov [Problems of assessing spatial heterogeneity of ^{137}Cs fallout for evaluation of erosion-accumulation rates]. Meteorologiya i Gidrologiya, 4, 30-45 (in Russian).

Higgitt, D.L., Froehlich, W., Walling, D.E. (1992). Applications and limitations of Chernobyl radiocaesium measurements in a Carpathian erosion investigation, Poland. Land Degradation and Rehabilitation 3, 15–26.

Improved Models for Estimating Soil Erosion Rates from Cesium-137 Measurements - Walling - 1999 - Journal of Environmental Quality - Wiley Online Library [WWW Document], n.d. (accessed 4.26.25).

Ito, E., Miura, S., Aoyama, M., Shichi, K. (2020). Global 137Cs fallout inventories of forest soil across Japan and their consequences half a century later. J. Environ. Radioact. 225, 106421. https://doi.org/10.1016/j.jenvrad.2020.106421

Ivanov, M.M. (2017). Geomorfologicheskiy podkhod k izucheniyu radioaktivnogo zagryazneniya malykh vodosborov v predelakh osvaivaemykh ravnin [Geomorphological approach to studying radioactive contamination in small catchments of cultivated plains]. Geomorfologiya i Paleogeografiya, (0), 30-45 (in Russian). https://doi.org/10.15356/0435-4281-2017-1-30-45

Izrael, Y.A. (2007). CHERNOBYL RADIONUCLIDE DISTRIBUTION AND MIGRATION. Health Phys. 93, 410–417. https://doi.org/10.1097/01.HP.0000285092.10598.41

J.T. Smith, P.G. Appleby, J. Hilton, N. (1997). Richardson, Inventories and fluxes of 210Pb, 137Cs and 241Am determined from the soils of three small catchments in Cumbria, UK, Journal of Environmental Radioactivity, Volume 37, Issue 2. https://doi.org/10.1016/S0265-931X(97)00003-9.Benoit, G., Rozan, T.F., n.d. 210Pb and 137Cs dating methods in lakes: a retrospective study 12.

Kirchner, G. (2013). Establishing reference inventories of Cs-137 for soil erosion studies: methodological aspects. Geoderma 211, 107–115. http://dx.doi.org/10.1016/j.geoderma.2013.07.011.

Kuchava, N., Imnadze, P., Nikolaishvili, I., Chkhartishvili, L. (2019). Case Study on Vertical Migration of 137Cs Radionuclide in Soil of Two Resorts in Georgia after 31 Years from Chernobyl Accident.

Kudelsky, A.V., Smith, J.T., Ovsiannikova, S.V., Hilton, J., 1996. Mobility of Chernobyl-derived 137Cs in a peatbog system within the catchment of the Pripyat River, Belarus. The Science of the Total Environment 188, 101-113.

Kuzmenkova, N.V., Ivanov, M.M., Alexandrin, M.Y., Grachev, A.M., Rozhkova, A.K., Zhizhin, K.D., Grabenko, E.A., Golosov, V.N. (2020). Use of natural and artificial radionuclides to determine the sedimentation rates in two North Caucasus lakes. Environ. Pollut. 262, 114269. https://doi.org/10.1016/j.envpol.2020.114269

Kuzmenkova Natalia, Golosov Valentin, Ivanov Maxim, Alexandrin Mikhail, Korneva Irina, Grabenko Evgeny, Rozhkova Alexandra, Bykhalova Olga (2023). Bottom sediment radioactivity of the six Caucasus lakes located in different altitude zones. Environ Sci Pollut Res 30, 50690–50702. DOI https://doi.org/10.1007/s11356-023-25838-4

Le Roux, G., De Vleeschouwer, F., Piotrowska, N., et al. (2012). High-altitude peat bog records of atmospheric deposition in the European Alps. The Holocene, 22(7), 751–762. DOI: 10.1177/0959683611434223

Linnik, V.G., Brown, J.E., Dowdall, M., Potapov, V.N., Surkov, V.V., Korobova, E.M., Volosov, A.G., Vakulovsky, S.M., Tertyshnik, E.G. (2005). Radioactive contamination of the Balchug (Upper Yenisey) floodplain, Russia in sedimentation processes and geomorphology. Sci. Total Environ. 399 (1–3), 233–251.

Linnik, V.G. (2011). Technogenic radionuclides in floodplains of the Techa and the middle part of the Yenisey Rivers. Vestnik (Series 5, Geography), 4. Moscow State University 24–30 (in Russian).

Lobb, D.A., Kachanoski, R.G., Miller, M.H. (1995). Tillage translocation and tillage erosion on shoulder slope landscape positions measured using cs-137 as a tracer. Canadian. Journal of Soil Science 75 (2), 211–218.

Łokas, E., Wachniew, P., Jodłowski, P., Gąsiorek, M. (2017). Airborne radionuclides in the proglacial environment as indicators of sources and transfers of soil material. J. Environ. Radioact. 178–179, 193–202. https://doi.org/10.1016/j.jenvrad.2017.08.018

Loughran R. J., Elliott G. L., Campbell B. L. and Shelley D. J. (1988). Estimation of soil erosion from caesium-137 measurements in a small, cultivated cathment in Australia. Appl. Radiot. Isot. 39, 1153.

Martynenko, V.P., Linnik, V.G., Govorun, A.P. et al. Comparison of the Results of Field Radiometry and Sampling in the Investigation of 137Cs Soil Content in Bryansk Oblast. Atomic Energy 95, 727–733 (2003). https://doi.org/10.1023/B:ATEN.0000010992.31484.3c.

Oldfield, F., Richardson, N., Appleby, P.G. (1995). Radiometric dating (210Pb, 137Cs, 241Am) of recent ombrotrophic peat accumulation and evidence for changes in mass balance. The Holocene 5, 141–148. https://doi.org/10.1177/095968369500500202

Oldfield, F., Wake, R., Boyle, J., et al. (1997). The late-Holocene history of Gormire Lake (NE England) and its catchment: A multiproxy reconstruction of past human impact. The Holocene, 7(1), 101-110.

Owens, P.N., Walling, D.E. (1996). Spatial variability of caesium-137 inventories at reference sites: an example from two contrasting sites in England and Zimbabwe. Appl. Rad. Isot. 47, 699-707.

Pearson, E.J., et al. (2019). Peatland carbon accumulation in a warming world: A case study from New Zealand. Global Change Biology, 25(12), 4254-4268.

Pearson, E.J., Royles, J., Amesbury, M.J., et al. (2019). Peatland carbon accumulation in a warming world: A case study from New Zealand. Global Change Biology, 25(12), 4254–4268. DOI: 10.1111/gcb.14834

Roos-Barraclough, F., Shotyk, W., Norton, S.A. (2002). *A 14,500-year record of peat accumulation in Switzerland.* The Holocene, 12(6), 687–696.

Sedighi, F., Darvishan, A.K., Golosov, V., Zare, M.R. (2020). Relationship between Mean Annual Precipitation and Inventories of Fallout Radionuclides (137Cs and 210Pbexcess) in Undisturbed Soils around the World: A Review. Eurasian Soil Sci. 53, 1332–1341. https://doi.org/10.1134/S1064229320090148

Shotyk, W., et al. (2002). A peat bog record of atmospheric Pb pollution since the Roman times. Science, 281(5383), 1635–1640.

Sutherland, R.A. (1996). Caesium-137 soil sampling and inventory variability in reference locations: a literature survey. Hydrol. Processes 10, 43±53

Tashilova, A.A., Ashabokov, B.A., Kesheva, L.A., Teunova, N.V. (2019). Analysis of Climate Change in the Caucasus Region: End of the 20th–Beginning of the 21st Century. Climate 7, 11. https://doi.org/10.3390/cli7010011

Tolonen, K., Warner, B.G., & Vasander, H. (1992). Ecology of Testaceans (Protozoa: Rhizopoda) in mires in southern Finland: I. Autecology. Archiv für Protistenkunde, 142(1-2), 119-138.

Tsitskishvili, M.S., Tsitskishvili, M.M., Chkhartishvili, A.G. (2020). Artificial Radionuclides in the Caucasus Int. Sci. Conf. "Modern Probl. Ecol. 7. (in Russian)

V. N. Golosov, "Special considerations for areas affected by Chernobyl fallout,"In Zapata (ed.) Handbook for the Assessment of Soil Erosion and Sedimentation Using Environmental Radionuclides (Kluwer, Dordrecht, 2002),pp. 165–183.

Van Pelt, R. S., Zobeck, T. M., Ritchie, J. C., & Gill, T. E. (2007). Validating the use of 137 Cs measurements to estimate rates of soil redistribution by wind. Catena, 70(3), 455–464. https://doi.org/10.1016/j.catena.2006.11.014

Varley A., A. Tyler, Y. Bondar, A. Hosseini, V. Zabrotski, M. Dowdall, (2018). Reconstructing the deposition 137Cs environment and long-term fate of Chernobyl at the floodplain scale through mobile gamma spectrometry, Environ. Pollut. 240, 191–199.

RESEARCH PAPER

SEAGRASSES (ZOSTERACEAE AND RUPPIACEAE) IN RUSSIA: DISTRIBUTION, DIVERSITY, PROSPECTS FOR FURTHER RESEARCH

A. Iurmanov[1, 2*], I. Popov[3], A. Gnedenko[4], Y. Lebedev[5], M. Kulikovskiy[2]

[1]Murmansk Arctic University, st. Kapitana Egorova, 15, Murmansk 183038, Russia;

[2]K.A. Timiryazev Institute of Plant Physiology Russian Academy of Sciences, st. Botanicheskaya, 35, Moscow, 127276, Russia

[3]Saint-Petersburg State University, n. Universitetskaya, 7/9, Saint-Petersburg, 199034, Russia;

[4]Institute of Geography Russian Academy of Sciences, st. Staromonetniy, 29, Moscow, 119017, Russia;

[5]RUDN University, st. Miklukho-Maklaya, 6, Moscow, 117198, Russia

***Corresponding author:** yurmanov-anton.ya.ru@yandex.ru

Received: June 25th 2025 / Accepted: November 12nd 2025 / Published: December 31st 2025

https://doi.org/10.24057/2071-9388-2025-4103

ABSTRACT. This work is dedicated to analysing the conditions conducive to the spatial succession of individual, extra-tropically persistent species. It also clarifies the distribution of seagrasses (Zosteraceae and Ruppiaceae) in different seas across three oceanic basins and the Caspian Sea, which is part of the inland drainage basin affecting the Russian Federation. A review of herbarium samples and literature on Russian seagrasses revealed five regions that differ in the number of Zosteraceae and Ruppiaceae species: the West Arctic and White Sea (3 species), the Russian section of the Baltic Sea (1 species), the Russian sections of the Black and Caspian Seas and the Sea of Azov (4 species), the south of the Russian Far East (9 species), and the north of the Russian Far East (2 species). The south of the Russian Far East is of particular interest as it serves as a refuge for some seagrasses. This is because they suffer from strong anthropogenic pressure in the main part of their range, which is located further south, whereas in Russia they experience no negative impact. In the Arctic, seagrasses have a wider distribution than was previously thought. This comprehensive study has enabled the development of new approaches to finding seagrass meadows in hard-to-access coastal areas of the Russian Federation, using remote sensing techniques and the assistance of citizen science volunteers.

KEYWORDS: seagrasses, Zosteraceae, Ruppiaceae, Seas of Russia, anthropogenic pressure

CITATION: Iurmanov A., Popov I., Gnedenko A., Lebedev Y., Kulikovskiy M. (2025). Seagrasses (Zosteraceae And Ruppiaceae) In Russia: Distribution, Diversity, Prospects For Further Research. Geography, Environment, Sustainability, 4 (18), 139-148
https://doi.org/10.24057/2071-9388-2025-4103

ACKNOWLEDGEMENTS: The work of Anton Iurmanov and Maxim Kulikovskiy was carried out with financial support under the state assignment of the Ministry of Science and Higher Education of the Russian Federation (theme 122 042 700 045-3). The work of Angelina Gnedenko was supported financially within the framework of the state assignment of the Institute of Geography of the Russian Academy of Sciences FMWS-2024-0007 (1 021 051 703 468-8). We wish to thank the Centre for Expedition Assistance for organising the expedition and RUDN University's Strategic Academic Leadership Program.

Conflict of interests: The authors reported no potential conflict of interests.

INTRODUCTION

Seagrasses are a group of underwater plants of the order Alismatales, widely distributed in the coastal waters of all continents except Antarctica (Hogarth 2015). Their aggregations often form 'underwater meadows' that resemble terrestrial ones. These meadows are habitats of high conservation value as numerous animals use them. Economic activity in the coastal zone directly or indirectly causes an increase in eutrophication, siltation and turbidity, and these processes harm seagrasses. Intentional extermination of these plants by humans also occurs because dried seagrasses resemble straw and are used as a raw material for the manufacture of various products (Duarte 2002; Short et al. 2011). The underwater meadows are suffering a global decline, and several species are considered threatened (Orth 2006).

A gradual and widespread increase in average annual atmospheric temperatures may, on the one hand, endanger existing seagrass meadows in equatorial and tropical regions due to changes in biotic and abiotic factors. On the other hand, it may contribute to the spread of these seagrasses in the Arctic region. Currently, the Russian Arctic remains an area that is extremely poorly studied in terms of seagrass distribution. This is due to its inaccessibility for research and the seasonality of this work. Seagrasses play an important role as a food source for waterfowl during their annual migrations to the Arctic during the nesting period. The use of satellite imagery is a promising method for assessing the distribution of marine vegetation. Furthermore, due to the

changing coastline caused by increasing warming (Tishkov et al. 2023), new areas with potential for seagrass colonisation may form in some locations. This requires further research to better understand these potential habitats.

The ecological value and vulnerability of seagrasses highlight the need for research into their distribution and abundance. Much of the information concerning seagrass distribution in Russian waters is published only in local journals. Consequently, this information is not sufficiently represented in international reviews (Short et al. 2007; Krause-Jensen, 2020), despite being significant, particularly for the Arctic and Far East. We aim to address this gap. Furthermore, our observations of Russia's coastal waters indicate they serve as a refuge for certain seagrass species. This is because the main parts of their ranges, located further south, experience considerable anthropogenic pressure, whereas in Russia, these species are not negatively impacted. We have gathered such data for one species, Phyllospadix iwatensis Makino (Iurmanov et al. 2022a), and hypothesised that a similar situation applies to other species. This paper evaluates that hypothesis and reviews information on seagrass distribution in Russian waters.

The aim of our research was to investigate the biogeographic distribution of marine Alismatales along the coastlines of the seas surrounding the Russian Federation, including the Caspian Sea. During the research, additional aims emerged. It became clear that it is necessary to develop specialised identification keys based on modern morphological descriptions of species. These keys will help us both during expeditions and when working with herbaria. Furthermore, in the future, we will be able to involve volunteers in clarifying the distribution areas of seagrasses along the coasts of the seas and oceans surrounding Russia. In recent years, scientific volunteerism has been actively developing in our country and has already proved its high effectiveness in the environmental research that we conduct (Shaikina et al. 2022; Tihonova et al. 2023; Vladimirov et al. 2023). Therefore, we decided to compile such a key.

A further additional aim relates to the prospects for further studies. Given that direct observation of vast areas is problematic, the use of remote methods appears promising. The use of satellite remote sensing of the Earth has proven to be an effective and economical method for studying shallow-water coasts (Kravtsova et al. 2021). This research method, limited by periods when a continuous ice cover is established, can be applied along the maritime border of the Russian Federation to identify promising territories for more detailed study (Short et al. 2007). We examined the effectiveness of remote sensing methods for surveying hard-to-reach coastal areas, such as Urup Island in the Kuril Islands and the Tersk Coast of the White Sea.

We developed a key for identifying the studied species based on literature sources and herbarium samples. Additionally, we used remote sensing techniques to conduct field surveys in remote areas such as the Kuril Islands in the Far East and Urup Island.

Materials and methods

We gathered publications on seagrass records and the state of their populations by examining the Russian Citation Index and Scopus databases. Additionally, we examined herbarium samples from the following institutions: Komarov Botanical Institute (LE), Saint Petersburg State University (LECB), Tsitsin Main Moscow Botanical Garden of the Russian Academy of Sciences (MHA), Moscow State University Faculty of Biology (MW), and Faculty of Geography (MWG), Institute of Marine Geology and Geophysics Far Eastern Branch Russian Academy of Sciences (SAK), Kamchatka Branch of the Pacific Geographical Institute of the Russian Academy of Sciences (Petropavlovsk-Kamchatsky), and the Herbarium of Kronotsky Nature Reserve (Elizovo). We also consulted the Atlantic Branch of the Institute of Oceanology, P.P. Shirshov, Russian Academy of Sciences (Kaliningrad) (herbarium acronym missing), and the Museum of the World Ocean (Kaliningrad). The GBIF database was also used. Our own observations were conducted from 2017 to 2022 in the Baltic Sea, Sea of Japan, Sea of Okhotsk, and the Pacific Ocean (Iurmanov et al. 2022a; Iurmanov et al. 2022b).

Finally, we characterised the obtained results in accordance with the 'bioregional model' of the world's seagrasses (Short et al. 2007). This involves identifying zones with an equal number of species. We used this model to define which species should be considered seagrasses, focusing on the families Zosteracea and Ruppiacea. This was necessary because there are several intermediate forms between seagrasses and other underwater plants, leading to disagreements among experts regarding definitions. During these studies, we analysed the diagnostic characters of the seagrass species (Tolmachev 1974; Wu et al. 2010) and created a new key for their identification.

When analysing the data collected through remote sensing, we found that multispectral satellite imagery from Sentinel-2, WorldView-2 satellites, and a series of Landsat, IKONOS, and QuickBird-2 satellites was predominant. Additionally, we noted some instances where hyperspectral aerial photography and unmanned aerial vehicles were used in certain studies.

Satellite images from the Landsat series are suitable for mapping the distribution of seagrasses and have been successfully used in this field for a long time (Zharikov et al. 2018). The capabilities of Sentinel satellite imagery are highly appreciated (Kuhwald et al. 2022; Li et al. 2022). However, except in cases where it is necessary to assess the dynamics of seagrass meadow distribution or a long series of satellite images is required, researchers prefer Landsat satellite imagery (Vidya et al. 2023; Pu et al. 2012).

The limited use of satellite imagery for seagrass mapping is due to technical challenges associated with the survey process. Different wavelengths of visible light penetrate water to different depths, and as wavelength increases, penetration depth decreases sharply. Consequently, only a limited number of channels are available for use in most common image processing systems. These channels, including blue, green, and red, form the basis for the primary information that is processed (Fig. 1).

When mapping the distribution areas of seagrass, underwater survey materials are typically used to provide general information about plant distribution patterns within the study area. This study primarily examines the potential use of satellite imagery to identify areas that require more detailed surveying, given limited field data and without the need for extensive underwater surveys. To assess the feasibility of using satellite images, several field observation sites were selected where the presence of seagrass was reliably established. Images from the Landsat-8 and Sentinel-2 satellites, which underwent atmospheric correction, were chosen for dates closest to the field observations (July 7, 2021 for Zostera marina L. and October 9, 2019 for *Phyllospadix iwatensis*).

Using Sentinel-2 imagery, a distribution map for *Phyllospadix iwatensis* was prepared in the coastal area of Urup Island. Images that had undergone atmospheric correction were used for automatic interpretation. The reference vector method was chosen as the algorithm for identifying algae habitats, as it has been recognised as one

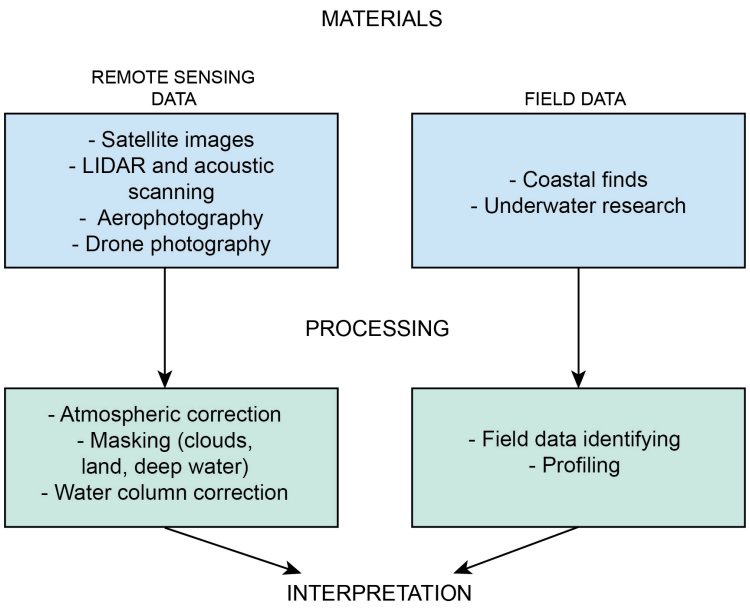

Fig. 1. A generalised scheme for conducting research on seagrasses using remote sensing data

of the most efficient for this purpose (Bakirman et al., 2016; Vidya et al., 2023). To ensure clear coverage of the entire coastline of the island with minimal sea swell, scenes taken on 30 September 2019 were selected as the most suitable based on their quality and coverage for creating the map. The Kuril Islands are generally characterised by a one-month shift in the growth season. In September, the condition of the vegetation cover allows for accurate interpretation.

One of the main challenges in analysing the distribution of seagrass on satellite images is the elimination of interference introduced into the incoming signal by the atmosphere, the sea surface with glare, and the water column. This interference affects the spectral brightness of underwater images and prevents the accurate determination of objects' true values without the influence of the water column. Atmospheric correction is a standard step in the analysis of any objects from satellite images, but there is debate about whether to correct for the water column and whether this step improves the results. In this study, images with only atmospheric corrections were used to compare visual representations of seagrass meadows in the waters of Russian seas from different survey systems.

Results

Distribution and diversity

Based on the results of this study, we have identified nine species of seagrass with established taxonomic status that grow in the waters of the Russian Federation. These species belong to the Zosteraceae (*Zostera marina, Zostera noltii* Hornem., *Zostera asiatica* Miki, *Zostera japonica* Aschers. and Graebn., *Zostera caespitosa Miki, Phyllospadix iwatensis* and *Phyllospadix juzepczukii* Tzvel.) and the Ruppiaceae (*Ruppia maritima* L. and *Ruppia cirrhosa* Grande). The distribution of seagrasses in the seas of Russia corresponds to the global bioregional model (Short et al. 2007), but the area of some bioregions is much larger. This applies to the Arctic and the northern part of the Far East. We identified five bioregions for the seagrasses (Fig. 2).

Bioregion 1. Western Arctic and White Sea

Three or four species of seagrass occur in the region. *Ruppia maritima, Zostera marina, Zostera noltii* were definitely reported, but the occurrence of *Ruppia cirrhosa* is

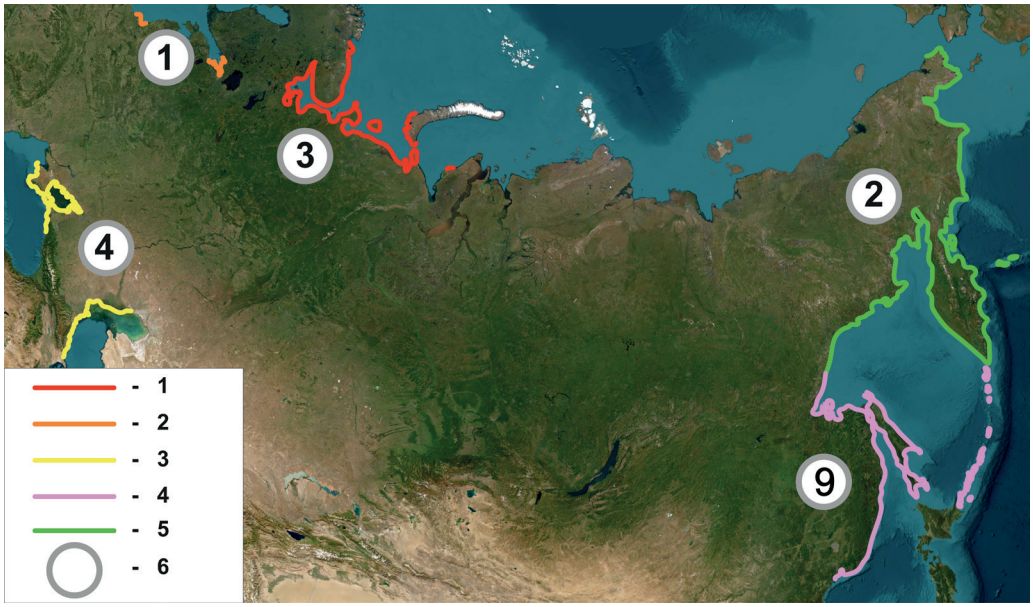

Fig. 2. Bioregions of seagrasses and their species richness: 1. Western Arctic and White Sea, 2. Russian section of the Baltic Sea, 3. Russian section of the Black and Caspian Seas, the Sea of Azov, 4. South of the Russian Far East; 5. North of the Russian Far East, 6. number of seagrass species

questionable. The region has been studied very unevenly. At least several tens of articles (Makarov and Spiridonov 2013; Sergienko et al. 2015, etc.) and one monograph (Vekhov 1992) have been published based on studies of a small plot of the White Sea located at its western 'corner'. However, the rest of the White Sea and the Russian Arctic have been studied hardly at all. This is because three biological stations are located at the western extreme of the White Sea. We found only one herbarium sample of seagrass from the eastern coast of the White Sea. Regarding the Russian section of the Barents Sea, a small number of records are known from the north of the Kola Peninsula at the state border and from Cheshskaya Bay (Vekhov 1992). Furthermore, *Zostera* marina was reported from Baydaratskaya Bay of the Kara Sea (Vidy — biologicheskie indikatory 2020), and several herbarium samples from the Yamal Peninsula are known (Fig. 3). The state of seagrass populations is considered normal, and the prospects for their commercial use have been discussed (Maksimovich et al. 2005). After a global decline caused by the myxomycete *Labyrinthula macrocystis* in the mid-20th century, recovery took place (Liubeznova 2013).

Bioregion 2. Russian section of the Baltic Sea

The seagrasses are almost absent. In the southern part (Kaliningradskaya oblast), remains of *Zostera* marina are often found in the wrack, but only one growing specimen is known (Volodina and Gerb 2013). Despite active surveys, no underwater meadows were found there. On the contrary, there is evidence of habitat loss. In 2021, our attempts to find them were similarly unsuccessful. The water was muddy, and algae dominated the seabed. In the centre of the southern section, a sewage treatment plant outlet significantly impacts the surrounding water area. In the northern part (Leningradskaya oblast), we did not find seagrasses, even in the wrack, although we examined the coasts of islands located in the centre of the Gulf of Finland, which is Russia's western outpost (Iurmanov et al. 2022b).

Bioregion 3. Russian section of the Black and Caspian Seas, the Sea of Azov

Four seagrass species are found in this area: *Ruppia cirrhosa, R. maritima, Zostera marina,* and *Z. noltii.* They have been studied since the mid-19th century. Most of the information concerns the coastal waters near Sevastopol city (Phillips et al. 2006), though some data for other locations are also available. Seagrasses are present throughout the Russian section of the Black Sea and in the southern part of the Sea of Azov (Milchakova and Phillips 2003; Stepanian 2009). A decline has been reported in areas affected by human activity (Lisovskaya 2011; Teyubova 2012). In a bay near Sevastopol (Kruglaya Bay), a succession of seagrass communities was observed. Initially, Zostera marina dominated, coexisting with *Z. noltii*, but then *Z. noltii* took over the site (Mironova et al. 2020). *Zostera marina* is considered a protected species in Crimea. A reduction in the abundance of *Zostera marina* was also noted on the northeastern coast of the Black Sea. In the Caspian Sea, a similar situation has been reported: an increase in Zostera noltii and a decrease in *Zostera marina* down to zero (Stepanian 2016). This occurred due to desalination, siltation, and pollution.

Bioregion 4. South of the Russian Far East

The region includes the coastal waters of Sakhalin, the nearest mainland, and the Kuril Islands. Seven species occur there: *Zostera marina, Zostera asiatica, Zostera noltii, Zostera japonica, Zostera caespitosa, Phyllospadix iwatensis, Phyllospadix juzepczukii, Ruppia maritima, Ruppia cirrhosa.* Herbarium samples of several other species exist: *Phyllospadix scouleri* Hook., *Zostera pacifica* S.Watson, *Zostera nana* Roth, *Zostera angustifolia* (Hornem.) Rchb., and *Ruppia occidentalis* S.Watson. However, these descriptions appear to be synonymous with those already mentioned. Most of the samples were collected near Vladivostok city, at the mouth of the Amur River, in the southern part of Sakhalin, and on

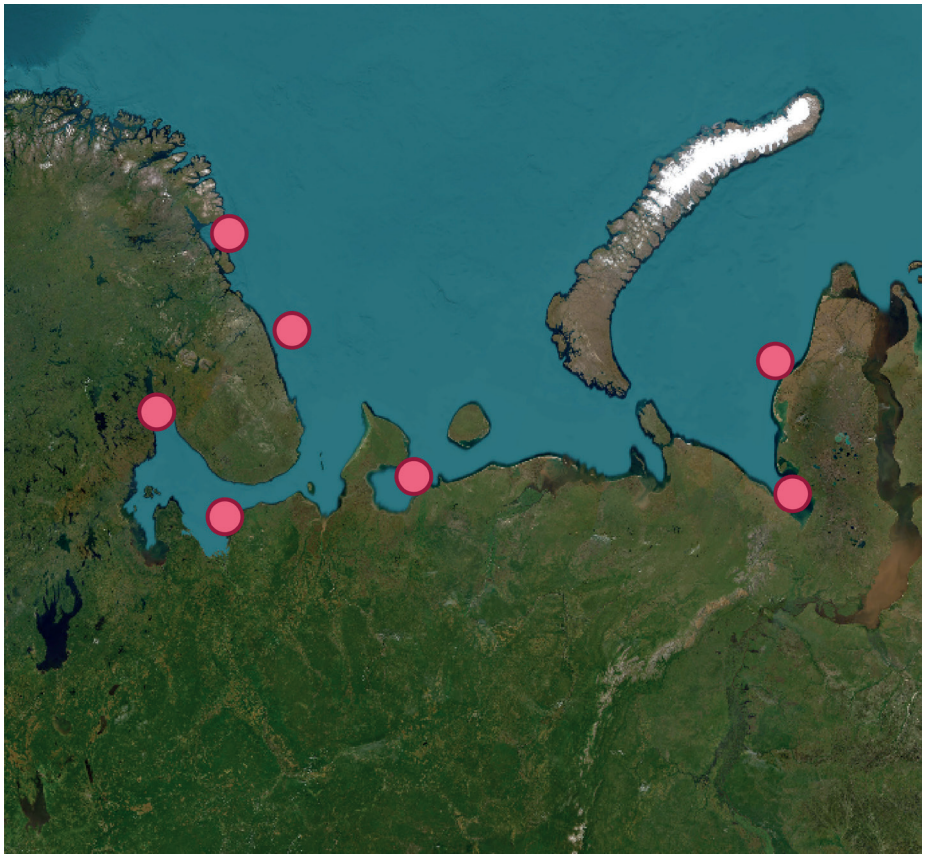

Fig. 3. Zostera marina registration points in the Western Arctic and White Sea Bioregion

Kunashir Island. We added several samples from Iturup and Urup islands (Iurmanov et al. 2022b). Publications indicate some records from the other southern Kurils (Evseeva 2007; Ivanova and Tsurpalo 2017). In general, however, the records cover only a small part of the coastline. Publications on the seagrasses of the Far East are relatively numerous (Aminina 2005; Kulepanov 2005; Blinova et al. 2015; Kulepanov and Drobyazin 2018). Physiological aspects and the role of seagrass as a substrate for fish spawning have been studied (Klimova et al. 2015). Details of their growth have also been investigated (Gusarova 2008; Ivanova and Tsurpalo 2013; Levenets and Turin 2014; Kalita and Skriptsova 2014, 2018; Levenets and Lebedev 2015; Sabitova et al. 2018). A survey of abundance along a long section of the Tatar Strait was carried out (Dulenin 2012). The issue of protection has not been raised. The seagrasses are considered common, and their use for economic purposes was discussed recently (Mitina et al. 2016). No negative trends have been reported.

The northern boundary of the 'bioregion' is not entirely clear because collection samples from the northern Kuril Islands and most of the Sea of Okhotsk are not available. Modelling the distribution of relatively southern species (*Phyllospadix iwatensis, Zostera asiatica*, and *Zostera japonica*) showed that they could occur up to the southern tip of Kamchatka and approximately the same latitude on the coast of the Sea of Okhotsk. Penetration into some areas of the eastern coast of Kamchatka and the Commander Islands is not excluded. However, seagrasses were studied on these islands, unlike the northern part of the Kuril Islands, and these southern species were not found. Therefore, we drew the boundary of the bioregion through the southern tip of Kamchatka (Fig. 2).

Bioregion 5. North of the Russian Far East

The region includes the northern part of the Sea of Okhotsk, the coastal waters of Kamchatka and the Commander Islands, the Russian section of the Bering Sea, and the southern part of the Chukchi Sea. Two species occur there: *Zostera marina* and *Ruppia cirrhosa*. Most of the collected specimens are known from the south of Kamchatka, near Petropavlovsk-Kamchatsky City. We also observed *Zostera marina* there in 2021. Other areas have been studied extremely fragmentarily. It is known that Zostera marina occurs on the Commander Islands (Mochalova and Yakubov 2004). A very small number of collected specimens, references in publications and other documents are known from other sites (Selivanova 2004). The northern border of the region is not well known (Fig. 5). It is believed that *Zostera marina* lives in the Chukchi Sea (Ministry of Natural Resources 2015). However, it is not known how far northwards it extends. In the neighbourhood, in Alaska, *Zostera marina* occurs in the southern part of the Chukchi Sea near the Bering Strait (McRoy 1968).

Key to families, genera and species

We developed a key, based on literature sources and herbarium samples (Tolmachev 1974; Wu et al. 2010), to identify the studied species. This key helps in the identification of families and genera of seagrasses (Table 1), as well as Zostera (Table 2), Phyllospadix (Table 3), and Ruppia (Table 4).

Fig. 4. Registration of seagrasses in the South of the Russian Far East bioregion: 1. *Phyllospadix iwatensis*, 2. *Zostera japonica*, 3. *Zostera asiatica*

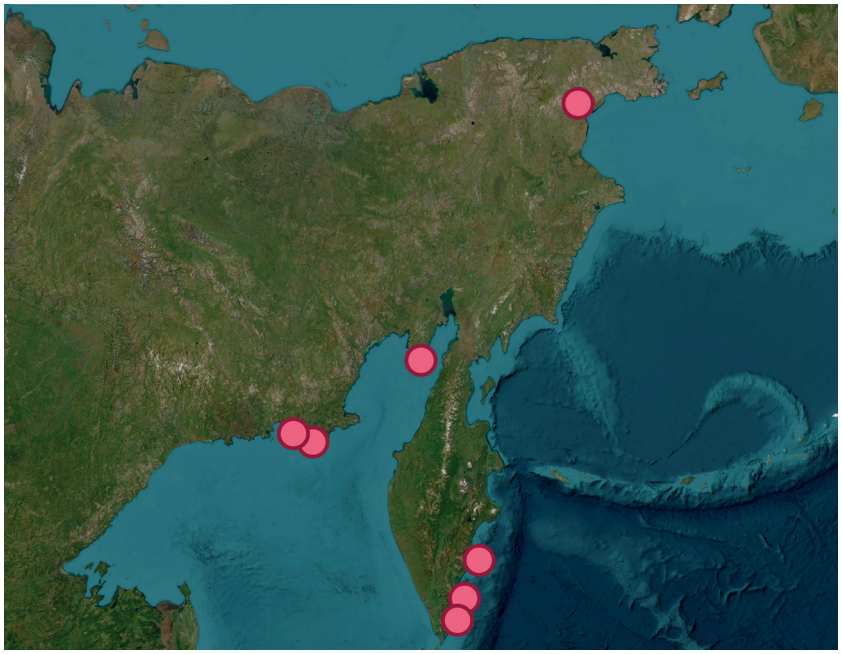

Fig. 5. Places of registration of *Zostera marina* in the north of the Far Eastern bioregion

Table 1. Families and genera identification

Level I	Level II	Result
Leaves 0.5-1.0 m long, narrow, linear (2-9 mm wide). Flowers unisexual, without perianth, collected in flat spikelets	Monoecious; ovary and fruits oval, stems elongated; Leaves 3-9 (11) veined	Zostera L., marine eelgrass
	Dioecious; ovary and fruits cordate, stems short, surrounded at the base by fibers of dead leaf sheaths; Leaves 3-5 veined	Phyllospadix Hook., surfgrass
Leaves extremely narrow, linear, probably filiform (in that case up to 15-20 cm). Flowers bisexual, collected in short spikelets	-	Ruppiaceae, widgeonweeds

Table 2. *Zostera* species identification

Level I	Level II	Level III	Result
stems over 50 cm long	Leaves 0.2-1 mm wide, 3-veined, apex apiculate. Stems 10-20 cm long. Inflorescence 1.5 cm long. Fruits smooth, 1.5-2 mm long	-	*Zostera noltii* Hornem.
	Leaves over 1 mm wide, stems over 20 cm long	Leaves 1.5-2 mm wide, apex rounded, 3-veined. Stems 20-30 (40) cm long. Fruits smooth, about 2 mm long, elliptical or narrow cylindrical	*Zostera japonica* Aschers. et Graebn.
		Leaves 3-6 mm wide, apex rounded, 5-7 veined. Stems up to 60 cm long. Fruits grooved, about 3.5 mm long, elliptical. Abundant creeping rhizomes, internodes short	*Zostera caespitosa* Miki
stems up to 50 cm long	Leaves 4-6 (8) mm wide, 5-7 veined, apex rounded. Stems 60-100(150) cm long. Fruits oblong, grooved, about 4 mm long	-	*Zostera marina* L.
	Leaves 10-15 mm wide, 9 (11) veined, apex apiculate. Stems up to 100 Stems. Fruits oblong, smooth, about 5 mm long	-	*Zostera asiatica* Miki

Table 3. *Phyllospadix* species identification

Level I	Result
Leaves 2-4.5 (5) mm wide, 5 or 3 veined, apex rounded, finely serrated. Fibers of dead leaf sheaths are abundant. Retinacules apiculate	*Phyllospadix iwatensis* Makino
Leaves 1.2-2.7 mm wide, 3 veined, apex rounded, finely serrated. Fibers of dead leaf sheaths at the base of the stem are few in number. Retinacules rounded	*Phyllospadix juzepezukii* Tzvel.

Table 4. *Ruppia species identification*

Level I	Result
Leaves 2-5 mm wide, apex apiculate. Stems 20-50 cm long. Peduncle strongly elongated (up to 10 cm or more), twisting into a spiral. Fruits ovoid or obliquely ovoid	*Ruppia cirrhosa* Grande
Leaves about 5 mm wide, apex apiculate. Stems up to 20 cm long. Peduncle 1-3 cm long, non-twisting. Fruits ovoid and curved	*Ruppia maritima* L.

Use of satellite imagery

The maps were prepared to compare the capabilities of visual interpretation of seagrass meadows at field observation stations in remote regions, specifically on the Tersk Coast of the White Sea and on Urup Island in the Kuril Ridge (Fig. 6).

It is noticeable that in the Landsat-8 image (Fig. 7) *Zostera* meadows are hardly visible because their distribution area captures a narrow but long strip of coastal shallow water. This makes them difficult to recognise at a spatial resolution of 30×30 metres from the image size. In contrast, the Sentinel-2 image allows for more accurate visual interpretation of the meadows and also provides extensive opportunities for automated processing.

A similar pattern can be observed in the *Phyllospadix iwatensis* sites located on the northern tip of Urup Island. A map of the distribution has been prepared for the coastal area of this island, showing that seagrasses are connected to gentle rock outcrops on the coastal cliffs and occupy relatively small areas (Fig. 8). At the same time, they are distributed fairly evenly along the coastline of the island and do not show a strict proximity to any particular coast. To a large extent, the distribution of *Phyllospadix iwatensis* is influenced by the structure of the coastal bottom, as all potential areas for its growth are limited to gentle rock formations at shallow depths.

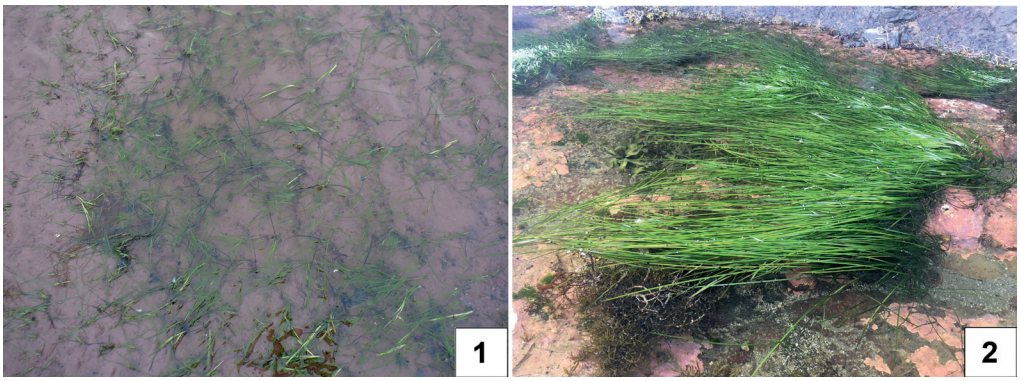

Fig. 6. Typical aggregation of *Zostera marina* (A) on the Tersk Coast of the White Sea (Photo by Mikhail Kuznetsov) and *Phyllospadix iwatensis* (B) on Urup Island in the Kuril Ridge at the northern coast of Urup Island (Photo by Anton Iurmanov)

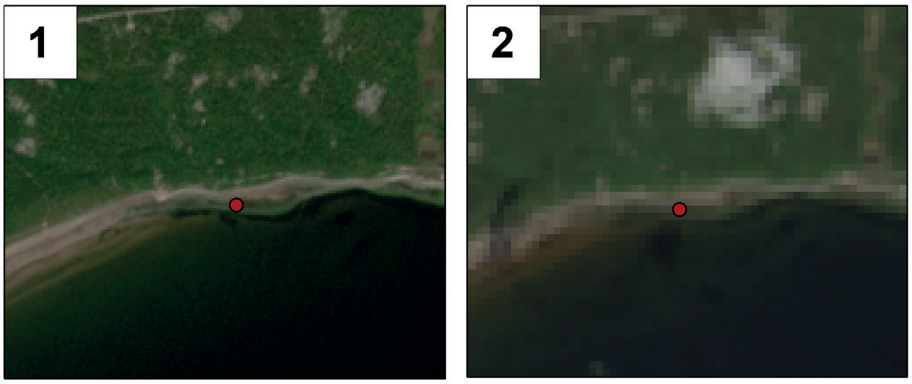

Fig. 7. Location of the point of discovery *Zostera marina* (Russia, Murmansk region) in pictures: 1. Sentinel-2, 2. Landsat-8

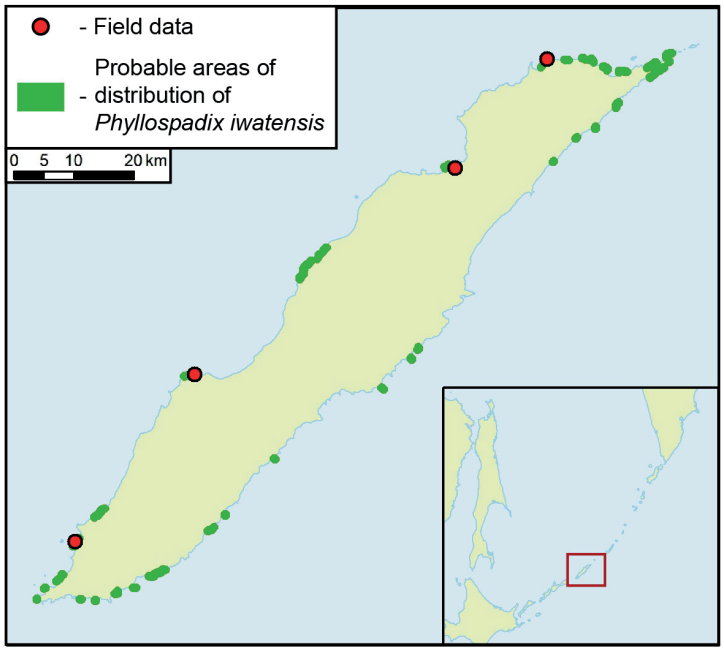

Fig. 8. The location of the identified and probable ranges of *Phyllospadix iwatensis* in the coastal waters of Urup Island (Kuril Islands, Russia), established by remote sensing

DISCUSSION

The dispersal of Alismatales plants occurs both vegetatively and through seed dispersal. However, there have not yet been enough studies to determine how long plant parts with roots and leaves can survive outside the substrate. Although long-distance dispersal is not common, it plays a significant role in the formation of new areas (McMahon et al. 2014). Based on this information, we can assume that these types of settlements could be the beginning of seagrass habitat formation (Iurmanov 2022; Iurmanov 2023).

Our observations of seagrass emissions on the shores of Russia indicate the complexity of the settlement process. The remains washed ashore appear to have grown elsewhere previously. However, if there are no large seagrass meadows close to the shore, no significant accumulations of emissions have been found. These emissions once again suggest that seagrass is distributed very unevenly across the water area. Several factors limit its occupation of new areas, ranging from substrate composition to human activity (Iurmanov et al. 2022).

In the case of *Phyllospadix iwatensis*, we found that it can grow in both surf-protected coastal areas and in areas affected by waves. This is thanks to its dense and robust turf, which allows the species to tolerate the substrate. It can therefore grow in surf zones as a habitat-forming agent

and occupy new habitats, unlike *Zostera marina* and *Zostera asiatica* (Iurmanov et al. 2022b), which cannot do this. The fruits of *Zostera asiatica* have a thick cuticle that prevents water from entering them before they open and release the seeds (Iurmanov et al. 2021). In the non-opening fruits of *Phyllospadix iwatensis*, our research found that they are similar to Prunus-type drupes. They have a differentiated inner sclerenchymal bone formed by the inner zone of the mesocarp and endocarp. Aerenchyme is also formed in the outer zone of the mesocarp in these fruits (Iurmanov et al. 2021). This fruit structure has adaptations for both hydrochory and endozoochory. The aerenchyme ensures the buoyancy of the single-seeded, non-opening diaspores, while the fruit bone mechanically protects the seeds from destruction.

Thus, although the specific habitats of various marine higher plant species indicate that the successful transfer of fruit or plant parts is insufficient for their establishment, and such material also requires optimal conditions, different adaptations for hydrochoric dispersal allow them to gradually expand their range and form new populations far from the original location (Iurmanov 2022; Iurmanov 2023).

The state of seagrasses in the southwest and west of Russia is similar to the usual situation in populated areas. They have survived in some locations, but overall, their numbers are declining. It is highly probable that they have recently become extinct in the Russian sector of the Baltic Sea. In the Black and Caspian Seas, their condition is also deteriorating. In the past, the remains of seagrasses on the shores were so numerous that they were actively used for economic purposes (Morozova-Vodyanitskaya 1939). However, this is no longer an issue as no commercial 'deposits' are available.

The biogeographical context of Russian Arctic seagrasses is particularly interesting. They have been found to be more widely distributed than previously thought (Krause-Jensen et al. 2014, 2020). Some authors previously believed that the Arctic was entirely unsuitable for seagrasses due to a lack of light (Blinova et al. 2014). However, they do exist there. Furthermore, their distribution is likely expanding (Krause-Jensen et al. 2014, 2020). As global warming progresses in the Arctic, seagrass populations may increase. This suggests that at least *Zostera marina* will gain new habitats. However, assessing these prospects is challenging. It is known that seagrasses can survive under ice (McRoy 1969). Nevertheless, the environment in the inner parts of the Russian Arctic is unlikely to be favourable for them. Despite global warming, conditions remain very cold. Arctic seas are primarily warming due to warm currents from the south. However, Novaya Zemlya Island acts as a barrier, meaning only the Barents Sea is warming rapidly.

The seas of the Russian Far East are particularly valuable for seagrasses. This might be because this region is thought to be a centre of origin for the Zosteraceae family (Iurmanov 2022), and consequently, a hotspot of their diversity. In addition to *Zostera marina*, several other species are found there. Some of these are considered vulnerable globally and have relatively small distribution areas. They were mainly described in the coastal waters of Japan, Korea, and the nearest Chinese territories. In the main part of their range, they are declining due to habitat loss. It has been found that they are quite widespread in the adjacent Russian territories. The usual factors that negatively impact seagrasses are not present there. At the same time, considering global warming, we might expect an expansion of their range and an increase in their numbers. Other seagrasses may also establish themselves there. However, studying this process presents a challenge. In the past, these plants attracted attention as a source of various products, but relevant research is now conducted rarely. Further improvement of remote sensing methods and the involvement of volunteers would help to address this.

To implement scientific volunteer projects aimed at monitoring the distribution and species diversity of marine meadows, we prepared an accessible guide for identifying seagrass species found in the seas surrounding the Russian Federation (Table 1–4). We also needed a unified framework for an observation system focused on phenology (Vladimirov et al. 2023). The importance of studying the phenology of seagrasses in Russia is determined by both fundamental tasks of studying habitat formation processes and practical tasks related to sustainable development. These include the ecosystem role of marine meadow communities in carbon dioxide fixation, primary production, creating shelter and a food base for marine animals, and protecting against coastal erosion.

These observations can be conducted in various locations, such as submerged seagrass beds, in the tidal zone, on the surface of waves, or washed ashore. Volunteers should record external factors such as the date, depth, water and air temperature, salinity, and describe the substrate. It will be important to identify the species of seagrass and determine whether it is a single plant or part of a meadow. They should also note the phenological stage (vegetative, budding, flowering, fruiting, or dying) of the seagrass. Additionally, volunteers may collect data on biomass. The organisation of this scientific volunteering project can serve as the basis for calibrating remote sensing techniques for marine meadows and determining the precise distribution of seagrass in Russia. This information can then be used to monitor its dynamics over time.

CONCLUSION

The seas of the Russian Far East are becoming a refuge for threatened sea grasses, which are declining in neighbouring southern areas. Seagrasses in the Russian Arctic are more widely distributed than previously thought and are probably expanding. Using remote sensing techniques, in conjunction with citizen science projects, will allow us to complete work on creating updated and detailed maps and inventories of seagrass flora, as well as establish a monitoring system.

REFERENCES

Aminina N. (2005). Main trends of the studies on algae and sea grasses of Far East. Isvestiya TINRO, 141: 348-354 [In Russian with English summary].

Blinova E., Yermakov I., Kamnev A., Krupina M., Stukolova I. (2014.) Grass weeds of the Russian seas: ecology, distribution, stocks, history of research. Part 2. Grass weeds of the north-west seas of Russia. Regional environmental issues, 5: 119-125 [In Russian with English summary].

Blinova E., Yermakov I., Kamnev A., Krupina M., Stukolova I. (2015). Seagrasses of the Russian seas: ecology, distribution, stocks, history of investigation. Part 3. Seagrasses of the Far Eastern seas of Russia. Regional environmental issues, 6: 16-27 [In Russian with English summary].

Duarte C. (2002). The future of seagrass meadows. Environmental Conservation, 29: 192-206.

Dulenin A. (2012). Resources and distribution of commercial macrophytes in the western Tartar Strait (Khabarovsk Territory). Izvestia TINRO, 170: 17-29 [In Russian with English summary].

Evseeva N. (2007). Macrophytobenthos of the coastal zone of southern Kuril Islands. In: Biology, state and environment of hydrobionts in Skhalin-Kuril region and its coastal waters. Proceedings of Sakhalin institute for fisheries. SakhNIRO, 9: 125-145. [In Russian].

Gusarova I. (2008). Macrophytobenthos of the northern Amur Bay. Izv TINRO, 155: 88-98 [In Russian with English summary].

Hogarth P. (2015). The Biology of Mangroves and Seagrasses. 3rdEd. Oxford etc.: Oxford University Press.

Iurmanov A., Romanov M., Bobrov A. (2021). Fruit morphology and histology of Zostera asiatica Miki and Phyllospadix iwatensis Makino (Zosteraceae) in connection with comparative carpology of Higher Alismatales. Botany Letters, 168(4): 1-7.

Iurmanov A., Popov I., Romanov M. (2022a). Seagrasses At The Islands Iturup And Urup Of Kuril Archipelago. Geography, Environment, Sustainability, 4(15): 39-43.

Iurmanov, A., Romanov M., Gerb M., Volodina A., Baikova I., Popov I., Markovets M. (2022b). Seagrass Zostera In the Russian Section Of the Baltic Sea. Geography, Environment, Sustainability, 2(15): 111-115.

Iurmanov A. (2022). Phylogenetic phytogeography of selected groups of seagrasses (Monocotylendoneae - Alismatales) based on analysing of genes 5.8S rRNA and RuBisCo large subunit. Geography, Environment, Sustainability, 15(1): 61-69.

Iurmanov A. (2023). Phylogenetic phytogeography of higher Alismatales: Posidoniaceae, Ruppiaceae, Cymodoceaceae, Zosteraceae, Potamogetonaceae: dis. ... kand. Biology 1.5.9. / Iurmanov A.A. Moscow. 206 p. [In Russian].

Ivanova M., Tsurpalo A. (2013). Composition and distribution of macrobenthos communities in the intertidal zone of Putyatin Island (Peter the Great Bay, Japan Sea). Izv. TINRO, 172: 149-160 [In Russian with English summary].

Ivanova M. and Tsurpalo A. (2017). The Phyllospadix iwatensis community in the intertidal zone of the Far Eastern seas of Russia. Izvestia TINRO, 188, 173–180 [In Russian with English summary].

Kalita T. and Skriptsova A. (2014). Current status of subtidal macrophyte communities in Ussuriysky and amursky bays, Sea of Japan. Russian Journal of Marine Biology, 40, 6. 427-434 [In Russian with English summary].

Kalita T., Skriptsova A. (2018). The Current State of the Zostera marina + Stephanocystis crassipes Community in the Eastern Bosphorus Strait, Sea of Japan. Russ J Mar Biol, 44: 25-35.

Klimova A., Klyukina R., Bonk A. and Klochkova N. (2015). The role of sea weeds in formation of spawning substrate of Pacific herring. Vestnik Kamchat GTU, 31, 60 – 66 [In Russian with English summary].

Kravtsova V., Vakhnina O., Chalova E. (2021). Methodological problems of studying the underwater relief in the river delta from satellite images (using the example of mapping the shoals of the Yenisei Delta). Water Resources, 48(4): 378-389.

Krause-Jensen D., Duarte C. (2014). Expansion of vegetated coastal ecosystems in the future Arctic. Frontiers in Marine Science, 1, 10.

Krause-Jensen D., Archambault P., Assis J., Bartsch I., Bischof K., Filbee-Dexter K., Dunton K., Maximova O., Ragnarsdóttir S., Sejr M., Simakova U., Spiridonov V., Wegeberg S., Winding M., Duarte C. (2020). Imprint of Climate Change on Pan-Arctic Marine Vegetation. Frontiers in Marine Science, 7.

Kulepanov V. and Drobyazin E. (2018). Species composition and quantitative distribution of seaweeds in the sublittoral zone and on the continental slope in the northwestern Japan Sea. Izvestiya TINRO, 195, 151–160 [In Russian with English summary].

Kulepanov V. (2005). Researches of macrophytobenthos at the coast of Primorye. Izvestiya TINRO, 141, 355-364 [In Russian with English summary].

Levenets I., Tyurin S. (2014). Macrophytes of Vostok Bay, Sea of Japan Biodiversity and Environment of Far East Reserves. Biodiversity and Environment of Far East Reserves 1: 36-48 [In Russian with English summary].

Levenets I. and Lebedev E. (2015). Diversity of the intertidal macrophytes of Far eastern marine biosphere reserve FEB RAS (Peter the Great bay, sea of Japan). Proceedings of Dalrybvtuz, 36, 37-48 [In Russian with English summary].

Lisovskaya O. (2011). Macrophytobenthos of the upper sections of shore zone of Russian coast of Black Sea. SPbGU, Saint-Petersbirg [In Russian].

Liubeznova N. (2013). Zostera is coming out of crisis. Priroda, 2: 95-96 [In Russian].

Makarov A., Spridonov V. (2013). Sea grasses: view from the cosmos. Priroda, 2: 91-94 [In Russian].

Maksimovich N., Ivanov M., Bukina M. (2005). Modern status and prospects for trade of sea grass Zostera marina L. in coastal waters of the Karelian coast of the White Sea. In: The study, sustainable use and conservation of natural resources of the White Sea. Proceedings of the IXth International Conference, 208-210. Petrozavodsk, 2005.

McMahon K. (2014). The movement ecology of seagrasses. Proc. Biol. Sci., 281(1795): 1-9.

McRoy C. (1968). The Distribution and Biogeography of Zostera marina (Eelgrass) in Alaska. Pac Sci, 22(4): 507-513.

McRoy C. (1969). Eelgrass under Arctic Winter Ice. Nature, 224: 818-819.

Milchakova, N.A., Phillips, R.C. 2003. Black Sea seagrasses. Marine Pollution Bulletin, 46, 695-699.

Ministry of Natural Resources and Ecology of the Russian Federation. Order No. 25-r dated September 22, 2015 On Approval of the List of Flora and Fauna Species that are Indicators of the Sustainable State of Marine Ecosystems in the Arctic Zone of the Russian Federation [In Russian].

Mironova N., Pankeeva T. (2020). Spatio-temporal changes in the macrophytobenthos of Kruglaya Bay (Black Sea). South of Russia-Ecology Development, 15: 125-139.

Mitina N., Malashenkov B. and Gordeev A. (2016) An Assessment of Natural Resource and Economic Potential of the Coastal Waters of the Middle Primorye. Gosudarstvennoye upravleniye, Elektronnny Vestnik. 58, 147-163 [In Russian with English summary].

Mochalova O., Yakubov V. (2004). Flora of Commander islands. BPI DVO RAN, Vladivostok. [In Russian].

Morozova-Vodianitskaya N. (1939). Zostera as an Object of Gathering in the Black Sea. Priroda, 8, 49-52. [In Russian].

Orth R. (2006). A Global Crisis for Seagrass Ecosystems. BioScience, 56, 987–996.

Phillips R., Milchakova N., Alexandrov V. (2006). Growth dynamics of Zostera in Sevastopol Bay (Crimea, Black Sea). Aquatic Botany, 85: 244-248.

Popov I., Iurmanov A. (2024). Recent surveys of the sea otter (Enhydra lutris) population on Kuril Islands. Pacific Conservation Biology, 30(6): 1-9.

Sabitova L., Skriptsova A., Cherbadgy I. (2018). Oxygen exchange and primary production of Zostera japonica Ascherson et Graebner, 1907 community in the Golubinyi Bay (Sea of Japan). Russian Journal of Marine Biology, 44,5: 415-423.

Selivanova O. (2004). Macrophytes of Russian shoal of Bering Sea, Commander islands and south-eastern Kanchatka. Dr. Thesis Kazan University [In Russian].

Sergienko L., Starodubtseva A., Smolkova O., Markovskaya E. (2015). Species of the genus Zostera L. (fam. Zosteraceae) in the flora of the western coast of White Sea. Fundamentalniye issledovaniya, 2-12: 2606-2612 [In Russian].

Shaikina M., Shipilina L., Gladilin A., Simakova K., Iurmanov A. (2022). Approaches to involving volunteers in solving phytoinvasion. In: Phytoinvasions. Materials of the All-Russian Scientific and Practical conference with international participation, 463-468. Moscow University Press, Moscow. [In Russian].

Short F., Carruthers T., Dennison W., Waycott M. (2007). Global seagrass distribution and diversity: A bioregional model. Journal of Experimental Marine Biology and Ecology, 350: 3-20.

Short F., Polidoro B., Livingstone S., Carpenter K., Bandeira S., Bujang J., Calumpong H., Carruthers T., Coles R., Dennison W., Erftemeijer P., Fortes M., Freeman A., Jagtap T., Kamal A., Kendrick G., Kenworthy W., La Nafie Y., Nasution I., Orth R., Prathep A., Sanciangco J., van Tussenbroek B., Vergara S., Waycott M., Zieman J. (2011). Extinction risk assessment of the world's seagrass species. Biological Conservation, 144: 1961-1971.

Stepanian O. (2009). Distribution of macroalgae and seaweed in the Azov Sea, Kerch Strait, and Taman Bay. Oceanology, 49: 361-367.

Stepanian O. (2016). Macrophytobenthos of the Caspian Sea: Diversity, Distribution, and Productivity. Oceanology, 56: 395-405.

Teyubova V. (2012). Raznoobrazie i ekologicheskie osobennosti makrofitobentosa rossijskogo sektora Chyornogo morya. PhD Thesis. Krasnodar, Kubanskij gosudarstvennyj universitet. [In Russian].

Tikhonova N., Ukhatova Yu., Zavarzin A., Vladimirov D., Iurmanov A. (2023). Fruits of the future: the results of the Fruits of Science project. Proceedings on Applied Botany, Genetics and Breeding, 184(2):245-250 [In Russian].

Tolmachev A. (1974). Determinant of higher plants of Sakhalin and the Kuril Islands. L.: Nauka. 372 P [In Russian].

Vekhov V. (1992). Zostera of the White Sea. Moscow: Moscow State University. (In Russian).

Vidy — biologicheskie indikatory sostoyaniya morskih arkticheskih ekosistem. (2020). Moskva: Fond «NIR». 383 pp. [In Russian].

Vladimirov D., Gladilin A., Gnedenko A., Glukhov A., Grudinskaya V., Zdravchev N., Lebedev P., Minin A., Mironenko I., Senator S., Simakova K., Tikhomirova A., Shaikina M., Shipilina L., Shiryaev A., Iurmanov A., Yantser O. (2023). The methodology of conducting phenological observations. Alpina PRO. Moscow [In Russian].

Volodina A. and Gerb M. (2013). Macrophytes of the coastal zone of the Russian sector of the southeastern part of the Baltic Sea (Kaliningrad region). Izvestiya KGTU, 28, 129-135. [In Russian with English summary].

Wu Z., Raven P., Hong D. (2010). Flora of China. Vol. 23 (Acoraceae through Cyperaceae). Science Press, Beijing, and Missouri Botanical Garden Press, St. Louis.

RESEARCH PAPER

CROSS-BORDER INTERACTIONS OF THE PSKOV REGION IN THE CONTEXT OF RESTRICTIONS: POLICY – PERCEPTION – PRACTICE

Kira A. Morachevskaya[1,2*], Alexander B. Sebentsov[1], Mikhail S. Karpenko[1], Andrei V. Radikevich[1,3]
[1]Institute of Geography Russian Academy of Sciences, 29 Staromonetny pereulok, 119017, Moscow, Russia
[2]Saint Petersburg State University, 7-9 Universitetskaya nab., 199034, Saint Petersburg, Russia
[3]Lomonosov Moscow State University, Leninskie gory, 1, 199991, Moscow, Russia
***Corresponding author:** k.morachevskaya@spbu.ru
Received: July 9th 2025 / Accepted: November 12nd 2025 / Published: December 31st 2025
https://doi.org/10.24057/2071-9388-2025-4161

ABSTRACT. This paper uses the 'Policy – Perception – Practice' approach to assess the impact of neighbourhood character dynamics and restrictions on cross-border relations in the Pskov region between 2013 and 2024. The information base includes the authors' database of documents that regulate various aspects of cross-border interactions in Russia, over 3,000 articles from Pskov media for 2013-2024, and expert interviews with government officials, as well as semi-structured interviews with the population in the regional capital and specific border towns. The analysis found that the cross-border relations of the Pskov region are asymmetric. Before the global pandemic and the geopolitical crisis of 2022, there was an emphasis on fostering cooperation with Latvia and Estonia, a collaboration that was institutionalised. The prevailing sentiment among the population, as shown by an analysis of media discourse, was that the Baltic borderland was seen only as a source of opportunities, while the Belarusian borderland was also viewed as a source of challenges. This finding underscores the imperative for cross-border cooperation to mitigate the potential for illegal activities, competitive economic pressures, illegal migration, and trade-related activities to grow without such collaboration. Despite a clear increase in the intensity of cross-border ties with Belarus after 2022, the study reveals significant shortcomings in the current approach to cross-border cooperation in Russia.

KEYWORDS: cross-border cooperation, discourse analysis, cross-border mobility, border resource, open border, asymmetric cross-border interactions

CITATION: Morachevskaya K. A., Sebentsov A. B., Karpenko M. S., Radikevich A. V. (2025). Cross-Border Interactions Of The Pskov Region In The Context Of Restrictions: Policy – Perception – Practice. Geography, Environment, Sustainability, 4 (18), 149-157
https://doi.org/10.24057/2071-9388-2025-4161

ACKNOWLEDGEMENTS: The research was carried out with the financial support of the project RSF №24-27-00400 'Adaptation of functions and territorial structures of border regions of Russia in the conditions of restrictions'.

Conflict of interests: The authors reported no potential conflict of interests.

INTRODUCTION

Cross-border relations between Russia and Western countries have been in crisis since 2022. At the same time, interest in establishing or expanding cooperation with so-called 'friendly states' began to grow. In this context, the question of introducing a programme similar to the Russia-EU cross-border cooperation programme on the border with friendly Belarus started to be raised at federal and regional levels in Russia[1]. This rhetoric has led to an increased need to analyse the directions, intensity, problems, and achievements of cross-border interactions along Russia's western borders.

Cross-border cooperation and the cross-border practices of the population are often seen as resources for peripheral territories. They demonstrably improve the quality of life for people living in border areas. In Christophe Sohn's words, the border can act as a resource. It produces asymmetric cross-border interactions, which are contacts that occur when people seek benefits in the neighbouring country (Sohn, 2014).

The Pskov region's position across multiple neighbourhoods was a significant factor in its selection as the testing region for this study. Extending from north to south, the region shares borders with three countries to the west: Estonia, Latvia, and Belarus. Despite numerous challenges in political relations with its Baltic neighbours, the period from 2004 to 2022 saw a noticeable increase in interaction between Russia, Latvia, and Estonia. This period

[1] The Ministry of Economic Development and the Ministry of Foreign Affairs of Russia, together with Belarusian colleagues, are developing a cross-border cooperation program within the framework of the Union State. [online] Available at: https://www.economy.gov.ru/material/news/minekonomrazvitiya_i_mid_rossii_sovmestno_s_belorusskimi_kollegami_razrabatyvayut_programmu_prigranichnogo_sotrudnichestva_v_ramkah_soyuznogo_gosudarstva.html (Accessed 14.10.2024).

was characterised by the implementation of various cross-border cooperation programmes, particularly those initiated under the Estonia-Latvia-Russia framework from 2007 to 2013. There were also Estonia-Russia and Latvia-Russia programmes from 2014 to 2020. It is also noteworthy that certain areas of the Pskov region were included within the scope of the Pskov-Livonia Euroregion. However, the effectiveness of the latter organisation has been subject to considerable debate (Barinov and Kiryushin, 2013).

During the same period, relations with Belarus developed against the backdrop of integration processes within the Union State and the Eurasian Economic Union (EAEU). However, various studies have repeatedly noted that this had little effect on the effectiveness of cooperation between the border regions of Russia and Belarus (Katrovskiy, 2022, Morachevskaya, 2016, Sebentsov et al., 2023). In the context of the declared priorities of integration, border cooperation was mentioned from time to time, though it lacked substantial support, particularly concerning financial instruments. Although there is a significant amount of literature on the institutionalised contacts between the Pskov region and Estonia, Latvia, and Belarus (Barinov and Kiryushin, 2013, Tsvetkova, 2017, Shlapeko, 2019), the role of neighbouring states in the everyday practices of the population has received almost no attention in studies (Barinov, 2011, Manakov, 2014). It can be hypothesised that the population of the depopulating Pskov region, which has a depressed economy, shows limited mobility. However, our previous research in the region (Morachevskaya, 2013, Sebentsov et al., 2023) shows that cross-border practices in the Russian-Estonian, Russian-Latvian (until 2022), and Russian-Belarusian border areas were quite varied and widely present among the population of the border areas and the city of Pskov.

This paper aims to answer how the dynamics of neighbourliness between 2013 and 2024 and restrictions influenced the characteristics of regional development. This is examined through the analysis of cross-border cooperation institutions, the population's cross-border practices, and perceptions of neighbours and borders.

The Policy-Perception-Practice (PPP) approach, which focuses on the interdisciplinary study of border activities, border policy, and border perception, has become a significant part of border studies (Kolosov, 2008, Kolosov and Scott, 2013). A main principle of this approach is that cross-border interactions depend on many factors, which can be divided into three main groups.

The term 'policy' is typically used to refer to the institutional framework that governs cross-border interactions. This includes security policy, foreign economic regulation, and the regulatory and legal framework for cooperation.

The concept of 'perception' includes elements such as images of a neighbouring country or region that reflect public opinion or shaped by public and media discourse. It also covers the cultural distance between the population of a country as a whole and the inhabitants of its border regions, historical narratives, political discourse, and the symbolic landscape (Kolosov and Sebentsov, 2019, O'Toal, 1996).

In a broad sense, the term 'practice' can be understood to denote the entire complex of cross-border interactions. These interactions may be defined as flows of people, information, goods, transport links, cross-border cooperation between authorities at different levels, and non-governmental organisations, among others.

One of the postulates of securitisation theory is that the perception of a particular situation in socio-political discourse frequently acts as the initial catalyst for changes in the prevailing state of affairs, affecting public institutions (Buzan et al., 1998) and international relations (Vendina et al., 2014). This assertion suggests that discourse is influenced by the politics and practice of cross-border interactions, and that discourse also influences these interactions. Consequently, our study will primarily comprise an examination of media discourse.

From the perspective of the discursive approach, the study of media materials in dynamics is most often based on analysing the general evolution of discourse. Such analysis includes the dynamics of the number of publications, their tonality, defining the internal structure of discourse based on key topics, and identifying cross-cutting motifs (Galkina and Popov, 2016). A systematic qualitative analysis of the entire array of news flows reveals key themes in a particular area and integrating ideas (Vendina et al., 2014). The evaluation of both the expectations and results of cross-border interactions in border regions is facilitated by long-term series in the assessment of discourse formed by the media (Kolosov and Sebentsov, 2019, Sebentsov et al., 2022, Sebentsov and Kolosov, 2020).

In the context of the Pskov region's cross-border relations, most researchers have concentrated on its borders with EU countries or Belarus. There is a lack of comparative analysis between these two types of neighbourhood relations (Gritskevich, 2016, Kolosov and Borodulina, 2006, Popkova, 2018, Sapogov et al., 2022). Regarding policy, some researchers have observed a paradoxical difference between the state of inter-state relations and the development of cross-border cooperation institutions on the borders with EU countries and on the internal borders of the Union State (Vardomskiy, 2008, Sebentsov and Lomakina, 2025).

Consequently, the analysis of policy, perception, and practice reflects the current reality and shapes the agenda for the future. In a rapidly changing geopolitical environment, this allows us to understand, on the one hand, the existing problems in the development of cross-border relations, and on the other hand, possible areas for cooperation.

MATERIALS AND METHODS

In the context of this study, the following methodology will be employed (Fig. 1). Firstly, an assessment of cooperation institutions as a reflection of policy will be made. Secondly, media discourse will be analysed. Thirdly, an analysis of the population's cross-border practices will be

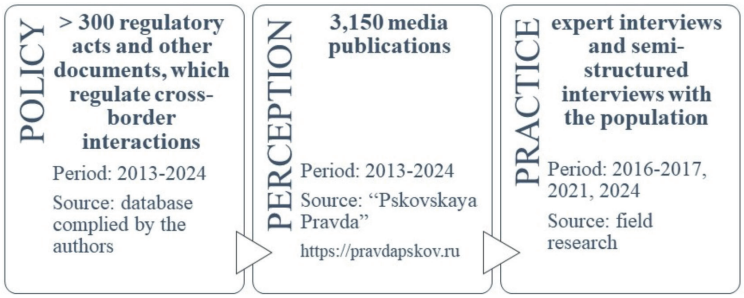

Fig. 1. Overview of study stages

conducted. The analysis of the institutionalisation of cross-border cooperation was based on over three hundred documents collected by the authors. These documents regulate various aspects of cross-border interactions across the entire Russian border and in the Pskov region.

A substantial proportion of the research data was provided by the Pskov media. At the preliminary stage, the media landscape of the Pskov region was analysed. To do this, the authors used the full-text database of print media 'Integrum', which contains four newspapers from the Pskov region: 'Pskovskie Novosti', 'Pskovskaya Pravda', 'AiF Pskov' and 'Pskovskaya Gubernia'. A preliminary analysis of the archive revealed that, firstly, the data for a number of newspapers is limited to specific years, and secondly, the thematic focus of the newspapers over a long period does not allow for a comprehensive assessment of the cross-border interactions of the Pskov region (for example, AiF Pskov focuses more on entertainment content). For this reason, it was decided to shift the main focus of the analysis to the region's key news media portal – Pskovskaya Pravda. This media resource was created based on the region's oldest newspaper. For the purposes of the study, the range of news topics covered by the media was important. Therefore, the degree of independence and other characteristics of the publication were not of fundamental importance.

A database comprising 3,150 publications was meticulously compiled for the period from 2013 to 2024, including the first nine months of 2024. This comprehensive compilation was conducted using the specific tags 'belarus*', 'latv*', and 'eston*'. The database was analysed quantitatively, examining the distribution of messages by topic (for which 12 thematic categories were used) and tone (positive, neutral, negative). The qualitative analysis involved identifying salient trends in the transformation of cross-border relations between the Pskov region and its neighbouring regions.

The data source, primarily used to assess the cross-border practices of the population, also included field research conducted by the authors in the Pskov region during 2016-2017, 2021, and 2024. This field research involved expert interviews with representatives of the authorities and semi-structured interviews with the population in various cities and districts of the region. These locations included Pskov and the border towns of Pytalovo, Pechory, Nevel, and Sebezh. The Sebezh district is given particular attention in the study due to its proximity to both Latvia and Belarus, and the strategic importance of the transport routes that cross the district, connecting it to both countries.

RESULTS

Institutions for cooperation in the Pskov border region

Until recently, the Pskov region reflected the institutional imbalance that had developed along Russia's borders by the late 1990s. As early as 1996, a Council for Cooperation was established between the border regions of Latvia, Russia, and Estonia. The Russian national authorities did not officially endorse the establishment of this Council. However, in 2003, the Pskov-Livonia Euroregion was established based on this Council. At the same time, the federal centre supported the region's collaboration with its European neighbours through the European TACIS programme. This programme helped implement several projects to improve border crossing points and encourage bilateral interaction. In the 2000s, even though both Estonia and Latvia joined NATO and the EU, cooperation between the three states became more institutionalised, developing within the framework of neighbourhood programmes. Initially, these programmes were carried out on a trilateral basis (from 2000 to 2013), and later on a bilateral basis, with separate programmes implemented with Estonia and Latvia respectively.

Cross-border cooperation with Belarus has not been as dynamic. The agreement on the development of mutually beneficial cooperation with the Vitebsk Regional Executive Committee, signed in 1993, remained for a considerable period the only framework document attesting to the cooperation between the two regions (Gorskaya, 2019). During the 2000s, twinning relations between a number of cities and districts in the Vitebsk and Pskov regions underwent accelerated development. As a result, a new agreement was signed with the Vitebsk Regional Executive Committee in 2015. Nevertheless, genuine cooperation was primarily confined to the visits of official delegations and the organisation of exhibition and fair activities.

The geopolitical crisis in relations with the West in 2022 brought about significant changes to the institutional environment of the border region. Almost all regional and municipal agreements with the Baltic countries were terminated, and Russia's participation in three cross-border programmes – Russia-Estonia, Russia-Latvia, and Interreg Baltic Sea Region — was discontinued. The operations of the Pskov-Livonia Euroregion, which had already seen a substantial reduction in activity during the pandemic, ceased entirely. In 2022, the cross-border activities of the Chudskoy Project organisation were completely paralysed. The presence of the Tartu 'branch' (Kolosov, Borodulina, 2006) and its high level of activity in implementing various environmental, educational, and social projects led to this organisation being regarded as a 'Euroregion-like' entity.

Concurrently, the focus of institutional cooperation shifted towards Belarus. The deepening of collaboration between Russia and Belarus within the Union State has allowed the Pskov and Vitebsk regions to proactively advocate for the creation of a cross-border cooperation programme between the two countries. Interviews conducted in the Vitebsk and Pskov regions in June 2024, and with representatives of the Border Policy Department of the Presidential Administration of Russia in October 2024, have led to the conclusion that the programme is being prepared with very little input from regional authorities. National authorities are more interested in the interregional aspect of this programme than the cross-border aspect. At this point, the border cooperation programme is seen solely as a way to establish cooperative links between large industrial companies, rather than as a method for developing cooperation between regional and local authorities and territorial communities.

The integration within the Union State has contributed to the institutionalisation of cooperation at the municipal level between districts in the Pskov Region and districts in neighbouring Belarusian regions. However, the absence of available financial resources, along with the lack of specific financial instruments from the Union State, means that specific cooperation projects based on these agreements cannot be expected to emerge.

The everyday practices of border residents: a view from the Sebezh district

Before 2020, residents of the Pskov region regularly travelled to Estonia, Latvia, and Belarus for various reasons. The frequency of these trips depended on several factors, including where people lived. Residents of Pskov and

nearby border districts travelled more often. Individual mobility also played a significant role, influenced by income levels and established habits. Between 2013 and 2021, incomes in the Estonian and Latvian border areas grew particularly quickly in real terms (Fig. 2). On the Russian side, income growth was more moderate, while incomes in Belarus remained stagnant. Additionally, currency exchange rate changes were important in shaping travel patterns. Comparable price levels, calculated using the World Bank method and adjusted for living standards in Russian regions, help explain the changes in cross-border travel. Unfavourable exchange rate movements made neighbouring countries (except Belarus) relatively more expensive for shopping, which made cross-border travel less appealing for Russians and more appealing for residents of the border areas of Latvia and Estonia.

The interviews demonstrated that the primary motivations for visiting Estonia included leisure activities such as day trips or weekend excursions to spas and swimming pools. Secondary motivations encompassed the acquisition of food and clothing and, less frequently, medical services (primarily for childbirth) and education, notably in Tartu. The motivations for travel to Latvia were comparable, with consumer purposes being the predominant factor.

It is evident that there was a high prevalence of trips from Latvia and Estonia to Russia, with the primary purpose of procuring petrol. In addition to this, residents of the Baltic states also purchased medicines and certain food products, such as pasta and cereals, in Russia.

Trips to Belarus were more common in the southern part of the Pskov region. However, for the population of the entire Pskov region, only trips for sanatorium and resort treatment were significant. In certain cases, individuals managed to obtain an education in Belarus. More often than not, these were either secondary specialised education programmes, which were generally better preserved in Belarus, or higher education programmes that were, on average, cheaper to obtain on a commercial basis than in Russia.

The Sebezh district of the Pskov region is unique because it is bordered by two countries, each with its own border crossing regime. This has led to various opportunities for cross-border activities among the local population. Until 2020, residents of the Sebezh district frequently visited neighbouring Latvia. Semi-structured interviews with the population revealed several reasons for this. Initially, the frequency and destinations of trips for purchasing food products were influenced by price differences, as mentioned before. Secondly, people travelled from Sebezh to Rezekne in Latvia for clothing and footwear, attracted by a wider selection, high quality, and reasonable prices. Thirdly, visits were made to a building supply store in Rezekne because no such store existed in Sebezh in earlier years. Fourthly, shuttle trading, particularly of approved food products, was a significant practice. Finally, due to the limited number of official car dealerships in the Sebezh district (and, for certain brands, in Pskov), Russian citizens sometimes had their vehicles serviced in neighbouring Latvia.

Concurrently, cross-border mobility showed a less pronounced asymmetrical pattern. Latvian residents also took advantage of price variations, with the Sebezh district being a popular destination for shopping. Sugar, cereals, pasta, flour, and similar items were in high demand among Latvian residents at retail outlets in Sebezh. The availability of medicines in Sebezh pharmacies contributed to this trend. As in other regions along the Russian border, it was customary for Latvian residents to travel to border petrol stations located on the Russian side.

The interviews conducted showed that cross-border mobility towards Belarus was generally less pronounced, and the range of motives was considerably more limited. Purchasing food products in Belarus was not a common practice, partly due to the widespread availability of Belarusian goods on the local market, including through mobile trade. A small number of labour ties exist, such as Belarusians working in the social sector, and educational ties involving training in specialised fields at vocational schools in Sebezh.

Cross-border interactions in media discourse

The shift in the character of interstate relations had consequences for both the institutional sphere and the cross-border practices of the local population. This shift was also reflected in media discourse.

In relation to the dynamics of mentions of neighbouring states, primarily Latvia and Estonia, on the Pskovskaya Pravda portal, 2013 stands out. This year coincided with a period of flourishing cross-border cooperation in the European direction (Fig. 3). It can be suggested that the geopolitical crisis of 2014 influenced the media's caution in mentioning the foreign context and led to a decrease in the intensity of external relations. The intensity of external relations decreased somewhat, so the number of news items tagged 'belarus*', 'eston*', and 'latv*' fell by almost half in subsequent years compared to 2013. In 2013,

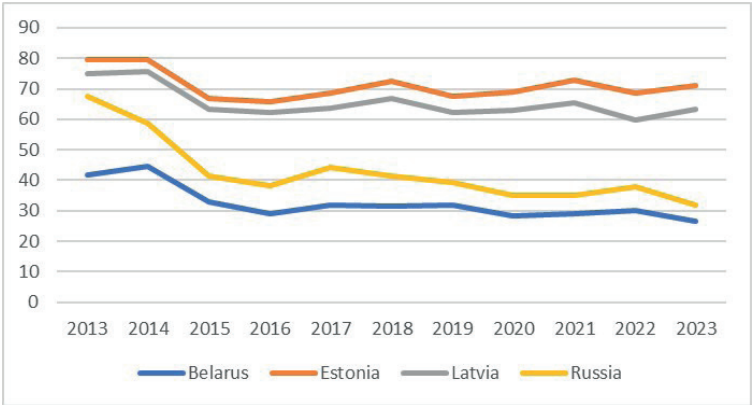

Fig. 2. Comparative price levels in borderlands, % to US price levels[2]

[2] The comparative price levels is the ratio of a purchasing power parity (PPP) conversion factor to the corresponding market exchange rate between different countries. It provides a measure of the differences in price level between the country and the United States by indicating the number of units of the common currency (US dollars) needed to buy the same volume of the aggregation level in each country. At the level of GDP, the price level ratio provides a measure of the differences in the general price levels of countries.

there was still active rhetoric of mutual support between countries in the event of any emergencies or tragic events in neighbouring regions.

The geopolitical crisis of 2014 was reflected in media discourse as a period of uncertainty concerning cross-border cooperation between the Pskov region and Latvia and Estonia. In this context, the media has recently started to address issues characterised by complete polarisation. On one hand, there is heated debate on the complex issue of bilateral relations: the Russian language in schools in the Baltic states. To lessen any potential discord with neighbouring nations, some news outlets use the narrative of 'Europe in our home', thereby aiming to reduce the perceived importance of any differences with these countries. Conversely, other topics emphasise the improvement of cross-border relations with Baltic countries. For example, there is a significant discussion about organising air traffic between Pskov and Riga. It can be suggested that this era of uncertainty is ending, with a prevailing consensus that cross-border cooperation aimed at improving the quality of life for people living in border regions should be exempt from political interference.

Since 2015, as evidenced by news reports and the results of our own interviews, there has been a noticeable trend of declining cross-border mobility to Latvia and Estonia. This decline is primarily due to economic reasons, such as changes in exchange rates, as highlighted in several news outlets. The reduction in the flow of people has also resulted in several negative institutional changes. These include the cancellation of booking options for border crossing queues and the closure of tax-free facilities at the border. These changes are being actively discussed in the media.

The period of cooling and uncertainty that characterised 2014–2015 gave way to a new phase in 2016, when cross-border cooperation became a prominent feature in media discourse. It is explicitly stated that this area should not be subject to any sanctions, as the quality of life of the population in border areas depends on it.

Such rhetoric significantly influences the optimism shown in business relations. The emergence of new small businesses focused on the EU market is a notable phenomenon in this regard. Headlines such as 'Pskov residents are invited to break into EU markets', while 'Latvian residents are invited to join the Moglino Special Economic Zone'[3] (2018) and 'We have studied the European market and understand what awaits us'[4] (2021) confirm the intention to maintain and develop economic ties between neighbouring regions.

It is evident that until 2020, the Baltic neighbours maintained a dominant presence within the information field, as shown by the greater number of mentions directed towards them compared to Belarus. It is also clear that the global pandemic of the novel coronavirus has had a significant impact on the nature and intensity of cross-border relations. However, before the events of 2022, which led to a major transformation in external relations with Western countries, Belarus had consistently ranked first. Firstly, it is important to note that in 2021, a number of restrictions on movement between Russia and Belarus, which had been introduced at all borders due to the COVID-19 pandemic, were lifted. Secondly, there was a significant increase in the number of news items concerning the situation at the border – the illegal import of tobacco products from Belarus into the Russian Federation. In 2021, excise duties on such goods were considerably increased in Russia (by 20%), leading to an increase in illegal flows of cigarettes from other EAEU countries.

The tone of mentions of Belarus, Latvia, and Estonia in Pskov news throughout the entire period is consistent with federal political discourse and the key geopolitical vector (Fig. 4). In 2023, a number of positive news items tagged 'latv*' and 'eston*' were observed. These items primarily concerned the participation of representatives from the Russian-speaking diaspora in Estonia and Latvia in cultural events, such as exhibitions and theatre performances, within the Pskov region. Regarding the Russian-Belarusian borderland, there has been a considerable amount of crime-related news over the years, partly due to the open nature of the border. The majority of negative incidents at the border pertain to representatives of third countries who commit various violations related to export-import operations.

The thematic structure of the news materials examined throughout the entire review period is highly diverse (Fig. 5), so the focus will be on some of the most significant features. History and culture were the predominant themes throughout the entire period. In the period leading up to the acute geopolitical crisis of 2022, despite the emergence of contradictions in the relationship between Russia and the Baltic states, the discourse continued to feature terms that indicated fairly close socio-cultural ties and a shared

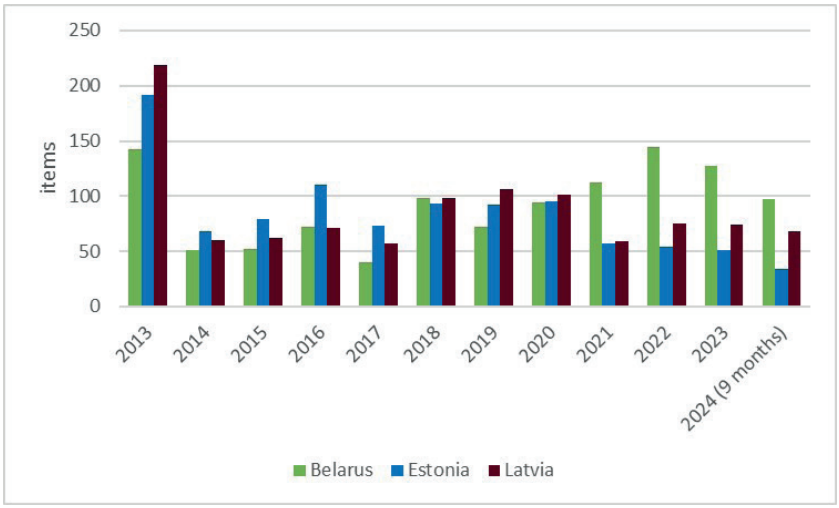

Fig. 3. Total number of news items mentioning the tags 'belarus*', 'eston*' and 'latv*' in 2013–2024

[3]Pskovskaya Pravda Official Website, (2018). Neighbors are forever. [online] Available at: https://pravdapskov.ru/society/0005218.html (Accessed 5.09.2024).

[4]Pskovskaya Pravda Official Website, (2021). German Petrushko presented an investment project at the forum in Kazan. [online] Available at: https://pravdapskov.ru/news/0024654.html (Accessed 5.09.2024).

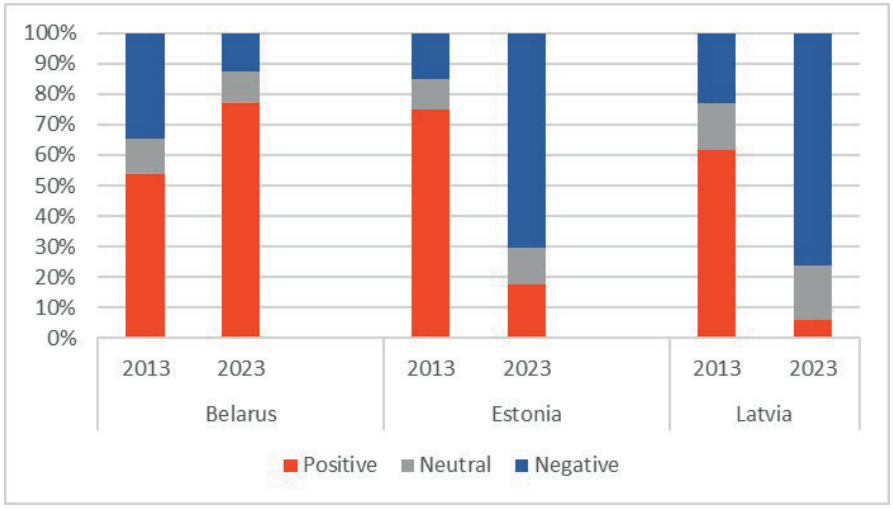

Fig. 4. Tone of news items mentioning the tags 'belarus*', 'eston*' and 'latv*' in 2013–2023

historical past. These included references to the Second World War, the Friendship Mound[5], the Hanseatic League, and Alexander Pushkin.

The second popular topic was borders and customs. News about incidents along the border is frequently featured in the media, although the context varies considerably between different sections. A paradoxical comparison can be drawn between the 'open' border with Belarus and the 'barrier' borders with Latvia and Estonia (prior to 2020). The former is a source of problems, while the latter is a resource ('the border location is not a limitation, but an opportunity'[6]; 'border resource',[7,8]). The open border has demonstrated unintended consequences, with research indicating that it can act as a conduit for crime and illegal activity. The media has repeatedly drawn attention to issues such as the illegal alcohol trade in markets, poaching (hunting and fishing) in the southern regions of the Pskov region, and illegal migration. The issue of competition between Belarusian and Russian producers is considered complex: 'Local producers are being squeezed out by Belarusians'[9].

The third topic, institutions, should be discussed separately (Fig. 3). News outlets have dedicated considerable coverage to projects implemented within the framework of cross-border cooperation programmes between Russia, Estonia, and Latvia. These projects cover diverse sectors, including transport, ecology, education, science, and tourism. The following quote from an article on this subject encapsulates the essence of this cross-border contact with our Baltic neighbours: 'The existence of unsolvable problems between neighbouring countries is to be avoided'[10].

It has only been since 2021 that specific plans for cooperation between the Pskov region and Belarus have been mentioned in the media. According to Pskovskaya Pravda (a news item from 2022), 'there has been a "reset" in relations between the Pskov region and the Vitebsk region'[11]. Issues concerning the potential for industrial cooperation, the synchronisation of special economic zone regimes, and rural development management are being raised. This new stage of constructive interaction has been marked by several notable developments. These include the establishment of agreements between enterprises and universities, the initiation of specific projects for personnel training in secondary vocational schools, the protection of transboundary lakes, the fostering of cooperation between trade unions, and the organisation of joint job fairs. In news coverage of Belarusian relations, labour market issues are often raised. This is particularly true regarding the recruitment of personnel to work in depopulated areas of the Pskov region, especially within the healthcare sector.

The status of a border crossing point has a considerable influence on the regional situation. The existence of an international border crossing point on the Russian-Latvian border distinguishes it significantly from the Estonian border, where border issues are barely discussed. Following 2022, the majority of news items related to the tags 'latv*' and 'eston*' concerned incidents where border guards or customs officers stopped someone or something at the border[12,13],.

DISCUSSION

The use of the PPP approach in analysing the Pskov region has helped identify several significant themes related to border dynamics and cross-border interactions.

[6] The Friendship Mound is a memorial complex erected on the border between Russia, Belarus and Latvia in memory of the cooperation between partisan units during the Second World War.

[6] Pskovskaya Pravda Official Website, (2016). Experience – for replication. [online] Available at: https://pravdapskov.ru/rubric/3/13792 (Accessed 5.09.2024).

[7] Pskovskaya Pravda Official Website, (2017). Sergey Pernikov: Cross-border cooperation is unique. [online] Available at: https://pravdapskov.ru/rubric/3/14832 (Accessed 5.09.2024).

[8] Pskovskaya Pravda Official Website, (2018). Envoy and Team. [online] Available at: https://pravdapskov.ru/politics/power/0003166.html (Accessed 5.09.2024).

[9] Pskovskaya Pravda Official Website, (2015). Pricier but closer to heart. [online] Available at: https://pravdapskov.ru/rubric/82/11714 (Accessed 5.09.2024).

[10] Pskovskaya Pravda Official Website, (2013). The Federation Council Committee on International Affairs, chaired by Mikhail Margelov, will host guests from Estonia. [online] Available at: https://pravdapskov.ru/news/12082 (Accessed 5.09.2024).

[11] Pskovskaya Pravda Official Website, (2022). A «reset» in relations occurred in the cooperation between Pskov Oblast and Vitebsk. [online] Available at: https://pravdapskov.ru/news/0031190.html (Accessed 5.09.2024).

[12] Pskovskaya Pravda Official Website, (2023). Pskov border guards detained two foreigners attempting to illegally cross Russia's state border. [online] Available at: https://pravdapskov.ru/news/0034825.html (Accessed 5.09.2024).

[13] Pskovskaya Pravda Official Website, (2024). Pskov customs officers intercepted two batches of smuggled cigarettes within a week. [online] Available at: https://pravdapskov.ru/news/0039903.html (Accessed 5.09.2024).

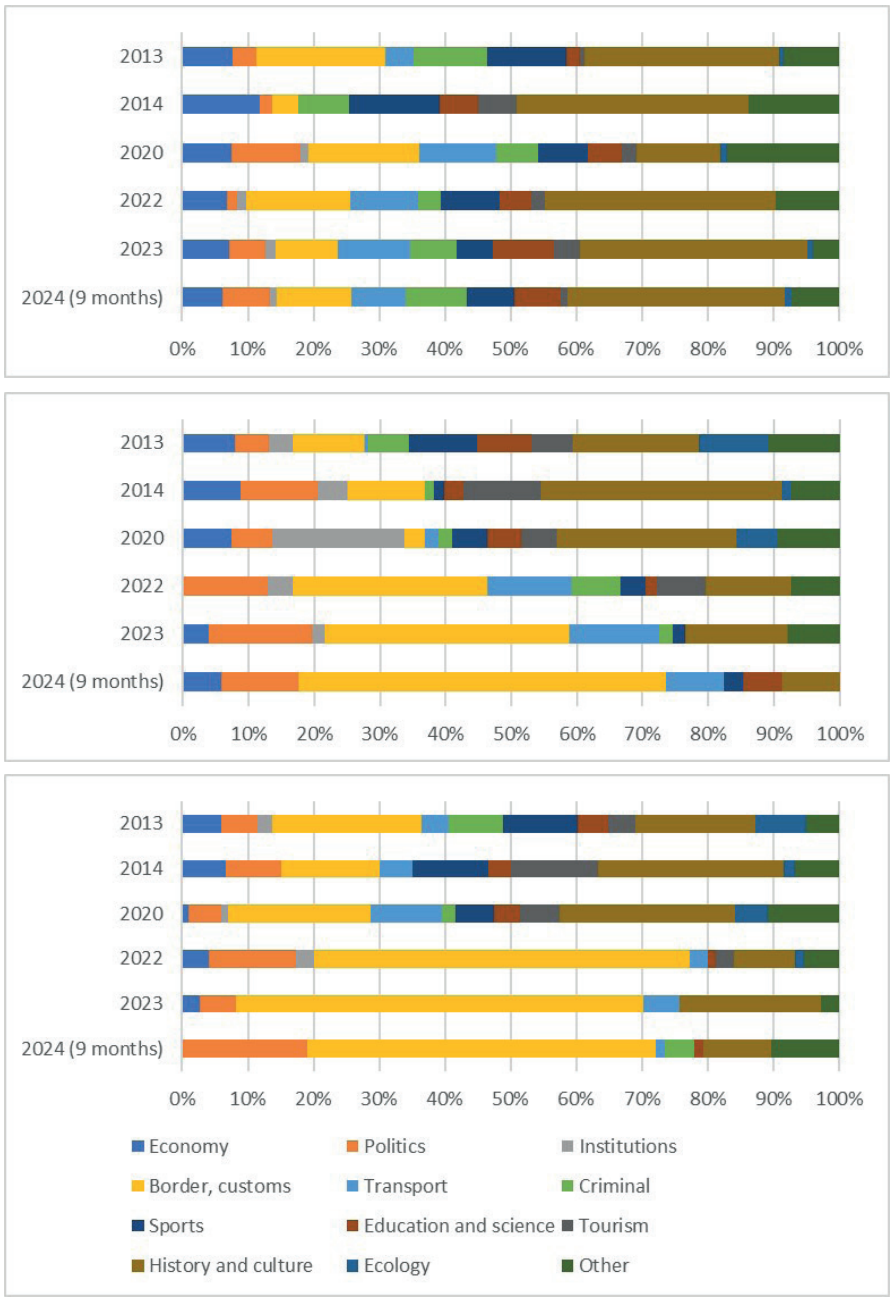

Fig. 5. Thematic structure of news items mentioning the tags 'belarus*', 'eston*' and 'latv*' in 2013–2024

Comparison with neighbours as an impetus for local development. A prominent theme that emerges from an examination of regional discourse concerns the tendency to compare with neighbouring regions. This tendency often favours the domestic context. The subjects to which the study is compared primarily relate to the social sphere and the quality of life in urban environments.

Media often discusses proposals to adopt practices from neighbouring countries. These include the organisation of taxi services and park development in Latvia, technology and maternity hospitals in Estonia, and waste collection, the state of houses, and streets in Belarus. Healthcare reorganisation in Belarus is also a topic. Examining this dynamic helps observe regional changes, partly driven by these comparisons. For example, in 2013, several news outlets reported on women from Pskov choosing to give birth in Estonian hospitals due to better facilities and medical equipment. By the end of 2014, a new perinatal centre was established in the region, meaning women in Pskov no longer needed to travel abroad for high-quality care.

The region's border location has resulted in two primary consequences. Firstly, it has fostered the development of new functions, and secondly, it has significantly influenced the growth of specific economic and social sectors. For example, an advertising campaign for new programme tacks at Pskov State University highlighted that graduates would possess the skills to work with or within businesses in neighbouring countries. The development of tourist locations in rural areas of the Pskov region in the form of eco-villages has been largely stimulated by the experience of neighbouring countries. The popularity of European cheeses and the ban on their import into Russia in 2014 led to the emergence of individual farmers in the Pskov region producing elite varieties of cheese. The examples provided demonstrate how political comparisons with neighbouring countries can stimulate internal changes in border regions.

Advertising the neighbour for life and everyday practices. Until 2020, there was considerable promotion of additional opportunities for residents of border areas. These opportunities are primarily associated with Latvia and Estonia, with Belarus not being mentioned in this context. Semi-structured interviews with residents of the Sebezh district suggest that the motivations for travelling to Latvia are considerably more varied than those for travelling to Belarus.

The news reports include details on purchasing apartments in Latvia and Estonia with funds from selling a two-room apartment in Pskov, and establishing a business in Latvia within a day. It was also explained how to start a business in Estonia after completing training at Pskov State University, the acquisition of real estate in Estonia, and a list of Estonian universities where graduates from Pskov schools can apply.

Such practices are characteristic of border regions and typically demonstrate the population's high adaptability to price fluctuations and changes in the range of goods and services on the domestic market.

Friendship and/or cooperation? As previously stated, interaction with the Baltic neighbours was largely institutionalised. In addition to border cooperation programmes, intergovernmental commissions and bilateral agreements with Estonia and Latvia resolved a host of constructive issues, including the control of fish catches in Lake Peipsi, mutual recognition of work experience in another country for pensioners, and schedules for border crossing points during peak periods. This interaction was described in the media as 'the wonders of cross-border cooperation'[14], and the principle of sharing experience was recommended.

However, despite the apparent absence of significant political and socio-cultural impediments, the Russian-Belarusian border region yielded only limited outcomes regarding border cooperation. As stated in an article in Pskovskaya Pravda in 2016[15], 'unfortunately, no large-scale projects have been implemented'.

One potential explanation for this phenomenon is the relative remoteness of neighbouring territories and the lack of attention they receive from national authorities. There is a lack of clearly defined mechanisms for interaction on the supranational agenda, including financial instruments for cooperation. The discourse about integration processes between Russia and Belarus scarcely addresses the issue of border regions. A number of indirect influences have been identified as contributing to the phenomenon under investigation. These include a variety of business practices, such as taxation and lending, state regulation of the economy, and a lack of external incentives for developing cooperative business ties in border areas. In the absence of incentives and preferences for cooperation, business representatives in the border region have revealed that they are not motivated to develop ties with the border regions of neighbouring countries. This finding suggests that legal institutionalisation and financial support for cooperation are crucial in transforming amicable relations into a productive partnership for addressing shared challenges.

One of the observations made in the study clearly expresses the effectiveness of cross-border interaction between the Pskov region and its neighbours, with the following quote: 'A good neighbour is better than a relative'[16].

CONCLUSIONS

The study's findings show that cross-border relations in the Pskov region developed in an asymmetrical manner until recently. Although cross-border cooperation between Russia and the EU is currently absent due to the geopolitical situation, institutionalised cooperation along the borders with the Baltic countries had developed before the COVID-19 pandemic. Efforts to establish cooperative institutions on the Belarusian side of the border were consequently unsuccessful.

The cross-border practices of the local population were also asymmetrical until 2020. Interviews demonstrated that travel destination choice was influenced not only by geographical residence but also by the possibility of satisfying certain needs. In any case, cross-border mobility towards Belarus was generally less intense, and the range of motives was significantly narrower.

A study of the perception of cross-border relations in the Pskov media also demonstrated the dominance of the Baltic neighbours in regional media discourse. Conversely, while the Baltic section of the border has been perceived almost exclusively as a resource for regional development until recently, the Belarusian section has been viewed as a source of various problems.

In the absence of adequate consideration of cross-border cooperation, an open border is associated with numerous disadvantages. These include, but are not limited to, the creation of an environment that encourages illegal activities, the facilitation of unfair competition among economic actors, and the occurrence of illegal migration and unbalanced export-import flows. At the same time, restrictions can reduce the border area's comparative advantages, such as the Pskov region's proximity to the EU market. However, they can also contribute to the development or enhancement of absolute advantages, including greater investment in the maintenance of intra-regional roads and increased tourist use of the internal territory.

Despite the geopolitical crisis of 2022, the importance of the neighbourhood with Belarus has grown significantly. However, the article's findings reveal considerable weaknesses in the current approach to cross-border cooperation and its institutionalisation. An open border between culturally and geographically close areas is essential, but it is not enough to foster cross-border cooperation. To encourage this, a specific cross-border cooperation programme should be created, drawing on the experience of cooperation with the European neighbours of the Pskov region. This programme should focus on a particular border area, consider the priorities for local and regional cooperation on both sides of the border, have a shared budget and common governing bodies, and establish clear criteria for selecting joint projects. Furthermore, it is important to involve not only national, regional, and local government representatives but also local communities in project activities.

[14] Pskovskaya Pravda Official Website, (2015). Wonders of cross-border cooperation. [online] Available at: https://pravdapskov.ru/rubric/17/11797 (Accessed 5.09.2024).

[15] Pskovskaya Pravda Official Website, (2016). Sergey Pernikov: We are not afraid of a shortage of personnel but rather their transfer from other enterprises. [online] Available at: https://pravdapskov.ru/rubric/3/13441 (Accessed 5.09.2024).

[16] Pskovskaya Pravda Official Website, (2018). Economics exam. [online] Available at: https://pravdapskov.ru/economics/investments/0004175.html (Accessed 5.09.2024).

REFERENCES

Barinov S.L. (2011). Barriers to cross-border sociocultural communication in the zone of Russia's new western frontier. Izv. Akad. Nauk, Ser. Geogr.,1, 45-54. (In Russian)

Barinov S.L., Kiryushin P.A. (2013). Nature and outcomes of the development of cross-border regions under various institutional conditions: The case of the Euroregions «Øresund,» «Pskov–Livonia,» and «Dnieper.» Vestnik mezhdunar. Org. Obrazov., Nauka, novaya ekonom., 8 (4), 196-213. (In Russian)

Buzan B., Wæver O., De Wilde J. (1998). Security: A New Framework for Analysis. Boulder: Lynne Rienner Publishers, DOI: https://doi.org/10.2307/2586187

Galkina T.A., Popov F.A. (2016). Russia's border with Abkhazia and South Ossetia at four scales (analysis of political discourse). Izv. Akad. Nauk, Ser. Geogr., 4, 109-118. (In Russian)

Gorskaya A.N. (2019). Cross-border cooperation between Pskov Oblast and the Republic of Belarus. Locus: People, Society, Cultures, Meaning, 4, 112-122. (In Russian)

Gritskevich Yu.N. (2016). Political discourse in the Pskov region in the context of media culture. In I. V. Moteyunajte ed. Cultural Landscape of Borderlands: Past, Present, Future: Proceedings of the II International Scientific Conference December 5–7, 2016 Volume II, Pskov: Pskovskij gosudarstvennyj universitet, 98-104. (In Russian)

Katrovskiy A.P. (2022). Regions of Russia bordering Belarus: Challenges to socio-economic development. In A.A. Mihajlova ed. Problems of Borderlands: New Trajectories for International Cooperation: Proceedings of the VI International Scientific and Practical Conference, Kaliningrad, October 20–21. Volume 6, Kaliningrad: Izdat. Baltijskogo Fed. Univers. im. Immanuila Kanta, 102-107. (In Russian)

Kolosov V., Scott J.W. (2013). Selected conceptual issues in border studies. Belgeo, 4, 9-21. DOI: https://doi.org/10.4000/belgeo.10532

Kolosov V.A. (2008). Geography of state borders: Ideas, achievements, practice. Izv. Akad. Nauk, Ser. Geogr., 5, 8-20. (In Russian)

Kolosov V.A., Borodulina N.A. (2006). The Russian-Estonian border: Barriers to perception and cross-border cooperation. Pskovskij regionolog. Zhurnal, 1, 145-157, DOI: https://doi.org/10.37490/S221979310022877-7. (In Russian)

Kolosov V.A., Sebentsov A.B. (2019). Regionalization processes in Northern Europe and the «Northern Dimension» program in Russian political discourse reflection. Baltic Region, 11(4), 76-92, DOI: https://doi.org/10.5922/2079-8555-2019-4-5.

Manakov A.G. (2014). Dynamics of cross-border contacts among the population of the western districts of Pskov Oblast in 2003–2013. Pskovskij regionolog. Zhurnal, 17, 98-107. (In Russian)

Morachevskaya K.A. (2013). Borderland and peripherality as factors in the development of Russian regions bordering Belarus. PhD Diss. (Geogr.). Moscow, 196. (In Russian)

Morachevskaya K.A. (2016). Institutional barriers to cross-border cooperation in the Russian-Belarusian borderlands. In Katrovskiy A.P. ed. Russian-Belarusian Borderlands: Problems and Prospects for Development. Proceedings of the International Scientific Conference October 13–14. Smolensk: Universum, 37-44. (In Russian)

O'Toal G. (1996). Critical Geopolitics: The Politics of Writing Global Space. Minneapolis: University of Minnesota Press, DOI: https://doi.org/10.2307/216022

Popkova L.M. (2016) Conflict discourse in Pskov's media space. In I. V. Moteyunajte ed. Cultural Landscape of Borderlands: Past, Present, Future: Proceedings of the II International Scientific Conference December 5–7, Volume II, Pskov: Pskovskij gosudarstvennyj universitet, 105-110. (In Russian)

Sapogov V.M., Manakov A.G., Terenina N.K. (2022). Cross-border cooperation between Pskov Oblast and Estonia and Latvia. In A.P. Klemyshov et al., ed., Cross-border Cooperation Along Russia's State Borders, 1 st. ed. Kaliningrad: Izdat. Baltijskogo Fed. Univers. im. Immanuila Kanta, 95-104. (In Russian)

Sebentsov A.B., Karpenko M.S., Gritsenko A.A., Turov N.L. (2022). Economic development as a challenge for «de facto states»: Post-conflict dynamics and perspectives in South Ossetia. Izv. Akad. Nauk, Ser. Geogr, 4, 485-502, DOI: https://doi.org/10.31857/S2587556622040094 (In Russian)

Sebentsov A.B., Kolosov V.A. (2020). The «Northern Dimension» of Russia-EU relations: Experience of spatial discourse analysis. Geogr. Sreda i zhivye sistemy, 2, 28-43, DOI: https://doi.org/10.18384/2712-7621-2020-2-28-43 (In Russian)

Sebentsov A.B., Lomakina A.I. (2025). Theory and practice of cross-border regionalization: Lessons for Russia. Polis: Polit. Issled., 2, 8-24, DOI: https://doi.org/10.17976/jpps/2025.02.05 (In Russian)

Sebentsov A.B., Morachevskaya K.A., Karpenko M.S. (2023). The Russian-Belarusian borderlands: Contradictions of integration and cross-border regionalization. From friendship to cooperation? Izv. Akad. Nauk, Ser. Geogr., 87(8), 1143-1162, DOI: https://doi.org/10.31857/S2587556623080150 (In Russian)

Shlapeko E.A. (2019). Specific features of cross-border cooperation in the Republic of Karelia and Pskov Oblast. Aktual. Probl. Sovremen.: nauka i obshchestvo, 4, 3-6. (In Russian)

Sohn C. (2014). Modelling cross-border integration: The role of borders as a resource. Geopolitics, 19(3), 587-608. DOI: https://doi.org/10.1080/14650045.2014.913029

Tsvetkova O.V. (2017). The role of local self-governance and intermunicipal cooperation in the development of border territories in the Russian Federation (on the example of Pskov Oblast). Politeks, 13(2), 65-76. (In Russian)

Vardomskiy L.B. (2008). Cross-border cooperation on Russia's «new and old» borders. Evraz. Ekon. Integr., 1, 90-108. (In Russian)

Vendina O.I., Kolosov V.A., Sebentsov A.B. (2014). Is the Baltic region part of the post-Soviet space? Mezdunarodnye processy, 12 (1-2), 76-92. (In Russian)

RESEARCH PAPER

COMPARATIVE ANALYSIS OF MACHINE LEARNING ALGORITHMS FOR LAND USE AND LAND COVER MAPPING: CASE STUDY OF BERRECHID-SETTAT REGION, MOROCCO

Youssef Laalaoui[1*], Naïma El Assaoui[1], Oumaima Ouahine[1]

[1]Geosciences, Water and Environment Laboratory, Earth Sciences Department, Faculty of Sciences, Mohammed V University in Rabat, 4 Ibn Battouta Avenue, 1014, Rabat, Morocco

***Corresponding author:** laalaoui.youssef@gmail.com

Received: April 4th 2025 / Accepted: November 12th 2025 / Published: December 31st 2025

https://doi.org/10.24057/2071-9388-2025-3980

ABSTRACT. This study analyses the spatiotemporal dynamics of Land Use and Land Cover (LULC) in the Berrechid-Settat area of Morocco throughout three reference years: 2010, 2015, and 2023. Satellite images from Landsat 7 (ETM+) and Landsat 8 OLI were processed using the Google Earth Engine (GEE) platform to facilitate quick access, preprocessing, and analysis of extensive datasets. To classify LULC changes and assess the efficacy of machine learning models, Random Forest (RF), Decision Tree (DT), and Support Vector Machine (SVM) were examined. These models were used to categorise five principal LULC classes: water bodies, forests, urban regions, vegetation, and barren lands. Our findings indicated that Random Forest consistently yielded the highest classification accuracy, achieving an Overall Accuracy (OA) of 91.84% and a Kappa Coefficient (KC) of 0.86 in 2023, thereby affirming its efficacy for multi-temporal land use and land cover mapping. The Decision Tree exhibited competitive performance in 2010 (87.36% OA, a KC of 0.79) but showed diminished stability in later years. The SVM displayed middling performance, particularly excelling in the classification of urban areas (about 94%) but exhibiting reduced accuracy for forest regions. This analysis emphasises the efficacy of GEE and Python libraries in analysing large satellite imagery and the proficiency of DT and RF models in land use and land cover classification. The results can guide regional planning and land management policies, fostering sustainable development.

KEYWORDS: Land Use Land Cover, Google Earth Engine, Support Vector Machine, Decision Tree, Random Forest

CITATION: Laalaoui Y., El Assaoui N., Ouahine O. (2025). Comparative Analysis Of Machine Learning Algorithms For Land Use And Land Cover Mapping: Case Study Of Berrechid-Settat Region, Morocco. Geography, Environment, Sustainability, 4 (18), 158-170

https://doi.org/10.24057/2071-9388-2025-3980

ACKNOWLEDGEMENTS: The authors wish to express their sincere gratitude to Dr. Thanh Thi Nguyen from the University of Kassel, Germany, for her valuable guidance, constructive feedback, and insightful discussions, which significantly contributed to improving the quality of this study.

Conflict of interests: The authors reported no potential conflict of interests.

INTRODUCTION

The alteration of LULC has a significant influence on ecological components (Bhungeni et al. 2024; Z. Zhao et al. 2024). This provides essential ecosystem services that are advantageous to both society and biodiversity. These services include the supply of drinkable water, support for farming activities, recreational opportunities, and the conservation of natural habitats. However, human-induced changes in LULC pose a substantial risk to the preservation of natural land cover and freshwater resources in various countries, particularly in watershed areas. Examining alterations in the Earth's surface is crucial for understanding ecological and societal transformations (Peterson and Levinson 2020). Traditional approaches and aerial imagery for data collection are time-intensive and often lack sufficient accuracy. The latest analysis techniques for satellite images now allow for more efficient detection of changes in LULC (Li et al. 2019). In recent years, remote sensing imaging has been increasingly utilised to identify changes in LULC and vegetation. The abundance of historical data and remote sensing imagery has made it convenient to study the impact of human activities on LULC (Ali and Johnson 2022). Classifying LULC is essential for detecting changes, and the approaches and strategies used for classifying LULC and extracting precise data from remote sensing images are highly adaptable. Mapping and monitoring LULC changes are essential for gaining insight into the spatial distribution of human activities on land and their impact on the natural environment (Dong et al. 2019). This knowledge is crucial for water resource managers and environmental health practitioners to formulate efficient environmental strategies.

Management plans and regulations. Remote sensing techniques have largely replaced conventional field

observation methods for LULC mapping. They offer a cost-efficient and effective way to gather spatiotemporal data across large areas. Remote sensing data can be systematically recorded, stored, and shared, making it a valuable resource for studying different landscapes. Many studies have shown that machine learning methods are very effective at classifying LULC using remote sensing data (Andrew et al. 2023).

The extensive body of research on LULC dynamics in Morocco is primarily limited by the lack of a uniform spatiotemporal scale and a generalised methodology. Most of the existing literature on the topic is either localised or methodologically constrained or temporally disjointed. This is often combined with the use of conventional classification methods such as maximum likelihood or minimum distance. These limitations make it difficult to ensure reliability due to the possibility of misclassification and low transferability across sensors. Most studies did not combine multi-temporal Landsat datasets from both Landsat 7 and Landsat 8 with uniform preprocessing, spectral harmonisation, and atmospheric correction, especially in the Berrechid–Settat region. This region is characterised by high rates of urban expansion and agricultural intensification but is exposed to increased pressure on water and land resources. Most of these studies did not include a comparative assessment of machine-learning methods using the same training and validation datasets. They have almost focused on assessing a single model or did not report significant statistical differences in accuracy metrics, which include Overall Accuracy, Producer's Accuracy, User's Accuracy, and Kappa. Finally, all regional studies demonstrated a lack of data due to the absence of efficient GEE-based computing for extensive, cloud-based analysis and standard temporal mosaicking. Consequently, this study tried to respond to this lack by (i) combining imageries from Landsat 7 ETM+ and Landsat 8 OLI within the same GEE workflow; (ii) rigorously comparing three robust classifiers, SVM, RF and DT, implemented under the same conditions; and (iii) investigating land use and land cover transitions for two decades, i.e., between 2010 and 2023, in a key agro-industrial corridor in Morocco. Thus, the approach presents not only the most up-to-date and consistently mapped landscape of Berrechid–Settat but also an adaptable methodology for studying other semi-arid regions grappling with similar environmental challenges and urban sprawl (Chomani and Pshdari 2024a).

The primary goal of our study is to categorise changes in LULC and assess the effectiveness of three machine learning algorithms. The classification process involved five LULC categories: vegetation, built-up areas, forests, barren land, and water bodies. The efficacy of these models was evaluated using accuracy metrics such as Overall Accuracy (OA), User's Accuracy (UA), Producer's Accuracy (PA), and Kappa Coefficient (KC). Our findings indicate that the DT model performed better in 2010, achieving an overall accuracy of 87.36% and a Kappa coefficient of 0.79, highlighting a strong agreement between the reference and classified data. By 2015, the RF model had emerged as the top performer with an overall accuracy of 88.74% and a Kappa coefficient of 0.81, while DT continued to perform strongly. In 2023, RF remained the best-performing model, with an OA of 91.84% and a KC of 0.86, underscoring its robustness in classifying LULC changes over time. The objective of this study is to enhance the existing knowledge on LULC classification and offer valuable insights for environmental management and policy development in the Berrechid-Settat area. Furthermore, it showcases the efficacy of GEE in efficiently obtaining and manipulating vast quantities of satellite imagery data, providing vital insights for land planning and management in the region, fostering sustainable development (Achahboun et al. 2023; Laalaoui et al. 2024; Sellami and Rhinane 2023).

MATERIALS AND METHODS

Study area

The Berrechid Settat area, situated in the Casablanca-Settat region of Morocco (Figure 1), has been chosen as the study location due to its diverse landscape (El Assaoui 2023; Elgendy and Abdelatif 2021). Berrechid Settat lies between the Casablanca region to the north and the Marrakech-Safi region to the south (Bouzekraoui et al. 2020).

The area is situated between longitudes 7° 43′ 48′ W and 7° 10′ 48′ W,
and the latitudes of 32° 57′ 36′ N and 33° 25′ 12′ N. The total land area measures 2062 square kilometres. It has varied topography, including agricultural plains, urbanised regions, and forests (Koukal et al. 2020).

The Berrechid Settat region is mainly known for its large agricultural areas, where a considerable amount of land is used for growing crops. It also includes forested areas with different amounts of tree cover, from dense forests to lighter woodlands. The area is experiencing significant urban expansion, with much development taking place in the areas on the outskirts of cities (El Assaoui Fouad Amraoui and El Mansouri 2015; Laalaoui et al. 2024).

Dataset

In this work, we employed Landsat satellite images, specifically utilising Landsat 7 for the year 2010 and Landsat 8 OLI for the years 2015 and 2023.

The Landsat satellites provide multispectral imagery with various resolutions (Pickens et al. 2020). For our analysis, we used the blue, green, red, near-infrared (NIR), and short-wave infrared (SWIR) bands (D. Chen et al. 2018). Additionally, several spectral indices were computed to improve classification accuracy.

All Landsat imagery was preprocessed in Google Earth Engine to ensure radiometric and temporal uniformity for the years 2010, 2015, and 2023. Specifically, for Landsat 8 OLI (2015, 2023) and Landsat 7 ETM+ (2010), we used the Collection 2 Surface Reflectance (SR) tier 1 products. Atmospheric correction was applied using LaSRC for Landsat 8 and LEDAPS for Landsat 7. Furthermore, masks were utilised to remove clouds, cloud shadows, dilated clouds, cirrus, and snow, based on the QA_PIXEL bitmask, and saturated pixels according to QA_RADSAT, retaining only clear observations. Additionally, the optical reflectance bands were adjusted using the Collection-2 SR scale and offset. Subsequently, these corrected images were clipped to the relevant year (from 1 January to 31 December) and Area of Interest (AOI). Composites were built using the median to generate a cloud-free image for this period, reducing residual cloud cover and avoiding Landsat-7 SLC-off striping artefacts. This cloud-free imagery dataset is spectrally consistent between Landsat sensors and across dates, serving as the input for LULC. Table 1 summarises the data, including the imagery acquisition and bands used (Achahboun et al. 2023; Bhungeni et al. 2024; Wachowska et al. 2018).

For each year, a composite image was generated by processing the entire Landsat dataset. Using Google Earth Engine (GEE), the median value for each pixel over the selected time period was computed. The code defines the Area of Interest (AOI) and retrieves Landsat image

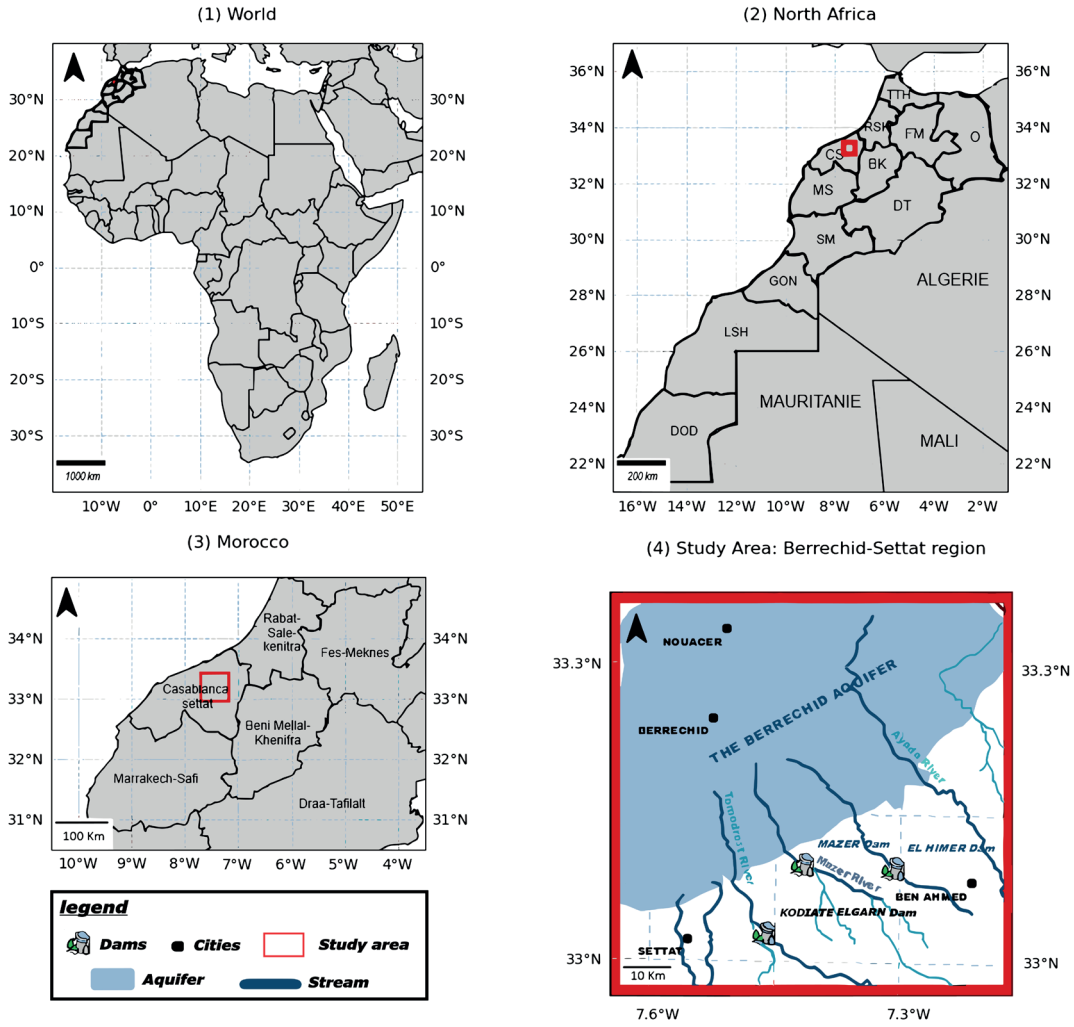

Fig. 1. The location of the study area (Berrechid-Settat area) Casablanca-Settat region

Table 1. Summary of imagery acquisition parameters for LULC classification in the Berrechid–Settat region

Year	Satellite / Sensor	Product Type	Collection	Acquisition Period	Spatial Resolution (m)	Processing Level	Nbr of Bands Used	Remarks
2010	Landsat 7 ETM+	Surface Reflectance (SR)	Collection 2 Tier 1	Jan 1 – Dec 31, 2010	30 m	LEDAPS atmospheric correction	6 spectral bands (B1–B5, B7)	used for LULC baseline classification
2015	Landsat 8 OLI	Surface Reflectance (SR)	Collection 2 Tier 1	Jan 1 – Dec 31, 2015	30 m	LaSRC atmospheric correction	6 spectral bands (B2–B7)	provides mid-decade LULC update
2023	Landsat 8 OLI	Surface Reflectance (SR)	Collection 2 Tier 1	Jan 1 – Dec 31, 2023	30 m	LaSRC atmospheric correction	6 spectral bands (B2–B7)	represents the most recent LULC status

collections for the specified years. Filters are applied to match the AOI and relevant dates, and the appropriate bands are selected for analysis. The composite images are created by calculating the median pixel value for each year and clipping the result to the AOI. These images are then displayed on the map using GEE's visualisation tools (Sellami and Rhinane 2023; Z. Zhao et al. 2024).

In the classification process, to promote class separability, multiple spectral indices were derived from the ATM-corrected Landsat datasets. Each index was selected to highlight a specific surface characteristic relevant to the land use and land cover (LULC) patterns of the Berrechid–Settat area. The Normalised Difference Vegetation Index (NDVI) was applied to highlight vegetated areas. Near-infrared (NIR) represents band 4 of LANDSAT 7 (L7) and band 5 of LANDSAT 8 (L8), while Red denotes band 3 from L7 and band 4 from L8. The Normalised Difference Built-up Index (NDBI) was used to identify urban and impervious patch areas by contrasting short-wave infrared and near-infrared bands B5 and B4 for L7, and B5 and B6 for L8. Water bodies were enhanced using the Normalised Difference Water Index (NDWI), which incorporates the green band B2 for L7 and B3 for L8, and the near-infrared band B4 for L7 and B5 for L8. The Bare Soil Index (BSI) (equation 4) was computed to determine bare and sparsely vegetated areas by integrating reflectance information from the blue, red, NIR, and SWIR spectral bands B1, B3, B4, B5 from L7, and B2, B4, B5, B6 for L8 (Harfouche et al. 2020). All indices were computed within the GEE environment and included as additional predictor layers to the reflectance composites, thus increasing the spectral feature space used by the machine-learning algorithms SVM, RF, and DT for land use and land cover classification (Aydin and Sefercik 2025; Dong et al. 2019; Harfouche et al. 2020).

The processed composite images were subsequently used for further analysis and classification with machine learning models (Du et al. 2018; Lee et al. 2017). This allowed for the detection of changes in land use and land cover (LULC) within the Berrechid-Settat area across the selected years.

After choosing the set of Landsat 7 images for the year 2010, as well as Landsat 8 OLI images for the years 2015 and 2023, the selected images underwent a cloud-masking process to guarantee the clarity and accuracy of the data. Subsequently, five datasets were created, comprising the blue (B2), green (B3), red (B4), near-infrared (B5), and short-wave infrared (B6) bands (J. Chen et al. 2017). In order to train and validate our data, sampling and validation were used. Independent reference data were collected using a stratified random design with a minimum of approximately 60 points per class (total n = 300) interpreted from high-resolution imagery and local knowledge. Validation points were withheld from training and enforced a ≥300 m buffer from training AOIs to limit spatial autocorrelation. These points were distributed proportionally to mapped class area (Belgiu and Drăguț, 2016). Accuracy was quantified using confusion matrices to derive OA, PA, UA, and Kappa, with 95% confidence intervals computed via bootstrap under a stratified estimator. This sample size provides stable per-class estimates for the five LULC categories: Vegetation, Built-up, Forest, Bareland, and Water Body.

The models were then examined by integrating the outcomes with testing data via accuracy assessments (Amin et al. 2024). Ultimately, the LULC maps were generated for the years 2010, 2015, and 2023. Figure 2 illustrates the Google Earth Engine (GEE) platform (Harfouche et al. 2020).

Classification Methods

To conduct a pixel-based supervised classification, a distinct collection of training samples was acquired for each year (2010, 2015, and 2023) (Conrad et al. 2020). The assignment of each training sample pixel to a LULC class was determined using additional data sources, such as high-resolution photography and pre-existing LULC maps. The categorisation was executed with Support Vector Machine (SVM), Random Forest (RF), and Decision Tree (DT) classifiers within the Google Earth Engine platform (El Assaoui et al. 2023; Kamusoko and Gamba 2016).

The three selected algorithms have been chosen for their reliable performance and complementary strengths in remote sensing. The SVM classifier is particularly recognised for its resilience to high-dimensional spectral data and few training samples, making it appropriate for a heterogeneous environment. The RF has ensured liability against overfitting and offers excellent performance on multi-class tasks through ensemble learning. The DT,

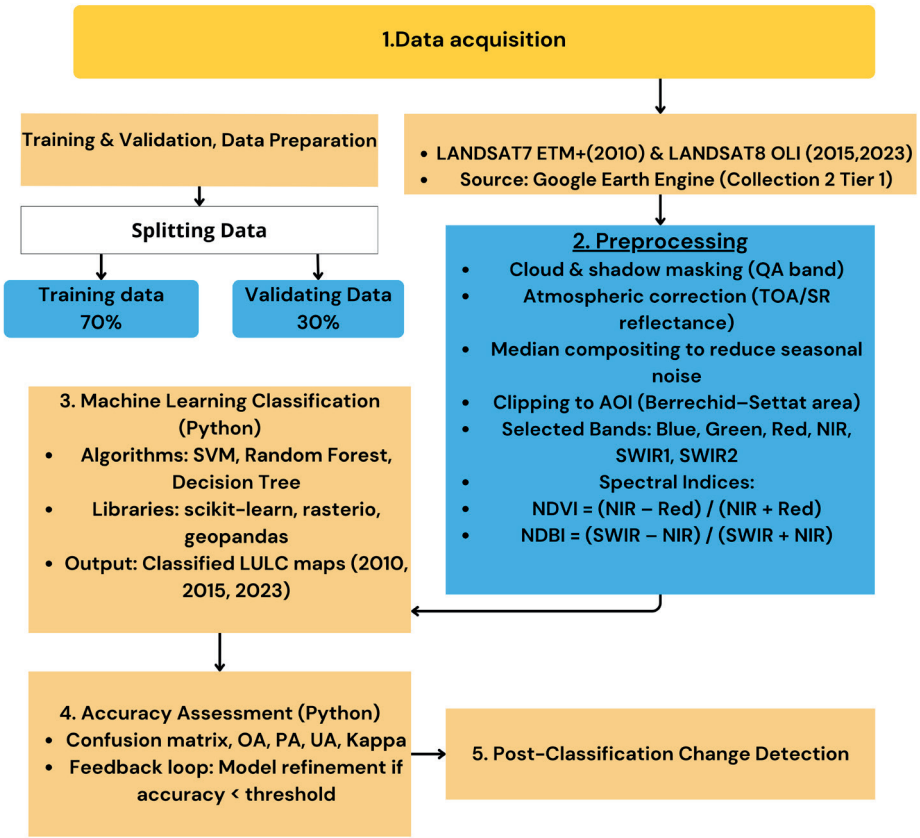

Fig. 2. A conceptual flowchart illustrating the methodology

Table 2. Name and Description of LULC Classes Scheme

ID	Class	Description
1	Vegetation	Agricultural land, grasslands, shrubs, and other types of vegetation cover.
2	Built-up	Residential, commercial, and industrial areas; roads; transportation networks; and urban infrastructure.
3	Forest	Dense forests, mixed forests, and open forests.
4	Barren lands	Sandy areas, rocky areas, barren land, and areas with minimal or no vegetation.
5	Water Bodies	Lakes, reservoirs, rivers, and other water features.

while the most straightforward method, does not suffer from the black box problem and is computationally accelerated. Therefore, it provides a perfect error metric with more complicated ensemble and kernel methods, offering interpretability and computational efficiency. Their combination enables a comprehensive evaluation of classification performance under differing algorithmic assumptions (Chomani and Pshdari 2024b; Feng et al. 2015).

The three classifiers used in this study for LULC categorisation are detailed below:

A Support Vector Machine (SVM) is a type of supervised learning algorithm used for both regression and classification. During the training phase, SVM classifiers construct an optimal hyperplane that effectively divides classes by minimising the misclassification of pixels from input datasets. Crucial factors for Support Vector Machines (SVM) include kernel functions, cost parameters, and gamma (Audebert et al. 2018).

Random Forest (RF) is an ensemble classifier that builds multiple decision trees using random subsets of the training data and attributes. The key input parameters for RF are the size of the training dataset and the number of trees created. In this study, 300 trees were used to improve the accuracy and performance of the classification.

A Decision Tree (DT) is a classification system that uses specified thresholds to make decisions. It splits nodes until it reaches terminal nodes. This approach involves grouping input data into distinct sets and then generating trees for the purpose of classification (Akar and Gormus 2021).

Data Processing

The LULC maps were produced entirely using Python-based workflows. Raster and vector datasets were imported and processed using libraries such as rasterio (v1.3.8), geopandas (v0.14.3), and numpy (v1.26.4). These tools facilitated image stacking, band alignment, and clipping of imagery to the Berrechid–Settat study area, preparing the data for classification. Only essential preprocessing tasks, such as cloud masking to remove pixels affected by cloud cover, were performed in Google Earth Engine (GEE). We used temporal aggregation methods, such as mean and median calculations, to fill in gaps left by cloud interference (Carlson et al. 2018; Wu 2020).

The LULC maps were produced entirely using Python-based workflows (He et al. 2020). High-resolution orthophoto images and pre-existing LULC maps were used to collect training and validation samples. These samples were saved as shapefiles and then imported into the Python environment to train the classifiers. The LULC classification in this study included five primary categories: forest, built-up land, barren land, bodies of water, and vegetation (Sharnagat et al. 2025).

Data normalisation, model training

For randomness in stratified sampling without attrition, maintaining the proportional representation of all LULC classes in both subsets was crucial for class balance. To reduce spatial autocorrelation and avoid overfitting, training and validation points were dispersed geographically within the AOI. A suitable minimum distance was also implemented between samples of the same class (Riche et al. 2024). This methodology enhanced the independence of the test data, which facilitated the model's generalisation. The samples were divided using the same ratios. Before training the model, min-max normalisation was applied to the spectral bands and resulting indices. This brought all features to a uniform scale of 0–1. This was achieved using the StandardScaler and MinMaxScaler functions from the scikit-learn.preprocessing package (v1.4.2) (Saqr et al. 2025). This standardisation helped to lessen the variations in range across the reflectance of different bands. It assisted the algorithms in maintaining numerical stability, particularly in distance-based models such as SVM and RF. This normalisation ensured that each feature contributed equally to classification, thereby improving the performance of all considered models through convergence.

After preparing the training and testing data, the models were run with default settings. First, supervised classification was implemented using the Scikit-learn library (v1.4.2). Parameters were specified for the SVM model, such as the kernel type (e.g., 'rbf'). After initialising the model, the 'fit()' function was used to train it on the training data. Predictions were then evaluated using the test data (Phan et al. 2020). The accuracy score function from Scikit-learn assesses the model's accuracy for the predictions. The datasets used in this study were generated through stratified random sampling, with 70% allocated for training and 30% for validation et al. 2020). The accuracy score function from Scikit-learn assesses the model's accuracy for the predictions. The datasets used in this study were generated through stratified random sampling, with 70% allocated for training and 30% for validation (Chomani and Pshdari 2024b; Lu et al. 2021).

Accuracy Assessment

Evaluation of classification accuracy was conducted by measuring overall accuracy (OA) and the Kappa coefficient (K), producer's accuracy (PA), and user's accuracy (UA). Their formulas are detailed below in equations 1, 2, 3, and 4 (Kobayashi et al. 2022). These metrics assess the quality of classification by quantifying the accuracy of the test data and the agreement between classified and reference data. Their calculations were performed using scikit-learn. metrics (V1.4.2), with functions such as confusion_matrix, classification_report, and cohen_kappa_score. Results were displayed and interpreted using matplotlib (V3.8.4) combined with seaborn (V0.13.2) for graphical display, statistics, and confusion matrices (Figure 5).

$$OA = \frac{Total\ Correctly\ Classified\ Pixels}{Total\ Sample\ Pixels} \times 100 \quad (1)$$

$$KC = \frac{Observed\ Accuracy - Change\ agreement}{1 - Chance\ Agreement} \quad (2)$$

$$PA = \frac{NO\ of\ correctly\ classified\ samples\ in\ a\ class}{Total\ No\ of\ referense\ samples\ in\ that\ class\ (column\ total)} \times 100 \quad (3)$$

$$UA = \frac{NO\ of\ correctly\ Classified\ Pixels\ in\ a\ class}{Total\ No\ of\ referense\ samples\ in\ that\ class\ (row\ total)} \times 100 \quad (4)$$

Where:

- Observed accuracy = Overall Accuracy (OA);
- Chance agreement is the proportion of agreement that could occur randomly based on the totals in the confusion matrix.

Kappa values range between 0 and 1, where:

- > 0.80 = strong agreement,
- 0.40–0.80 = moderate agreement,
- < 0.40 = weak agreement.

Predicting and Exporting Data

The final step involved using the trained models to generate predictions and exporting the results as GeoTIFF files (Dong et al. 2019). While various tools such as GDAL or GeoPandas/Geocube are available, they are not well-suited for large-scale geographic operations (Drusch et al. 2017). An efficient approach using the rasterio library is presented below (Gerber et al. 2018).

First, the original input image is retrieved, and metadata attributes such as height, width, and CRS are extracted. The input image is then preprocessed to align with the data used during model training. If additional features like NDVI or elevation were included during training, they must be combined with the input image before proceeding. This process ensures scalability for generating predictions over large geographic areas (Jiang et al. 2021). The results are saved in GeoTIFF format for further analysis.

Once the model training and validation were complete, each machine learning classifier was applied to the entire Landsat imagery to predict the LULC category for each year of the study: 2010, 2015, and 2023. The prediction process was then performed using the 'predict()' function from the scikit-learn library (v1.4.2), which resulted in pixel-wise classification outcomes. Finally, the resulting arrays were restructured and converted to raster formats using rasterio (v1.3.8) to ensure the geospatial conformity of the final outputs with the imagery. The classified rasters were then exported as GeoTIFF files for further processing and map production (Peterson and Levinson 2020). High-quality theme map production and post-processing were carried out using matplotlib (v3.8.4), geopandas (v0.14.3), and rasterio.plot modules. A unique colour scheme was assigned to each land category, including vegetation, urban, forest, barren land, and water body (Gerber et al. 2018; Wu 2020). Additional map elements, such as the title, legend, north arrow, and scale bar, were included to improve map interpretation. All the final maps were exported at a resolution of 600 dpi, which is suitable for publishing and scientific sharing. This process helped to create accurate geo-referenced outputs that showed the precise spatial distribution and temporal changes of LULC in the area of interest (Sharnagat et al. 2025; Q. Zhao et al. 2021).

RESULTS AND DISCUSSION

Mapping the Spatial Distribution of LULC Classes

Fig. 3 shows the LULC classification maps produced by three machine learning algorithms: SVM, RF, and DT, over the 13 years of the study. For each classifier, these colour-coded images display the spatial distribution pattern of five LULC classes: vegetation, built-up, forest, bareland, and water body. SVM's classification exhibits much smoother and more homogeneous class boundaries, whereas RF and DT show local heterogeneity. In contrast, the green colour representing bareland varies more across the years, indicating the classifiers' sensitivity to spectral variation. These multi-model maps offer a suitable platform for visual comparison of spatial patterns and temporal dynamics, which highlighted the observation of continuous urban expansion and a slight reduction in vegetation cover between 2010 and 2023.

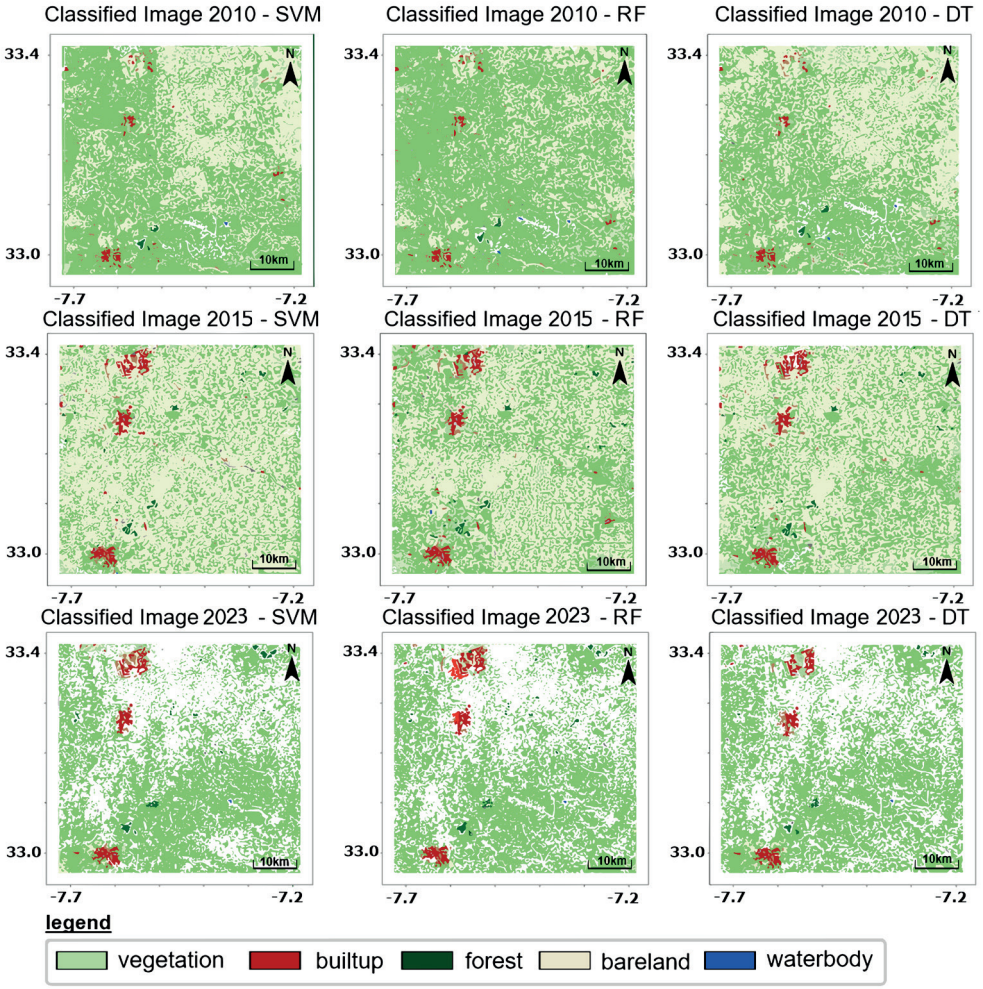

Fig. 3. LULC classification maps of the AOI for 2010, 2015, and 2023 generated using Support Vector Machine (SVM), Random Forest (RF), and Decision Tree (DT) classifiers

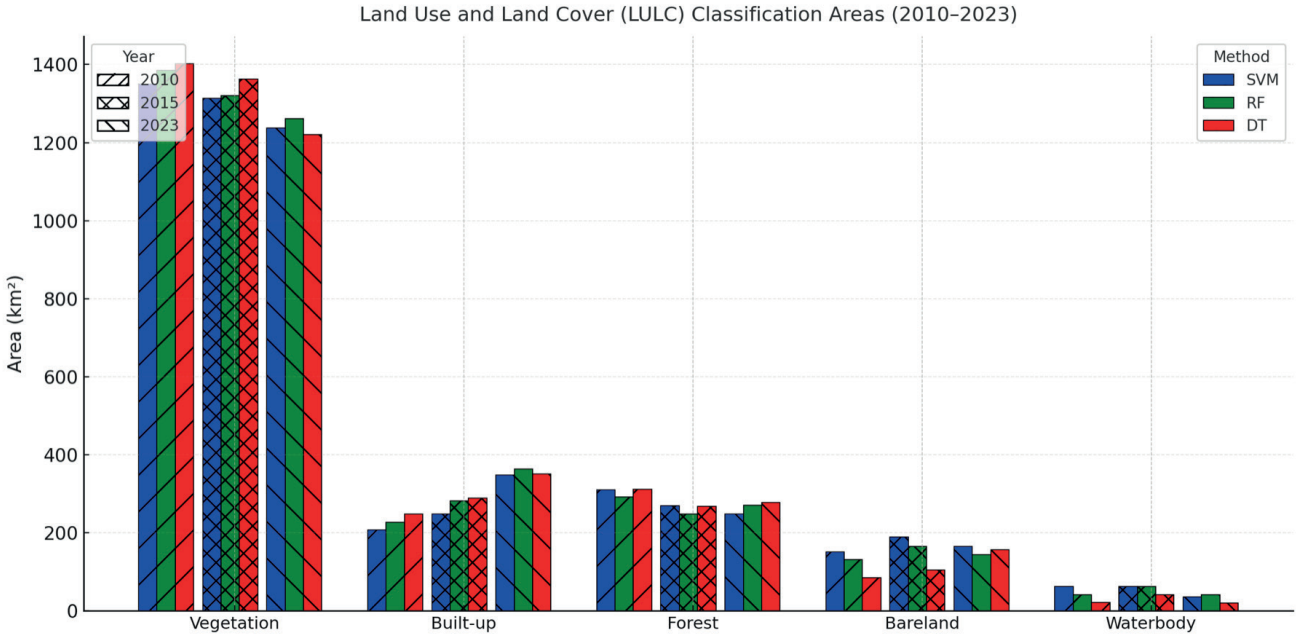

Fig. 4. Comparison of LULC class areas (in km^2) in the AOI for 2010, 2015, and 2023, derived from Support Vector Machine (SVM), Random Forest (RF), and Decision Tree (DT) classifiers. The bar chart highlights differences between models and changes over time across five major LULC categories: vegetation, built-up, forest, bareland, and water body

The classified area distributions, as shown in Figure 4 and Table 3, reveal distinct temporal shifts and model-based fluctuations in the AOI over 13 years of the study. Vegetation, covering approximately 1200 to 1400 km^2 across all classifiers, continues to dominate this class. However, it decreased slightly by 2023, while built-up areas increased from about 200 km^2 in 2010 to over 300 km^2 in 2023. This data aligns well with the area's ongoing urban expansion and agricultural land modification (Du et al. 2018). The forest class maintained intermediate values between 250–350 km^2 with little temporal change across models and years. Bareland, however, showed a gradual reduction from 150–200 km^2 to less than 100 km^2 in 2023. Water bodies represented the smallest fraction, less than 70 km^2, with a barely noticeable reduction over time (Carrara et al. 2024; Congalton and Green 2019). DT classifiers produced slightly higher vegetation estimates in 2010 compared to other classifiers. RF outputs were more balanced and consistent in the following years, particularly for built-up and bareland classes. The SVM model performed between these two methods, yielding slightly lower vegetation and higher built-up estimates due to its effectiveness in distinguishing mixed spectral signatures (Ali and Johnson 2022). Generally, the three algorithms reported similar temporal trends, which increases confidence in our classification methodology. RF is, however, the most suitable method for multi-temporal LULC mapping in this region because of its stable intra-class ratio and consistent spatial predictions (Meghraoui et al. 2024).

Evaluation of the Mapping Precision of Machine Learning Algorithms

Each model operated on a confusion matrix derived from 30% of the entire figure 5. A confusion matrix is a statistical construct that illustrates the correlation between the actual class (ground truth) and the predicted or generated map (Nicolau et al. 2023). The confusion matrices derive overall accuracy (OA), Kappa coefficient, user's accuracy (UA), and producer's accuracy (PA) by land use/land cover type (Belgiu and Csillik 2018). Therefore, the confusion matrices yield the following OA and Kappa coefficients for the classification trees. The SVM confusion matrix shows an OA of 91.7% and a Kappa coefficient of 0.810. The RF confusion matrix shows an OA of 91.84% and a Kappa of 0.86. The DT confusion matrix shows an OA of 91.16% and a Kappa of 0.68. A Kappa of 0.845 was recorded for 2023. Table 4 and Figure 5 show the overall model performance over the years and classifications. However, the RF model had the highest overall OA and Kappa from all datasets. The classes performed across the models. The built-up land use class was achieved in all models with UA and PA exceeding 97% for 2023 RF. SVM and DT also had UA and PA exceeding 89%. On the other hand, the forest class performed less well with SVM, showing a PA as low as 75.2% in 2023 (Wang et al. 2018). Similarly, the numerical classifications for bare land and waterbody. The only inconsistency is the 81% PA for forest classification in 2020, which is still a decent score but 6% lower than the DT for forest classification accuracy. Where the forest category was not accurately represented was in built-up areas. This is similar to how the forest was perfectly classified in 2020 across all three models. However, all three models struggled with this over the years, with SVM again showing the highest omission errors (El Assaoui et al. 2015; J. Jiang et al. 2025). This resembles a replica of a city covered up by what should have been classified as non-built-up pixel values. Where SVM struggled, the RF model excelled, achieving the best classification for built-up in 2023 at 88.4%. The lowered classification accuracy for some classes in 2023 means that for bareland and waterbody classes, DT's PA values were lower than RF and SVM. However, it still achieved fairly good accuracy for built-up and vegetation classes (Congalton and Green 2019).

CONCLUSION

The study has illustrated the effectiveness of various machine learning algorithms, including SVM, RF, and DT, in categorising land use and land cover (LULC) changes in the Berrechid Settat region for the years 2010, 2015, and 2023 (El Assaoui et al. 2021; Kussul et al. 2017). A comprehensive assessment of accuracy measurements, such as Overall Accuracy (OA), Kappa Coefficient, User's Accuracy (UA), and Producer's Accuracy (PA), shows that each approach has distinct advantages and disadvantages when used for different LULC classes.

Table 3. LULC Classification Areas and Percentages (2010, 2015, 2023)

Class	2010 - SVM		2010 - RF		2010 - DT	
	Area (km^2)	(%)	Area (km^2)	(%)	Area (km^2)	(%)
Vegetation	1350.20	65.48	1385.25	67.18	1402.57	68.02
Builtup	207.23	10.05	226.92	11.01	247.65	12.01
Forest	309.63	15.02	292.18	14.17	310.95	15.08
Bareland	151.56	7.35	131.14	6.36	84.34	4.09
Waterbody	61.88	3.00	41.45	2.01	21.65	1.05
Class	2015 - SVM		2015 - RF		2015 - DT	
	Area (km^2)	(%)	Area (km^2)	(%)	Area (km^2)	(%)
Vegetation	1312.67	63.66	1319.70	64.00	1362.16	66.06
Builtup	248.68	12.06	281.46	13.65	288.76	14.00
Forest	268.88	13.04	247.85	12.02	268.22	13.00
Bareland	188.67	9.15	165.58	8.03	104.34	5.06
Waterbody	62.27	3.02	61.88	3.00	41.28	2.00
Class	2023 - SVM		2023 - RF		2023 - DT	
	Area (km^2)	(%)	Area (km^2)	(%)	Area (km^2)	(%)
Vegetation	1237.51	60.01	1261.53	61.18	1220.50	59.19
Builtup	348.48	16.93	363.94	17.65	351.37	16.55
Forest	247.85	12.02	270.43	13.11	278.12	13.12
Bareland	165.62	8.03	144.52	7.01	156.35	7.38
Waterbody	35.04	1.71	41.34	2.00	20.74	1.01

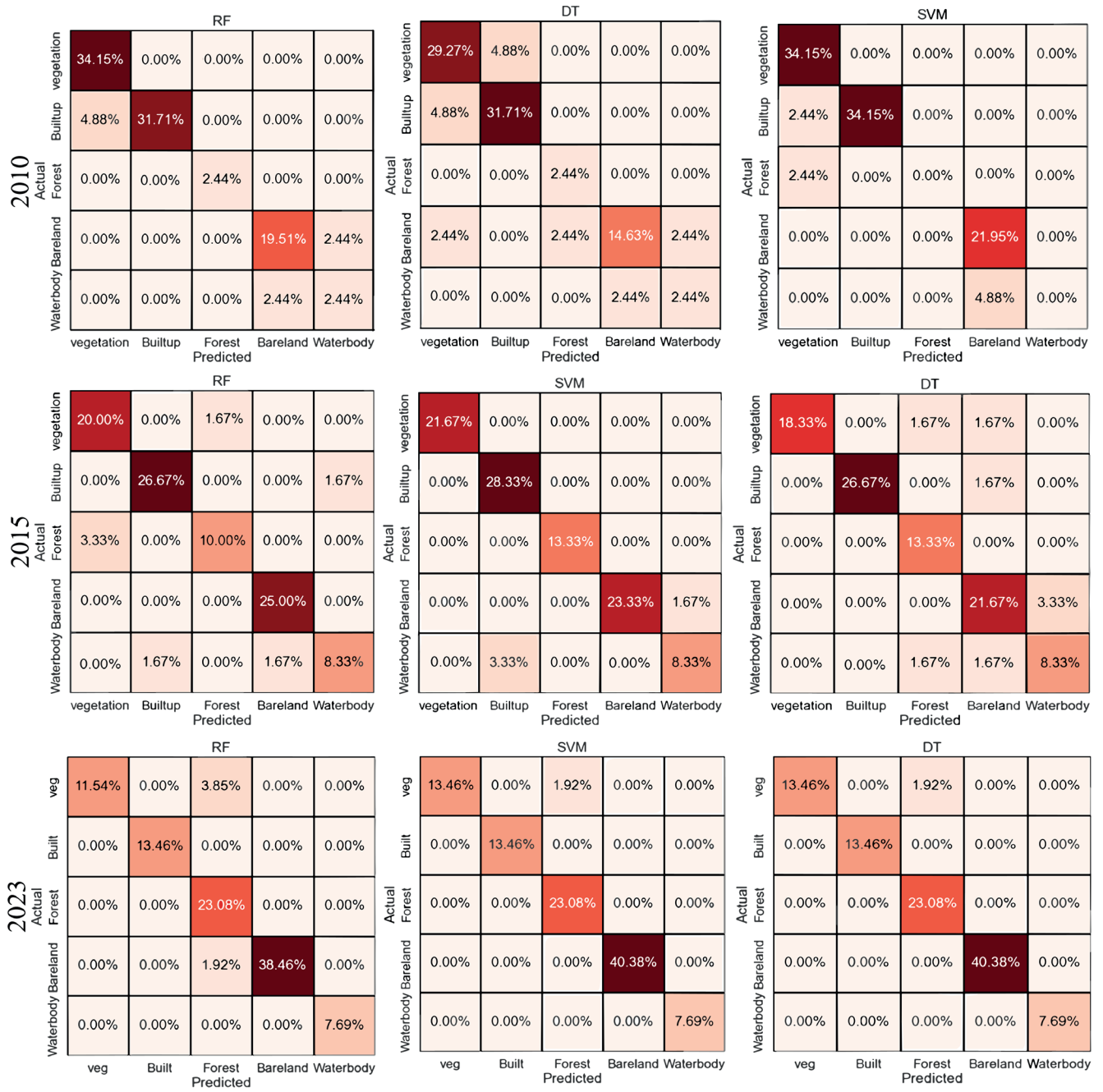

Fig. 5. Confusion matrices for 2010, 2015, and 2023

Table 4. Classification Accuracy Metrics (2010, 2015, 2023)

Year	Classifier	LULC Class	UA (%)	CE (%)	PA (%)	OE (%)	OA & KC
2010	SVM	Vegetation	90.42	9.58	84.85	15.15	84.19% and 0.766
		Builtup	94.20	5.80	90.05	9.95	
		Forest	81.81	18.19	79.05	20.95	
		Bareland	66.10	33.90	69.65	30.35	
		Waterbody	0.00	100.00	0.00	100.00	
	RF	Vegetation	89.20	10.80	83.10	16.90	82.26% and 0.736
		Builtup	94.00	6.00	90.95	9.05	
		Forest	100.00	0.00	100.00	0.00	
		Bareland	94.90	5.10	91.45	8.55	
		Waterbody	94.70	5.30	90.95	9.05	
	DT	Vegetation	90.00	10.00	88.05	11.95	87.36% and 0.794
		Builtup	94.20	5.80	90.95	9.05	
		Forest	100.00	0.00	100.00	0.00	
		Bareland	94.50	5.50	91.35	8.65	
		Waterbody	93.20	6.80	90.75	9.25	
2015	SVM	Vegetation	91.22	8.78	90.45	9.55	85.39% and 0.768
		Builtup	95.00	5.00	95.65	4.35	
		Forest	82.61	17.39	84.65	15.35	
		Bareland	66.90	33.10	75.25	24.75	
		Waterbody	83.30	16.70	71.44	28.56	
	RF	Vegetation	90.00	10.00	88.70	11.30	88.74% and 0.811
		Builtup	94.80	5.20	96.55	3.45	
		Forest	86.69	14.31	75.02	24.98	
		Bareland	95.70	4.30	97.05	2.95	
		Waterbody	95.50	4.50	96.55	3.45	
	DT	Vegetation	90.80	9.20	93.65	6.35	88.16% and 0.799
		Builtup	95.00	5.00	96.55	3.45	
		Forest	79.96	20.04	100.00	0.00	
		Bareland	95.30	4.70	96.95	3.05	
		Waterbody	94.00	6.00	96.35	3.65	

2023	SVM	Vegetation	94.32	5.68	91.70	8.24	88.49% and 0.810
		Builtup	98.10	1.85	96.90	3.09	
		Forest	85.71	14.28	85.90	17.60	
		Bareland	70.00	29.90	76.5	23.41	
		Waterbody	100.00	0.00	100.00	0.00	
	RF	Vegetation	93.10	6.82	89.95	10.05	91.84% and 0.857
		Builtup	97.90	2.04	97.80	2.14	
		Forest	70,80	29,60	75,20	24,76	
		Bareland	98,80	1,18	98,30	1,70	
		Waterbody	98,60	1,33	97,80	2,18	
	DT	Vegetation	93.90	6.10	94.90	5.10	91.16% and 0.845
		Builtup	98.10	1.90	97.80	2.18	
		Forest	68.30	31.60	81.70	18.21	
		Bareland	98.40	1.52	98.20	1.75	
		Waterbody	97.10	2.84	97.60	2.32	

Random Forest (RF) consistently achieved the highest accuracy throughout all years, particularly excelling in the classification of built-up, water body, and barren lands categories (Fentaw and Abegaz 2024), attaining elevated user's accuracy (UA) and producer's accuracy (PA) values. This indicates that RF is an effective model for land use and land cover (LULC) mapping, especially in intricate systems characterised by significant spatial variability. Conversely, the Support Vector Machine (SVM) exhibited commendable performance. Nevertheless, it faced difficulties in distinguishing certain classes, such as forest and bare ground (Baatz et al. 2025), resulting in more omission errors for these categories. The Decision Tree (DT) displayed similar accuracy across many classes but showed a slight decrease in performance, especially for smaller or more heterogeneous categories such as water body and barren land.

A notable discovery is that all models successfully distinguished the built-up class, which is essential for tracking urban expansion and land development in swiftly urbanising areas such as Berrechid-Settat. The forest class presented the most significant obstacle among all models, highlighting the necessity for enhanced spectral feature selection or the integration of supplementary data to improve forest classification accuracy (Andrew et al. 2023; Drusch et al. 2017).

In summary, RF has demonstrated the highest reliability for LULC classification in this area, especially for classes with distinct spectral signatures, such as built-up areas and aquatic bodies (Dharumarajan and Hegde, 2022). SVM and DT offered significant insights, particularly regarding processing efficiency and the management of intricate decision boundaries. This study highlights the importance of model selection in remote sensing applications and provides a foundation for future research focused on improving LULC classification accuracy through more sophisticated hybrid models or by including other data sources such as topography and climate factors (Alshari and Gawali 2021; Amazirh et al. 2024; El Assaoui et al. 2023).

This analysis offers a thorough understanding of LULC dynamics in the region, providing significant insights for land management, urban planning, and environmental monitoring.

Our functional framework for land monitoring could be useful in regional urban planning and water management initiatives. However, the classification accuracy could be improved by using Sentinel-2 imagery or higher-resolution data, or by incorporating an object-based approach to the research. Furthermore, future research should focus on including socio-economic and hydro-climatic variables to better explain the drivers of LULC changes.

REFERENCES

Achahboun C., Chikhaoui M., Naimi M. and Bellafkih M. (2023). Crops Classification Using Machine Learning And Google Earth Engine. Proceedings - SITA 2023: 2023 14th International Conference on Intelligent Systems: Theories and Applications. DOI: 10.1109/SITA60746.2023.10373760

Akar O. and Gormus K.S. (2021). Land Use and Land Cover Classification Using Machine Learning and Deep Learning Algorithms. Environmental Monitoring and Assessment, 193(2), 59. DOI: 10.1007/s10661-021-08853-y

Ali K. and Johnson B.A. (2022). Land-use and land-cover classification in semi-arid areas from medium-resolution remote-sensing imagery: A deep learning approach. Sensors, 22(22), 8750.

Alshari E.A. and Gawali B.W. (2021). Development of classification system for LULC using remote sensing and GIS. Global Transitions Proceedings, 2(1), 8–17.

Amazirh A., Ouassanouan Y., Bouimouass H., Baba M.W., Bouras E.H., Rafik A., Benkirane M., Hajhouji Y., Ablila Y. and Chehbouni A. (2024). Remote Sensing-Based Multiscale Analysis of Total and Groundwater Storage Dynamics over Semi-Arid North African Basins. Remote Sensing, 16(19). DOI: 10.3390/rs16193698

Amin G., Imtiaz I., Haroon E., Saqib N.U., Shahzad M.I. and Nazeer M. (2024). Assessment of Machine Learning Algorithms for Land Cover Classification in a Complex Mountainous Landscape. Journal of Geovisualization and Spatial Analysis, 8(2), 34. DOI: 10.1007/s41651-024-00195-z

Andrew O., Apan A., Paudyal D.R. and Perera K. (2023). Convolutional Neural Network-Based Deep Learning Approach for Automatic Flood Mapping Using NovaSAR-1 and Sentinel-1 Data. ISPRS International Journal of Geo-Information, 12(5). DOI: 10.3390/ijgi12050194

Assaoui N.E. (2023). Use of Remote Sensing and GIS to Study the Evolution of Irrigated Areas and Their Impact on Groundwater in a Semi-Arid Region (Morocco). In: Z. A. Ergüler, R. Hadji, H. I. Chaminé, J. Rodrigo-Comino, A. Kallel, B. Merkel, M. Eshagh, H. Chenchouni, S. Grab, M. Karakus, S. Khomsi, J. Knight, M. Bezzeghoud, M. Barbieri, S. Panda, A. C. Benim, and H. El-Askary eds., Selected Studies in Geotechnics, Geo-informatics and Remote Sensing , 75–79. Springer Nature Switzerland.

Assaoui N.E., Sadok A. and Charafi M. (2021). Analysis of a water supply intake from a silted dam using two-dimensional horizontal numerical modeling: Case of Mechraa Hammadi dam (Morocco). Materials Today: Proceedings, 45, 7718–7724. DOI: https://doi.org/10.1016/j.matpr.2021.03.337

Audebert N., Le Saux B. and Lefèvre S. (2018). Deep learning for classification of hyperspectral data: A comparative review. Remote Sensing, 10(2), 157. DOI: 10.3390/rs10020157

Aydin I. and Sefercik U.G. (2025). Multispectral UAV-based LULC mapping performance improvement by integrating precise NDSM data and machine learning algorithms. Earth Science Informatics, 18(2). DOI: 10.1007/s12145-025-01841-w

Baatz R., Ghazaryan G., Hagenlocher M., Nendel C., Toreti A. and Rezaei E.E. (2025). Drought research priorities, trends, and geographic patterns. Hydrology and Earth System Sciences, 29(5), 1379–1393. DOI: 10.5194/hess-29-1379-2025

Belgiu M. and Csillik O. (2018). Comparison of random forest and support vector machine classifiers for large area land cover mapping. Remote Sensing, 10(1), 6. DOI: 10.3390/rs10010006

Belgiu M. and Drăguț L. (2016). Random forest in remote sensing: A review of applications and future directions. ISPRS Journal of Photogrammetry and Remote Sensing, 114, 24–31. DOI: 10.1016/j.isprsjprs.2016.01.011

Bhungeni O., Ramjatan A. and Gebreslasie M. (2024). Evaluating Machine-Learning Algorithms for Mapping LULC of the uMngeni Catchment Area, KwaZulu-Natal. Remote Sensing, 16(12), 2219.

Bouzekraoui H., El Asri Z., Ouikhalfan M. and Benyaich A. (2020). Urban sprawl and land degradation in the Casablanca-Settat region of Morocco: Analysis and implications. Urban Planning and Development, 146(3), 05020011. DOI: 10.1061/(ASCE)UP.1943-5444.0000594

Carlson D., Montealegre A.L. and Inoue Y. (2018). Geospatial analysis of land cover change using time-series Landsat imagery on Google Earth Engine. International Journal of Remote Sensing, 39(7), 1978–1995. DOI: 10.1080/01431161.2017.1407044

Carrara P., Bordogna G. and De Carolis G. (2024). Spatial Data Infrastructure for Remote Sensing: A Comprehensive Analysis. DOI: 10.20944/preprints202404.0593.v1

Chen D., Bi B., Luo Z.H., Yang Y.W., Webber M. and Finlayson B. (2018). A scientometric review of water research on the Yangtze river. Applied Ecology and Environmental Research, 16(6), 7969–7987. DOI: 10.15666/aeer/1606_79697987

Chen J., Hu Y., Fan W., Zhang Y. and Wang L. (2017). Urban land cover classification using integrated multispectral and texture analysis with Landsat 8 imagery. Remote Sensing, 9(4), 316. DOI: 10.3390/rs9040316

Chomani K. and Pshdari S. (2024a). Evaluation of Different Classification Algorithms for Land Use Land Cover Mapping. Kurdistan Journal of Applied Research, 9(2), 13–22. DOI: 10.24017/science.2024.2.2

Chomani K. and Pshdari S. (2024b). Evaluation of Different Classification Algorithms for Land Use Land Cover Mapping. Kurdistan Journal of Applied Research, 9(2), 13–22. DOI: 10.24017/science.2024.2.2

Congalton R.G. and Green K. (2019). Assessing the accuracy of remotely sensed data: principles and practices. CRC Press.

Conrad C., Schönbrodt-Stitt S., Loew A. and Sorensen R. (2020). A pixel-based classification framework for improving land cover mapping through spatial and temporal integration. Remote Sensing of Environment, 247, 111920. DOI: 10.1016/j.rse.2020.111920

Dharumarajan S. and Hegde R. (2022). Digital mapping of soil texture classes using Random Forest classification algorithm. Soil Use and Management, 38(1), 135–149. DOI: 10.1111/sum.12668

Dong J., Xiao X., Menarguez M.A., Zhang G., Qin Y. and Roy D.P. (2019). Mapping paddy rice planting area in northeastern Asia with Landsat 8 images, time series, and rasterio library. International Journal of Applied Earth Observation and Geoinformation, 78, 65–74. DOI: 10.1016/j.jag.2019.01.012

Drusch M., Gascon F., Berger M. and Duesmann B. (2017). Sentinel-2: ESA's optical high-resolution mission for GMES operational services. Remote Sensing of Environment, 221, 255–261. DOI: 10.1016/j.rse.2017.05.032

Du T.L.T., Du Bui D., Nguyen M.D. and Lee H. (2018). Satellite-based, multi-indices for evaluation of agricultural droughts in a highly dynamic tropical catchment, Central Vietnam. Water (Switzerland), 10(5). DOI: 10.3390/w10050659

El Assaoui Fouad Amraoui N. and El Mansouri B. (2015). MODÉLISATION NUMERIQUE DE L'EFFET DES CHANGEMENTS CLIMATIQUES SUR LA NAPPE DE BERRECHID (MAROC) , Vol. 11, Issue 23, 1857–7881.

El Assaoui N., Bouiss C. and Sadok A. (2023). Assessment of Water Erosion by Integrating RUSLE Model, GIS and Remote Sensing – Case of Tamdrost Watershed (Morocco). Ecological Engineering & Environmental Technology, 24(3), 43–53. DOI: 10.12912/27197050/159530

ElAssaoui N., Amraoui F. and El Mansouri B. (2015). Modeling of climate changes impact on groundwater Resources of Berrechid Aquifer. International Journal of Innovative Research in Science Engineering and Technology, 4(7), 5681–5694.

Elgendy N. and Abdelatif T. (2021). Land use and land cover dynamics in Morocco: Insights into the spatial and temporal changes. Journal of African Earth Sciences, 179, 104163. DOI: 10.1016/j.jafrearsci.2021.104163

Feng Q., Gong J., Liu J. and Li Y. (2015). Flood mapping based on multiple endmember spectral mixture analysis and random forest classifier—The case of Yuyao, China. Remote Sensing, 7(9), 12539–12562.

Fentaw A.E. and Abegaz A. (2024). Analyzing Land Use/Land Cover Changes Using Google Earth Engine and Random Forest Algorithm and Their Implications to the Management of Land Degradation in the Upper Tekeze Basin, Ethiopia. Scientific World Journal, 2024. DOI: 10.1155/2024/3937558

Gerber F., Skakun S., Brown M.E. and Justice C.O. (2018). Automated geospatial data processing and visualization in Python using rasterio and GDAL. Computers & Geosciences, 118, 1–10. DOI: 10.1016/j.cageo.2018.05.014

Gohr C., Rodríguez G., Belomestnykh S., Berg-Moelleken D., Chauhan N., Engler J.-O., Heydebreck L.V., Hintz M.J., Kretschmer M., Krügermeier C., Meinberg J., Rau A.-L., Schwenck C., Aoulkadi I., Poll S., Frank E., Creutzig F., Lemke O., Maushart M., … Von Wehrden H. (2025). Artificial intelligence in sustainable development research. Nature Sustainability, 8(8), 970–978. DOI: 10.1038/s41893-025-01598-6

Harfouche A., Achard F. and Eva H.D. (2020). Time-series analysis of Landsat imagery for detecting forest cover changes in tropical regions. Forests, 11(8), 827. DOI: 10.3390/f11080827

He Y., Ding H. and Li P. (2020). Assessment of supervised machine learning classifiers for mapping land cover with Sentinel-2 imagery in Google Earth Engine. Remote Sensing, 12(1), 83. DOI: 10.3390/rs12010083

Jiang B., Dungan J.L., Matin A., Zarecor S. and Song X. (2021). A workflow for geospatial data integration and analysis using GDAL and rasterio libraries. Environmental Modelling & Software, 140, 105064. DOI: 10.1016/j.envsoft.2021.105064

Jiang J., Cai D., Yang Q. and Huang M. (2025). Scientometric insights into urban sustainability: exploring the vulnerability-adaptation-settlements nexus for climate resilience. Frontiers in Environmental Science, 13. DOI: 10.3389/fenvs.2025.1596271

Kamusoko C. and Gamba J. (2016). Machine learning techniques for land cover mapping in rural areas using Landsat 8 data: A comparison of SVM and RF classifiers. Remote Sensing, 8(9), 753. DOI: 10.3390/rs8090753

Kobayashi A., Hu C. and Andrefouet S. (2022). Improving accuracy in land cover classification and change detection using ensemble learning with pixel-based and object-based methods. International Journal of Remote Sensing, 43(2), 503–522. DOI: 10.1080/01431161.2021.1952635

Koukal T., Panferov O., Medina J.G. and Rouabhi A. (2020). Land cover changes and agricultural developments in Morocco: An assessment of spatial trends from 2000 to 2019. Remote Sensing Applications: Society and Environment, 19, 100357. DOI: 10.1016/j.rsase.2020.100357

Kussul N., Lavreniuk M., Skakun S. and Shelestov A. (2017). Land Use and Land Cover Classification Using Deep Learning Algorithms on Sentinel-2 Imagery. IEEE Journal of Selected Topics in Applied Earth Observations and Remote Sensing, 10(9), 3479–3490. DOI: 10.1109/JSTARS.2017.2724559

Laalaoui Y., Elassaoui N. and Ouahine O. (2024). Balancing urban growth and the sustainability of groundwater and agricultural land: Case of the berrechid-settat area. E3S Web of Conferences, 489, 04012.

Lee J., Xu P. and Ho H.T. (2017). Land cover classification for urban areas using Google Earth Engine and machine learning algorithms. Remote Sensing, 9(3), 248. DOI: 10.3390/rs9030248

Li W., Fu H., Yu L. and Wang L. (2019). A review of remote sensing-based land cover and land use change detection systems and models: Classification and assessment. Sensors, 19(9), 2326. DOI: 10.3390/s19092326

Lu D., Weng Q. and Li G. (2021). Evaluation of training sample sizes and class distribution on machine learning classifiers for land cover classification using Google Earth Engine. International Journal of Applied Earth Observation and Geoinformation, 100, 102327. DOI: 10.1016/j.jag.2021.102327

Meghraoui K., Sebari I., Pilz J., Ait El Kadi K. and Bensiali S. (2024). Applied Deep Learning-Based Crop Yield Prediction: A Systematic Analysis of Current Developments and Potential Challenges. Technologies, 12(4). DOI: 10.3390/technologies12040043

Nicolau A., Pires L.F. and Segovia J.A. (2023). Accuracy assessment: Quantifying classification quality. Lecture Notes in Geoinformation and Cartography, 235–254. DOI: 10.1007/978-3-031-26588-4_7

Peterson D.L. and Levinson D.H. (2020). Land use and land cover changes and their environmental implications in the Mediterranean basin. Environmental Science & Policy, 114, 245–254. DOI: 10.1016/j.envsci.2020.09.004

Phan T.N., Kuch V. and Lehnert L.W. (2020). Land cover classification using Google Earth Engine and random forest classifier—The role of image composition. Remote Sensing, 12(15), 2411.

Pickens A.H., Patel N., Senf C., Heurich M. and Hostert P. (2020). Remote sensing of vegetation cover dynamics and land cover change using Landsat data in complex landscapes. Remote Sensing of Environment, 242, 111770. DOI: 10.1016/j.rse.2020.111770

Riche A., Ricci R., Melgani F., Drias A. and Souissi B. (2024). Machine Learning Approach to LULC Forecasting. 2024 IEEE Mediterranean and Middle-East Geoscience and Remote Sensing Symposium (M2GARSS), 59–63. DOI: 10.1109/M2GARSS57310.2024.10537270

Saqr A.M., Kartal V., Karakoyun E. and Abd-Elmaboud M.E. (2025). Improving the Accuracy of Groundwater Level Forecasting by Coupling Ensemble Machine Learning Model and Coronavirus Herd Immunity Optimizer. Water Resources Management, 39(11), 5415–5442. DOI: 10.1007/s11269-025-04210-w

Sellami E.M. and Rhinane H. (2023). A new approach for mapping land use/land cover using google earth engine: a comparison of composition images. The International Archives of the Photogrammetry, Remote Sensing and Spatial Information Sciences, 48, 343–349.

Sharnagat N., Nema A.K., Mishra P.K., Patidar N., Kumar R., Suryawanshi A. and Radha L. (2025). State-of-the-Art Status of Google Earth Engine (GEE) Application in Land and Water Resource Management: A Scientometric Analysis. Journal of Geovisualization and Spatial Analysis, 9(1), 16. DOI: 10.1007/s41651-025-00218-3

Wachowska M., Kowalczyk A. and Kozak J. (2018). Using remote sensing for land cover classification and change detection: A comparative approach between machine learning algorithms. International Journal of Applied Earth Observation and Geoinformation, 75, 108–118. DOI: 10.1016/j.jag.2018.08.002

Wang J., Gong P. and Zhang B. (2018). Comparative evaluation of machine learning classifiers for land cover classification based on Landsat and Sentinel-2 data. International Journal of Remote Sensing, 39(16), 5604–5624. DOI: 10.1080/01431161.2018.1490972

Wu Q. (2020). geemap: A Python package for interactive mapping with Google Earth Engine. Journal of Open Source Software, 5(51), 2305.

Zhao Q., Yu L., Li X., Peng D., Zhang Y. and Gong P. (2021). Progress and trends in the application of google earth and google earth engine. Remote Sensing, 13(18). DOI: 10.3390/rs13183778

Zhao Z., Islam F., Waseem L.A., Tariq A., Nawaz M., Islam I.U., Bibi T., Rehman N.U., Ahmad W., Aslam R.W., and others. (2024). Comparison of three machine learning algorithms using google earth engine for land use land cover classification. Rangeland Ecology & Management, 92, 129–137.

RESEARCH PAPER

MAJORITY FILTER FOR ENHANCING PIXEL-BASED RANDOM FOREST LAND COVER CLASSIFICATION IN SUKAJAYA DISTRICT, BOGOR REGENCY

Fathan Aldi Rivai[1*], Boedi Tjahjono[1], Khursatul Munibah[1], Adenan Yandra Nofrizal[2]

[1]Department of Soil Science and Land Resources, Faculty of Agriculture, IPB University, Dramaga Main Road, 16680, Bogor Regency, Indonesia

[2]Department of Applied Geoinformatics and Cartography, Faculty of Science, Charles University, Albertov 6, 128 43, Prague, Czech Republic

Received: July 29th 2025 / Accepted: November 12nd 2025 / Published: December 31st 2025

***Corresponding author:** r.fathan.aldi@gmail.com

https://doi.org/10.24057/2071-9388-2025-4183

ABSTRACT. High-quality land cover data are essential for environmental policy, spatial planning, and ecosystem monitoring. However, pixel-based classification methods, while widely used due to their practicality, often suffer from salt-and-pepper noise, which undermines map reliability. This study aimed to integrate Random Forest (RF) classification and majority filtering to enhance the quality of land cover mapping in Sukajaya District, Bogor Regency. RF was applied to Sentinel-2 image data with varying numbers of trees (ntree) to determine the optimal model performance. Subsequently, majority filtering was applied to each classification result to reduce noise and improve spatial coherence. The evaluation employed multiple accuracy metrics, including User's Accuracy (UA), Producer's Accuracy (PA), F1-Score, Overall Accuracy (OA), and Kappa Coefficient (KC). Comprehensive accuracy increased with the ntree until reaching an optimal point. Beyond this point, additional ntree resulted in diminishing returns. Applying majority filtering as a post-processing procedure led to further improvements in classification accuracy. While majority filtering can reduce classification noise and improve the visual quality of land cover maps, it also carries the risk of removing small, accurately classified land cover patches. This consequence is rarely discussed in similar studies. These findings highlight the importance of integrating pixel-based machine learning classification with majority filtering in land cover classification workflows, while emphasising a trade-off that tends to favour visual accuracy over the preservation of spatial detail.

KEYWORDS: Diminishing return, Majority filter, Pixel-based classification, Random Forest, Salt-and-pepper noise

CITATION: Rivai F. A., Tjahjono B., Munibah K., Nofrizal A. Y. (2025). Majority Filter For Enhancing Pixel-Based Random Forest Land Cover Classification In Sukajaya District, Bogor Regency. Geography, Environment, Sustainability, 4 (18), 171-182
https://doi.org/10.24057/2071-9388-2025-4183

Conflict of interests: The authors reported no potential conflict of interests.

INTRODUCTION

Land cover is a critical aspect of the Earth's surface and a key consideration in territorial policymaking. It reflects the spatial distribution of ecosystems and provides quantitative indications of land-based service potentials (Anthony et al., 2024). This information supports evidence-based planning by offering an objective foundation for assessing environmental conditions (Aslam et al., 2024). When analysed temporally, land cover data can be used to identify landscape dynamics (Qacami et al., 2023). Variations in land cover types influence carbon stock differences, making it a vital component in emissions accounting (Solomon et al., 2018; Zhu et al., 2022). This data also plays a crucial role in hydrological process modelling (Mensah et al., 2022) and habitat suitability assessments for biodiversity conservation (Edosa and Erena, 2024). Collectively, these applications highlight the strategic importance of land cover in supporting conservation policies and adaptation to environmental change.

Land cover mapping using field surveys demands considerable time and resources. The development of geographic information systems, remote sensing technologies, and machine learning algorithms has increased the efficiency of this process. Random Forest (RF) is one of the most commonly used algorithms for land cover classification. This algorithm uses a bootstrap aggregation (bagging) method by building multiple decision trees from random subsets of the training data (Altman and Krzywinski, 2017; Rivai et al., 2023). At each node, RF randomly chooses a subset of features to improve model diversity (Ibrahim, 2023). It is particularly effective at managing imbalanced training data (Chahal et al., 2024), which makes it highly suitable for land cover classification tasks. In these tasks, training data across different classes are usually uneven, especially when the proportions of land cover are very uneven.

RF is a reliable algorithm for land cover classification, with the number of trees (ntree) being its most critical hyperparameter. RF is widely used in pixel-based land cover classification due to its ability to deliver high accuracy with relatively efficient computational performance. This approach is considered more practical than object-based methods, which require complex and computationally

intensive segmentation steps (Ye et al., 2023; Behera et al., 2024). Consequently, pixel-based classification remains a common approach for generating land cover maps. However, pixel-based classification results often suffer from salt-and-pepper noise. This refers to pixels that are classified differently from their surrounding areas (Ebrahimy et al., 2021; El-Deen Taha and Mandouh, 2024; Fu et al., 2017). This issue is frequently overlooked in land cover classification studies. The focus is typically placed on improving overall accuracy without adequately addressing the presence of noise. Although statistical accuracy may appear high, such noise can distort area estimations for each class and lead to misinterpretation of the results. This presents a challenge when the output is intended to support decision-making processes.

Studies aimed at improving image quality have shown that majority filtering effectively removes salt-and-pepper noise in raster data (Olariu et al., 2022; Maleki et al., 2024). Salt-and-pepper noise typically appears as isolated pixels with values that differ from their neighbours, affecting both visual interpretation and quantitative analysis. Majority filtering tackles this by substituting the central pixel with the most common value among its surrounding pixels (Bayazit et al., 2025). This process helps to reduce local anomalies without significantly distorting the image structure. Applying this technique to the outputs of pixel-based classification can improve the accuracy and overall quality of land cover data generated using machine learning algorithms.

Sukajaya District, located in Bogor Regency, holds strategic importance within a conservation area due to its position in a mountainous region. Research by Tjahjono et al., (2024) indicates that Sukajaya District is highly prone to landslides. The local government has implemented ecologically oriented strategies to preserve the environmental quality of the area. Land cover mapping is crucial for generating accurate data to support environmentally based policy decisions. To effectively and efficiently detect detailed land cover features using open-source data, Sentinel-2 imagery with a 10 m resolution is well-suited for classification purposes. This study aims to enhance the quality of pixel-based RF land cover classification in Sukajaya District. To achieve high classification accuracy while minimising salt-and-pepper noise, the ntree was tuned and post-processing was applied using a majority filter to reduce noise and improve spatial coherence.

MATERIALS AND METHODS

Study Area

Sukajaya District is an administrative district within Bogor Regency, West Java Province (Fig. 1). Administratively, Sukajaya District shares borders with several districts in two regencies. To the west, it borders Cipanas and Lebakgedong Districts (Lebak Regency). To the south, it borders Cibeber District (Lebak Regency) and Nanggung District (Bogor Regency). To the east, it borders Nanggung and Cigudeg Districts (Bogor Regency). To the north, it borders Jasinga District (Bogor Regency). Situated within the Halimun Mountains and characterised by intense human activities, land use in Sukajaya District has become increasingly fragmented across different land cover types. This situation has led to more noticeable landscape fragmentation between land cover classes (Pramesti et al., 2025). Sukajaya District's varied landscape makes it an ideal study area for evaluating the performance of the RF classification algorithm and the use of majority filtering to improve land cover map accuracy. This is crucial for supporting spatial planning.

Materials

The administrative boundary of Sukajaya District was obtained from the Ina-Geoportal website. Sentinel-2 imagery from the year 2024 was used for land cover classification. Harmonised surface reflectance data from Sentinel-2 were retrieved via Google Earth Engine (GEE) and cloud masking was applied to remove contaminated pixels. To further reduce residual artefacts and temporal inconsistencies, a median filter was applied. All bands used in the analysis were resampled to a spatial resolution of 10 m using the nearest neighbour method, which preserves

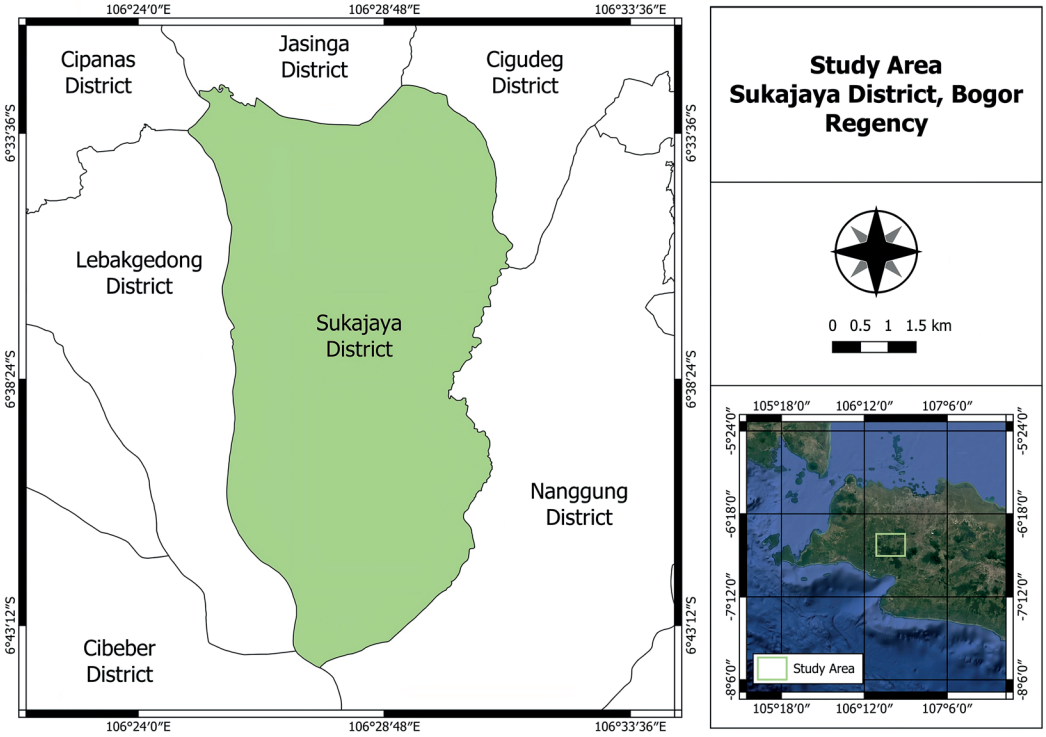

Fig. 1. The Map of Sukajaya District

original pixel values without introducing interpolation, thereby maintaining the integrity of the reflectance data. The specific Sentinel-2 bands used in the classification are listed in Table 1.

Land cover classes were defined following field surveys conducted in Sukajaya District. The classes and the number of datasets per class are presented in Table 2. The dataset consists of points derived from field verification and interpretation using Google Earth. This dataset was split using a 70/30 ratio, with 70 percent used as training data and 30 percent as validation data, following common practice in machine learning applications (Joseph, 2022). Consistently, the training data were used for land cover classification using the RF algorithm, with the ntree increasing incrementally from 100 to 700 in steps of 100. The validation data were used to assess the classification accuracy of both the RF results and the outputs after majority filtering in the post-processing stage.

Methods

Random Forest for Land Cover Classification

Random Forest (RF) is a supervised machine learning algorithm that works by building multiple decision trees in parallel during training, a technique called ensemble learning. The algorithm then combines the voting results from each tree to produce a more stable final decision (Breiman, 2001). The RF algorithm was implemented using GEE, which uses the Statistical Machine Intelligence and Learning Engine (SMILE) library as its backend. The SMILE RF library allows for efficient large-scale processing of geospatial data (Aji et al., 2024). This efficiency is achieved through direct integration with GEE's geospatial datasets and its support for parallel training. The number of trees (ntree) was tuned from 100 to 700 in steps of 100. With 10 Sentinel-2 bands, the number of variables per split was set to three, following the default setting of the square root of the input features.

Majority Filtering

Majority filtering is an image processing method used to reduce salt-and-pepper noise. It replaces the value of a central pixel with the majority value of its neighbouring pixels (S. Liu and Gu, 2017). Majority filtering was applied using the Sieve feature in QGIS to improve the land cover classification results from RF. This process uses an 8-neighbour rule (Ávila-Mosqueda et al., 2025), which considers all adjacent neighbouring pixels to determine the majority value for the central pixel. The majority filter assigns a pixel value based on the dominant value among its neighbouring pixels (Svoboda et al., 2022; Al-Aarajy et al., 2024). Mathematically, the original raster R consists of pixel values *R(i,j)*, where *i* and *j* represent the pixel coordinates. For each pixel (*i,j*), a local window *N(i,j)* is defined, which includes neighbours within a certain radius. The new pixel value *R'(i,j)* is calculated by taking the mode of *N(i,j)*, as shown in Equation 1:

$$R'(i,j) = mode\,(N(i,j)) \quad (1)$$

Here, *R'(i,j)* is the new pixel value obtained after applying majority filtering, and mode*(N(i,j))* is the most frequent value within the local window *N(i,j)*.

Table 1. Sentinel-2 bands used

Band	Description	Wavelength (nm)	Resolution (m)	Resample Resolution Used (m)
B2	Blue	490	10	10
B3	Green	560	10	10
B4	Red	665	10	10
B5	Red Edge 1	705	20	10
B6	Red Edge 2	740	20	10
B7	Red Edge 3	783	20	10
B8	Near Infrared (NIR)	842	10	10
B8A	Narrow NIR	865	20	10
B11	Short Wave Infrared 1	1610	20	10
B12	Short Wave Infrared 2	2190	20	10

Table 2. The amount of training and validation data collected for each land cover class

Land cover class	Data training amount	Data validation amount
Water body	405	173
Forest	401	172
Mixed garden	407	174
Oil palm plantation	412	177
Rice field	401	172
Bare land	169	72
Built-up area	403	173

Land Cover Class-based Accuracy Assessment

The classification results of the Random Forest model for each tested tree number, both without and with majority filtering, were evaluated based on accuracy per land cover class. The commonly used accuracy metrics in land cover classification are User's Accuracy (UA) and Producer's Accuracy (PA). UA represents the probability that a classified label is correct. This means it shows how accurately the pixels classified into a certain class truly belong to that class in the validation data. The formula for UA is presented in Equation 2.

$$UA_c = TP_c / \left(TP_c + FP_c \right) \quad (2)$$

PA indicates the classifier's ability to correctly identify pixels belonging to a specific class. It measures how many pixels from the actual class are correctly classified. The formula for PA is presented in Eq. 3.

$$PA_c = TP_c / \left(TP_c + FN_c \right) \quad (3)$$

When the number of validation samples is unbalanced across classes, it is recommended to use the F1-Score as an additional metric. This is because the F1-Score combines UA and PA into a single harmonic metric (Amin et al., 2024). The dataset sizes between subsets are unbalanced, resulting in unequal validation data for each land cover class. Therefore, in addition to calculating UA and PA, this research also uses the F1-Score metric. The formula for calculating the F1-Score is presented in Eq. 4.

$$F1_c = \left(2 \times UA_c \times PA_c \right) / \left(UA_c + PA_c \right) \quad (4)$$

Here, $F1_C$ is the F1-score for class c, UA_C is the user's accuracy for class c, PA_C is the producer's accuracy for the land cover class c, TP_C is the number of pixels correctly classified as class c, FP_C is the number of pixels incorrectly classified as class c but actually belong to other classes, and FN_C is the number of pixels that belong to class c but were misclassified as other classes.

Comprehensive Accuracy Assessment

The accuracy of the RF classification results, including tree number tuning and majority filtering, was assessed using Overall Accuracy (OA) and the Kappa Coefficient (KC). OA represents the percentage of total pixels or samples that were correctly classified when compared to the validation data. The formula for calculating OA is presented in Eq. 5.

$$OA = \sum_{i=1}^{K} TP_i / N \quad (5)$$

TP_i is the number of pixels correctly classified as class i. K is the total number of land cover classes. N is the total number of validation pixels across all classes.

Kappa coefficient (KC) is a statistical metric that measures the level of agreement between classification results and reference data, after correcting for the possibility of chance agreement. In short, KC accounts for the probability that a classification was correct purely by chance. The formula for calculating KC is presented in Equation 6.

$$k = \left(P_o - P_e \right) / \left(1 - P_e \right) \quad (6)$$

P_o is the number of correctly classified pixels divided by the total number of validation pixels, and P_e is derived from the product of the marginal totals in the classification and reference data.

RESULTS

Land Cover Raster from Random Forest with and without Majority Filtering

Pixel-based RF classification was conducted for each tested ntree without a majority filter. The results are illustrated in Fig. 2, and the corresponding land cover areas are presented in Fig. 3. The resulting land cover maps show variations in area depending on the ntree applied.

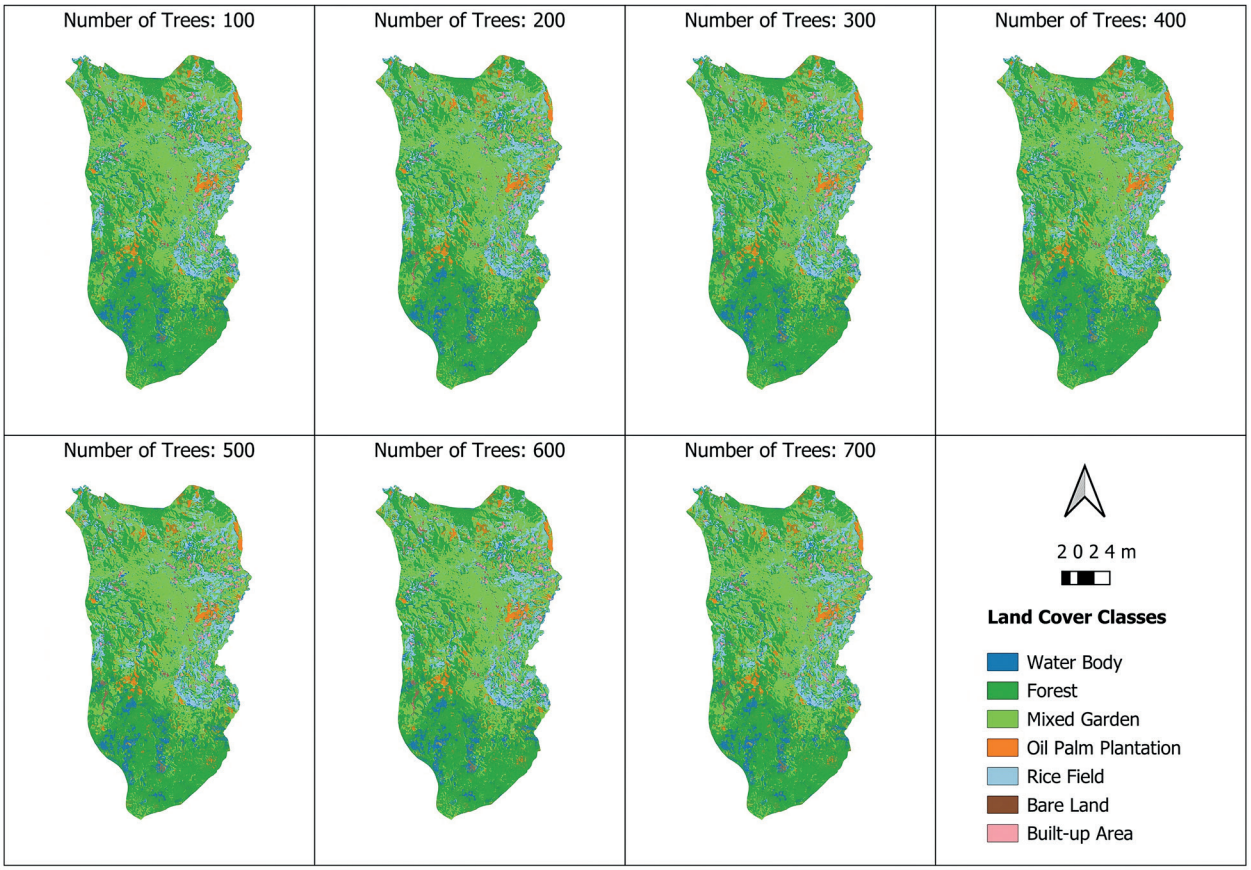

Fig. 2. Land cover classification using Random Forest without majority filter post-processing

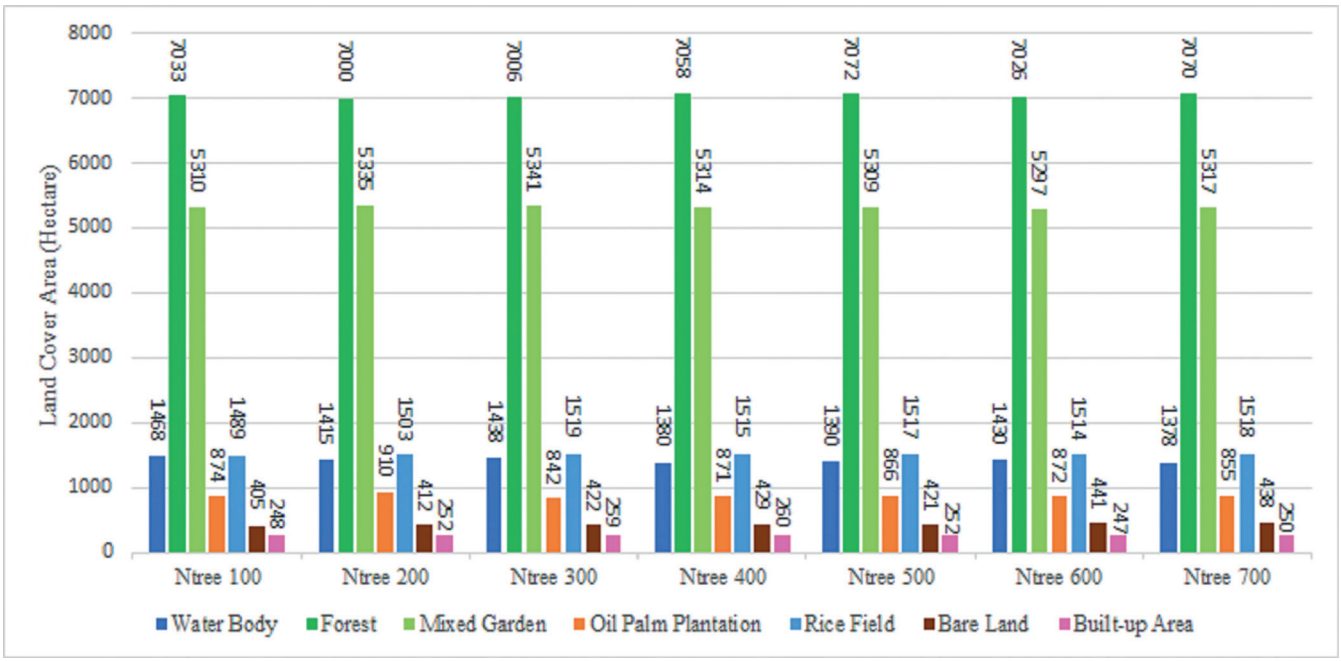

Fig. 3. Land cover class area from Random Forest classification without majority filter post-processing

Consistently, forest appeared as the dominant land cover, ranging from 7,000 to 7,070 ha. This was followed by mixed garden (5,297 to 5,341 ha), rice field (1,489 to 1,503 ha), water body (1,378 to 1,468 ha), oil palm plantation (842 to 910 ha), and bare land (405 to 441 ha). The smallest land cover class was built-up area, ranging from 247 to 259 ha. Despite these results, the classification outputs still show salt-and-pepper noise. This is characterised by small, scattered pixels that differ from the dominant surrounding class. This limitation comes from the pixel-based classification approach. In this method, each pixel is treated independently without considering the spatial pattern around it. This reduces both the accuracy and the visual quality of the land cover raster data.

Through the application of a majority filter, these noise speckles can be replaced by aligning pixel values with the dominant surrounding class. The post-processing results of the majority filter are shown in Fig. 4, and the area of each land cover class is presented in Fig. 5. The filtered output displays the same ranking of land cover areas from largest to smallest as in the unfiltered classification. However, differences in area are observed following the application of the majority filter. Forest remains the dominant land cover, ranging from 7,243 to 7,303 ha, followed by mixed garden (5,540 to 5,598 ha), rice field (1,481 to 1,505 ha), water body (1,091 to 1,151 ha), oil palm plantation (695 to 754 ha), and bare land (360 to 399 ha). Built-up area continues to represent the smallest land cover class, with an area between 261 and 273 ha.

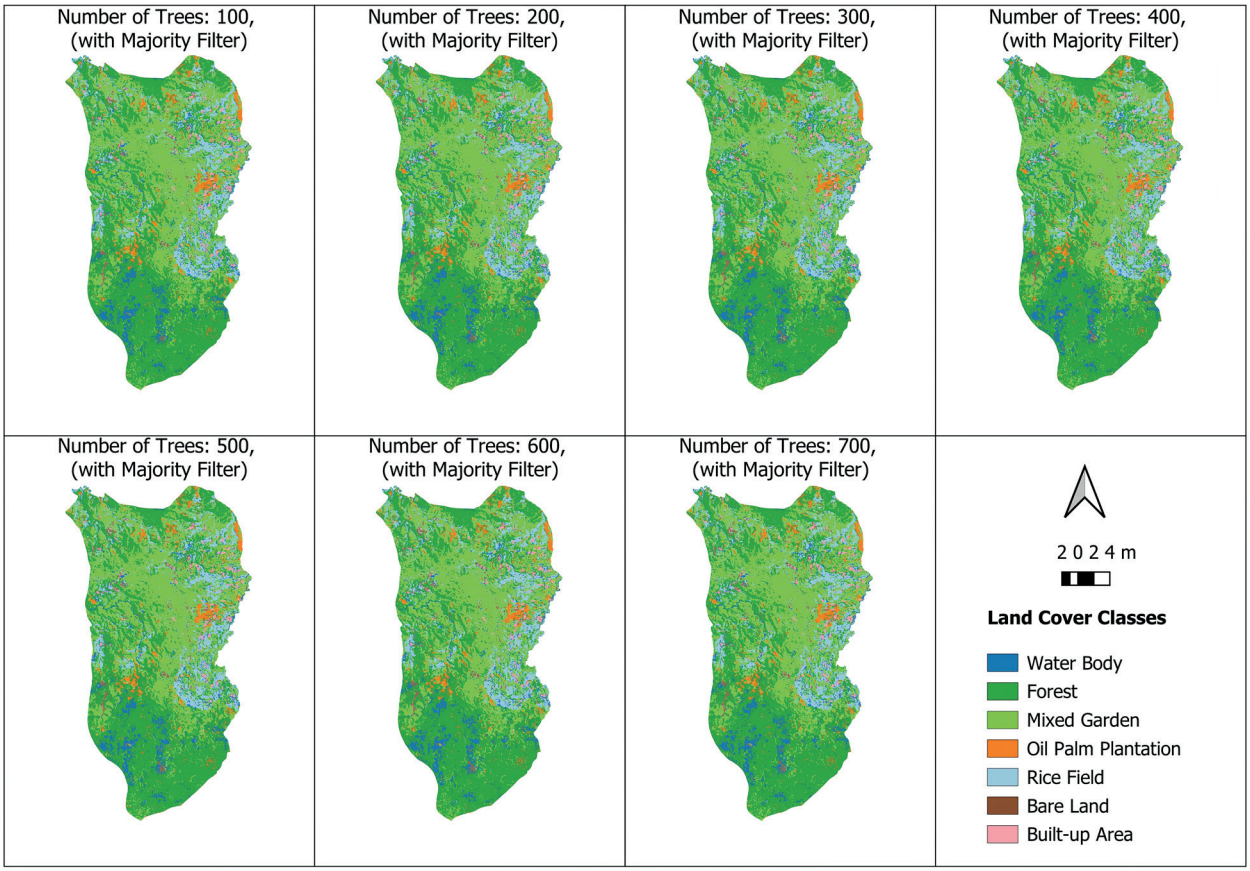

Fig. 4. Land cover classification using Random Forest with majority filter post-processing

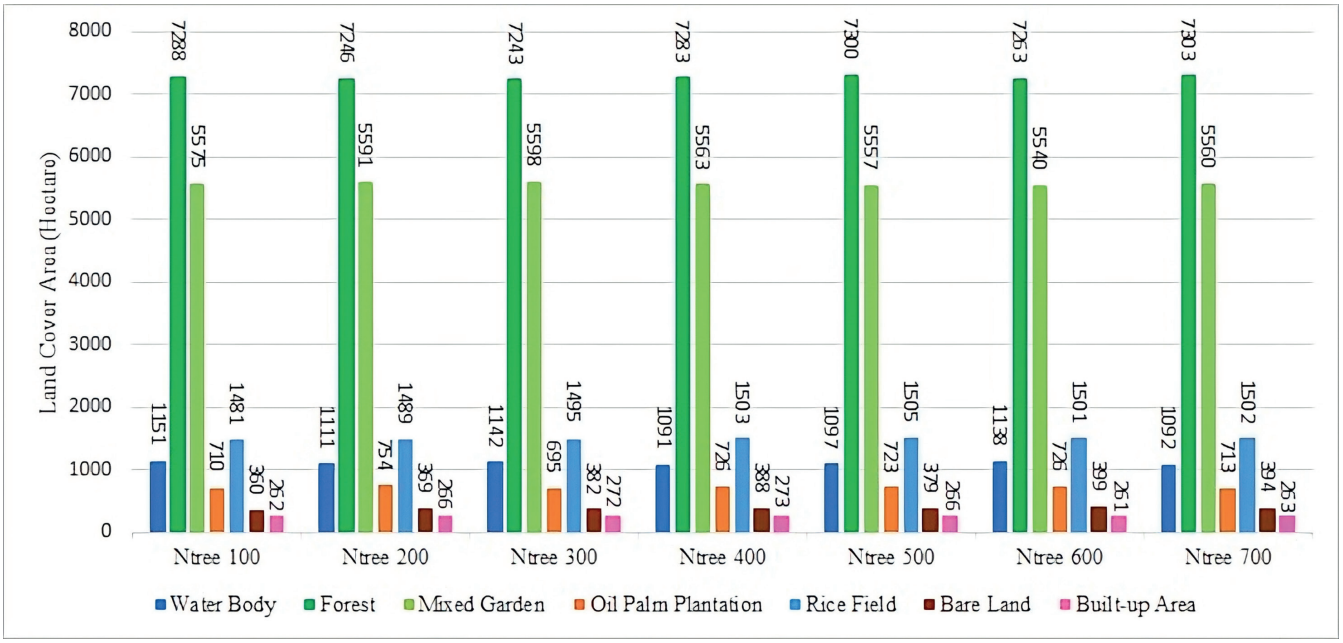

Fig. 5. Land cover class area from Random Forest classification with majority filter post-processing

A zoomed-in view is presented in Fig. 6 to illustrate in greater detail the differences between land cover classification results before and after applying the majority filter. The RF classification results using ntree values ranging from 100 to 700 without majority filtering display scattered speckles consisting of one to four pixels. These patterns give the impression of randomly distributed land cover patches with extremely small areas, approximately 100 to 400 m2. After applying the majority filter to each classification output across different ntree values, these speckles are eliminated. The majority filter works by reassigning pixel values to the most dominant land cover class within their neighbourhood, effectively transforming isolated pixels into more homogeneous clusters. As a result, small fragmented patches tend to shrink, while larger contiguous areas are expanded.

Accuracy of Land Cover Classification Per-Class with and without Majority Filtering

Visually, the majority filter enhances the quality of the land cover classification results. To better understand its impact on classification accuracy, an assessment was carried out for each land cover class. The classification accuracy per class was evaluated using User's Accuracy (UA) (Table 3), Producer's Accuracy (PA) (Table 4), and the F1-Score metric (Table 5).

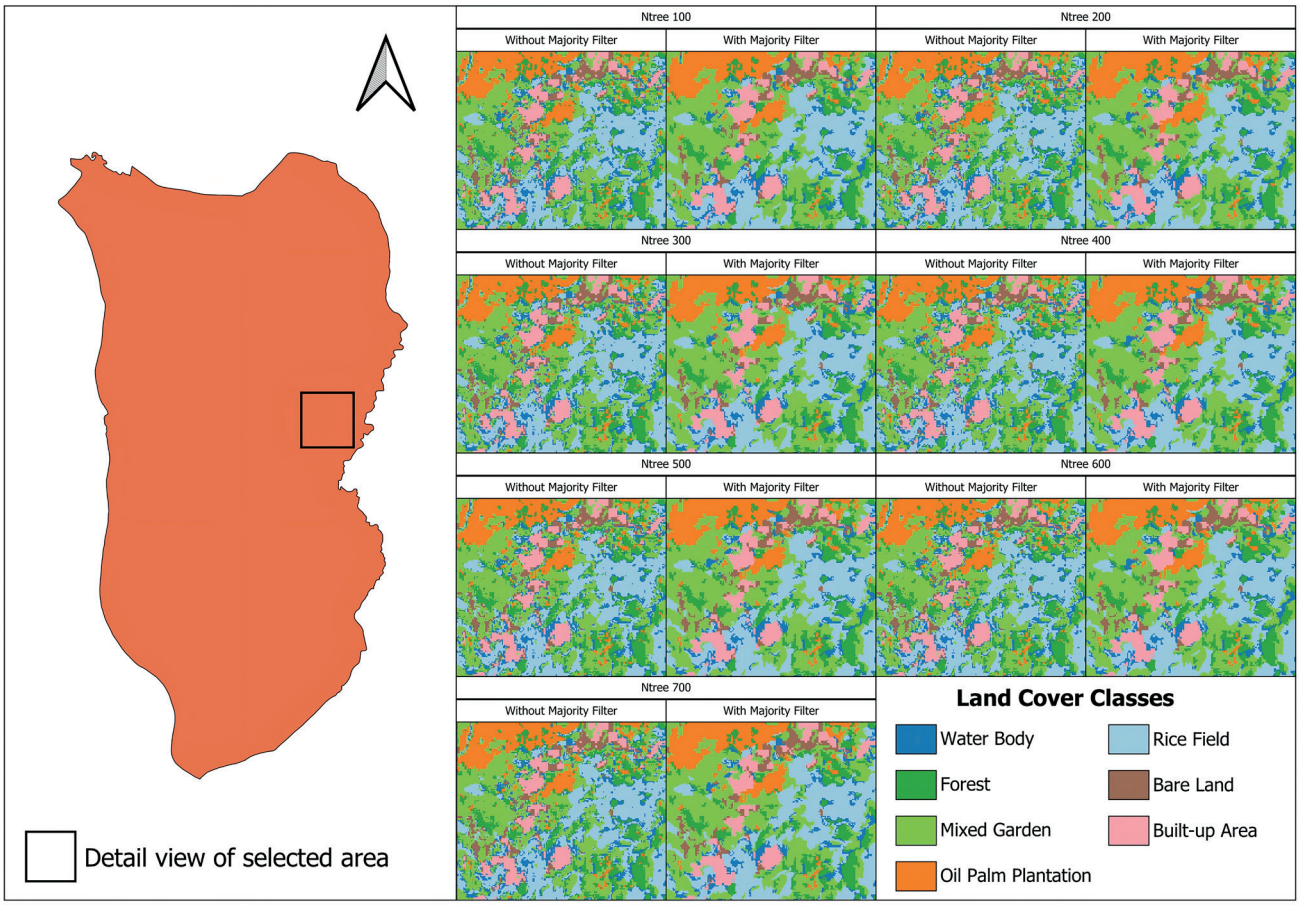

Fig. 6. Zoom-in comparison of land cover classification features using ntree 100–700 without and with majority filtering

The lowest accuracy values were observed for the bare land and water body classes. This can be attributed to the tropical wet conditions in Sukajaya District, where frequent rainfall causes bare land to become moist and appear non-homogeneous, complicating the classification process. This contrasts with bare land classifications in arid desert regions, which tend to be easier to classify (Darem et al., 2023; Du et al., 2023; Elmahdy and Mohamed, 2023). Similarly, water bodies in Sukajaya District are generally shallow, with partially exposed land and surrounding vegetation extending over the edges, resulting in high variability in conditions. This contributes to the reduced classification accuracy for this class. In contrast, other land cover classes that are relatively more homogeneous exhibit higher accuracy. Overall, classification accuracy is influenced by the degree of homogeneity within a land cover class; the more homogeneous the class, the higher its classification accuracy.

Based on UA values before and after applying the majority filter, accuracy shifts were generally positive, indicating that the majority filter improved the per-class accuracy of the land cover classification. This suggests a trend of increased accuracy in most land cover classes after the filter was applied, although variations in accuracy changes between classes were observed. Exceptions were found in the mixed garden class (except at ntree 200), bare land (ntree 400), and built-up area (ntree 400), which experienced decreases in accuracy. On average, the absolute change in UA reached 2.10 percentage points, showing that the majority filter had a measurable impact on classification accuracy. Based on PA values before and after the majority filter, only the bare land class showed a decline in accuracy, while the oil palm plantation class showed no improvements in accuracy. These results were consistent across ntree values from 100 to 700. The average absolute change in PA was calculated at 2.13 percentage points.

Based on F1-Score values before and after the application of the majority filter, the mixed garden class experienced a decrease in accuracy only at ntree 500. The bare land class showed an increase in accuracy only at ntree 600 and 700. Aside from these exceptions, a consistent improvement in accuracy was observed across ntree values from 100 to 700. The average absolute change was 1.88 points, reinforcing the finding that the filter tends to enhance the balance between UA and PA, despite slight variations in response across classes. Accuracy reductions in specific land cover classes based on UA, PA, and F1-Score metrics may occur when those classes are represented as small fragments. Although such fragments may have been correctly classified initially, the majority filter replaces them with the dominant surrounding class, thereby reducing the accuracy for those specific land cover categories.

Comprehensive Accuracy Assessment of Land Cover Classifications Before and After Majority Filtering

The comprehensive classification performance was evaluated using OA and KC, as shown in Fig. 7. In the first RF classification experiment with ntree set to 100, the map achieved a comprehensive accuracy with an OA of 81.94% and a KC of 78.72%. As the ntree value increased in increments of 100, the performance of the RF classifier improved, reaching its peak at ntree 400 for land cover classification. At this point, the model achieved an OA of 83.02% and a KC of 79.99%. Therefore, in this model, ntree 400 represents a plateau. A plateau refers to the stage where further increases in ntree do not result in additional performance gains (Probst and Boulesteix, 2018). When ntree was further increased in increments of 100, the accuracy exhibited diminishing returns. This indicates that after the RF model reaches its optimal accuracy, increasing the ntree may lead to a decline in performance. Similar results were also reported by Liu et al. (2021), who found that once the optimal ntree is reached, further increases in ntree can result in decreased performance.

Table 3. User's accuracy per land cover class from Random Forest classification (Ntree 100–700) without and with majority filtering

Method	User's Accuracy						
	Water Body	Forest	Mixed Garden	Oil Palm Plantation	Rice Field	Bare Land	Built-up Area
RF Ntree 100	67.20	78.60	75.90	94.50	81.30	67.90	99.40
RF Ntree 200	69.30	79.50	74.70	94.00	81.30	68.40	99.40
RF Ntree 300	69.80	80.70	75.60	95.60	81.50	70.20	99.40
RF Ntree 400	70.40	81.00	75.10	95.60	81.50	70.20	99.40
RF Ntree 500	70.40	79.70	75.40	96.10	82.80	66.10	99.40
RF Ntree 600	69.60	81.80	75.30	95.10	82.80	64.40	99.40
RF Ntree 700	70.00	80.80	75.10	94.50	82.40	65.00	99.40
RF Ntree 100 with Majority Filter	70.30	81.00	75.30	95.00	87.20	68.50	99.40
RF Ntree 200 with Majority Filter	72.90	80.90	75.30	95.10	86.50	69.80	99.40
RF Ntree 300 with Majority Filter	74.60	82.10	73.80	96.10	87.60	70.40	99.40
RF Ntree 400 with Majority Filter	75.90	82.30	75.00	97.70	83.70	68.50	98.80
RF Ntree 500 with Majority Filter	74.90	80.80	72.70	96.60	88.70	68.50	99.40
RF Ntree 600 with Majority Filter	72.80	82.80	74.40	96.70	87.60	68.50	99.40
RF Ntree 700 with Majority Filter	76.30	82.10	74.90	96.10	84.30	69.10	99.40

Table 4. Producer's Accuracy per land cover class from Random Forest classification (Ntree 100 – 700) without and with Majority Filtering

Method	Producer's Accuracy						
	Water Body	Forest	Mixed Garden	Oil Palm Plantation	Rice Field	Bare Land	Built-up Area
RF Ntree 100	71.10	79.10	74.10	97.20	86.00	52.80	96.00
RF Ntree 200	71.70	76.70	74.70	97.70	88.40	54.20	95.40
RF Ntree 300	73.40	77.90	74.70	97.70	89.50	55.60	95.40
RF Ntree 400	72.80	79.10	74.70	97.70	89.50	55.60	95.40
RF Ntree 500	72.80	79.70	74.10	97.70	89.50	54.20	95.40
RF Ntree 600	74.00	78.50	73.60	98.30	89.50	52.80	95.40
RF Ntree 700	72.80	78.50	73.00	97.70	90.10	54.20	95.40
RF Ntree 100 with Majority Filter	74.00	82.00	78.70	97.20	87.20	51.40	96.50
RF Ntree 200 with Majority Filter	74.60	81.40	78.70	97.70	89.50	51.40	96.50
RF Ntree 300 with Majority Filter	76.30	82.60	77.60	97.70	90.70	52.80	96.50
RF Ntree 400 with Majority Filter	76.30	83.70	77.60	97.70	89.50	51.40	96.50
RF Ntree 500 with Majority Filter	75.70	83.10	76.40	97.70	91.30	51.40	96.50
RF Ntree 600 with Majority Filter	77.50	81.40	77.00	98.30	90.70	51.40	96.50
RF Ntree 700 with Majority Filter	76.30	82.60	77.00	97.70	90.70	52.80	96.50

Table 5. F1-Score per land cover class from Random Forest classification (Ntree 100–700) without and with majority filtering

Method	F1-Score						
	Water Body	Forest	Mixed Garden	Oil Palm Plantation	Rice Field	Bare Land	Built-up Area
RF Ntree 100	69.10	78.80	75.00	95.80	83.60	59.40	97.60
RF Ntree 200	70.50	78.10	74.70	95.80	84.70	60.50	97.30
RF Ntree 300	71.50	79.30	75.10	96.60	85.30	62.00	97.30
RF Ntree 400	71.60	80.00	74.90	96.60	85.30	62.00	97.30
RF Ntree 500	71.60	79.70	74.80	96.90	86.00	59.50	97.30
RF Ntree 600	71.70	80.10	74.40	96.70	86.00	58.00	97.30
RF Ntree 700	71.40	79.60	74.10	96.10	86.10	59.10	97.30
RF Ntree 100 with Majority Filter	72.10	81.50	77.00	96.10	87.20	58.70	97.90
RF Ntree 200 with Majority Filter	73.70	81.20	77.00	96.40	88.00	59.20	97.90
RF Ntree 300 with Majority Filter	75.40	82.30	75.60	96.90	89.10	60.30	97.90
RF Ntree 400 with Majority Filter	76.10	83.00	76.30	97.70	86.50	58.70	97.70
RF Ntree 500 with Majority Filter	75.30	81.90	74.50	97.20	90.00	58.70	97.90
RF Ntree 600 with Majority Filter	75.10	82.10	75.70	97.50	89.10	58.70	97.90
RF Ntree 700 with Majority Filter	76.30	82.30	75.90	96.90	87.40	59.80	97.90

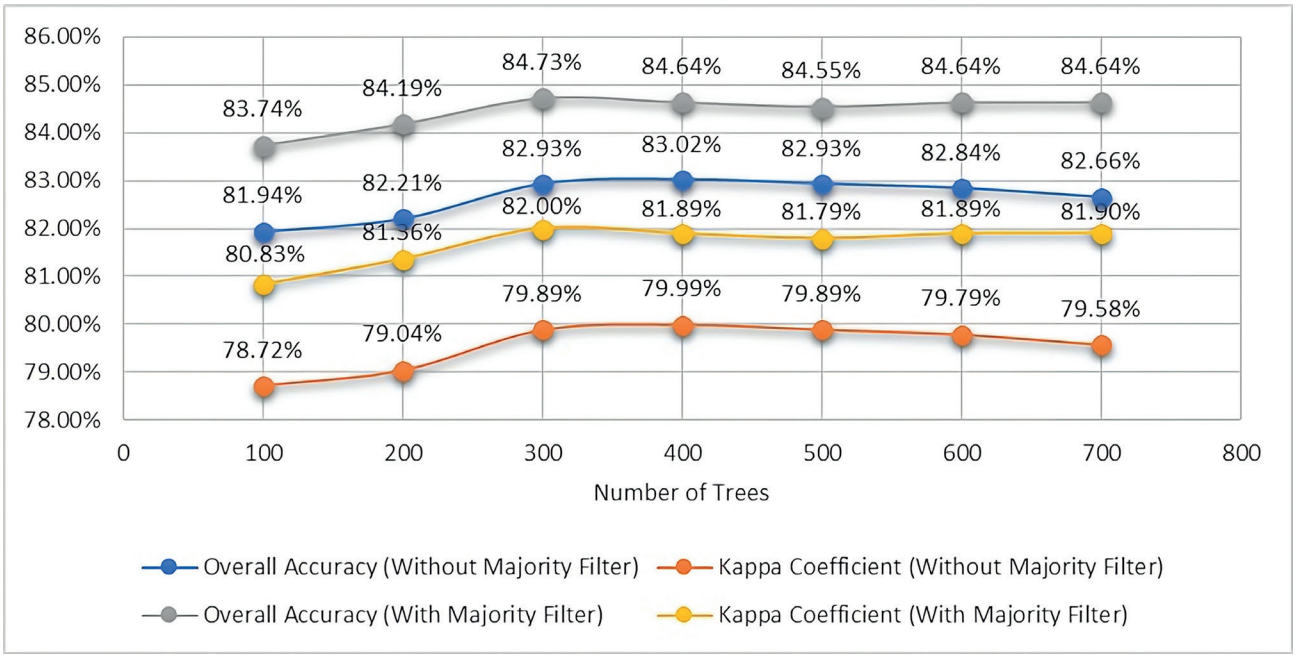

Fig. 7. Comprehensive accuracy of land cover classification using Random Forest (Ntree 100 – 700) with and without majority filter post-processing

After applying the majority filter, changes were observed in both OA and KC. Both metrics increased, confirming that post-classification processing with a majority filter can improve land cover classification quality by addressing salt-and-pepper noise. On average, OA increased by 1.80 percentage points, while KC saw a larger average improvement of 2.11 percentage points. However, this also led to a shift in the point of optimal accuracy. In the original classification results, the highest accuracy was achieved with an ntree value of 400. After majority filtering, the highest accuracy was instead observed with an ntree value of 300. Initially, the classification at ntree 400 had an OA of 83.02% and a KC of 79.99%, while ntree 300 had an OA of 82.93% and a KC of 79.89%. After the majority filter was applied, ntree 300 improved by 1.80 percentage points in OA and 2.11 percentage points in KC. In contrast, ntree 400 only improved by 1.62 percentage points in OA and 1.90 percentage points in KC. These findings confirm that the majority filter consistently enhances land cover classification quality. However, the extent of improvement does not directly correspond to the accuracy levels before post-processing. This is likely due to the inherent differences in classification outcomes produced by varying ntree settings, which lead to variations in the pixels most susceptible to reclassification during majority filtering.

Identical accuracy results were observed for ntree values of 400, 600, and 700 after applying the majority filter, despite their OA values being different before this filtering process. This indicates that although the initial classification results varied, the final outputs became identical after applying the majority filter, particularly in the areas used for validation. In other words, initial differences in classification had little impact on accuracy values because the majority filter produced uniform maps in the validation areas. However, a slight distinction remains in the KC values. The KC for ntree 400 and 600 remained the same after filtering, while the value for ntree 700 was slightly higher by 0.01 percentage points. This is due to the nature of the KC, which accounts for chance agreement. As a result, minor variations in classification patterns can still be detected, even when OA values are identical.

DISCUSSION

The study results indicate that majority filtering plays a vital role in enhancing the spatial coherence of land cover classification maps produced by RF by reducing salt-and-pepper noise. This finding aligns with the application of majority filtering demonstrated by Chen et al. (2023), where salt-and-pepper noise, consisting of minority pixels, is replaced by the majority class of neighbouring pixels. Although numerous studies have applied this technique and emphasised the advantages in reducing classification noise and enhancing spatial coherence, few have critically examined potential drawbacks. One notable yet often overlooked consequence is the removal of pixels that were correctly classified but belong to small, fragmented land cover patches. Such areas, despite being accurate representations of actual land cover, are susceptible to elimination due to excessively small spatial size. This effect is evident in the water body, oil palm plantation, rice field, and bare land classes, which consistently from ntree 100 to 700 experienced reductions in area after majority filtering. Conversely, land cover types characterised by larger fragment sizes such as forest, mixed garden, and built-up area consistently from ntree 100 to 700 showed increases in area.

Both the results with and without majority filtering consistently show that forest remains the dominant land cover in Sukajaya District, while built-up areas are the least extensive. Nevertheless, noticeable changes in area are clearly observed. The results after applying majority filtering are considered better, as the salt-and-pepper noise has been removed. Forest dominance is expected, as Sukajaya District, which spans from mountainous areas to the foothills, partly lies within a National Park forest area. Mountainous regions are often designated as protected zones, making forest cover the dominant class (Li et al., 2022). Findings from other highland regions consistently show that forest is the predominant land cover type (Adhikari et al., 2022; Ismail et al., 2021; Ratnayake et al., 2024). In the Himalayas, where permanent snow exists, forest is the second most dominant class after snow (Singh and Pandey, 2021). However, the presence of plantations or agricultural land as classes competing with forest for dominance is also frequently observed in areas that have

undergone deforestation. These differences largely depend on conservation policies and their enforcement, which shape human activities and the intensity of anthropogenic land use (Chen et al., 2025).

Through tuning the ntree, it was found that accuracy per land cover class generally improved, but some classes experienced a decline. The claim by Kuntla and Manjusree (2020) that majority filtering reduces commission errors and thus improves per-class accuracy cannot be fully accepted. This study demonstrates that, in the case of the bare land class, almost all ntree values tested showed decreases in both area and accuracy. This is because bare land is the most fragmented class, making it highly susceptible to negative externalities from majority filtering.

In studies using RF, tuning the ntree is typically performed to achieve high accuracy (Manafifard, 2024). Logically, the plateau point of ntree in RF is expected to yield higher accuracy than other ntree values, both before and after majority filtering. Although this has not been definitively proven, the present study suggests that accuracy can improve beyond the plateau point after post-classification majority filtering. The shift of maximum accuracy from ntree 400 (before filtering), which was considered the plateau in this experiment, to ntree 300 (after filtering) indicates that the relationship between the RF ntree tuning parameter and classification accuracy is not strictly linear when majority filtering is applied in post-processing. Even though ntree 400 initially produced the best overall accuracy, after majority filtering the best results shifted to ntree 300. This suggests that models with slightly lower initial performance may produce better results after majority filtering, depending on how the post-filtering changes align with the validation data locations.

It is important to emphasise that majority filtering is a post-classification procedure and does not affect the internal learning dynamics of the RF model. However, different ntree values can yield slightly different classification patterns (Sun and Ongsomwang, 2023). These differences influence the distribution of salt-and-pepper noise, which in turn determines the susceptibility of pixels to the majority filtering process. This phenomenon reflects the inherent randomness of the RF algorithm, arising from the bootstrapping process and random feature selection during tree construction, which ultimately affects the classification results (Salman et al., 2024). Consequently, although ntree 400 may produce the highest initial accuracy, the combination of noise distribution, filtering effects, and coincidentally more favourable variability at ntree 300 with slightly lower initial accuracy can lead to a more optimal improvement after majority filtering. Moreover, the accuracy difference between ntree 400 and ntree 300 prior to filtering is very small.

The phenomenon of identical OA values for ntree 400, 600, and 700 after filtering, despite different values before filtering, highlights the limitation of OA. OA only measures the proportion of correctly classified samples and does not account for agreement due to chance. In contrast, KC, which adjusts for random agreement, remains more sensitive in distinguishing model performance. This underscores the importance of using multiple accuracy metrics in land cover map evaluation. For this reason, land cover classification studies often employ both OA and KC as evaluation tools (Zeferino et al., 2020). These findings emphasise the importance of integrating pixel-based machine learning classification algorithms with spatial majority filtering techniques to support operational land cover mapping.

Majority filtering has proven effective in enhancing the spatial coherence of classification results and reducing noise. Therefore, studies that rely on pixel-based classification for purposes such as land cover change analysis (Kaur et al., 2023), urban expansion (Zhang et al., 2021), deforestation monitoring (Silva et al., 2022), estimating carbon stock changes (Wahyuni et al., 2025), soil erosion assessment (Belay and Mengistu, 2021), delineating geohazard-prone areas (Tempa and Aryal, 2022), and projecting land cover dynamics (Hakim et al., 2020) should apply majority filtering as a post-processing step to produce cleaner and more accurate results. Majority filtering also has the potential to remove small land cover patches that may have been correctly classified but are spatially vulnerable to being filtered out. This creates a trade-off between the visual accuracy gained from the positive effects of majority filtering and the preservation of spatial details that risk being lost due to its negative effects. Nevertheless, the overall benefits of applying majority filtering outweigh its side effects.

CONCLUSIONS

This study demonstrates that the RF algorithm can classify pixel-based land cover from Sentinel-2 imagery in Sukajaya District, Bogor Regency, with a performance plateau reached at ntree 400. However, the initial classification results still exhibit salt-and-pepper noise due to the inherent limitations of the pixel-based approach. The application of majority filtering improves land cover classification accuracy. This improvement allows performance to surpass that of the model with the best parameters before filtering, as evidenced by the accuracy of ntree 300 exceeding that of ntree 400 after filtering. Majority filtering affects land cover classes. Classes with large but fragmented patches tend to increase in size, whereas classes initially composed of small units tend to decrease. Overall, majority filtering effectively enhances the quality of classification results. It is recommended as a standard component in the workflow for pixel-based land cover classification. This supports evidence-based planning by offering an objective foundation for assessing environmental conditions.

REFERENCES

Adhikari J.N., Bhattarai B.P., Rokaya M.B. and Thapa T.B. (2022). Land use/land cover changes in the central part of the Chitwan Annapurna Landscape, Nepal. PeerJ, 10, e13435. DOI: 10.7717/peerj.13435

Aji A., Husna V.N. and Purnama S.M. (2024). Multi-Temporal data for land use change analysis using a machine learning approach (google earth engine). International Journal of Geoinformatics, 20(4), 19–28. DOI: 10.52939/ijg.v20i4.3145

Al-Aarajy K.H.A., Zaeen A.A. and Abood K.I. (2024). Supervised classification accuracy assessment using remote sensing and geographic information system. TEM Journal, 13(1), 396–403. DOI: 10.18421/TEM131-41

Altman N. and Krzywinski M. (2017). Ensemble methods: bagging and random forests. Nature Methods, 14(10), 933–934. DOI: 10.1038/nmeth.4438

Amin G., Imtiaz I., Haroon E., Saqib N. us, Shahzad M.I. and Nazeer M. (2024). Assessment of machine learning algorithms for land cover classification in a complex mountainous landscape. Journal of Geovisualization and Spatial Analysis, 8(34), 1–19. DOI: 10.1007/s41651-024-00195-z

Anthony T., Shohan A.A.A., Oludare A., Alsulamy S., Kafy A. Al and Khedher K.M. (2024). Spatial analysis of land cover changes for detecting environmental degradation and promoting sustainability. Kuwait Journal of Science, 51(100197). DOI: 10.1016/j.kjs.2024.100197

Aslam R.W., Shu H., Naz I., Quddoos A., Yaseen A., Gulshad K. and Alarifi S.S. (2024). Machine learning-based wetland vulnerability assessment in the Sindh Province Ramsar site using remote sensing data. Remote Sens., 16(928). DOI: 10.3390/rs16050928

Ávila-Mosqueda S.V., van Tussenbroek B.I. and Garza-Pérez J.R. (2025). Changes in seagrass landscape configuration in a Caribbean Reef Lagoon indicate an ecosystem shift after repeated disturbances. Coasts, 5(8). DOI: 10.3390/coasts5010008

Bayazit M., Dönmez C. and Berberoglu S. (2025). Assessing the efficiency of pixel-based and object-based image classification using deep learning in an agricultural Mediterranean plain. Environ. Monit. Assess., 197(155), 1–20. DOI: 10.1007/s10661-024-13431-2

Behera D.K., Pujar G.S., Kumar R. and Singh S.K. (2024). A comprehensive approach towards enhancing land use land cover classification through machine learning and object-based image analysis. Journal of the Indian Society of Remote Sensing, 53, 731–749. DOI: 10.1007/s12524-024-01997-w

Belay T. and Mengistu D.A. (2021). Impacts of land use/land cover and climate changes on soil erosion in Muga watershed, Upper Blue Nile basin (Abay), Ethiopia. Ecological Processes, 10(1). DOI: 10.1186/s13717-021-00339-9

Breiman L. (2001). Random forests. Machine Learning, 45, 5–32.

Chahal A., Gulia P., Gill N.S., Yahya M., Haq M.A., Aleisa M., Alenizi A., Khan A.A. and Shukla P.K. (2024). Predictive analytics technique based on hybrid sampling to manage unbalanced data in smart cities. Heliyon, 10(e39275). DOI: 10.1016/j.heliyon.2024.e39275

Chen J., Sasaki J., Guo Z. and Endo M. (2023). UAV-based seagrass wrack orthophotos classification for estimating blue carbon. Estuarine, Coastal and Shelf Science, 293. DOI: 10.1016/j.ecss.2023.108476

Chen W., Yuan Y., Gu T., Ma H. and Zeng J. (2025). What factors drove the global cropland expansion into highlands? Earth's Future, 13, e2024EF005337. DOI: 10.1029/2024EF005337

Darem A.A., Alhashmi A.A., Almadani A.M., Alanazi A.K. and Sutantra G.A. (2023). Development of a map for land use and land cover classification of the Northern Border Region using remote sensing and GIS. Egyptian Journal of Remote Sensing and Space Science, 26(2), 341–350. DOI: 10.1016/j.ejrs.2023.04.005

Du H., Li M., Xu Y. and Zhou C. (2023). An ensemble learning approach for land use/land cover classification of arid regions for climate simulation: A case study of Xinjiang, Northwest China. IEEE Journal of Selected Topics in Applied Earth Observations and Remote Sensing, 16, 2413–2426. DOI: 10.1109/JSTARS.2023.3247624

Ebrahimy H., Mirbagheri B., Matkan A.A. and Azadbakht M. (2021). Per-pixel land cover accuracy prediction: A random forest-based method with limited reference sample data. ISPRS Journal of Photogrammetry and Remote Sensing, 172, 17–27. DOI: 10.1016/j.isprsjprs.2020.11.024

Edosa B.T. and Erena M.G. (2024). Wildlife habitat suitability analysis and mapping the former dhidhessa wildlife sanctuary using GIS-based analytical hierarchal process and weighted linear combination methods. Heliyon, 10(e33921). DOI: 10.1016/j.heliyon.2024.e33921

El-Deen Taha L.G. and Mandouh A.A. (2024). Assessment of Random Forest and Neural Network for improving land use/ land cover mapping from LIDAR data and RGB image: A case study of Magaga-El-Menia Governorate, Egypt. Geoplanning: Journal of Geomatics and Planning, 11(1), 17–30. DOI: 10.14710/geoplanning.11.1.17-30

Elmahdy S.I. and Mohamed M.M. (2023). Regional mapping and monitoring land use/land cover changes: a modified approach using an ensemble machine learning and multitemporal Landsat data. Geocarto International, 38(1). DOI: 10.1080/10106049.2023.2184500

Fu B., Wang Y., Campbell A., Li Y., Zhang B., Yin S., Xing Z. and Jin X. (2017). Comparison of object-based and pixel-based random forest algorithm for wetland vegetation mapping using high spatial resolution GF-1 and SAR data. Ecological Indicators, 73, 105–117. DOI: 10.1016/j.ecolind.2016.09.029

Hakim A.M.Y., Matsuoka M., Baja S., Rampisela D.A. and Arif S. (2020). Predicting land cover change in the Mamminasata area, Indonesia, to evaluate the spatial plan. ISPRS Int. J. Geo-Inf., 9(481). DOI: 10.3390/ijgi9080481

Ibrahim M. (2023). Evolution of random forest from decision tree and bagging: A bias-variance perspective. DUJASE, 7(1), 66–71. DOI: 10.3329/dujase.v7i1.62888

Ismail M.H., Aik D.H.J., Alias M.A., Muharam F.M. and Zaki P.H. (2021). Land Use/Land Cover (LULC) Changes in Cameron Highlands, Malaysia: Explore the Impact of the LULC Changes on Land Surface Temperature (LST) Using Remote Sensing. In: Climate Impacts on Sustainable Natural Resource Management , 279–301. wiley. DOI: 10.1002/9781119793403.ch14

Joseph V.R. (2022). Optimal ratio for data splitting. Stat. Anal. Data Min.: The ASA Data Sci. Journal, 15, 531–538. DOI: 10.1002/sam.11583

Kaur H., Tyagi S., Mehta M. and Singh D. (2023). Time series (2001/2002–2021) analysis of earth observation data using Google Earth Engine (GEE) for detecting changes in Land Use Land Cover (LULC) with specific reference to forest cover in East Godavari Region, Andhra Pradesh, India. J. Earth Syst. Sci., 132(86), 1–16. DOI: 10.1007/s12040-023-02099-w

Kuntla S.K. and Manjusree P. (2020). Development of an automated tool for delineation of flood footprints from SAR imagery for rapid disaster response: a case study. Journal of the Indian Society of Remote Sensing, 48(6), 935–944. DOI: 10.1007/s12524-020-01125-4

Li B. V, Jenkins C.N. and Xu W. (2022). Strategic protection of landslide vulnerable mountains for biodiversity conservation under land-cover and climate change impacts. PNAS, 19(2), e22113416118. DOI: 10.1073/pnas.2113416118/-/DCSupplemental

Liu D., Zhang X., Zheng T., Shi Q., Cui Y., Wang Y. and Liu L. (2021). Optimisation and evaluation of the random forest model in the efficacy prediction of chemoradiotherapy for advanced cervical cancer based on radiomics signature from high-resolution T2 weighted images. Archives of Gynecology and Obstetrics, 303, 811–820. DOI: 10.1007/s00404-020-05908-5

Liu S. and Gu G. (2017). Improving the impervious surface estimation from hyperspectral images using a spectral-spatial feature sparse representation and post-processing approach. Remote Sens., 9(456). DOI: 10.3390/rs9050456

Maleki R., Wu F., Oubara A., Fathollahi L. and Yang G. (2024). Refinement of cropland data layer with effective confidence layer interval and image filtering. Agriculture, 14(1285). DOI: 10.3390/agriculture14081285

Manafifard M. (2024). A new hyperparameter to random forest: application of remote sensing in yield prediction. Earth Science Informatics, 17(1), 63–73. DOI: 10.1007/s12145-023-01156-8

Mensah J.K., Ofosu E.A., Yidana S.M., Akpoti K. and Kabo-bah A.T. (2022). Integrated modeling of hydrological processes and groundwater recharge based on land use land cover, and climate changes: a systematic review. Environmental Advances, 8(100224). DOI: 10.1016/j.envadv.2022.100224

Olariu H.G., Malambo L., Popescu S.C., Virgil C. and Wilcox B.P. (2022). Woody plant encroachment: Evaluating methodologies for semiarid woody species classification from drone images. Remote Sens., 14(1665). DOI: 10.3390/rs14071665

Pramesti T.V., Rushayati S.B. and Prasetyo L.B. (2025). Evaluating ecosystem recovery on degraded lands restoration using satellite-based spatial indicators in Mount Halimun Salak National Park, Indonesia. Ecological Engineering & Environmental Technology, 26(8), 363–374. DOI: 10.12912/27197050/208417

Probst P. and Boulesteix A.-L. (2018). To tune or not to tune the number of trees in random forest. Journal of Machine Learning Research, 18, 1–18. http://jmlr.org/papers/v18/17-269.html.

Qacami M., Khattabi A., Lahssini S., Rifai N. and Meliho M. (2023). Land-cover/land-use change dynamics modeling based on land change modeler. Annals of Regional Science, 70, 237–258. DOI: 10.1007/s00168-022-01169-z

Ratnayake S.S., Reid M., Larder N., Hunter D., Ranagalage M., Kogo B., Dharmasena P.B. and Kariyawasam C.S. (2024). Knowing the lay of the land: changes to land use and cover and landscape pattern in village tank cascade systems of Sri Lanka. Frontiers in Environmental Science, 12, 1353459. DOI: 10.3389/fenvs.2024.1353459

Rivai F.A., Asy'ari R., Fadhil M.H., Jouhary N.A., Saenal N., Ardan F., Pohan A., Pramulya R. and Setiawan Y. (2023). Analysis of land use and land cover changes using random forest through Google Earth Engine in Depok City. SSRS Journal B: Spatial Research, 1, 1–12.

Salman H.A., Kalakech A. and Steiti A. (2024). Random forest algorithm overview. Babylonian Journal of Machine Learning, 2024, 69–79. DOI: 10.58496/bjml/2024/007

Silva C.A., Guerrisi G., Del Frate F. and Sano E.E. (2022). Near-real time deforestation detection in the Brazilian Amazon with Sentinel-1 and neural networks. European Journal of Remote Sensing, 55(1), 129–149. DOI: 10.1080/22797254.2021.2025154

Singh G. and Pandey A. (2021). Evaluation of classification algorithms for land use land cover mapping in the snow-fed Alaknanda River Basin of the Northwest Himalayan Region. Applied Geomatics, 13(4), 863–875. DOI: 10.1007/s12518-021-00401-3

Solomon N., Pabi O., Annang T., Asante I.K. and Birhane E. (2018). The effects of land cover change on carbon stock dynamics in a dry Afromontane forest in northern Ethiopia. Carbon Balance and Manage., 13(14), 1–13. DOI: 10.1186/s13021-018-0103-7

Sun J. and Ongsomwang S. (2023). Optimal parameters of random forest for land cover classification with suitable data type and dataset on Google Earth Engine. Frontiers in Earth Science, 11, 1188093. DOI: 10.3389/feart.2023.1188093

Svoboda J., Štych P., Laštovička J., Paluba D. and Kobliuk N. (2022). Random Forest classification of Land Use, Land-Use Change and Forestry (LULUCF) using Sentinel-2 data—A case study of Czechia. Remote Sensing, 14(5). DOI: 10.3390/rs14051189

Tempa K. and Aryal K.R. (2022). Semi-automatic classification for rapid delineation of the geohazard-prone areas using Sentinel-2 satellite imagery. SN Applied Sciences, 4(5). DOI: 10.1007/s42452-022-05028-6

Tjahjono B., Firdania I. and Trisasongko B.H. (2024). Modeling landslide hazard using machine learning: a case study of Bogor, Indonesia. Journal of Natural Resources and Environmental Management, 14(2), 407–414. DOI: 10.29244/jpsl.14.2.407

Wahyuni N.I., Soemarno and Hasyim A.W. (2025). Estimating carbondioxide emission and mitigation strategies from land use and land cover change in Banyuwangi. J-PAL, 16(1), 9–14. DOI: 10.21776/ub.jpal.2025.016.01.02

Ye Z., Yang K., Lin Y., Guo S., Sun Y., Chen X., Lai R. and Zhang H. (2023). A comparison between Pixel-based deep learning and Object-based image analysis (OBIA) for individual detection of cabbage plants based on UAV Visible-light images. Computers and Electronics in Agriculture, 209. DOI: 10.1016/j.compag.2023.107822

Zeferino L.B., Souza L.F.T. de, Amaral C.H. do, Fernandes Filho E.I. and Oliveira T.S. de. (2020). Does environmental data increase the accuracy of land use and land cover classification? International Journal of Applied Earth Observation and Geoinformation, 91. DOI: 10.1016/j.jag.2020.102128

Zhang X., Estoque R.C., Murayama Y. and Ranagalage M. (2021). Capturing urban heat island formation in a subtropical city of China based on Landsat images: implications for sustainable urban development. Environmental Monitoring and Assessment, 193(3). DOI: 10.1007/s10661-021-08890-w

Zhu L., Xing H. and Hou D. (2022). Analysis of carbon emissions from land cover change during 2000 to 2020 in Shandong Province, China. Scientific Reports, 12(1). DOI: 10.1038/s41598-022-12080-0

ges.rgo.ru/jour/

ISSN 2542-1565 (Online)